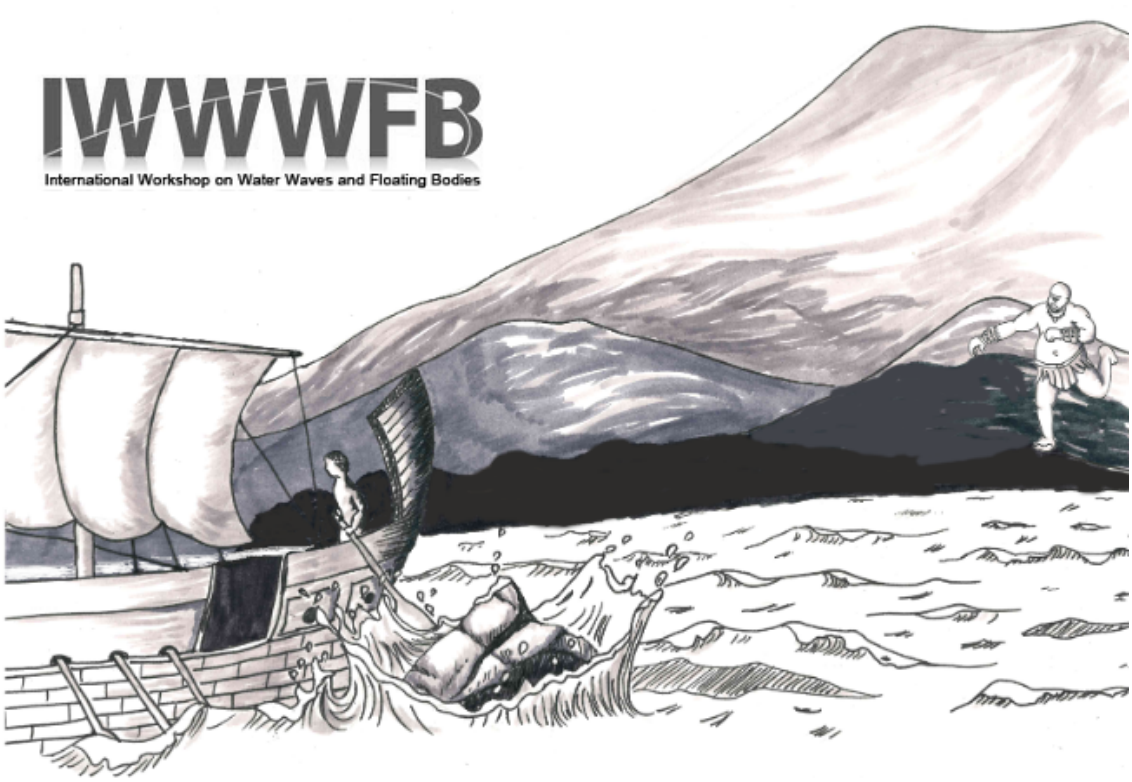

Proceedings of the 37th International Workshop on Water Waves and Floating Bodies

Giardini Naxos, 10th-13th April 2022

Editors: Alessandro Iafrati
Giuseppina Colicchio

Index

M. Amini-Afshar, H.B. Bingham, *The Challenges of Computing Wave Added Resistance Using Maruo's Formulation and The Kochin Function*……1

M.E. Bitsch, A.D. Melander, A.P. Engsig-Karup, *A High-order Pseudospectral Incompressible Navier-Stokes Free Surface Model in 2D*……5

S. Boral, T. Sahoo, M.H. Meylan F*lexural gravity wave amplitudes in the vicinity of blocking point under shallow water approximation*……9

X. Chen, L. Diebold and Y. Choi *Speed-effect restoring forces on ship motions*……13

Y. Chen, M. Hayatdavoodi, B. Zhao, R. C. Ertekin *Waves generated by moving disturbances on the seafloor*……17

D. Clamond *Derivation of some steady gravity wave equations for uneven bottoms*……21

G. Colicchio, M. Antuono *New cut cell method for finite differences approximation of the Poisson Equations applied to a semi-averaged model for water waves propagation*……25

S. Das, M.H. Meylan *Time dependent motion due to sinusoidal ocean bottom oscillation*……29

F. De Vita, M. Lorenzo, P. Pezzutto, F. De Lillo, F. Bosia, M. Onorato *Energy budgets in the interaction between a surface gravity wave and a sumberged cylindrical resonator*……33

A. Del Buono, A. Iafrati *Multisection approach for the vertical water impact of a fuselage*……37

H. Ding, J. Zang *Numerical investigation of the survivability of a wave energy converter*……41

E.C. Edwards, M. Hann, D. Greaves, D.K.P. Yue *Generalizing the optimal axisymmetric point-absorber wave energy converter to irregular waves*……45

F. G. Eroglu, N. T. M¨ucke, A. P. Engsig-Karup *Reduced Order Modelling for Dispersive and Nonlinear Water Wave Modelling*……49

M. Gao, S. Draper, L. Chen, H. Wolgamot, L. Cheng *Modelling a dam break flow in a moving reference frame*……53

J. Grue *On the generation process of upstream waves by a pressure distribution at critical speed*……57

R. Hascoët *Level-Crossing Conditioning in second-order water waves*……61

J. He, F. Noblesse *Theoretical foundation of a new type of panel method*……65

J. Huang, R. Porter *Wave power extraction from a metamaterial cylinder with internal paddle power take off mechanism*……69

S. Jin, T. Tosdevin, M. Hann, D. Greaves *Experimental study on short design waves for extreme response of a floating hinged raft wave energy converter*……73

M.B.M. Khan, M.H. Meylan, H. Behera *Generalised hybrid element method for oscillatory motion of multiple floating structures in oblique regular waves*……77

A. Lamei, M.Hayatdavoodi, H.R. Riggs *Elastic Responses of Wind-tracing Floating Offshore Wind Turbines*……82

H. Liang, H. Santo, M. Si D*ecomposition of ship waves and time-frequency spectrograms*……86

Y. Liu , S. Zheng, H. Liang, P. Cong *Wave energy absorption amongst arrays of point absorbers with a non-regular geometry*……90

M. Lorenzo, P. Pezzutto, F. Bosia, C. Camporeale, F. De Lillo, F. De Vita, C. Manes, F. Ventrella, M. Onorato *METAREEF, a sustainable submerged floating metamaterial structure to attenuate surface gravity waves*……94

S.Malenica, J.N. Newman *Added mass and damping of structures with angular symmetry*……98

P. Marleaux, T.I. Khabakhpasheva, M. Abdel-Maksoud, A.A. Korobkin, K. Maki *High-speed vessel moving along the edge of ice field*……102

N. Mokus, F. Montiel *Floe size distributions in irregular sea states*……106

Y-S. Nam, J-H. Lee, Y. Liu, Y. Kim *Enhanced Wave-Field Reconstruction Based on Stochastic Characteristics of Shadowing Effects*……110

E. Renzi, F. Dias *Modelling design waves in a Numerical Wave Flume based on a higher-order Moving Particle Semi-Implicit Method*……114

S. Saha, S. Das, S.N. Bora *Trapped waves within the blocking frequency under compressed sea ice and two-dimensional current*……118

Y.M. Scolan *Analysis of the pressure field in a breaking wave*……122

Y.A. Semenov, Y.N. Savchenko, G.Y. Savchenko *Impulsive impact of a body submerged in an open container*……126

K. Shishmarev, K. Zavyalova, T. Khabakhpasheva *Steady-state motion of a load on an ice cover with linearly variable thickness in a channel*……130

C. Stavropoulou, M. Goteman *A very simple park interaction factor*……134

I.V. Sturova *The Cauchy-Poisson problem for a fluid with a shear flow and non-uniform compressed ice cover*……138

R. Subramanian, R.F. Beck *Body-Exact Computations of Vertical Plane Motions*……142

C. Tong, Y. Shao, H.B. Bingham, F.-C.W. Hanssen *A study of a fixed trapezoidal section in regular waves using a generalized weak-scatterer model*……146

M. van der Eijk, P.R. Wellens *Experimental and numerical 2D wedge entry in water with entrained air*……150

J. Visbech, A.P. Engsig-Karup, H.B. Bingham *Efficient Computation of the Linear Radiation Problem using a Spectral Element Method*……154

Q. Xiao, R. Calvert, S.Q. Yan, T. Adcock ,T.S. van den Bremer *The wave-induced drift of objects of finite size*……158

Z. Xie, M.Brocchini, P. Lin *Numerical Simulation of Turbulent Structures under Breaking Waves*……162

J. Xu, D.Z. Ning, L. Chen, C.W. Zhang, B. Teng *Local resonances within an array of C-shaped cylinders in water waves*……166

H. Xu, M. Greco, C. Lugni *Influence of Rigid/Deformable Foil Shape on the Hydrodynamic Loads and Performance*……170

J. Yang, J. Yao, X. Zhang *On the modulation of a plane wave to oblique perturbations in finite water depth*……174

J. Yao, X. Zhang, R.F. Beck *Nonlinear Effect on Ship Generated Mini-tsunamis*……178

Z-M. Yuan *Wave-passing by ships in a single file formation*……182

Z. Zhang, K.J. Maki, L.J. Doctros *Two-Dimensional Planing in Water of Finite Depth*……186

B.B. Zhao, T.Y. Zhang, L.J. Li, Z. Wang, W.Y. Duan, M. Hayatdavoodi *Extension of MCC-FS model to bottom time-varying problems*……190

S. Zheng, R. Porter, H. Liang, D. Greaves *Water wave interaction with an annular metamaterial cylinder*.....194

K. Zheng, B.B. Zhao, W.Y. Duan *Experimental study on wave breaking and evolution of wave groups with high steepness*.....198

Z. Zhu, B-S. Kim, S. Wang, Y. Kim *Study on Numerical PMM Tests in Incident Waves*.....202

ISBN: 978-88-7617-052-2 (print)
ISBN: 978-88-7617-053-9 (online)
April 2022
Editors: Alessandro Iafrati, Giuseppina Colicchio
Cover: Giuseppina Colicchio
Publisher: Institute of Marine Engineering CNR-INM, National Research Council of Italy

37th International Workshop on Water Waves and Floating Bodies, Giardini Naxos, Italy (Sicily), 10-13 April 2022

The Challenges of Computing Wave Added Resistance Using Maruo's Formulation and The Kochin Function

Mostafa Amini-Afshar* and Harry B. Bingham

Technical University of Denmark, Department of Mechanical Engineering
Section for Fluid Mechanics, Coastal and Maritime Engineering
*maaf@mek.dtu.dk, hbb@mek.dtu.dk

1 Introduction

Maruo's formulation [1] for the wave drift force on bodies with forward speed (added resistance), requires calculation of finite and semi-infinite integrals containing the Kochin function. With this abstract we intend to highlight and discuss some computational challenges related to these integrals in further detail through several two- and three-dimensional (2D, 3D) example calculations.

2 The formulation

According to Maruo's formulation [1, 2] the added resistance R_w can be computed by

$$R_w = \frac{\rho}{4\pi}\left\{-\int_{-\infty}^{\bar{k}_1} + \int_{\bar{k}_2}^{\bar{k}_3} + \int_{\bar{k}_4}^{\infty}\right\} \frac{\bar{\kappa}\,(m - K\cos\beta)}{\sqrt{\bar{\kappa}^2 - m^2}}\,|H(m)|^2\,dm, \tag{2.1}$$

in which ρ is the fluid density, $K = \omega_0^2/g$ is the wave number and β is the heading angle, with ω_0 the wave frequency, and g the gravitational acceleration. The integration bounds are

$$\bar{k}_1 = -\frac{\kappa_0}{2}\left(1 + 2\tau + \sqrt{1+4\tau}\right), \quad \bar{k}_3 = \frac{\kappa_0}{2}\left(1 - 2\tau - \sqrt{1-4\tau}\right),$$
$$\bar{k}_2 = -\frac{\kappa_0}{2}\left(1 + 2\tau - \sqrt{1+4\tau}\right), \quad \bar{k}_4 = \frac{\kappa_0}{2}\left(1 - 2\tau + \sqrt{1-4\tau}\right).$$

Here $\kappa_0 = g/U^2$ and $\tau = U\omega/g$, U as the forward speed of the body and ω as the encounter frequency. Note that if $\tau > \frac{1}{4}$ then $\bar{k}_3 = \bar{k}_4 = \kappa_0\tau$, and the last two integrals are merged in to one semi-infinite integral in $[\bar{k}_2\ \infty]$. The Kochin function is defined by an integration over the body surface $\boldsymbol{S}_b$

$$H(m) = \iint_{\boldsymbol{S}_b}\left(\phi_B\frac{\partial}{\partial n} - \frac{\partial\phi_B}{\partial n}\right)e^{\bar{\kappa}z + \mathrm{i}\left(xm + y\sqrt{\bar{\kappa}^2 - m^2}\right)}ds, \tag{2.2}$$

where $\partial/\partial n$ denotes the derivative normal to the body surface, ϕ_B is the combined radiation and scattering velocity potential and $\bar{\kappa}(m) = \frac{1}{g}\left(\omega + mU\right)^2$. In the context of the 2D strip theory, (2.2) can be expressed by

$$H(m) = \int_L e^{\mathrm{i}xm}\left[\int_{Cx} e^{\bar{\kappa}z}e^{\mathrm{i}y\sqrt{\bar{\kappa}^2 - m^2}}\left\{\left(\mathrm{i}\sqrt{\bar{\kappa}^2 - m^2}N_y + \bar{\kappa}N_z\right)\psi_B - \left(\frac{\partial\psi_B}{\partial N}\right)\right\}dl\right]dx, \tag{2.3}$$

where N denotes the normal vector to each 2D section C_x in the $y-z$ plane, and L is length of the body. The total 2D disturbance potential is ψ_B. Using the method of equivalent line source, Kashiwagi [2, 3] proposed also an equivalent equation for the Kochin function inside his *Enhanced Unified Theory*. In the 2D strip theory, this alternative equation takes the following form

$$H(m) = \int_L e^{\mathrm{i}xm}\left[\int_{C_x} e^{\nu z}e^{\mathrm{i}\nu y}\left\{\left(\mathrm{i}\nu N_y + \nu N_z\right)\psi - \left(\frac{\partial\psi}{\partial N}\right)\right\}dl\right]dx, \tag{2.4}$$

in which ψ is either the radiation ($\nu = \omega^2/g$) or the scattering velocity potential ($\nu = K$).

3 Calculations and Discussions

We believe there are two unsolved issues related to the computation of wave added resistance using (2.1), and the 3D Kochin function (2.2) or its 2D equivalent (2.3). The first is evaluation of the semi-infinite integrals. For many years, in order to avoid the associated *computational difficulties*, these integrals have either been neglected completely (arguing that their contribution is negligible), or have been computed by assuming an *artificial* and *arbitrary* submergence of the z- coordinate of the floating body (asserting that it is necessary for *convergence*). Even if we assume that the added resistance can be calculated using only the middle integral in (2.1), then we are faced with a second issue which is the poor comparison between Maruo's far-field method and the well-established near-field method for *floating bodies*, (the best comparison yet achieved in our calculations is related to a floating spheroid [4]). In what follows we discuss these matters using 2D and 3D computations.

3.1 Alternative and Original form of the Kochin Function (2D)

To our best knowledge the semi-infinite integrals have never been treated completely, except by Prof. Kashiwagi through the alternative form of the Kochin function (2.4) and the Enhanced Unified Theory (see for example [2, 3]). In a recent paper [5] we have employed this alternative form inside our in-house strip-theory code which is an implementation of the classical STF strip theory using the low-order BEM and the zero-speed Green function. Note that Kashiwagi uses an elegant semi-analytical method to compute these integrals, but in our work we truncate the integration where there is almost zero contribution to the final results. Using these computations, we have illustrated the relative contributions of the semi-infinite integrals to the added resistance. An example is shown in figure 1. In the plot the subscripts on H and the superscripts on R_w denote the contribution to the corresponding integral in (2.1). The Froude number is given by Fr, B is the beam of the vessel, and A is the wave amplitude. As can be seen, the semi-infinite integrals play an important role in computing the added resistance, and should not be neglected. This fact has already been emphasized by Prof. Kashiwagi. It is also important to note that for $\tau > 1/4$ there is no finite integral in (2.1), and neglecting the third integral is in fact equivalent to cutting-off the semi-infinite integral at $\bar{k}_3 = \bar{k}_4$. In addition we have conducted a convergence study of the computations based on the original formulation (2.3) for the added resistance of the Wigley hull. See figure 2. The computation for added resistance of a prismatic barge is also shown in figure 3. In order to ensure accuracy in case of a highly oscillatory Kochin function for large m values, we employed a *spectral* integration scheme for the integral along x. According to these computations the convergence of the added resistance based on the original form (2.3) is achieved, however in neither of these cases are the converged results anything close to the correct solutions based on the alternative form of the Kochin function. This is also true if we consider only the middle integral in (2.1) for the added resistance, which has become common practice in the literature. For the Wigley hull the converged results are unrealistically large. In the next section we illustrate this issue further using 3D computations and only based on the original 3D form (2.2). The 3D

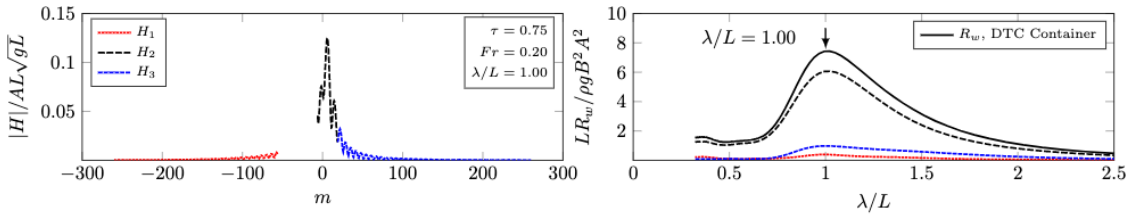

Figure 1: (Left) The Kochin function related to three integrals in (2.1). (Right) Illustration of relative contribution of the semi-infinite integrals to the added resistance of the DTC Container. Note the computations are based on the ***alternative*** form of the Kochin function (2.4)

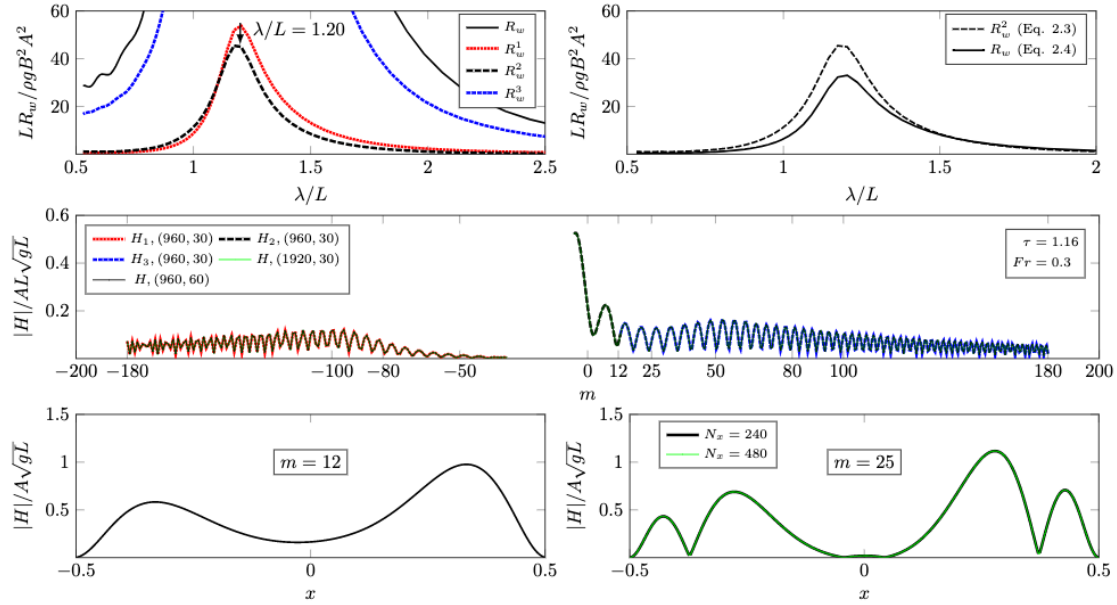

Figure 2: First row: Illustration of relative contribution of the semi-infinite integrals to the added resistance of the Wigley hull based on the ***original*** form of the Kochin function (2.3). Second row: Convergence of the Kochin function in terms of number of 2D sections and number of panels (N_x, N_p). Third row: The Kochin function along the body for $m = 12$ and 25 in case of $\lambda/L = 1.20$.

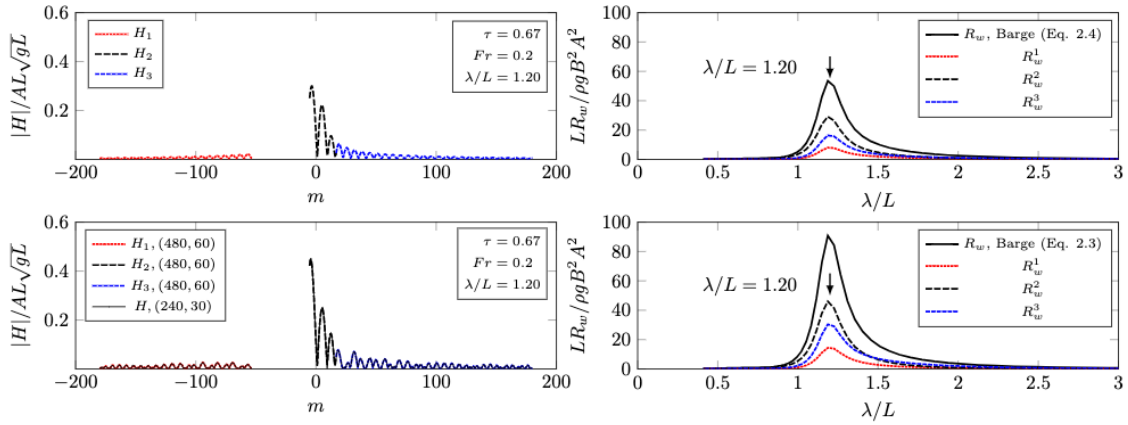

Figure 3: Illustration of relative contribution of the semi-infinite integrals to the added resistance of the barge, $L/B = 10$ and $L/T = 16$ with T as the draft. Top: The computations based on the ***alternative*** form of the Kochin function (2.4). Bottom: The computations based on the ***original*** form of the Kochin function (2.3).

computations are performed using the open-source solver OW3D-Seakeeping which is based on 4th order finite difference-method. Note that these results are based on the Neumann-Kelvin linearization and for $\beta = \pi$

3.2 Floating Bodies (3D)

Two geometries are considered: the Wigley hull type I (free in heave and pitch), and the Modified Wigley hull (free in surge, heave, pitch) as defined by [6]. For both hulls, a convergence study is conducted for the added resistance based on the near-field formulation and Maruo's far-filed method (2.1). See the first and the second rows in figure 4. On the left side, the Kochin functions H_1, H_2, H_3 corresponding to the peak value of the added resistance are plotted. On the right side, convergence for the far-field added resistance (based on only the middle integral) is illustrated. The numbers in the parentheses denote the total number of grid points on the body, normalized by the number of grid points for the coarsest grid. We have not included the contribution from the first and the third integral R_w^1, R_w^3, as this leads to unrealistically large added resistances similar to the 2D computations from the previous section. As the integral for the Kochin function (2.2) contains oscillatory terms, in our computation we ensured that the integral bounds $\bar{k}_2$ and $\bar{k}_3$ are below the grid Nyquist wave number π/l_a. Here l_a is the average grid spacing along the waterline. For the near-field method only the final converged results are shown. Note also that for the Wigley I hull, we have improved our computational accuracy compared with our previous results presented in 32th IWWWFB [7]. As can be seen from the results in figure 4, the converged far-field results (based on only the middle integral) do not compare well with the converged near-field solutions. Moreover it is seen that H_1 and H_3 corresponding to the semi-infinite integrals are also converged.

3.3 Submerged Bodies (3D)

The significance of the semi-infinite integrals is extremely low in the case of submerged bodies. A well-known example from the literature is the added resistance of the fixed submerged spheroid with $L/B = 5$ and the submergence depth of $\hat{d} = 0.75B$. See the results in the third row of figure 4. The BEM solutions are according to [8]. Note that we have included all three integrals from (2.1), even though this was not necessary as the Kochin functions H_1, H_3 are almost zero over the corresponding integration ranges. Apparently this fact that the semi-infinite integrals can be left out of the computation for a submerged body, has been generalized by some researchers to the computations for floating bodies. As we have shown in the previous sections this is not a correct generalization.

4 Conclusions

Using 2D strip-theory and 3D models, we have illustrated the convergence of the calculations for the wave added resistance based on Maruo's method (2.1)-(2.3). By this we have tried to highlight two unsolved problems related to Maruo's formulation and floating bodies. First, the inclusion of the semi-infinite integrals, and second the fact that the added resistance is still predicted to be substantially higher than other reference solutions, even when the semi-infinite integrals are ignored. With regard to the first issue, it is known that some researchers use *poor convergence* as an excuse for introducing an arbitrary submergence of the z- coordinate in the original formulation $e^{\bar{\kappa}(z-\epsilon)}$. By doing so they *damp* these high added resistance values, and can *tune* their models in

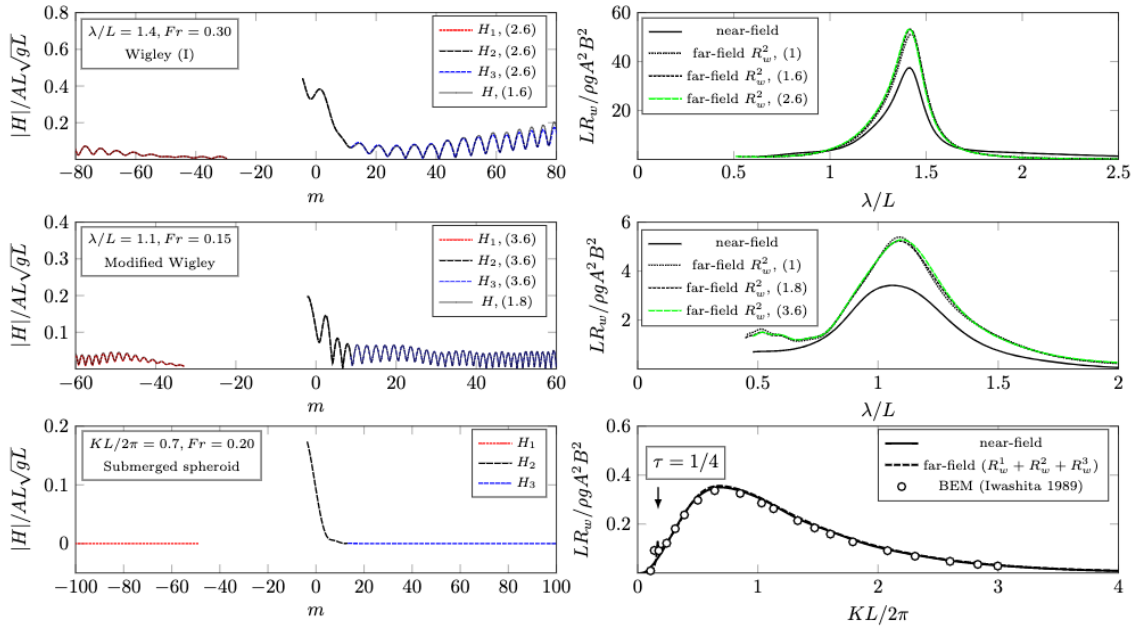

Figure 4: 3D computations based on (2.2). Left: The Kochin function (H_1, H_2, H_3) at the peak value of the added resistance. Right: Added resistance considering only the middle integral R_w^2. for the floating bodies, and considering all three integrals $R_w^1 + R_w^2 + R_w^3$ for the submerged spheroid.

order to achieve good agreement with measurements. With regard to the second problem, [9] has attributed the high added resistances to the fact that potential-flow models overpredict the body motions due to lack of viscous damping. This is in spite of the fact that only the symmetric modes (surge-heave-pitch) are considered in their work. Accordingly they achieve reasonable agreement with experimental data by introducing a damping model to reduce the motion and accordingly the added resistance. Obviously this would have a direct effect also on their near-field solutions, which has not been mentioned in that research. To conclude, we are left with an open question of what is the actual computational problem (if not convergence) in evaluating the integrals and the original forms of the Kochin function (2.2), (2.3) for floating geometries.

Acknowledgment

This research has been funded by the ShippingLab project (`https://shippinglab.dk`), and its financial support is highly appreciated.

References

[1] H. Maruo, "Wave resistance of a ship in regular head seas," *Bulletin of the Faculty of Engineering, Yokohama National University*, vol. vol. 9, 1960.

[2] M. Kashiwagi, "Prediction of surge and its effect on added resistance by means of the enhanced unified theory," in *Transactions of the West-Japan Society of Naval Architects 89*, pp. 77–89, The Japan Society of Naval Architects And Ocean Engineers, 1995.

[3] M. Kashiwagi, "Added resistance, wave-induced steady sway force and yaw moment on an advancing ship," *Ship Technology Research (Schiffstechnik)*, vol. 39, no. 1, pp. 3–16, 1992.

[4] M. Amini-Afshar and H. B. Bingham, "Accurate evaluation of the kochin function for added resistance using a high-order finite difference-based seakeeping code," in *33th International Workshop on Water Waves and Floating Bodies, Guidel-Plages, France*, 2018.

[5] M. Amini-Afshar and H. B. Bingham, "Added resistance using Salvesen–Tuck–Faltinsen strip theory and the Kochin function," *Applied Ocean Research*, vol. 106, p. 102481, 2021.

[6] M. Kashiwagi, T. Ikeda, T. Sasakawa, *et al.*, "Effects of forward speed of a ship on added resistance in waves," *International Journal of Offshore and Polar Engineering*, vol. 20, no. 3, pp. 196–203, 2010.

[7] M. Amini-Afshar and H. B. Bingham, "Implementation of the far-field method for calculation of added resistance using a high order finite-difference approximation on overlapping grids," in *32th International Workshop on Water Waves and Floating Bodies*, (Dalian, Liaoning, China), 2017.

[8] H. Iwashita and M. Ohkusu, "Hydrodynamic forces on a ship moving with forward speed in waves," *Journal of the Society of Naval Architects of Japan*, vol. 1989, no. 166, pp. 187–205, 1989.

[9] S. Liu, A. Papanikolaou, and G. Zaraphonitis, "Prediction of added resistance of ships in waves," *Ocean Engineering*, vol. 38, no. 4, pp. 641–650, 2011.

A High-order Pseudospectral Incompressible Navier-Stokes Free Surface Model in 2D

Max E. Bitsch, Anders D. Melander, and Allan P. Engsig-Karup
Department of Applied Mathematics and Computer Science
Technical University of Denmark, 2800 Kgs. Lyngby, Denmark
Email: maxbitsch@gmail.com

Simulation of water waves and taking into account the sea floor to estimate sea states are important for the design of offshore structures. We propose a new high-order accurate pseudospectral method for solving the incompressible Navier-Stokes equations with a free surface. The work is motivated by the lack of high-order accurate free surface water wave models which include viscous and rotational effects. The numerical scheme utilizes Fourier and Chebyshev basis functions for the numerical discretization and enables exploiting the fast Fourier transform (FFT) algorithm for efficiency reasons. A key feature is an explicit-implicit pressure-correction method designed to work with general Runge-Kutta (RK) methods used for temporal integration that fulfills mass balance and a pressure-velocity coupling. Another key feature is the use of a Fourier-continuation technique for solving numerical wave tank problems on finite (non-periodic) domains. As a starting point towards establishing the solver, we provide benchmark results to demonstrate accuracy and convergence using established cases used for potential flow solvers. We present numerical case results for i) nonlinear stream function wave solutions and ii) steep solitary wave reflection in a numerical wave tank in this abstract.

GOVERNING EQUATIONS

We consider the general - potentially 3D - incompressible flow with constant properties governed by the Navier-Stokes equations on the following form:

$$\nabla \cdot \mathbf{v} = 0, \tag{1a}$$

$$\partial_t \mathbf{v} + \mathbf{v}\nabla \cdot \mathbf{v} = -\frac{1}{\rho}\nabla p + \mathbf{g} + \nu \nabla^2 \mathbf{v}, \tag{1b}$$

with $\mathbf{v}$ being the velocity field $[u, v, w]^T$, ∇ the gradient operator $[\frac{\partial}{\partial x}, \frac{\partial}{\partial y}, \frac{\partial}{\partial z}]^T$, ρ the density, p the pressure, $\mathbf{g}$ the gravitational acceleration $[0, 0, -g]^T$, and ν the kinematic viscosity. The equations describes conservation of mass and momentum, respectively, and both must be fulfilled to ensure accurate results. The total pressure p is split into its static and dynamic parts $p = p_D + p_S$ with $p_S = \rho g(\eta - z)$, where $\eta(x, y, t)$ is the water free surface. Atmospheric pressure is ignored and the pressure on the free surface is assumed to be zero. The evolution of the free surface elevation is governed by the kinematic boundary condition, which ensures that free surface particles remain on the free surface

$$\frac{\partial \eta}{\partial t} + u|_{z=\eta}\frac{\partial \eta}{\partial x} + v|_{z=\eta}\frac{\partial \eta}{\partial y} = w|_{z=\eta}, \tag{2}$$

where $|_{z=\eta}$ denotes evaluation at the free surface level. The constantly evolving free surface elevation yields a time-dependent domain for which nonlinear waves requires re-discretization of the computational domain. To avoid this the Navier-Stokes equations are solved in a time-invariant σ-domain that is achieved by applying a modified version of the classical σ-transform

$$\sigma = \frac{2z + 2h(x, y) - d(x, y, t)}{d(x, y, t)}, \quad -1 \leq \sigma \leq 1, \tag{3}$$

where $h(x,y)$ is the elevation of the seabed and $d(x,y,t) = \eta(x,y,t) + h(x,y)$ is the total depth. The current σ-transform differs from the usual as it ranges from -1 to 1 due to the support of the Chebyshev basis The transformation limits the number of solvable problems as it does not allow for overturning or breaking waves since this leads to spatial singularities. Applying the chain rule, the Navier-Stokes equations is transformed to the σ-domain as,

$$\nabla_\sigma \cdot \mathbf{v} = 0, \tag{4a}$$

$$\partial_t \mathbf{v} + \mathbf{v}_\sigma \nabla \cdot \mathbf{v} = -\frac{1}{\rho}(\nabla_\sigma p_D + \nabla p_S) + \mathbf{g} + \nu \nabla_\sigma^2 \mathbf{v}, \tag{4b}$$

where the velocity in the σ-direction and the derivative operator is given as:

$$\mathbf{v}_\sigma = [u, v, w_\sigma]^T, \quad w_\sigma = \frac{\partial \sigma}{\partial t} + u\frac{\partial \sigma}{\partial x} + v\frac{\partial \sigma}{\partial y} + w\frac{\partial \sigma}{\partial z}, \tag{5a}$$

$$\nabla_\sigma = \left[\frac{\partial}{\partial x} + \frac{\partial \sigma}{\partial x}\frac{\partial}{\partial \sigma}, \frac{\partial}{\partial y} + \frac{\partial \sigma}{\partial y}\frac{\partial}{\partial \sigma}, \frac{\partial \sigma}{\partial z}\frac{\partial}{\partial \sigma}\right]^T. \tag{5b}$$

The σ-derivatives are evaluated from (3) by using the chain rule,

$$\begin{aligned} &\frac{\partial \sigma}{\partial t} = -d^{-1}\left(\frac{\partial d}{\partial t} + \sigma\frac{\partial d}{\partial t}\right), \quad \nabla\sigma = d^{-1}\left(2\nabla h - \nabla d - \sigma\nabla d\right), \\ &\nabla^2\sigma = d^{-1}\left(2\nabla^2 h - \nabla^2 d - \sigma\nabla^2 d - 2\nabla\sigma\nabla d\right), \quad \frac{\partial \sigma}{\partial z} = 2d^{-1}, \end{aligned} \tag{6}$$

where the time derivative of the depth is evaluated at the free surface from the kinematic boundary condition (2) and projected down into the domain.

NUMERICAL DISCRETIZATION

A method of lines approach is used to discretize the governing equation in time. The momentum equation (4b) and the free surface equation (2) are advanced in time by employing an explicit-implicit pressure-correction method using a general RK method from [1] (here for velocity)

$$\mathbf{v}^{(k)} = \sum_{l=1}^{k} \alpha_{kl}\mathbf{v}^{(l-1)} + \beta_{kl}\Delta t f(\mathbf{v}^{(l-1)}), \quad k = 1, 2, ..., s, \tag{7}$$

with $\mathbf{v}^{(0)} = \mathbf{v}^n$, $\mathbf{v}^{(s)} = \mathbf{v}^{n+1}$ and $f(\cdot)$ being the σ-transformed momentum (4b). Conservation of mass is ensured at each time step by applying a pressure-correction method originally proposed by [2], where the pressure is determined such that the velocity field is divergence free. Continuity needs to be satisfied at each RK-stage, hence the divergence $\nabla_\sigma^{(k)} \cdot \mathbf{v}^{(k)}$ at stage k must vanish. Note that the derivative operator is also denoted with the stage index as it is time-dependent on the discrete level due to the σ-transform. Let $\hat{f}(\cdot)$ be the momentum equation without the dynamic pressure and the divergence at stage k becomes

$$\nabla_\sigma^{(k)} \cdot \mathbf{v}^{(k)} = \nabla_\sigma^{(k)} \cdot \sum_{l=1}^{k} \alpha_{kl}\mathbf{v}^{(l-1)} + \beta_{kl}\Delta t\left[\hat{f}(\mathbf{v}^{(l-1)}) - \frac{1}{\rho}\nabla_\sigma^{(l-1)} p_D^{(l-1)}\right]. \tag{8}$$

We set $\nabla_\sigma^{(k)} \cdot \mathbf{v}^{(k)} = 0$ and by isolating the pressure, the velocity field at stage k becomes divergence free by solving the Poisson type problem

$$\nabla_\sigma^{(k)} \cdot \nabla_\sigma^{(k-1)} p_D^{(k-1)} = \frac{\rho}{\beta_{kk}\Delta t}\nabla_\sigma^{(k)} \cdot \hat{\mathbf{v}}^{(k)}, \tag{9}$$

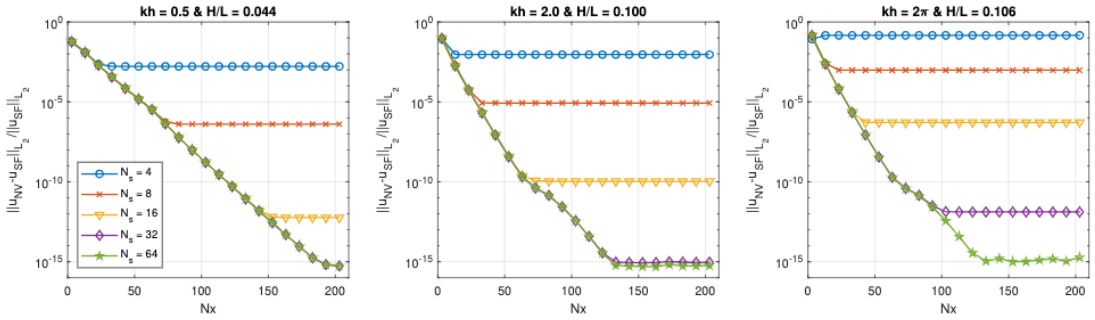

Figure 1: Relative L_2-error of the velocity u measured against a stream function solution for kh = 0.5, 2.0 and 2π with maximum theoretical steepness of 75%.

where the velocity without the pressure $\hat{\mathbf{v}}^{(k)}$ is given as:

$$\hat{\mathbf{v}}^{(k)} = \sum_{l=1}^{k-1} \alpha_{kl}\mathbf{v}^{(l-1)} + \beta_{kl}\Delta t f(\mathbf{v}^{(l-1)}) + \alpha_{kk}\mathbf{v}^{(k-1)} + \beta_{kk}\Delta t \hat{f}(\mathbf{v}^{(k-1)}). \tag{10}$$

The boundary value problem is solved with a zero Dirichlet pressure boundary condition at the free surface and a no-slip Neumann condition at wall boundaries, where the latter is determined in a similar fashion as the Poisson problem resulting in:

$$\mathbf{n} \cdot \nabla_\sigma^{(k-1)} p_D^{(k-1)} = \frac{\rho}{\beta_{kk}\Delta t}\mathbf{n} \cdot \hat{\mathbf{v}}^{(k)}, \tag{11}$$

with $\mathbf{n}$ being the normal vector. The velocity without pressure (10) can now be corrected with the newly obtained pressure to determine the final divergence free velocity. The Poisson type equation consists of mixed-stage derivative operators and it is necessary to advance the free surface to stage k before the Poisson equation is set up. The presented results uses the classical explicit fourth-order RK-scheme.

The governing equations are discretized in a 2D σ-domain using a pseudospectral method based on Fourier modes in the horizontal direction evaluated at N_x equidistant nodes and Chebyshev polynomials in the vertical σ-direction evaluated at N_s+1 Chebyshev-Gauss-Lobatto nodes. The Fourier basis is inherently periodic, hence enforcing boundary conditions are only necessary at the free surface and the seabed. A collocation approach is used to represent the free surface, the velocities, and the pressure, which are discretized in nodal space by global Lagrange interpolation polynomials $l_j(x_i)$ with the Cardinal property that $l_j(x_i) = \delta_{ij}$, where δ_{ij} is Kroneckers delta. The derivatives in the horizontal direction are evaluated discreetly in modal space by FFT and the vertical derivatives are evaluated by fast Chebyshev transform (FCT). Mixed derivatives are evaluated by repeated use of the FFT and FCT. These discrete evaluations makes the computations of the derivatives scalable as they both have work effort $\mathcal{O}(N \log N)$. Nonlinear terms are evaluated at collocation points by direct products, that are susceptible to aliasing, which can be damped through mild spectral filtering.

NONLINEAR ACCURACY

The accuracy of the nonlinear model is shown in Fig. 1 where the relative L_2-error of the bulk velocity u is shown. The error is computed for a 2D nonlinear stream function wave with limiting steepness of 75% and dimensionless depth $kh = 0.5$, 2.0, and 2π. The test shows spectral convergence and that more horizontal resolution is needed on shallow water and more

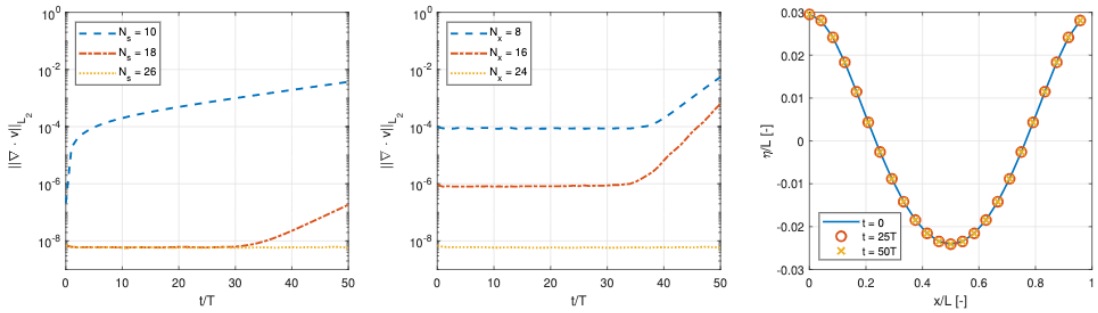

Figure 2: Stream function wave for kh 2.0 with maximum theoretical steepness of 40% and $\Delta t = T/100$. Divergence for different resolution with constant $N_x = 24$ (left) and constant N_s=26 (middle), and a comparison of the free surface elevation for $N_x = 24$ and N_s=26. (right)

vertical resolution is needed on deep water, which is as expected due to the decay of modal coefficients for the stream function.

Stability of the model is highly dependent on the divergence which can be seen in Fig. 2 (left and middle) for a 2D nonlinear stream function wave propagating for 50 wave periods with limiting steepness of 40% and $kh = 2.0$. The test hints that the vertical resolution is of great importance for the stability but the magnitude of the divergence is governed by the horizontal resolution. Fig. 2 (right) show the free surface elevation for the stable wave propagation test where excellent agreement with the constant low divergence can be observed.

The model's ability to cope with nonlinear shallow-water waves is tested by colliding two identical 2D solitary waves, essentially replicating a solitary wave reflecting off a vertical wall. The free surface elevation of the solitary wave at attachment (η_a), maximum wave run up (η_0), and detachment (η_d) from the wall are shown in Fig. 3 with a comparison to results from [3]. The maximum run up is determined up to $a/h = 0.6$ as it was found by [4] that a jet occurs for larger a/h, hence breaking the invertibility of the σ-transform.

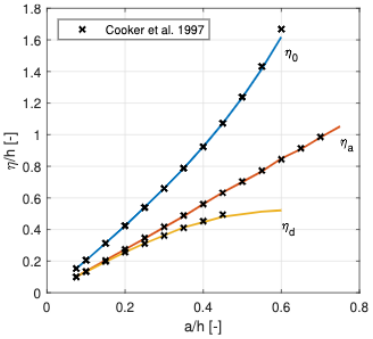

Figure 3: Attachment (η_a), maximum wave run up (η_0) and detachment (η_d) curves for reflection of a solitary wave.

At the workshop we plan to show i) a spectral filter for dealiasing of nonlinear simulations for improving model robustness and ii) an extension of the wave tank used for the reflecting solitary wave with a benchmark comparison to experimental results of a submerged bar test [5].

REFERENCES

[1] Shu, C.-W., and Osher, S. 1988. *Efficient implementation of essentially non-oscillatory shock-capturing schemes.* Journal of computational physics 77(2), 439–471.

[2] Chorin, A. J. 1968. *Numerical solution of the Navier-Stokes equations.* Mathematics of computation 22(104), 745–762.

[3] Cooker, M., Weidman, P., and Bale, D. 1997. *Reflection of a high-amplitude solitary wave at a vertical wall. Journal of Fluid Mechanics 342*, 141–158.

[4] Chambarel, J., Kharif, C., and Touboul, J. 2009. *Head-on collision of two solitary waves and residual falling jet formation.* Nonlinear processes in geophysics 16(1), 111–122.

[5] Beji, S., and Battjes, J. 1993. *Experimental investigation of wave propagation over a bar.* Coastal Engineering 19(1-2), 151–162.

Flexural gravity wave amplitudes in the vicinity of blocking point under shallow water approximation

Susam Boral[1], **Trilochan Sahoo**[1], **Michael H Meylan**[2]
[1]Dept. of Ocean Engineering and Naval Architecture, IIT Kharagpur, India
[2]School of Mathematical and Physical Sciences, The University of Newcastle, Australia
E-mail Address of the presenting author: susamboral@gmail.com

1 INTRODUCTION

Recently, there has been significant progress in studying the blocking of flexural gravity waves. Das et al. [1; 2] investigated the criteria for occurrences of flexural gravity wave blocking in homogeneous and two-layer fluids. Boral et al. [3] studied the wave amplitudes of flexural waves in the vicinity of the saddle as well as blocking points. Similarly, Barman et al. [4; 5] studied the wave scattering of flexural gravity wave due to ice-crack and bottom undulation in the context of wave blocking, and demonstrated the occurrence of removable discontinuities at the blocking points. In the present study, the characteristics of flexural gravity waves are studied near the saddle point as well as the blocking points for weakly varying compressive force in shallow water. The study reveals that the amplitude of flexural gravity waves in the vicinity of the saddle and blocking points satisfy the hyper-Airy and Airy differential equation, respectively, under the shallow water approximation. Using WKB theory, the asymptotic solution of the hyper-Airy differential equation is obtained for matching the far-field solution with the near field solution. Moreover, the simulation of time-dependent wave propagation is demonstrated using the spectral method in the proximity of the saddle point.

2 FORMULATION OF MATHEMATICAL MODEL

In the present section, a mathematical model consisting of an infinitely extended floating elastic plate is developed under the assumption of small amplitude structural response and shallow water approximation. The interaction of gravity waves with the infinitely extended floating elastic plate/ice sheet generates the flexural gravity waves. Besides, a two-dimensional Cartesian coordinate system is assumed to represent the fluid domain with x-axis along the mean position of the plate covered surface and y-axis acting vertically downward. In addition, the fluid is assumed to be inviscid, incompressible and the flow is considered irrotational. Moreover, the plate is assumed to be thin, isotropic and homogeneous. Thus, the equation of continuity in the case of long waves yields

$$\frac{\partial \zeta}{\partial t} - h\frac{\partial^2 \Phi}{\partial x^2} = 0, \tag{1}$$

with $\Phi(x,t), \zeta(x,t)$ and h being the velocity potential, floating plate deflection and water depth respectively. The equation of motion associated with the long flexural gravity waves yields [5]

$$EI\frac{\partial^4 \zeta}{\partial x^4} + N\frac{\partial^2 \zeta}{\partial x^2} + \rho_p d\frac{\partial^2 \zeta}{\partial t^2} + \rho g\zeta = \rho\frac{\partial \Phi}{\partial t}. \tag{2}$$

where E is the Young's modulus, $I = d^3/12(1-\nu^2)$ with d and ν being the plate thickness and Poisson ratio respectively, N is the lateral compressive force, g is the acceleration due to gravity, ρ is the water density, ρ_p is the plate density and P_s is the pressure acting upon the floating elastic plate/ice sheet. Finally, combining Eqs. (1) and (2), the flexural gravity wave equation in shallow water is obtained as

$$D\frac{\partial^6 \zeta}{\partial x^6} + Q\frac{\partial^4 \zeta}{\partial x^4} + \gamma_p\frac{\partial^4 \zeta}{\partial x^2 \partial t^2} + \frac{\partial^2 \zeta}{\partial x^2} = \frac{1}{gh}\frac{\partial^2 \zeta}{\partial t^2}, \tag{3}$$

where $D = EI/\rho g$, $Q = N/\rho g$ and $\gamma_p = \rho_p d/\rho g$.

3 DERIVATION AND ANALYSIS OF DISPERSION RELATION

Assuming the motion is simple harmonic in time t with angular frequency ω, the plate deflection is written as

$$\zeta(x,t) = \mathrm{Re}\left\{\zeta_0 e^{\mathrm{i}(kx-\omega t)}\right\}, \tag{4}$$

with ζ_0 being the known amplitude. Substituting Eq. (4) in Eq. (3), the dispersion relation is obtained as

$$\omega^2 = \frac{gk^2h(Dk^4 - Qk^2 + 1)}{1 + gk^2h\gamma_p}. \tag{5}$$

It is worth mentioning that $\gamma_P \ll 1$; thus, the inertia term is neglected in the subsequent discussion as in [5]. Moreover, the phase and group velocities are derived in the form

$$c = \frac{\omega}{k} = \sqrt{gh(Dk^4 - Qk^2 + 1)}; \qquad c_g = \frac{d\omega}{dk} = \frac{gkh(3Dk^4 - 2Qk + 1)}{\omega}. \tag{6}$$

It is pertinent to mention that the phase velocity c vanishes for $Q = Q_c = 2\sqrt{D}$ m^2 and $k = k_c = (1/D)^{1/4}$ m^{-1}, whilst the group velocity c_g attains zero minimum for $Q = Q_{cg} = \sqrt{3D}$ m^2 and $k = k_{cg} = (1/3D)^{1/4}$ m^{-1}. Noticeably, both c_g and dc_g/dk vanish for Q_{cg} and k_{cg}. Further, Q_c and Q_{cg} are referred to as the buckling limit and threshold of blocking of compressive force respectively, whereas k_c and k_{cg} are known as the critical wavenumber and saddle point respectively [1]. may be noted that the vanishing of group velocity i.e., the existence of optima in the dispersion relation leading to the occurrences of flexural gravity wave blocking.

In Fig. 1, the dispersion curve is exhibited versus wavenumber for different values of compressive force. Figure 1 demonstrates that no wave blocking occurs for $Q < Q_{cg}$, whilst for $Q > Q_{cg}$ the dispersion curve possesses two optima which correspond with the primary (higher wavenumber) and secondary (lower wavenumber) blocking points. In addition, three propagating wave modes exist for any frequency within the limits of the blocking point.

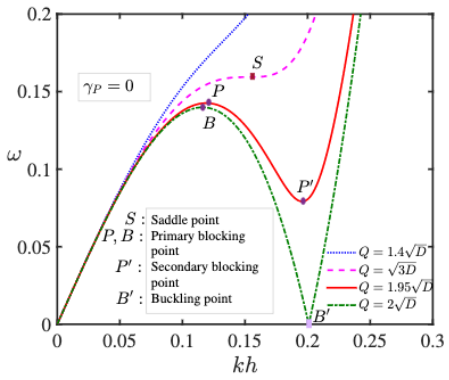

Figure 1: Dispersion curves for different values of Q with $\gamma_P = 0$, $EI = 5 \times 10^8$ Pa.

4 WAVE AMPLITUDE NEAR SADDLE AND BLOCKING POINTS

In the present section, emphasis is given for determining the wave amplitude in the vicinity of saddle as well as the blocking points for weakly varying compressive force $Q(x)$ in two different subsections.

4.1 WAVE AMPLITUDE NEAR SADDLE POINT

In the vicinity of saddle point, the wave amplitude $a(x,t)$ can be written as [3]

$$a(x,t) \equiv a(\varepsilon^{1/6}x, \varepsilon^{1/6}t), \tag{7}$$

with $\varepsilon \ll 1$ being a small parameter. Thus, the deflection of floating elastic plate $\zeta(x,t)$ is written in the form

$$\zeta(x,t) = a(\varepsilon^{1/6}x, \varepsilon^{1/6}t)e^{\mathrm{i}(kx-\omega t)}. \tag{8}$$

Next, we set $\overline{k}^4 = Dk^4$, $\overline{Q} = Q/\sqrt{D}$ and $\overline{\omega}^2 = (\sqrt{D}/gh)\omega^2$ and the overbar is omitted in the subsequent discussions. Consequently, substituting Eq. (8) in Eq. (3) and considering weakly varying compressive force $Q = Q(\varepsilon^{1/2}x)$, the Taylor series expansion of the compressive force Q about the saddle point, say $x = x_0$, yields

$$Q(\varepsilon^{1/2}x) = Q_0 + \varepsilon^{1/2}(x - x_0)Q'(x_0) + ..., \tag{9}$$

where $Q_0 = Q(x_0)$. Using Eq. (9) in Eq. (3) and comparing different powers of ε as in [3], it is obtained that

$$O(1) : \omega^2 = k^6 - Q_0k^4 + k^2, \tag{10}$$

$$O(\varepsilon^{1/6}) : \frac{\partial a}{\partial t} + c_g\frac{\partial a}{\partial x} = 0, \tag{11}$$

$$O(\varepsilon^{1/3}) : -\frac{\partial^2 a}{\partial t^2} + \left(15k^4 - 6Q_0k^2 + 1\right)\frac{\partial^2 a}{\partial x^2} = 0, \tag{12}$$

$$O(\varepsilon^{1/2}) : 4ik(Q_0 - 5k^2)\frac{\partial^3 a}{\partial x^3} - \left\{(x - x_0)Q'(x_0)k^4\right\}a = 0, \tag{13}$$

...

It may be noted that Eq. (10) is the dispersion relation of the long flexural gravity wave. On the other hand, the group velocity vanishes in the vicinity of the saddle point. Thus, Eq. (11) reveals that wave amplitude a is independent of time t in the proximity of saddle point. Again, at the saddle point both $c_g = 0$ and $dc_g/dk = 0$ [1], which ensures that Eq. (12) is trivially satisfied. Subsequently, Eq. (13) provides the solution near the saddle point. Consequently, $O(\varepsilon^m)$ for $m > 1/2$ is neglected. Setting $\xi = (x - x_0)\left\{\dfrac{Q'(x_0)k^3}{20k^2 - 4Q_0}\right\}^{1/4}$, Eq. (13) can be rewritten as

$$\frac{d^3a}{d\xi^3} - \mathrm{i}\xi a = 0, \tag{14}$$

which is known as the hyper-Airy differential equation. Using the WKB theory [3], the asymptotic solution of Eq. (14) for $\xi \to -\infty$ is obtained as

$$a(\xi) \sim (-\xi)^{-1/3}e^{3e^{-\pi\mathrm{i}/6}\gamma(-\xi)^{4/3}/4}, \tag{15}$$

where γ is the cube root of unity. In the present study, the asymptotic solution is considered for $\gamma = -(1+\mathrm{i}\sqrt{3})/2$ due to the fact that it is decaying to the right and oscillatory in nature to the left about the point x_0. By solving Eq. (14) and using Eq. (15), the wave amplitude a is obtained in the form

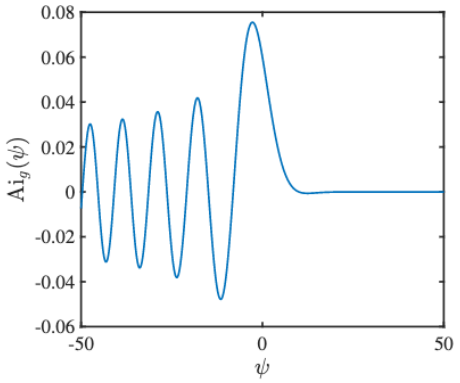

Figure 2: Generalised Airy function $\mathrm{Ai}_g(\psi)$

$$a \approx \frac{a_m}{(-\xi_m)^{-1/3}e^{3e^{-\pi\mathrm{i}/6}\gamma(-\xi_m)^{4/3}/4}}\mathrm{Ai}_g(\xi),$$

with

$$\mathrm{Ai}_g(\xi) = \frac{1}{\pi}\int_0^\infty \cos\left(\frac{\tau^4}{4} + \xi\tau\right)d\tau,$$

being the generalised Airy function, a_m being the amplitude at the point $x = x_m$, where $x_m = x_0 - O(\alpha)$ with α being very small which is similar to the thickness of the boundary layer as in [3].

4.2 WAVE AMPLITUDE NEAR BLOCKING POINTS

It may be recalled from section 3 that the group velocity vanishes in the close neighbourhood of primary as well as secondary blocking points. Thus, proceeding in a similar manner as in subsection 4.1 and considering $Q = Q(\varepsilon^{1/3}x)$, it can be easily derived that the wave amplitude near the blocking points satisfies

$$\frac{d^2a}{dx^2} - \frac{(x - x_0)Q'(x_0)k^4}{15k^4 - 6Q(x_0)k^2 + 1}a = 0, \tag{16}$$

which is the well-known Airy differential equation. The solution of Eq. (16) yields the amplitude $a(x)$ near the primary/secondary blocking point in terms of the Airy function $\mathrm{Ai}(x)$.

5 TIME-DOMAIN SIMULATION

In the present section, the time domain simulation of flexural gravity wave propagation in the vicinity of the saddle point is demonstrated. Figure 3 demonstrates that no wave transmission occurs beyond

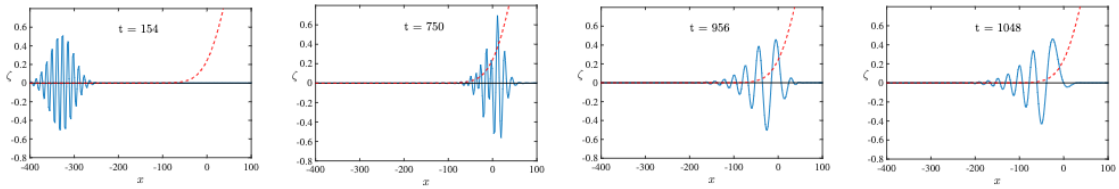

(a) (b) (c) (d)

Figure 3: Gaussian pulse near the saddle point with slowly varying $Q(x)$ in red dashed line.

the saddle point ($x = 80$ m). Figure 3a reveals the Gaussian pulse for time $t = 154$ s. On the other hand, Fig. 3b depicts that the incoming wave amplitude attains a higher value in the proximity of the saddle point beyond which it decays, which is similar to the characteristics of generalized Airy function as in Fig. 2. Figures 3c and 3d exhibit that wave reflection occurs from the saddle point [3].

ACKNOWLEDGEMENT

The authors acknowledge the support received from the MHRD, Govt. of India through Apex Committee of SPARC vide grant number SPARC/2018-2019/P751/SL. S.B. acknowledges the financial support from the CSIR, New Delhi, India, through the senior research fellowship vide file no: 09/081(1345)/2019-EMR-I.

REFERENCES

[1] Das, S., Sahoo, T., and Meylan, M. H. 2018. *Dynamics of flexural gravity waves: from sea ice to Hawking radiation and analogue gravity.* Proc. R. Soc. A: Math. Phys. Eng. Sci. 474(2209), 20170223.

[2] Das, S., Sahoo, T., and Meylan, M. H. 2018. *Flexural-gravity wave dynamics in two-layer fluid: blocking and dead water analogue. J. Fluid Mech. 854*, 121–145.

[3] Boral, S., Meylan, M. H., and Sahoo, T. 2021. *Time-dependent wave propagation on a variable Winkler foundation with compression. Wave Motion 106*, 102792.

[4] Barman, S. C., Das, S., Sahoo, T., and Meylan, M. H. 2021. *Scattering of flexural-gravity waves by a crack in a floating ice sheet due to mode conversion during blocking. J. Fluid Mech. 916*.

[5] Barman, S. C., Boral, S., Sahoo, T., and Meylan, M. H. 2021. *Bragg scattering of long flexural gravity waves by an array of submerged trenches and the analysis of blocking dynamics.* AIP Adv. 11(11), 115308.

Speed-effect restoring forces on ship motions

Xiaobo Chen[1], **Louis Diebold**[1] and **Youngmyung Choi**[2]

[1]Research Department, Bureau Veritas Marine & Offshore, Paris, France
[2]Dept. Naval Architecture and Ocean Engineering, PNU, Busan, Republic of Korea
xiao-bo.chen@bureauveritas.com

Following a new decomposition of radiation forces into the sum of added mass, damping and restoring components, it is shown that the speed-effect restoring forces are critically important not only to keep the theoretical consistency but also to predict ship motions with much improved accuracy.

1 Unsteady potential of time-harmonic flow

We define a Cartesian coordinate system translating at the speed U with the ship in the positive x-direction. The z-axis is positive upwards with the origin at the undisturbed free surface. Relative to this reference frame, there exists an ambient flow $-U\boldsymbol{i}$ opposing the ship forward direction. The presence of ship in this ambient flow creates a ship-shaped steady flow around the hull, called base flow $\mathbf{W} = U\nabla(\bar{\phi} - x)$. In addition to this base flow, there should be a wavy steady flow $\nabla\phi$. When the ship oscillates about the reference frame or/and in incoming waves, there exists also an unsteady flow $\nabla\psi$. The wavy steady and unsteady flows are called perturbation flow and represented by the velocity potential $\Phi = \phi + \psi$. All velocity potentials $(\bar{\phi}, \phi, \psi)$ satisfy the Laplace equation in the fluid. The total flow $\mathbf{W} + \nabla\Phi$ satisfies the kinematic and dynamic conditions written in the combined form

$$\begin{aligned} &\Phi_{tt} + g\Phi_z + 2\mathbf{W}\cdot\nabla\Phi_t + \mathbf{W}\cdot\nabla(\mathbf{W}\cdot\nabla\Phi) + \nabla\Phi\cdot(\mathbf{W}\cdot\nabla)\mathbf{W} \\ &= -2\nabla\Phi\cdot\nabla\Phi_t - (\mathbf{W}+\nabla\Phi)\cdot(\nabla\Phi\cdot\nabla)\Phi - \nabla(\mathbf{W}\cdot\nabla\Phi)\cdot\nabla\Phi - gU\bar{\phi}_z - \mathbf{W}\cdot(\mathbf{W}\cdot\nabla)\mathbf{W} \end{aligned} \tag{1}$$

on the free surface $z = \eta$ which is defined by

$$\eta = -\frac{1}{g}\Big[(\partial_t + \mathbf{W}\cdot\nabla)\Phi + \frac{1}{2}\nabla\Phi\cdot\nabla\Phi + \frac{1}{2}(\mathbf{W}\cdot\mathbf{W} - U^2)\Big] \tag{2}$$

The above equations (1) for potentials $\Phi = \phi + \psi$ and (2) for wave elevations are fully nonlinear with quadratic and cubic products of potentials and the assumption of time independence concerns only the base flow $\mathbf{W}$. Obtaining solutions of such problems with accuracy is extremely difficult if not impossible.

We assume now the base flow $\mathbf{W} = U\nabla(\bar{\phi} - x)$ is of order $O(1)$ while the perturbation flows $\Phi = \phi + \psi$ are of smaller order $o(1)$ comparing to the base flow $(\bar{\phi} - x)$ in the same way presented in Sclavounos (1995). Thus, the quadratic and cubic products of (ϕ, ψ) on the right-hand side of (1) are ignored. Furthermore, the free-surface elevation η is also assumed to be of smaller order $o(1)$ which is true for small or moderate speed. The Taylor expansion of all terms in (1) with respect to $z = 0$ can be used to express the boundary condition on the mean free surface. Finally, the frequency-domain expression of unsteady potential is scaled and written as

$$\psi = \Re\mathrm{e}\big\{\varphi\,\mathrm{e}^{-\mathrm{i}\omega_e t}\big\}L\sqrt{gL} \tag{3}$$

with ω_e the encounter frequency, g the acceleration due to gravity and L the ship length. The base flow $\mathbf{W} = U\mathbf{w}$ with $\mathbf{w} = \nabla\bar{\phi} - \boldsymbol{i}$ is used to obtain the linear boundary condition for the unsteady flow φ

$$\varphi_z - \omega^2\varphi - 2\mathrm{i}\tau\mathbf{w}\cdot\nabla\varphi + F_\mathrm{r}^2\mathbf{w}\cdot\nabla(\mathbf{w}\cdot\nabla\varphi) + F_\mathrm{r}^2\nabla\varphi\cdot(\mathbf{w}\cdot\nabla)\mathbf{w} + \bar{\phi}_{zz}(\mathrm{i}\tau\varphi - F_\mathrm{r}^2\mathbf{w}\cdot\nabla\varphi) = 0 \tag{4}$$

on the mean free surface $z = 0$. In (4), we have used the notations $\omega = \omega_e\sqrt{L/g}$ for dimensionless encounter frequency, $F_\mathrm{r} = U/\sqrt{gL}$ the Froude number and $\tau = \omega F_r$ the Brard number. Without considering the presence of ship, the classical Neumann-Kelvin linearisation can be derived by taking $\bar{\phi} = 0$ (then $\mathbf{w} = -\boldsymbol{i}$) in (4)

$$\varphi_z - \omega^2\varphi + 2\mathrm{i}\tau\varphi_x + F_\mathrm{r}^2\varphi_{xx} = 0 \tag{5}$$

which is widely used in many previous studies. The Neumann-Kelvin boundary condition (5) can be illustrated as the uniform stream penetrating in and through the ship hull (physically unacceptable) as shown by the left part of Figure 1. The linearisation based on the ship-shaped stream (4) is illustrated on the right part of Figure 1 which is physically acceptable.

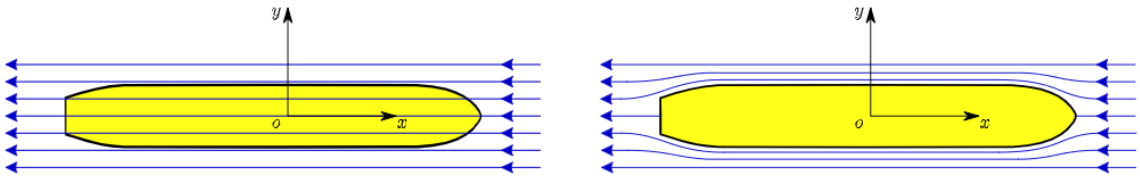

Figure 1: Uniform stream (left) *vs* ship-shaped stream (right) as the base flow in the linearisation

The boundary condition on the ship hull is written on H at its mean position

$$\frac{\partial}{\partial n}\varphi = \begin{cases} -\varphi_n^I & \text{diffraction} \\ \sum_{j=1}^{6}\left(-\mathrm{i}\omega\xi_j n_j + F_{\mathrm{r}}\xi_j m_j\right) & \text{radiations} \end{cases} \tag{6}$$

The potential φ^I representing incoming waves is well known. The six elementary motions are denoted by ξ_j for $j = 1, 2, \cdots, 6$ including the translations $\boldsymbol{T} = (\xi_1, \xi_2, \xi_3)$ and rotations $\boldsymbol{R} = (\xi_4, \xi_5, \xi_6)$. The vector components $\{n_j\}$ for $j = 1, 2, \cdots, 6$ are elements of the generalized normal vector $\{\boldsymbol{n}, \boldsymbol{r}\wedge\boldsymbol{n}\}$ defined in (13) and $\{m_j\}$ for $j = 1, 2, \cdots, 6$ are those of m_j terms

$$(m_1, m_2, m_3) = -(\boldsymbol{n}\cdot\nabla)\mathbf{w} \quad \text{and} \quad (m_4, m_5, m_6) = -(\boldsymbol{n}\cdot\nabla)(\boldsymbol{r}\wedge\mathbf{w}) \tag{7}$$

given in Newman (1978), depending on the ship-shaped stream $\mathbf{w}$ and the position vector $\boldsymbol{r}$. The normal vector $\boldsymbol{n} = (n_1, n_2, n_3)$ is defined positive inwards to the fluid.

This linearised boundary value problem with the condition (4) on the mean free surface and the condition (6) on the ship hull has been solved in Chen et al. (2021) by using the Green function associated with a pulsating and translating source with the viscous effect, and developing its analytical integration on the hull and on the free surface. The boundary integral equation includes that on the hull, that on the zone of free surface in the vicinity of ship and one over the waterplane inside the ship to ensure the good conditioned system of solutions. Numerical results in excellent agreement with experimental measurements shows that the method in Chen et al. (2021) provides well a reliable and practical method to evaluate wave loading and induced ship motions. One of important features in this new Green function method concerning a new decomposition of radiation forces is presented here.

2 Decomposition of radiation forces

According to the boundary condition (6) on the ship hull H, the time-harmonic potential φ can be written as the sum $\varphi = \varphi^D + \varphi^R$ of the diffraction φ^D and radiation φ^R. The radiation potential φ^R is further decomposed as

$$\varphi^R = -\mathrm{i}\omega\sum_{j=1}^{6}\xi_j\varphi_j^n + F_{\mathrm{r}}\sum_{j=1}^{6}\xi_j\varphi_j^m \tag{8}$$

in which the first 6 elementary potentials are due to ship velocities $-\mathrm{i}\omega\xi_j$ for $j = 1, 2, \cdots, 6$ and the second 6 potentials associated with ship's motions interacting with the base flow $\mathbf{w}$ via m_j terms. The boundary conditions on the hull for $(\varphi_j^n, \varphi_j^m)$ are then written by

$$\frac{\partial}{\partial n}\varphi_j^n = n_j \quad \text{and} \quad \frac{\partial}{\partial n}\varphi_j^m = m_j \tag{9}$$

for $j = 1, 2, \cdots, 6$. The time-harmonic pressure scaled with $(\rho g L)$ can be obtained by Bernoulli's equation

$$p^R = -\Big[-\mathrm{i}\omega\varphi^R + F_{\mathrm{r}}(\mathbf{w}\cdot\nabla\varphi^R)\Big] = \sum_{j=1}^{6}\xi_j\Big[\omega^2\varphi_j^n + \mathrm{i}\tau\big(\mathbf{w}\cdot\nabla\varphi_j^n + \varphi_j^m\big) - F_{\mathrm{r}}^2\mathbf{w}\cdot\nabla\varphi_j^m\Big] \tag{10}$$

by introducing the radiation potential (8) and considering the notation for the time derivative of the time-harmonic potential $\psi_t = -\mathrm{i}\omega\varphi$. In addition, the hydrostatic pressure p^H and that p^S due to the base flow are written by

$$p_0 = p^H + F_{\mathrm{r}}^2 p^S \quad \text{with} \quad p^H = -z \quad \text{and} \quad p^S = -\frac{1}{2}(\mathbf{w}\cdot\mathbf{w} - 1) = -\frac{1}{2}\big(\nabla\bar{\phi}\cdot\nabla\bar{\phi} - 2\bar{\phi}_x\big) \tag{11}$$

which yield the usual hydrostatic stiffness due to the spatial variations of p^H and of the ship hull associated with the ship motion, and the speed-effect restoring forces due to the variations linked to the base-flow pressure p^S.

The radiation forces including linear forces scaled by $(\rho g L^3)$ and torque moments scaled by $(\rho g L^4)$, are defined as the reaction of fluid via pressure on the ship hull against the acceleration, velocity and displacement of the ship, under the chosen reference system associated with the mean position of the ship

$$\boldsymbol{F}^R = -\iint_H p^R\boldsymbol{N}\,\mathrm{d}s - \iint_H\big(\boldsymbol{X}\cdot\nabla p_0 + p_0\boldsymbol{R}\wedge\big)\boldsymbol{N}\,\mathrm{d}s - \oint_\Gamma(\eta^R - X_3)p_0\boldsymbol{N}\,\mathrm{d}l \tag{12}$$

for $i = 1, 2, \cdots, 6$. In (12), $\boldsymbol{N}$ is called generalized normal vector, and $\boldsymbol{X}$ the displacement vector

$$\begin{aligned} &\boldsymbol{N} = \{\boldsymbol{n}, \boldsymbol{r} \wedge \boldsymbol{n}\} = \{n_1, n_2, n_3, n_4, n_5, n_6\} \\ &\boldsymbol{X} = \boldsymbol{T} + \boldsymbol{R} \wedge \boldsymbol{r} = \{X_1, X_2, X_3\} \qquad \text{with} \quad \boldsymbol{r} = \{x - x_0, y - y_0, z - z_0\} \end{aligned} \tag{13}$$

associated with the translation/rotation $(\boldsymbol{T}/\boldsymbol{R})$ and the position vector $\boldsymbol{r}$ with respect to the reference point $\boldsymbol{r}_0 = (x_0, y_0, z_0)$. The notation $\boldsymbol{R} \wedge \boldsymbol{N} = \{\boldsymbol{R} \wedge \boldsymbol{n}, \boldsymbol{R} \wedge (\boldsymbol{r} \wedge \boldsymbol{n})\}$ is adopted. The waterline integral is resultant from the integration on the intermittant surface between the local free-surface elevation $\eta^R = -\mathrm{i}\omega\varphi^R + F_\mathrm{r}(\mathbf{w} \cdot \nabla\varphi^R)$ and the vertical displacement of the waterline. This term often omitted in many studies is kept in Chen (2021). In addition to the projection of gravity force on the moving ship, we write

$$\boldsymbol{F}^R + \{\boldsymbol{0}, (\boldsymbol{R} \wedge \boldsymbol{r}_G) \wedge \boldsymbol{G}\} = -\sum_{j=1}^{6} \xi_j \big(-\omega^2 A_{ij} - \mathrm{i}\omega B_{ij} + C_{ij}\big) \tag{14}$$

in which A_{ij}, B_{ij} and C_{ij} on the right-hand side are called added-mass, damping and stiffness coefficients, respectively, following their respective association with the acceleration, velocity and displacement of the ship. The gravity $\boldsymbol{G}$ scaled by $(\rho g L^3)$ is equal to $(0, 0, -V/L^3)$ with V the buoyant volume in still water and $\boldsymbol{r}_G$ the center of gravity.

Among all terms in (12) and (14), the simplest ones are associated with the hydrostatic pressure $p^H = -z$

$$-\iint_H \big(\boldsymbol{X} \cdot \nabla p^H + p^H \boldsymbol{R} \wedge\big)\boldsymbol{N}\,\mathrm{d}s + \{\boldsymbol{0}, (\boldsymbol{R} \wedge \boldsymbol{r}_G) \wedge \boldsymbol{G}\} = -\sum_{j=1}^{6} \xi_j H_{ij} \tag{15}$$

in which H_{ij} is called hydrostatic restoring coefficients given in all textbooks. In a similar way, the contribution by p^S defined in (11) can be written by

$$-F_\mathrm{r}^2 \iint_H \big(\boldsymbol{X} \cdot \nabla p^S + p^S \boldsymbol{R} \wedge\big)\boldsymbol{N}\,\mathrm{d}s + F_\mathrm{r}^2 \oint_\Gamma X_3 p^S \boldsymbol{N}\,\mathrm{d}l = -F_\mathrm{r}^2 \sum_{j=1}^{6} \xi_j S_{ij} \tag{16}$$

where S_{ij} is called speed-effect restoring coefficients. Concerning the radiation forces due to the time-harmonic pressure p^R defined by (10) and the free-surface elevation η^R along the waterline, we decompose them

$$-\iint_H p^R \boldsymbol{N}\,\mathrm{d}s - F_\mathrm{r}^2 \oint_\Gamma \eta^R p_0^S \boldsymbol{N}\,\mathrm{d}l = -\sum_{j=1}^{6} \xi_j \Big(-\omega^2 R_{ij}^{\omega} - \mathrm{i}\tau R_{ij}^{\tau} + F_\mathrm{r}^2 R_{ij}^{F_\mathrm{r}}\Big) \tag{17}$$

with the components

$$\begin{cases} R_{ij}^{\omega} = -\displaystyle\iint_H \varphi_j^n n_i\,\mathrm{d}s + F_\mathrm{r}^2 \oint_\Gamma \varphi_j^n p_0^S n_i\,\mathrm{d}l \\ R_{ij}^{\tau} = -\displaystyle\iint_H \big(\mathbf{w} \cdot \nabla\varphi_j^n + \varphi_j^m\big) n_i\,\mathrm{d}s + F_\mathrm{r}^2 \oint_\Gamma \big(\mathbf{w} \cdot \nabla\varphi_j^n + \varphi_j^m\big) p_0^S n_i\,\mathrm{d}l \\ R_{ij}^{F_\mathrm{r}} = -\displaystyle\iint_H \big(\mathbf{w} \cdot \nabla\varphi_j^m\big) n_i\,\mathrm{d}s + F_\mathrm{r}^2 \oint_\Gamma \big(\mathbf{w} \cdot \nabla\varphi_j^m\big) p_0^S n_i\,\mathrm{d}l \end{cases} \tag{18}$$

By introducing (15), (16) and (17) back to (12) and following the usual notations, the coefficients (A_{ij}, B_{ij}, C_{ij}) on the right-hand side of (14) are given by

$$\begin{cases} A_{ij} = \Re\mathrm{e}\Big\{R_{ij}^{\omega} + \mathrm{i}(F_\mathrm{r}/\omega)R_{ij}^{\tau} - (F_\mathrm{r}^2/\omega^2)\big(R_{ij}^{F_\mathrm{r}} - R_{ij}^{S}\big)\Big\} \\ B_{ij} = \Im\mathrm{m}\Big\{\omega R_{ij}^{\omega} + \mathrm{i}F_\mathrm{r} R_{ij}^{\tau} - (F_\mathrm{r}^2/\omega)R_{ij}^{F_\mathrm{r}}\Big\} \\ C_{ij} = H_{ij} + F_\mathrm{r}^2\,\big(S_{ij} + R_{ij}^{S}\big) \end{cases} \tag{19}$$

The terms R_{ij}^S in above (19) are defined by the limit at zero frequency of the component $R_{ij}^{F_\mathrm{r}}$ given in (18)

$$R_{ij}^{S} = R_{ij}^{F_\mathrm{r}}(\omega \to 0) \tag{20}$$

which are purely real.

3 Speed-effect restoring forces and ship motions

The new decomposition (14) of radiation forces (plus gravity contribution) into added-mass (A_{ij}), damping (B_{ij}) and restoring coefficients (C_{ij}) given by (19) includes two speed-effect restoring coefficients S_{ij} contributed by the steady pressure (16) and R_{ij}^S by the "unsteady" pressure at the limit of zero frequency (20). The speed-effect restoring

forces R_{ij}^S are subtracted from the added-mass coefficients so that A_{ij} in (19) tend to a *finite* value at $\omega \to 0$ unlike the classical added-mass coefficients which tend to infinity as $O(\omega^{-2})$ by ignoring the speed-effect restoring forces.

In addition to the classical hydrostatic restoring coefficients H_{ij} defined by (15), the total restoring coefficients C_{ij} in (19) are augmented by the speed-effect components $(S_{ij} + R_{ij}^S)$ multiplied by the factor $F_{\rm r}^2$. These additional components are then negligible for $F_{\rm r} \to 0$ as expected. The component R_{ij}^S can be approximated by

$$R_{ij}^S = -\iint_H n_i (\mathbf{w} \cdot \nabla \bar{\varphi}_j^m)\, {\rm d}s + O(F_{\rm r}^2) \tag{21}$$

by ignoring the waterline integral of order $O(F_{\rm r}^2)$ on the right-hand side of (18). The zero-frequency "unsteady" potentials $\bar{\varphi}_j^m$ associated with the m_j terms can be approximated by

$$\{\bar{\varphi}_j^m\}_{j=1,2,\cdots,6} = -\{\mathbf{w}, \boldsymbol{r} \wedge \mathbf{w}\} + O(F_{\rm r}^2) \tag{22}$$

since they satisfy

$$\frac{\partial}{\partial n}\bar{\varphi}_j^m = \boldsymbol{n} \cdot \nabla \bar{\varphi}_j^m = m_j \quad \text{and} \quad \frac{\partial}{\partial z}\bar{\varphi}_j^m = 0 \tag{23}$$

on the hull for $j = 1, 2, \cdots, 6$ and on the mean free surface for $j = (1, 2, 6)$, respectively.

On the other side, the component S_{ij} defined by (16) is converted into another form in Chen (2021)

$$\{S_{ij}\}_{i=1,2,6} = \iint_H \{\nabla p^S, \boldsymbol{r} \wedge \nabla p^S\} n_j \, {\rm d}s \tag{24}$$

for $j = (1, 2, 6)$. Introducing (8) for $\bar{\varphi}_j^m$ in (21) and (11) for p^S in (24), we can show that

$$S_{jj} + R_{jj}^S = 0 \tag{25}$$

for $j = (1, 2, 6)$, i.e., in the horizontal directions (surge, sway and yaw). This cancellation of the speed-effect restoring forces in the horizontal directions is expected to be consistent with physics. On the contrary, the neglect of the component S_{ij} should induce non-physical restoring forces represented by R_{ij}^S and the accuracy of ship motions could be affected, in particular, in the horizontal directions where no other restoring forces are present.

Even in the vertical directions (heave, roll and pitch) where the hydrostatic restoring forces are dominant, the influence of speed-effect restoring forces S_{ij} is significant. Indeed, the speed-effect restoring coefficients S_{ij} are computed based on the ship-shaped stream $\mathbf{w}$ and introduced in the added-mass coefficients (19) in place of $(-R_{ij}^S)$. The comparison of A_{55} is depicted on the left of Figure 2, and that of pitch RAO on the right of the figure. It is shown that the inclusion of S_{ij} is critically important to predict ship motions with accuracy.

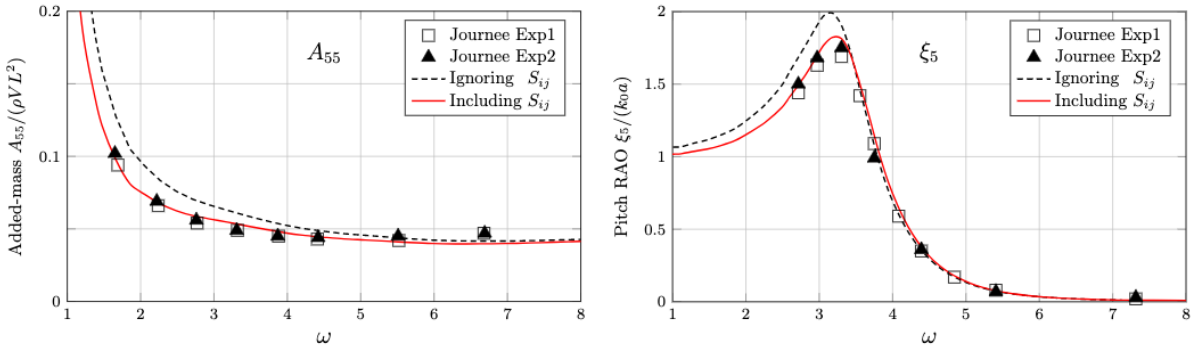

Figure 2: Added-mass coefficient (left) and Pith RAO (right) including (solid) the speed-effect restoring forces S_{ij} *versus* those ignoring S_{ij} (dashed), comparing with measurements of head-sea tests on Wigley IV hull at $F_{\rm r} = 0.3$ in Journee (1992).

References

[1] Sclavounos P. (1995) Computation of wave ship interactions. In Advances in Marine Hydrodynamics, Ed. Ohkusu M. *Computational Mechanics Publications*, 177-231.

[2] Newman J.N. (1978) The theory of ship motions. *Advance in Applied Mechanics*, 18, 221-283.

[3] Chen X.B., Choi Y.M., Malenica S. and Derbanne Q. (2021) Developpement d'une nouvelle methode pour l'evaluation de la tenue a la mer d'un navire anime d'une vitesse d'avance dans la houle. *Proceedings of ATMA'2021*, Paris (France), 1-18.

[4] Chen X.B. (2021) Ship motion theory – Wave loading and induced motions. *Techn. Report of Bureau Veritas.*

[5] Journee J.M.J. (1992) Experiments and calculations on four Wigley hullforms. *Delft Univ. Techn. Ship Hydromechanics Lab*, Report No.909.

Waves generated by moving disturbances on the seafloor

Yongbo Chen[a], Masoud Hayatdavoodi[a,b], BinBin Zhao[a] and R. Cengiz Ertekin[a,c]

a. College of Shipbuilding Engineering, Harbin Engineering University, Harbin, China
b. School of Science and Engineering, University of Dundee, Dundee DD1 4HN, UK
c. Department of Ocean & Resources Engineering, University of Hawaii, HI 96822, USA

Email: mhayatdavoodi@dundee.ac.uk

Introduction

Moving disturbances on the seafloor have been used by e.g., Tuck & Hwang (1972) to generate long waves to study tsunami run-up. Bottom moving disturbances can also be used as wave-makers to generate long waves in laboratory e.g., by Jamin et al. (2015). In principle, waves may be generated by a bottom disturbance, moving or oscillating in the vertical or horizontal direction. The bottom disturbance may be a continuous surface or discrete (in the case of a piston located on the seafloor). In this study, waves generated by moving disturbances on the sea floor are studied by use of the Level I Green-Naghdi (GN) equations. Attention is confined to waves generated by continuous bottom surface which is allowed to move in either vertical or horizontal direction. Results are compared with existing laboratory experiments and available numerical data. The model is then used to study waves generated by oscillatory bottom disturbances.

The level I Green-Naghdi Equations

Green et al. (1974) showed that the exact three-dimensional equations of motion of an inviscid and incompressible fluid (Euler's equations) can be simplified by making a single assumption about the distribution of the vertical velocity. The resultant equations are known as the GN equations, and they satisfy the nonlinear boundary conditions and the conservation of mass exactly, and postulate the integrated form of the conservation of momentum and energy laws. The GN equations are classified based on the assumption made about the distribution of the vertical velocity over the fluid column. In the Level I GN equations, used in this study, the vertical velocity varies linearly from the seafloor to the free surface. Consequently, (due to the continuity equation) the horizontal velocity is invariant over the water column in the Level I GN equations. These conditions are mostly applicable to the unsteady and nonlinear fluid motions in shallow waters, the subject of this study.

A rectangular Cartesian coordinate system (x_1, x_2) is used, where the origin is at the still-water level (SWL), with x_1 pointing to the right, and x_2 pointing upward against gravity. Ertekin (1984) provided a compact form of the Level I GN equations. In two dimensions the equations are given by

$$\eta_{,t} + \{(h+\eta-\alpha)u_1\}_{,x_1} = \alpha_{,t}, \tag{1}$$

$$\dot{u}_1 + g\eta_{,x_1} + \frac{\hat{p}_{,x_1}}{\rho} = -\frac{1}{6}\{[2\eta+\alpha]_{,x_1}\ddot{\alpha} + [4\eta-\alpha]_{,x_1}\ddot{\eta} + (h+\eta-\alpha)[\ddot{\alpha}+2\ddot{\eta}]_{,x_1}\}, \tag{2}$$

$$u_2(x_1,x_2,t) = \dot{\alpha} + \frac{x_2+h-\alpha}{h+\eta-\alpha}(\dot{\eta}-\dot{\alpha}), \tag{3}$$

$$\bar{p}(x_1,t) = \frac{\rho}{2}(h+\eta-\alpha)(\ddot{\alpha}+\ddot{\eta}+2g) + \hat{p}, \tag{4}$$

where $\alpha(x_1,t)$ is the bottom profile of the fluid sheet, $\eta(x_1,t)$ is the free surface, measured from the SWL, h is the water depth, g is the gravitational acceleration and ρ is the fluid mass density. The subscripts after commas denote partial derivatives with respect to the variables, while the superposed dots mean first and second material derivatives. $\bar{p}$ is the pressure at the bottom profile and $\hat{p}$ is the pressure on the free surface and $\hat{p}=0$ in this study without loss in generality. All the variables in this manuscript are dimensionless using ρ, g, and h as a dimensionally independent set, hence

$$x_1^{'} = \frac{x_1}{h}, \quad \eta^{'} = \frac{\eta}{h}, \quad \alpha^{'} = \frac{\alpha}{h}, \quad u_1^{'} = \frac{u_1}{\sqrt{gh}}, \quad t^{'} = t\sqrt{\frac{g}{h}}. \tag{5}$$

For simplicity, the superscript ($'$) are removed from all variables in the foregoing.

Continuous bottom disturbance

The system of equations (1) to (4) is solved to determine the impact of moving bottom disturbances on fluid. In this study, attention is confined to cases where the bottom disturbance is described by a continuous function, i.e. $\alpha(x_1,t)$ is continuous at all times. Cases where the bottom is discontinuous shall be considered in the future. The solution approach of the problem is described below.

At any given time, Eqs. (1) and (2) are solved for two unknowns, η and u_1, with $\alpha(x_1,t)$ given as a known function. For a given $\alpha(x_1,t)$, Eq. (1) contains only time derivatives of function η. Hence, at a given time step, surface elevation is determined explicitly by use of Eq. (1). The first and second material derivatives of η are given by $\dot{\eta} = \eta_{,t} + u_1\eta_{,x_1}$ and $\ddot{\eta} = \dot{\eta}_{,t} + u_1\dot{\eta}_{,x_1}$. Substituting $\eta_{,t}$ and $\eta_{,tt}$ (obtained from Eq. (1)) into $\ddot{\eta}$, gives

$$\ddot{\eta} = \ddot{\alpha} + (h+\eta-\alpha)(u_{1,x_1}^2 - u_{1,x_1t} - u_1u_{1,x_1x_1}). \tag{6}$$

Substituting Eq. (6) and material derivatives, $\dot{\alpha}$, $\ddot{\alpha}$ and $\ddot{\alpha}_{,x_1}$ into Eq. (2), gives

$$\begin{aligned}
&u_{1,t} + u_1u_{1,x_1} + g\eta_{,x} = \\
&-\eta_{,x_1}[\alpha_{,tt} + u_{1,t}\alpha_{,x_1} + 2u_1\alpha_{,x_1t} + u_1u_{1,x_1}\alpha_{,x_1} + u_1^2\alpha_{,x_1x_1}] \\
&-\frac{1}{2}(h+\eta-\alpha)[\alpha_{,x_1tt} + u_{1,x_1t}\alpha_{,x_1} + u_{1,t}\alpha_{,x_1x_1} + 2u_{1,x_1}\alpha_{,x_1t} \\
&+2u_1\alpha_{,x_1x_1t} + u_{1,x_1}^2\alpha_{,x_1} + u_1u_{1,x_1x_1}\alpha_{,x_1} + 3u_1u_{,x_1}\alpha_{,x_1x_1} + u_1^2\alpha_{,x_1x_1x_1}] \\
&-\frac{1}{2}(h+\eta-\alpha)(u_{1,x_1}^2 - u_{1,x_1t} - u_1u_{1,x_1x_1})[(2\eta-\alpha)_{,x_1}] \\
&-\frac{1}{3}(h+\eta-\alpha)^2(u_{1,x_1}u_{1,x_1x_1} - u_{1,x_1x_1t} - u_1u_{1,x_1x_1x_1}).
\end{aligned} \tag{7}$$

Equation (7) is similar to that given by Ertekin (1984) for a flat and stationary seafloor, involving the following additional terms due to the moving bottom disturbance: $\alpha_{,x_1tt}$, $2u_{1,x_1}\alpha_{,x_1t}$, $2u_1\alpha_{,x_1x_1t}$, $\alpha_{,tt}$ and $2u_1\alpha_{,x_1t}$. Equations (1) and (7), η and u_1 are solved numerically by use of the finite different method. Equation (7) forms a tridiagonal matrix of u_1, which is solved by use of a Gaussian Elimination method. Then u_2 and $\bar{p}$ are obtained explicitly by Eqs. (3) and (4). Discussion on the applicability of high level GN equations to generation of long waves by a moving bottom disturbance can be found in Zhao et al. (2011).

Results and Discussion

Results include comparisons with available data, followed by results of the GN model for waves generated by a moving bottom. A sketch of an arbitrary-shaped bottom disturbance on an otherwise flat bottom is shown in Fig. 1.

In a study by Tinti & Bortolucci (2000), waves generated by a disturbance moving horizontally on the seafloor are investigated by use of shallow water wave approximation method. The bottom disturbance is given by

$$\alpha(x_1,t) = \begin{cases} \frac{H_s}{2}[1 - cos(\frac{2\pi}{L_s}(x_1 - x_s))], & x_s \le x_1 \le x_e, \\ 0, & x_1 < x_s, x_1 > x_e, \end{cases} \tag{8}$$

where $L_s = 10$ and $H_s = 0.01$. The bottom disturbance moves along x_1 with constant velocity V_s. Shown in Fig. 2, the snapshots of wave profiles calculated by the GN equations are compared with those of Tinti & Bortolucci (2000). Figure 2 shows that two waves are generated: one wave with distinguishable peak and trough propagates in the same direction as the bottom disturbance while the other wave with almost only one trough propagates in the opposite direction. Overall, very good agreement is observed between the results.

Next, the laboratory experiments conducted by Hammack (1973), in which the bottom disturbance oscillates vertically, is considered. The bottom disturbance on the seafloor is given by

$$\alpha(x_1,t) = H_s(t) * H((\frac{L_s}{2})^2 - (x_1 - x_0)^2), \quad x_1 \ge 0, \tag{9}$$

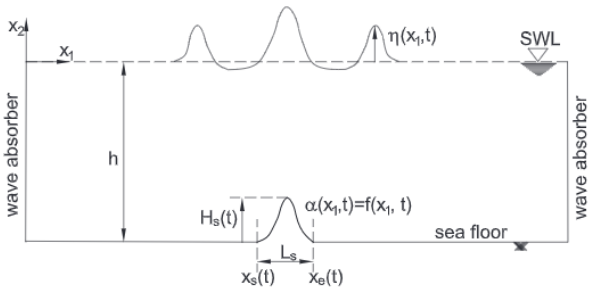

Figure 1: A sketch of the numerical wave tank with an arbitrary-shaped bottom disturbance, defined by a continuous function $f(x_1, t)$. x_s and x_e are the starting and ending position of the bottom disturbance, and $L_s = x_e - x_s$ is the disturbance length.

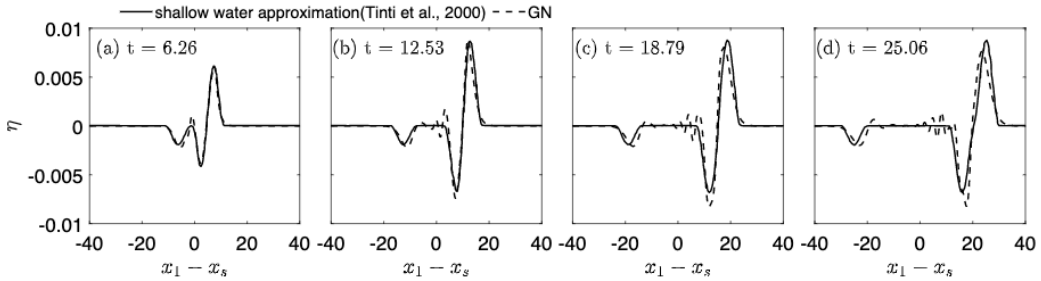

Figure 2: Snapshots of surface elevation at (a) $t = 6.26$, (b) $t = 12.53$, (c) $t = 18.79$ and (d) $t = 25.06$, obtained by the GN model and shallow water approximation of Tinti & Bortolucci (2000). The bottom disturbance moves with constant speed of $V_s = 0.639$ and stops at $t = 26.06$.

where $L_s = 24.4$, x_0 is the coordinate of the middle point of the moving disturbance, $x_0 = \frac{x_s+x_e}{2}$ and $H()$ is the unit step function (whose value is zero for negative arguments and one for positive arguments). $H_s(t)$ is given by

$$H_s = H_0(1 - e^{-qt}), \quad t \geq 0, \tag{10}$$

where H_0 is the oscillating amplitude of the bottom disturbance and q is constant. For the purpose of this comparison, we make sure that the bottom surface is continuous (i.e., the edges of the bottom disturbance are made smooth).

Time series of water surface elevation downstream of the obstacle are shown in Fig. 3, where results of the GN model are compared with the laboratory measurements of Hammack (1973) and the Boussinesq model of Fuhrman & Madsen (2009). At $x_1 = x_e$ and $x_1 = x_e + 20$, GN results show better agreement with the laboratory experiments. Both GN and Boussinesq models (Fuhrman & Madsen (2009)) overestimate the surface elevation at $x_1 = x_e + 180$ and $x_1 = x_e + 400$. Overall, there is close agreement between results of the two models and the laboratory measurements.

In this part, we study waves generated by a continuous moving bottom disturbance whose shape is described by the following hyperbolic function:

$$\alpha(x_1, t) = H_s(t) * R(x_1) * sech^2(x_1 - x_0). \tag{11}$$

The bottom disturbance oscillates vertically, defined by $H_s(t) = H_0 sin(\omega t)$ where ω is the oscillation frequency of the bottom surface. The ramp function is given as $R(x_1) = e^{\frac{-(x_1-x_0)^2}{\sigma^2}}$, where σ is a constant, controlling the effective width of $R(x_1)$.

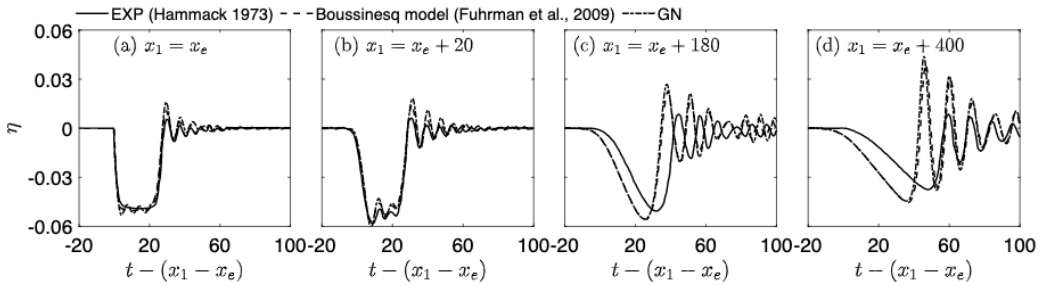

Figure 3: Time series of wave surface elevation recorded at (a) $x_1 = x_e$, (b) $x_1 = x_e + 20$, (c) $x_1 = x_e + 180$ and (d) $x_1 = x_e + 400$, downstream of the disturbance. $H_0 = -0.1$ and $q = 0.978$.

Figure 4 shows snapshots of wave surface elevation and bottom disturbances with $H_0 = 0.05$, 0.1 and 0.15. Wave profiles are very close to each other at $x_1 \geq x_0 + \frac{L_s}{2}$ with $H_0 = 0.1$ and 0.15. This can also be seen in Fig. 5 where time series of the surface elevation are recorded at four gauges.

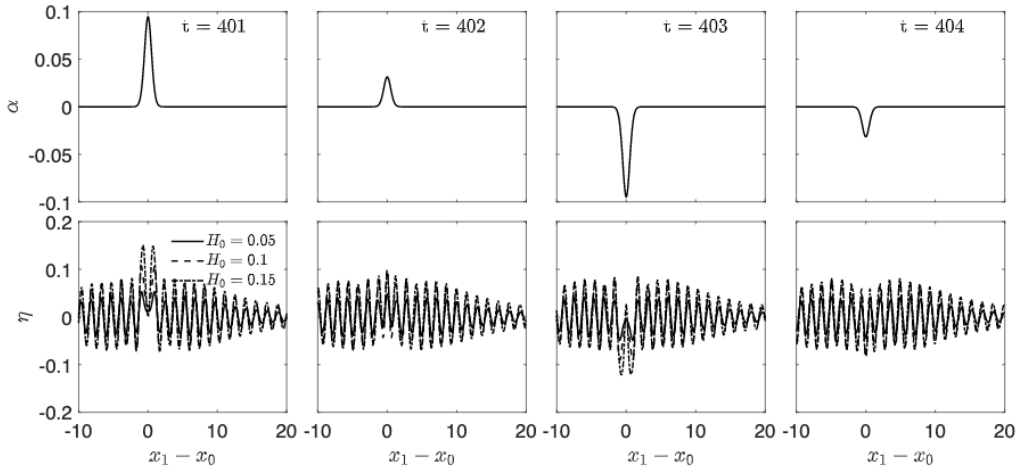

Figure 4: Snapshots of waves generated by the oscillating bottom disturbance with $H_0 = 0.05$, 0.1 and 0.15, $L_s = 4$, $\omega = 1.57$ and $\sigma = 1$.

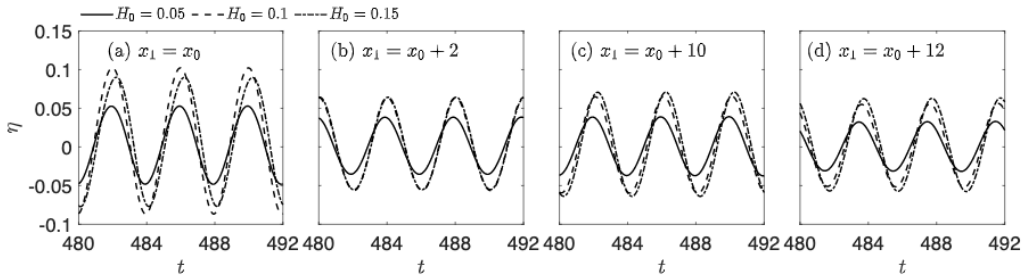

Figure 5: Time series of the wave surface elevation generated by the oscillating bottom disturbance with $H_0 = 0.05$, 0.1 and 0.15, $L_s = 4$, $\omega = 1.57$ and $\sigma = 1$.

Shown in Fig. 5, the oscillatory waves generated by a vertically oscillating disturbance have the same frequency as the moving disturbance and propagate with no change in their frequency. The wave height seems to increase as the oscillation height of the bottom disturbance increases, but the relationship appears to be nonlinear. Overall, the GN model developed in this study shows promising accuracy to study nonlinear waves generated by bottom disturbances.

References

Ertekin, R. C. (1984), *Soliton Generation by moving disturbances in shallow water: theory, computation and experiment*, Ph.D. Dissertation, University of California, Berkeley.

Fuhrman, D. R. & Madsen, P. A. (2009), 'Tsunami generation, propagation, and run-up with a high-order Boussinesq model', *Coastal Engineering* **56**(7), 747–758.

Green, A. E., Laws, N. & Naghdi, P. (1974), 'On the theory of water waves', *Proceedings of the Royal Society of London. A. Mathematical and Physical Sciences* **338**(1612), 43–55.

Hammack, J. L. (1973), 'A note on tsunamis: their generation and propagation in an ocean of uniform depth', *Journal of Fluid Mechanics* **60**(4), 769–799.

Jamin, T., Gordillo, L. et al. (2015), 'Experiments on generation of surface waves by an underwater moving bottom', *Proceedings of the Royal Society of London. A. Mathematical and Physical Sciences* **471**(2178), 20150069.

Tinti, S. & Bortolucci, E. (2000), 'Energy of water waves induced by submarine landslides', *Pure and Applied Geophysics* **157**(3), 281–318.

Tuck, E. O. & Hwang, L.-S. (1972), 'Long wave generation on a sloping beach', *Journal of Fluid Mechanics* **51**(3), 449–461.

Zhao, B. B., Duan, W. Y. & Webster, W. C. (2011), 'Tsunami simulation with Green–Naghdi theory', *Ocean Engineering* **38**(2), 389–396.

Derivation of some steady gravity wave equations for uneven bottoms

Didier Clamond
Laboratoire J. A. Dieudonné, Université Côte d'Azur, CNRS UMR 7351,
Parc Valrose, F-06108 Nice cedex 2, France.
didier.clamond@univ-cotedazur.fr

1 Introduction

Two-dimensional steady surface waves are fundamental because complex gravity wave fields are often described as interaction between such waves. In constant depth, several efficient numerical algorithms are available and mathematical results (existence, unicity, stability, etc.) are already well-known. The situation is not so advanced for uneven bottoms due to its higher complexity.

A key tool for dealing with water waves is conformal mapping that transforms the (generally unknown) physical domain into a chosen geometry (strip, circle, half-plane, etc.). To the linear approximation, the conformal mapping can be determined independently of the wave field because the upper boundary is flat and the lower boundary is given. This is not the case for the fully nonlinear equations since the shape of the upper boundary is unknown. However, the mapping can be easily obtained as function of the free surface (to be determined) and of the (given) bottom profile. Indeed, for a bottom given by a sufficiently regular function, the latter can be continued to an holomorphic function providing a solution of the conformal mapping, as shown in section 3 below. With this formal solution of the conformal mapping, several equations for the free surface can then be obtained. This is illustrated in section 4 with Byatt-smith [1], Nekrasov [2] and Babenko [3] equations generalised for uneven bottoms of arbitrary (smooth) profile.

2 Physical assumptions, definitions and notations

The fluid is homogeneous, the pressure is zero at the impermeable free surface, while the (uneven) seabed is impermeable. Let be $\{x, y\}$ a Cartesian coordinate system moving with the wave, x being the horizontal coordinate and y the upward vertical one; $y = -d(x)$ and $y = \eta(x)$ denote, respectively, the equations of the bottom and of the free surface. The origin $y = 0$ of the vertical direction is chosen such that η has zero Eulerian average, i.e.,

$$\langle\, \eta \,\rangle \stackrel{\text{def}}{=} \lim_{L\to\infty} \frac{1}{2L} \int_{-L}^{L} \eta(x)\, \mathrm{d}x \;=\; 0, \tag{1}$$

hence $y = 0$ is the equation of the mean surface elevation (the still-water level) and $d(x) > 0$. The mean water depth is denoted $\bar{d} \stackrel{\text{def}}{=} \langle d \rangle$ for brevity. The bottom shape $d(x)$ is a given analytic function that can be extended to complex x.

Let be ϕ, ψ, u and v the velocity potential, the stream function, the horizontal and vertical velocities, respectively, such that $u = \partial_x\phi = \partial_y\psi$ and $v = \partial_y\phi = -\partial_x\psi$. The velocity potential satisfies the well-known system of equations

$$\partial_x^2\phi \,+\, \partial_y^2\phi \;=\; 0 \qquad \text{for} \quad -\,d(x) \,\leqslant\, y \,\leqslant\, \eta(x), \tag{2}$$

$$\partial_y\phi \,+\, d'\,\partial_x\phi \;=\; 0 \qquad \text{at} \quad y \,=\, -d(x), \tag{3}$$

$$\partial_y\phi \,-\, \eta'\,\partial_x\phi \;=\; 0 \qquad \text{at} \quad y \,=\, \eta(x), \tag{4}$$

$$2\,g\,\eta \,+\, (\partial_x\phi)^2 \,+\, (\partial_y\phi)^2 \;=\; B \qquad \text{at} \quad y \,=\, \eta(x), \tag{5}$$

where $g > 0$ is the downward constant acceleration of gravity, B is a Bernoulli constant and primes denote the (total) derivative with respect of x. The mean-level condition (1) yields a definition of

the Bernoulli constant, i.e., $B = \langle u_\mathrm{s}^2 + v_\mathrm{s}^2 \rangle$ where, as general notation, subscripts 's' denote the quantities written at the free surface — e.g., $\phi_\mathrm{s}(x) = \phi(x, y = \eta(x))$ — and subscripts 'b' denote the quantities written at the seabed — e.g., $\phi_\mathrm{b}(x) = \phi(x, y = -d(x))$. Note that, for example, $u_\mathrm{s} = (\partial_x \phi)_\mathrm{s} \neq \partial_x(\phi_\mathrm{s}) = u_\mathrm{s} + \eta' v_\mathrm{s}$.

The system (2)–(5) is reduced introducing the complex potential $f \stackrel{\text{def}}{=} \phi + \mathrm{i}\psi$ (with $\mathrm{i}^2 = -1$) and the complex velocity $w \stackrel{\text{def}}{=} u - \mathrm{i}v$ that are holomorphic functions of $z \stackrel{\text{def}}{=} x + \mathrm{i}y$, i.e., $f = f(z)$ and $w = \mathrm{d}f/\mathrm{d}z$. The complex conjugate is denoted with a star (e.g., $z^* = x - \mathrm{i}y$).

The flow being steady, the impermeable free surface and bottom are streamlines, hence ψ_s and ψ_b are constant. A reference velocity is then $c \stackrel{\text{def}}{=} (\psi_\mathrm{b} - \psi_\mathrm{s})/đ$. In constant depth, c corresponds to Stokes' second definition of phase velocity, that is the phase velocity observed in the frame of reference without mean flow.

3 Conformal mapping and its formal resolution

The bottom and the free surface being streamlines, it is advantageous to make the change of independent complex variable $z = x + \mathrm{i}y \mapsto \zeta \stackrel{\text{def}}{=} (\mathrm{i}\psi_\mathrm{s} - f)/c$, that conformally maps the fluid domain $x \in \mathbb{R}$ and $y \in [-d(x), \eta(x)]$ into the strip $\alpha \stackrel{\text{def}}{=} \mathrm{Re}(\zeta) \in \mathbb{R}$ and $\beta \stackrel{\text{def}}{=} \mathrm{Im}(\zeta) \in [-đ, 0]$. This conformal mapping yields $c/w = -\mathrm{d}z/\mathrm{d}\zeta$ and the Cauchy–Riemann relations $\partial_\alpha x = \partial_\beta y$ and $\partial_\beta x = -\partial_\alpha y$.

By definition of the conformal mapping, z and ζ are related by the relation [4]

$$z(\zeta) \;=\; x_\mathrm{b}(\zeta + \mathrm{i}đ) \;-\; \mathrm{i}\,d(x_\mathrm{b}(\zeta + \mathrm{i}đ)) \;=\; z_\mathrm{b}(\zeta + \mathrm{i}đ), \tag{6}$$

where $x_\mathrm{b}(\zeta + \mathrm{i}\,đ)$ and $d(x_\mathrm{b}(\zeta + \mathrm{i}đ))$ are analytic continuations of the functions $x_\mathrm{b}(\alpha)$ and $d(x_\mathrm{b}(\alpha))$, respectively. Indeed, at the bottom $\zeta = \alpha - \mathrm{i}\,đ$, the relation (6) yields

$$z_\mathrm{b}(\alpha) \stackrel{\text{def}}{=} z(\zeta = \alpha - \mathrm{i}đ) \;=\; x_\mathrm{b}(\alpha) \;-\; \mathrm{i}\,d(x_\mathrm{b}(\alpha)) \;=\; z_\mathrm{b}(\alpha), \tag{7}$$

as it should be, while at the free surface $\zeta = \alpha + \mathrm{i}0$, (6) gives

$$z_\mathrm{s}(\alpha) \stackrel{\text{def}}{=} z(\zeta = \alpha) \;=\; x_\mathrm{b}(\alpha + \mathrm{i}đ) \;-\; \mathrm{i}\,d(x_\mathrm{b}(\alpha + \mathrm{i}đ)) \;=\; z_\mathrm{b}(\alpha + \mathrm{i}đ), \tag{8}$$

so once $x_\mathrm{b}(\alpha)$ is known, and $d(x)$ being prescribed, $z(\zeta)$ is known everywhere. Separating real and imaginary parts and introducing Taylor expansions around the bottom, the solution (6) at the free surface yields

$$x_\mathrm{s}(\alpha) \;=\; \cos[đ\,\partial_\alpha]\, x_\mathrm{b}(\alpha) + \sin[đ\,\partial_\alpha]\, d(x_\mathrm{b}(\alpha)), \quad y_\mathrm{s}(\alpha) \;=\; \sin[đ\,\partial_\alpha]\, x_\mathrm{b}(\alpha) - \cos[đ\,\partial_\alpha]\, d(x_\mathrm{b}(\alpha)). \tag{9a,b}$$

Note that, eliminating x_b between equations (9), one gets

$$y_\mathrm{s}(\alpha) \;=\; \tan[đ\,\partial_\alpha]\, x_\mathrm{s}(\alpha) \;-\; \sec[đ\,\partial_\alpha]\, d(\cos[đ\,\partial_\alpha]\, x_\mathrm{s}(\alpha) + \sin[đ\,\partial_\alpha]\, y_\mathrm{s}(\alpha))\,. \tag{10}$$

This expression is explicit for y_s in constant depth but, in general, it is implicit for varying bottoms.

For later convenience, we introduce the self-adjoint positive-definite pseudo-differential operators $\mathscr{C} \stackrel{\text{def}}{=} \partial_\alpha \cot[đ\,\partial_\alpha]$ and $\mathscr{S} \stackrel{\text{def}}{=} \partial_\alpha \operatorname{csc}[đ\,\partial_\alpha]$ that acts on a pure frequency as

$$\mathscr{C}\,\exp(\mathrm{i}k\alpha) \;=\; k\,\coth(k\,đ)\,\exp(\mathrm{i}k\alpha), \qquad \mathscr{S}\,\exp(\mathrm{i}k\alpha) \;=\; k\,\operatorname{csch}(k\,đ)\,\exp(\mathrm{i}k\alpha).$$

Thus, these operators are easily computed and inverted in Fourier space. With these operators, we have in particular

$$\frac{\mathrm{d}\,x_\mathrm{s}}{\mathrm{d}\alpha} \;=\; \mathscr{C}\,y_\mathrm{s} \;+\; \mathscr{S}\,d(x_\mathrm{b})\,, \qquad \frac{\mathrm{d}\,x_\mathrm{b}}{\mathrm{d}\alpha} \;=\; \mathscr{S}\,y_\mathrm{s} \;+\; \mathscr{C}\,d(x_\mathrm{b})\,, \tag{11a,b}$$

relating x to the free surface y_s.

4 Equations for the free surface

Once the conformal mapping has been solved as function of the free surface, an equation for the latter must be derived. Exploiting the holomorphy of different functions, various equations can be obtained. Here, we give generalisations to uneven bottoms of some well-known equations, but many other can be derived. Though not difficult, these derivations are a bit lengthly and thus they are not detailed here. (Similar derivations in constant depth can be found in [5].)

The generalised equations below are written as pseudo-differential equations for simplicity, but their integral formulations are easily obtained expressing the pseudo-differential operators as convolution integrals, e.g., for any function f

$$\mathscr{C}\, f(\alpha) \;=\; \frac{1}{2\,đ} \fint_{-\infty}^{\infty} \coth\!\left(\frac{\alpha-\gamma}{2\,đ\,/\,\pi}\right) \frac{\mathrm{d}\, f(\gamma)}{\mathrm{d}\gamma}\, \mathrm{d}\gamma, \qquad \mathscr{C}^{-1}\, f(\alpha) \;=\; -\frac{1}{\pi} \int_{-\infty}^{\infty} \ln\tanh\left|\frac{\alpha-\gamma}{4\,đ\,/\,\pi}\right| f(\gamma)\, \mathrm{d}\gamma,$$

$$\mathscr{S}\, f(\alpha) \;=\; \frac{\pi}{4\,đ^2} \int_{-\infty}^{\infty} \operatorname{sech}\!\left(\frac{\alpha-\gamma}{2\,đ\,/\,\pi}\right)^2 f(\gamma)\, \mathrm{d}\gamma, \qquad \sec[đ\,\partial_\alpha]\; f(\alpha) \;=\; \frac{1}{2\,đ} \int_{-\infty}^{\infty} \operatorname{sech}\!\left(\frac{\alpha-\gamma}{2\,đ\,/\,\pi}\right) f(\gamma)\, \mathrm{d}\gamma.$$

For periodic domains, the corresponding integrals can be easily obtained periodising the kernels.

4.1 Generalised Byatt-Smith equation

The Bernoulli equation at the free surface (5) yields, after conformal mapping and exploiting the relations (10),

$$(\, B \;-\; 2\, g\, y_{\mathrm{s}}\,) \left\{ [\,\mathscr{C}\, y_{\mathrm{s}} \;+\; \mathscr{S}\, d(x_{\mathrm{b}})]^2 \;+\; \left(\frac{\mathrm{d}\, y_{\mathrm{s}}}{\mathrm{d}\alpha}\right)^2 \right\} \;=\; c^2, \tag{12}$$

together with — from (11b) —

$$x_{\mathrm{b}} \;=\; \sigma\, \alpha \;+\; \partial_\alpha^{-1}\, [\,\mathscr{S}\, y_{\mathrm{s}} \;+\; \mathscr{C}\, d(x_{\mathrm{b}}) \;-\; \sigma\,]\,. \tag{13}$$

with $\sigma \stackrel{\mathrm{def}}{=} \lim_{\Lambda\to\infty} (2\Lambda)^{-1} \int_{-\Lambda}^{\Lambda} (\mathrm{d}x_{\mathrm{b}}(\alpha)/\mathrm{d}\alpha)\, \mathrm{d}\alpha$ and where ∂_α^{-1} is the integration operator providing an antiderivative with zero average. The equation (12) can be rewritten

$$y_{\mathrm{s}} \;+\; \sec[đ\,\partial_\alpha]\, d(x_{\mathrm{b}}) \;=\; \mathscr{C}^{-1} \left[\frac{c^2}{B - 2 g y_{\mathrm{s}}} \;-\; \left(\frac{\mathrm{d}\, y_{\mathrm{s}}}{\mathrm{d}\alpha}\right)^2 \right]^{\frac{1}{2}}, \tag{14}$$

that is the generalisation for uneven bottoms of the equation studied by Byatt-Smith [1] in constant depth.

4.2 Generalised Nekrasov equation

Exploiting the holomorphy of the function $\ell(\zeta) \stackrel{\mathrm{def}}{=} \log(-w/c) = -\log(\mathrm{d}z/\mathrm{d}\zeta)$ and denoting $\theta \stackrel{\mathrm{def}}{=} -\operatorname{Im}\ell$ the inclination angle of a streamline, we have

$$\theta_{\mathrm{b}}(\alpha) \;=\; -\arctan\big(d'(x_{\mathrm{b}})\big)\,, \qquad \theta_{\mathrm{s}}(\alpha) \;=\; \arctan\left(\frac{\mathrm{d}\, y_{\mathrm{s}}}{\mathrm{d}\alpha} \,\Big/\, \frac{\mathrm{d}\, x_{\mathrm{s}}}{\mathrm{d}\alpha}\right), \tag{15a,b}$$

so θ_{b} is prescribed by the (given) bottom slope and θ_{s} has to be determined. After some rather lengthly algebra, one obtains

$$\theta_{\mathrm{s}} \;=\; \sec[đ\,\partial_\alpha]\, \theta_{\mathrm{b}} \;+\; \mathscr{C}^{-1} \left\{ \frac{g\, c\, \sin(\theta_{\mathrm{s}})}{K_{\mathrm{N}} \;-\; 3\, g\, c\, \partial_\alpha^{-1}\, \sin(\theta_{\mathrm{s}})} \right\}, \tag{16}$$

where θ_{b} is given by (15a) and with the integration constant

$$K_{\mathrm{N}} \;=\; \lim_{\Lambda\to\infty} \frac{1}{2\,\Lambda} \int_{-\Lambda}^{\Lambda} \frac{c^3\, \cos(\theta_{\mathrm{s}})^3}{(\mathrm{d}x_{\mathrm{s}}/\mathrm{d}\alpha)^3}\, \mathrm{d}\alpha. \tag{17}$$

An equation for x_b as function of θ_s can be derived from (13), i.e.,

$$x_\mathrm{b} \;=\; \sigma\,\alpha \;+\; \partial_\alpha^{-1}\left[\,\frac{B}{2\,g\,đ} \;-\; \sigma \;+\; \mathscr{C}\,d(x_\mathrm{b}) \;-\; \frac{\mathscr{S}\left(K_\mathrm{N} \;-\; 3\,g\,c\,\partial_\alpha^{-1}\,\sin(\theta_\mathrm{s})\right)^{2/3}}{2\,g}\,\right]. \tag{18}$$

The equations (16) and (18), together with (15a), form a generalisation of the Nekrasov equation [2] for uneven bottoms.

Note that Krasovskii [6] and others, considered such a generalisation but only for periodic (generally sinusoidal) bottoms and/or mild slopes. Our approach here is also valid for non-periodic bottoms and it is not restricted to small variations of the mean depth. Actually, it can be extended to overturning bottoms.

4.3 Generalised Babenko equation

Exploiting the holomorphy of the complex velocity $w(\zeta)$, after some algebra not detailed here, a generalised Babenko equation [3] for y_s is obtained as

$$B\,\mathscr{C}\,y_\mathrm{s} \;-\; g\,y_\mathrm{s}\,\mathscr{C}\,y_\mathrm{s} \;-\; \tfrac{1}{2}\,g\,\mathscr{C}\,y_\mathrm{s}^2 \;+\; \left(\tfrac{1}{2}\,B \;-\; g\,y_\mathrm{s}\right)\mathscr{S}\,d(x_\mathrm{b}) \;=\; K_\mathrm{B} \;-\; \tfrac{1}{2}\,c\,\partial_\alpha^{-1}\,\mathscr{S}\,v_\mathrm{b}, \tag{19}$$

together with

$$v_\mathrm{b} \;=\; \frac{c\,d'(x_\mathrm{b})}{1+d'(x_\mathrm{b})^2}\left(\frac{\mathrm{d}\,x_\mathrm{b}}{\mathrm{d}\alpha}\right)^{-1} = \frac{c\,d'(x_\mathrm{b})}{1+d'(x_\mathrm{b})^2}\,\frac{1}{\mathscr{S}\,y_\mathrm{s} \;+\; \mathscr{C}\,d(x_\mathrm{b})}, \tag{20}$$

and the integration constant

$$K_\mathrm{B} \;=\; \lim_{\Lambda\to\infty}\,\frac{B}{2\,\Lambda}\int_{-\Lambda}^{\Lambda}\left[\,\frac{y_\mathrm{s}}{đ} \;-\; \frac{g\,đ}{2\,B}\,\frac{y_\mathrm{s}^2}{đ^2} \;+\; \frac{d(x_\mathrm{b})}{2\,đ}\,\right]\mathrm{d}\alpha, \tag{21}$$

x_b being given by (13). In constant depth, a Babenko equation [5] is recovered, that is quadratic in nonlinearities. However, its generalisation to uneven bottoms is highly nonlinear, in general.

Babenko-like equations have been of great help for mathematical proofs [7] and numerical algorithms [5], in infinite and constant depth. Their efficiency for uneven bottoms remain to be demonstrated due to their highly nonlinear nature.

REFERENCES

[1] Byatt-Smith, J. G. B. 1970. *An exact integral equation for steady surface waves. Proc. R. Soc. Lond. A 315*, 405–418.

[2] Nekrasov, A. I. On steady waves on the surface of a heavy fluid. In *Trudy Vseross S'ezda Matematikov* (1928), pp. 258–262.

[3] Babenko, K. I. 1987. *Some remarks on the theory of surface waves of finite amplitude. Sov. Math. Dokl. 35*, 599–603.

[4] Clamond, D. 1999. *Steady finite-amplitude waves on a horizontal seabed of arbitrary depth. J. Fluid Mech. 398*, 45–60.

[5] Clamond, D., and Dutykh, D. 2018. *Accurate fast computation of steady two-dimensional surface gravity waves in arbitrary depth. J. Fluid Mech. 844*, 491–518.

[6] Krasovskii, Y. P. 1962. *On the theory of steady-state waves of finite amplitude.* USSR Comput. Math. & Math. Phys. 1(4), 996–1018.

[7] Buffoni, B., Dancer, E. N., and Toland, J. F. 2000. *The regularity and local bifurcation of steady periodic water waves.* Arch. Rat. Mech. Anal. 152(3), 207–240.

New cut cell method for finite differences approximation of the Poisson Equations applied to a semi-averaged model for water waves propagation

Giuseppina Colicchio[1,2], **Matteo Antuono**[1]
[1] CNR-INM, Institute of Marine Engineering, Rome, Italy.
[2] AMOS, Marine Technology Department, NTNU, Trondheim, Norway.
giuseppina.colicchio@cnr.it

1 INTRODUCTION

In incompressible fluids approximation, both finite-differences and finite-volumes solutions of the Poisson equation rely on a gridding of the fluid domain. The most straightforward way to grid the domain is to use a mesh fitted to the fluid boundaries. However, the generation of body fitted grids is time-consuming and relies on the experience of the people for a good quality representation of the fluid flow; in fact, poor meshes can cause non-physical results and undermine the stability of the solution. Moreover, for moving boundaries (e.g. the free surfaces), the boundary deformation can change the topology of the domain and a new gridding is necessary. To avoid all these problems, immersed boundary methods have been devised to describes solid boundaries on Cartesian grids. A full analysis of all the immersed boundaries methods can be found in [1]. There, they are catalogued as a) indirect Boundary Conditions (BC) with a forcing extending into the fluid region and b) direct BC either in the form of Ghost Cell methods in Finite-Differences approaches and Cut-Cell methods in Finite-Volumes approaches. In this work a Cut-Cell approach is devised for finite-differences modelling, taking into account both still or moving boundaries with either Neumann or Dirchlet conditions.

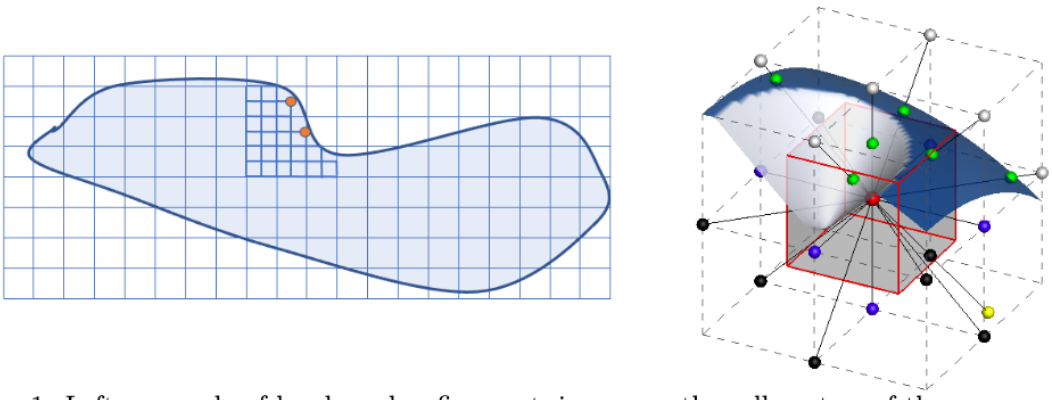

Figure 1: Left: example of local mesh refinement; in orange the cell centers of the coarse grid where care must be taken for the interpolation from the finer mesh. Right: Definition of the 20-points stencil for a cell cut by the domain boundaries. The actually used points in equation (5) are plotted in red, green, blue, black and yellow.

Left part of figure 1 shows how Adaptive Mesh Refinement (AMR) is also introduced into the modelling without significant changes in the way the boundary conditions are treated but for some points. Differently from what is done in [2], where an energy bound is set up on the boundary, here, the geometry of boundary is reconstructed on the Cartesian grid cells to describe even the finest detail of the surface geometry.

2 MATHEMATICAL FORMULATION

The aim of this work is to solve the classical Poisson equation $\nabla^2\phi = RHS$ on an irregular domain represented on a Cartesian grid with both Neumann and Dirchlet BC. The classical second order accurate 7-points stencil is used to discretize equation in points well inside the fluid domain. In the cell centre P_0, close to the boundaries, the function ϕ_0, is written as combination of ϕ_i in the surrounding points P_i at a distance $(\Delta x_i, \Delta y_i, \Delta z_i)$ from P_0. The forth order accurate interpolation of the function ϕ around the point P_i (either in the fluid domain or on the Dirchlet boundary) can be written using a Taylor expansion as:

$$\begin{aligned}
\phi_i - \phi_0 &= \frac{\partial\phi_0}{\partial x}\Delta x_i + \frac{\partial\phi_0}{\partial y}\Delta y_i + \frac{\partial\phi_0}{\partial z}\Delta z_i + \frac{\partial^2\phi_0}{\partial x^2}\frac{\Delta x_i^2}{2} + \frac{\partial^2\phi_0}{\partial y^2}\frac{\Delta y_i^2}{2} + \frac{\partial^2\phi_0}{\partial z^2}\frac{\Delta z_i^2}{2} + \\
&+ \frac{\partial^2\phi_0}{\partial x\partial y}\Delta x_i\Delta y_i + \frac{\partial^2\phi_0}{\partial x\partial z}\Delta x_i\Delta z_i + \frac{\partial^2\phi_0}{\partial y\partial z}\Delta y_i\Delta z_i + \frac{\partial^3\phi_0}{\partial x^3}\frac{\Delta x_i^3}{6} + \frac{\partial^3\phi_0}{\partial y^3}\frac{\Delta y_i^3}{6} + \\
&+ \frac{\partial^3\phi_0}{\partial z^3}\frac{\Delta z_i^3}{6} + \frac{\partial^3\phi_0}{\partial x^2\partial y}\frac{\Delta x_i^2}{2}\Delta y_i + \frac{\partial^3\phi_0}{\partial x^2\partial z}\frac{\Delta x_i^2}{2}\Delta z_i + \frac{\partial^3\phi_0}{\partial y^2\partial x}\frac{\Delta y_i^2}{2}\Delta x_i + \\
&+ \frac{\partial^3\phi_0}{\partial y^2\partial z}\frac{\Delta y_i^2}{2}\Delta z_i + \frac{\partial^3\phi_0}{\partial z^2\partial x}\frac{\Delta z_i^2}{2}\Delta x_i + \frac{\partial^3\phi_0}{\partial z^2\partial y}\frac{\Delta z_i^2}{2}\Delta y_i + \frac{\partial^3\phi_0}{\partial x\partial y\partial z}\Delta x_i\Delta y_i\Delta z_i
\end{aligned} \tag{1}$$

Similarly, in the point P_j (on a Neumann boundary), the derivative of function ϕ normal to the Neumann boundary can be written as

$$\begin{aligned}
\frac{\partial\phi_j}{\partial n} &= \frac{\partial\phi_0}{\partial x}n_{xj} + \frac{\partial\phi_0}{\partial y}n_{yj} + \frac{\partial\phi_0}{\partial z}n_{zj} + \frac{\partial^2\phi_0}{\partial x^2}\Delta x_j n_{xj} + \frac{\partial^2\phi_0}{\partial y^2}\Delta y_j n_{yj} + \frac{\partial^2\phi_0}{\partial z^2}\Delta z_j n_{zj} + \\
&+ \frac{\partial^2\phi_0}{\partial x\partial y}(\Delta y_j n_{xj} + \Delta x_j n_{yj}) + \frac{\partial^2\phi_0}{\partial x\partial z}(\Delta x_j n_{zj} + \Delta z_j n_{xj}) + \frac{\partial^2\phi_0}{\partial y\partial z}(\Delta y_j n_{zj} + \Delta z_i n_{yj}) + \\
&+ \frac{\partial^3\phi_0}{\partial x^3}\frac{\Delta x_j^2}{2}n_{xj} + \frac{\partial^3\phi_0}{\partial y^3}\frac{\Delta y_j^2}{2}n_{yj} + \frac{\partial^3\phi_0}{\partial z^3}\frac{\Delta z_i^2}{2}n_{zj} + \frac{\partial^3\phi_0}{\partial x^2\partial y}(n_{xj}\Delta x_j\Delta y_j + n_{yj}\frac{\Delta x_j^2}{2}) + \\
&+ \frac{\partial^3\phi_0}{\partial x^2\partial z}(n_{xj}\Delta x_j\Delta z_j + n_{zj}\frac{\Delta x_j^2}{2}) + \frac{\partial^3\phi_0}{\partial y^2\partial x}(n_{yj}\Delta x_j\Delta y_j + n_{xj}\frac{\Delta y_j^2}{2}) + \\
&+ \frac{\partial^3\phi_0}{\partial y^2\partial z}(n_{yj}\Delta y_j\Delta z_j + n_{zj}\frac{\Delta y_j^2}{2}) + \frac{\partial^3\phi_0}{\partial z^2\partial x}(n_{zj}\Delta x_j\Delta z_j + n_{xj}\frac{\Delta z_j^2}{2}) + \\
&+ \frac{\partial^3\phi_0}{\partial z^2\partial y}(n_{zj}\Delta y_j\Delta z_j + n_{yj}\frac{\Delta z_j^2}{2}) + \frac{\partial^3\phi_0}{\partial x\partial y\partial z}(n_{xj}\Delta y_j\Delta z_j + n_{yj}\Delta x_j\Delta z_j + n_{zj}\Delta x_i\Delta y_j)
\end{aligned} \tag{2}$$

with (n_{xj}, n_{yj}, n_{zj}) the normal-unitary vector to the the boundary through point P_j.

Both the Taylor expansions are written with 19 terms. Supposing that the normal derivatives are known in N_n points and the values of the function ϕ is known in N_m points (with $N_n + N_m = 19$), it is possible to multiply each of the equations (1) by a coefficient a_i and each of the equations (2) by a coefficient b_j so that summing them we have:

$$\begin{aligned}
&\textstyle\sum_i^{N_m} a_i(\phi_i - \phi_0) + \sum_j^{N_n} b_j\frac{\partial\phi_j}{\partial n} = \\
=\ &\tfrac{\partial\phi_0}{\partial x}(\textstyle\sum_i^{N_m} a_i F_1 + \sum_j^{N_n} G_1) + \tfrac{\partial\phi_0}{\partial y}(\sum_i^{N_m} a_i F_2 + \sum_j^{N_n} b_j G_2) + \tfrac{\partial\phi_0}{\partial z}(\sum_i^{N_m} a_i F_3 + \sum_j^{N_n} b_j G_3) + \\
+\ &\tfrac{\partial^2\phi_0}{\partial x^2}(\textstyle\sum_i^{N_m} a_i F_4 + \sum_j^{N_n} b_j G_4) + \tfrac{\partial^2\phi_0}{\partial y^2}(\sum_i^{N_m} a_i F_5 + \sum_j^{N_n} b_j G_5) + \tfrac{\partial^2\phi_0}{\partial z^2}(\sum_i^{N_m} a_i F_6 + \sum_j^{N_n} b_j G_6) + \\
+\ &\tfrac{\partial^2\phi_0}{\partial x\partial y}(\textstyle\sum_i^{N_m} a_i F_7 + \sum_j^{N_n} b_j G_7) + \tfrac{\partial^2\phi_0}{\partial x\partial z}(\sum_i^{N_m} a_i F_8 + \sum_j^{N_n} b_j G_8) + \tfrac{\partial^2\phi_0}{\partial y\partial z}(\sum_i^{N_m} a_i F_9 + \sum_j^{N_n} b_j G_9) + \\
+\ &\tfrac{\partial^3\phi_0}{\partial x^3}(\textstyle\sum_i^{N_m} a_i F_{10} + \sum_j^{N_n} b_j G_{10}) + \tfrac{\partial^3\phi_0}{\partial y^3}(\sum_i^{N_m} a_i F_{11} + \sum_j^{N_n} b_j G_{11}) + \\
+\ &\tfrac{\partial^3\phi_0}{\partial z^3}(\textstyle\sum_i^{N_m} a_i F_{12} + \sum_j^{N_n} b_j G_{12}) + \tfrac{\partial^3\phi_0}{\partial x^2\partial y}(\sum_i^{N_m} a_{i13} + \sum_j^{N_n} b_j G_{13}) + \\
+\ &\tfrac{\partial^3\phi_0}{\partial x^2\partial z}(\textstyle\sum_i^{N_m} a_i F_{14} + \sum_j^{N_n} b_j G_{14}) + \tfrac{\partial^3\phi_0}{\partial y^2\partial x}(\sum_i^{N_m} a_i F_{15} + \sum_j^{N_n} b_j G_{15}) + \\
+\ &\tfrac{\partial^3\phi_0}{\partial y^2\partial z}(\textstyle\sum_i^{N_m} a_i F_{16} + \sum_j^{N_n} b_j G_{16}) + \tfrac{\partial^3\phi_0}{\partial z^2\partial x}(\sum_i^{N_m} a_i F_{17} + \sum_j^{N_n} b_j G_{17}) + \\
+\ &\tfrac{\partial^3\phi_0}{\partial z^2\partial y}(\textstyle\sum_i^{N_m} a_i F_{18} + \sum_j^{N_n} b_j G_{18}) + \tfrac{\partial^3\phi_0}{\partial x\partial y\partial z}(\sum_i^{N_m} a_i F_{19} + \sum_j^{N_n} b_j G_{19})
\end{aligned} \tag{3}$$

where the coefficients F_α depende on $\Delta x_i, \Delta y_i, \Delta z_i$ (see equation (1)) and the G_β depende on $\Delta x_j, \Delta y_j, \Delta z_j, n_{xj}, n_{yj}, n_{zj}$ from equation (2).

In order to have that the left hand side of equation (3) represents a second order accurate approximation of the Laplacian operator in point P_0, we have to impose that the coefficient of each of the derivative of ϕ_0 is null but for those of $\frac{\partial^2\phi_0}{\partial x^2}$, $\frac{\partial^2\phi_0}{\partial y^2}$ and $\frac{\partial^2\phi_0}{\partial z^2}$. Each of these last coefficients has to be equal to 1. So we identify a system of 19 equations with 19 unknowns (the N_m a_i coefficients and the N_n b_j coefficients). Practically, we define a linear system

$$\mathbf{M} \left\{ \begin{array}{c} \mathrm{a}_i \\ \mathrm{b}_j \end{array} \right\} = \{I_{19}\} \tag{4}$$

where $\{I_{19}\}$ is a vector with all its elements equal to zero but for the 4th, 5th and 6th ones and where the solution vector $\{a_i, b_j\}^T$ is later used to approximate the Laplacian operator from the left hand side of equation (3), namely:

$$\nabla^2\phi_o \simeq \sum_i^{N_m} (a_i\phi_i) - \left(\sum_i^{N_m} a_i\right)\phi_0 + \sum_j^{N_n} \left(b_j \frac{\partial\phi_j}{\partial n}\right) + O(\Delta P^2) \tag{5}$$

Practically we have enlarged the stencil to 20 points close to the domain boundaries. In same cases, system (4) becomes overdetermined. To overcome this problem, a Singlular Value Decomposition SVD is used.

2.1 Definition of the points on the stencil

To identify the 20-points of the stencil close to the boundary, we refer to the right side of figure 1. There, the cell of interest is plotted with red edges and it is cut by the boundary surface represented with a dark and light blue surface. The two colors indicate two different boundary conditions that can be given on that surface. In the same picture, the blue spheres represents the classical 7-points stencil. Other 12 points are used here and shown in black. Actually, some of those points, as the top ones (shaded in gray), are outside of the fluid domain. For this reason, they are substituted with the green points, that are the intersection between the boundary surface and the line connecting the cell-center with those outside points. In this particular case, two of those points are characterized by a kind of boundary condition while four are characterized by the other BC.

The last point for the solution of system (4) should be possibly inside the domain. To satisfy this requirement, it is obtained using $\mathbf{n}$, the unitary normal vector to the boundary surface in the closest point to the cell centre, pointing inside the domain. This new point is represented in yellow in figure 1 and it is at distance $(2N(n_x)\Delta x, 2N(n_y)\Delta y, 2N(n_z)\Delta z)$ from the cell centre, where $N(f)$ stands for nearest whole number to f.

2.2 Local Mesh Refinment

To handle different mesh sizes, the solution of the Poisson equations is based on an iterative process similarly to [3]. *S0: At the first iteration level*, the solution is calculated on the coarsest subsiding mesh as described in paragraph 2.1; *Sl: then the solution on any further level of refinement* is calculated only on that level with Dirchlet BC on the border with a coarser mesh. *CH: At the end of this up-level process*, the solutions form the local finest level is interpolated on the coarsest mesh. If the difference between the interpolated value and the initial coarsest solution is lower than a threshold value, the solution can be accepted as it is. Otherwise, on the coarsest level, these interpolated values are used to recalculate the forcing term of the Poisson

equation in the refined region, taking into account the details that the coarse mesh is unable to see and the whole process from *S0* to *CH* is repeated. Particular care has to be taken for the cell centers highlighted in orange in the left side of figure 1. There, the set of points used for the interpolation from the finer mesh should be deprived of those points outside the fluid domain.

3 APPLICATION TO THE SEMI-AVARAGED MODEL

In [4], the Depth Semi Averaged Model (DSAM) was applied to the study of the interaction of a solitary wave with a submerged obstacle. In that case, an indirect immersed boundary condition has been applied to the solution of the Poisson equation $\nabla^2\Gamma = \nabla \cdot \left(\frac{\mathbf{M}}{d}\right)$ for Γ the semi-averaged vertical velocity component written as $\Gamma = \int_z^\eta w dz$, where w is the vertical component of the velocity, h the local bathymetry, d is the local water depth and $\mathbf{M}$ is the generalized mass flux.

In [4], the results from DSAM were compared with those obtained with OpenFOAM characterized by a mesh three times finer. The results were in reasonable good agreement but for the local interaction with the upper edges of the submerged obstacle. Figure 2 shows the comparison of water heigh obtained with the Navier-Stokes solver (bottom part of the panels) with the indirect immersed boundary on the left and with the Cut-Cell method on the right for DSAM. When interacting with the backward facing step, the new Cut-Cell method allows to better capture the details of the interaction with the edge. After that time step, the high steepness of the free surface causes a local mesh refinement that allows to reach the breaking of the wave front. However, the details of the breaking cannot be modelled in DSAM and they are not fully captured by OpenFOAM without any further refinement.

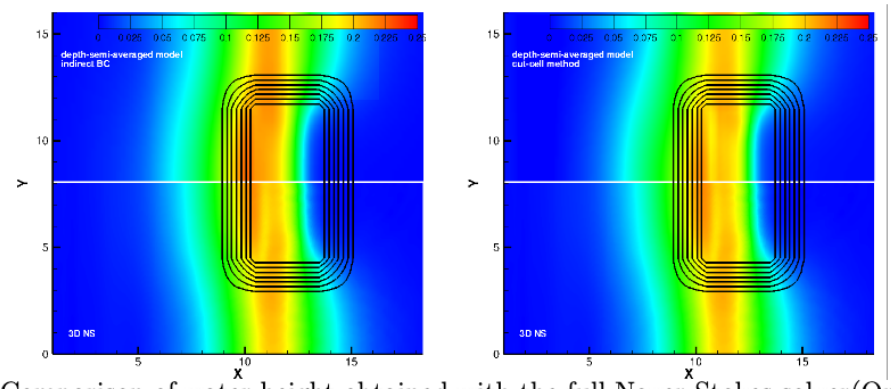

Figure 2: Comparison of water height obtained with the full Naver-Stokes solver(OpenFOAM) versus the solution of DSAM with indirect immersed BC (left side) and with Cut-Cell method (right).

REFERENCES

[1] Mittal, R., and Iaccarino, G. 2005. *Immersed Boundary Methods. Annu. Rev. Fluid Mech. 37*, 239–261.

[2] Sharan, N., Brady, P., and Livescu, C. 2021. *Finite-difference Cartesian cut-cell method for hyperbolic systems. AIAA 2021-0746*.

[3] Martin, D., and Cartwright, K. Oct 1996. Solving poisson's equation using adaptive mesh refinement. Tech. Rep. UCB/ERL M96/66, EECS Department, University of California, Berkeley.

[4] Colicchio, G., and Antuono, M. 2020. *Study of the interaction of a solitary wave with a submerged obstacle through a depth semi-averaged model. 35th IWWWFB*.

Time dependent motion due to sinusoidal ocean bottom oscillation

Santu Das[1] **and Michael H. Meylan**[2]
[1]Mathematical and Computational Sciences (Physical Sciences Division),
Institute of Advanced Study in Science and Technology, Guwahati 781035, India
[2]School of Information and Physical Sciences, College of Engineering, Science and Environment,
University of Newcastle, NSW 2308, Australia
Email: santudas20072@gmail.com

1 INTRODUCTION

Coastal areas, including land-mass and water, have always been a significant part of human civilisation. More than 600 million people live in a coastal region within 10 m of elevation, which accounts for 10 per cent of the world population. On top of that, approximately 2.4 billion people, around 40 per cent of the total world population, live within 100 Kms of the coastline. Any threat to the coastal region thus possesses an enormous amount of potential damage to the world population, a country's economy, natural food resources, to name a few. Among all the natural calamities, Tsunamis possess a grave threat which is evident from the recent accounts of destruction caused by 2004 Indian Ocean, 2011 Tohoku Oki, 2018 Sulawesi and Palu Tsunami, which were caused following submarine earthquakes. Predicting and simulating Tsunami waves is of obvious importance in providing a reliable warning system. In particular, the inclusion of compressibility allows for the simulation of acoustic gravity waves, which have been proposed as a method for early warning [1, 2, 3]. It has also been shown that a Tsunami model based on a compressible ocean is more accurate than a model with an incompressible ocean [2]. Many other authors have shown this [4, 5, 2, 6]. It is also essential to simulate different kinds of motions of the ocean bottom. An appropriate model taking the water compressibility into account and that can cater to such changes in the initial time-domain displacement is developed in this work.

2. MATHEMATICAL FORMULATION

We consider free-surface gravity wave propagation in a compressible ocean of finite depth h. The physical problem is formulated in a two-dimensional Cartesian coordinate system having z- axis pointing upwards and x- axis horizontal. The ocean bed is characterised as rigid. A wave propagation due to the ocean floor disturbance is realised both towards the positive and negative x- direction under the assumption of linearised water wave theory. The flow is considered irrotational. We are interested in calculating the time-dependent motion of the fluid due to a movement of the seafloor, simulating the generation of a Tsunami in two dimensions. We consider time-dependent growth $l(t)$ of a fixed displacement function $\mathcal{X}(x)$ of the ocean bottom between $-b$ and b. We note that it would be

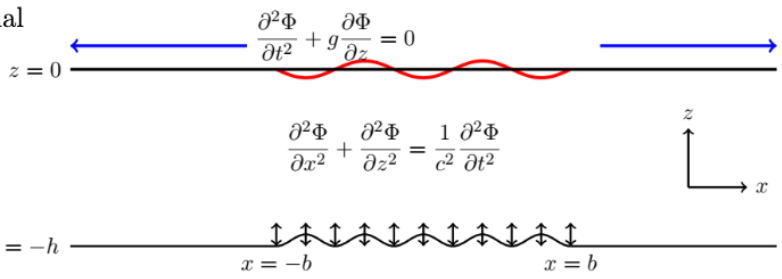

Figure 1: Schematic diagram of the single frequency problem with sinusoidal oscillating bottom profile.

straightforward to generalise to more complex motions which were not separable using linearity. Under these assumptions, the small amplitude displacement of the seafloor $\tilde{h}$ is given by

$$\tilde{h}(x,t) = l(t)\mathcal{X}(x)\mathcal{H}(b^2 - x^2),$$

where Φ is the displacement potential, g is the acceleration due to gravity, $c = \dfrac{K_0}{\rho_0}$ is the speed of sound in water, K_0 being the bulk modulus and ρ_0 is the undisturbed density of the whole water region, and $\mathcal{H}(\cdot)$ represents Heaviside unit step function. The boundary value problem we wish to solve is given by

$$\nabla^2\Phi(x,z,t) = \frac{1}{c^2}\frac{\partial^2\Phi}{\partial t^2} \qquad \text{in} \quad -h < z < 0, \tag{1a}$$

$$\Phi_{tt} + g\Phi_z = 0 \qquad \text{at} \quad z = 0, \tag{1b}$$

$$\Phi_z = l(t)\mathcal{X}(x)\mathcal{H}(b^2 - x^2) \qquad \text{at} \quad z = -h. \tag{1c}$$

We calculate the single frequency solution considering a sinusoidal bottom profile. We consider a block of the ocean bottom between $-b$ and b with a sinusoidal surface which is oscillating vertically with a unit amplitude and angular frequency ω (see Fig. 1) in the following form:

$$\zeta^m(x,t) = \exp\left(\mathrm{i}\frac{m\pi x}{b}\right)\mathcal{H}(b^2 - x^2)e^{\mathrm{i}\omega t} = \zeta_c^m(x,t) + \mathrm{i}\zeta_s^m(x,t), \quad m \in \mathbb{Z} \text{ (set of integers)}$$

where

$$\zeta_c^m(x,t) = \cos\left(\frac{m\pi x}{b}\right)\mathcal{H}(b^2 - x^2)e^{\mathrm{i}\omega t}, \quad \text{and} \quad \zeta_s^m(x,t) = \sin\left(\frac{m\pi x}{b}\right)\mathcal{H}(b^2 - x^2)e^{\mathrm{i}\omega t}, \tag{2}$$

In this case the displacement potential can be written as $\Phi(x,z,t) = \phi^m(x,z)\exp(\mathrm{i}\omega t)$ and ϕ^m satisfies the following equations

$$\nabla^2\phi^m(x,z,) = -\frac{\omega^2}{c^2}\phi^m \qquad \text{in} \quad -h < z < 0,$$

$$-\omega^2\phi^m + g\phi_z = 0 \qquad \text{at} \quad z = 0,$$

$$\phi_z^m = \exp\left(\mathrm{i}\frac{m\pi x}{b}\right)\mathcal{H}(b^2 - x^2) \qquad \text{at} \quad z = -h.$$

The problem will be solved by applying Fourier transformation of the form

$$\mathcal{F}(k,z) = \int_{-\infty}^{\infty}\phi^m(x,z)\exp(-\mathrm{i}kx)dx, \tag{4}$$

whose inverse Fourier transformation is given by

$$\phi^m(x,z) = \frac{1}{2\pi}\int_{-\infty}^{\infty}\mathcal{F}(k,z)\exp(\mathrm{i}kx)dk, \tag{5}$$

The potential $\phi(x,z,\omega)$ is obtained as

$$\begin{aligned}
\phi^m(x,z,\omega)|_{|x|<b} = b(-1)^m \Bigg\{ & \frac{4\mu_0\cosh\mu_0(z+h)e^{-\mathrm{i}k_0 b}(m\pi\mathrm{i}\sin(k_0x) + k_0 b\cos(k_0x))}{k_0(m^2\pi^2 - k_0^2b^2)(2\mu_0 h + \sinh 2\mu_0 h)} \\
& + \sum_{n=1}^{N}\frac{4\mu_n\cos\mu_n(z+h)e^{-\mathrm{i}k_n b}(m\pi\mathrm{i}\sin(k_nx) + k_n b\cos(k_nx))}{k_n(m^2\pi^2 - k_n^2b^2)(2\mu_n h + \sin 2\mu_n h)} \\
& + \sum_{n=N+1}^{\infty}\frac{4\mu_n e^{-\lambda_n b}\cos(\mu_n(z+h))(\mathrm{i}m\pi\sinh(\lambda_n x) + \lambda_n b\cosh(\lambda_n x))}{\lambda_n(m^2\pi^2 + \lambda_n^2b^2)(2\mu_n h + \sin(2\mu_n h))}\Bigg\} \\
& - (-1)^m\frac{\xi_m\cosh\xi_m z + (\omega^2/g)\sinh\xi_m z}{\xi_m\mathcal{D}(\xi_m,h)}e^{\mathrm{i}m\pi(x+b)/b}, \text{ where } \xi_m = \sqrt{\frac{m^2\pi^2}{b^2} - \frac{\omega^2}{c^2}}.
\end{aligned} \tag{6}$$

The solution for cosine type bottom ($\cos(m\pi x/b)$) can be retrieved as

$$\phi_c^m(x,z,\omega) = \frac{\phi^m(x,z,\omega) + \phi^{-m}(x,z,\omega)}{2}.$$

The region-wise explicit forms for the potential function turn out to be

$$\phi_c^m(x,z,\omega)|_{|x|>b} = b^2(-1)^m \left\{ \frac{-4\mathrm{i}\mu_0 \sin(k_0 b)\cosh(\mu_0(z+h))e^{\mp \mathrm{i}k_0 x}}{(m^2\pi^2 - k_0^2 b^2)(2\mu_0 h + \sinh(2\mu_0 h))} \right.$$
$$\left. + \sum_{n=1}^{N} \frac{-4\mathrm{i}\mu_n \sin(k_n b)\cos(\mu_n(z+h))e^{\mp \mathrm{i}k_n x}}{(m^2\pi^2 - k_n^2 b^2)(2\mu_n h + \sin(2\mu_n h))} - \sum_{n=N+1}^{\infty} \frac{4\mu_n \sinh(\lambda_n b)\cos(\mu_n(z+h))e^{\mp \lambda_n x}}{(m^2\pi^2 + \lambda_n^2 b^2)(2\mu_n h + \sin(2\mu_n h))} \right\} \quad (7)$$

The upper sign is for $x > b$ and the lower sign is for $x < -b$. When $|x| < b$, the following form of $\phi_c^m(x,z,\omega)$ is obtained:

$$\phi_c^m(x,z,\omega)|_{|x|<b} = b^2(-1)^m \left\{ \frac{4\mu_0 \cosh(\mu_0(z+h))e^{-\mathrm{i}k_0 b}\cos(k_0 x)}{(m^2\pi^2 - k_0^2 b^2)(2\mu_0 h + \sinh(2\mu_0 h))} \right.$$
$$\left. + \sum_{n=1}^{N} \frac{4\mu_n \cos(\mu_n(z+h))e^{-\mathrm{i}k_n b}\cos(k_n x)}{(m^2\pi^2 - k_n^2 b^2)(2\mu_n h + \sin(2\mu_n h))} + \sum_{n=N+1}^{\infty} \frac{4\mu_n e^{-\lambda_n b}\cos(\mu_n(z+h))\cosh(\lambda_n x)}{(m^2\pi^2 + \lambda_n^2 b^2)(2\mu_n h + \sin(2\mu_n h))} \right\}$$
$$- \frac{\xi_m \cosh \xi_m z + \frac{\omega^2}{g}\sinh \xi_m z}{\xi_m \left(\xi_m \sinh(\xi_m h) - \frac{\omega^2}{g}\cosh(\xi_m h)\right)} \cos\left(\frac{m\pi x}{b}\right), \quad \text{where} \quad \xi_m = \sqrt{\frac{m^2\pi^2}{b^2} - \frac{\omega^2}{c^2}}. \quad (8)$$

Similarly, the same for the sine type bottom ($\sin(m\pi x/b)$) can be obtained as

$$\phi_s^m(x,z,\omega) = \frac{\phi^m(x,z,\omega) - \phi^{-m}(x,z,\omega)}{2\mathrm{i}},$$

and the potential functions in the regions $|x| > b$ and $|x| < b$ can easily be computed. We now return to our primary problem of a finite time growth of the ocean bottom between $-b$ and b. We write $\mathcal{X}(x)$ as a Fourier series

$$\mathcal{X}(x) = \left(\sum_{m=0}^{\infty} \zeta_c^m \cos\left(\frac{m\pi x}{b}\right) + \zeta_s^m \sin\left(\frac{m\pi x}{b}\right) \right) \quad (9)$$

Applying a Fourier transformation in time (which is equivalent to a Laplace transform since the fluid is at rest)

$$\hat{\Phi}(x,z,\omega) = \int_0^{\infty} \Phi(x,z,t)e^{-\mathrm{i}\omega t}dt, \quad (10)$$

we can find the solution as

$$\hat{\Phi}(x,z,\omega) = \mathcal{W}(\omega)\left(\sum_{m=0}^{\infty} \zeta_c^m \phi_c^m(x,z,\omega) + \zeta_s^m \phi_s^m(x,z,\omega) \right) \text{ where } \mathcal{W}(\omega) = \int_0^{\infty} l(t)e^{-\mathrm{i}\omega t}dt.$$

Now taking the inverse Fourier transformation, we obtain the potential function as

$$\Phi(x,z,t) = \frac{1}{2\pi}\int_{-\infty}^{\infty} \hat{\Phi}(x,z,\omega)e^{\mathrm{i}\omega t}d\omega = \mathrm{Re}\left\{ \frac{1}{\pi}\int_0^{\infty} \hat{\Phi}(x,z,\omega)e^{\mathrm{i}\omega t}d\omega \right\}. \quad (11)$$

We present here a formula for the surface elevation which is

$$\eta(x,t) = \frac{1}{\pi}\sum_{m=0}^{\infty}\zeta_m^c \mathrm{Re}\left\{\int_0^\infty \mathcal{W}(\omega,\tau) f_c^m(x,\omega) e^{\mathrm{i}\omega t} d\omega\right\} + \frac{1}{\pi}\sum_{m=1}^{\infty}\zeta_s^m \mathrm{Re}\left\{\int_0^\infty \mathcal{W}(\omega,\tau) f_s^m(x,\omega) e^{\mathrm{i}\omega t} d\omega\right\}.$$

The first integral in the RHS represents the surface elevation when $\cos(m\pi x/b)$ type bottom is considered, and the second term represents the same for $\sin(m\pi x/b)$ type bottom. The quantities $f_c^m(x,\omega)$ and $f_s^m(x,\omega)$ are defined by

$$f_c^m(x,\omega) = \left.\frac{\partial \phi_c^m(x,z,\omega)}{\partial z}\right|_{z=0} \quad \text{and} \quad f_s^m(x,\omega) = \left.\frac{\partial \phi_s^m(x,z,\omega)}{\partial z}\right|_{z=0}.$$

3 RESULTS

The surface profiles for a flat profile and for a Gaussian profile of the form $\mathcal{X} = \exp(-6(x/20000)^2)$ are shown for $\tau = 10$s, $l_{\max} = 1$, $b = 20$ Km and $h = 5$ Km in which

$$l(t) = \frac{l_{\max} t}{\tau}\mathcal{H}(t(\tau - t)) + l_{\max}\mathcal{H}(t-\tau) \quad \text{with} \quad \mathcal{W}(\omega,\tau) = l_{\max}\frac{\left(e^{-\mathrm{i}\omega\tau} - 1\right)}{\tau\omega^2}.$$

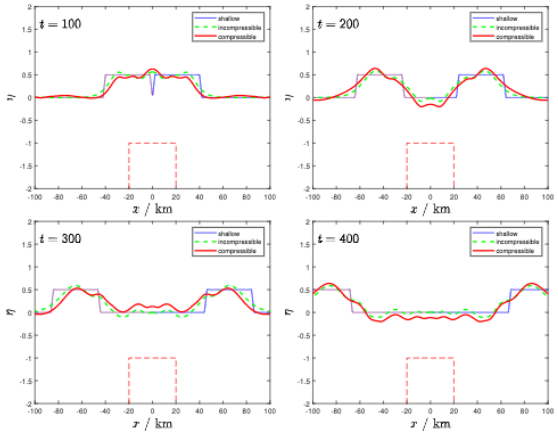

Figure 2: The bottom displacement is shown as a red dashed line for illustration only. The incompressible shallow water solution is also given along with the incompressible solution.

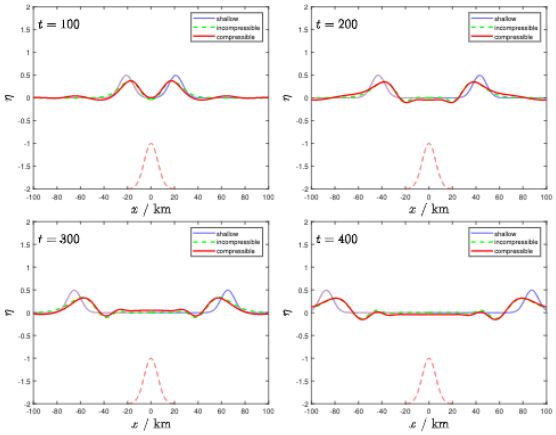

Figure 3: As in Fig. 2 except the bottom displacement is given by a Gaussian function.

REFERENCES

[1] C.A. Oliveira, T., and Kadri, U. 2016. *Pressure field induced in the water column by acoustic-gravity waves generated from sea bottom motion.* J. Geophys. Res-Oceans 121(10), 7795–7803.

[2] Nosov, M. A. 1999. *Tsunami generation in compressible ocean.* Phys. Chem. Earth Pt. B 24(5), 437–441.

[3] Stiassnie, M. 2010. *Tsunamis and acoustic-gravity waves from underwater earthquakes.* J. Eng. Math. 67(1-2), 23–32.

[4] Sells, C. C. L. 1965. *The effect of a sudden change of shape of the bottom of a slightly compressible ocean.* Philos. Tr. R. Soc. S-A 258(1092), 495–528.

[5] Yamamoto, T. 1982. *Gravity waves and acoustic waves generated by submarine earthquakes.* Int. J. Soil Dyn. Earthq. Eng. 1(2), 75–82.

[6] Nosov, M. A., and Kolesov, S. V. 2007. *Elastic oscillations of water column in the 2003 Tokachi-oki tsunami source: in-situ measurements and 3-D numerical modelling.* Nat. Hazard. Earth Sys. 7(2).

Energy budgets in the interaction between a surface gravity wave and a sumberged cylindrical resonator

Francesco De Vita[1*], Matteo Lorenzo[2], Paolo Pezzutto[2], Filippo De Lillo[2], Federico Bosia[3], Miguel Onorato[2]
[1]DMMM, Politecnico di Bari, 70125 Bari, Italy
[2]Dipartimento di Fisica, Universitá di Torino, 10129 Torino, Italy
[3]DISAT, Politecnico di Torino, 10129 Torino, Italy
[*]francesco.devita@poliba.it

HIGHLIGHTS

In this work, we investigate the energy transfer between a surface propagating wave and a sumberged resonator. We provide evidence that close to resonance conditions, not only is the energy transfer enhanched, but also the viscous dissipation rate, due to increased velocity differences between the wave and the resonator.

1 INTRODUCTION

Metamaterials are engineered materials developed to control standard properties of wave propagation such as dispersion, refraction or diffraction. They were first developed in the field of optics [1] and then extended to phononic crystals and elastic waves [2]. Metamaterials are typically arranged in periodic patterns and their dispersion relation can display band gaps, *i.e.* frequency regions of forbidden propagation. Similar effects have been reported also for surface gravity waves propagating over a periodic structure [3].

In this context, the METAREEF project aims at developing a novel device for coastal protection based on the idea of metamaterials and their enhanced wave control. The device is composed of a lattice of reversed pendula anchored to the seabed. The interplay between the propagating wave and the submerged device can produce wave filtering, depending on the ratio between the wave frequency and the natural frequency of the pendula [4]. Although in the past potential theory has been successfully used to describe wave forcing on submerged structures, recently it has been shown that viscosity can play an important role, especially close to resonant conditions [5]. For this reasons, Direct Numerical Simulations (DNS) of the Navier-Stokes equations can represent a powerful tool to understand the energy exchange between the wave and the submerged structure.

In this work, we present results of DNS simulations of a wave propagating over a sumberged horizontal resonator, oscillating about an equilibrium position, which is an approximation of the reversed pendula of the METAREEF device. The aim is to provide evidence that the resonators absorb energy from the wave, which is dissipated inside the fluid by viscous stresses. Results are presented in terms of energy budget and velocity distributions.

2 Governing Equations

The physical problem is governed by the Navier-Stokes equations for multiphase flows:

$$\rho(\partial_t \mathbf{u} + \mathbf{u} \cdot \nabla \mathbf{u}) = -\nabla p + \nabla \cdot (\mu \mathbf{D}) + \rho \mathbf{g} + \mathbf{f} \tag{1}$$

$$\nabla \cdot \mathbf{u} = 0 \tag{2}$$

with $\mathbf{u} = (u, w)$ the velocity field, p the pressure field, $\mathbf{D}$ the deformation tensor defined as $D_{ij} = (\partial_i u_j + \partial_j u_i)/2$, $\mathbf{g}$ the gravity vector and $\mathbf{f}$ the Immersed Boundary Method force which enforces the no-slip boundary condition at the solid boundary. The material properties ρ and μ of the fluid are related to the volume fraction field $\mathcal{F}(\mathbf{x}, t)$ as

$$\rho(\mathcal{F}) = \mathcal{F}\rho_1 + (1 - \mathcal{F})\rho_2 \tag{3}$$
$$\mu(\mathcal{F}) = \mathcal{F}\mu_1 + (1 - \mathcal{F})\mu_2, \tag{4}$$

where ρ_1, ρ_2, μ_1 and μ_2 are the density and viscosity of the two fluids; the volume fraction field (defined as the volumetric ratio of the two fluids in each computational cell) is advected by the flow with the following equation

$$\partial_t \mathcal{F} + \nabla \cdot (\mathcal{F}\mathbf{u}) = 0. \tag{5}$$

The dynamic of the resonator is modelled by the Newton's law

$$m\frac{d^2X}{dt^2} + \kappa(X - X_0) = F \tag{6}$$

where X is the position of the centre of mass of the resonator, m its mass, κ is the elastic constant, X_0 the equilibrium position and F the horizontal component of the integral of the hydrodynamic forces acting on it. This force is computed by integrating the surface forces tensor, pressure (p) and the viscous stress tensor ($\boldsymbol{\tau}$) over the surface of the solid body as follows:

$$\mathbf{F} = \int_S (\boldsymbol{\tau} - p\mathbf{I}) \cdot \mathbf{n} dS. \tag{7}$$

Details on the implementation and validation of the solver can be found in [6].

3 Results

We simulate a monochromatic sinusoidal wave propagating inside a unit periodic 2D squared domain of size λ, the wavelenght of the wave. The initial surface elevation and velocity field are taken from linear theory. Since the water depth is equal to $h = \lambda/2$ the wave angular frequency ω_w can be estimated using the dispersion relation in deep-water condition $\omega_r = \sqrt{gk}$, with $k = 2\pi/\lambda$ the wavenumber. The resonator is located at the center of the domain in the horizontal direction ($X_0 = \lambda/2$) and the submergence is $d = -r - 3a$, r being the radius of the resonator and a the initial wave amplitude. The natural frequency of the resonator can be estimated by considering the added mass term $\omega_r = \sqrt{\kappa/(m + \rho_w V)}$, where V is the volume of the resonator and ρ_w the density of the surrounding fluid. The simulation parameters are the following: Reynolds number $Re = \rho_w g^{1/2}\lambda^{3/2}/\mu_w = 10^5$, density ratio $\rho_a/\rho_w = 1/850$, viscosity ratio $\mu_a\mu_w = 1.92 \cdot 10^{-2}$, resonator radius $r/\lambda = 0.1$ and density $\rho_r = \rho_w/2$.

In [4] it has been shows that based on the ratio between the wave frequency and the resonator frequency $\Omega = \omega_r/\omega_w$, wave energy dissipation can change significantly. The wave mechanical energy E^w is given by the sum of the kinetic ($\mathcal{K}$) and potential ($\mathcal{U}$) contribution:

$$E^w(t) = \mathcal{K}^w(t) + \mathcal{U}^w(t) = \frac{1}{2}\int_0^\lambda \int_{-h}^\eta \left(\rho_w |\mathbf{u}|^2 + \rho_w g z\right) dz dx - \bar{\mathcal{U}^w} \tag{8}$$

with $\bar{\mathcal{U}^w}$ the potential energy of the still water level. Similarly, the resonator energy E^r can be computed as

$$E^r(t) = \frac{1}{2}\left[mU^2 + \kappa(X - X_0)^2\right] \tag{9}$$

with U the velocity of the center of mass of the resonator.

In [4], the dissipation was estimated by fitting the time evolution of the wave mechanical energy with an exponential expression, similar to the linear theory decay $E^w(t) = E^w(t = 0)e^{-4\nu k^2 t}$. Here, instead, we directly compute the dissipation rate by viscous stresses as

$$\mathcal{P}^w(t) = \int_0^{\lambda} \int_{-h}^{\eta} 2\mu \left[\left(\frac{\partial u}{\partial x} \right)^2 + \left(\frac{\partial v}{\partial y} \right)^2 + \frac{1}{2} \left(\frac{\partial u}{\partial y} + \frac{\partial v}{\partial x} \right)^2 \right] dxdz \tag{10}$$

at every timestep of the simulation. The amount of energy dissipated at time t is then computed as $\mathcal{D}^w(t) = \int_0^t \mathcal{P}^w dt$.

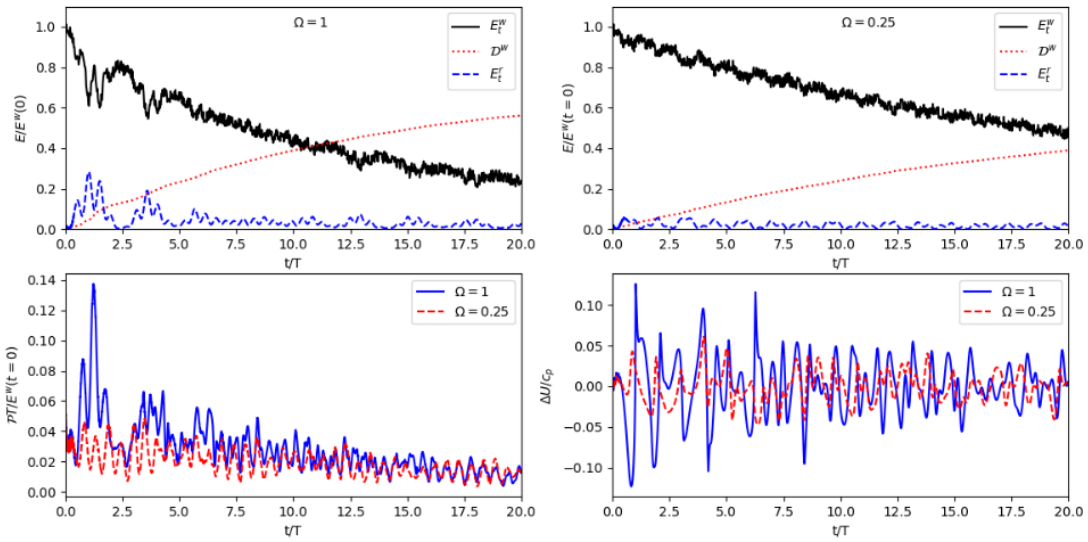

Figure 1: Time history of wave and resonator mechanical energy and dissipation for the case $\Omega = 1$ (top left panel) and $\Omega = 0.25$ (top right panel); instantaneous dissipation rate for the two cases (bottom left panel); instantaneous velocity difference between the wave and the resonator (bottom right panel).

The time history of the wave and resonator mechanical energy are shown in fig.1 (top panels) alongside the dissipated energy. Energy is normalized with the initial wave mechanical energy $E^w(t = 0)$ and time is made non-dimensional using the wave period $T = 2\pi/\omega_w$. For the case $\Omega = 1$, close to resonance conditions, the energy absorbed by the resonator reaches a maximum of about 30% of the initial wave mechanical energy; instead, when $\Omega = 0.25$ the maximum energy of the resonator is about 10%. This energy then is partially returned to the wave and partially dissipated by viscous stresses. Looking at the instantaneous dissipation rate (fig.1 bottom left panel), it can be seen that in resonance conditions not only the energy transfer, but also the dissipation rate increases. This implies that the increased absorbed energy by the resonator leads to an increase in viscous dissipation. Since this term is proportional to the velocity gradient (see eq.(10)) we compute the difference between the resonator velocity U and the interface velocity at the same horizontal coordinate $\Delta U(t) = u(x = X, z = \eta, t) - U(t)$. Results, reported in the bottom right panel of fig. 1, clearly show that in the case $\Omega = 1$ the velocity difference can reach values about 4 times greather than for $\Omega = 0.25$ and exhibits a maximum about the maximum dissipation rate (compare with the bottom left panel). The differences in the velocity field are highlighted in figure 2 where the color map of the horizontal

velocity is reported, after one wave period. The overall mechanism can be explained as follows: when the frequency of the wave and the resonator are comparable, the elastic force acts on a timescale similar to the hydrodynamic forcing on the resonator and its motion does not follow the wave. On the other hand, when the timescale of the elastic force is larger, the resonator follows the wave motion more easily, with a reduced dissipation.

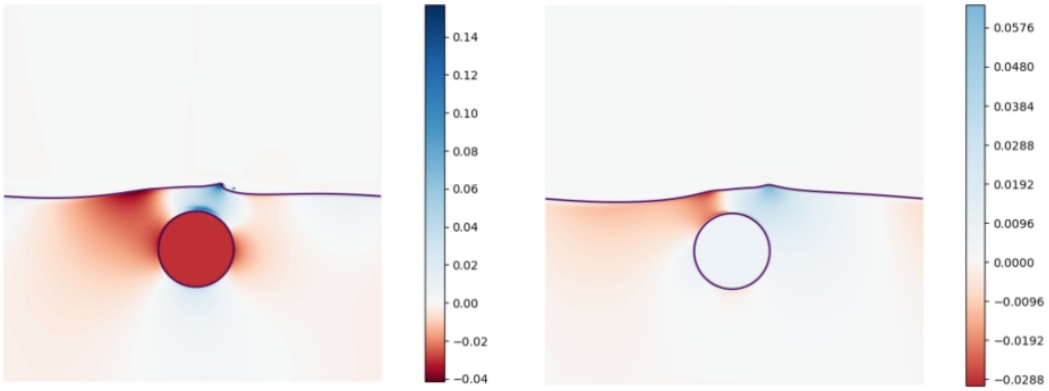

Figure 2: Horizontal velocity colormap after one wave period: $\Omega = 1$ (left panel), $\Omega = 0.25$ (right panel). Velocity is made non-dimensional using the phase velocity.

REFERENCES

[1] Pendry, J. 2001. *Electromagnetic materials enter the negative age.* Physics World 14(9), 47.

[2] Hussein, M. I., Leamy, M. J., and Ruzzene, M. 2014. *Dynamics of phononic materials and structures: Historical origins, recent progress, and future outlook.* Applied Mechanics Reviews 66(4).

[3] Hu, X., Shen, Y., Liu, X., Fu, R., and Zi, J. 2003. *Complete band gaps for liquid surface waves propagating over a periodically drilled bottom.* Physical Review E 68(6), 066308.

[4] De Vita, F., De Lillo, F., Bosia, F., and Onorato, M. 2021. *Attenuating surface gravity waves with mechanical metamaterials.* Physics of Fluids 33(4), 047113.

[5] Jin, S., Patton, R. J., and Guo, B. 2018. *Viscosity effect on a point absorber wave energy converter hydrodynamics validated by simulation and experiment. Renewable Energy 129*, 500 – 512.

[6] De Vita, F., De Lillo, F., Verzicco, R., and Onorato, M. 2021. *A fully Eulerian solver for the simulation of multiphase flows with solid bodies: Application to surface gravity waves. Journal of Computational Physics 438*, 110355.

Multisection approach for the vertical water impact of a fuselage

Alessandro Del Buono*, Alessandro Iafrati
CNR-INM, INstitute of Marine engineering, 00128 Rome, Italy
*alessandro.delbuono@inm.cnr.it

1 INTRODUCTION

Although aircraft ditching is a rare event in the aeronautical field, it needs to be considered in the design phase to guarantee safety and ensure the certifications' respect. Besides experimental tests [1, 2] and high-fidelity approaches [3], the use of fast and efficient solvers, albeit of lower fidelity, is of primary interest to aircraft manufacturers to have a quick but at the same time accurate estimate of the hydrodynamic loads acting on the aircraft, to be effectively exploited in its conceptual and preliminary design phases. This is particularly true during the aircraft optimization process where many different configurations have to be analyzed. In this perspective, fully non-linear potential flow models, although remaining low fidelity approaches but being fully non-linear, provide accurate details, like pressure distribution, and should allow capturing some hydrodynamics phenomena occurring in ditching problems like cavitation and ventilation [1]. An idea should be developing a 2D+t procedure which exploits a 2D fully non-linear potential flow model [4, 5] to describe the hydrodynamics of the aircraft ditching phenomenon. The 2D+t approach is based on a slender body approximation and reduces the 3D problem into a series of 2D cross section problems, with the shape of the section changing in time, in an earth-fixed frame of reference. As a first step through the implementation of a 2D+t approach, this paper presents a multisection procedure for computing the vertical water impact of a fuselage. Differently from the 2D+t method, in the multisection procedure the forward velocity in the longitudinal direction is not considered and the shape of the 2D sections don't change in time during the immersion. The proposed multisection procedure is based upon a 2D fully non linear potential flow hybrid BEM-FEM solver proposed in [6, 7]. The hybrid BEM-FEM approach has shown in the past good capabilities in describing the hydrodynamics of 2D water impact problems both in water entry with constant velocity [6, 7] and in the combined water entry/exit with varying speed [8]. The numerical investigation aims to preliminarily verify the procedure here proposed through its application to a guided drop test of a scaled fuselage.

2 MULTISECTION PROCEDURE

The vertical water impact of a fuselage is here faced with a multisection approach where the 3D water entry problem is approximated by a series of the 2D water entry problems of the different fuselage cross sections. In this way the 3D problem is split into a series a 2D boundary value problem which are solved independently by using the hybrid BEM-FEM solver. The multisection algorithm is based on a three-step procedure, described in the following, and shown in figure 1.

- Step 1. Let consider the impacting fuselage on the x-z plane. Starting from the point where the fuselage touches the water the first time, a number of equally spaced vertical space-fixed cross planes intersecting the fuselage are introduced.
- Step 2. When the body reaches a fixed initial depth, necessary to start the numerical simulation [8], the first space-fixed plane is activated. The corresponding 2D section on the y-z plane is derived by linear interpolation between the fuselage sections closer to the

activated plane. This is the 2D body geometry that the hybrid BEM-FEM solver uses to solve the 2D water entry problem.

- Step 3. After certain time steps, other space-fixed sections are activated as the lower intersection with the fuselage contour reaches the fixed initial depth. The corresponding 2D sections are derived and the water entry simulation starts on each new activated section.

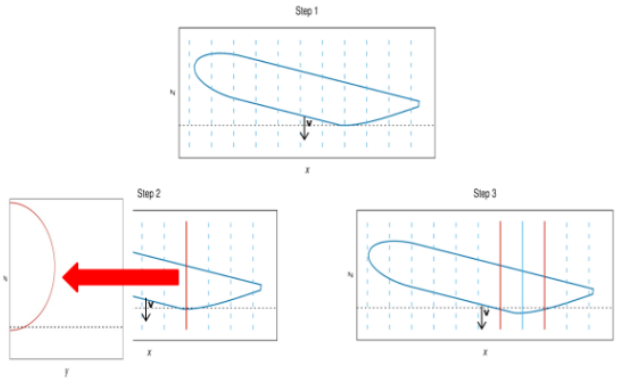

Figure 1: Multisection procedure.

The third step of the multisection procedure described above is the most critical one from a numerical point of view. It requires paying particular attention to the choice of the initial discretization of the new activated section. Indeed, in this work, during the firsts numerical test on the multisection procedure, it was observed that an inadequate discretization does not allow the formation of the jet and the evolution of the solution. This critical aspect is similar to what was observed in [9] for the water entry of an asymmetric body. In that case, the criticality was the correct definition of the initial discretization, in particular the choice of the amplitude of the first panel on the two sides of the free surface. To overcome this criticality, in [9] the initial discretizzation was defined by considering the relationship on the velocity singularity at the intersection point between the body contour and the free surface

$$u_z \propto \sigma r^{\sigma-1}, \quad \sigma = \frac{\pi}{2(\pi-\beta)}, \tag{1}$$

where r is the distance from the intersection point (*i.e.* the half width of the firsts panel on the free surface, $r = dx/2$) and β is the deadrise angle. Thus fixing the amplitude of the first panel on one side, the amplitude of the first panel on the other side is chosen to have the same order of the vertical velocity at the two intersection points. In this way, the discretization guarantees the formation of the jet on both sides of the body and the evolution of the solution [9]. In this paper, in order to define the size of the first panel for the new activated section, the relationship (1) is coupled with the Courant number, C,

$$C = \frac{udt}{dx}, \tag{2}$$

used to determine the time step dt. In equation (2) u and dx are the flow velocity and the amplitude of the panel, respectively. Setting $dx = 2r$, considering $u \simeq u_z$ at the initial step of new activated section and being dt governed by the previous activated sections, the following relationship is proposed for the choice of the first panel amplitude of the new activated section

$$dx = \left(\frac{\sigma 2^{\sigma-1} dt}{C}\right)^{1/(2-\sigma)}. \tag{3}$$

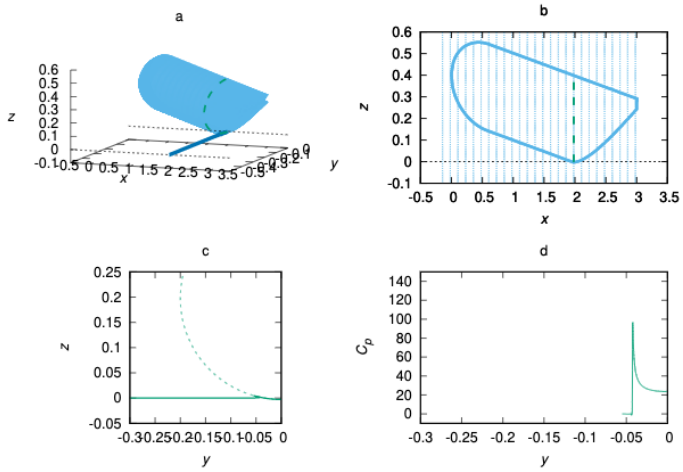

Figure 2: Overview at t=0.006s. a) 3D view. b) x-z plane: the dashed line represents the activated section. c) y-z plane: free surface (continue line) and 2D section (dashed line). d) pressure coefficient distribution acting on the activated section.

3 WATER ENTRY OF A SCALED FUSELAGE

A simple drop test case of a scaled fuselage has been chosen to verify the implemented procedure. The body is characterized by circular cross sections and impacts the water with a decelerated vertical velocity. At the beginning of the fuselage water entry, only the first fixed section is activated, which is represented by a green dashed line in figures 2a-b, where the fuselage on a global 3D view and on the x-z plane are respectively shown at time $t = 0.006s$. The light blue dashed lines in figure 2b represent the equally spaced vertical space-fixed cross planes introduced. The corresponding 2D water entry problem of the first activated section is solved and the results in terms of free surface shape and pressure coefficient distribution are depicted in figures 2c-d: as the solution is symmetrical, only the results on the y-negative side of the domain are shown. The flow rises along the body contour and a thin jet is formed (see figure 2c); moreover, the pressure coefficient on the wetted area is characterized by a peak just behind the jet root (see figure 2d). At a later time instant, $t = 0.027s$, the wetted area of the whole entering fuselage expanded and the second section has been activated: it is represented by a magenta dashed line in figures 3a-b. Also for the new activated section the corresponding 2D water entry problem is computed providing the free surface configuration and the pressure acting along the 2D section. Results in terms of the free surface shape and the pressure coefficient distribution for the two activated sections at time $t = 0.027s$ are shown in figures 3c-d. In the first one, green curves, the flow has continued rising the body contour and the pressure has decreased due to both the body deceleration and the increase of the local jet angle at the jet root. In the second one, magenta curves, a thin jet has been formed and a peak of pressure occurs at the jet root. The same behaviour in terms of free surface evolution and pressure coefficient distribution, can be observed by following other sections activated later, which will be shown during the workshop, thus highlighting that the algorithm in equation (3) works well.

4 CONCLUSION

The vertical water impact of a scaled fuselage with decelerated entry velocity has been presented. The problem was approximately studied with a multisection procedure exploiting a 2D fully non-linear potential flow solver based on a hybrid BEM-FEM approach. The test has shown that the formula for defining the initial discretizzation of the new activated sections works reasonably well. Indeed, in each section the jet is formed and the simulation updates as

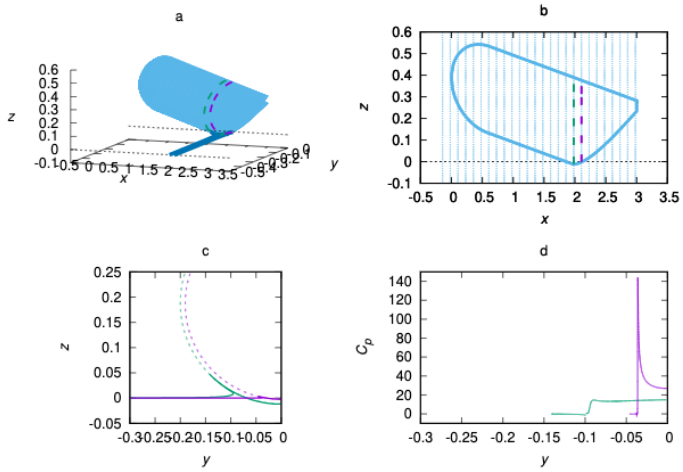

Figure 3: Overview at t=0.027s. a) 3D view. b) x-z plane: the dashed lines represent the activated sections. c) y-z plane: free surface (continue line) and 2D section (dashed line). d) pressure coefficient distribution acting on the activated sections.

expected, and the 2D solver provides, for each activated section, a hydrodynamics description in terms of free surface shape evolution and pressure distribution along the wetted area.

REFERENCES

[1] Iafrati, A., and Grizzi, S. 2019. *Cavitation and ventilation modalities during ditching.* Physics of Fluids 31(5), 052101.

[2] Iafrati, A., Grizzi, S., and Olivieri, F. 2021. *Experimental Investigation of FluidâStructure Interaction Phenomena During Aircraft Ditching.* AIAA Journal 59(5).

[3] Climent, H., Viana, J., Sanchez Iglesias, F., and Espinosa de los Monteros, J. Comparative analysis of different methods to compute ditching loads. In 4^{th} *Aerospace Structural Impact Dynamics International Conference* (4-6 June, Madrid, Spain, 2019).

[4] Iafrati, A., and Broglia, R. Hydrodynamics of planing hulls: a comparison between RANS and $2D + t$ potential flow models. In 27^{th} *Symposium on Naval Hydrodynamics* (5-10 October, Seoul, Korea, 2008), pp. 795–813.

[5] Sun, H., and Faltinsen, O. M. 2011. *Dynamic motions of planing vessels in head seas. Journal of Marine Science and Technology 16*, 168–180.

[6] Battistin, D., and Iafrati, A. 2004. *A numerical model for the jet flow generated by water impact. Journal of Engineering Mathematics 48*, 353–374.

[7] Iafrati, A., and Battistin, D. Hydrodynamics of water entry in presence of flow separation from chines. In 8^{th} *International Conference on Numerical Ship Hydrodynamics* (22-25 September, Busan, Korea, 2003).

[8] Del Buono, A., Iafrati, A., Bernardini, G., and Tassin, A. 2021. *Water entry and exit of 2D and axisymmetric bodies. Journal of Fluids and Structures 103*, 103269.

[9] Iafrati, A. Hydrodynamics of asymmetric wedges impacting the free surface. In *European Congress on Computational Methods in Applied Sciences and Engineering, ECCOMAS 2000* (11-14 September, Barcelona, Spain, 2000).

Numerical investigation of the survivability of a wave energy converter

Haoyu Ding*, Jun Zang
Centre for Infrastructure, Geotechnical and Water Engineering, Department of Architecture and Civil Engineering, University of Bath, BA2 7AY, U.K.
*E-mail: hd484@bath.ac.uk

HIGHLIGHTS

The survivability of a wave energy converter (WEC) buoy is investigated numerically in this research. Various wave conditions with varying wave heights and wave steepness, including regular waves and focussed waves are considered. Both laminar flow and turbulence flow solvers are used to examine the performance, efficiency and accuracy in computing motion responses of and forces on the wave energy devices. Surge decay of the WEC buoy and results of different regular waves interacting with the WEC buoy are presented. A focused wave is generated by OpenFOAM as an extreme wave condition aiming to conduct further survival investigation on the WEC system.

1 INTRODUCTION

The research on wave energy convertors (WECs) has attracted great interests, however, there are still many challenges remaining in the development of effective, reliable and economically viable WECs. Because WECs are always exposed to the harsh marine environments, survivability under extreme marine environments that cause extreme loads and large responses is one of the challenges that are needed to be addressed. To assess and analyse the survivability of WECs, identifying survival conditions, quantifying loadings and responses of WECs and characterising the pressure and velocity field of WECs under survival conditions are required. Numerical modelling is an efficient and feasible option to meet these requirements and carry out a series of test cases for WEC systems with different incident wave conditions. In addition, the numerical modelling tools for analysing WEC survivability should have the capability of dealing with breaking waves, large free surface deformations and large motion responses. OpenFOAM® has been proved to be an accurate and mature viscous flow model for simulating wave-structure interactions even under violent waves [1]. This research aims to apply OpenFOAM® to investigate the survivability of a WEC system as part of a joint EPSRC project.

2 NUMERICAL METHOD

For this survival study, large motion responses of floating WEC buoy may occur in extreme wave conditions. Thus, the application of an overset mesh can enhance the capability of OpenFOAM models for simulating large amplitude motions. The solver, *overInterDyMFoam*, is employed for dynamic mesh to simulate the interactions between fluid and floating structure on overset mesh. Waves are generated and dissipated by using the relaxation-based wave generation toolbox *waves2Foam* proposed in [2]. The Navier-Stokes equations, which is introduced below, are utilised for *interFOAM* to describe the two-phase flow. These equations are written as a mass conservation equation and momentum equation by Newton's second law, which are showed below respectively:

$$\frac{\partial \rho}{\partial t} + \nabla \cdot (\rho \mathbf{u}) = 0 \tag{1}$$

$$\frac{\partial \rho \mathbf{u}}{\partial t} + \nabla \cdot (\rho \mathbf{u}\mathbf{u}^T) = -\nabla P - (\mathbf{g} \cdot \mathbf{x})\nabla \rho + \nabla \cdot (\mu \nabla \mathbf{u}) + \sigma_t k_\gamma \nabla \gamma \tag{2}$$

where $\mathbf{u} = (u, v, w)$ is the flow velocity vector, ρ is the density of fluid, $\mathbf{x} = (x, y, z)$ is the Cartesian coordinate vector, P is the pressure in excess of the hydrostatic part, $\mathbf{g}$ is the acceleration due to gravity, μ refers to the dynamic viscosity, σ_t and k_γ are the surface tension coefficient and the surface

curvature, respectively. When water waves are simulated, both water and air are solved simultaneously by Eq. 1 and 2.

To track the shape and position of the free surface, the volume of fluid (VOF) method has been employed in OpenFOAM®. The transport equation of the VOF field can be yielded as:

$$\frac{\partial \gamma}{\partial t} + \nabla \cdot (\vec{U}\gamma) = 0 \tag{3}$$

Where, γ is the volume fraction. $\gamma = 0$ is for air, 1 is for water and intermedia value is for the mixture of two fluids at the interface. This equation shows the relationship between the velocity field and γ in each cell. While, in order to keep tracking accurate free surface, an additional convective is included in the transport equation to provide a sharper interface resolution. The velocity field is modelled by corresponding gas and liquid velocities denoted by $\vec{U}_{\mathrm{g}}$ and $\vec{U}_{\mathrm{l}}$, respectively. The velocity field can be yielded by weighed averages as $\vec{U} = \gamma\vec{U}_{\mathrm{l}} + (1-\gamma)\vec{U}_{\mathrm{g}}$. According to this equation for velocity field, the new transport equation of VOF can be written as:

$$\frac{\partial \gamma}{\partial t} + \nabla \cdot (\vec{U}\gamma) + \nabla[\vec{U}_r\gamma(1-\gamma)] = 0 \tag{4}$$

Where $\vec{U}_r = \vec{U}_{\mathrm{l}} - \vec{U}_{\mathrm{g}}$. In the simulation of OpenFOAM®, two immiscible fluids are considered as one effective fluid throughout the flow domain. The physical properties, including density and dynamic viscosity, can be denoted as weighed averages by using of volume fraction γ.

$$\phi = \gamma\phi_{water} + (1-\gamma)\phi_{air} \tag{5}$$

Based on this method, these physical properties can be equal to the properties of each fluid in their corresponding occupied regions and varying only across the interface.

3 NUMERICAL SETUP

A WEC structure under development by the Swedish company CorPower Ocean has been investigated in [3] by a series of tank tests. The WEC buoy is selected in this research as part of an EPSRC joint project for the numerical investigations on the survivability of WEC structures. Figure 1 shows the buoy shape and the dimension of the WEC buoy in a full scale. A laboratory model scale of 1:16 was chosen in [3]. To compare with the experimental results directly, the numerical model scale used in this research is also selected to be 1:16.

In the numerical wave tank, water depth is 3.125 m, which follows the setup in the experiments. The WEC buoy is restrained by a vertical mooring line which is attached to the bottom of the WEC buoy and connected to a fixed point at the depth of 3.09 m. A pretensioned force of the mooring line in the vertical direction (the direction of z-axis in Figure 1(b)) is applied on the WEC buoy, and the pretensioned force equals to 515 N at the equilibrium position of the WEC buoy. The total mass of the buoy is 19.1 kg. The axial stiffness of the mooring line is set to 202 N/m.

A cross-section of the numerical wave tank from side view is shown in Figure 2(a). The mesh around free surface boundary and around the WEC buoy are refined from the background mesh, where overset mesh is applied in this research. Figure 2(b) shows the cylindrical overset mesh domain around the WEC buoy, which will have the same movement as the floating buoy during the numerical simulations. And the background mesh shown in Figure 2(a) is static mesh, which will be kept fixed during the simulations. The data information is transferred between the background mesh and the overset mesh. In this way, the deformation of mesh in traditional dynamic mesh can be avoided and the capacity of numerical wave tank to large amplitude motions can be enhanced.

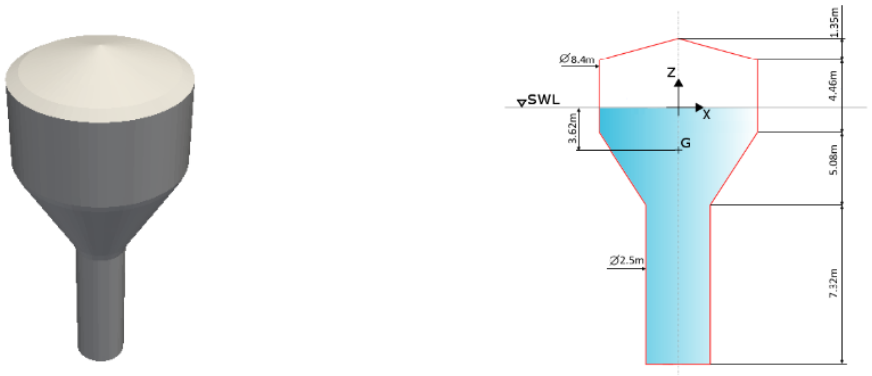

(a) (b)

Figure 1: (a) illustration of a WEC buoy shape and (b) dimension of the WEC buoy in real scale.

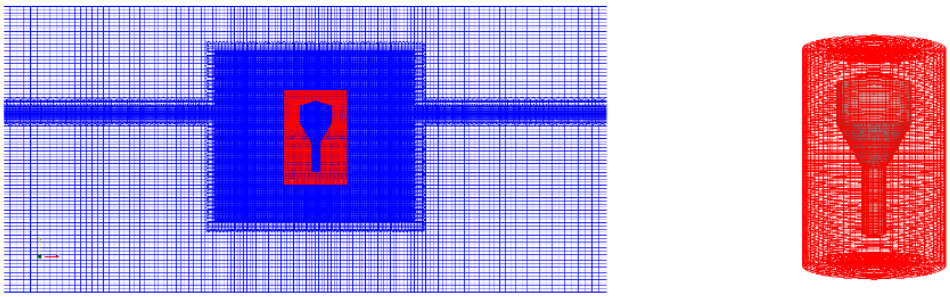

(a) (b)

Figure 2: (a) one cross-section of the numerical wave tank in OpenFOAM from side view to show the mesh around the WEC buoy, (b) overset mesh around the WEC buoy.

3 RESULTS

Surge decay of the WEC buoy with a mooring line restraint are simulated first and compared with experimental results to validate the numerical prediction of motion responses. The axial stiffness of mooring line is 202 N/m in the experimental scale in [3]. In the surge decay test, the initial position of the WEC buoy is 0.1 m away from the equilibrium potion in the horizontal direction and the mooring line gives a restoring force in surge. Figure 3 shows the comparison of the surge decay between numerical results and experimental results, which shows an agreement. Both numerical model and physical experiment have predicted the resonance period of ~ 4 s for surge in this setup. The mooring line simulated in our numerical model is considered as a linear spring, there may be differences between the linear spring in the numerical model and the physical experiment. Thus, the buoy simulated by the numerical model decays slightly faster than that in the experiment. While the differences of the surge decay amplitudes in Figure 3 between numerical results and experimental results are minor. In general, the numerical model shows a good performance on representing the motion of this WEC buoy.

Some test cases with regular waves interacting with the WEC buoy are carried out, and the surge and heave response are presented in Figure 4(a). Figure 4(a) shows the surge and heave response amplitude operator (RAO) as a function of *kh*, where RAO = amplitude of response / incident wave amplitude, *k* is wave number, *h* is water depth and *kh* is employed to denote different incident wave conditions. The heave RAO at *kh* = 2.52 is larger than the values of *kh* = 1.53 and 5.59. While the surge RAO in this wave condition keeps increasing with the decrease of *kh*, and the surge RAO of *kh*

from 2.52 to 1.53 increases significantly faster than that of *kh* from 5.59 to 1.53. It is obvious that the response of the WEC buoy is sensitive to the changes of incident wave conditions. To assess the survivability of the WEC buoy further, extreme wave conditions are also generated in the numerical model to simulate the interactions between the WEC buoy and extreme waves. The focused waves are applied for the short-term survival investigations in [1]. This research also utilises the focused waves for further survival investigations on this WEC buoy. Figure 4(b) shows a focused wave generated in the numerical model by New Wave theory and based on JOWSWAP spectrum. The significant wave height (H_s) is 0.55 m, the peak period (T_p) is 2.75 s and the peak-enhancement factor (γ) is 5 in Figure 4(b).

Further results on the WEC buoy interacting with this extreme wave condition and a range of varying wave conditions will be presented during the workshop.

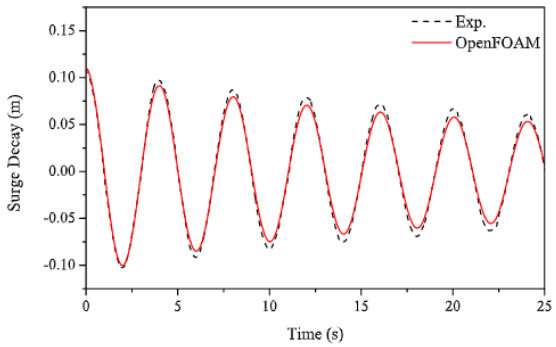

Figure 3: comparisons between OpenFOAM results and experimental results of surge decay of the WEC buoy in time histories.

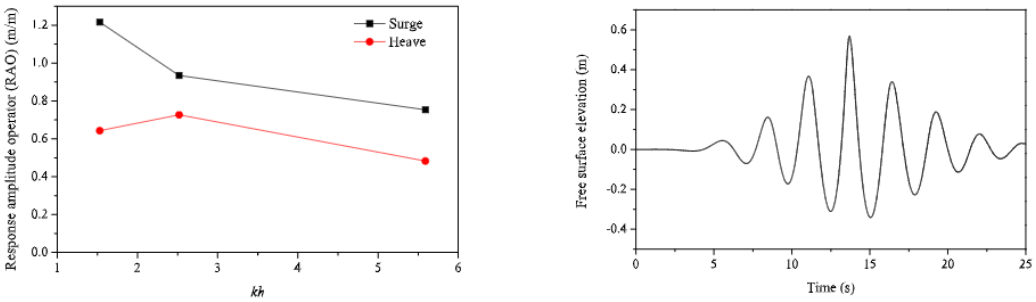

Figure 4: (a) Surge and heave response amplitude operator as a function of dimensionless wave number, *kh*, (b) free surface elevations of a focused wave generated in OpenFOAM numerical wave tank in time histories.

REFERENCES

[1] Ransley, E.J., Greaves, D., Raby, A., Simmonds, D., Hann, M., 2017. *Survivability of wave energy converters using CFD*. Renewable Energy, 109, 235-247.
[2] Jacobsen, N.G., Fuhrman, D.R., Fredsøe, J., 2012. *A wave generation toolbox for the opensource CFD library: OpenFoam®*. International Journal of Numerical Method Fluids, 70, 1073-1088.
[3] Todalshaug, J.H., Ásgeirsson, G.S., Hjálmarsson, E., Maillet, J., Möller, P., Pires, P., Guérinel, M., Lopes, M., 2016. *Tank testing of an inherently phase-controlled wave energy converter*. International Journal of Marine Energy, 15, 68-84.

Generalizing the optimal axisymmetric point-absorber wave energy converter to irregular waves

Emma C. Edwards[1,2*], Martyn Hann[1], Deborah Greaves[1], Dick K. P. Yue[2]
[1] School of Engineering, Computing and Mathematics, University of Plymouth, Plymouth, UK
[2] Mechanical Engineering, Massachusetts Institute of Technology, Cambridge, MA, USA
*emma.c.edwards@plymouth.ac.uk

HIGHLIGHTS

We extend analysis which found the optimal shape of an axisymmetric point-absorber wave energy converter for a monochromatic wave, called $\mathcal{S}_O$, to irregular waves. We show that as the incident wave spectrum width increases, the optimal resonant wavenumber for $\mathcal{S}_O$ decreases and the optimal power take-off coefficient increases.

1 INTRODUCTION AND THEORY

In [1], we perform an optimization of geometry of an axisymmetric point-absorber wave energy converter (WEC), in which we assume a monochromatic unidirectional incident wave, all within the context of linearized potential theory. The optimization framework involves ensuring maximum power (derived in [2]), specifying practical motion constraints and then minimizing surface area as a proxy for cost. We carry out a nonlinear optimization for a broad range of geometries for four different constraint regimes, for the problem of a WEC moving and extracting energy in the heave-mode only, as well as the full 3D problem of a WEC moving and extracting energy in heave, surge and pitch. In this paper, we focus on the shape that results from the heave-only problem, where the heave motion is constrained to be no more than three times the incident wave amplitude, and the draft of the body times the wavenumber over the heave motion is required to be larger than 0.1. This shape, which we call $\mathcal{S}_O$, is shown in figure 1.

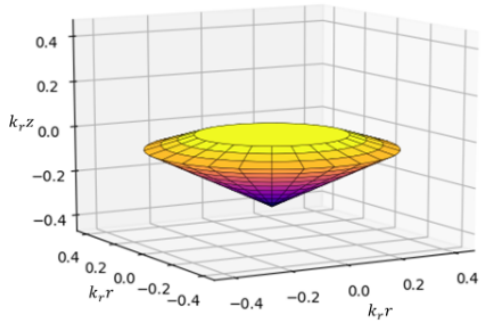

Figure 1: Shape $\mathcal{S}_O$, the optimal shape for an axisymmetric heaving WEC [1]

In this paper we extend the analysis to irregular waves. Instead of performing a full new optimization, we assume the shape to be $\mathcal{S}_O$, and we develop a methodology to determine how the optimal properties of $\mathcal{S}_O$ depend on the incident sea-state, described by a spectrum. As shown in figure 1 and described in [1] and [3], geometric descriptions of $\mathcal{S}_O$ are nondimensionlized by incident resonant wavenumber k_r. In this paper, we will determine what k_r of $\mathcal{S}_O$ should be to maximize power given an incident spectrum, and how this depends on spectrum width and shape. Specifically, this tells us how the optimal size of $\mathcal{S}_O$ depends on the incident sea state.

For regular waves, there is a known expression for the optimal power take-off (PTO) coefficient ([2], [3]), but for irregular waves there is no such expression. Therefore, we also look in this paper how the optimal PTO coefficient depends on spectrum width and shape.

We assume linear potential flow, deep water, heave-only motion, and a PTO modeled as a linear damper with damping coefficient β_{33}. The incident sea state is assumed unidirectional. We consider three types of incident spectrum. The first, a top-hat spectrum, is described by

$$S_{TH}(k) = \begin{cases} 1/(2\delta), & \text{if } k_m - \delta < k < k_m + \delta \\ 0, & \text{otherwise,} \end{cases} \tag{1}$$

where k_m is the mean wavenumber. The second, a Gaussian spectrum, is described by

$$S_G(k) = \frac{1}{\sigma\sqrt{2\pi}} \exp\left(\frac{-1}{2}\frac{(k-k_m)^2}{\sigma^2}\right), \tag{2}$$

where σ is the standard deviation. Finally, the Bretschneider spectrum is described by

$$S_B(k) = \frac{5}{16}\frac{k_m^2}{\sqrt{k^5 g}} H_S^2 \exp\left(\frac{-5k_m^2}{4k^2}\right), \tag{3}$$

where H_S is the significant wave height, and k_m is the modal wavenumber. We define $[f]^S \equiv \int f(k)S(k)dk$. To quantify the extractable power, given an incident spectrum $S(k)$, we look at the 'spectrum capture width,'

$$W^S = [P(\beta_{33})]^S / [\Pi]^S, \tag{4}$$

where $P(k, \beta_{33})$ is extractable power at wavenumber k with PTO coefficient β_{33} and $\Pi(k)$ is incident power per unit crest-length at wavenumber k. Note that β_{33} cannot change for different wavenumbers. To compare PTO coefficient with the optimal value for a monochromatic wave, we define

$$\beta'_{33} = \frac{\beta_{33}}{B_{33}(k_r)}. \tag{5}$$

For the top-hat spectrum (equation 1), the spectrum width, Δ, is measured by half-width of the spectrum, $\delta/2$, and for the Gaussian spectrum (equation 2), Δ is measured by the half-width at half-max. We nondimesionalize Δ, k_r and W^S by mean or modal wavenumber k_m.

We define $\mathcal{W}$ to be the maximum $k_m W^S$ for a given β'_{33} and spectrum, and $\mathcal{K}$ to be the optimal k_r/k_m that gives that $\mathcal{W}$. Furthermore, we define β'^*_{33} to be the optimal value of β'_{33} for a given spectrum, with $\mathcal{W}^*$ being the corresponding maximum $\mathcal{W}$ and $\mathcal{K}^*$ the corresponding optimal $\mathcal{K}$. We determine how $\beta'^*_{33}, \mathcal{K}^*$ and $\mathcal{W}^*$ change with different shape (type) and width, Δ/k_m, of spectra.

2 RESULTS AND DISCUSSION

Figures 2 a) and b) show that the optimal resonant wavenumber $\mathcal{K} = k_r/k_m$ decreases as Δ/k_m increases, for both the top-hat and Gaussian spectra. Because $\mathcal{K} < 1$, we see that for wider spectra the optimal WEC is not in resonance at the mean/modal wavenumber of the spectrum. Figure 2 c) and d) show that there is an optimal β'_{33} for each spectra, which increases as Δ/k_m increases. That is, the optimal PTO coefficient is larger for wider spectra. Figure 3 shows that, as Δ/k_m increases, $\mathcal{W}^*$ a) increases for top-hat spectra but b) stays approximately constant for Gaussian spectra. Furthermore, figures 3 a) and b) show that $\mathcal{K}^*$ decreases and β'^*_{33} increases with increasing Δ/k_m for both types of spectra.

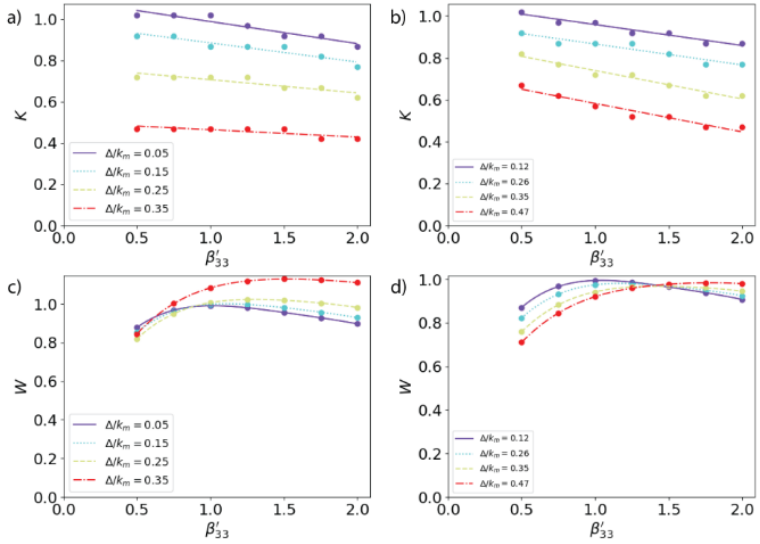

Figure 2: The optimal $\mathcal{K} = k_r/k_m$ as a function of β'_{33}, for different Δ/k_m values for (a) the top-hat spectra, and (b) Gaussian spectra, and the corresponding $\mathcal{W} = k_m W^S$ values, for (c) the top-hat spectra and (d) Gaussian spectra

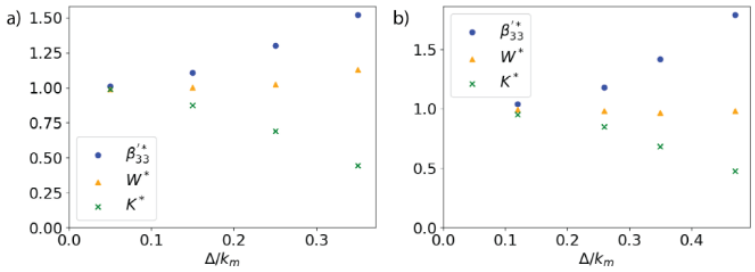

Figure 3: The optimal $\beta_{33}{}'*$, and corresponding maximum $\mathcal{W}^*$ and optimal $\mathcal{K}^*$, as functions of Δ/k_m for (a) the top-hat spectra and (b) the Gaussian spectra

And finally, we consider a more realistic incident sea state by considering the Bretschneider spectrum (equation 3). The Bretschneider spectrum differs from the other two spectra we consider because: (i) it is not symmetric– the spectrum is wider above the peak than below it, and (ii) its width is not changeable. We calculate that the width below k_m at half-max is $\Delta/k_m = 0.37$, and above k_m it is $\Delta/k_m = 0.89$. For the Bretschneider spectrum we calculate $\beta'^*_{33} = 1.5, \mathcal{K}^* = 0.84$, and $\mathcal{W}^* = 0.74$. This extractable power is less and the optimal resonant wavenumber is larger than an equivalently wide symmetric spectrum. We hypothesize that this is because of the asymmetry of the spectrum. Since there is not as much energy at small wavenumbers for the Bretschneider spectrum, having a smaller $\mathcal{K}$ will not be as beneficial, and thus the resonant wavenumber should be close to the modal wavenumber.

When determining $\mathcal{S}_O$ in [1], we apply constraints (following from [4]) on (i) the body heave body motion ξ_3 relative to the incident wave amplitude A: $\alpha_3 < \alpha_0$, where $\alpha_3 = |\xi_3|/A$ and α_0 is the design constraint, and (ii) wavenumber k times draft at the centerline H relative to α_3: $\epsilon_3 > \epsilon_0$, where $\epsilon_3 = kH/\alpha_3$ and ϵ_0 is the design constraint.

For irregular waves, the 'spectrum motion constraint' becomes $\alpha_3^S < \alpha_0^S$ where

$$\alpha_3^S = \left(\left[(|\xi_3|/A)^2 \right]^S / [1]^S \right)^{1/2}, \tag{6}$$

and α_0^S is the design constraint. The 'spectrum steepness constraint' becomes $\epsilon_3^S > \epsilon_0^S$, where

$$\epsilon_3^S = \left([1]^S / \left[\left(\frac{|\xi_3|/A}{kH} \right)^2 \right]^S \right)^{1/2}, \tag{7}$$

and ϵ_0^S is the design constraint. For the Bretschneider spectrum, using the optimized parameters of $\mathcal{K}^* = 0.84$ and $\beta_{33}^{'*} = 1.5$, we calculate $\alpha_3^S = 1.62$ and $\epsilon_3^S = 0.19$. If $\alpha_0^S = 3$ and $\epsilon_0^S = 0.1$, the calculated values clearly adhere to the spectrum motion and steepness constraints. If stricter motion constraints were desired, the methodology described in this paper is general and could therefore be applied to a different shape.

3 CONCLUSION

In a recent paper, we perform an optimization of the geometry of an axisymmetric point-absorber WEC. In this paper, we extend analysis on the optimized shape, called $\mathcal{S}_O$ and shown in figure 1, to irregular waves. We consider top-hat and Gaussian spectra to investigate how width and shape of spectrum influences the optimal resonant wavenumber of $\mathcal{S}_O$ and optimal PTO coefficient, and we also consider a Bretschneider spectrum to study a more realistic sea-state. We show that as the spectrum width increases, the optimal resonant wavenumber of $\mathcal{S}_O$ decreases and the optimal PTO coefficient increases. Compared to the idealized spectra, the extractable power for the Bretschneider spectrum is less, and the optimal resonant wavenumber is larger than an equivalently wide symmetric spectrum.

These conclusions give us insights into WEC design. Namely, when designing a WEC in irregular waves, it should be larger than if it was in resonance at the peak wavenumber, and the size increases with wider spectra. The PTO should not be tuned to be equal to the radiation damping at resonance, as was the case for regular waves, and should be larger with wider spectra. When designing a WEC for a particular location the spectrum shape is an important part of the design consideration. While we begin with the optimized shape found from regular waves, our methodology of determining size and PTO of the WEC is general and could be used for any WEC shape and incident spectrum. It would be interesting to perform a full optimization of the shape in irregular waves to compare the result to $\mathcal{S}_O$. Finally, this work assumes linear potential flow, so physical modelling and/or higher-order methods (i.e. [5]) should be used for further analysis.

REFERENCES

[1] Edwards, E. C. and Yue, D. K. P. Optimisation of the geometry of axisymmetric point-absorber wave energy converters. *J. Fluid Mech.*, 933, 2022.

[2] Evans, D. V. A theory for wave-power absorption by oscillating bodies. *J. Fluid Mech.*, 77(1):1–25, 1976.

[3] Edwards, E. C. *Optimization of the Geometry of Axisymmetric Point-absorber Wave Energy Converters.* PhD thesis, Massachusetts Institute of Technology, 2020.

[4] Evans, D. V. Maximum wave-power absorption under motion constraints. *Appl. Ocean Res.*, 3(4):200–203, 1981.

[5] Michele, S., Renzi, E., and Sammarco, P. Weakly nonlinear theory for a gate-type curved array in waves. *J. Fluid Mech.*, 869:238–263, 2019.

Reduced Order Modelling for Dispersive and Nonlinear Water Wave Modelling

F. G. Eroglu [1,3,*], **N. T. Mücke**[2,4], **A. P. Engsig-Karup**[3]

[1]Dept. of Mathematics, Faculty of Science, Bartın University, 74110 Bartın, Turkey
[2]CWI, Science Park 123, 1098 XG Amsterdam, Netherlands
[3]Dept. of Appl. Math. and Computer Science, Technical University Denmark, Lyngby, Denmark
[4]Mathematical Institute, Utrecht University, Utrecht, Netherlands
[*]Corresponding author, e-mail: fguler.eroglu@gmail.com

1 INTRODUCTION

This abstract describes our recent work on employing reduced-order modelling (ROM) to solve fully nonlinear potential flow equations (FNPF) to achieve faster turn-around time than a full order model (FOM) based on the spectral element method (SEM) [1]. We propose a POD-Galerkin based model-order reduction approach to reduce the cost of the solve step in the Laplace problem. If repeated simulations are needed for applications, e.g. in optimization loops with varying parameters, it may become prohibitively expensive to run many FOM simulations in practical times. Reduced-order modelling techniques were introduced to eliminate the time-consuming behaviour of high-dimensional numerical methods and reduce the load on computational resources without compromising overall accuracy. The proper orthogonal decomposition (POD) method is one of the most effective snapshot-based reduced-order modelling techniques and is considered in this work. The basic idea of using POD is to generate a low-dimensional model with few degrees of freedom using the most dominant features of the system, thereby significantly reducing the computational time and cost.

2 MATHEMATICAL FORMULATION

We consider the Eulerian FNPF model, cf. complete derivation in [2]. Mass continuity is expressed in terms of the Laplace equation for the scalar velocty potential ϕ within the fluid volume (Ω) subject to a free surface condition (Γ^{FS}) and impermeable walls and sea floor (Γ^{b})

$$\phi = \tilde{\phi}, \quad z = \eta \quad \text{on} \quad \Gamma^{FS}, \tag{1a}$$

$$\nabla^2 \phi = 0, \quad -h(x,y) < z < \eta \quad \text{in} \quad \Omega, \tag{1b}$$

$$\mathbf{n} \cdot \nabla \phi = 0, \quad z = -h(x,y) \quad \text{on} \quad \Gamma^{b}, \tag{1c}$$

and subject to the nonlinear free surface boundary conditions in the time domain (T)

$$\frac{\partial \eta}{\partial t} = -\boldsymbol{\nabla}\eta \cdot \boldsymbol{\nabla}\tilde{\phi} + \tilde{w}(1 + \boldsymbol{\nabla}\eta \cdot \boldsymbol{\nabla}\eta) \qquad \text{in} \quad \Gamma^{\mathrm{FS}} \times T, \tag{2a}$$

$$\frac{\partial \tilde{\phi}}{\partial t} = -g\eta - \frac{1}{2}\left(\boldsymbol{\nabla}\tilde{\phi} \cdot \boldsymbol{\nabla}\tilde{\phi} - \tilde{w}^2(1 + \boldsymbol{\nabla}\eta \cdot \boldsymbol{\nabla}\eta)\right) \quad \text{in} \quad \Gamma^{\mathrm{FS}} \times T, \tag{2b}$$

where the '$\sim$' symbol is used for free surface (FS) variables. The equations are widely used to describe both free surface flow as well as wave-structure interaction and have been subject to many investigations for decades when it comes to the design of flexible and efficient numerical schemes. While the numerical discretization of FNPF equations is well-established, in recent years, renewed attention has been given to make progress with CFD solvers, where FNPF models as medium fidelity models are demonstrated to be several orders of magnitude faster than CFD solvers for non-breaking wave and wave-structure simulations, and couplings of these types of solvers can be exploited for enabling high-fidelity CFD-FNPF simulations.

3 NUMERICAL DISCRETIZATION

The numerical discretization of the model equations (1) is based on the σ-transformed SEM scheme detailed in [1] (with the $\mathcal{K}$-matrix defined for the σ-formulation). The numerical scheme for the Laplace equation is given here in brevity. Find $\phi(t,x,z)$ satisfying $\mathcal{L}\phi = \mathbf{b}$, where

$$\mathcal{L}_{ij} = -\sum_{k=1}^{N^k} \int_{\Omega^{c,k}} (\mathcal{K}(\eta(t))\nabla^c N_j) \cdot \nabla^c N_i \mathrm{d}\boldsymbol{x}, \quad b_i = \sum_{s=1}^{N^s} \oint_{\Gamma^{c,s}} N_i \mathbf{n} \cdot \left(\mathcal{K}(\eta(t)) \nabla^c \left(\sum_{j=1}^{N^p} \phi_j N_j \right) \right) \mathrm{d}\boldsymbol{x}, \quad \text{(3a)}$$

for $i = 1, ..., N^p$. Here N^k is the number of elements, N^s is boundary segments, and $N^p = N^i + N^b$ is total grid points in the σ-transformed domain Ω^c. We use the decomposition

$$\mathcal{L} = \begin{pmatrix} \mathcal{L}_{bb} & \mathcal{L}_{bi} \\ \mathcal{L}_{ib} & \mathcal{L}_{ii} \end{pmatrix}, \ \phi = \begin{pmatrix} \phi_b \\ \phi_i \end{pmatrix}, \ \mathbf{b} = \begin{pmatrix} b_b \\ b_i \end{pmatrix}, \quad \mathcal{L} \in \mathbb{R}^{N^p \times N^p}, \quad \mathbf{b} \in \mathbb{R}^{N^p}, \quad \text{(3b)}$$

where the subscripts b and i correspond to the free surface boundary and the inner variables, respectively. The system is defined in terms of the unknown inner values in the modified form

$$\mathcal{L}^* \phi_i = \mathbf{b}^*, \quad \mathcal{L}^* \in \mathbb{R}^{N^i \times N^i}, \quad \mathbf{b}^* \in \mathbb{R}^{N^i}, \quad \text{(3c)}$$

where $\mathcal{L}^* = \mathcal{L}_{ii} - \mathcal{L}_{ib}\mathcal{L}_{bb}^{-1}\mathcal{L}_{bi}$ and $\mathbf{b}^* = b_i - \mathcal{L}_{ib}\mathcal{L}_{bb}^{-1} b_b$. The Laplace problem has $b_i = 0$.

4 PROJECTION-BASED MODEL ORDER REDUCTION

Now, we present the essentials of the POD setting that is used to generate a reduced basis. For further details of the method, see [3]. First, POD starts with an ensemble of snapshots, $\{\phi(x,z,t_i)\}_{i=1}^{N^S}$. This is a set of FOM solutions obtained by solving the system of equations (3), at different time instances, $t_j = 1, 2, ..., N^S$, to the Laplace problem. These are collected in a snapshot matrix

$$\mathcal{S} = [\phi_{j,1}, \phi_{j,2}, ..., \phi_{j,N^S}], \quad \mathcal{S} \in \mathbb{R}^{N^p \times N^S}. \quad \text{(4)}$$

We then seek to generate a POD basis for constructing a reduced-order system from the snapshots matrix, $\mathcal{S}$, by using the singular value decomposition (SVD), $\mathcal{S} = \mathcal{U}\Sigma\mathcal{V}^T$. The aim is to express the solution in terms of a reduced basis using the eigenvectors of the SVD such that $\phi_i^l(x,z,t) = \mathcal{V}_l \mathbf{a}(t)$. For this ansatz, we use the N^l most important modes in the reduced basis, and construct an intrusive POD-Galerkin projection of the Laplace system. This gives rise to a reduced basis system of equations in the form

$$\mathcal{L}^\dagger \mathbf{a} = \mathbf{b}^\dagger, \quad \mathcal{L}^\dagger \in \mathbb{R}^{N^l \times N^l}, \quad \mathbf{b}^\dagger \in \mathbb{R}^{N^l}, \quad \text{(5)}$$

where the system is defined from $\mathcal{L}^\dagger = \mathcal{V}_l^T \mathcal{L}^* \mathcal{V}_l$ and $\mathbf{b}^\dagger = \mathcal{V}_l^T \mathbf{b}^*$. Hence, it is possible to solve the reduced system of equations which from snapshot data learns basis functions that capture the variations in the solution with respect to time when the free surface boundary condition is changing.

Remark, the reduced system matrix (5) is dense, and hence it becomes intrinsically difficult to scale the system degree of freedom (N^p) to large-scale as is possible in a p-multigrid accelerated FNPF-SEM solver [4]. Hence, the advantage of acceleration of the FNPF-SEM solver lies in the ability to reduce the cost of simulation for certain problem sizes and parametrizations. From the solution to the linear system (5), the FOM solution is estimated $\phi_i \approx \phi_i^l$ after which the vertical free surface velocity $\tilde{w}$ is computed in the usual way from ϕ, recalling $(u, w) = (\partial_x, \partial_z)\phi$, to obtain closure in the free surface time-stepping problem (2).

5 NUMERICAL STUDIES

This section presents partial results of our numerical experiments for accelerating the FNPF-SEM solver through using POD-Galerkin for the Laplace solve step. Our first numerical experiment assesses the potential of using ROM for acceleration of the Laplace problem by considering nonlinear stream function waves. This is a relevant benchmark for nonlinear wave propagation subject to variations in the dispersion (kh) and nonlinear wave (H/L) parameters. Here $k = 2\pi/L$ is wave number, L is wave length, and H is wave height. In Figures 1a-1c, we present results of a convergence test, where a fixed spatial resolution is used with N^p =144 nodes in the mesh. The elements are quadrilaterals with expansions of polynomial order $P = 6$, meshed in terms of a single vertical layer and four elements in the horizontal direction. We vary the nonlinearity of the waves such that $H/L = 0.1, 10, 40, 70, 98$ % of the theoretical $(H/L)_{max}$. From sampling the variation of the free surface evolution across a wave period, a basis is constructed using the POD procedure in each case. More than 99% of the variation in the waves are captured with few modes ($N^l < 15$) in each case due to a strong exponential decay in the singular modes. This translates into a possible acceleration of up to about x100 times of the Laplace solve step. Similar results are given in Figures 1d-1f for a higher resolution case with a mesh

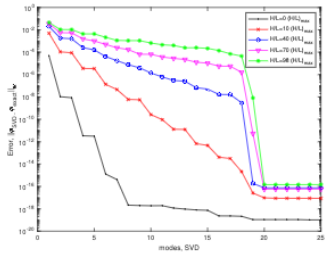

(a) Convergence tests, ϕ, $kh = 2\pi.(N_x^k, N_\sigma^k) = (4, 1)$.

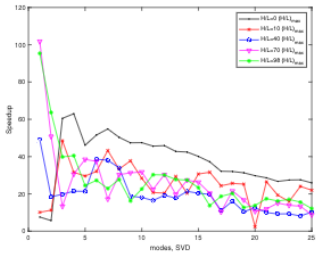

(b) Speedup estimates, $kh = 2\pi.\ (N_x^k, N_\sigma^k) = (4, 1)$.

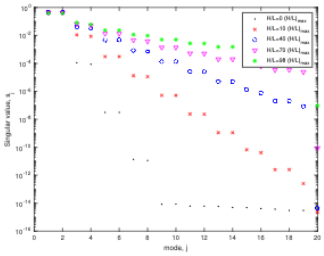

(c) Singular values, $kh = 2\pi.\ (N_x^k, N_\sigma^k) = (4, 1)$.

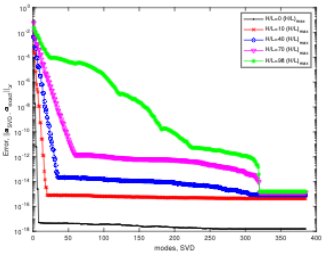

(d) Convergence tests, ϕ, $kh = 2\pi.\ (N_x^k, N_\sigma^k) = (64, 16)$.

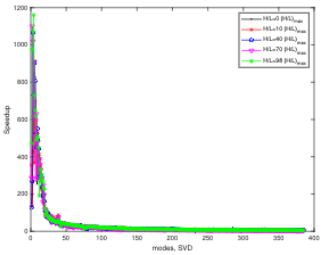

(e) Speedup estimates, $kh = 2\pi.\ (N_x^k, N_\sigma^k) = (64, 16)$.

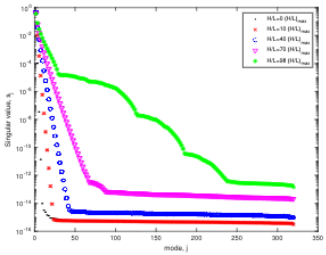

(f) Singular values, $kh = 2\pi.\ (N_x^k, N_\sigma^k) = (64, 16)$.

Figure 1

consisting of N^p =36864 nodes in a layered configuration with $(N_x^k, N_\sigma^k) = (64, 16)$ elements. The potential speedup is for this setup up to 2-3 orders of magnitude in the low accuracy tolerance level regime, and with increasing potential the more resolution in the vertical as it is most important to capture details near the free surface. The former results presented build up to testing a POD-Galerkin ROM for a more realistic case. We consider the experiments due to Beji & Battjes (1994) of harmonic generation resulting from dispersive and nonlinear waves passing a submerged bar inside a numerical wave tank in 2D as the second experiment. The setup is based on Case A of the experiments. The input wave is generated in the numerical wave tank using a stream function solution at undisturbed depth 0.4m with a wave height of 2cm and a wave period of 2.02s. In this setup, the FOM model uses a configuration

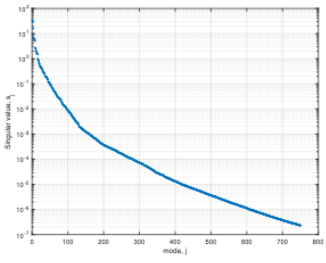

(a)

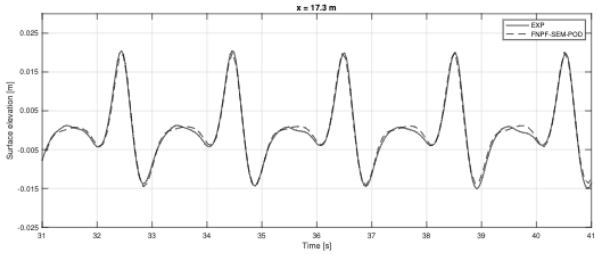

(b)

Figure 2: Harmonic generation over a submerged bar in 2D. (a) Singular values of the snapshot matrix, and (b) numerical results obtained from the FNPF-SEM-ROM model at gauge 6.

$(N_x^k, N_\sigma^k, P) = (103, 1, 6)$, and snapshots are generated by running a simulation until t_{final}=20s. The final FNPF-SEM-ROM results are obtained by then running the entire simulation until t_{final}=41s with wave generation and absorption. When the basis has been generated using a POD offline, we run the same simulation online with only N^l =500 modes in the reduced system (5). Results are presented in Figure 2b for Gauge 6 at 17.3m in the experiments using the setup from [1]. Remark, the speedup potential is currently reduced, since the computational complexity of constructing the Laplace operator is similar to FOM simulations as it is updated through a global assembly before projection at every RK stage of en ERK4 scheme for the time-integration due to the time-dependent coefficients of the σ-transformed Laplace equation (3a).

CONCLUSIONS

The results obtained from numerical experiments demonstrate that the potential speedup is influenced by both dispersion and nonlinearity parameters as expected. For the most nonlinear waves, the rank of the SVD increases, requiring more POD modes and lowering the potential speedup. However, our tests indicate a significant reduction of system size is possible in the range of linear to mildly nonlinear waves and for problems, where there is a need for significant spatial resolution in the vertical. The latter suggests a significant potential for acceleration of wave-structure problems, where the POD-Galerkin approach can be used to account also for the parametrisation of geometric features of structures.

ACKNOWLEDGEMENT

This research has been supported by TÜBİTAK (The Scientific and Technological Research Council of Turkey) with a "2219-International Postdoctoral Research Fellowship Program for Turkish Citizens" scholarship.

REFERENCES

[1] Engsig-Karup, A. P., Eskilsson, C., and Bigoni, D. 2016. *A stabilised nodal spectral element method for fully nonlinear water waves. Journal of Computational Physics 318(2)*, 1–21.

[2] Engsig-Karup, A. P., Glimberg, L. S., Nielsen, A. S., and Lindberg, O. Fast hydrodynamics on heterogenous many-core hardware. In *Designing Scientific Applications on GPUs* (2013), R. Couturier, Ed., Lecture notes in computational science and engineering, CRC Press / Taylor & Francis Group.

[3] Eroglu, F., Kaya, S., and Rebholz, L. 2017. *A Modular Regularized Variational Multiscale Proper Orthogonal Decomposition for Incompressible Flows. Computer Methods in Applied Mechanics and Engineering 325*, 350–368.

[4] Engsig-Karup, A. P., and Laskowski, W. L. 2021. *An efficient p-multigrid spectral element model for fully nonlinear water waves and fixed bodies.* International Journal for Numerical Methods in Fluids 93(9), 2823–2841.

Modelling a dam break flow in a moving reference frame

Min Gao*, Scott Draper, Lifen Chen, Hugh Wolgamot, Liang Cheng
Oceans Graduate School, The University Western Australia, Perth, WA 6009, Australia.
*Email: min.gao@research.uwa.edu.au

1 INTRODUCTION

Wave overtopping onto the deck of a vessel during severe sea conditions may cause significant damage to topside structures and/or even result in ship loss. Methods for more reliable prediction of green water loads on topside structures therefore remains a key priority for industry.

Over the last 2-3 decades a significant body of research has investigated green water loading on different types of structures placed at different locations on the deck. In some of these studies, the vessel has been held fixed for simplicity. However, it has been shown that vessel motion can influence green water loads. For example, Buchner (1995) emphasized the important role of the vertical velocity of the deck on the pressure on the deck, whilst Zhu et al., (2009) analysed green water on both fixed and oscillating vessels (free in heave and pitch), and stated that the ship motion must be taken into account otherwise the green water loads would be underestimated.

These earlier works showed that vessel motion could influence green water in different ways. Motions affect (i) the general wave-structure interaction and the amount of fluid that enters onto the deck and (ii) the flow behaviours of the on-deck water. In screening of sea-states for green water loads it is straightforward to account for the effect of motions on freeboard exceedance, which is essentially (i), but there is little account taken of (ii). This latter effect could impact the accuracy of screening; events with similar freeboard exceedance but different vessel motion may result in significantly different loads.

In terms of understanding the effect of vessel motion on green water flow on deck, it is not immediately obvious if vessel motions will generally increase or decrease green water loads for the same freeboard exceedance. This is because local (upwards) accelerations of the deck are expected to increase green water flow velocity. However, these accelerations will be maximum when the vessel is displaced downwards in heave and pitch, at which point the upward slope of the pitched deck will act to slow green water. To explore this trade-off further, the present study investigates dam break flows in a moving reference frame that undergoes vessel-like motions (specifically heave and/or pitch motions). Whilst a dam break is not a perfect analogy for green water flow, many researchers have noted and demonstrated the similarities between shipped water and dam break flow (e.g. Buchner, 1995). More advanced modelling approaches could be used to explore the effect of vessel motion on green water (e.g. Greco and Lugni, 2012), but the simple dam break analogy shown in Fig. 1 is an efficient way to explore the problem.

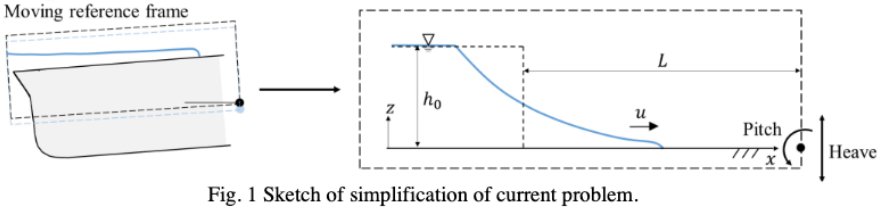

Fig. 1 Sketch of simplification of current problem.

2 PROBLEM DEFINITION AND SOLUTION

As in the classical dam break model, in this work a dam is defined in terms of its initial height h_0 located within a moving reference frame (Fig. 1). Heave displacement and pitch rotation of the reference frame containing the dam break are modelled as sinusoidal functions of time with period T_h and T_p, and amplitudes $a_h(T_h/2\pi)^2$ and $\alpha_p(T_p/2\pi)^2$, respectively. Here, a_h and α_p are the peak heave acceleration and pitch rotational acceleration, respectively. Phases of the motions ϕ_h and ϕ_p are defined relative to the time of the initial dam break. The last parameter needed to define the problem is the distance between the initial dam location and the point about which the reference frame rotates, denoted by L. Combining these parameters with the acceleration due to gravity g, leads to several non-dimensional parameters, including the normalized accelerations ($a_h/g, a_p/g = \alpha_p L/g$), periods ($T_h/(h_0/g)^{1/2}, T_p/(h_0/g)^{1/2}$) and radius of rotation L/h_0 in addition to the relative phase of the motions.

To determine practical ranges for these non-dimensional parameters a seakeeping analysis for a Floating, Production, Storage and Offloading (FPSO) unit located on the North West Shelf of Australia has been

undertaken (using the same model and sea states as those adopted in Chen et al., 2019) The results of this analysis show that in events leading to freeboard exceedance, the vertical motion at the bow due to pitch was around three times that due to heave. Taking the peak wave period to be equal to the periods of motion T_h and T_p, and the maximum freeboard exceedance to be the initial dam height h_0, the analysis indicates the following ranges: a_h/g =0.04~0.08, a_p/g =0.14~0.24, $T_h/(h_0/g)^{1/2}$ =12.5~28.2, and $T_p/(h_0/g)^{1/2}$ =15.5~28.2. With respect to ϕ_h and ϕ_p, the vessel heave and pitch at the time of maximum freeboard exceedance showed some variation, but were often associated with the time of minimum heave and pitch (resulting in negative freeboard/vertical motion); hence these can be assumed to take values that ensure minimum pitch and heave when the dam breaks. The normalised radius L/h_0 of the pitch had a mean value of about 40.

Over this non-dimensional parameter-space the dam break problem has been simulated using both CFD and the Shallow Water Equations (SWEs). In the CFD simulations, the Navier-stokes equations are solved using the *interDyMFoam* provided by an open source CFD package OpenFOAM to describe the flow motion in a moving frame. The computational domain is forced to heave and pitch with a prescribed motion and the Volume of Fluid method is used to track the free surface. In the SWE simulations, the 1D shallow water equations (Eq. 1) have been solved using the Harten Lax van Leer Riemann solver (Harten et al., 1983)

$$\frac{\partial h}{\partial t}+\frac{\partial hu}{\partial x}=0, \qquad \frac{\partial uh}{\partial t}+\frac{\partial u^2h}{\partial x}=-0.5\frac{\partial(a_z h^2)}{\partial x}+a_x h, \tag{1}$$

where u represents the depth-averaged horizontal velocity, h is the water depth and both a_z and a_x represent additional accelerations introduced by the vessel motion, including the Coriolis, centripetal and Euler components. These terms are modelled following the approach derived in Huang and Hsiung (1996).

3 SIMULATION RESULTS

Fig. 2a presents free surface profiles obtained from CFD simulations of dam break events in a fixed reference frame, and an oscillating reference frame representing relatively large vessel motion (parameters are given in caption). Results are plotted at three typical instants : $1.1(h_0/g)^{1/2}=0.05T_h=0.05T_p$, $4.39(h_0/g)^{1/2}=0.2T_h$ and $10.96(h_0/g)^{1/2}=0.5T_h$. It can be seen that the motion does not drastically alter the flow profile but does result in noticeable changes. For instance, for the moving dam break the water surface elevation reduces faster upstream of the dam (x <0) owing to the downward pitch of the vessel, whilst the upstream profile still maintains a similar run-out speed due to the increased acceleration due to motion. To investigate these changes in surface profile in more detail, Fig. 2b plots the horizontal momentum flux for both dam break scenarios. This momentum flux has been calculated using a set of numerical gauges orientated normal to the bed and spaced $0.1h_0$ apart. It can be seen that the momentum flux for the moving dam break is different from the fixed case; at the first time instant the momentum flux is larger due to motion, whilst it is lower at the two later times. Noting that the Froude number of the flow on deck is large, the horizontal momentum flux should correlate well with the load on large structures capable of completely deflecting the flow, implying that the motion is increasing the damage potential of the dam break flow in this example.

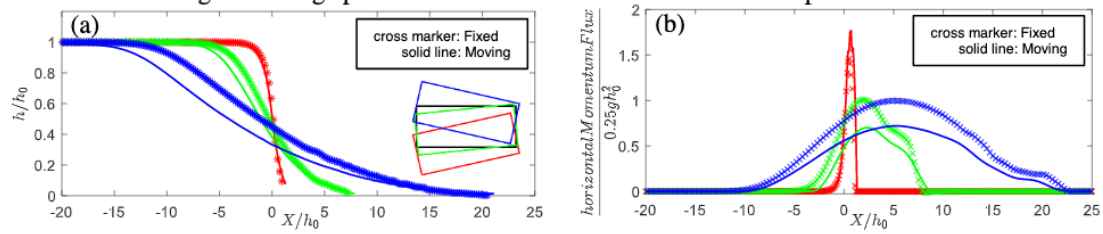

Fig. 2 Free surface profile (a) and horizontal momentum flux (b) at three instants in time (cross-referenced in Fig. 3) obtained from CFD for a fixed and representative moving reference frame with (a_h/g =0.08, a_p/g =0.24, and $T_p/\sqrt{h_0/g}=T_h/\sqrt{h_0/g}$= 21.9). Phases chosen to ensure minimum pitch and heave when the dam breaks. L/h_0 =40. A cartoon on lower left of Fig.(a) shows the position of the moving frame at three time instants and the fixed frame(black).

3.1 The evolution of momentum flux in time

A number of characteristics associated with green water flow influence load. In this abstract, we focus on momentum flux which, as noted above, is likely to be a good indication of the load on large structures. In more general scenarios, both the depth and the velocity of the flow can also be important for predicting loads. We define the maximum horizontal momentum flux in space at any time instant as the Maximum Momentum Flux (MMF). For reference, the MMF of a fixed dam break flow on a flat bed modelled using the SWEs is $0.25gh_0^2$ and is constant in time (e.g. Chanson, 2006).

The evolution of MMF calculated using CFD and the SWE solver for a heaving, pitching and combined heaving and pitching dam break is shown in Fig. 3. The MMF of a classical dam break in a fixed reference frame is also presented as a reference to distinguish the effect of vessel motion. The three example cases shown have the largest normalised acceleration across the practical ranges described in Section 2, hence they display the most evident effects of vessel motion on MMF. It can be seen that as the dam initially breaks, the MMF increases to a peak value, followed by a drop which is similar to that observed for the fixed dam break. Following this, the MMF oscillates in time owing to the heave and pitch motions which result in varying acceleration and bed slope, whilst for the fixed dam break the MMF becomes constant in time and close to the analytical estimate of $0.25gh_0^2$. Based on these observations, two typical stages in the dam break flow are identified: (i) the initial stage where the CFD result has a sharp increase in MMF followed by a rapid descent; and (ii) the later stage where the MMF fluctuates and the results from CFD and SWE agree with each other well. Across the range of parameters considered in this study, the duration of the initial stage did not vary significantly, lasting approximately $(2.7\sim3.1)(h_0/g)^{1/2}$.

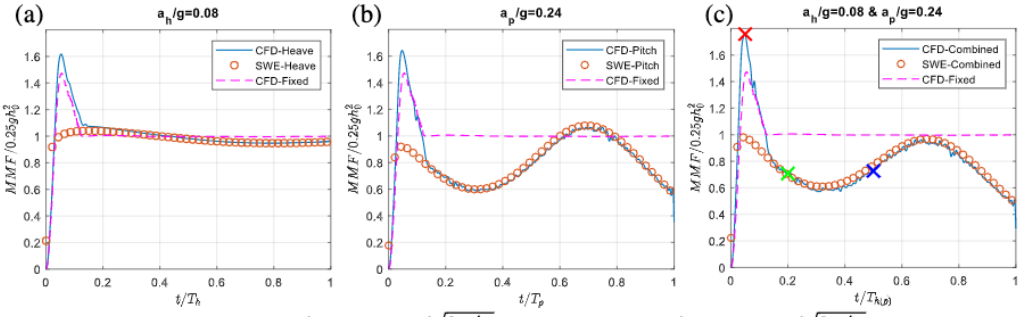

Fig. 3 Evolution of MMF for (a) heave ($a_h/g = 0.08, T_h/\sqrt{h_0/g}$= 21.9), (b) pitch ($a_p/g = 0.24, T_h/\sqrt{h_0/g}$= 21.9) and (c) combined heave and pitch with (a_h/g =0.08, a_p/g =0.24, and $T_p/\sqrt{h_0/g} = T_h/\sqrt{h_0/g}$= 21.9). Crosses indicate the time instants in Fig. 2

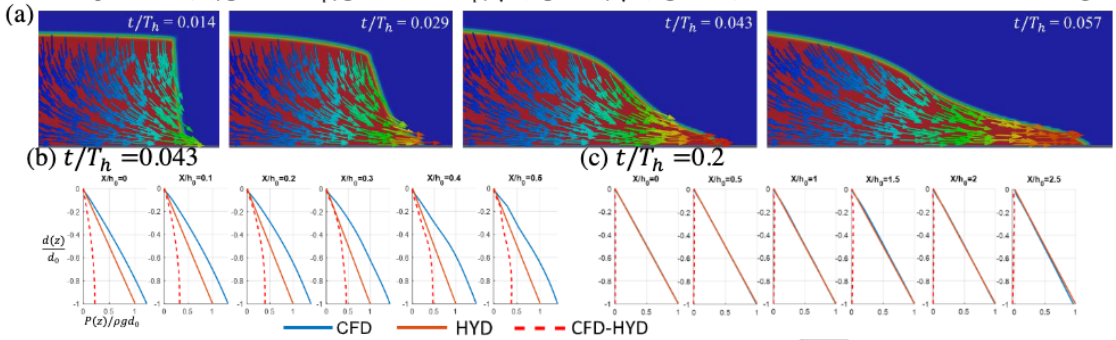

Fig. 4 (a) Velocity vectors at different times for a heaving dam break ($a_h/g = 0.08, T_h/\sqrt{h_0/g}$= 21.9). Pressure distribution with depth in (b) the initial stage ($t/T_H = 0.043$) and (c) the later stage ($t/T_H = 0.2$) at six locations for the same heave case. d_0 represents water depth on bed at that location, whilst $d(z)$ and $P(z)$ represent depth and pressure through the water column. The pressure obtained from CFD is referred as "CFD", and hydrostatic pressure is referred to as "HYD".

The results in Fig.3 are consistent with the experimental and numerical study by Stansby et al. (1998), which indicated that the analytical solution of SWEs agrees with the experimental measument only after a bore is established. The velocity vectors from CFD at a few instants in time are shown in Fig. 4a for a heaving dam break just after release. It can be seen that the vertical flow funnels into a horizontal jet which results in an increase in MMF during the initial stage of the dam break. This funnelling is associated with a non-hydrostatic pressure distribution with depth (Fig. 4b), explaining the lack of agreement with the SWEs during the initial stage. In contrast, at later times (Fig. 4c), the pressure distribution with depth becomes hydrostatic satisfying the shallow water assumption. The results from CFD and the SWEs agree well with each other at this time.

3.2 Peak MMF

The peak MMF in time provides an upper bound estimate of damage potential. This peak is plotted in Fig. 5 for heaving cases (left), pitching cases (middle) and combined heaving and pitching cases (right) for a range of normalised acceleration and period. In each plot the peak MMF has been normalized by the peak MMF of the classical dam break calculated using CFD and the phase of the motions is chosen to ensure minimum heave and pitch when the dam breaks. The assumption T_p=T_h and a_p=3a_h is used in the combined case, as suggested by the seakeeping analysis mentioned in Section 2. Focusing first on heave, it can be seen that heave motion always results in an increase in peak MMF. This increase is almost linear with normalised acceleration (hence

it essentially increases local gravity) and is not sensitive to normalised period over the range of parameters considered because it happens during the initial stage of the dam break. For pitch the same is not true; for sufficiently large normalised period the peak MMF reduces to values close to and below that for a fixed dam break. This is because for these cases the pitch angle (shown using contour lines in Fig. 5) increases when the dam break occurs, which acts to reduce the MMF. Nevertheless, for the vast majority of the parameter space the peak MMF is increased, indicating that acceleration effects are more important than slope effects for most practical scenarios. Comparing the heave and pitch only cases, it is clear that that increase in peak MMF is bigger in the latter case. This is not unexpected given that the range of normalised pitch accelerations (chosen based on the seakeeping analysis) are larger than those due to heave, emphasising the relative importance of pitch motion. Finally, in the combined heave and pitch scenarios, the heave acceleration effectively adds to the acceleration induced by pitch. This results in a further increase in peak MMF up to values of close to 20% over the range of parameters considered.

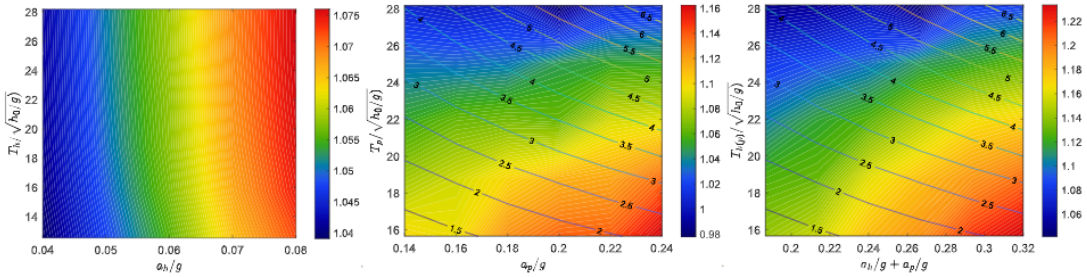

Fig. 5 Peak MMF of heave(left), pitch(middle) and combined(right) case obtained from CFD. The contour line with number is the angle of pitch motion in degree.

4 CONCLUSIONS

The dam break flow in a moving reference frame is numerically studied as an approximation of green water flow on a moving deck. As for fixed dam break flow, two stages in the evolution of the dam break are identified; the initial non-hydrostatic stage that has a sharp increase in horizontal MMF followed by a rapid descent, and the later hydrostatic stage where the MMF oscillates in time. In the initial stage, the MMF reaches its largest value. This peak may be higher or lower than that observed in a classic (fixed) dam break flow, but over the majority of the parameter space believed to be relevant to ship motions, heave and pitch lead to increases in peak MMF. These increases are typically on the order of 5-20%, hence they are not insignificant but at a level where fixed models are still likely to provide useful insight into green water loading. For times that do not coincide with peak MMF, motion can lead to an increase or decrease in MMF compared to a fixed dam break depending on the phase of the deck oscillation.

During the workshop these findings will be compared to experimental data for a simplified FPSO geometry (similar to that modelled in Chen et al. 2021), recently tested at 1:64 scale in the large wave basin at Shanghai Jiao Tong University. Simultaneous measurements of vessel motion, relative wave elevation and load on a topside structure placed close to the bow, allow inference of the effect of vessel motion on green water load.

ACKNOWLEDGEMENT

This work was supported by the ARC Industrial Transformation Research Hub for Offshore Floating Facilities which is funded by the Australian Research Council, Woodside Energy, Shell, Bureau Veritas and Lloyds Register (Grant no. IH140100012). The support in resources provided by the Pawsey Supercomputing Centre. HW is supported by an Australian Research Council (ARC) Early Career Fellowship (DE200101478).

REFERENCES

Buchner, B. The impact of green water on FPSO design. 1995 Houston, TX, United states. Offshore Technology Conference, 45-57.

Chanson, H. Analytical solutions of laminar and turbulent dam break wave. Proceedings of the International Conference on Fluvial Hydraulics, River Flow, 2006. 465-474.

Chen, L., Taylor, P. H., Draper, S., Wolgamot, H., Milne, I. A. & Whelan, J. R. 2019. Response based design metocean conditions for a permanently moored FPSO during tropical cyclones: Estimation of greenwater risk. *Applied Ocean Research*, 89, 115-127.

Greco, M. & Lugni, C. 2012. 3-D seakeeping analysis with water on deck and slamming. Part 1: Numerical solver. *Journal of Fluids and Structures*, 33, 127-147.

Harten, A., Lax, P. D. & Van Leer, B. 1983. On Upstream Differencing and Godunov-Type Schemes for Hyperbolic Conservation Laws. *SIAM Review,* 25**,** 35-61.

Huang, Z. & Hsiung, C.-C. 1996. Nonlinear Shallow-Water Flow on Deck. Journal of Ship Research, 40, 303-315.

Stansby, P. K., Chegini, A. & Barnes, T. C. D. 1998. The initial stages of dam-break flow. *Journal of Fluid Mechanics,* 374**,** 407-424.

Zhu, R., Miao, G. & Lin, Z. 2009. Numerical Research on FPSOs With Green Water Occurrence. *Journal of Ship Research,* 53**,** 7-18.

Chen, L. F., Taylor, P. H., Ning, D. Z., Cong, P. W., Wolgamot, H., Draper, S. & Cheng, L. 2021. Extreme runup events around a ship-shaped floating production, storage and offloading vessel in transient wave groups. Journal of Fluid Mechanics, 911, A40.

On the generation process of upstream waves by a pressure distribution at critical speed

John Grue
Department of Mathematics, University of Oslo, Norway
johng@math.uio.no

1 Background and motivation

Wave effects from ships moving along shallow waterways continue to be of interest. The ship speed (U) relative to the shallow water speed ($c_0 = \sqrt{gh}$, g the acceleration of gravity, h the water depth), expressed by the Froude number ($Fr = U/c_0$), is typically subcritical ($Fr < 1$) but may in certain circumstances become critical ($Fr = 1$). This case is investigated here.

At subcritical speed, the waves due to high speed vessels ($Fr < 0.7$) in the Bay of Tallinn were measured, obtaining that a major part of the wave energy was due to components near the edge of the wave wake (Torsvik et al., 2015). Also at subcritical speed, conventional ships moving along the shallow waterways of Oslofjorden in Norway regularly generate an upstream mini-tsunami, where the wave generation occurs at the shallow depth changes of the water (Grue, 2017).

At critical speed ($Fr = 1$), water continuously piles up at the ship's bow. The wave energy spreads laterally. If the water is horizontally unbounded, a frontal system of three-dimensional, curved solitary waves is developed. This has been computed using nonlinear long wave theories such as the Kadomtsev-Petviashvili equation and variants of the Boussinesq equations, most notably by Lee and Grimshaw (1990) and Li and Sclavounos (2002). See also the references in these papers. If the motion takes place in a narrow channel, a sequence of long-crested solitary waves are formed (e.g., Wu, 1987). The big cruiseferries with a car-deck moving along the Oslofjorden may have a speed that for a short while is close to the shallow water speed. Questions concerning the upstream wave generation at $Fr = 1$ may be: What determines the incipient wavelength? How fast and strong is the process?

Figure 1: High P1 (low P2) pressure systems corresponding to depression (elevation).

We explore these questions by a set of fully dispersive and strongly nonlinear simulations. We combine simulations with two different moving pressure systems. One is a depression corresponding to a ship. This corresponds to a high pressure (Figure 1). We denote this by pressure system P1. This will generate a bow wave of elevation, and eventually a system of upstream three-dimensional solitons. A second pressure system is of elevation, of similar shape as the depression system, but where the draught is negative. This corresponds to a low pressure system. We denote this by pressure system P2. This has a negative bow

wave, and there are no upstream waves. Instead, a long crested wave system fixed to the elevation pressure, of speed corresponding to $Fr = 1$ with a clearly defined wavelength develops. The wavelength defined by the P2-system is used as reference length of the waves of the P1-system (Figure 2).

2 Method

The fluid layer has constant depth h. A frame of reference is introduced. The driving pressure system (ship) is moving along the x-direction. Its position is $x_0(t)$, with $U = \dot{x}_0$. The vertical coordinate is y with $y = 0$ in the mean free surface. The lateral coordinate is z, and t is time. The moving surface pressure is specified by $P(x, z, t) = -\rho g Y_0(x - x_0, z)$ $(Y_0 < 0)$.

Potential flow is assumed. The velocity potential is a superposition between a steady part with no waves (ϕ_0) plus an unsteady part representing the waves (ψ). ϕ_0 satisfies $(\partial\phi_0/\partial n)\sqrt{1 + |\nabla_1\zeta|^2} = V_0 = -U(\partial Y_0/\partial x)$ on $y = \zeta = Y_0 + \eta$ where η denotes the wave surface, $\partial/\partial n$ the normal derivative out of the fluid and ∇_1 the horizontal gradient. The rigid lid condition applies at $y = 0$ outside the region of the applied pressure, as well as at $y = -h$. Both potentials satisfy the Laplace equation in the fluid. Variable $v = (\partial\psi/\partial n)\sqrt{1 + |\nabla_1\zeta|^2}$, where $\partial\psi/\partial n$ is the normal derivative of ψ, is defined along the surface. The solution, obtained by an integral equation over the upper surface of the fluid, connects the potential and its normal derivative. The integral equation expressed in terms of Fourier transform over the horizontal plane (e.g., Grue, 2017) reads:

$$\hat{V}_0 + \hat{v} = kT\,(\hat{\phi}_0 + \hat{\psi}) + n.l.t.1, \tag{1}$$

where a hat denotes Fourier transform in the horizontal plane, $k = |(k_x, k_z)|$ the absolute value of the wavenumber vector in the Fourier domain, $T = \tanh(kh)$, and $n.l.t.1$ includes nonlinear contributions. The term $n.l.t.1$ is evaluated using two approximations including i) quadratic terms and ii) quadratic plus cubic terms, where results of the approximations are compared. The kinematic and dynamic boundary conditions at the wave surface are expressed in the Fourier transformed version:

$$\hat{\eta}_t - kT\,\hat{\psi} = n.l.t.1, \tag{2}$$

$$\hat{\psi}_t + g\hat{\eta} = U\mathbf{i}k_x\hat{\phi}_0 + n.l.t.2. \tag{3}$$

The term $U\mathbf{i}k_x\hat{\phi}_0$ in (3) contributes to the bow wave, and $n.l.t.2$ includes the (exact) nonlinear terms of the Bernoulli equation for the pressure.

3 Results

Simulations are carried out with the high pressure system P1 using $P_1 = -\rho g Y_0$ and with the low pressure system P2 using $P_2 = \rho g Y_0$, both with $Y_0 < 0$. The shape is given by $Y_0 = -d_0 \exp\Big(-[(x - x_0)/(l_0/2)]^6 - [z/(w_0/2)]^6\Big)$ where (l_0, w_0, d_0) denote the (length,width,draught). The dimensions of the big cruiseferries of Color Line are chosen with $l_0 = 210$ m, $w_0 = 35$ m and $d_0 = 6.8$ m, making a deplacement of 36 000 m^3. A

water depth of $h = 14$ m is a realistic measure at a site where the mini-tsunami occurs. The numerical wave tank is $(L_x, L_z) = (250h, 250h)$. The resolution is $N_x = N_z = 760$ in each direction. The equations are integrated by a matlab script. Heun's method with $\Delta t = 0.2\sqrt{h/g}$ is used for the time integration. The integration is very robust. No smooting is applied. Products are anti-aliased in the Fourier domain. The simulations are fully dispersive and strongly nonlinear.

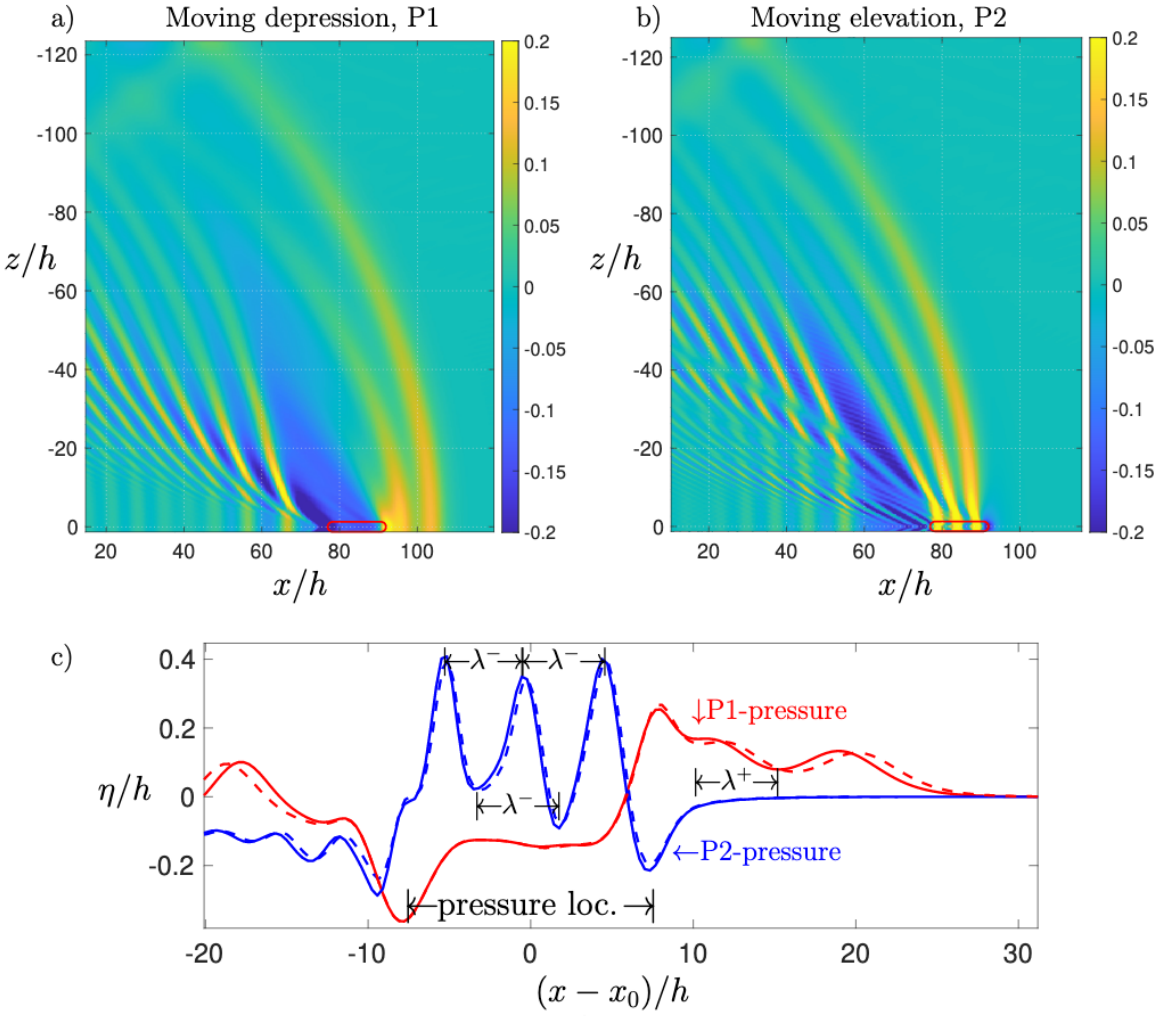

Figure 2: Elevation in color scale ($t = 200\sqrt{h/g}$) driven by moving a) high pressure, P1 (ship), b) low pressure, P2. The location of the pressure system is indicated by the red contour. c) Elevation along the x-axis for high pressure, P1 (red) and low pressure, P2 (blue). $t = 200\sqrt{h/g}$ (solid line) and $t = 220\sqrt{h/g}$ (dashed). Wavelengths λ^+ (λ^-) of the P1(P2) systems indicated. $Fr = 1$.

Figure 2a shows the upstream wave system as well as the downstream waves due to the (high-) pressure system, P1. Two upstream three-dimensional solitons are generated. The present fully dispersive and strongly nonlinear calculations generalise the asymptotic and long wave simulations by Lee and Grimshaw (1990) and Li and Sclavounos (2002), as well

as other calculations referenced in these papers. Some of these calculations were made for rather long, wide and shallow pressure distributions fitting to the long wave regime.

Figure 2b shows the waves resulting from the inverted (low-) pressure system, P2. This artifice is used to illustrate of the dispersive contribution to the upstream wave generation of the P1-system. A depression is observed ahead of the P2-pressure. A short wave train with three crests is attached to the moving pressure. Figure 2c illustrates the elevation along the x-axis. The wave group generated by the P2-system, attached to the moving pressure, is characterised by a wave speed corresponding to $Fr = 1$. Moreover, a wavelength is clearly defined. We denote this by λ^-. The computations show that this wavelength, between the three crests and between the two troughs, is the same, where $\lambda^- \simeq 4.95h$. The corresponding wavenumber of $hk^- \simeq 1.27$ is in the intermediate depth range.

As regards the upstream waves due to the P1 system, the waves emerge from the bow wave. A trough to trough wave length (λ^+) of the wave, right upstream of the bow wave is defined (see figure 2c). This wavelength increases with time. However, at the inception, this trough to trough wave length is equally long as the wavelength attached to the P2-system (λ^-). In the calculation $\lambda^+ \simeq 4.83h$ at $t = 200\sqrt{h/g}$ while it is $\lambda^+ \simeq 5.89h$ at the later time $t = 220\sqrt{h/g}$. This implies that $\lambda^+ \simeq \lambda^-$ at the inception of the upstream wave generation. This illustrates the dispersive effect of the upstream generation of three-dimensional solitons at $Fr = 1$.

We note that the dispersive properties discussed here are very visible in calculations where the pressure (ship) is moving past a depth change, where the speed increases from subcritical to critical (calculations not shown). However, the wavelength attached to the moving pressure is more clearly defined by λ^- developing by the P2-system.

In the present simulations two curved upstream solitary waves were generated. The pressure system has moved a distance of 200 water depths corresponding to 2.8 km with $h = 14$ m. In reality the shoal (of $h = 14$ m) extends a few hundred meters.

4 References

Grue, J. (2017) Ship generated mini-tsunamis. J. Fluid Mech. 816, 142-166.

Lee, S.-J., and Grimshaw, R.H.J. (1990) Upstream-advancing waves generated by three-dimensional moving disturbances. Phys. Fluids A: Fluid Dynamics 2, 194.

Li, Y., and Sclavounos, P.D. (2002) Three-dimensional nonlinear solitary waves in shallow water generated by an advancing disturbance. J. Fluid Mech. 470, 383-410.

Torsvik, T., Soomere, T., Didenkulova, I., and Sheremet, A. (2015) Identification of ship wake structures by a time-frequency method. J. Fluid Mech. 765, 229-251.

Wu, T.Y. (1987) Generation of upstream advancing solitons by moving disturbances. J. Fluid Mech. 184: 75–99.

LEVEL-CROSSING CONDITIONING IN SECOND-ORDER WATER WAVES

Romain Hascoët

ENSTA Bretagne, CNRS UMR 6027, IRDL, 2 rue François Verny, 29806 Brest Cedex 9, France
romain.hascoet@ensta-bretagne.fr

1 INTRODUCTION

The present study investigates the effect of second-order nonlinearities on wave statistics conditioned to free-surface upcrossing. An upcrossing event is defined as the free-surface upcrossing a given level (i.e. a given altitude) at a position fixed in the reference frame of the mean flow (i.e. the reference frame where the mean fluid velocity field is zero). Based on a trivariate Edgeworth expansion [1], an analytical approximation is derived for the conditional distribution of a second-order wave variable, given free-surface upcrossing.

This analytical model has been applied to three different wave variables: the vertical component of the fluid velocity, the horizontal component of the fluid velocity (both derived from the second-order velocity potential, considered at the mean water level), and the free-surface slope. For these three wave variables, the analytical approximations of their conditional distributions, given upcrossing, have been compared with numerical results obtained from Monte Carlo simulations of second-order irregular seas. These comparisons are used to assess the applicative scope of the analytical model.

2 EDGEWORTH APPROXIMATION

As a first step, an expression is required for the non-conditioned joint distribution of η, $\dot{\eta}$, and ξ, where η is the sea surface elevation, $\dot{\eta}$ its time derivative, and ξ is a third wave kinematic variable. The free surface elevation η is modeled as a stationary differentiable random process, which implies that its time derivative has a zero mean, $E[\dot{\eta}] = 0$. Without loss of generality, it is also assumed that $E[\eta] = E[\xi] = 0$ (if necessary, the random variables of the considered problem can be redefined such that their means are equal to zero). Besides, in order to make analytical expressions more compact, the triad $(\chi = \eta/\sigma_\eta, \dot{\chi} = \dot{\eta}/\sigma_{\dot{\eta}}, \zeta = \xi/\sigma_\xi)$ is introduced, where σ_η, $\sigma_{\dot{\eta}}$, σ_ξ are the standard deviations of η, $\dot{\eta}$, ξ. An approximation for the non-conditional joint distribution of $(\chi, \dot{\chi}, \zeta)$ can be obtained from the Edgeworth expansion of the related probability density function, truncated to the leading order. This approximation takes the form [2]

$$\begin{aligned}\hat{f}_{\chi,\dot{\chi},\zeta} = &\frac{1}{(2\pi)^{3/2}\sqrt{1-\rho^2-\dot{\rho}^2}} J_3 \\ &\times \left[1 + \frac{1}{6}\left(\lambda_{300}H_{300} + 3\lambda_{201}H_{201} + 3\lambda_{120}H_{120} + 6\lambda_{111}H_{111}\right.\right. \\ &\left.\left. + 3\lambda_{102}H_{102} + \lambda_{030}H_{030} + 3\lambda_{021}H_{021} + 3\lambda_{012}H_{012} + \lambda_{003}H_{003}\right)\right].\end{aligned} \tag{1}$$

A "hat" symbol has been used in Eq. (1) to differentiate the Edgeworth approximation, $\hat{f}_{\chi,\dot{\chi},\zeta}$, from the exact probability density function, $f_{\chi,\dot{\chi},\zeta}$. The function J_3 is given by:

$$J_3(\chi,\dot{\chi},\zeta) = \exp\left\{-\frac{1}{2}\frac{(1-\dot{\rho}^2)\chi^2 + (1-\rho^2)\dot{\chi}^2 + \zeta^2 - 2\rho\chi\zeta - 2\dot{\rho}\dot{\chi}\zeta + 2\rho\dot{\rho}\chi\dot{\chi}}{1-\rho^2-\dot{\rho}^2}\right\}. \tag{2}$$

The coefficients

$$\rho = E[\chi\zeta]\,, \tag{3}$$

$$\dot{\rho} = E[\dot{\chi}\zeta]\,, \tag{4}$$

are the non-conditional correlation coefficients of the pairs (χ,ζ) and $(\dot{\chi},\zeta)$. Note that the variables $(\eta,\dot{\eta})$ and their standardized counterparts $(\chi,\dot{\chi})$, non-conditioned, are uncorrelated. The functions H_{abc} are trivariate Hermite polynomials, defined by:

$$H_{abc}(\chi,\dot{\chi},\zeta) = \frac{(-1)^{a+b+c}}{J_3(\chi,\dot{\chi},\zeta)}\frac{\partial^a}{\partial\chi^a}\frac{\partial^b}{\partial\dot{\chi}^b}\frac{\partial^c}{\partial\zeta^c}J_3(\chi,\dot{\chi},\zeta)\,. \tag{5}$$

As calculations will show, explicit expressions for the third-order (i.e. $a+b+c=3$) Hermite polynomials, appearing in Eq. (1), are not required in the present study. The coefficients λ_{abc} (with $a+b+c=3$) are the third-order cumulants of the approximated probability distribution. They may be expressed as:

$$\lambda_{abc} = E\left[\chi^a\dot{\chi}^b\zeta^c\right]\,,\ \text{for}\ a+b+c\leq 3\,. \tag{6}$$

In the present context of second-order water waves, the cumulants can be analytically computed from the linear and quadratic transfer functions of the related wave variables (see e.g. Longuet-Higgins 1963 [3]).

3 APPLYING RICE'S FORMULA TO EDGEWORTH'S APPROXIMATION

The conditional distribution of a wave variable ξ, given that the free-surface elevation, η, up-crosses the level ℓ, may be expressed in terms of generalised Rice's formula

$$f_{\xi|\eta\uparrow\ell}(\xi) = \frac{\displaystyle\int_0^{+\infty}\tau' f_{\eta,\dot{\eta},\xi}(\ell,\tau',\xi)\,\mathrm{d}\tau'}{\displaystyle\int_0^{+\infty}\tau' f_{\eta,\dot{\eta}}(\ell,\tau')\,\mathrm{d}\tau'} = \frac{1}{\sigma_\xi}\frac{\displaystyle\int_0^{+\infty}\tau f_{\chi\dot{\chi}\zeta}(\tilde{\ell},\tau,\xi/\sigma_\xi)\,\mathrm{d}\tau}{\displaystyle\int_0^{+\infty}\tau f_{\chi,\dot{\chi}}(\tilde{\ell},\tau)\,\mathrm{d}\tau}\,, \tag{7}$$

where $\tilde{\ell}=\ell/\sigma_\eta$. When the distributions $f_{\chi\dot{\chi}\zeta}$ and $f_{\chi,\dot{\chi}}$ are replaced by their truncated Edgeworth expansions, the following approximation is obtained:

$$\hat{f}_{\xi|\eta\uparrow\ell}(\xi) = \frac{1}{\sigma_\xi}\frac{\displaystyle\int_0^{+\infty}\tau\hat{f}_{\chi\dot{\chi}\zeta}(\tilde{\ell},\tau,\xi/\sigma_\xi)\,\mathrm{d}\tau}{\displaystyle\int_0^{+\infty}\tau\hat{f}_{\chi,\dot{\chi}}(\tilde{\ell},\tau)\,\mathrm{d}\tau}\,, \tag{8}$$

where $\hat{f}_{\chi,\dot{\chi}}$ is the leading-order Edgeworth approximation of the joint probability density function of χ and $\dot{\chi}$. The integral at the denominator of Eq. (8) is a normalisation factor which has been already computed in [4], where Longuet-Higgins investigates the upcrossing frequency of the second-order free surface elevation. It can be expressed in the following form:

$$\int_0^{+\infty}\tau\hat{f}_{\chi,\dot{\chi}}(\tilde{\ell},\tau)\,\mathrm{d}\tau = \frac{1}{2\pi}e^{-\frac{1}{2}\tilde{\ell}^2}\left[1+\frac{\lambda_{300}}{6}H_3(\tilde{\ell})+\frac{\lambda_{120}}{2}H_1(\tilde{\ell})\right]\,, \tag{9}$$

where H_3 and H_1 are the third and first univariate probabilist's Hermite polynomials. The computation of the numerator of Eq. (8) is more involved. It may be decomposed as follows:

$$\mathscr{F}(\tilde{\ell},\zeta) = \int_0^{+\infty}\tau\hat{f}_{\chi\dot{\chi}\zeta}(\tilde{\ell},\tau,\zeta)\,\mathrm{d}\tau \tag{10}$$

$$= \alpha_{000}G_1(\tilde{\ell},\zeta) + \sum_{a+b+c=3}\alpha_{abc}\mathscr{I}_{abc}(\tilde{\ell},\zeta) \tag{11}$$

where G_1 is given by

$$G_1(\tilde{\ell},\zeta) = \int_0^{+\infty} \tau J_3(\tilde{\ell},\tau,\zeta)\,\mathrm{d}\tau\,, \tag{12}$$

the functions $\mathscr{I}_{abc}$ (with $a+b+c=3$) are given by

$$\mathscr{I}_{abc}(\tilde{\ell},\zeta) = \int_0^{+\infty} \tau H_{abc}(\tilde{\ell},\tau,\zeta) J_3(\tilde{\ell},\tau,\zeta)\,\mathrm{d}\tau\,. \tag{13}$$

The coefficients α_{000} and α_{abc} ($a+b+c=3$) are numerical factors whose expressions can be identified by substituting Eq. (1) into Eq. (10). Inspired by a method initially proposed in [4],[1] the integrals $\mathscr{I}_{abc}$ may be analytically computed by using a combination of integrations by parts and Hermite polynomial algebra. The detailed steps of the calculation are a bit lengthy and not reproduced here. All calculations done, $\mathscr{F}$ can be expressed in the following form:

$$\begin{aligned}\mathscr{F}(\tilde{\ell},\zeta) =& \Gamma_0(\tilde{\ell},\zeta) G_0(\tilde{\ell},\zeta) + \Gamma_1(\tilde{\ell},\zeta) G_1(\tilde{\ell},\zeta) \\ &+ \left[\beta_1 H_{100}(\tilde{\ell},0,\zeta) + \beta_2 H_{010}(\tilde{\ell},0,\zeta) + \beta_3 H_{001}(\tilde{\ell},0,\zeta)\right] J_3(\tilde{\ell},0,\zeta)\,,\end{aligned} \tag{14}$$

where G_0 is defined as

$$G_0(\tilde{\ell},\zeta) = \int_0^{+\infty} J_3(\tilde{\ell},\tau,\zeta)\,\mathrm{d}\tau\,. \tag{15}$$

The first-order trivariate Hermite polynomials, H_{100}, H_{010}, H_{001}, can be readily obtained from Eq. (5). The terms β_1, β_2, β_3 are numerical coefficients which can be expressed as a function of the coefficients α_{abc}. Γ_0 and Γ_1 are respectively second-order and third-order bivariate polynomials. The functions G_0 and G_1 can be expressed in closed-form, making use of the Gauss error function. The full explicit expressions of these different terms are a bit lengthy and are not reproduced in the present abstract.

4 ILLUSTRATIVE EXAMPLE

In Section 3, the analytical approximation of the conditional distribution, given free-surface upcrossing, has been derived for any wave variable – noted as ξ above (or ζ in standardized form). In the present section, as an illustrative example, the model is applied to a specific wave variable: the vertical component of the fluid velocity, denoted as w (derived from the velocity potential considered at the mean water level). The assumed sea state is short-crested with a significant wave height $H_s = 4$ m and a peak period $T_p = 10$ s. The water depth is infinite. The conditional distribution of w, given upcrossing of the level ℓ by η, is shown in Figure 1. The results are shown for the linear wave model and the second-order wave model. For the second-order wave model, the Edgeworth-based approximation (calculated by substituting Eqs. 9-14 into Eq. 8) is compared with numerical results obtained from multiple Monte Carlo realizations of the considered sea state. Within the linear wave model (dashed line), w, given upcrossing, follows a Rayleigh distribution which is independent of the actual crossing level, ℓ. When second-order wave nonlinearities are introduced, the conditional distribution of w, given upcrossing, is not of Rayleigh type anymore and it does depend on the altitude of the crossing level. In Figure 1, two different altitudes are considered: $\ell = +H_s/2$ (grey); $-H_s/2$ (black). In the present example, the Edgeworth-based analytical approximation (dotted lines) reproduces quite faithfully the results obtained from the Monte Carlo simulations (solid lines).

In order to better assess the scope of the analytical model, it has been applied to a series of configurations, where the sea state properties and the considered wave variable have been varied. For the sea state, the effects of changes in the wave direction distribution, wave camber and water

[1] In [4], Longuet-Higgins deals with bivariate Hermite polynomials, instead of the trivariate Hermite polynomials appearing in Eq. (13).

depth have been investigated. Regarding the wave variable, in addition to w, the wave slope, and the horizontal component of the fluid velocity (both considered along the average wave direction), have been also considered. In some cases, it has been found that the Edgeworth-based approximation provides results that are less satisfactory than those reported in the example of Fig. 1. The limitations of the Edgeworth-based approximation are partly related to the polynomial nature of the correction (the expression into square brackets in Eq. 1) applied to the Gaussian baseline. It translates to two different kinds of spurious features which may develop in the analytical approximation: (i) spurious oscillatory features; (ii) negative probability densities (which have no mathematical meaning). These limitations will be qualitatively and quantitatively discussed during the workshop.

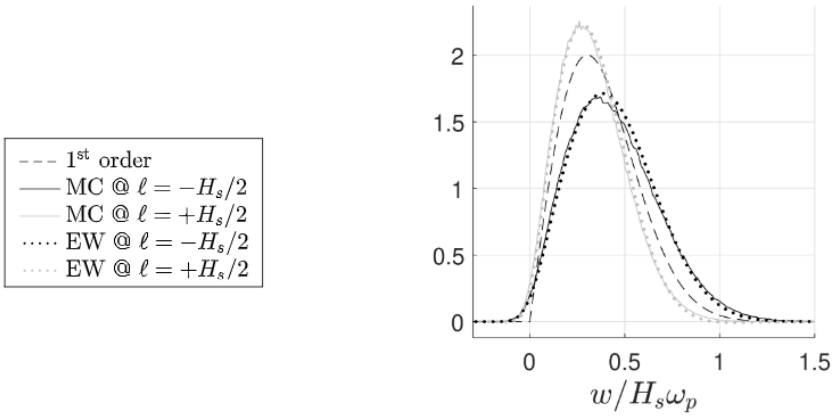

Figure 1: Conditional distribution of w, given free-surface upcrossing. The conditional distribution obtained from the linear wave model (a Rayleigh distribution) is shown as a dashed line (labelled as '1st order' in the legend); it does not depend on the elevation of the crossing level. The conditional distribution obtained from the second-order wave model is shown for two different crossing level elevations: $\ell = -H_s/2$ (black); $+H_s/2$ (grey). Results obtained from the Monte Carlo simulations (labelled as 'MC') are shown as solid lines; the approximations based on Edgeworth expansions (labelled as 'EW') are shown as dotted lines.

REFERENCES

[1] Edgeworth, F. Y. 1906. *The generalised law of error, or law of great numbers*. Journal of the Royal Statistical Society 69(3), 497–539.

[2] Jensen, J. J. 1996. *Second-order wave kinematics conditional on a given wave crest*. Applied Ocean Research 18(2), 119–128.

[3] Longuet-Higgins, M. S. 1963. *The effect of non-linearities on statistical distributions in the theory of sea waves*. Journal of Fluid Mechanics 17(3), 459–480.

[4] Longuet-Higgins, M. S. 1964. *Modified Gaussian distributions for slightly nonlinear variables*. *Radio Sci. D 68*, 1049–1062.

Theoretical foundation of a new type of panel method

Jiayi He (hejiayifans@gmail.com) and **Francis Noblesse** (noblfranc@gmail.com)

School of Naval Architecture, Ocean & Civil Engineering, Shanghai Jiao Tong University, Shanghai, China

Highlights

This abstract summarizes the main features of a new type of panel method, which is based on the Fourier-Kochin method and a weakly-singular boundary-integral flow representation sans waterline integral.

1 Introduction: main features of existing panel methods in marine hydrodynamics

The classical Green function and boundary-integral method implemented in the panel methods used in ship and offshore hydrodynamics are essentially based on applications of Green's fundamental identity

$$\int_{\mathcal{D}} dv\,(\varphi\,\nabla^2_{\boldsymbol{\xi}} G - G\,\nabla^2_{\boldsymbol{\xi}}\varphi) = \int_{\Sigma} da\,\mathbf{m}\cdot(\varphi\,\nabla_{\boldsymbol{\xi}} G - G\,\nabla_{\boldsymbol{\xi}}\varphi) \tag{1}$$

to the flow potential $\varphi(\boldsymbol{\xi})$ and the Green function $G(\boldsymbol{\xi},\mathbf{x})$ that satisfies the free-surface boundary condition relevant to the class of problems under consideration. The unit vector $\mathbf{m}$ in (1) is normal to the closed boundary surface Σ that encloses the flow region $\mathcal{D}$. Although application of Green's basic relation (1) is straightforward in principle, the formulation of integral equations that are well suited for practical applications in ship and offshore hydrodynamics involves nontrivial issues.

In particular, the region where the Green function G in (1) is defined is larger than the flow region $\mathcal{D}$ outside the body surface Σ^H. Specifically, G exists in the lower half space for flows around ships and offshore structures, i.e. in the region outside the hull-surface Σ^H of the body (ship or offshore structure) as well as inside the body. The Green function contains waves that propagate in every direction, including inside the structure, and these waves can result in non-physical waves (eigensolutions) inside the body and spurious solutions for some special wave frequencies, called 'irregular frequencies'. The formulation of a boundary-integral flow representation unaffected by irregular frequencies is nontrivial and indeed has been considered in numerous studies for diffraction-radiation of acoustic or water waves. This issue was recently considered in [1] where a review of the literature related to irregular frequencies may be found and Green's basic identity (1) is applied to a flow-model, called 'rigid-waterplane flow-model', of diffraction-radiation of regular waves by an offshore structure.

Another fundamental difficulty involved in the formulation of a boundary-integral flow representation based on Green's identity (1) is that application of this identity to flows around ships advancing at a constant speed V in calm water or in regular waves of (encounter) frequency ω result in an integral around the mean wetted waterline of the ship. This line integral, called waterline integral hereafter, is a source of notorious difficulties that are well documented in the literature.

Moreover, the Green functions G associated with the free-surface boundary conditions in marine hydrodynamics are defined by singular Fourier integrals and are quite complicated. Indeed, the evaluation of G and $\nabla_{\boldsymbol{\xi}} G$ and the subsequent integration of these functions, which involve complicated singularities, over the hull surface of a ship or offshore structure is a major basic difficulty of panel methods in ship and offshore hydrodynamics.

Lastly, Green's identity (1) involves surface distributions of sources and dipoles associated with the Green function G and its gradient $\nabla_{\boldsymbol{\xi}} G$, which is more singular than G and causes a discontinuity across the dipole distribution.

Thus, there are plenty of good reasons for seeking alternative ways of evaluating potential flows around ships and offshore structures.

2 A weakly-singular boundary-integral flow representation sans waterline integral

An alternative to the classical boundary-integral representation of potential flow around a ship steadily advancing in calm water or in regular waves, which is obtained from Green's identity (1) and involves a waterline integral as was already noted and is well known, is given in [2, 3]. This flow representation is

$$\phi = \int_{\Sigma^H} da\,[G\,q^H + \mathbf{G}\cdot(\mathbf{n}\times\nabla_{\boldsymbol{\xi}}\varphi)] + \int_{\Sigma^F} d\xi\,d\eta\,G\,[q^F - (\mathrm{i}f + F\,\partial_\xi)\,p^F] \text{ where } \mathbf{G} \equiv (0, \partial^\xi_\zeta G, -\partial^\xi_\eta G) \tag{2}$$

is a vector Green function that is related to, and easily determined from, the scalar Green function G. The notation ∂^ξ in (2) means integration with respect to ξ. The boundary-integral flow representation (2) provides an integral equation to determine the flow that corresponds to a prescribed flux $q^H \equiv \mathbf{n}\cdot\nabla_{\boldsymbol{\xi}}\varphi$ at the body surface Σ^H and prescribed distributions of pressure p^F and flux q^F at the free surface Σ^F, in accordance with the free-surface boundary condition $\partial_\zeta\varphi+(\mathrm{i}f+F\partial_\xi)^2\varphi = (\mathrm{i}f+F\partial_\xi)p^F - q^F$ where $F \equiv V/\sqrt{gL}$ and $f \equiv \omega\sqrt{L/g}$.

The boundary-integral flow representation (2) does not involve a waterline integral. Another notable feature of the flow representation (2) is that it is weakly singular. Indeed, the vector Green function $\mathbf{G}$ defined in (2) is no more singular than the scalar Green function G and the integral over the body surface Σ^H in (2) accordingly is continuous across Σ^H. Lastly, the flow representation (2) is shown in [1, 3] to be free from irregular frequencies.

The boundary-integral flow representation (2) is obtained in [3] via an application of Green's basic identity (1) to the flow-model, called 'rigid-waterplane flow-model', previously used in [1] for diffraction-radiation of regular waves by offshore structures. It is notable and interesting that the boundary-integral flow representation (2), obtained in [3] via Green's classical identity (1) applied to the 'rigid-waterplane flow-model' as was just noted, is identical to the representation of potential flow around a ship steadily advancing in *calm* water obtained in [2] via an analysis based on a *different* flow-model. This flow-model, associated with the theory called Neumann-Michell theory [4, 5], strictly considers the flow outside the ship hull-surface Σ^H but accounts for the (linear) contribution to the integral over Σ^H that stems from the narrow band of water bounded by the undisturbed free surface and its linear approximation.

Moreover, the 'rigid-waterplane flow-model' and the usual 'free-waterplane flow-model' considered in [1] for diffraction-radiation of regular waves by offshore structures are shown in [3] to yield identical boundary-integral flow representations.

That different linear flow-models yield identical flow representations lends credence to the analysis based on the rigid-waterplane flow-model used in [3] for ship motions in regular waves.

Thus, the flow representation (2) holds for the general case $V\omega \neq 0$ as well as for the special cases $\omega = 0$ or $V = 0$. The flow representation (2) and the consistent expressions for the Green function (associated with optimal Rankine-Fourier decompositions) given in [10] therefore provide a common mathematical basis for the analysis of wave diffraction-radiation by ships and offshore structures.

A main element of the derivation of the flow representation (2) from Green's identity (1) is the identity

$$\int_{\Sigma^H} da\,[(\varphi-\phi)\,\mathbf{n}\cdot\nabla_{\boldsymbol{\xi}}G + (\mathbf{n}\times\nabla_{\boldsymbol{\xi}}\varphi)\cdot\mathbf{G}] = \int_\Gamma d\eta\,(\varphi-\phi)\,\partial_\zeta^\xi G\,, \tag{3}$$

where $\mathbf{G}$ is the vector Green function defined in (2). The identity (3), given in [2, 3], holds for a *general* Green function G, which may be associated with various free-surface boundary conditions, or even boundary conditions associated with other boundary-value problems such as those related to very large floating structures or ice-engineering. Indeed, the identity (3) is general, and can be further generalized. This identity explains how the waterline integral that is obtained if $V \neq 0$ via applications of Green's basic identity (1) can be eliminated.

3 Main features of the Fourier-Kochin method

A core issue in the computation of potential flow around a ship or an offshore structure (body) consists in evaluating flows created by distributions of singularities over the panels (typically flat/curved triangles/quadrilaterals) commonly used to approximate the body surface. This basic issue is considered within the framework of the Fourier-Kochin (FK) method in [6–10]. The FK approach entails two tasks.

The first task consists in evaluating the Kochin (or amplitude) functions, denoted as $\mathcal{A}$ hereafter, associated with a given distribution of singularities. This task, which essentially amounts to integrating the elementary wave function $e^{k\,z\,+\,\mathrm{i}\,k\,(x\cos\gamma\,+\,y\sin\gamma)}$ over a panel, can be performed easily and efficiently, and indeed is a trivial task that evidently is incomparably simpler than the panel-integration of G and $\nabla_{\boldsymbol{\xi}}G$ that is required in the 'direct Green function method' used in current panel methods. The simplicity of the panel-integration in the FK method in fact is a compelling advantage of that method over the direct Green function method.

However, the second task in the FK method is anything but trivial. This task consists in evaluating singular double Fourier integrals of the general form

$$\phi^F(\mathbf{x}) = \frac{1}{\pi}\int_{-\pi}^{\pi} d\gamma \int_0^\infty dk\,\frac{\mathcal{A}(k,\gamma)\,e^{\,\mathrm{i}\,k\,(x\cos\gamma\,+\,y\sin\gamma)}}{\Delta(k,\gamma)+\mathrm{i}\,\epsilon\,\Delta_1(k,\gamma)} \quad \text{where } \epsilon = +0 \tag{4a}$$

and (k,γ) are related to the Cartesian Fourier variables $(\alpha,\beta) = k\,(\cos\gamma, \sin\gamma)$. Moreover, $\Delta(k,\gamma)$ and $\Delta_1(k,\gamma)$ denote dispersion functions associated with the class of flows under consideration. In particular, one has $\Delta \equiv (f+F\alpha)^2/k - 1$ for flows around ships steadily advancing in regular waves. The singular double Fourier integral

(4a) is considered in [6–10] for *general* dispersion functions Δ and Δ_1, i.e. for a broad class of dispersive media, and a *general* amplitude (Kochin) function $\mathcal{A}$ associated with arbitrary compact distributions of singularities.

The flow potential ϕ^F defined by the singular double Fourier integral (4a) is expressed in [6–10] as

$$\phi^F(\mathbf{x}) = \phi^W(\mathbf{x};C) + \phi^L(\mathbf{x};C) \tag{4b}$$

where ϕ^W is given by a single (one-fold) Fourier integral along the dispersion curve(s) defined by the dispersion relation $\Delta = 0$, and ϕ^L is given by a regular (non-singular) double Fourier integral. Specifically, for a single closed dispersion curve that surrounds the origin $k = 0$ of the Fourier plane (α,β), as for the dispersion curve related to the ring waves created by a ship advancing in regular waves at $V\omega/g < 1/4$), the component ϕ^W in the fundamental decomposition (4b) is given by the single Fourier integral

$$\begin{aligned} &\phi^W(\mathbf{x}) = \mathrm{i}\int_{-\pi}^{\pi} d\gamma\, \Theta\, \frac{\mathcal{A}(k_*,\gamma)}{\Delta_k(k_*,\gamma)}\, e^{\,\mathrm{i}\,k_*\,(x\cos\gamma + y\sin\gamma)} \;\text{ where }\; k_* = k_*(\gamma) \\ &\text{and }\; \Theta \equiv \mathrm{erf}[k_*\,(x\cos\gamma + y\sin\gamma)/C] - \mathrm{sign}[\Delta_1(k_*,\gamma)\,\Delta_k(k_*,\gamma)]\;. \end{aligned} \tag{4c}$$

The component ϕ^L is given by the double Fourier integral

$$\phi^L(\mathbf{x}) = \frac{1}{\pi}\int_{-\pi}^{\pi} d\gamma \int_0^{\infty} dk\, \mathcal{A}^L(k,\gamma)\, e^{\,\mathrm{i}\,k\,(x\cos\gamma + y\sin\gamma)} \;\text{ where} \tag{4d}$$

$$\mathcal{A}^L = \frac{\mathcal{A}(k,\gamma)}{\Delta(k,\gamma)} - \frac{\mathcal{A}(k_+^*,\gamma)\, e^{-C^2(k/k_+^*-1)^2/4}}{(k-k_+^*)\,\Delta_k(k_+^*,\gamma)} + \frac{\mathcal{A}(k_-^*,\gamma-\pi)\, e^{-C^2(k/k_-^*+1)^2/4}}{(k+k_-^*)\,\Delta_k(k_-^*,\gamma-\pi)} \;\text{ with }\; \left\{\begin{matrix} k_+^* \equiv k_*(\gamma) \\ k_-^* \equiv k_*(\gamma-\pi) \end{matrix}\right\}.$$

In expressions (4c-d), $\Delta_k \equiv \partial_k\Delta(k,\gamma)$ and $k_*(\gamma)$ denotes the root of the dispersion relation $\Delta(k,\gamma) = 0$.

The decomposition (4b), given here for a single closed dispersion curve surrounding the origin $k = 0$ of the Fourier plane, holds for general dispersion functions, which typically define several dispersion curves (as is the case in ship hydrodynamics). The component ϕ^W in (4b) represents waves and is defined by a (one-fold) Fourier integral along every dispersion curve defined by the dispersion relation $\Delta = 0$. The component ϕ^L in (4b) is defined by a double Fourier integral with integrand that is smooth everywhere (notably at the dispersion curve) and is dominant near the origin of the Fourier plane, as is numerically illustrated in [6–10].

The wave component ϕ^W and the component ϕ^L in the fundamental decomposition (4b) both involve a positive real number C, although the sum $\phi^W + \phi^L$ is independent of C in accordance with the fact that the decomposition (4) does not involve approximations, i.e. is *exact*. The decomposition (4b) therefore is not unique, and in fact corresponds to a family of alternative decompositions.

In particular, the classical definition of the *principal value of a singular integral*, as well as the *technique of contour integration* in the complex (Fourier) plane, are shown in [6–10] to correspond to the two special choices $C = \infty$ or $C = 0$ in (4b-d). It is also shown in [6–10] that these two classical choices for C are not optimal. In particular, the component ϕ^L includes waves that cancel out the waves defined by the component ϕ^W in large flow regions if C is chosen too large, and the components ϕ^W and ϕ^L are *not smooth* (although the sum ϕ^F is smooth) if C is chosen as $C = 0$. Indeed, an optimal choice for C in (4b-d) and a corresponding *optimal* waves/local-effect (WL) decomposition in which the wave and local components ϕ^W and ϕ^L are *smooth* and ϕ^L represents a *non-oscillatory local* disturbance is shown in [6–10] to be $C \approx 1/2$. This optimal choice is also justified in [10] via an elementary theoretical consideration.

The WL decomposition (4) and the similar flow representation given in [6–10] for dispersion curves represented in the Cartesian form $\alpha = \alpha^*(\beta)$ hold for *arbitrary dispersion functions* Δ and Δ_1 as was already noted. These general WL decompositions are applied in [6–10] to the specific dispersion functions associated with particular classes of flows in ship and offshore hydrodynamics, specifically diffraction-radiation of regular waves by offshore structures in deep water or in finite water depth, and deep-water flows around ships steadily advancing in calm water or in regular waves. These particular applications yield simple expressions, well suited for numerical evaluation, that can be used for the practical evaluation of flows created by *general* compact distributions of singularities for major classes of flows of interest in marine hydrodynamics.

Another notable feature of the FK method expounfded in [10] is that it is based on an optimal Rankine-Fourier (RF) decomposition $G = G^R + G^F$ of the Green functions G associated with the free-surface boundary conditions relevant to ship and offshore hydrodynamics. Thus, the FK theory expounded in [10] involves two optimal flow decompositions related to the Rankine-Fourier decomposition $G = G^R + G^F$ and the previously-noted choice of the parameter C in (4b-d) in the waves/local-flow (WL) decomposition. Indeed, the RF decomposition and the WL decomposition both are non-unique, and optimal decompositions can then be used.

4 Conclusion: a new type of panel methods

The new boundary-integral flow representation (2), together with the Fourier-Kochin (FK) method for evaluating flows created by general distributions of singularities given in [6–10], provide a mathematical basis for a new type of panel method that offers several compelling advantages over the classical 'direct-Green-function' approach pursued for the past fifty years.

In particular, the boundary-integral flow representation (2) is weakly singular, does not involve a waterline integral and is free from irregular frequencies. Moreover, the FK method circumvents the basic difficulties associated with the numerical evaluation of Green functions G and the subsequent integration of G and ∇G over hull-surface panels. Lastly, the major numerical evaluations involved in the FK method, implemented in the manner expounded in [10], are proportional to the number N of panels, whereas the direct-Green-function method requires evaluation and subsequent panel-integration of N^2 singular functions G and ∇G.

In short, the fundamental results given in [3, 10] and summarized in this abstract lay the foundation of panel methods that are considerably simpler than existing methods (notably because the complexities associated with the evaluation and subsequent panel-integration of Green functions are avoided in the FK method) and more robust (because the notorious difficulties related to the line integral around the waterline of a steadily advancing ship are moot) and moreover are expected to be far more efficient than current panel methods (notably because main computations are proportional to the number of panels).

References related to boundary-integral flow representations and the Fourier-Kochin method

[1] J. He, H. Wu, C.-J. Yang, R.-C. Zhu, W. Li, F. Noblesse. Diffraction-radiation of regular water waves and irregular frequencies: a straightforward flow modeling approach and analysis. Eur. J. Mech. B/Fluids 90 (2021) 7-14.

[2] J. He, H. Wu, C.-J. Yang, R.-C. Zhu, W. Li, F. Noblesse. Boundary-integral representation sans waterline integral for flows around ships steadily advancing in calm water. Eur. J. Mech. B/Fluids 89 (2021) 259-266.

[3] J. He, F. Noblesse. Boundary-integral flow representation sans waterline integral in ship and offshore hydrodynamics. Eur. J. Mech. B/Fluids. Submitted.

[4] J. He, Y. Zhu, C. Ma, C.-J. Yang, W. Li, F. Noblesse. Boundary integral representations of steady flow around a ship. Eur. J. Mech. B/Fluids 72 (2018) 152-163.

[5] F. Noblesse, F. Huang, C. Yang. The Neumann-Michell theory of ship waves. J. Eng. Math. 79 (2013) 51-71.

[6] J. He, H. Wu, R.-C. Zhu, C.-J. Yang, F. Noblesse. Practical flow-representations for arbitrary singularity-distributions in ship and offshore hydrodynamics, with applications to steady ship waves and wave diffraction-radiation by offshore structures, Eur. J. Mech. B/Fluids 83 (2020) 24-41.

[7] J. He, H. Wu, R.-C. Zhu, C.-J. Yang, F. Noblesse. Practical evaluation of flows due to arbitrary singularity distributions in the 3D theory of ship motions in regular waves at $\tau < 1/4$. Eur. J. Mech. B/Fluids 83 (2020) 212-225.

[8] J. He, H. Wu, R.-C. Zhu, C.-J. Yang, F. Noblesse. Practical evaluation of flows due to arbitrary singularity distributions in the 3D theory of ship motions in regular waves at $0.3 < \tau$. Eur. J. Mech. B/Fluids 85 (2021) 8-20.

[9] H. Wu, J. He, R.-C. Zhu, C.-J. Yang, F. Noblesse. Practical representation of flows due to general singularity distributions for wave diffraction-radiation by offshore structures in finite water depth. Eur. J. Mech. B/Fluids 89 (2021) 1-14.

[10] J. He, C.-J. Yang, F. Noblesse. Optimal Fourier-Kochin flow representations in ship and offshore hydrodynamics: Theory. Eur. J. Mech. B/Fluids. Submitted.

Wave power extraction from a metamaterial cylinder with internal paddle power take off mechanism

J. Huang, R. Porter
School of Mathematics, University of Bristol, Bristol BS8 1UG, UK
jin.huang@bristol.ac.uk, richard.porter@bristol.ac.uk

1 INTRODUCTION

Originating in the field of electromagnetics, the term metamaterial is used to describe a microstructure which interacts with the wavefield to create unusual effects not normally associated with scattering in ordinary settings. The microstructure is usually formed by a periodic arrangement of elements whose design contributes to the macroscopic properties of the metamaterial. In water waves, one such metamaterial device used recently by a number of authors is a closely-spaced periodic array of thin vertical bottom-mounted plates. For example, it has been shown in [1], [2] that submerged rectangular ridges are capable of perfectly transmitting negatively-refracted plane incident waves. When plate arrays are formed into vertical circular cylinders extending through the depth [3] have demonstrated that there is capacity for the cylinder to absorb significantly more wave energy than an equivalent rigid cylinder operating in rigid body motion, exploiting the internal resonance associated with the metamaterial properties of the plate array microstructure. [3] considered placing a damping condition on the internal free surface of the cylinder and imagined how this could be representative of a physical mechanical absorbing mechanism. Meanwhile, in a separate study of [4] in which narrow vertical absorbing paddles were placed around the surface of a vertical cylinder also showed the ability of a circular cylinder to absorb more energy than in rigid body motion.

In this paper, we return to [3] and consider a more realistic way to extract the power from the internal resonance promoted by the metamaterial structure. We arrange a pair of hinged paddles with springs and dampers about the midplane of each channel. The paddles are excited by water waves to rotate around the hinge points and the dampers are used to control the power absorption. To simplify the mathematical problem, an assumption is made in which the discrete paddle displacement in discrete channels is replaced by a continuous double-sided paddle displacement along the centreplane of a cylinder occupied with a continuous effective medium. The results show that this new type of wave energy converter (WEC) can capture significantly larger energy in almost all incident wave frequencies and angles when compared to the traditional WECs operating in rigid body motion.

2 PROBLEM FORMULATION

As shown in Fig.1, a parallel array of closely-spaced vertical thin plates aligned with y-axis are confined within a circular cylinder of radius a centred at the origin in the water of depth h and density ρ. Between adjacent plates, there are a pair of paddles hinged at $z=-c$ with the identical damping, γ, and spring, κ. The paddles are fitted above rigid walls occupying $-h<z<-c$. The paddles are perpendicular to the plates and symmetrically distributed on either side of the symmetry plane of the cylinder. Power is generated under the action of a regular wave with the amplitude A which propagates at an angle β to the positive x-axis. It should be noted that there is no fluid between the two rows of paddles and the separation between these two rows must be large enough that the paddles do not come into contact in operation.

The whole fluid domain is divided into two regions: an outer region $\Omega_1=\{r>a, 0\le\theta<2\pi, -h\le z\le 0\}$ and an inner region $\Omega_2=\{r\le a, 0\le\theta<2\pi, -h\le z\le 0\}$, where (r,θ) is the polar coordinate.

Linear potential theory is used to study the present problem and in which the fluid motion is described by a velocity potential $\Re[\phi(x,y,z)\mathrm{e}^{\mathrm{i}\omega t}]$, where ω is the assumed angular frequency. Therefore,

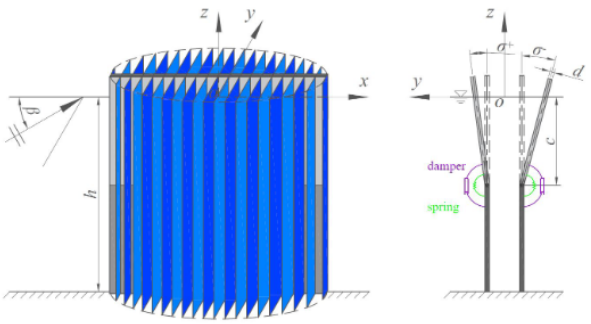

Figure 1: Sketch for the metamaterial cylinder with paddles.

the time-independent velocity potentials $\phi_k(x,y,z)$ satisfy

$$\nabla^2\phi_k(x,y,z)=0 \quad \text{in} \quad \Omega_k \quad (k=1,2). \tag{1}$$

with

$$\frac{\partial\phi_k}{\partial z}=\frac{\omega^2}{g}\phi_k \quad \text{on} \quad z=0, \quad \text{and} \quad \frac{\partial\phi_k}{\partial z}=0 \quad \text{on} \quad z=-h. \tag{2}$$

In the inner region, the velocity potential also satisfies no-flow conditions on either side of each vertical channel wall. On the underlying assumption that the the width of the channel is much smaller its length and water depth a multiscale homogenisation (e.g. Porter (2021)) can be used to replace the combined internal fluid/structure by an effective medium governing equation

$$\frac{\partial^2\phi_2}{\partial y^2}+\frac{\partial^2\phi_2}{\partial z^2}=0 \quad \text{in} \quad \Omega_2. \tag{3}$$

The velocity potential $\phi_2(x,y,z)$ also satisfies kinematic and dynamic boundary conditions on the surface of paddles. Since the width of the paddles is assumed small and the number of the paddles consequently large, we assume that the pitch angles of the two paddle rows can be expressed as continuous functions, $\sigma^{\pm}(x)$, of position x. For modelling simplicity, the distance of between the two row of paddles and the thickness of the paddles (assumed much smaller than the radius of the cylinder), are set to zero in the present study. Thus, the time-harmonic kinematic condition on the two rows of paddles at $y=0^{\pm}$, $-a<x<a$ is written

$$\frac{\partial\phi_2(x,y,z)}{\partial y}=\begin{cases}-\mathrm{i}\omega\sigma^{\pm}(x)(z+c), & -c<z<0\\ 0, & -h<z<-c\end{cases} \tag{4}$$

and the dynamic condition expressed as

$$(-\omega^2 I_c+\mathrm{i}\omega\gamma+\kappa+C)\sigma^{\pm}(x)=\mathrm{i}\omega\rho\int_{-c}^{0}\phi_2(x,0^{\pm},z)(z+c)\,\mathrm{d}z, \qquad -a<x<a \tag{5}$$

where $I_c=\frac{1}{3}\rho_s cd\left(c^2+\frac{1}{2}d^2\right)$ and $C=\frac{1}{2}\rho gd(\frac{1}{6}d^2+c^2)-\frac{1}{2}\rho_s gc^2d$ are the moment inertia and restoring moment per unit width for the paddles hinged along the center of the bottom edge. Here ρ_s represents the density the paddle.

Applying the continuity of pressure and flux on the interface of the inner and outer regions, we can obtain the corresponding matching conditions on the interface

$$\phi_1=\phi_2, \quad \text{and} \quad \frac{\partial\phi_1}{\partial r}=\frac{\partial\phi_2}{\partial y}\sin\theta, \quad \text{on} \quad r=a. \tag{6}$$

Since the structure possesses geometric symmetry about $y=0$, the total potential can be written as the sum of potential which are symmetric and anti-symmetric about $y=0$, i.e.

$$\phi_k=(\phi_k^s+\phi_k^a)/2, \quad (k=1,2), \quad \text{where} \quad \begin{cases}\phi_k^s(x,-y,z)=\phi_k^s(x,y,z),\\ \phi_k^a(x,-y,z)=-\phi_k^a(x,y,z).\end{cases} \tag{7}$$

Consequently, we only need to consider solutions in the upper half domain ($y \geq 0$) provided we apply appropriate conditions on $y = 0$ and introduce functions $\sigma^{s,a}(x)$ from which $\sigma^{\pm}(x) = \frac{1}{2}(\sigma^s(x) \pm \sigma^a(x))$.

In the outer region, the solutions for the symmetric potential ϕ_1^s satisfying Eqs. (1), (2) and (7) can be written as

$$\phi_1^s = -\frac{\mathrm{i}gA}{\omega} \sum_{m=0}^{\infty} \cos m\theta \left[2\epsilon_m \mathrm{i}^m \cos m\beta J_m(kr)\psi_0(z) + A_{m0}^s H_m(kr)\psi_0(z) + \sum_{n=1}^{\infty} A_{mn}^s K_m(k_n r)\psi_n(z) \right], \tag{8}$$

where the first term in the bracket represents the (symmetric) incident wave and the second and third terms represent the scattered response. Here, $\epsilon_0 = 1$ and $\epsilon_m = 2$, $(m \geq 1)$, k_n $(n = 1, 2, \dots)$ are the real positive roots of the dispersion equation $\omega^2 = -gk_n \tan k_n h$ while k is the wave number defined by $k_0 = -\mathrm{i}k$, $\psi_n(z)$ are the vertical eigenfunctions defined by $\psi_n(z) = \cos k_n(z + h)/\cos k_n h$ and A_{mn}^s are the undetermined coefficients.

By applying the method of separation of variables, the symmetric velocity potential ϕ_2^s in the inner region satisfying Eqs. (2) and (3) can be written as

$$\phi_2^s = -\frac{\mathrm{i}gA}{\omega} \sum_{n=0}^{\infty} \left[C_n^s(x)\mathrm{e}^{-k_n y} + D_n^s(x)\mathrm{e}^{k_n y} \right] \psi_n(z). \tag{9}$$

To solve the resulting problem, it is convenient to expand the unknown functions $C_n^s(x)$ and $D_n^s(x)$ in Eq. (9) in a series of Chebyshev polynomials as $[C, D]_n^s(x) = \sum_{p=0}^{\infty} [C, D]_{n,p}^s T_p(x/a)$ where $C_{n,p}^s$ and $D_{n,p}^s$ are unknown coefficients to be determined.

The expressions for the anti-symmetric potentials ϕ_k^a in the inner and outer regions can be obtained after replacing cos functions with sin functions and replacing the superscript s with a.

By applying the symmetric/antisymmetric versions of the boundary conditions (4), (5), (6) to the expressions given above, and using the orthogonality of trigonometric functions, and vertical eigenfunctions $\psi_n(z)$, and after truncating the infinite series that result to finite series, a closed system of equations with unknowns $A_{mn}^{s/a}$, $C_{np}^{s/a}$ and $D_{np}^{s/a}$ can be formulated. Once these coefficients are determined, the wave elevation in the wave field can be calculated using the linearised kinematic condition on the free surface ($\eta = \frac{\mathrm{i}\omega}{g}\phi|_{z=0}$). The mean power absorption can be evaluated by integrating the time-averaged product of pressure and velocity over the paddle surfaces and this results in

$$P = \frac{\rho\omega}{4} \Im \left\{ \int_{-a}^{a} \int_{-c}^{0} \left[\phi_2^s(x, 0^+, z) \frac{\partial \phi_2^{s*}(x, 0^+, z)}{\partial y} + \phi_2^a(x, 0^+, z) \frac{\partial \phi_2^{a*}(x, 0^+, z)}{\partial y} \right] \mathrm{d}z\, \mathrm{d}x \right\} \tag{10}$$

where $*$ represents the complex conjugate. In order to represent the results in a meaningful way, the non-dimensional power $\bar{P}$ is defined as $\bar{P} = kP/P_i$ where $P_i = \frac{1}{2}\rho g A^2 c_g$ represents the incident wave power per unit width of the wave front and $c_g = (\omega/2k)(1 + 2kh/\sinh 2kh)$ is the group velocity.

3 RESULTS

We consider a metamaterial cylinder of radius a is in the water of depth $h = 2a$ at the incident wave angle $\beta = \pi/4$ with the paddles attached to a constant non-dimensional damping $\bar{\kappa} = \kappa/(\rho a c^2\sqrt{gh}) = 0.2$ and spring $\bar{\gamma} = \gamma/(\rho g a c^2) = 0.2$. We consider four cases with the same paddle thickness $d = 0.1a$ and density $\rho_s = 2\rho$ but different paddle lengths, c. Fig. 2(a) shows the non-dimensional power $\bar{P}$ generated by the paddles against the incident wave frequency. It shows that the paddle length has little influence on the power extraction. The maximum mean power generated by an equivalent axisymmetric WEC operating in combined rigid-body heave and surge/pitch motion under this non-dimensionalisation is $\bar{P} = 3/2$ ([5]). For the present device, it can be found that $\bar{P} > 2$ for $ka > 1$. Fig. 2(b) and (c) show the amplitudes of the paddle motion at $ka = 1$. Although the paddle length is different, the horizontal displacements of the paddles at the mean surface are of the same order of

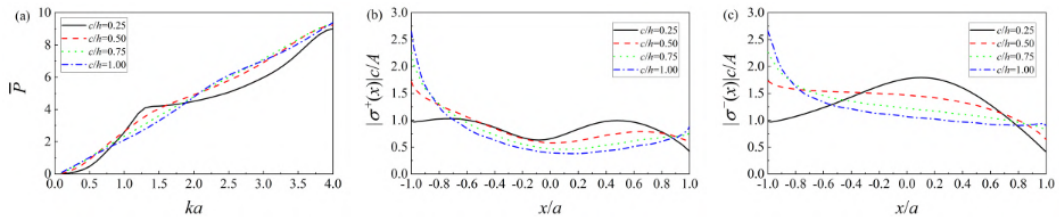

Figure 2: In (a) non-dimensional power generated by the metamaterial cylinder of radius a in water of depth $h = 2a$ for an incident wave angle $\beta = \pi/4$ with dimensionless damping $\bar{\gamma} = 0.2$ and spring $\bar{\kappa} = 0.2$. In (b) and (c) the corresponding amplitudes of the paddle motion at $ka = 1$.

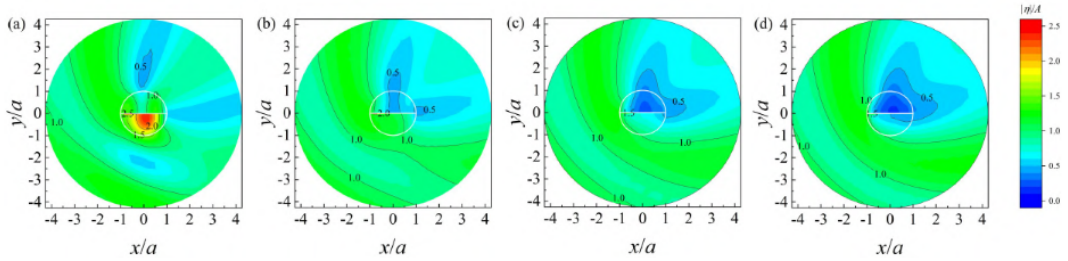

Figure 3: The wave elevation $h = 2a$ at $ka = 1$ and $\beta = \pi/4$ with the damping $\bar{\gamma} = 0.2$ and spring $\bar{\kappa} = 0.2$: (a) $c/h = 0.25$; (b) $c/h = 0.50$; (c) $c/h = 0.75$; (d) $c/h = 1.00$.

magnitude as the incident wave amplitude. Upside and leeside of the cylinder, the paddle tends to moves more with greater amplitude as paddle length increases.

The corresponding wave elevations at $ka = 1$ are presented in Fig. 3. Although the horizontal displacements of the paddles are similar to incident wave heights, the wave elevation – especially inside the metamaterial cylinder – are quite different. With the longer paddle length, the wave amplitudes induced by the paddles are relatively small. Remarkably, when the hinge point is close to the sea bed, the wave elevations on surfaces of the paddles become relatively calm.

Fig. 4 shows a contour plot of the dimensional wave power $\bar{P}$ generated by the metamaterial cylinder with the paddle length $c/h = 1.0$ against the non-dimensional frequency ka and incident wave angle β (due to symmetry, we need only consider $0 \le \beta \le \pi/2$).

The plot shows that, for most $ka \lesssim 3$, the power is not sensitive to the incident wave angle implying that this type of WEC can absorb high power from all wave directions.

Acknowledgements: This work was supported by the EPSRC, grant number EP/V04740X/1

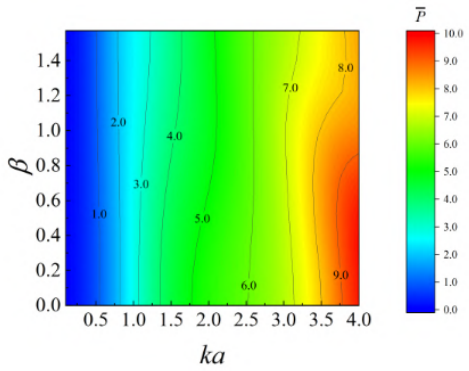

Figure 4: The contour of dimensional wave power generated by the metamaterial cylinder with the paddle length $c/h = 1$ against the non-dimensional frequency ka and incident wave angle β.

REFERENCES

[1] Porter, R. 2021. *Plate arrays as a perfectly-transmitting negative refraction metamaterial. Wave Motion 100*, 102673.

[2] Marangos, C., and Porter, R. 2021. *Shallow water theory for structured bathymetry. Proc. Roy. Soc. A. 477*, 102724.

[3] Zheng, S., Porter, R., and Greaves, D. 2020. *Wave scattering by an array of metamaterial cylinders. J. Fluid Mech. 903*, A50.

[4] Porter, R., Zheng, S., and Greaves, D. 2021. *Extending limits for wave power absorption by axisymmetric devices. J. Fluid Mech. 924*, A39.

[5] Evans, D. V. 1976. *A theory for wave power absorption by oscillating bodies. J. Fluid Mech. 77*, 1–25.

Experimental study on short design waves for extreme response of a floating hinged raft wave energy converter

Siya Jin*, Tom Tosdevin, Martyn Hann, Deborah Greaves
School of Engineering, Computing and Mathematics, University of Plymouth, UK
* Corresponding author <siya_jin@126.com>

1 INTRODUCTION

Predicting extreme responses with respect to a long-term return period (e.g., 50-year) is of great importance for the design of an offshore structure. The established method is to conduct a large number of long-duration (1-hour/3-hour) simulations to predict the design loads/responses [1, 2]. If the system response can be well modelled via a linear transfer function, the long-term analysis is easy to achieve. The analysis will be considerably time-consuming if a time-domain nonlinear response model is required and even impractical using a computational fluid dynamics (CFD) method or physical tank testing.
To speed up the design procedure, there has been continuous interest in investigating the potential of using a short design wave (SDW) to replace long-duration irregular wave tests (IR) [3, 4]. Several standards have suggested that SDWs can be applied on fixed offshore structures, while applying SDWs on the design loads of floating offshore structures needs to be verified with further numerical simulations and experimental results before they can become established tools. In present work, four types of SDW are investigated experimentally on a designed 1:50 scale floating hinged raft wave energy converter (WEC): (1) the New Wave (NW) which is a single wave series obtained based on the frequency content of the wave spectrum; (2) the most likely extreme response wave (MLER) which is a single wave series obtained via the frequency content of the response spectrum; (3) the conditioned NW (CNW) which is a group of waves generated by embedding the single NW into a series of short random irregular backgrounds; and (4) the conditioned random response wave (CRRW) which is a group of waves generated by embedding the MLER into a series of random irregular backgrounds. For the CNW and CRRW, 20 wave series are run in this work.

2 EXPERIMENTAL DESCRIPTIONS

2.1 Experiment Model

A designed 1:50 scale two-body hinged raft WEC was built and tested. Its main geometric dimension and the mooring layout are described in Fig. 1 and Table 1. With the constraint of the hinge, the device has 13 degrees of freedom (DOF): 6 DOF (surge, sway, heave, roll, pitch and yaw) for each raft and the relative hinge angle between the fore raft and aft raft. 4 aerial mooring lines were used to secure the device. Each mooring line consists of a stiff rope using polyethylene fibers and a linear spring with calibrated stiffness of 7.35 N/m. The motions of the two rafts were measured by a Qualisys optical tracking system. A rotary sensor was installed to record the relative hinge angle. 4 load cells were used to capture the mooring loads at the fairleads. In this work, response of the relative hinge angle is studied to demonstrate the application of SDWs on this floating structure.

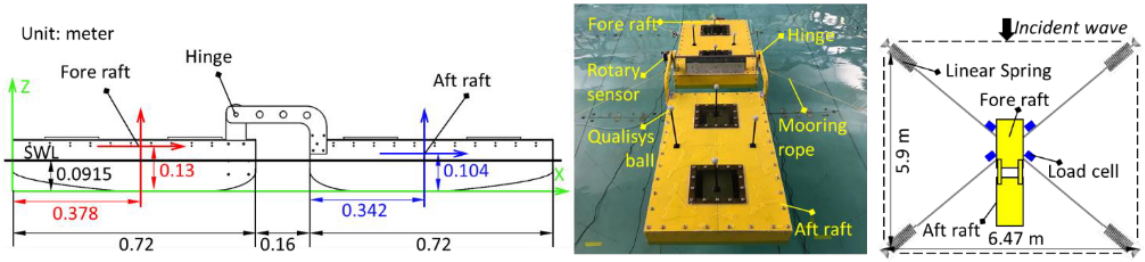

(a) (b) (c)

Fig. 1. (a) Dimensions of the designed 1:50 scale hinged raft WEC. The green, red and blue coordinates represent the global coordinate, the centre of gravity (CoG) of the fore raft and the CoG of the aft raft, respectively. (b) Experiment model. (c) Mooring layout.

Table 1. Main parameters of the 1:50 scale hinged raft model. The order of the inertias is I_{XX}, I_{YY}, I_{ZZ}.

Parameters	**Value**
Length of the fore raft [m]	0.72
Length of the aft raft [m]	0.72
Draft of the WEC [m]	0.0915
Width of the WEC [m]	0.435
Mass of fore raft [kg]	25.125
Mass of aft raft [kg]	25.125
Inertias of fore raft [kgm^2, kgm^2, kgm^2]	0.49, 2.06, 2.23
Inertias of aft raft [kgm^2, kgm^2, kgm^2]	0.49, 2.06, 2.23
Spring stiffness [N/m]	7.35
Spring initial pretension [N]	2.5

2.2 Test cases

The Billia Croo site (58.96 °N, 3.38 °W) at the European Marine Test Centre (EMEC) in the UK, is considered here as the operational site. The hourly reanalysis data of 1979/01/01–present from the European Centre for Medium-Range Weather Forecasts (ECMWF) are used to obtain the extreme sea states related to a long-term return period [5]. The long-term variation of sea states is described by a joint distribution achieved by fitting the signifiant wave height (H_S) distribution via a Weilbull distribution and fitting the peak wave period (T_P) via a H_S conditional log-normal distribution. As a result, the 50-year environmental contour line is obtained and plotted in Fig. 2(a), which gives a set of H_S - T_P to represent the extreme sea states having the largest probablity to generate design reponse.

Table 2. Description of the test cases under 1:50 scale for model testing.

Wave Parameter				**IR**	**SDW**
H_S **[m]**	T_P **[s]**	f_P **[rad/s]**	γ		
0.22	2.2	2.86	1	IR-50year-1	NW-50year-1, MLRW-50year-1, CRW-50year-1, CRRW-50year-1
			3.3	IR-50year-2	NW-50year-2, MLRW-50year-2, CRW-50year-2, CRRW-50year-2
0.05	1.1	5.71	1	IR-R-1	NW-R-1, MLRW-R-1, CRW-R-1, CRRW-R-1
			3.3	IR-R-2	NW-R-2, MLRW-R-2, CRW-R-2, CRRW-R-2

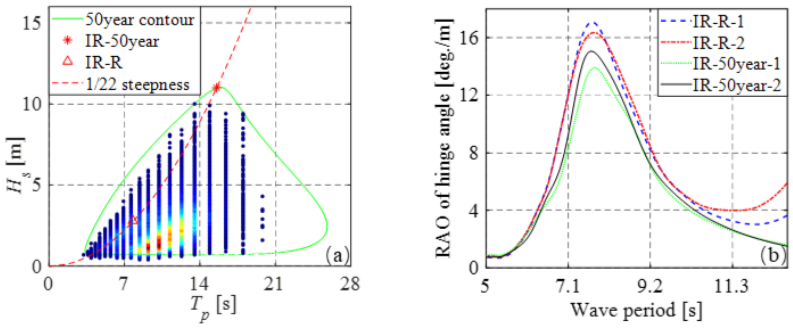

Fig. 2. (a) Schematic of the waves for the EMEC site in full scale. (b) RAOs of the relative hinge angle in full scale.

Considering the linear wave with no breaking, two wave conditions along the 1/22 steepness line are determined to study, as decipted in Fig. 2(a): one is the wave hitting the desired 50-year contour line with the largest H_S, called 50year; another is the wave at the targeted hinge resonance of the device, called R (see Fig. 2(b)). The long-duration IRs are modelled by the JONSWAP spectrum with two different gamma (γ) values. Then, 4 types of SDW are tested on the WEC. The detailed test program is described in Table 2.

3 RESULTS AND DISCUSSION

3.1 Impact of Proceeding Wave Effect and Transient Dynamics

Fig. 3 shows the comparison of the NWs with different γ at the same wave condition and the generated relative hinge angle responses. Clearly, NW-R-1 and NW-R-2 achieve the same focused peak value at 45 second, while they have different proceeding waves before 45 seconds, which leads the WEC to generate different peaks of hinge angle. This may indicate the disadvantage of NW for dynamically floating structures in that the wave with large amplitude is not the only factor to produce extreme response and the proceeding waves before the peak can also be of considerable importance for the extreme response of a dynamically floating structure.
Fig. 4 compares the results from NWs at two wave conditions: R and 50year. As observed, NW-R-1 with much smaller H_S but with targeted response resonance period produces a larger response reaction than NW-50year-1 which has higher H_S. This indicates that NW with large focus amplitude may not generate the extreme response for floating structures and a design wave such as the MLER that considers the transient dynamics of a device (i.e., response RAO) may perform better.

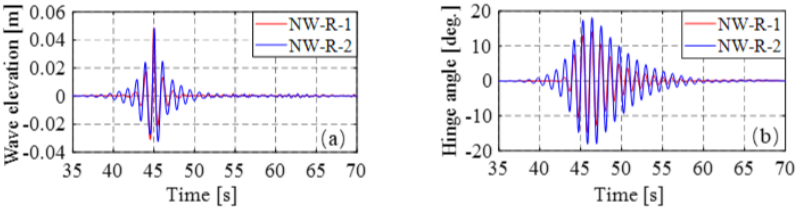

Fig. 3. Examples of proceeding wave effect on this floating hinged raft WEC under wave conditions of NW-R-1 and NW-R-2. (a) Wave elevation. (b) Hinge angle response.

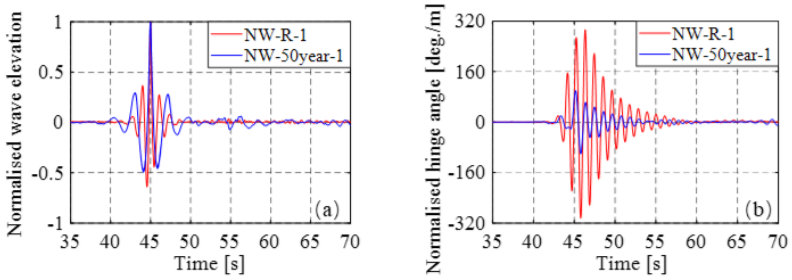

Fig. 4. Examples of transient dynamics effect on this floating hinged raft WEC under wave conditions of NW-R-1 and NW-50year-1. (a) Normalised wave elevation. (b) Normalised hinge angle response.

3.2 SDWs for Extreme Response

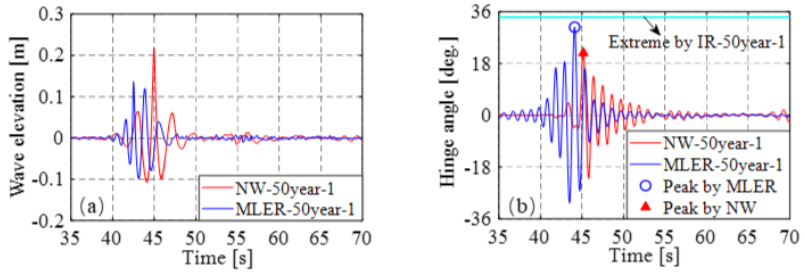

Fig. 5. Comparison of NW and MLER under wave condition of 50year-1. (a) Wave profiles of NW-50year-1 and MLER-50year-1. (b) Hinge angle responses generated.

Fig. 5 shows the physically measured results from NW and MLER under wave condition of 50year-1. As seen, the wave profile MLER with consideration of the response RAO is totally different from the profile of the NW. Furthermore, the MLER with smaller peak amplitude leads to a larger hinge angle of 31 degree, which is quite close to the extreme target of 34 degree through long-duration IR wave, compared with that from NW.
Fig. 6 shows the probability distributions of the hinge angle for different sea states tested. The presented distributions are obtained by physical model testing under IR waves with the Rayleigh distribution based on

the zeroth spectral moment of the hinge angle response. For comparison, results from 20 CNWs, 20 CRRWs, a single NW and a MLER are also shown. The design response studied here is that with exceedance probability of 10^{-2}. Clearly, the physically obtained distributions more or less fit well those from the Rayleigh distribution. This states that the hinge angle response is mainly linear under the sea states studied. Then, the figure shows that using response conditioned SDWs such as MLER and CRRW produce hinge angles at lower exceedances compared with wave based SDWs such as NW and CNW. Using MLER generates hinge angles fitting well with the target 10^{-2} exceedance probability, while NW considerably underpredict the extreme response. With consideration of random backgrounds, both CNW and CRRW could generate hinge angle reaching exceedance probability of 10^{-2}, while a considerably higher percentile is required for CNW and the hinge angles predicted from CNWs have greater variations.

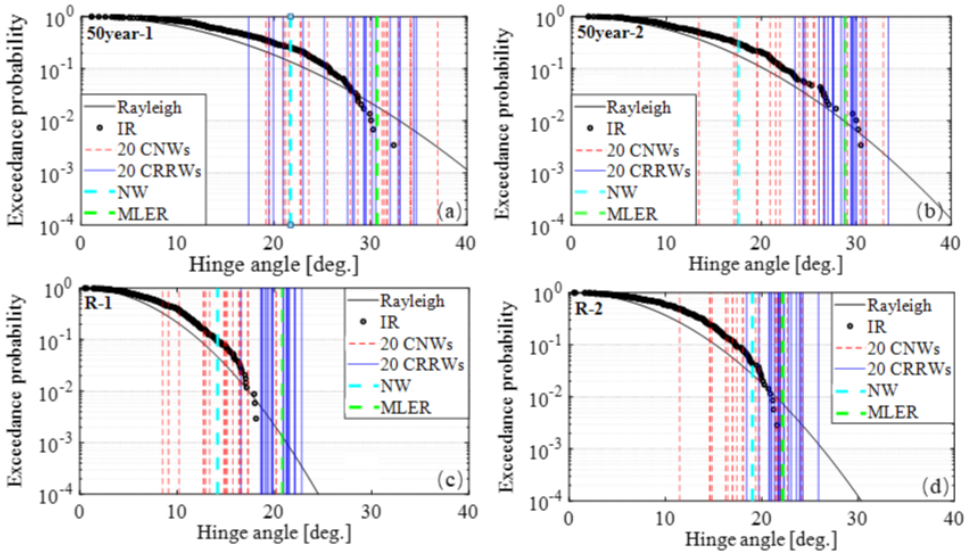

Fig. 6. Comparison of IR, CNW, CRRW, NW and MLER for relative hinge angle response. The theoretical probability distributions are described by the Rayleigh distribution. (a) Under 50year-1. (b) Under 50year-2. (c) Under R-1. (d) Under R-2.

4. Conclusion

This study has carried out a series of physical model tests to investigate the application of SDWs for generating extremes on a 1:50 scale floating hinged raft WEC. It has been found that response conditioned design waves such as the MLER and CRRW have better performance than wave conditioned SDWs such as NW and CNW for generating extremes on a floating structure. Other design responses are worth investigating, such as mooring load, bending moment, etc., in future work. Application of SDWs under wave conditions with high nonlinearity and even wave breaking is also of interest to study.

ACKNOWLEDGEMENT

This work was conducted within the Supergen Offshore Renewable Energy Hub (EP/S000747/1) funded by Engineering and Physical Sciences Research Council (EPSRC).

REFERENCES

[1] NORSOK STANDARD: N-003. Actions and action effects. 2007.
[2] IEC, Marine energy - Wave, tidal and other water current converters - Part 2: Design requirements for marine energy systems. Technical Specification IEC TS 62600-2. 2016.
[3] Hansen, P.F. and L.P. Nielsen, On the New Wave model for the kinematics of large ocean waves. Ocean Waves, 1995.
[4] P.H. Taylor, P. Jonathan, and L.A. Harland. Time domain simulations of jack-up dynamics with the extremes of a Gaussian process. in 14th Int Conf Offshore Mech Arct Eng.
[5] ECMWF. https://www.ecmwf.int/.

Generalised hybrid element method for oscillatory motion of multiple floating structures in oblique regular waves.

Mohamin B M Khan[1], **Michael H. Meylan**[2], **Harekrushna Behera**[1]
[1]Department of Mathematics, SRM Institute of Science and Technology, Kattankulathur 603203, India
[2]School of Mathematical and Physical Sciences, University of Newcastle, Callaghan 2308, Australia
E-mail: muhaymin77@gmail.com

HIGHLIGHTS

- The hydrodynamics and wave interaction with multiple surface piercing floating structures with arbitrary cross-sections are examined.
- The system is modelled under linear water wave theory and the boundary problem is solved using a *hybrid element method* combining eigenfunction expansion and boundary element method.
- The simulation involves instantaneous coupling the equations of motion for the moultiple floating structures and the fluid potentials.
- The hydrodynamics are studied using frequency dependent coefficients for wave forces, wave reflection and transmission.

1. INTRODUCTION

The hydrodynamics of floating structures are essential in design and engineering of the categories ocean structures like wave energy devices, free surface breakwaters, offshore platforms, ships etc., which has a significant impact in the areas of coastal engineering, environmental protection, recreation, and various marine facility designs. A significant aspect in floating body hydrodynamics is the steady oscillating motion of the structure at the free surface. The oscillations of a floating body were the first consistently examined by studying the superimposition of wave harmonics [1], and the transient motions of a freely floating structure that simultaneously solved the time-domain fluid-motion and rigid-body dynamics of the system [2]. Since then many researchers have theortically examined the problem using methods like Galerkin approximation and finite element formulation [3], classical matched eigenfunction expansion method [4][5], Boussinesq-type equations and eigenmode expansion [6] etc. These and other works collectively expounded the hydrodynamics of such systems using scattered, radiated and diffracted potentials, as well as wave forces, surface elevations and hydrodynamic coefficients. In spite of the large amount of literature on floating breakwaters in numerical, analytical and experimental approaches, the growing complexity of current and upcoming models has reignited the need for fast and stable numerical schemes that can instantaneously couple the fluid forces in the system and dynamics of an arbitrary floating body.

In the current work, the hydrodynamics of a general system of multiple floating structures, each having vertical oscillations is modeled using linear water wave theory. The simulation involves coupling the equations of motion for the floating body and the fluid potentials. The boundary value problem is solved using hybrid-element method combining eigenfunction expansion and boundary element methods (EFEM-BEM). The hydrodynamics are studied using frequency dependent coefficients. Results for multiple box type floating breakwaters are presented in this scenario. In addition to reducing wave load excitation on the floating structures, the study will enhance the understanding of the impacts of various physical parameters for minimizing incident wave energy, wave reflection, and transmission.

2. MATHEMATICAL FORMULATION

Wave interaction with multiple floating structures is modeled using the linear water wave theory and solved using a hybrid element method EFEM-BEM. The fluid-structure interaction is considered in a cartesian co-ordinate system wherein the fluid is modeled as inviscid, incompressible and irrotational,

due to which a scalar velocity potential $\Phi(x, y, z, t)$ can be defined satisfying $\nabla^2\Phi = 0$. The configuration in Fig. 1 consists of N floating structures A_j having different widths r_j, where $j = 1, 2, \cdots N$, over a uniform seabed at water depth $z = -h$. The spacing between the structures j and $j+1$ is l_j, and the distances d_j are defined recursively as $d_1 = r_1,\ d_{j+1} = (d_j + l_j + r_{j+1}),\ j = 2, \cdots, (N-1)$. Thus, the fluid domain under consideration is divided into the water region A_0, with outer regions one the sea- and lee- side labelled as O_1 and O_2, respectively. It is presumed that the incident wave makes an angle θ, with the $x-$ axis and the fluid flow is simple harmonic in time with angular frequency ω. The existing velocity potential in the three regions is of the form $\Phi(x, z, t) = \Re\{\phi(x, z)e^{-\mathrm{i}(k_y y - \omega t)}\}$, and $k_y = k_0 \sin\theta$, where k_0 is the progressive wave number, and the spatial velocity potentials $\phi(x, z)$ are solutions to the Helmholtz equation

$$\left(\frac{\partial^2}{\partial x^2} + \frac{\partial^2}{\partial z^2} - k_y^2\right)\phi = 0 \tag{1}$$

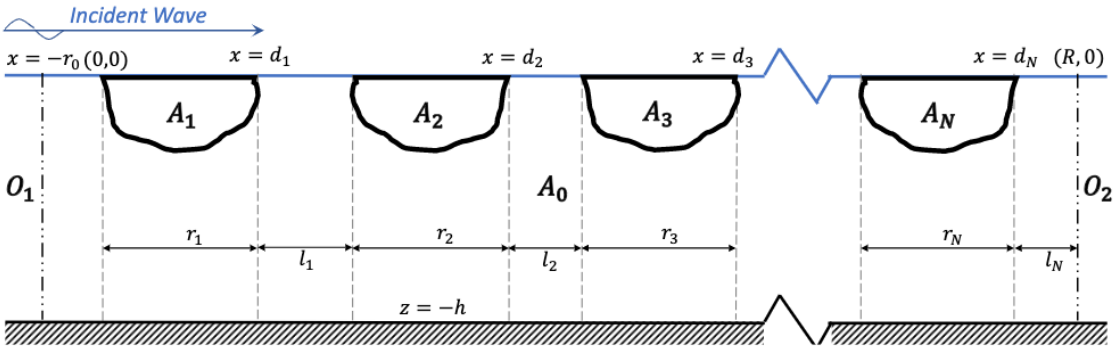

Figure 1: Schematic for the wave scattering configuration of multiple floating structures over a uniform seabed.

The mean free surface is governed by kinematic and dynamic boundary conditions which are combined to give the linearized free surface boundary condition as

$$\frac{\partial\phi}{\partial z} - K\phi = 0, \text{ for } z = 0 \text{ in } A_0, O_1, O_2, \tag{2}$$

where $K = \omega^2/g$, and the bottom boundary condition on the rigid sea floor is

$$\frac{\partial\phi_j}{\partial z} = 0, \text{ for } z = -h \text{ in } A_0, O_1, O_2. \tag{3}$$

On the fluid-structure interface S_j between structure A_j and water region A_0, $j = 1, 2, \cdots N$, assuming the uniform vertical displacement η_j, the oscillatory motion is governed by the following N pair of equations for $j = 1, 2, \cdots N$

$$\frac{\partial\phi}{\partial \boldsymbol{n}} = \frac{\partial\eta_j}{\partial t}(\boldsymbol{k}.\boldsymbol{n}) \tag{4}$$

$$m_j\frac{\partial^2\eta_j}{\partial t^2} = -\rho_j g\eta_j + i\omega\rho_j\int_{S_j}\frac{\partial\phi}{\partial t}(\boldsymbol{k}.\boldsymbol{n})\ ds, \tag{5}$$

where $\boldsymbol{k}$ is the unite vector in z-direction, $\boldsymbol{n}$ is the outward normal to the region A_0, ρ_j is the structure density, and m_j is the structure mass. The radiation conditions for outer regions O_1 and O_2 are

$$\phi_{O_1} = \left(I_0 e^{-\mathrm{i}q_0 x} + \mathscr{R}_0 e^{\mathrm{i}q_0 x}\right)\zeta_0(k_0, z) \quad \text{as} \quad x \to -\infty, \tag{6}$$

$$\phi_{O_2} = \mathscr{T}_0 e^{-\mathrm{i}q_0 x}\zeta_0(k_0, z) \qquad \text{as} \quad x \to \ \infty, \tag{7}$$

where I_0 is the known incident amplitude, $\mathscr{R}_0$ and $\mathscr{T}_0$ are the undetermined constants. $\zeta_0(k_0, z)$ is the eigenfunction in the outside region O_1 with $q_0 = \sqrt{k_0^2 - k_y^2}$.

3. SOLUTION METHODOLOGY

The numerical modeling of the wave action against N floating structures is undertaken using the hybrid element method (EFEM-BEM) applied on the three domains. The above boundary value problem is tackled using the eigenfunction expansion of the potential in the outer regions O_1, O_2 combined with a boundary element method in the inner fluid domain. The fundamental solution Green's function, derived using Green's theorem, is implemented to convert the BVP into a boundary integral equation. The domain of infinite water region is constricted by using fictitious auxiliary boundaries defined at $x = -r_0$ and $x = R = d_N + l_N$ where r_0 and l_N are defined for auxiliary boundaries on left and right of the $N-$structure array. The velocity potentials from eigenfunction expansion method are used to evaluate the boundary conditions on auxiliary boundaries and subsequently used in the boundary element formulation that begins with $\mathcal{G}_0 \equiv \mathcal{G}(\boldsymbol{x}, \boldsymbol{x}_0)$ as the fundamental solution to Laplace equation when it satisfies $\nabla^2 \mathcal{G}_0 + \delta_{\boldsymbol{x}_0} = 0$, where $\delta_{\boldsymbol{x}_0}$ is the Dirac delta distribution at the source point $\boldsymbol{x}_0$. Thus $\mathcal{G}_0$ represents a radially symmetric solution field emanating from a unit source concentrated at $\boldsymbol{x}_0$ and extending to infinity. Implementing the fundamental solution $\mathcal{G}_0$ and the potential ϕ into the *Green's* 2^{nd} *identity*, the boundary integral representation can be formalized as follows:
Let ϕ be a harmonic function in $\Gamma \in \mathbb{R}^2$, a simple open and connected domain with boundary $\partial\Gamma$. Then $\phi(\boldsymbol{x}_0)$ for $\boldsymbol{x}_0 \in \Omega$ can be expressed as

$$\phi(\boldsymbol{x}_0) = \int_{\partial\Gamma} \left(\mathcal{G}(\boldsymbol{x}, \boldsymbol{x}_0) \frac{\partial \phi(\boldsymbol{x})}{\partial \boldsymbol{n}} - \phi(\boldsymbol{x}) \frac{\partial \mathcal{G}(\boldsymbol{x}, \boldsymbol{x}_0)}{\partial \boldsymbol{n}} \right) d\boldsymbol{x} \tag{8}$$

where $\mathcal{G}(\boldsymbol{x}, \boldsymbol{x}_0)$ is the fundamental solution of the Laplace equation and

$$\mathcal{G}(\boldsymbol{x}, \boldsymbol{x}_0) = -\frac{1}{2} \ln |\boldsymbol{x} - \boldsymbol{x}_0|_2 \quad \text{and} \quad \frac{\mathcal{G}(\boldsymbol{x}, \boldsymbol{x}_0)}{\partial \boldsymbol{n}} = -\frac{\boldsymbol{n} \cdot (\boldsymbol{x} - \boldsymbol{x}_0)}{||\boldsymbol{x} - \boldsymbol{x}_0||_2^2} \tag{9}$$

In case of oblique waves, the the fundamental solution to the Helmholtz equation Eq. (1) is Green's function $\mathcal{G}$ satisfying

$$\frac{\partial^2 \mathcal{G}}{\partial x^2} + \frac{\partial^2 \mathcal{G}}{\partial z^2} - k_y^2 \mathcal{G} = \delta(x - x_0)\, \delta(z - z_0)\,, \text{ given by} \tag{10}$$

$$\mathcal{G}(x,\, z\,;\, x_0,\, z_0) = -\frac{\mathrm{K}_0(k_y r)}{2\pi}, \quad \text{and} \quad \frac{\partial \mathcal{G}}{\partial \boldsymbol{n}} = \frac{k_y}{2\pi} \mathrm{K}_1(k_y r) \frac{\partial r}{\partial \boldsymbol{n}}, \tag{11}$$

where $r = \sqrt{(x - x_0)^2 + (z - z_0)^2}$ is the distance between (x_0, z_0) and (x, z) (i.e. source point to field point), K_0, K_1 are the second kind modified Bessel functions of 0^{th} order, 1^{st} order, respectively. In both cases of normal and oblique waves, for a closed domain Γ having boundary $\partial\Gamma$ the boundary integral representation from Eq. (8) is given by

$$\int_{\partial\Gamma} \left(\mathcal{G}(\boldsymbol{x}, \boldsymbol{x}_0) \frac{\partial \phi(\boldsymbol{x})}{\partial \boldsymbol{n}} - \phi(\boldsymbol{x}) \frac{\partial \mathcal{G}(\boldsymbol{x}, \boldsymbol{x}_0)}{\partial \boldsymbol{n}} \right) d\boldsymbol{x} = \begin{cases} 0, & \boldsymbol{x}_0 \text{ outside } \Gamma, \\ \frac{1}{2}\phi(\boldsymbol{x}_0), & \boldsymbol{x}_0 \text{ on } \partial\Gamma, \\ \phi(\boldsymbol{x}_0), & \boldsymbol{x}_0 \text{ inside } \Gamma, \end{cases} \tag{12}$$

Eqs. (12) are solved for the entire boundary $\partial\Gamma$ of the three domains using constant element boundary element method (BEM). The physical boundaries of the domains $\partial\Gamma_j$ are discretized into finite number of elements on which the values of ϕ and $\phi_{\boldsymbol{n}}$ are taken as constant. Implementing the boundary conditions, the integral equations are discretized, following which the kernels are integrated using Gaussian integration to evaluate the integral coefficients. The resulting system of equations is solved as a matrix equation and the unknown potentials are evaluated.

3.1 Velocity potentials in the outer region using eigenfunction expansion

In particular, due to the absence of a structure in the outer regions O_1 and O_2 and approximation of

a uniform bottom bed bottom bed, the velocity potentials are deduced by the eigenfunction expansion method, such that for $k_n,\ n = 1, 2, \cdots$ modes, the spatial velocity potential satisfying Eq. (1) along with Eqs. (2)-(3) and Eqs. (6)-(7) in the outer region are given by a combination of eigenfunctions and expressed as

$$\phi_{O_1} = I_0 e^{-\mathrm{i}q_0(x+r_0)}\zeta_0(k_0,z) + \sum_{n=0}^{\infty} \mathscr{R}_n\ e^{\mathrm{i}q_n(x+r_0)}\zeta_n(k_n,z) \quad \text{at} \quad \Gamma_L, \tag{13}$$

$$\phi_{O_2} = \sum_{n=0}^{\infty} \mathscr{T}_n\ e^{-iq_n(x-R)}\zeta_n(k_n,z) \quad \text{at } \Gamma_R, \tag{14}$$

where $\zeta_n(k_n,z)$ are given by $\zeta_n(k_n,z) = \left(\dfrac{\mathrm{i}g}{\omega}\right)\dfrac{\cosh k_n(z+h)}{\cosh k_n h}$, with k_n satisfying the dispersion relation $\omega^2 = gk_n\tanh(k_n h)$. The undetermined constants $\mathscr{R}_n$ and $\mathscr{T}_n$ are evaluated using orthogonality of eigenfunctions ζ_n in the outside regions as

$$\mathscr{R}_n + \delta_{n0} = \frac{1}{\mathscr{E}_n}\int_{-h}^{0} \phi_{O_1}(z)\Big|_{x=-r_0}\ \zeta_n(k_n,\ z)\,dz, \tag{15}$$

$$\mathscr{T}_n = \frac{1}{\mathscr{E}_n}\int_{-h}^{0} \phi_{O_2}(z)\Big|_{x=R}\ \zeta_n(k_n,z)\,dz, \tag{16}$$

where $\mathscr{E}_n = \displaystyle\int_{-h}^{0} {\zeta_n}^2(k_n,z)\,dz = -\left(\frac{g^2}{\omega^2}\right)\frac{k_n h + \sinh(k_n h)\cosh(k_n h)}{2k_n\cosh^2(k_n h)}$ and δ_{n0} is the Kronecker delta function. The derivative of potential is given as

$$\frac{\partial\phi_{O_1}}{\partial \boldsymbol{n}}\bigg|_{x=-r_0} = -\frac{\partial\phi_{O_1}}{\partial x}\bigg|_{x=-r_0} = \mathrm{i}q_0 I_0\zeta_0(k_0,\ z) - \sum_{n=0}^{\infty}\mathrm{i}q_n\mathscr{R}_n\zeta_n(k_n,\ z)\,. \tag{17}$$

Substituting for $\mathscr{R}_n$ from Eq.(15) in Eq.(17) and truncating the infinite series after N-terms, it is derived that

$$\frac{\partial\phi_{O_1}}{\partial \boldsymbol{n}}\bigg|_{x=-r_0} = \Omega\left[\phi_{O_1}(z)\Big|_{x=-r_0}\right] + 2\mathrm{i}q_0 I_0\zeta_0, \text{ where } \Omega \text{ is given by} \tag{18}$$

$$\Omega\left[\phi_{O_1}(z)\Big|_{x=-r_0}\right] = -\sum_{n=0}^{N}\frac{\mathrm{i}q_n}{\mathscr{E}_n}\left\{\int_{-h}^{0}\phi_{O_1}(s)\,\zeta_n(k_n,\ s)\,ds\right\} I_n(k_n,\ z)\,. \tag{19}$$

The integral $\displaystyle\int_{-h}^{0}\phi_{O_1}(s)\,\zeta_n(k_n,\ s)\,ds$ is evaluated using the same boundary element discretization as in the evaluation of Green's function and its normal derivative on the auxiliary boundary, which in turn gives the matrix factorization of Ω. Thus, the integral is evaluated exactly, which in turn gives the matrix factorization of Ω. Finally, Eqs. (12) and (19) are solved to derive a final matrix equation to determine the unknown constants of the outer solution.

4. RESULTS

In the following results, upto three structures of rectangular shape are considered. The optimal parameters $r_j/h = 0.5, l_j/h = 0.5, \forall j$ and $\theta = 10^\circ$, kept fixed, unless otherwise stated. The observations here are mainly discussed for wave scattering by the system and wave forces on the multiple structures in varied configurations. The reflection, transmission and dissipation coefficients (K_r, K_t and K_d) and vertical wave force on structure A_j are calculated as

$$K_r = \left|\frac{\mathscr{R}_0}{I_0}\right|,\quad K_t = \left|\frac{\mathscr{T}_0}{I_0}\right|,\quad K_d = 1 - K_r^2 - K_t^2,\quad F_v = \frac{i\omega}{gh^2}\int_{S_j}\phi(\boldsymbol{k}.\boldsymbol{n})\ ds. \tag{20}$$

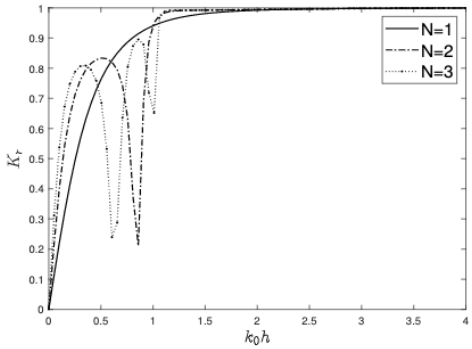

(a) Reflection coefficient

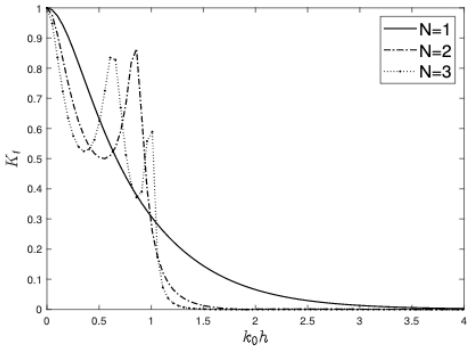

(b) Transmission Coefficient

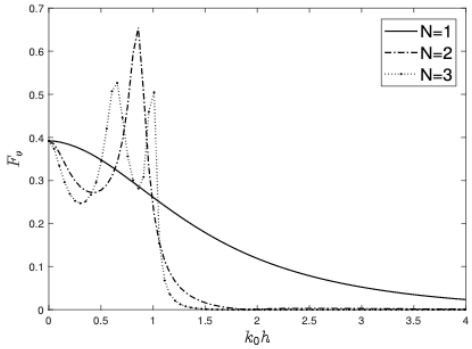

(c) Vertical force on lee-side structure

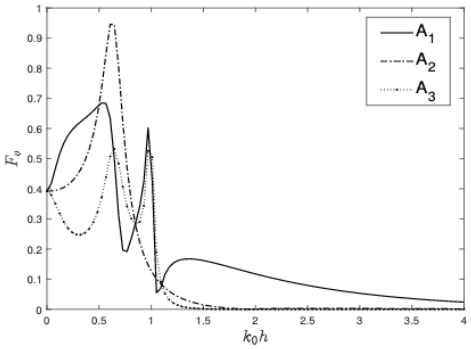

(d) Vertical force on each structure

Figure 2: Frequency dependence of hydrodynamics coefficients for multiple floating structures.

The above figures illustrate the frequency dependence of the hydrodynamic coefficients by plotting K_r, K_t and F_v against non-dimensional wavenumber k_0h. It is noticeable that with increase in the number of structures, the oscillatory patterns in the reflection and transmission coefficients increase (Figs.2(a),2(b)), indicating interference of incoming, reflected and radiated waves. This is also indicated by the vertical wave force on the lee side structure (Fig.2(c)) and wave forces on different structures (Fig.2(d)). The peaks and troughs in F_v correspond to interference of the waves that result in increasing oscillations in the floating bodies. These results agree with those already found in the literature, signifying the accuracy of the proposed method.

REFERENCES

[1] Ursell, F. 1964. *The decay of the free motion of a floating body.* Journal of Fluid Mechanics 19(2), 305–319.

[2] Yeung, R. 1982. *The transient heaving motion of floating cylinders.* Journal of engineering mathematics 16(2), 97–119.

[3] Sannasiraj, S., Sundar, V., and Sundaravadivelu, R. 1998. *Mooring forces and motion responses of pontoon-type floating breakwaters.* Ocean Engineering 25(1), 27–48.

[4] Zheng, Y., You, Y., and Shen, Y. 2004. *On the radiation and diffraction of water waves by a rectangular buoy.* Ocean engineering 31(8-9), 1063–1082.

[5] Zheng, Y., Shen, Y., You, Y., Wu, B., and Jie, D. 2006. *Wave radiation by a floating rectangular structure in oblique seas.* Ocean Engineering 33(1), 59–81.

[6] Mohapatra, S., and Guedes Soares, C. 2015. *Wave forces on a floating structure over flat bottom based on Boussinesq formulation. Renewable Energies Offshore. London: Taylor & Francis*, 335–342.

Elastic Responses of Wind-tracing Floating Offshore Wind Turbines

Azin Lamei[a], **Masoud Hayatdavoodi**[a,b] **and H. Ronald Riggs**[c]

a. School of Science and Engineering, University of Dundee, Dundee DD1 4HN, UK
b. College of Shipbuilding Engineering, Harbin Engineering University, Harbin, China
c. Civil and Environmental Engineering Dep., University of Hawaii, Honolulu, Hawaii 96822, USA

Email: alamei@dundee.ac.uk

This study is concerned with the motion analysis and structural responses of a multi-unit floating offshore wind turbine to combined wave and wind loads. Three wind turbines are placed on an equilateral triangular platform. A single-point mooring system is used to allow the structure to rotate in response to the environmental loads. Hydrodynamic and aerodynamic loads are determined by use of the linear diffraction theory and the blade element momentum method, respectively and the elastic response of the entire structure is determined by use of a finite element analysis. The responses of the fully flexible structure to co-directional and misaligned wind and wave loads are studied.

Introduction

Floating platforms that can support multiple wind turbines are introduced to potentially reduce the cost of floating offshore wind turbines. While placing multiple turbines on the same floating structure may reduce costs compared to multiple individual platforms, it adds to the complexities associated with the motion analysis and elastic response of the system to the environmental loads. In this study, a numerical approach is presented to obtain the elastic motions of multi-unit floating offshore wind turbines (FOWTs) to combined wind and wave loads. Here, a multi-unit wind-tracing triangular platform is considered. The platform consists of three pontoons and three columns at the corners, shown in Fig. 1 (a). Three 5 MW NREL wind turbines are installed on top of each column. To minimize the wake effects on the trailing wind turbine, the distance between each hub centre of the rotors is set to $2.2\,D_r = 277.2\ m$, where D_r is the rotor diameter. The draft of the structure is $d = 16\ m$. The structure is moored to the seabed with a single-point mooring system. A submerged turret bearing is located under the pontoons. Three taut cables connect the bottom of the columns of the platform to the turret and the turret is connected to the seabed with four catenary mooring lines. The turret can be located in an infinite number of horizontal and vertical locations under the platform. In an optimization study for the specific platform design, the preferred location of the turret is 64 m under SWL, along the x-axis and 40.05 m away from the trailing column. Further details about this concept can be found in Li et al. (2019).

A numerical tool is developed for aeroelasticity and hydroelasticity analysis of FOWTs in the frequency domain. The structural analysis of the entire FOWT is carried out with the finite element method. The aerodynamic loads on the rotors are obtained with blade element momentum method, and linear diffraction wave theory is used for the hydrodynamic loads on the floating structure. Herein, responses of the rigid and flexible structures to wave loads are determined and compared. Then, responses of the fully flexible structure to combined wind and wave loads for various incoming wave directions are obtained.

Combined Wave and Wind Impact on Elastic Bodies

A FOWT is typically under simultaneous effect of wind, wave and current loads and the mooring forces of the structure. The presented approach only considers the effect of wind and wave loads and the mooring forces of the FOWT. Hydrodynamic loads on the FOWT platform is computed by the linear wave diffraction theory. The total load on a floating structure is given by the sum of external hydrodynamic pressure force, hydrostatic restoration forces and mooring line loads. Linear hydroelasticity analysis is based on extending the rigid body degrees of freedom with generalized modes to include the deformation of the body. The mode shapes of the structure are obtained with the finite element method and the displacement of the structure is expressed with a reduced modal basis. In this case, the hydrostatic stiffness includes the change in the hydrostatic pressure and the structural geometric stiffness. The complete formulation developed by Huang & Riggs (2000) is applied. In the absence of wind loads, the equation of motion of the elastic body is written as

$$\xi_j[-\omega^2(M_{ij} + a_{ij}) + i\omega(\,b_{ij}) + (\,c_{ij,moor} \,+\, c_{ij})] \;=\; AX_i, \quad i,j = 1,2,\cdots m, \tag{1}$$

where $6 \leq m$ is the number of generalized modes, M_{ij} is the modal structural mass matrix, and a_{ij}, b_{ij} and c_{ij} are the added mass, hydrodynamic damping and hydrostatic stiffness coefficient matrices, respectively. Moreover, $c_{ij,moor}$ is the stiffness matrix of the mooring lines. X_i is the amplitude of wave excitation force divided by the wave amplitude A and is presented in complex form, ω is the wave frequency and ξ_j is the complex body response phasor in mode j.

The aerodynamic loads on the rotor is computed by the steady blade element momentum method. For a FOWT, the total thrust force on the rotor depends on the relative motion of the platform

$$T(V_{rel}) = \frac{1}{2}\rho A_r C_T(V_{rel}^2), \tag{2}$$

where ρ is the air density, A_r is the rotor projected area, and C_T is the thrust coefficient. The relative incoming wind speed on the rotor, V_{rel}, is defined as $V_{rel} = V_0 - V_h$, where V_0 is the incoming wind speed on a fixed rotor, and V_h is the speed of the hub centre, along the direction of the incoming wind. In frequency domain, V_h is expressed as $i\omega(\xi_1 + \xi_5(z_h - z_{cg}))$, where z_h and z_{cg} are the vertical coordinates at the hub and the centre of gravity. For a FOWT, assuming that the structure speed at the tower top, V_h is small, the thrust force with relative incoming wind speed, Eq. (2) can be approximated by Taylor series,

$$T(V_{rel}) = \frac{1}{2}\rho A_r C_T(V_0^2) - \rho A_r C_T(V_0\ i\omega(\xi_1 + \xi_5(z_h - z_{cg}))). \tag{3}$$

where the second order and higher terms are discarded. In Eq. (3), the first term represents the thrust force on a fixed tower and it is assumed that it is an excitation force in surge acting at the top of the structure by the incoming wind. The wind force is harmonic and with the same frequency as the incident waves, and the wind direction is always orthogonal to the rotor, parallel to the x-direction. We assume that the integrated aerodynamic normal force over the blades act at the hub centre and eventually is transferred to the tower top. Hence, we can obtain the wind load phase angle following the same approach as in MacCamy & Fuchs (1954) for wave-interaction with a circular cylinder i.e.

$$F_{1,W} = \frac{1}{2}C_T\rho V_0^2 A_r \cos(\omega t - \delta_{\text{aero}}), \tag{4}$$

where $F_{1,W}$ is the thrust force on a fixed rotor in surge and δ_{aero} is the phase angle of the inline force and it is determined as

$$\delta_{\text{aero}}(kr_0) \ = \ -\tan^{-1}\left[\frac{Y_1^{'}(kr_0)}{J_1^{'}(kr_0)}\right], \tag{5}$$

in which, k is the wave number, $J_p(kr)$ and $Y_p(kr)$ are the Bessel functions of the first and the second kind of order p, respectively, and r_0 is the top diameter of the tower. Furthermore, the second term in Eq. (3) can be rewritten as $i\omega(\xi_1 + \xi_5(z_h - z_{cg}))\rho C_T V_0$, where $\rho C_T V_0$ represents an aerodynamic damping coefficient, B_{aero}, for a FOWT. The total aerodynamic load vector acting on the centre of gravity, F_W is the sum of the wind load on the rotor and the tower calculated following a similar approach. The wind load vector, F_W, and the aerodynamic damping matrix, $B_{aero,mat}$ on the rotor are added to right-hand side and the left-hand side of the the equation of motion of a floating platform in frequency domain, Eq. (1), respectively. To determine the responses of a FOWT to combined wind and wave loads we have,

$$\xi_j[-\omega^2(M_{ij} + a_{ij}) + i\omega(\ b_{ij} + \ B_{aero,mat}\ ) + (\ c_{ij,moor} \ + \ c_{ij})] \ = \ AX_i \ + \ F_W\ , \quad i,j = 1,2,\cdots m. \tag{6}$$

The computations of the wind-tracing platform are carried out in HYDRAN-XR, (NumSoft Technologies 2020). HYDRAN-XR is a potential-flow solver integrated with finite element analysis and can consider single and multi-unit floating offshore wind turbines. HYDRAN-XR has been enhanced to include the wind loads on single and multi-unit FOWT

Here, rather than applying the total wind force at the hub centre as indicated above, the aerodynamic load is applied across the front face of the blades. Likewise, the wind load on the tower is distributed on its area facing the inflow wind. In aerodynamic analysis, the normal wind force on the annular control volumes over the blades are computed and distributed over the front face nodes of the rotor. Similarly, the aerodynamic damping coefficient is obtained with local thrust coefficients on each control volume and assigned to the front nodes of the blades. The final wind load vector, F_W, and aerodynamic damping matrix on the centre of gravity of the structure is obtained and added to the equation of motion of the FOWT in frequency domain. The equation of motion is solved for the translational and rotational modes of the structure together with the generalized modes, accounting for aeroelasticity and hydroelasticity of the FOWT.

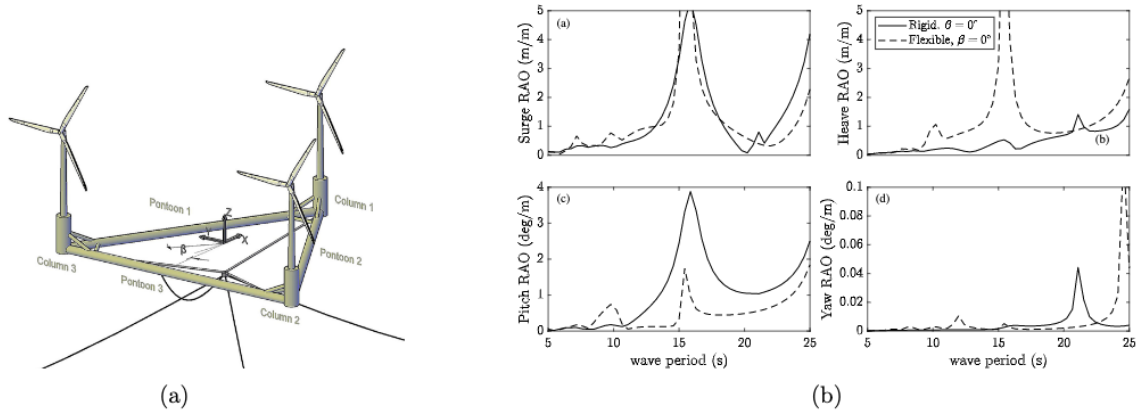

Figure 1: (a) Schematic of the wind-tracing multi-unit FOWT and (b) comparison of RAOs of the rigid and flexible structures to waves with $\beta = 0°$, in the absence of wind.

Results and Discussion

Results are presented in three parts, namely (*i*) comparison of the rigid and flexible responses to wave loads (in the absence of wind), (*ii*) comparison of the responses of a SPAR FOWT to combined wind and wave loads with laboratory measurements and (*iii*) responses of the flexible structure to combined wind and wave loads for several incoming wave directions.

An earth-fixed Cartesian coordinate system is chosen with its origin on the still water level, and z-axis pointing upwards in the positive direction. The translation motions, surge (ξ_1), sway (ξ_2), and heave (ξ_3), are parallel to the x-, y- and z-axes, respectively and the rotational motions, roll(ξ_4), pitch (ξ_5), and yaw (ξ_6), are about the x-, y- and z-axes, respectively.

The response amplitude operators (RAOs) of the wind-tracing FOWT are computed for the rigid and flexible structures. The RAOs in surge, heave, pitch and yaw for the rigid and flexible structures are compared over the wave period in headseas, $\beta = 0°$ in Fig. 1(b).

The surge RAOs of both rigid and flexible wind-tracing FOWTs are approximately similar over the wave period. However, the rigid structure undergoes larger pitch RAOs compared with the flexible body. Moreover, a new peak at approximately 15 s is introduced to the heave RAOs when the flexibility of the wind-tracing FOWT is included. The yaw RAOs of both rigid and flexible structures are approximately zero except at $T = 22$ s and $T = 24$ s, where a peak is computed for the rigid body and the flexible body, respectively.

Next, the motions of a 5 MW SPAR FOWT to waves and steady wind loads are computed and compared with laboratory measurements conducted by Ahn & Shin (2017). The laboratory experiments are carried out for a model with a scaling ratio of 1 : 128 with waves and rated wind speed of the 5 MW wind turbine, 11.4 m/s. The SPAR FOWT is moored with three catenary mooring lines in 320 s water depth and a draft of 120 m. The FOWT is modelled with respect to the prototype dimensions and its RAOs in surge, heave and pitch are compared with laboratory measurements by Ahn & Shin (2017) in Fig. 3. In general, an excellent agreement is observed between the numerical results by HYDRAN-XR and the laboratory measurements.

Finally, wind- and wave-induced responses of the fully flexible wind-tracing FOWT is computed in the frequency domain for co-directional and misaligned wind and wave loads. In our approach, with steady blade element momentum method, it is assumed that the incoming wind is always orthogonal to the rotors. Thus, the misalignment of wind and waves are modelled by varying the incoming wave direction. The wind load on the towers and the rotors of the wind-tracing FOWT is computed at wind speed 11.4 m/s. Figure 3 presents the RAOs of the wind-tracing FOWT in its rigid body modes for wave heading angles $\beta = 0°$, $45°$, $90°$ and $135°$, and wave periods from 5 s to 25 s. Shown in Fig. 3, heave RAOs do not change significantly by increasing the wave heading angles. However, in surge and pitch, RAOs with $\beta = 0°$ are larger than the responses with higher wave heading angles. Moreover, surge and pitch RAOs are both at their minimum with $\beta = 90°$. Furthermore, the wind-tracing FOWT experience largest motions in sway, roll and yaw when the wind load direction is perpendicular to the incoming wave

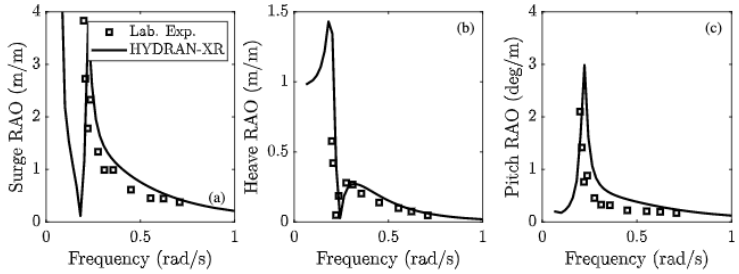

Figure 2: Comparison of the wave-induced RAOs of the SPAR FOWT computed by HDYRAN-XR and the laboratory measurements of Ahn and Shin (2017).

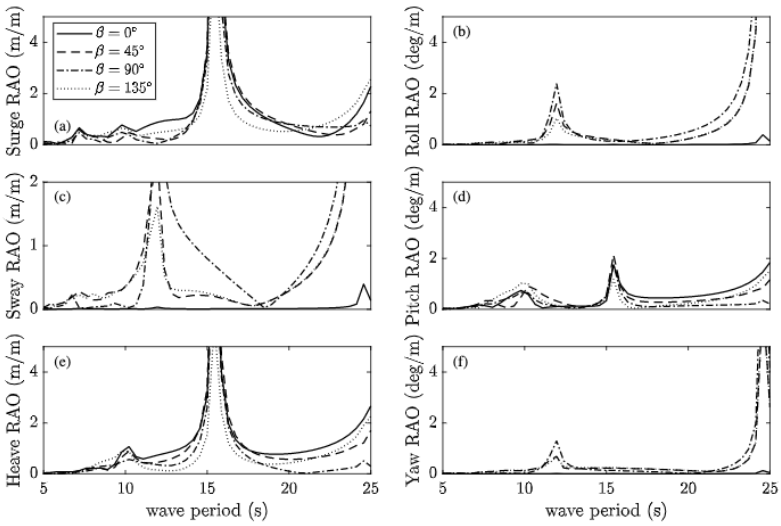

Figure 3: RAOs of the wind-tracing FOWT for codirectional and misaligned wind and wave loads, with wave heading angles $\beta = 0°$, 45°, 90° and 135°.

loads, *i.e.* $\beta = 90°$

Acknowledgement This work is partially funded by the CBJ-Ocean Engineering of Hong Kong.

References

Ahn, H. J. & Shin, H. (2017), 'Model test and numerical simulation of OC3 spar type floating offshore wind turbine', *International Journal of Naval Architecture and Ocean Engineering* **11**(1), 1–10.

Huang, L. L. & Riggs, H. R. (2000), 'The hydrostatic stiffness of fexible foating structures for linear hydroelasticity', *Marine Structures* **13**, 91–106.

Li, S., Lamei, A., Hayatdavoodi, M. & Wong, C. (2019), Concept design and analysis of wind-tracing floating offshore wind turbines, *in* 'Proceedings of the ASME 2019 2nd International Offshore Wind Technical Conference, November 3-6, St. Julian's, Malta', ASME, pp. 1–8.

MacCamy, R. & Fuchs, R. (1954), *Wave forces on piles: A diffraction theory*, Tech. Memo. No. 69, Beach Erosion Board. Army Corps of Engineers, 1-17.

NumSoft Technologies (2020), HYDRAN-XR, hydrodynamic response analysis with integrated structural finite element analysis, version 20.1, Technical report, Numsoft Technologies.

Abstract for 37th IWWWFB, Giardini Naxos, Italy - April 10-13, 2022

Decomposition of ship waves and time-frequency spectrograms

Hui Liang, Harrif Santo, Michael Si

Technology Centre for Offshore and Marine, Singapore (TCOMS), 118411, Singapore

E-mail: liang_hui@tcoms.sg

Highlights

- The viscous-ship-wave Green function [1] is applied to study wave patterns generated by a ship hull;
- The KHP approximation [2, 3] is conducted rendering a decomposition of transverse and divergent waves;
- Time-frequency spectrograms are analysed to study the amplitudes of transverse and divergent waves.

1 Green function and Hogner model

The ship-wave Green function represents the flow induced by a point singularity (source, sink, or dipole) with unit strength translating steadily along a straight path in calm water, and it is an essential building block to constructing the boundary integral equation to model free-surface flows by an advancing ship hull within the linear potential theory. As reported in [4], however, very short and steep divergent waves exist when both source and flow-field points are on the free surface. Moreover, the wave amplitude is unbounded as the flow-field point approaches the track of the source point. To eliminate these unphysical behaviours, fluid viscosity is accounted for as in [1]. Under the influence of fluid viscosity effects, and singular behaviour is eliminated, and steep short waves are severely damped out. This viscous-ship-wave Green function is then used as the fundamental solution to construct the boundary integral equation to model wave patterns by a ship hull.

A frame of reference $Oxyz$ translating with the ship at a constant speed U in the direction of the positive x-axis is defined with the Oxy plane coinciding with the undisturbed free surface and z-axis orienting positively upward. Following [1], the viscous-ship-wave Green function is

$$4\pi G = -1/r + 1/d + G^F, \quad \text{with } \{r, d\} = \sqrt{(x-\xi)^2 + (y-\eta)^2 + (z \mp \zeta)^2}, \tag{1}$$

where $\mathbf{x} \equiv (x, y, z)$ and $\boldsymbol{\xi} \equiv (\xi, \eta, \zeta)$ denote the flow-field point and source point, respectively, and G^F is the free-surface term in the form of a double Fourier integral. The free-surface term G^F can be decomposed into a non-oscillatory local-flow component G^L and a wave component G^W dominant in the far field, given by

$$G^L = \frac{2\kappa}{\pi}\mathrm{Im}\int_{-1}^{1} \mathrm{e}^Z E_1(Z)\mathrm{d}q, \quad \text{with } Z = -\mathrm{i}\kappa\sqrt{1-q^2}[-|x-\xi| + \mathrm{i}\sqrt{1-q^2}(z+\zeta) - \mathrm{i}q(y-\eta)], \tag{2}$$

$$G^W = 4H(\xi - x)\mathrm{Im}\int_{-\infty}^{\infty} \kappa \exp\left\{\kappa(1+q^2)(z+\zeta) + 4\epsilon\kappa(x-\xi)\frac{(1+q^2)^3}{1+2q^2} + \mathrm{i}\kappa\sqrt{1+q^2}[(x-\xi) - q(y-\eta)]\right\}\mathrm{d}q, \tag{3}$$

where $\mathrm{e}^u E_1(u)$ is the complex exponential-integral function, κ is defined as $\kappa = g/U^2$, and ϵ is a parameter associated with viscous effects defined as $\epsilon = g\nu/U^3$.

To model free-surface flows around a ship hull, the highly simple but realistic Hogner model [5] is adopted. The flow induced by an advancing ship hull is represented by a source distribution with strength n_ξ over the mean wetted hull surface

$$\phi(\mathbf{x}) = \iint_{\Sigma^H} n_\xi G(\mathbf{x}, \boldsymbol{\xi})\mathrm{d}S, \tag{4}$$

where Σ^H denotes the mean wetted hull surface, and n_ξ is the component in x-direction of the vector normal to the ship hull. Introducing polar coordinates $(x, y) = h(-\cos\gamma, \sin\gamma)$, where γ is measured from the negative x-axis, the potential induced by the ship hull in the far field ($h/L \gg 1$) is written in a Fourier-Kochin form [6]

$$\phi^W(\mathbf{x}) = \iint_{\Sigma^H} n_\xi G^W(\mathbf{x}, \boldsymbol{\xi})\mathrm{d}S = \frac{\kappa}{\pi}\mathrm{Im}\int_{-\infty}^{\infty} A(\mathbf{x}, q)\mathrm{e}^{\mathrm{i}\kappa h\psi(q,\gamma)}\mathrm{d}q, \tag{5}$$

where the Kochin function $A(\mathbf{x}, q)$ and phase function $\psi(q, \gamma)$ are written as:

$$A(\mathbf{x}, q) = \iint_{\Sigma^H} n_\xi \exp\left[\kappa(1+q^2)(z+\zeta) + 4\epsilon\kappa(x-\xi)\frac{(1+q^2)^3}{1+2q^2} + \mathrm{i}\kappa\sqrt{1+q^2}(\xi + q\eta)\right]\mathrm{d}S, \tag{6}$$

$$\psi(q, \gamma) = \sqrt{1+q^2}(\cos\gamma - q\sin\gamma). \tag{7}$$

2 Uniform KHP approximation

The uniform asymptotic approximation to the wavenumber integral (5) is considered. Unlike the classical CFU approximation [7] involving the Airy function and its derivative, the KHP approximation [2, 3] only involves elementary functions. Moreover, the KHP approximation is able to provide an explicit decomposition of transverse and divergent waves that exist inside the cusps of the wave pattern.

Within Kelvin's wedge $\gamma < \gamma_c \equiv 19°28'$, there are two stationary points requiring the vanishing of the first-order derivative of the phase function, i.e. $\psi'(q,\gamma) = 0$, and they are given by

$$q_\pm = (1 \pm Q)\cot\gamma/4, \quad \Rightarrow \quad \psi''_\pm \equiv \psi''(q_\pm,\gamma) = \mp\frac{4}{\sqrt{3}}\frac{Q\sin\gamma}{\sqrt{(1\pm Q)(1\mp Q/3)}}, \quad \text{with } Q = \sqrt{1-8\tan^2\gamma}. \tag{8}$$

At the cusp $\gamma = \gamma_c$, two stationary points coalesce $q_- = q_+ = q_c = 1/\sqrt{2}$, and both first- and second-order derivatives of the phase function are nil, e.g.: $\psi'(q_c,\gamma_c) = \psi''(q_c,\gamma_c) = 0$. The third- and fourth-order derivatives at q_c are

$$\psi'''_c \equiv \psi'''(q_c,\gamma_c) = -4\sqrt{6}/9, \quad \text{and} \quad \psi''''_c \equiv \psi''''(q_c,\gamma_c) = 8\sqrt{3}/9. \tag{9}$$

Outside Kelvin's wedge $\gamma > \gamma_c$, two stationary points turn to two complex saddle points which are a complex conjugate pair. By deforming the integration path, only the contribution of the saddle point at which the imaginary part of ψ'' is larger than zero matters, and the selected saddle point is

$$q_o = (1-\mathcal{Q})\cot\gamma/4, \quad \Rightarrow \quad \psi''_o \equiv \psi''(q_o,\gamma) = \frac{4}{\sqrt{3}}\frac{\mathcal{Q}\sin\gamma}{\sqrt{(1-\mathcal{Q})(1+\mathcal{Q}/3)}}, \quad \text{with } \mathcal{Q} = \mathrm{i}\sqrt{8\tan^2\gamma - 1}. \tag{10}$$

Based on [3], the approximation to wave pattern inside the cusp $\gamma \le \gamma_c$, combining ones due to Kelvin and Havelock, is written as

$$\phi^W(\mathbf{x}) \approx \frac{\kappa}{\pi}\mathrm{Im}\left[F_-^{KH}\mathrm{e}^{\mathrm{i}(\kappa h\psi_- + \pi/4)} + F_+^{KH}\mathrm{e}^{\mathrm{i}(\kappa h\psi_+ - \pi/4)}\right], \tag{11}$$

where the functions $F_\pm^{KH}$ are defined as

$$F_\pm^{KH} = (1-\mathrm{e}^{-u^{4/3}})\frac{\sqrt{2\pi}A_\pm}{\sqrt{\kappa h|\psi''_\pm|}} + \mathrm{e}^{-u^{4/3}}\frac{C_H^* A_c}{(\kappa h|\psi'''_c|)^{1/3}}\left[1 \mp \frac{\Gamma(2/3)}{\Gamma(1/3)}\left(\frac{A'_c}{A_c} - \frac{\psi''''_c}{6\psi'''_c}\right)\left(\frac{6}{\kappa h\psi'''_c}\right)^{1/3}\right], \tag{12}$$

with $C_H^* \equiv \Gamma(1/3)/6^{1/6} \approx 1.987334$, and $u = 3\kappa h|\psi_+ - \psi_-|/4$. Eq. (11) provides an explicit decomposition of the two systems of waves consisting of transverse waves and divergent waves associated with the first term and second term, respectively, in the square bracket of Eq. (11). At the cusp, there is a phase difference $\pi/2$ of transverse and divergent waves. The approximation to wave pattern outside the cusp $\gamma \ge \gamma_c$, which combines approximations due to Havelock and Peters, is written as

$$\phi^W(\mathbf{x}) \approx \frac{\kappa}{\pi}\mathrm{Im}\left[F_o^{HP}\mathrm{e}^{\mathrm{i}(\kappa h\psi_o + \pi/4)}\right], \tag{13}$$

where the function F_o^{HP} is defined as

$$F_o^{HP} = (1-\mathrm{e}^{-v^{4/3}})\frac{\sqrt{2\pi}A_o}{\sqrt{\kappa h\psi''_o}} + \mathrm{e}^{-v^{4/3}}\frac{(1-\mathrm{i})C_H^* A_c}{(\kappa h|\psi'''_c|)^{1/3}}\left[\mathrm{e}^{-2v/3} + \mathrm{i}\frac{\Gamma(2/3)}{\Gamma(1/3)}\left(\frac{A'_c}{A_c} - \frac{\psi''''_c}{6\psi'''_c}\right)\left(\frac{6}{\kappa h\psi'''_c}\right)^{1/3}\right], \tag{14}$$

with $v = 3\kappa h\,|\mathrm{Im}(\psi_o)|/2$.

3 Wave patterns

For illustrative purposes, wave patterns generated by a modified Wigley hull model are considered, and the geometry of the Wigely hull is defined as

$$y = \pm\frac{L}{10}[(1-X^2)(1-Z^2)(1+0.2X^2) + Z^2(1-Z^8)(1-X^2)^4], \quad \text{where } X = \frac{2x}{L} \text{ and } Z = \frac{10z}{L}, \tag{15}$$

with $-L/2 \le x \le L/2$ and $-L/10 \le z \le 0$. In Eq. (15), L denotes the length of Wigley hull, and the Froude number associated with ship's speed is defined as $F = U/\sqrt{gL}$. Fig. 1 exhibits contour plots of wave patterns generated by the modified Wigley hull at $F = 0.4$, 0.6, and 0.8, respectively. Wave patterns together with their decomposition into transverse and divergent waves inside the cusp are displayed in the left, middle, and right subplots, respectively. The white dashed line in the left subplot corresponds to the cusp. At $F = 0.4$, the amplitude of transverse waves is appreciably larger than that of divergent waves, whereas the tendency is reversed at $F = 0.8$. The amplitudes of two wave systems are comparable at $F = 0.6$. Therefore, divergent waves play an increasingly dominant role with the increasing ship's velocity. Moreover, short divergent waves disappear near the track under the joint influences of fluid viscosity effects and ship hull interference effects as expounded in [1] and [8], respectively.

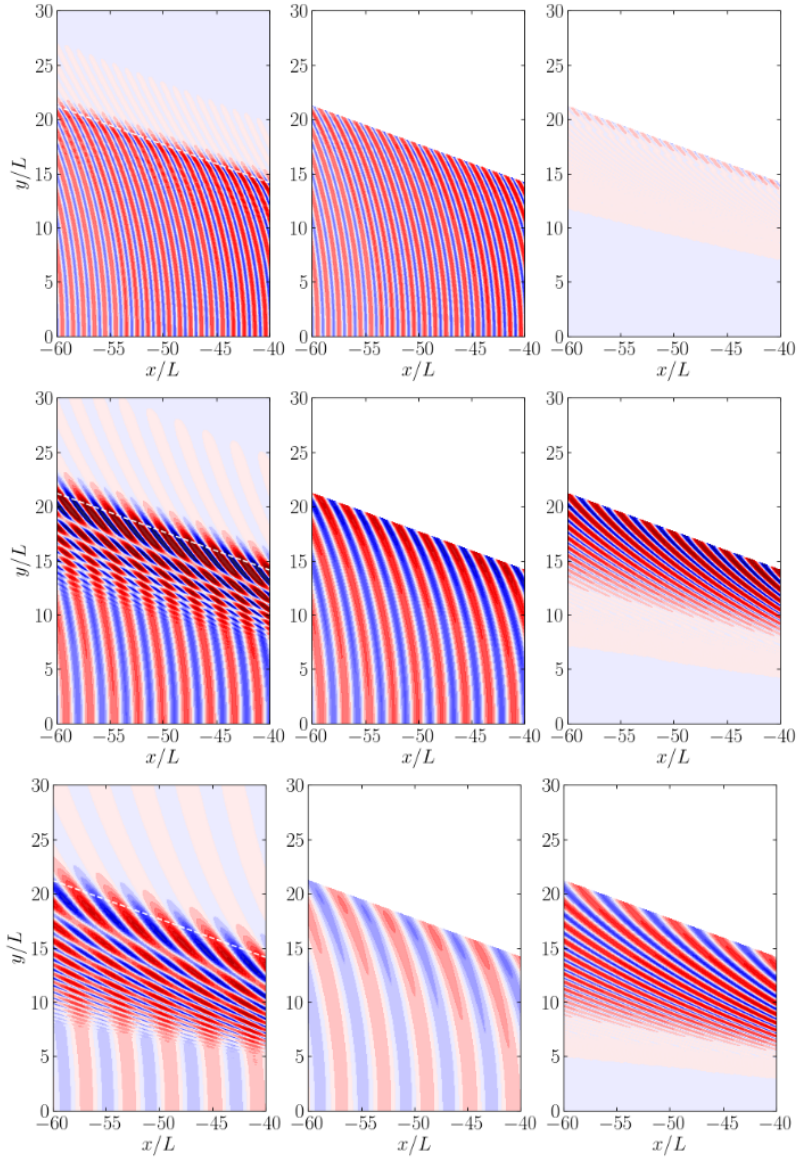

Figure 1: Wave patterns as well as decomposition into transverse waves and divergent waves for $F = 0.4$, 0.6, and 0.8 displayed in the top, middle, and bottom rows, respectively.

4 Time-frequency spectrogram

To further study the amplitudes of transverse and divergent waves inside Kelvin's wedge, the time-frequency spectrogram is studied. Based on the geometrical relation as in Fig. 2, we can obtain the frequencies of transverse waves and divergent waves measured at the sensor location [9]

$$\omega_{\pm} = \frac{g}{2\sqrt{2}U}\sqrt{\chi^2 \pm \chi\sqrt{\chi^2 - 8} + 4}, \quad \text{with } \chi \equiv Ut/y, \tag{16}$$

where y denotes the lateral distance between the sensor and ship's sailing line, and $t = 0$ corresponds to the time instant when the mid-ship is aligned with the sensor location. Eq. (16) gives rise to two branches plotted by the black line in Fig. 3. The lower and upper branches correspond to the frequencies of transverse waves and divergent waves at the sensor location. Two branches intersect at $Ut/y = 2\sqrt{2} = 1/\tan\gamma_c$ when the cusp of Kelvin's wake meets the sensor. With the time marching, the frequency of transverse waves is nearly constant, whereas that of divergent waves is steadily increasing. Besides, Fig. 3 shows time-frequency spectrograms of wave patterns generated by the modified Wigley hull at $y/L = 20$ for $F = 0.4$, 0.6, and 0.8 displayed in the left,

middle, and right subplots. The frequencies of transverse waves and divergent waves determined by spectrograms are in good agreement with the dispersion relation given by Eq. (16) as expected. At $F = 0.4$ as in the left subplot, divergent waves are inconsequential in consistency with top subplot in Fig. 1. With the increasing the Froude number, divergent waves are playing an increasingly important role. With the time marching, however, the amplitude of divergent waves at the sensor location diminishes. At the sensor location, the lateral distance from ship's sailing line keeps constant, whereas the inline distance is consistently increasing resulting in the decreasing of the polar angle γ. As elucidated in [1] and [8], divergent waves are largely damped out under influences of fluid viscosity and ship hull interference. Therefore, the sensor can only measure divergent waves over a period of time. Comparing three subplots, the duration of divergent waves is increasing with ship's speed.

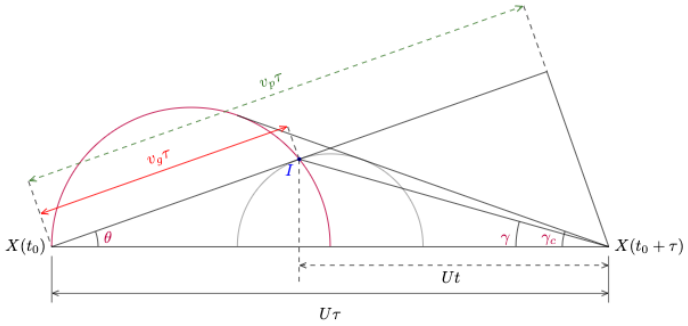

Figure 2: Ship wave dispersion. I is the sensor's position, $v_p = U\cos\theta$ the phase velocity, $v_g = 0.5U\cos\theta$ the group velocity, 'purple semi-circle' the boundary of energy at $t_0 + \tau$ generated by the ship at time instant t_0, $U\tau$ the inline distance sailed from t_0 to $t_0 + \tau$, and Ut the inline distance from the sensor to the ship at $t_0 + \tau$.

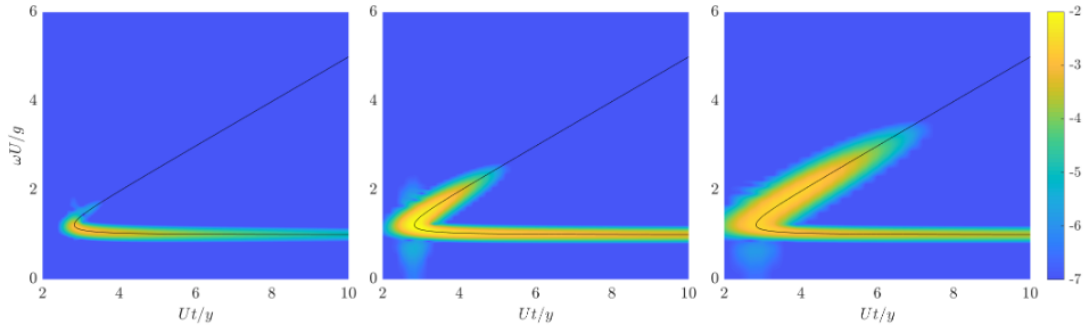

Figure 3: Spectrograms of ship-generated waves for $F = 0.4$ (left), 0.6 (middle), and 0.8 (right).

H.L. highly appreciates discussions with X.B. Chen at Bureau Veritas and R. Pethiyagoda at Queensland University of Technology. This research is supported by A*STAR under its RIE 2020 Industry Alignment Fund (A19F1a0104).

References

[1] H. Liang, & X. B. Chen, Viscous effects on the fundamental solution to ship waves. *J. Fluid. Mech.*, 879: 744–774, 2019.

[2] H. Wu, J. He, Y. Zhu, & F. Noblesse, The Kelvin–Havelock–Peters farfield approximation to ship waves. *Eur. J. Mech. (B/Fluids)*, 70: 93–101, 2018.

[3] H. Liang, H. Wu, J. He, & F. Noblesse, Kelvin–Havelock–Peters approximations to a classical generic wave integral. *Appl. Math. Model.*, 77: 950–962, 2020.

[4] F. Ursell, On Kelvin's ship-wave pattern. *J. Fluid. Mech.*, 8: 418–431, 1960.

[5] E. Hogner, Contributions to the theory of ship waves. *Ark. Mat. Astr. Fys.*, 17: 1–50, 1923.

[6] H. Wu, J. He, H. Liang, & F. Noblesse, Influence of Froude number and submergence depth on wave patterns. *Eur. J. Mech. (B/Fluids)*, 75: 258–270, 2019.

[7] C. Chester, B. Friedman, & F. Ursell, An extension of the method of steepest descents. *Math. Proc. Camb. Phil. Soc.*, 53: 599-611, 1959.

[8] H. Wu, J. Wu, J. He, R. Zhu, C. J. Yang, & F. Noblesse, Wave profile along a ship hull, short farfield waves, and broad inner Kelvin wake sans divergent waves. *Phys. Fluids*, 31: 047102, 2019.

[9] R. Pethiyagoda, S. W. McCue, & T. J. Moroney, Spectrograms of ship wakes: identifying linear and nonlinear wave signals. *J. Fluid. Mech.*, 811: 189–209, 2017.

Wave energy absorption amongst arrays of point absorbers with a non-regular geometry

Yingyi Liu[a], Siming Zheng[b], Hui Liang[c] & Peiwen Cong[d]

[a]Research Institute for Applied Mechanics, Kyushu University, Fukuoka 8168580, Japan; liuyingyi@riam.kyushu-u.ac.jp

[b]School of Engineering, Computing and Mathematics, University of Plymouth, Drake Circus, Plymouth PL4 8AA, United Kingdom; siming.zheng@plymouth.ac.uk

[c]Technology Centre for Offshore and Marine, Singapore (*TCOMS*), 118411, Singapore; lianghuistar@gmail.com

[d]State Key Laboratory of Coastal and Offshore Engineering, Dalian University of Technology, Dalian 116024, China; pwcong@dlut.edu.cn

1. INTRODUCTION

The interaction theory presented by Kagemoto & Yue (1986) and refined by many other scholars is effective in wave effects on multiple surface-piercing bodies. In this work, by virtue of a boundary element method using the hybrid dipole-source formulation (Liu *et al.* 2021), interactions among point absorber arrays are considered. Based on the fundamental theoretical result that the maximum mean power generated by an axisymmetric heaving converter is equivalent to that contained in $\lambda/2\pi$ length of an incident wave crest (Evans 1979; Falnes 1980), the array performance can be numerically predicted. Given that regular shapes such as cylinders are often used for the individual device in an array, a non-regular geometry is preferred. Moreover, the characteristics in the interactions amongst devices in association with different layouts is also of particular interest.

2. THEORY AND METHODOLOGY

2.1. *Wave scattering amongst multiple floating bodies*

Let us consider a train of regular incident waves that propagates to the positive x-direction and transmits with a small amplitude A, a heading angle β measured from the positive x-axis, and a wave number k, in water of a finite depth h. In terms of polar coordinates (r_j, θ_j, z_j), the ambient wave potential incident to body j can be expressed as a summation of partial cylindrical waves incident to the body j:

$$\phi_j^A(r_j,\theta_j,z_j) = -\frac{\mathrm{i}gA}{\omega}\frac{\cosh k(z_j+h)}{\cosh kh}\mathrm{e}^{\mathrm{i}k(x_j\cos\beta+y_j\sin\beta)}\sum_{q=-\infty}^{\infty}J_q(kr_j)\mathrm{e}^{\mathrm{i}q(\pi/2+\theta_j-\beta)}. \tag{1}$$

Eq. (1) can be further written as the following compact form

$$\phi_j^A(x_j,y_j,z_j) = \{a_j^I\}^T\{\psi_j^I\}, \tag{2}$$

in which $\{\psi_j^I\}$ is a scalar vector of the basis function that is also named as the incident partial wave component

$$\left\{\psi_j^I\right\}_{lq} = \begin{cases} \frac{\cosh k(z_j+h)}{\cosh kh}J_q\left(kr_j\right)\mathrm{e}^{\mathrm{i}q\theta_j}, & l=0 \\ \cos k_l\left(z_j+h\right)I_q\left(k_lr_j\right)\mathrm{e}^{\mathrm{i}q\theta_j}, & l\geqslant 1 \end{cases}, \tag{3}$$

where J_q is the Bessel function of the first kind of order q, and I_q is the modified Bessel function of the first kind of order q, l represents numbering of the eigen-expansion mode.

In arrays of floating bodies, each individual body not only experiences the ambient incident plane wave, but also outgoing waves that are scattered from all the other neighboring bodies in the arrays. The scattered waves from body i can then be expressed as incident waves to body j:

$$\phi_i^S(r_i,\theta_i,z_i) = \{A_i^S\}^T[T_{ij}]\{\psi_j^I\}, \tag{4}$$

where $\{A_i^S\}$ is a scalar vector of the scattering coefficients, and the T-transfer matrix is derived from Graf's addition theorem:

$$[T_{ij}]_{nn}^{mq} = \begin{cases} H_{m-q}(kL_{ij})\mathrm{e}^{\mathrm{i}\alpha_{ij}(m-q)}, & n=0 \\ K_{m-q}(k_nL_{ij})\mathrm{e}^{\mathrm{i}\alpha_{ij}(m-q)}(-1)^q, & n\geqslant 1 \end{cases}. \tag{5}$$

where H_{m-q} is the zeroth-order Hankel function of the first kind; K_{m-q} is the zeroth-order modified Bessel function of the second kind; L_{ij} is the distance between the centers (origins of the local coordinate systems) of body i and j; α_{ij} is the angle at body i between the positive x-direction and the line joining the center of i to that of j in an anti-clockwise direction. Note that Eq. (5) holds true for any integer m, and any non-negative integer n, when $r_j \leqslant L_{ij}$. On the basis of Eq. (4), the total wave potentials that incident to body j can be expressed as a summation of the ambient incident plane wave and all scattered waves from the other bodies. Using a so-called diffraction transfer matrix $[D_j]$ as defined in Liu *et al.* (2021) based on the hybrid dipole-source formulation, the scattered wave from body j and all the incident waves to the same body can be connected via

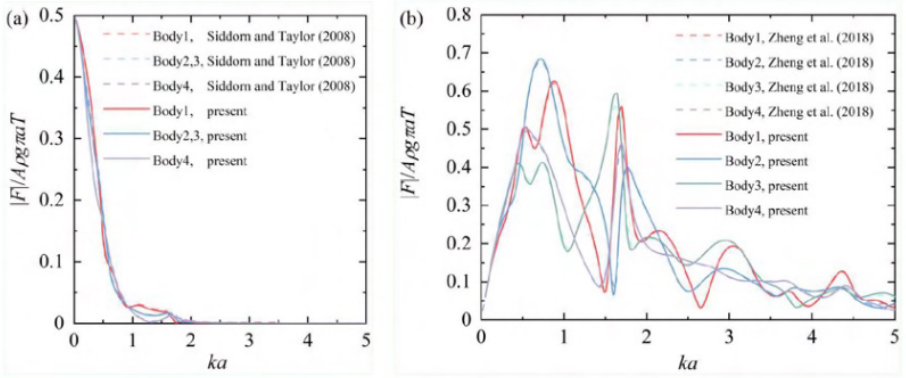

Figure 1: Excitation forces acting on each body of the four-cylinder array, $\beta = \pi/4$: (a) vertical force F_z; (b) horizontal force F_x.

the following relation

$$\{A_j^S\} = [D_j] \cdot (\{a_j^I\} + \sum_{\substack{i=1 \\ i \neq j}}^{N_B} [T_{ij}]^T \{A_i^S\}), \quad (j = 1, 2, ..., N_B). \tag{6}$$

from which the scattering coefficients can be numerically solved, where N_B stands for the number of bodies in the arrays.

Wave excitation forces can then be calculated via pressure integration over each body using matrix operations:

$$F_{j,p}^E = \left\{\eta_j^E\right\} \left\{G_{j,p}^E\right\}, \tag{7}$$

where $F_{j,p}^E$ is interpreted as the excitation force in the p^{th} degree of freedom of body j. $G_{j,p}^E$ is named as the force transfer matrix with the following form

$$\left\{G_{j,p}^E\right\} = \mathrm{i}\omega\rho \iint_{S_B^j} \left(\left\{\psi_j^I\right\} + [D_j]^T \left\{\psi_j^S\right\}\right) n_{j,p} \mathrm{d}S, \tag{8}$$

where n_p is the p^{th} component of the normal vector on the immersed body surface; S_B^j denotes the immersed body surface; ρ denotes the water density. The overall expansion coefficients of the total waves that incident to body j read

$$\left\{\eta_j^E\right\} = \left\{a_j^I\right\}^T + \sum_{\substack{i=1 \\ i \neq j}}^{N_B} \left\{A_i^S\right\}^T [T_{ij}]. \tag{9}$$

Following a similar approach, wave radiation forces acting on body j can be evaluated as

$$F_{j,t}^{R,i,p} = \begin{cases} \left\{\eta_j^{R,i,p}\right\} \left\{G_{j,t}^E\right\}, & i \neq j \\ \mathrm{i}\rho \left(a_{j,p} + \omega b_{j,p}\right) + \left\{\eta_j^{R,i,t}\right\} \left\{G_{j,t}^E\right\}, & i = j \end{cases} \tag{10}$$

where $a_{j,p}$ and $b_{j,p}$ are respectively the added mass and the radiation damping of body j in the p^{th} degree of freedom due to its own unitary motion in the same mode when the body is in isolation; $F_{j,t}^{R,i,p}$ is interpreted as the radiation force of body j in the t^{th} degree of freedom due to the motion of body i in p^{th} degree of freedom.

2.2. *Wave power and interaction factor*

It is common to use the so-called interaction factor to evaluate the performance of arrays of wave energy converters. The interaction factor q is defined as a function of the wave number k and the incident wave angle β and can be numerically evaluated by

$$q(k, \beta) = \frac{2\pi}{\lambda N_B} \frac{\left(\sum_{j=1}^{N_B} P_j(k, \beta)\right)_{\max}}{P_W}, \tag{11}$$

where P_j represents the wave power of each converter in the arrays. Physically, $q < 1$ indicates that the wave interactions have a destructive effect on the power absorption of the wave farm. In contrast, if $q > 1$, the park effect is constructive. The maximum absorbed power of an entire array can be calculated as (Evans 1979, etc.)

$$\left(\sum_{j=1}^{N} P_j(k, \beta)\right)_{\max} = \frac{1}{8} \left\{F^E\right\}^* [B_{\text{rad}}]^{-1} \left\{F^E\right\}, \tag{12}$$

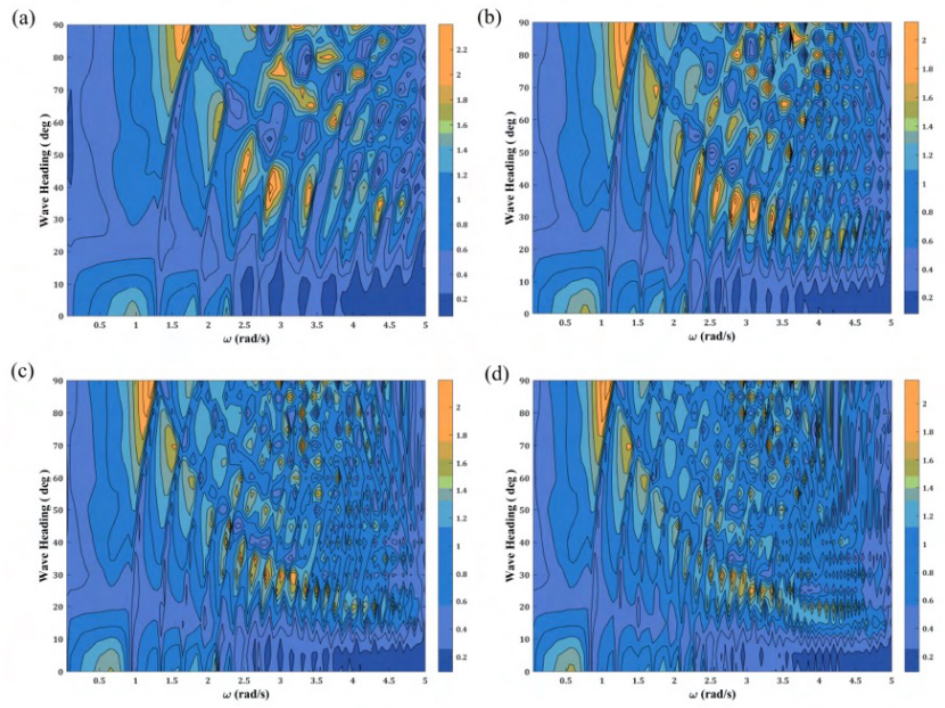

Figure 3: q-factor of a single array of CorPower-like point absorbers against the device spacing s: (a) $s = 2D$; (b) $s = 3D$; (c) $s = 4D$; (d) $s = 5D$.

where $\{F^E\}$ is a scalar vector of complex amplitudes of the wave excitation forces; $[B_{\text{rad}}]$ represents the radiation damping matrix; the asterisk $*$ denotes the complex conjugate transpose. In Eq. (11), P_W is the time-averaged incident wave power per unit crest-width and defined by

$$P_W = \frac{1}{4}\rho g A^2 \sqrt{\frac{g}{k}\tanh kh}\left(1 + \frac{2kh}{\sinh 2kh}\right). \tag{13}$$

3. RESULTS AND DISCUSSIONS

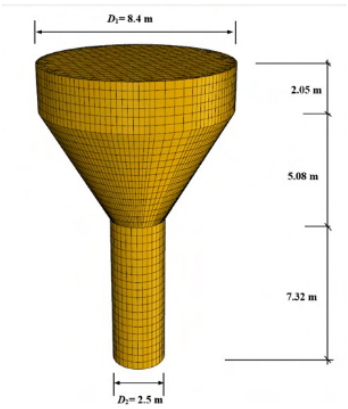

Figure 2: Device geometry and surface meshing.

Verification is firstly performed via a four-cylinder benchmark problem given in Siddorn & Taylor (2008). The geometry of each body is a truncated vertical cylinder of radius $r = a$, draught $T = 2a$, being placed in water of depth $h = 4a$. The foursquare layout of the array separates neighboring cylinders by a distance of $s = 4a$ for an incident wave heading angle of $\beta = \pi/4$. Figure 1 shows that our present results agree well with those from theoretical methods documented in Siddorn & Taylor (2008) and Zheng *et al.* (2018).

Numerical computations are carried out for a line array along the x-axis of 7 evenly-spaced CorPower-like heaving point abosrbers and a double array in parallel involving 7×2 evenly-spaced point abosrbers of the same type. The surface of the individual device is discretised using 765 panels on the immersed body surface and 46 panels on the waterplane cross-sectional area. The mesh and dimensions of the device are given in Figure 2.

Variations of the q-factor versus the device spacing s, the wave heading angle β, and the wave angular frequency ω are displayed in Figure 3 and 4. It is found that the q-factor distributions of a single array are more regular than those of a double array. There are some remarkable "bright spot" regions indicating that the wave energy absorption there is locally optimised against wave conditions. For a single array, the lower the wave frequency is, the larger the wave heading tends to be in

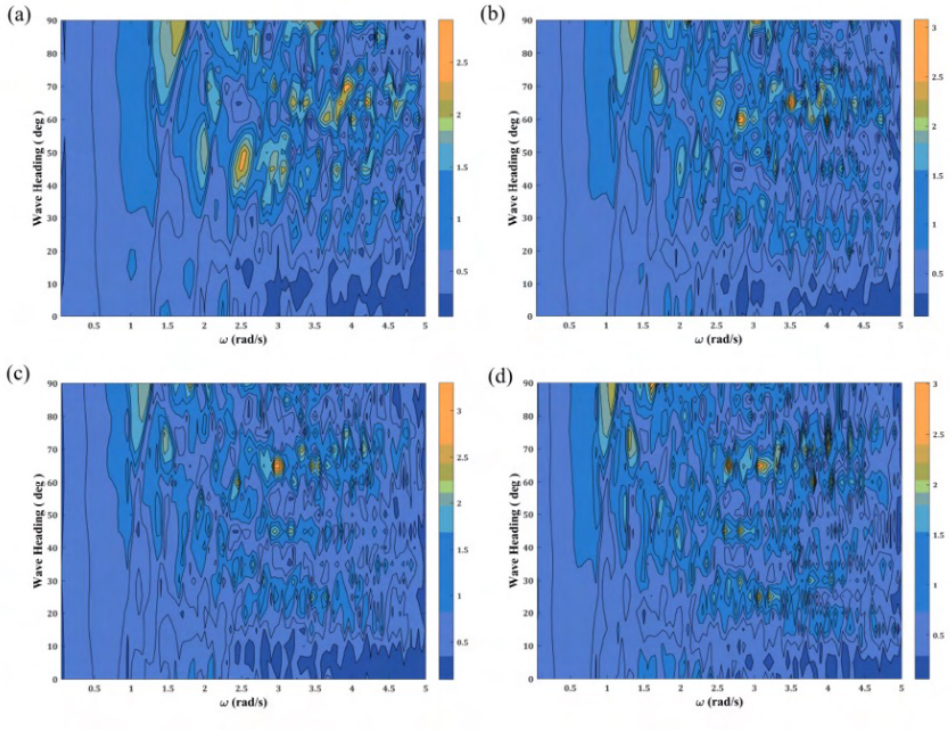

Figure 4: q-factor of a double-parallel array of CorPower-like point absorbers against the device spacing s: (a) $s = 2D$; (b) $s = 3D$; (c) $s = 4D$; (d) $s = 5D$.

association with the centre of a spot region. In contrast, for a double array, the distribution of spot regions are rather randomised, indicating much stronger interactions amongst the devices as the scattered waves not only come from neighboring devices in row but also in column. In addition, both cases suggest that the number (or density) of the spot regions increases with the device spacing. More results will be presented at the workshop regarding other interesting phenomena in the point absorber arrays including those in staggered arrangement.

4. CONCLUSIONS

Wave interactions with multiple axisymmetric point absorbers is presented. Good agreement is found with the theoretical methods for cylinders. The method is applied to non-regularly shaped CorPower-like heaving devices in a line array and a double array in parallel. It is found that there are "bright spot" regions where wave energy absorption is optimised and the distribution of such regions becomes randomised in a double array. Moreover, the density of spot regions increases with the device spacing and the size varies with the frequency.

ACKNOWLEDGEMENTS

This work was supported by Grant-in-Aid for Early-Career Scientists (JSPS Grant Number JP18K13939). The surface mesh of the CorPower-like device provided by Iñaki Zabala of SENER Ingeniería y Sistemas, S.A., Spain is greatly appreciated.

REFERENCES

Evans, DV 1979 Some theoretical aspects of three-dimensional wave-energy absorbers. In *Proc. 1st Symp. Wave Energy Utilization*, pp. 78–112.

Falnes, Johannes 1980 Radiation impedance matrix and optimum power absorption for interacting oscillators in surface waves. *Applied ocean research* **2** (2), 75–80.

Kagemoto, H. & Yue, D. K. P. 1986 Interactions among multiple three-dimensional bodies in water waves: an exact algebraic method. *Journal of fluid mechanics* **166**, 189–209.

Liu, Yingyi, Liang, Hui, Kashiwagi, Masashi & Cong, Peiwen 2021 Alternative approaches of evaluating diffraction transfer matrix and radiation characteristics using the hybrid source-dipole formulation. *Applied Ocean Research* **114**, 102769.

Siddorn, P & Taylor, R Eatock 2008 Diffraction and independent radiation by an array of floating cylinders. *Ocean Engineering* **35** (13), 1289–1303.

Zheng, S., Zhang, Y. & Iglesias, G. 2018 Wave–structure interaction in hybrid wave farms. *Journal of Fluids and Structures* **83**, 386–412.

METAREEF, a sustainable submerged floating metamaterial structure to attenuate surface gravity waves

Matteo Lorenzo[1*], Paolo Pezzutto[1], Federico Bosia[2], Carlo Camporeale[3], Filippo De Lillo[1], Francesco De Vita[4], Costantino Manes[3], Francesco Ventrella[1], Miguel Onorato[1]

[1]Dipartimento di Fisica, Università degli Studi di Torino, 10129 Torino, Italy
[2]DISAT, Politecnico di Torino, Corso Duca degli Abruzzi 24, 10129 Torino, Italy
[3]DIATI, Politecnico di Torino, Corso Duca degli Abruzzi 24, 10129 Torino, Italy
[4]DMMM, Politecnico di Bari, Via Orabona 4, 70125 Bari, Italy
[*]matteo.lorenzo@unito.it

1 INTRODUCTION

Tethered floating breakwaters, built as a regular lattice of reversed pendula [1] provide an attractive option for beach management. With respect to rubble mound breakwaters, this type of structures has small impact on water circulation. Without localized refraction/diffraction effects, the formation of tombolos and stagnating pools between them is prevented. Moreover, if the floaters are kept below the water surface, their visual impact from the shore is negligible, similar to artificial reefs. On the other hand, in the presence of rising sea levels, tethered floats are much more adaptable than artificial reefs. The environmental impact of point-wise hinged floaters is very small throughout the entire the operating life of the structure, from deployment to decommissioning. Depending on their efficiency, the cost-effectiveness of beach protection using tethered floats is favourable compared to the current hard-engineering strategies. Tethered floating breakwaters have been studied since the late 70s with extensive laboratory and field tests, exploring different configurations for the anchoring and submergence of the floats [2, 3, 4].

The models proposed for the efficiency of these devices are based on experimental results obtained with waves impacting on a single float (single row of floats) [2, 4]. The underlying hypothesis is that subsequent floats behave with the same efficiency. This means that the only wave attenuation mechanism that has been considered so far is fluid drag dissipation, while wave scattering has been considered negligible [4]. Of course, wave reflection from a single float (or row) might be small, but, in principle, in regular structures, we must consider possible wave scattering that may emerge from a collective behaviour.

This phenomenon is typical of metamaterials that are engineered structures designed to interact with waves and manipulate their propagation properties, such as phase and group velocity, or to produce effects such as negative refraction, cloaking, superlensing and absorption. In terms of wave attenuation, the key concept is that metamaterial dispersion relation may be non-monotonic or even involve *bandgaps*, *i.e.* ranges of frequencies for which wave propagation is inhibited [5].

2 METAREEF

The purpose of METAREEF is to investigate to which extent the concept of metamaterial wave control can be applied to an efficient attenuation system for surface gravity waves. The periodic structure of METAREEF is designed as a lattice of submerged inverted pendula, in which each pendulum is anchored to the seabed (fig.1a).

Using direct numerical simulations of the Navier-Stokes equation in its two-dimensional form with periodic boundary conditions, free boundary and moving bodies, De Vita et al. [6, 7]

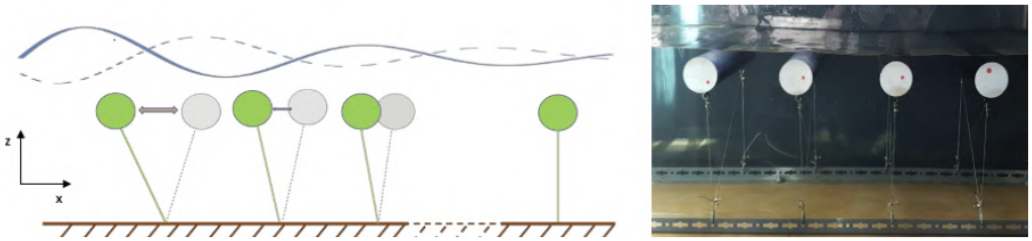

Figure 1: METAREEF device. a) Basic design concept with energy attenuation of the incident wave along x direction. b) Experimental configuration with 4 pendula.

showed that large energy attenuation is possible if the wave and the pendula resonances are characterized by similar frequencies. As the number of resonators is increased, the range of attenuated frequencies also grows. The periodic configuration considered in [7] is going to be updated in the form of a numerical flume. This will help in understanding the fluid dynamics around the pendula to better understand the dissipation processes.

Here, we consider physical experiments with the purpose of characterizing the dissipation and reflection processes, while looking for possible collective behaviours. While the structure to be considered should be a lattice of spherical floats, the preliminary tests are performed in a 2DV configuration, using a line of cylindrical pendula (fig.1b).

3 EXPERIMENTAL SET-UP

Experiments are performed at the "G. Bidone" Hydraulics and Fluid Dynamics laboratory of the Politecnico di Torino, in a 55 m long channel, 0.6 m wide and 1 m deep, equipped with a piston-type wavemaker. Resistance wave gauges are placed before and after the device to measure the surface elevation. Incident and reflected wave fields are separated with a windowed least squares scheme [8]. In order to minimize the uncertainty for the incident and reflected fields, six gauges are placed on the ocean side of the device, while transmitted waves are measured with only one gauge. The duration of the timeseries is limited accordingly, removing any effect of the reflection from the channel end and the wavemaker.

The metamaterial is made up of an array of submerged cylinders anchored to the bottom, with their axes parallel to the wave crests (fig.1b). Cylinders are made with commercial pvc pipes (diameter is 82 mm with wall thickness of 3 mm), filled with air so as to be much less dense than water and waterproofed with polyurethane foam. The length of the pendulum is fixed, with a distance between the bottom of the flume and the top of the cylinder equal to 43 cm. Cylinders are braced with two additional cables in order to constrain the motion in the plane as far as possible. The resonant frequency of the pendulum is estimated empirically to be approximately equal to 0.6 Hz.

As a first validation, we maintained the system as linear as possible, by keeping the amplitude of waves equal to 1 cm for the range of tested frequencies (0.4 to 1.4 Hz). Tests were carried out by varying the mutual distance (L), the number of oscillators and the water height (h), keeping the periodic configuration.

Reflection and transmission coefficients (C_R and C_T) are computed as ratios between energies (spectral zero-th moments) and dissipation coefficients are consequently calculated as $C_D = 1 - C_R - C_T$.

4 RESULTS AND DISCUSSION

In Figure 2 the dissipation coefficients are plotted against the frequency of the incident waves.

In the left plot (fig.2a), each curve represents a configuration with a different number of pendula with the same mutual distance between the pendula (equal to 24 cm) and the same water height. Increasing the number of pendula (up to 11), the dissipation around the resonant frequency (0.6Hz) increases, as predicted numerically [7].

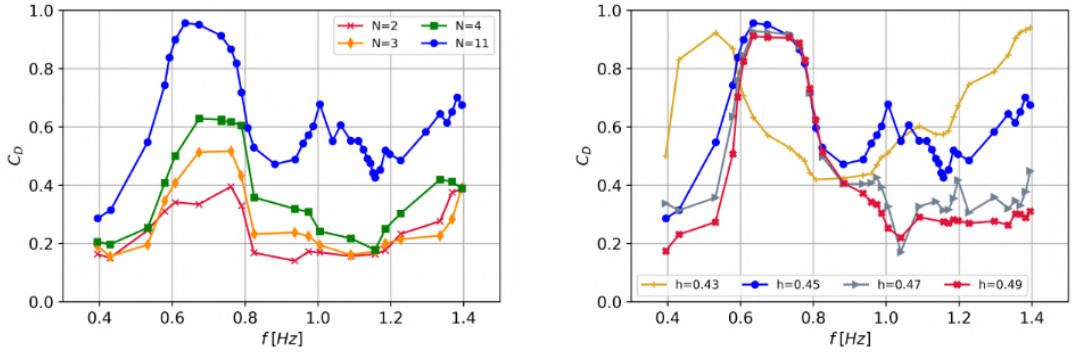

Figure 2: Dissipated energy as function of the generated waves' frequency. a) L = 0.24m, a = 0.01m, h = 0.45m. Each series represents a configuration with a different number of resonators. b) L = 0.24m, a = 0.01m, 11 cylinders. Each series represent a different water level. Blue-dotted line represents the same configuration.

The right panel (fig.2b) shows results for the 11 cylinders configuration; here each curve represent a different water level. The behavior changes drastically as the water height decreases to 43 cm, corresponding to the cylinder location at the still water level, with dissipation increasing below the modal frequency. This appears consistent with previous studies ([9]), which concluded that, for long waves, an emerging device is more effective. Short waves lose significant energy only if the wave amplitude is comparable with the gap between the mean water level and the top of the cylinders.

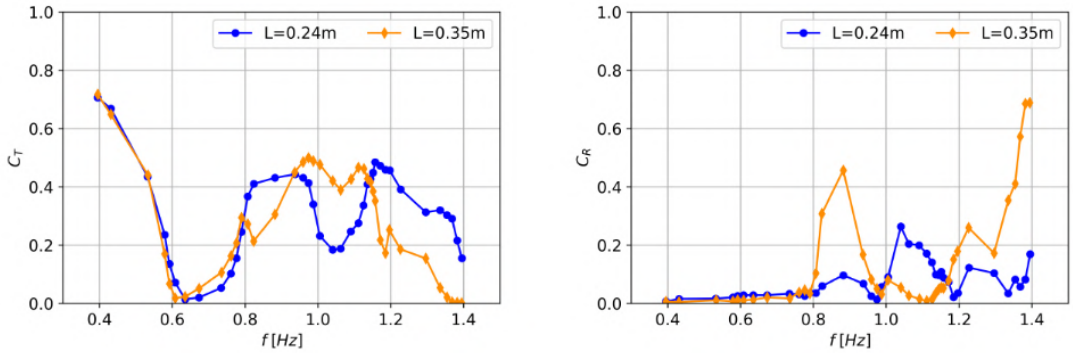

Figure 3: 11 cylinders configuration with a = 0.01m, h = 0.45m. On the left Transmitted energy (a) and on the right Reflected energy (b) as function of the generated waves' frequency for different mutual distances.

In fig.3 we compare transmission (3a) and reflection coefficients (3b) for two different mutual distances (L). It is interesting to see that the reflection, although almost negligible for the whole range (3b), is characterized by sharp peaks, and that the position of the peaks changes with L.

Further analysis is required to understand the origin of the peaks, but it appears certain that the wave reflection depends on the geometry of the metamaterial.

Comparing fig.3a (L=0.24m) with the corresponding dissipation (fig.2) and reflection (fig.3b), we see that the efficiency of the system mainly depends on dissipation, especially in the low frequency range around the modal resonance. Moreover, in this range, the metamaterial geometry seems to be unimportant. For shorter waves, the contribution of the reflection is not negligible (see *e.g.* the through in fig. 3a around $1.05Hz$ and the corresponding peak in fig. 3b).

ACKNOWLEDGMENTS

All authors have been funded by Compagnia di San Paolo Progetto d'Ateneo/Fondazione San Paolo "Metapp", n. CSTO160004. and Proof of concept "Metareef" grant. Furthermore, M. Onorato, F. Bosia, F. De Lillo and M. Lorenzo acknowledge the EU, H2020 FET Open "Bio-Inspired Hierarchical MetaMaterials" grant No. 863179.

REFERENCES

[1] Dai, J., Wang, C. M., Utsunomiya, T., and Duan, W. 2018. *Review of recent research and developments on floating breakwaters.* Ocean Engineering 158(March), 132–151.

[2] Agerton, D. J., Savage, G. H., and Stotz, K. C. 1977. *Design, analysis and field test of a dynamic floating breakwater. Coastal Engineering 1976 3*, 2792–2809.

[3] Jones, D. B. 1978. An Assessment of transportable breakwaters with reference to the container off-loading and transfer system (COTS). Tech. rep., Civil Engineering Laboratory, Port Hueneme, California.

[4] Seymour, R. J., and Hanes, D. M. aug 1979. *Performance Analysis of Tethered Float Breakwater.* Journal of the Waterway, Port, Coastal and Ocean Division 105(3), 265–280.

[5] Hussein, M. I., Leamy, M. J., and Ruzzene, M. 2014. *Dynamics of phononic materials and structures: Historical origins, recent progress, and future outlook.* Applied Mechanics Reviews 66(4).

[6] De Vita, F., De Lillo, F., Verzicco, R., and Onorato, M. 2021. *A fully Eulerian solver for the simulation of multiphase flows with solid bodies: Application to surface gravity waves. Journal of Computational Physics 438*.

[7] De Vita, F., De Lillo, F., Bosia, F., and Onorato, M. 2021. *Attenuating surface gravity waves with mechanical metamaterials.* Physics of Fluids 33(4).

[8] Zelt, J. A., Skjelbreia, J. E., and Wave Technologies. 1993. *Estimating incident and reflected wave fields using an arbitrary number of wave gages. Proceedings of the Coastal Engineering Conference 1*, 777–788.

[9] Sergiienko, N. Y., Cazzolato, B. S., Ding, B., Hardy, P., and Arjomandi, M. 2017. *Performance comparison of the floating and fully submerged quasi-point absorber wave energy converters. Renewable Energy 108*, 425–437.

Added mass and damping of structures with angular symmetry

by S. Malenica[1] & J. N. Newman[2]

[1] Bureau Veritas, France <sime.malenica@bureauveritas.com>

[2] MIT and WAMIT, Inc., USA <jnn@mit.edu>

(37th IWWWFB – Giardini Naxos, Italy, 10-13 April 2022)

1 Introduction

Structures that are axisymmetric about a vertical axis have obvious symmetry properties. With respect to the added-mass and damping coefficients, these are unchanged by rotation of the body or coordinate system about the vertical axis, through an arbitrary angle θ. In such cases the coefficients for surge and sway are identical, with no coupling between these modes. The same properties apply for roll and pitch. Our objective here is to show that similar properties exist for structures that are not axisymmetric, if the geometry is unchanged by rotation about the vertical axis through an angle $\theta = 2\pi/N$ with N an integer and $N \geq 3$. The examples include structures with multiple columns or floats that are equally spaced around a circle, and single cylinders with polygonal shape such as equilateral triangles or pentagons. Figure 1 shows several examples with $N = 3$.

The symmetry properties to be derived here are obvious for cases such as a square cylinder or square array of circular columns, but not for other cases, especially if N is odd. Unlike circular and square cylinders, the radiated waves can be quite different for surge and sway, as shown for the triangular cylinder in Figure 2. Thus it is surprising to find that the added mass and damping matrices for this structure have almost the same forms as for axisymmetric bodies; the only difference is a nonzero moment due to yaw. Two alternative proofs are presented in the following Sections.

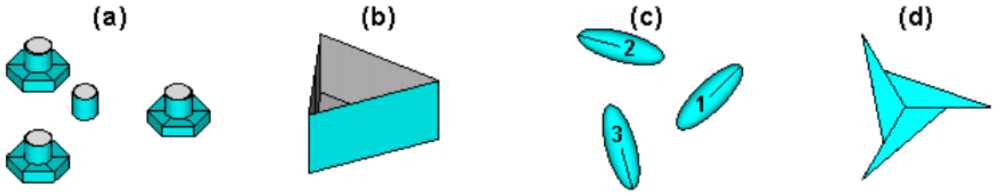

Figure 1: Examples of structures where the geometry is unchanged by rotation about the vertical axis through the angle $2\pi/3$. (a): wind-turbine floats; (b) equilateral triangular cylinder; (c) spheroids at 45° angles; (d) 6-sided cylinder. (a) and (b) are symmetrical about the vertical planes that include the center of the structure and a body or vertex; (c) and (d) are asymmetric.

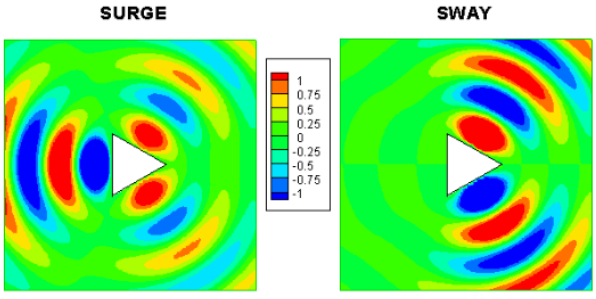

Figure 2: Contour plots of the free-surface elevations due to surge and sway of the triangular cylinder shown in Figure 1(b). The cylinder sides are 2m wide by 1m draft, the fluid depth is infinite and the wavelength in the far field is 2m. The elevations shown in the legend are per unit amplitude of surge and sway.

2 Symmetry relations based on rotation of the coordinate system

The structure is assumed to be rigid, with six degrees of motion. The added mass and damping are represented by 6×6 matrices $\mathbf{A}$ and $\mathbf{B}$, with coefficients A_{ij} and B_{ij}. The row index i represents the three components of the force ($i = 1, 2, 3$) and moment ($i = 4, 5, 6$). The column index j represents the modes of translation ($j = 1, 2, 3$) and rotation ($j = 4, 5, 6$). These are defined with respect to the Cartesian coordinate system x, y, z, with the z-axis vertical. $\mathbf{A}$ and $\mathbf{B}$ are symmetric matrices, with $A_{ij} = A_{ji}$ and $B_{ij} = B_{ji}$. Only the added mass is considered in the following analysis; the derivation for the damping matrix is identical.

If the matrix $\mathbf{A}$ is partitioned into four 3×3 sub-matrices $\mathbf{A}_{mn}$, and the coordinate system is rotated about the z-axis by the angle θ, the matrix $\mathbf{A}^*$ in the new system is given by

$$\mathbf{A}^* = \begin{bmatrix} \mathbf{A^*}_{11} & \mathbf{A^*}_{12} \\ \mathbf{A^*}_{21} & \mathbf{A^*}_{22} \end{bmatrix} = \begin{bmatrix} \mathbf{Q}\mathbf{A}_{11}\mathbf{Q}^T & \mathbf{Q}\mathbf{A}_{12}\mathbf{Q}^T \\ \mathbf{Q}\mathbf{A}_{21}\mathbf{Q}^T & \mathbf{Q}\mathbf{A}_{22}\mathbf{Q}^T \end{bmatrix} \tag{1}$$

where the transformation matrix $\mathbf{Q}$ is defined in the form

$$\mathbf{Q} = \begin{bmatrix} \cos\theta & \sin\theta & 0 \\ -\sin\theta & \cos\theta & 0 \\ 0 & 0 & 1 \end{bmatrix} = \begin{bmatrix} c & s & 0 \\ -s & c & 0 \\ 0 & 0 & 1 \end{bmatrix}. \tag{2}$$

Here $c = \cos\theta$ and $s = \sin\theta$. After evaluating the matrix products the sub-matrix $\mathbf{A^*}_{11}$ is

$$\mathbf{A}^*_{11} = \begin{bmatrix} A_{11}c^2 + A_{12}sc + A_{21}sc + A_{22}s^2 & -A_{11}sc + A_{12}c^2 - A_{21}s^2 + A_{22}sc & A_{13}c + A_{23}s \\ -A_{11}cs - A_{12}s^2 + A_{21}c^2 + A_{22}cs & A_{11}s^2 - A_{12}cs - A_{21}sc + A_{22}c^2 & -A_{13}s + A_{23}c \\ A_{31}c + A_{32}s & -A_{31}s + A_{32}c & A_{33} \end{bmatrix}. \tag{3}$$

Since the geometry of the structure is unchanged by rotation through an angle $\theta = 2\pi/N$, rotation of the coordinates through the same angle does not change the added-mass matrix. Thus $\mathbf{A^*}_{11} = \mathbf{A}_{11}$. Equating the coefficients in these two sub-matrices gives a set of equations which can be reduced to the following forms if $s \neq 0$:

$$\left.\begin{aligned} (A_{11} - A_{22})s - (A_{12} + A_{21})c = 0 \\ (A_{11} - A_{22})c + (A_{12} + A_{21})s = 0 \end{aligned}\right\}, \qquad \left.\begin{aligned} A_{13}(1 - c) - A_{23}s = 0 \\ A_{13}s + A_{23}(1 - c) = 0 \end{aligned}\right\}. \tag{4}$$

These equations are homogeneous and the determinants $s^2 + c^2$ and $s^2 + (1 - c)^2$ are nonzero. Thus

$$A_{11} - A_{22} = 0, \quad A_{12} + A_{21} = 0, \quad A_{13} = 0, \quad A_{23} = 0. \tag{5}$$

Following the same procedure for the other sub-matrices gives the results

$$A_{14} - A_{25} = 0, \quad A_{15} + A_{24} = 0, \quad A_{16} = 0, \quad A_{26} = 0, \tag{6}$$

$$A_{41} - A_{52} = 0, \quad A_{42} + A_{51} = 0, \quad A_{43} = 0, \quad A_{53} = 0, \tag{7}$$

$$A_{44} - A_{55} = 0, \quad A_{45} + A_{54} = 0, \quad A_{46} = 0, \quad A_{56} = 0. \tag{8}$$

Since $\mathbf{A}$ is symmetric, $A_{12} = A_{21} = 0$ and $A_{45} = A_{54} = 0$. After using (5-8) and imposing symmetry it follows that

$$\mathbf{A} = \begin{bmatrix} A_{11} & 0 & 0 & A_{14} & A_{15} & 0 \\ 0 & A_{11} & 0 & -A_{15} & A_{14} & 0 \\ 0 & 0 & A_{33} & 0 & 0 & A_{36} \\ A_{14} & -A_{15} & 0 & A_{44} & 0 & 0 \\ A_{15} & A_{14} & 0 & 0 & A_{44} & 0 \\ 0 & 0 & A_{36} & 0 & 0 & A_{66} \end{bmatrix}. \tag{9}$$

These results are based on the fact that $\mathbf{A}^* = \mathbf{A}$ when $\theta = 2\pi/N$, but they imply more general conclusions. Indeed, they have been derived without explicitly assigning the angle θ of the rotated coordinate system. Since the equations (4) are homogeneous the solutions (5) do not depend on θ, and similarly for the solutions (6-8) for the other sub-matrices. Thus the matrix $\mathbf{A}^*$ is independent of θ. This means that the added mass and damping are independent of the angle of rotation of the coordinate system, as in the case of an axisymmetric structure.

If the structure is symmetrical about the $x - z$ plane, as in Figure 1(a,b), $A_{14} = 0$ and $A_{36} = 0$. In that case the only difference in (9) relative to an axisymmetric structure is the nonzero coefficient A_{66}, representing the added moment of inertia due to yaw.

3 Symmetry relations based on the individual force matrix for one body

A triangular array with $N = 3$ bodies is considered to simplify the analysis. The bodies are centered on a circle at polar angles $\theta_n = (n-1)(2\pi/3)$ $(n = 1, 2, 3)$ or, equivalently, at $\theta = 0$ and $\theta = \pm(2\pi/3)$. The entire structure moves as a rigid body with six degrees of freedom, as in Section 2. The added mass corresponding to the force and moment on the body n is represented by the 6×6 matrix $\mathbf{a}^{(n)}$ with coefficients $a_{ij}^{(n)}$. In general these matrices are full and asymmetric, as in the example described in Section 4. The matrix for the entire structure is

$$\mathbf{A} = \mathbf{a}^{(1)} + \mathbf{a}^{(2)} + \mathbf{a}^{(3)}. \tag{10}$$

Since the geometry is unchanged by rotation through the angles $\theta = \pm(2\pi/3)$ it follows that $\mathbf{a}^{(2)}$ and $\mathbf{a}^{(3)}$ can be related to $\mathbf{a}^{(1)}$ using the transformation matrix (2) with 3×3 sub-matrices, in a similar manner to (1) except that the transformation here is in the opposite sense. Thus for $(n = 2, 3)$,

$$\mathbf{a}^{(n)} = \begin{bmatrix} \mathbf{a}_{11}^{(n)} & \mathbf{a}_{12}^{(n)} \\ \mathbf{a}_{21}^{(n)} & \mathbf{a}_{22}^{(n)} \end{bmatrix} = \begin{bmatrix} \mathbf{Q}_n^T \mathbf{a}_{11}^{(1)} \mathbf{Q}_n & \mathbf{Q}_n^T \mathbf{a}_{12}^{(1)} \mathbf{Q}_n \\ \mathbf{Q}_n^T \mathbf{a}_{21}^{(1)} \mathbf{Q}_n & \mathbf{Q}_n^T \mathbf{a}_{22}^{(1)} \mathbf{Q}_n \end{bmatrix} \tag{11}$$

where $\mathbf{Q}_n$ is defined by (2) with $\theta = \theta_n$.

In the following equations it is convenient to omit the superscript 1 for the coefficients of the matrix $\mathbf{a}^{(1)}$. Thus $a_{ij} \equiv a_{ij}^{(1)}$. After the indicated multiplications the results are similar to (3) except for the signs of terms which are linear in $s = \sin\theta_n$. However these terms cancel when the sum in (9) is evaluated, since $\sin\theta_3 = -\sin\theta_2$, and it follows that

$$\mathbf{A}_{11} = \begin{bmatrix} a_{11} & a_{12} & a_{13} \\ a_{21} & a_{22} & a_{23} \\ a_{31} & a_{32} & a_{33} \end{bmatrix} + 2 \begin{bmatrix} a_{11}c^2 + a_{22}s^2 & a_{12}c^2 - a_{21}s^2 & a_{13}c \\ -a_{12}s^2 + a_{21}c^2 & a_{11}s^2 + a_{22}c^2 & a_{23}c \\ a_{31}c & a_{32}c & a_{33} \end{bmatrix}. \tag{12}$$

After substituting $c = \cos(2\pi/3) = -1/2$, $c^2 = 1/4$ and $s^2 = 3/4$, and combining the two matrices in (12),

$$\mathbf{A}_{11} = (3/2) \begin{bmatrix} a_{11} + a_{22} & a_{12} - a_{21} & 0 \\ a_{21} - a_{12} & a_{11} + a_{22} & 0 \\ 0 & 0 & 2a_{33} \end{bmatrix}. \tag{13}$$

Thus

$$A_{11} = A_{22} = \tfrac{3}{2}(a_{11} + a_{22}), \tag{14}$$

$$A_{33} = 3a_{33}. \tag{15}$$

Since $\mathbf{A}$ is symmetric, $a_{12} - a_{21} = 0$ and it follows that

$$A_{12} = A_{21} = 0. \tag{16}$$

Repeating the same process for the other sub-matrices gives the results

$$A_{44} = A_{55} = \tfrac{3}{2}(a_{44} + a_{55}), \tag{17}$$

$$A_{66} = 3a_{66}, \tag{18}$$

$$A_{14} = A_{25} = A_{41} = A_{52} = \tfrac{3}{2}(a_{14} + a_{25}) = \tfrac{3}{2}(a_{41} + a_{52}), \tag{19}$$

$$A_{15} = -A_{24} = A_{51} = -A_{42} = \tfrac{3}{2}(a_{15} - a_{24}) = \tfrac{3}{2}(a_{51} - a_{42}), \tag{20}$$

$$A_{36} = A_{63} = 3a_{36} = 3a_{63}. \tag{21}$$

All of the other coefficients A_{ij} not included in (14-21) are equal to zero. These results are consistent with (9).

This analysis has been described for three separate bodies, but it can be applied more generally to structures such as those shown in Figures 1(a,b,d) simply by dividing the submerged surface into three angular sectors and replacing the pressure force on each body by the force acting on the corresponding sector. The extension for $N > 3$ follows by summing (10) over all bodies. If N is odd the same analysis can be followed for each pair of bodies which are symmetrically centered about $\theta = 0$. The final results are unchanged, except that the factors 3 and $\frac{3}{2}$ in (14-21) are replaced by N and $N/2$.

4 Numerical example

Table 1 shows the added-mass and damping coefficients for the spheroids in Figure 1(c). The spheroids are prolate, with length 3m and diameter 1m. The centers are on a circle of radius 2m. The axis of each spheroid is in the plane of the free surface, oriented at 45° from the tangent to the circle. The added-mass coefficients are normalized by the fluid density ρ and the damping coefficients by $\rho\omega$ where ω is the frequency. The wavenumber $K = \omega^2/g = 1m^{-1}$ and the fluid depth is infinite.

The matrices $\mathbf{A}$ and $\mathbf{B}$ in the upper part of Table 1 are the coefficients for the complete structure. These have the same form as the matrix (9). Since this structure is asymmetrical A_{14}, A_{25} and A_{36} are nonzero and $A_{14} = A_{25}$. The same properties apply for B_{14}, B_{25} and B_{36}. (If the spheroids were oriented at zero or 90° relative to the tangent the structure would be symmetric about the $x - z$ plane and these coefficients would all be equal to zero.) The matrices $\mathbf{a}^{(1)}$ and $\mathbf{b}^{(1)}$ in the lower part of Table 1 represent the force and moment on spheroid 1. The coefficients for spheroids 2 and 3 can be evaluated using (11); the sums for all three spheroids are the same as the coefficients in $\mathbf{A}$ and $\mathbf{B}$.

A

1.3164	0.0000	0.0000	-0.0036	-0.3448	0.0000
0.0000	1.3164	0.0000	0.3448	-0.0036	0.0000
0.0000	0.0000	0.2601	0.0000	0.0000	1.0643
-0.0036	0.3448	0.0000	5.2618	0.0000	0.0000
-0.3448	-0.0036	0.0000	0.0000	5.2618	0.0000
0.0000	0.0000	1.0643	0.0000	0.0000	6.9598

B

0.3122	0.0000	0.0000	0.0967	0.5644	0.0000
0.0000	0.3122	0.0000	-0.5644	0.0967	0.0000
0.0000	0.0000	0.6887	0.0000	0.0000	-0.2616
0.0967	-0.5644	0.0000	3.9414	0.0000	0.0000
0.5644	0.0967	0.0000	0.0000	3.9414	0.0000
0.0000	0.0000	-0.2616	0.0000	0.0000	1.9662

$\mathbf{a}^{(1)}$

0.4482	-0.3717	-0.4244	-0.1956	-0.1112	-0.6891
-0.3717	0.4294	0.1799	0.1187	0.1932	1.0465
0.1657	-0.0055	0.0867	0.0034	-1.6749	0.3548
-0.0575	-0.0441	0.1674	0.0757	-0.0825	-0.2543
-0.2739	0.0551	-0.3408	-0.0825	3.4322	-0.4552
-0.7727	0.8578	0.3548	0.2253	0.4006	2.3199

$\mathbf{b}^{(1)}$

0.0438	-0.1141	0.1751	0.0026	0.1497	-0.4613
-0.1141	0.1643	-0.0817	-0.2266	0.0618	0.3423
-0.1946	0.0089	0.2296	-0.0032	-1.1651	-0.0872
0.0476	-0.0346	-0.0639	0.1519	-0.1454	0.0824
0.3417	0.0169	-0.3952	-0.1454	2.4756	0.0920
-0.2156	0.3451	-0.0872	-0.4331	0.1678	0.6554

Table 1: Added-mass (left) and damping coefficients (right) for the spheroids shown in Figure 1(c). The upper matrices $\mathbf{A}$ and $\mathbf{B}$ are for the complete structure. The lower matrices $\mathbf{a}^{(1)}$ and $\mathbf{b}^{(1)}$ are for the individual force and moment on the first spheroid.

5 Discussion

Structures with angular symmetry have been considered, where the geometry is unchanged by rotation about the vertical axis through an angle $2\pi/N$, with N an integer and $N \geq 3$. For this type of structure the added-mass and damping coefficients for surge and sway are equal, and uncoupled. The same properties apply for roll and pitch. The general form of the coefficients is shown in the matrix (9). If the structure is symmetric about a vertical plane, as in most cases of practical importance, the only difference compared to an axisymmetric structure is the nonzero added moment of inertia due to yaw.

These properties apply only to the force and moment due to body motions, and not to the exciting forces in incident waves or other properties such as the radiated wave patterns shown in Figure 2. However there are integral relations which apply. For example the total energy in the radiated waves is related to the damping coefficients; thus the two wave patterns shown in Figure 2 radiate the same amount of energy. Similarly, the integrals of the square of the exciting forces over all wave directions can be related to the damping coefficients using the Haskind relations; thus the integrals of the squares of the exciting forces in surge and sway (or the moments in roll and pitch) have the same value.

The case $N = 2$ is an exception. When $\theta = \pi$ the coefficients of $\mathbf{A}^*$ are equal to $\pm A_{ij}$, providing no relations between different added-mass or damping coefficients. A vertical flat plate in the $x - z$ plane is an obvious example, where the surge added mass is zero and the sway added mass is nonzero.

High-speed vessel moving along the edge of ice field

P. Marleaux[1], **T.I. Khabakhpasheva**[2], **M. Abdel-Maksoud**[1], **A.A. Korobkin**[2], **K. Maki**[3],

[1] Institute for Fluid Dynamics and Ship Theory, Hamburg University of Technology, Germany
[2] School of Mathematics, University of East Anglia, Norwich, UK
[3] Department of Naval Architecture and Marine Engineering, University of Michigan Ann Arbor, MI, USA

1 Introduction

We are concerned with motion of a high-speed vessel that operates in close proximity of an ice field. The presence of the floating ice sheet changes the hydrodynamic forces acting on the vessel. The waves generated by the ship may break the ice near its edge.

In the present study, the ice is continuous with constant thickness and identical material properties in all directions at every point. The ice is modeled as a thin elastic semi-infinite plate. The rest of the water surface is free of ice. The ship moves in open water of finite depth, see Fig. 1. The flow generated by the ship is nonlinear and potential. Viscous and surface tension effects are not included in the present model. The problem is challenging because the moving vessel causes the ice

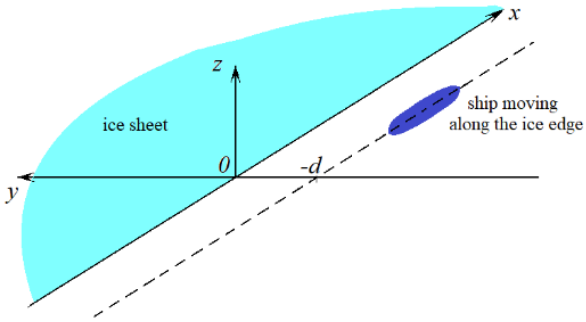

Figure 1: Sketch of the problem.

deflection which in turn modifies the vessel motions. The problem is coupled, generally speaking. The coupling is expected to be weak if the vessel moves far enough from the ice edge. We shall find the conditions of ice and the vessel motion where the presence of the ice field affects the vessel motions.

The forces acting on the ship and the ship motions are computed by the 2D+t approach. Within this approach the three-dimensional flow is approximated by several two-dimensional earth fixed flow problems. As the ship moves forward it causes unsteady flow in each cross-plane, which is solved using a boundary element method based on potential theory. General requirements for the validity of 2D+t theory are that the ship hull is slender and moves fast. Corrections are typically needed at the transom stern as the physically required drop to atmospheric pressure is not captured by the 2D+t approximation. For the ship moving in open water of constant depth, the flow is symmetric with respect to the symmetry plane of the ship. If the ship moves along either a vertical wall or an ice edge, then the flow is not symmetric and there are forces acting on

the ship in the transverse direction. Disturbances generated by the ship in the elastic ice propagate both from the ice edge, which are consistent with the 2D+t approach, and along the edge, which leads to interaction between the cross-planes.

In case of open water and constant forward speed of the ship, it is sufficient to use a single cross-plane to approximate the three-dimensional wave field because the temporal development of the flow in a earth fixed cross-plane can be directly translated to the spatial distribution of the wave field along the ship axis. This is also the case if the ice sheet is modeled by a rigid plate of constant thickness, as there is no interaction between the respective cross planes If the ice sheet is modeled as elastic, then all cross-planes need to be modeled simultaneously. This is comparable to previously published problems with the ship moving in incident waves, where interaction between the flows in the cross planes is implied by the unsteady ship motion [1; 2]. However, in our problem, it is not clear how to describe the deflection of the ice sheet within the 2D+t approach, which does not account for the hydroelastic waves propagating in the direction of the ship motion.

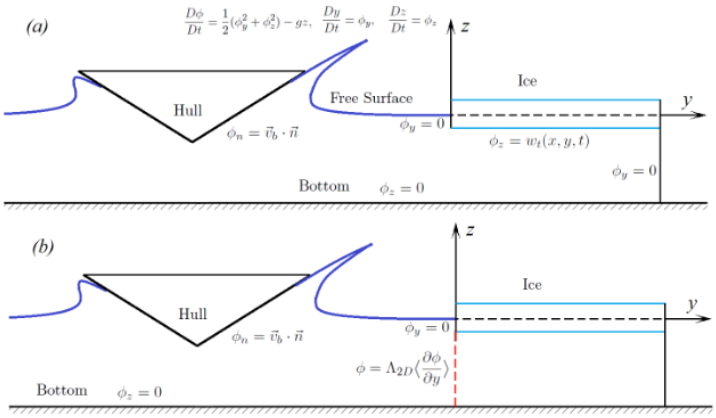

Figure 2: Boundary conditions in a cross plane for the BEM 2D+t (a) and 2D+t with the non-local boundary condition on the fictitious vertical boundary (b).

The idea of the present study is to use the domain decomposition method dividing the flow domain into the domain of open water, $y < 0$, where the ship moves, and the domain covered with ice, $y > 0$. We model the flow in the ice covered region and the ice deflection caused by the ship moving near the ice edge as linear and match the velocity potential in the ice covered region with the potential of nonlinear flow in the open water region at a fictitious boundary shown in Fig. 2 by the vertical dashed line. To this aim, we shall solve the linear problem in the ice covered region, and find a non-local relation between the velocity potential under the ice and its normal derivative at the fictitious vertical wall at the ice edge. This relation is suggested to use as the boundary condition for the non-linear problem in the open water region with the ship. The boundary element method, which is used to solve the flow in each cross-plane for the open-water region $y < 0$, incorporates fully non-linear free surface boundary conditions. This enables it to capture important flow effects associated with high speed ships such as spray evolution and flow separation at chines. Details on the implementation can be found in [1]. Due to the potential flow assumptions made for the flow solver, viscous effects are neglected.

This approach is tested first for the rigid ice model, where the 2D+t approach is well applicable with a single cross plane needed for computations. The rigid-ice plate can be included in the boundary element method without using the 3D or 2D non-local boundary condition at $y = 0$.

In this way we can investigate the applicability of the non-local boundary condition and gain experience of working with this condition. We consider using the boundary element method for both open water and ice-covered regions as too extensive. Note that non-local boundary condition at $y = 0$ does not include the memory effect for the rigid ice model.

2 Non-local boundary condition

We consider here only the ice-covered region, $y > 0$, $-\infty < x < \infty$ and $-H < z < 0$, where H is the water depth and $z = 0$ is the position of the ice/water interface at equilibrium. The ice sheet of constant mass per unit area m_i and rigidity D_i corresponds to the half-plane $y > 0$. The ice deflection $w(x, y, t)$ is governed by the linear Kirchhoff-Love equation of a thin elastic plate,

$$m_i w_{tt} + D_i \nabla^4 w = p(x, y, w(x, y, t), t) \qquad (y > 0,\ t > 0), \tag{1}$$

where $p(x, y, z, t)$ is the hydrodynamic pressure acting on the ice/water interface $z = w(x, y, t)$. This linear model of continuous elastic ice plate is acceptable because ice breaks for relative elongations of ice elements (strains) of order of 10^{-4}. Large and moderate deformations of the ice plate lead to ice breaking before such non-linear deformations are achieved. The plate equation (1) is solved subject to the zero initial conditions, $w(x, y, 0) = 0$ and $w_t(x, y, 0) = 0$, free-free boundary conditions at the edge of the ice plate, and the far-field condition, $w(x, y, t) \to 0$ as $x^2 + y^2 \to \infty$ and $t < +\infty$.

We assume that the equations of the flow under the ice sheet and corresponding boundary conditions can be linearised, even if the flow outside the ice-covered region is fully nonlinear. The linear theory of hydroelasticity provides the following equations describing the flow under the ice:

$$\phi_{xx} + \phi_{yy} + \phi_{zz} = 0 \quad (-H < z < 0,\ y > 0,\ |x| < \infty), \qquad \phi \to 0 \quad (x^2 + y^2 \to \infty),$$

$$\phi_z = 0 \quad (z = -H,\ \ y > 0,\ |x| < \infty), \qquad \phi_z = w_t(x, y, t) \quad (z = 0,\ y > 0,\ |x| < \infty). \tag{2}$$

The hydrodynamic pressure on the ice/water interface is given by the linearised Bernoulli equation,

$$p(x, y, w(x, y, t), t) = -\rho \phi_t - \rho g w(x, y, t),$$

where ρ is the liquid density and g is the gravitation acceleration. We assume that the normal velocity of the flow on the fictitious vertical boundary of the ice covered region is given,

$$\phi_y(x, 0, z, t) = G(x, z, t) \qquad (H < z < 0,\ y = 0,\ -\infty < x < \infty,\ t \geq 0). \tag{3}$$

We shall solve the problem (1)-(3) and determine the potential $\phi(x, 0, z, t)$ at the vertical fictitious boundary as an operator acting on $G(x, z, t)$ in the form $\phi(x, 0, z, t) = \Lambda <G>$. The latter relation is suggested to be used as a boundary condition at the fictitious boundary of the open water region with a ship moving there.

To solve the problem (1)-(3), we use the Fourier transform in the x-direction and the normal mode method in the vertical z-direction. The velocity potential $\phi(x, y, z, t)$ is sought in the form $\phi(x, y, z, t) = \phi_0(x, y, z, t) + \Phi(x, y, z, t)$, where $\phi_0(x, y, z, t)$ is the solution of the problem (2)-(3), where $w_t(x, y, t) = 0$. Correspondingly, $\Phi(x, y, z, t)$ is the solution of the problem (1)-(3), where $\Phi_y(x, 0, z, t) = 0$ on the fictitious boundary and the right hand side in (1) reads $-\rho\Phi_t - \rho\phi_{0t} - \rho g w(x, y, t)$. The potential ϕ_0 is the solution of the problem for the rigid ice model. Note that the solution of this problem exists only if the integral of the function $G(x, z, t)$ over the fictitious boundary is zero. We start with the potential $\phi_0(x, y, z, t)$. This potential satisfies Laplace's

equation and the conditions $\phi_{0z} = 0$ at $z = -H$ and $z = 0$. The resulting relation on the fictitious boundary reads

$$\phi_0(x,0,z,t) = \int_{-\infty}^{\infty}\int_{-H}^{0} \frac{\partial \phi_0}{\partial y}(x_0,z_0,0,t) k_{3D}(x-x_0,z,z_0)\mathrm{d}x_0\mathrm{d}z_0, \tag{4}$$

$$k_{3D}(x-x_0,z,z_0) = -\frac{1}{2\pi}\Bigg\{\frac{1}{\sqrt{(x-x_0)^2+(z-z_0)^2}} + \frac{1}{\sqrt{(x-x_0)^2+(2H+z+z_0)^2}} + \frac{\pi}{H}S_R(|x-x_0|,2H+z+z_0) + \frac{\pi}{H}S_R(|x-x_0|,|z-z_0|)\Bigg\},$$

$$S_R(x,\zeta) = \sum_{k=1}^{\infty}\left[\frac{1}{\sqrt{(2\pi k-\pi\zeta/H)^2+(\pi x/H)^2}} + \frac{1}{\sqrt{(2\pi k+\pi\zeta/H)^2+(\pi x/H)^2}} - \frac{1}{\pi k}\right].$$

The relation (4) written within the 2D+t approach without interaction between cross planes is

$$\phi_0(x,0,z,t) = \int_{-H}^{0} \frac{\partial \phi_0}{\partial y}(x_0,z_0,0,t) k_{2D}(z,z_0)\mathrm{d}z_0, \quad k_{2D}(z,z_0) = \frac{1}{\pi}\log\left|\cos\left(\frac{\pi z}{H}\right) - \cos\left(\frac{\pi z_0}{H}\right)\right|. \tag{5}$$

Note that here $z = 0$ corresponds to the ice-water interface but not to the equilibrium level of the liquid, see Fig. 2. The lower part of the ice edge is submerged in water, which makes the derivative $\phi_{0,y}(x,z,0,t) = O(|z|^{-\frac{1}{3}})$ to be singular at the lower corner of the ice edge.

3 Numerical results

The computer code *impact2d* which was developed at TUHH, has been adjusted to account for rigid level ice by implementing the proposed boundary conditions (4) and (5). Condition (5) is consistent with classical 2D+t theory, where a single cross plane is used to approximate the 3D flow. This problem is also solved directly by using panels on the rigid boundaries of the ice-covered region without considering any conditions on the fictitious boundary. Additionally, condition (4) has been implemented. As it requires integration along the x-axis, all cross planes need to be modelled simultaneously. In that regard it is considered a first step towards implementation of elastic ice sheets. The results obtained with the respective approaches are compared to each other throughout the study. The results of the comparison will be presented at the Workshop.

Acknowledgment

This study is funded by the US Office of Naval Research project titled “Energy-Efficient Operations in the Arctic Environment of Advanced Naval Vessels”.

References

[1] H. Simonis, P. Marleaux, and M. Abdel-Maksoud. Numerical analysis of semi-displacement vessels in head waves. In *Proceedings of the 33rd Symposium on Naval Hydrodynamics*, Osaka, Japan, 2020. October 18-23.

[2] H. Sun and O. M. Faltinsen. Dynamic motions of planing vessels in head seas. *Journal of Marine Science and Technology*, 16(2):168–180, April 2011. doi: 10.1007/s00773-011-0123-4.

Floe size distributions in irregular sea states

Nicolas Mokus, Fabien Montiel
Department of Mathematics and Statistics, University of Otago, Dunedin, New Zealand
nmokus@maths.otago.ac.nz

Highlights

We develop and implement an efficient multiple scattering model to study the wave-induced breakup of sea ice floes. We use it to observe the emergence of a floe size distribution after repeated breakup events. We find the resulting distribution is right-skewed and better approximated by a lognormal model than the often used Pareto model.

1 Introduction

Sea ice is a distinctive feature of both polar oceans. By drastically altering the ocean surface albedo and interrupting the fluxes of matter, kinetic energy, and thermal radiation between oceans and atmosphere, it has an extensive impact on their circulations and the Earth's climate. The marginal ice zone (MIZ) is the transition belt between an ice-free ocean and the pack ice. It features a collection of ice floes of varying sizes, distinguishing it from a continuous ice cover, and is notably affected by waves. The shape of this floe size distribution (FSD) has been an active topic of research for decades [1]. Wave activity is one of the drivers of the FSD evolution which, in turn, controls wave propagation. Smaller floes are more sensible to melt, and lower ice concentration allows waves to propagate further into the MIZ, introducing a positive feedback loop. Therefore, representing the FSD in global climate models is necessary to improve their accuracy and enhance their long-term forecast capabilities.

Remote sensing observation of floe sizes have suggested the FSD follows a Pareto (power law) distribution [1, 2]. This led to its adoption in various modelling studies. However, recent field observations [3, 4], laboratory experiments [5, 6] and numerical models [7, 8] propose contrasting distributions. The role of wave activity in the emergence of the Pareto distribution [3], and even the validity of this statistical model [9, 10], are unclear. In a recent modelling study [11], we combine FSDs obtained under monochromatic forcings to simulate the FSD resulting from a wave spectrum. We find the lognormal distribution is a strong parametric alternative to the Pareto distribution. In this abstract, we show that this model is also appropriate for the FSD produced by repeated breakup under polychromatic wave forcing.

2 Mathematical model

2.1 Wave scattering

Our model is based on linear water wave theory. We consider the scattering of surface gravity waves propagating in the x direction, in a two-dimensional fluid domain of constant depth H, by an array of ice floes modelled as visco-elastic floating plates [12] with free edge boundary conditions. Floes are non-overlapping so that individual floes are separated by open water, delimiting homogeneous sub-domains. Floe j is identified by the coordinate of its left edge, x_j, and its length, L_j. This geometry is illustrated on Figure 1. The fluid velocity derives from a

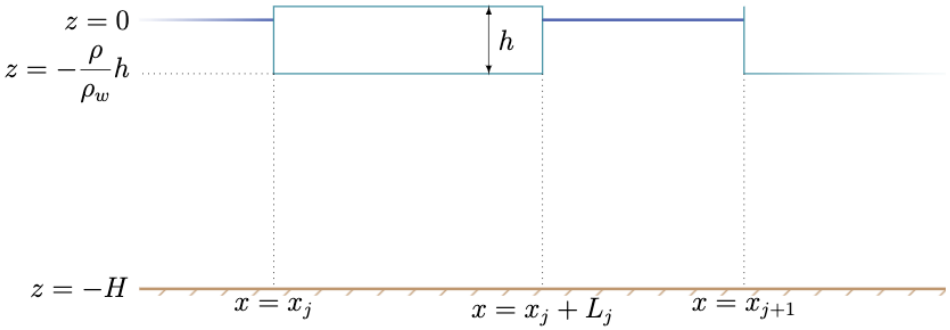

Figure 1: Geometry of the model at rest.

scalar, time-harmonic potential Φ solution of Laplace's equation. We further assume separation of space and time variables so that $\Phi = \mathrm{Re}\left[\phi\left(x,z\right)\exp(-i\omega t)\right]$ with ω a prescribed angular frequency. We note g the acceleration of gravity, D the floes flexural rigidity, h their thickness, ρ their density, γ their viscosity, ρ_w the fluid density. The ensuing boundary conditions on the fluid top surface and at the impervious seabed lead to the dispersion relations

$$k\tanh\left(kH\right) = \frac{\omega^2}{g} \quad ; \quad \left(\frac{D}{\rho_w g}k^4 + 1 - \frac{\omega^2}{g}\frac{\rho}{\rho_w}h - i\frac{\gamma\omega}{\rho_w g}\right)k\tanh\left(k\left(H - \frac{\rho}{\rho_w}h\right)\right) = \frac{\omega^2}{g} \tag{1}$$

with respective roots k^w and k^f in respectively open water and ice-covered sub-domains.

The potential ϕ is expanded onto these wave modes in every sub-domain, and the expansion coefficients are determined to ensure continuity of pressure and velocity across the horizontal interfaces between adjacent sub-domains. It fully determines the spatial part of Φ in the whole domain. More details on the solution method can be found in [11].

2.2 Breakup parametrisation

Strain is often used to parametrise wave-induced breakup [13]. Here, we consider the maximum strain undergone by each floes. We use the plane stress approximation so that for a given ice floe, this maximum strain, in absolute value, is located on either top or bottom surface of the floe. The motion of the bottom surface is derived from the wave field, fully characterised by ϕ, so that

$$\tilde{\varepsilon}\left(x,\omega\right) = \frac{h}{2\omega}\left|\mathrm{Re}\left[i\frac{\partial^2}{\partial x'^2}\frac{\partial\phi}{\partial z}\right]\right|. \tag{2}$$

Our model solves for the scattering of a monochromatic wave. The strain field undergone by the floes is a consequence of this monochromatic forcing. To estimate the strain field resulting from a developed sea, we introduce the theoretical Pierson-Moskowitz spectrum

$$S(\omega) = c_1\frac{g^2}{\omega^5}\exp\left(-c_2\frac{g^2}{\omega^4 {H_s}^2}\right) \tag{3}$$

where $c_1 = 8.1\times10^{-3}$, $c_2 = 3.24\times10^{-2}$ are non-dimensional constants. This spectrum is parametrised by the significant wave height $H_s = 4\sqrt{\int_0^{+\infty} S(\omega)\mathrm{d}\omega}$. Using the superposition principle, the strain under such a forcing can be written as

$$\varepsilon(x) = \frac{\int_{\omega_{\min}}^{\omega_{\max}} \tilde{\varepsilon}(x,\omega)S(\omega)\mathrm{d}\omega}{\int_{\omega_{\min}}^{\omega_{\max}} S(\omega)\mathrm{d}\omega} \tag{4}$$

where the bounds $\omega_{\min}, \omega_{\max}$ are used for numerical integration, ensuring we capture a significant part of the spectrum, Equation (4) being evaluated on 200 equally spaced angular frequencies.

As in [11], we set floe j to break when $\max_{x' \in [0, L_j]} \varepsilon_j(x') > \varepsilon_c$ where ε_c is an empirically determined strain threshold. We situate the breakup point at $x_b = \operatorname{argmax} \varepsilon_j$ so that a floe of length L_j breaks into two floes of length x_b and $L_j - x_b$.

2.3 Numerical experiment

Our experiment is summarised by the following steps:

1. The domain is initialised with a single, semi-infinite floe.
2. The scattered wave field is determined for 200 frequencies between $\omega_{\min}$ and $\omega_{\max}$.
3. The ensuing strain field is derived from Equation 4. All floes meeting the breakup condition are split and the domain updated.
4. Steps 2 and 3 are repeated until none of the floes break.
5. The resulting finite lengths are recorded.

To account for wave dispersion, at each iteration individual waves are assigned a phase sampled uniformly in $[0, 2\pi)$. Additionally, after every breakup event floes are assigned random new locations, preserving their order, to enforce they do not overlap. These sources of randomness impact the resulting FSD. Therefore, we run the same simulation several times, to obtain an ensemble of FSDs.

3 Preliminary results and conclusions

We investigate the behaviour of the model under small-amplitude wave forcing, setting $H_s = 1\,\mathrm{m}$. The ice properties are set to $h = 1\,\mathrm{m}$, $\gamma = 20\,\mathrm{Pa\,s\,m^{-1}}$, $\varepsilon_c = 4 \times 10^{-5}$. The resulting distributions are right-skewed. We average them over 40 model realisations. Specifically, these 40 sets of floe lengths are assembled into a single dataset, which is equivalent to averaging count histograms computed on the same bins. We estimate, by maximum likelihood, parameters for a Pareto distribution (following a common assumption in wave–sea ice modelling) and for a lognormal distribution. In Figure 2, we compare these parametric distributions to a kernel density estimate of the FSD.

Even though the lognormal distribution does not perfectly fit the data, especially for larger floe lengths, it is a better match than the Pareto distribution. The predicted mode of a Pareto distribution is the smallest admissible floe size, while our empirical distribution clearly is not monotonic. This reinforces our recent modelling findings [11] and suggest a reappraisal of the de facto power law assumption adopted in the modelling community [14, 15].

The polychromatic parametrisation used here differs from the one used in [11]. The results are qualitatively similar but differ quantitatively, as shown in Figure 2. It is not clear which one of these parametrisations has more physical significance. Additional observational data is needed to confirm or invalidate these statistical models. We do not attempt at this stage to evaluate the impact of empirical parameters such as ε_c or γ on these results. This will be discussed during the presentation.

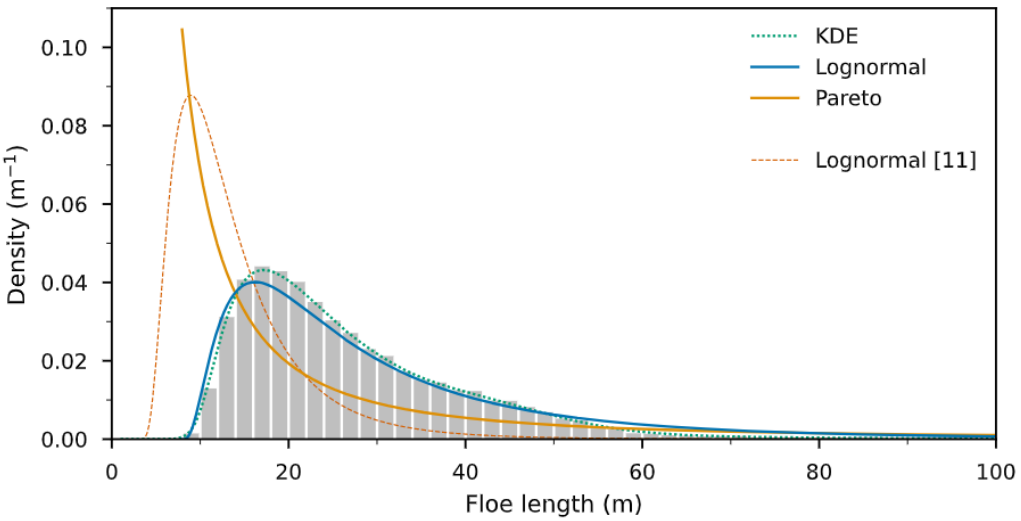

Figure 2: Average FSD over 40 model realisations. Two non-parametric density estimates (histogram, kernel density) are compared to two parametric models. The histogram bin width is 2 m. The lognormal fit to a similar configuration, obtain by combining monochromatic FSDs [11], is added for comparison.

REFERENCES

[1] Rothrock, D. A., and Thorndike, A. S. 1984. *Measuring the sea ice floe size distribution.* Journal of Geophysical Research 89(C4), 6477.

[2] Toyota, T., Takatsuji, S., and Nakayama, M. 2006. *Characteristics of sea ice floe size distribution in the seasonal ice zone.* Geophysical Research Letters 33(2).

[3] Herman, A., Wenta, M., and Cheng, S. May 2021. *Sizes and Shapes of Sea Ice Floes Broken by Waves–A Case Study From the East Antarctic Coast. Frontiers in Earth Science 9*.

[4] Dumas-Lefebvre, E., and Dumont, D. 2021. *Aerial observations of sea ice break-up by ship waves. The Cryosphere Discussions 2021*, 1–26.

[5] Dolatshah, A., Nelli, F., Bennetts, L. G., Alberello, A., Meylan, M. H., Monty, J. P., and Toffoli, A. Sept. 2018. *Letter: Hydroelastic interactions between water waves and floating freshwater ice.* Physics of Fluids 30(9), 091702.

[6] Herman, A., Evers, K.-U., and Reimer, N. Feb. 2018. *Floe-size distributions in laboratory ice broken by waves.* The Cryosphere 12(2), 685–699.

[7] Montiel, F., and Squire, V. A. Oct. 2017. *Modelling wave-induced sea ice break-up in the marginal ice zone.* Proceedings of the Royal Society A: Mathematical, Physical and Engineering Science 473(2206), 20170258.

[8] Herman, A. Nov. 2017. *Wave-induced stress and breaking of sea ice in a coupled hydrodynamic discrete-element wave–ice model.* The Cryosphere 11(6), 2711–2725.

[9] Clauset, A., Shalizi, C. R., and Newman, M. E. J. Nov. 2009. *Power-Law Distributions in Empirical Data.* SIAM Review 51(4), 661–703.

[10] Stern, H. L., Schweiger, A. J., Zhang, J., and Steele, M. Jan. 2018. *On reconciling disparate studies of the sea-ice floe size distribution. Elementa: Science of the Anthropocene 6*.

[11] Mokus, N. G. A., and Montiel, F. 2021. *Wave-triggered breakup in the marginal ice zone generates lognormal floe size distributions. The Cryosphere Discussions 2021*, 1–33.

[12] Robinson, N., and Palmer, S. Nov. 1990. *A modal analysis of a rectangular plate floating on an incompressible liquid.* Journal of Sound and Vibration 142(3), 453–460.

[13] Kohout, A. L., and Meylan, M. H. Sept. 2008. *An elastic plate model for wave attenuation and ice floe breaking in the marginal ice zone.* Journal of Geophysical Research 113(C9).

[14] Williams, T. D., Bennetts, L. G., Squire, V. A., Dumont, D., and Bertino, L. Nov. 2013. *Wave–ice interactions in the marginal ice zone. Part 1: Theoretical foundations. Ocean Modelling 71*, 81–91.

[15] Boutin, G., Lique, C., Ardhuin, F., Rousset, C., Talandier, C., Accensi, M., and Girard-Ardhuin, F. Mar. 2020. *Towards a coupled model to investigate wave–sea ice interactions in the Arctic marginal ice zone.* The Cryosphere 14(2), 709–735.

Enhanced Wave-Field Reconstruction Based on Stochastic Characteristics of Shadowing Effects

Yoon-Seo Nam[1], Jae-Hoon Lee[1], Yuming Liu[2] and *Yonghwan Kim[1]

[1] Department of Naval Architecture and Ocean Engineering, Seoul National University, Seoul, Korea
[2] Department of Mechanical Engineering, Massachusetts Institute of Technology, Cambridge, MA, USA
*yhwankim@snu.ac.kr

1 INTRODUCTION

In order to analyze the performance of ships and offshore platforms on a real-time basis, the phase-resolved prediction for a surrounding wave field is required. The sensing mechanism of a marine radar involves modulation effects such as shadowing which engender non-physical effects in the radar image. Therefore, post-processing, that is, the wave-field reconstruction should be performed to scale the image intensity and to remove the non-physical components. In the present study, we propose an enhanced reconstruction method based on the stochastic characteristics of the shadowing effect.

2 THEORETICAL BACKGROUNDS

A radar beam with a slope (μ) is assumed to be emitted from the radar that is located far away from the origin of the coordinate system. In the coordinate system (x, z), the x-axis is aligned with the radar ray and z=0 indicates the mean sea surface. The wave elevation (ζ) and wave slope (q) are considered independent zero-mean Gaussian random processes with the standard deviation of σ and w, respectively. The spatial autocorrelation function of the wave elevation is denoted by *acf*. Moreover, the random variables at the origin (x=0) are abbreviated as (ζ_0, q_0), and variables at x are abbreviated as (ζ_1, q_1) to simplify expressions. The coordinate system and definitions are summarized in Fig. 1. Then, the shadowing function, $S(\zeta_0, q_0, \mu; \sigma, w)$ is defined with respect to the given variables, which represents the probability that the shadowing will not occur at the origin. The general form of the shadowing function is as follows:

$$S(\zeta_0, q_0, \mu; \sigma, w) = \begin{cases} \exp\left[-\int_0^\infty g(x)dx\right] & \mu \geq q_0 \\ 0 & \mu < q_0 \end{cases} \tag{1}$$

where $g(x)$ indicates the conditional probability that the waves between [x, x+dx] interfere with the radar ray when no shadowing occurs between [0, x]. The conditional shadowing probability can be expressed by introducing a joint Gaussian probability density function, $P_4(\zeta_0, \zeta_1, q_0, q_1)$, such that:

$$g(x) = \frac{\int_\mu^\infty (q_1 - \mu) P_4(\zeta_0, \zeta_0 + \mu x, q_0, q_1) dq_1}{\int_{-\infty}^\infty \int_{-\infty}^{\zeta_0 + \mu\tau} P_4(\zeta_0, \zeta_1, q_0, q_1) d\zeta_1 dq_1}. \tag{2}$$

Particularly, $g(x)$ can be calculated with or without considering the spatial autocorrelation effects. The details about the evaluation of $g(x)$ without the correlation effects can be found in [1], and an enhanced computation with the correlation is presented in [2]. Based on the derived conditional probabilities in the previous studies, $S(\zeta_0, q_0, \mu; \sigma, w)$ can be computed.

Further stochastic characteristics independent of the standard deviation of wave elevations (σ) can be derived from the shadowing function. The Smith function, $S(\mu; w)$, which denotes the probability of not shadowing, is defined by averaging the shadowing function over (ζ_0, q_0):

$$S(\mu; w) = \int_{-\infty}^\infty \int_{-\infty}^\infty S(\zeta_0, q_0, \mu; \sigma, w) \frac{1}{2\pi\sigma w} \exp\left(-\frac{\zeta_0^2}{2\sigma^2} - \frac{q_0^2}{2w^2}\right) d\zeta_0 dq_0. \tag{3}$$

For a sequence of consecutive radar images, the illumination ratio (the ratio of not shadowed time to the entire measurement duration at a certain location) can be obtained. Hence, it is possible to estimate the mean surface slope in each azimuthal direction ($w_{est}(\theta)$) from the radar images by fitting the illumination ratio with the Smith function. Details about the mean surface slope estimation are presented in [3].

Based on the estimated mean surface slope and the relationship between sea state parameters, we propose the following estimation for the significant wave height, which is required to scale the image intensity according to the total energy of an ocean wave field:

$$H_S = \frac{g w_{total} T_4^2}{\pi^2} \tag{4}$$

where $w_{total} = \sqrt{w_{est}(\theta)^2 + w_{est}\left(\theta + \frac{\pi}{2}\right)^2}$, $T_4 = 2\pi\left(\frac{m_0}{m_4}\right)^{1/4}$.

Here, m_n indicates the n^{th} spectral moment computed by the FFT analysis on the radar image sequence. Furthermore, it is possible to estimate the expected variance (energy) of the image intensity. In the present study, the Smith variance is proposed, which represents the ratio between the expected variances of the shadowed (ζ_s) and original wave-field (ζ). Explicit formulation of the Smith variance is as follows:

$$V(\mu; w) = \frac{\mathrm{var}(\zeta_s)}{\mathrm{var}(\zeta)} = \frac{1}{\sigma^2}\int_{-\infty}^{\infty}\int_{-\infty}^{\infty}\zeta_0^2 S(\zeta_0, q_0, \mu_0; \sigma, w)\frac{1}{2\pi\sigma w}\exp\left(-\frac{\zeta_0^2}{2\sigma^2} - \frac{q_0^2}{2w^2}\right)d\zeta_0 dq_0 \tag{5}$$

where $\zeta_s(x,t) = \begin{cases} \zeta(x,t) & \textit{no shadowing} \\ 0 & \textit{shadowing} \end{cases}$.

By adopting the mean-shift modification method proposed by Zinchenko [4], the radar image can be modified to resemble the shadowed wave field. Subsequently, the calibration of image intensity based on the Smith variance is conducted so that the energy level could be uniform in the entire measurement domain such as an ocean wave field. For this purpose, the radar image intensity (ρ) is divided by the square root of the expected variance at each location (r, θ) as follows:

$$\rho_c(r,\theta) = \frac{\rho(r,\theta)}{\sqrt{V(\mu(r); w_{est}(\theta))}} \qquad \text{where } \mu(r) = r / h_r. \tag{6}$$

Here, h_r is the radar height.

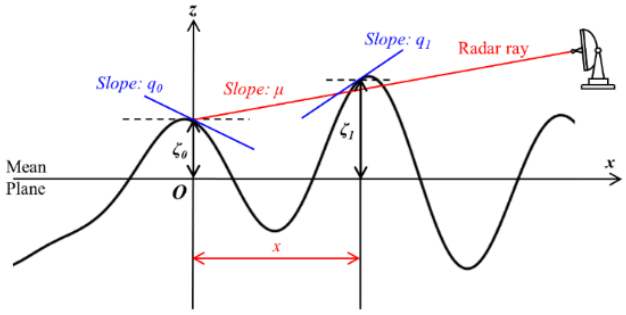

Fig. 1 Coordinate system and definitions

3 COMPUTATION RESULT

Synthetic radar images are generated to validate the proposed wave-field reconstruction method. To this end, a short-crested wave data of Beaufort scale 7 (H_S=4.0 m and T_{mean}=7.7 s) is synthesized based on the linear superposition of random wave components. The main propagation direction and the spreading angle are χ_M=180.0 deg and χ_S=60.0 deg, respectively. Moreover, the assumed minimum and maximum sensing radius are $R_{\min}$=200.0 m and $R_{\max}$=2000.0 m with the spatial resolution dx=dy=10.0 m. The length of the time window is T=100.0 s and the time interval between two successive radar images is set to dt=1.0 s. Subsequently, the geometrical shadowing effect is reflected to generate the synthetic image intensity with the radar height of h_r=40 m. The intensity of the shadowed point is set to be zero, whereas the non-shadowed points are rescaled into an 8-bit grey scale (0-255). The generated synthetic wave data and radar image are shown in Fig. 2.

First, the mean surface slope is estimated by fitting the illumination ratio with the Smith function as presented in Fig. 3(a). The estimated mean surface slopes with and without considering the spatial autocorrelation effect

are compared in Fig. 3(b). The exact mean surface slope is computed based on the analytic integration of a given wave spectrum. As shown in the figure, the mean surface slope estimation is more accurate when the spatial autocorrelation effects are taken into account for the derivation of the Smith function. Accordingly, the accuracy of the H_S estimation is also improved due to the correlation effects (without correlation: $H_{S,est}/H_{S,exact}$=1.178, with correlation: $H_{S,est}/H_{S,exact}$=1.051).

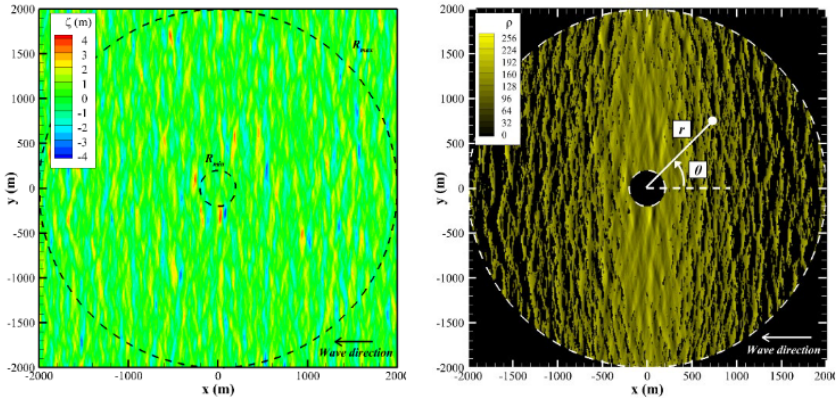

(a) Synthetic wave data (b) Synthetic radar image

Fig. 2 Synthetic wave-field and radar image: Short-crested waves of Beaufort scale 7 (H_S=4.0 m, T_{mean} = 7.7 s)

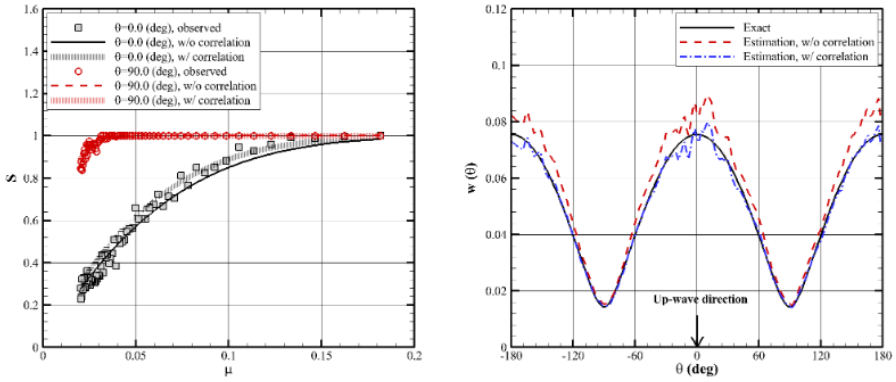

(a) Fitting with Smith function (b) Estimated mean surface slope

Fig. 3 Estimation of the mean surface slope by fitting with Smith function

Fig. 4 presents the observed variance of radar image intensities. It can be confirmed that the variance is non-uniform because of the dependence of shadowing effects on the azimuth; the shadowing effects are severe for the main propagation direction and weak in cross-wave direction. The expected variance is evaluated with the mean surface slope according to Eq. (5), and compared with the observed variance for each azimuthal direction. The estimated and observed variances are in good agreement as shown in Fig. 4(b).

Lastly, the radar image intensity is calibrated with the theoretically derived variance. Subsequently, the general wave-field reconstruction is conducted based on the 3D FFT & IFFT analysis techniques. Fig. 5 shows the reconstructed results with or without the energy-level calibration. As shown in Fig. 5(a), the reconstructed wave elevation is overestimated in the cross-wave direction due to the nonhomogeneous energy distribution. On the other hand, mitigation of the overestimation by the calibration is confirmed (refer to Fig. 5(b)). When the results are assessed through the root-mean-square (RMS) error between the exact and reconstructed wave fields, the accuracy is enhanced by about 10% for the whole measurement domain by the calibration.

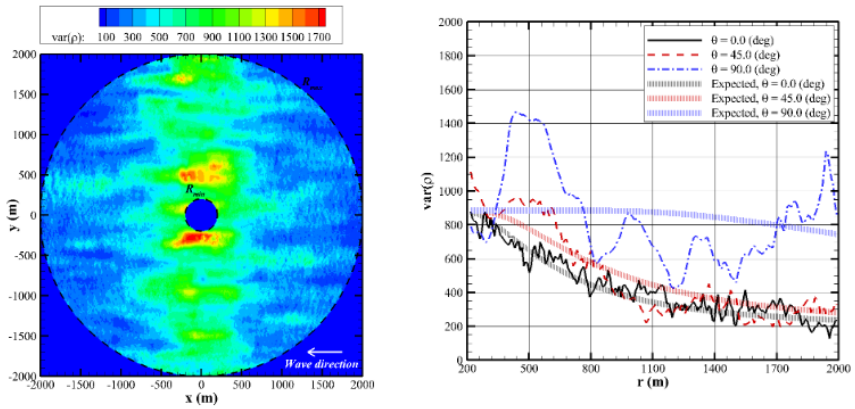

(a) Variance distribution (b) Variance in each direction

Fig. 4 Variance of radar image intensity: Short-crested waves of Beaufort scale 7 (H_S=4.0 m, T_{mean} = 7.7 s)

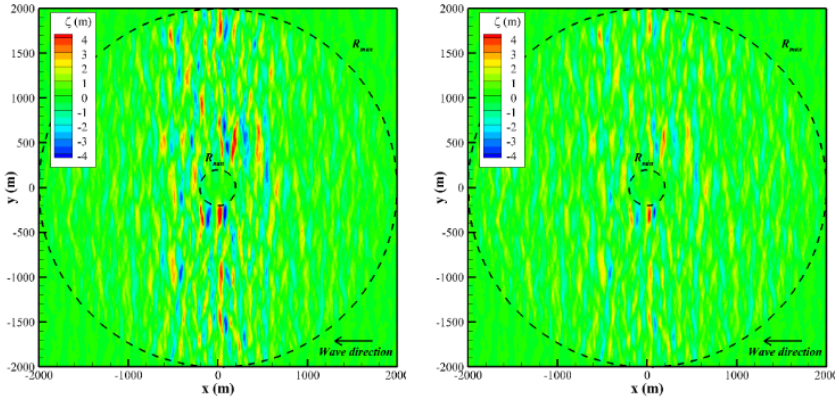

(a) w/o calibration (b) w/ calibration

Fig. 5 Reconstructed wave-field: Short-crested waves of Beaufort scale 7 (H_S=4.0 m, T_{mean} = 7.7 s)

4 CONCLUSIONS

The following conclusions can be made throughout this study:

- The accuracy of the significant wave height estimation is improved by considering the spatial autocorrelation effects in the shadowing function.
- The non-uniformity of the reconstructed wave field can be mitigated by applying the energy-level calibration based on the theoretically derived variance of radar image intensities.

ACKNOWLEDGEMENT

This study is supported by the DSME-SNU Future ocean cluster (FOC) center through the project “Development of Core Technology for Real-Time Digital Twin of Ship Operation in Seaways” (Project No.0690-2020014). Their financial and administrative supports are highly appreciated.

REFERENCES

[1] Smith, B., 1967. Geometric shadowing of a random rough surface, *IEEE transactions on antennas and propagation*, 15, 668-671.

[2] Bourlier, C. & Berginc, G., 2003. Shadowing function with single reflection from anisotropic Gaussian rough surface. Application to Gaussian, Lorentzian and sea correlations, *Waves in random and complex media*, 13:1, 27-58.

[3] Gangeskar, R., 2014. An algorithm for estimation of wave height from shadowing in X-band radar sea surface images, *IEEE transactions on geoscience and remote sensing*, 52(6), 3373-3381.

[4] Zinchenko, V., Vasilyev, L., Halstensen, S.O., Liu, Y., 2021. An improved algorithm for phase-resolved sea surface reconstruction from X-band marine radar images, *J. Ocean Engineering and Marine Energy*, 7, 97-114.

Modelling design waves in a Numerical Wave Flume based on a higher-order Moving Particle Semi-Implicit Method

Emiliano Renzi[1] **& Frederic Dias**[2,3]

1. Department of Mathematical Sciences, Loughborough University, LE11 3TU, UK
2. School of Mathematics and Statistics, University College Dublin, Belfield, Dublin 4, Ireland
3. ENS Paris-Saclay, CNRS, Centre Borelli, Université Paris-Saclay, Gif-sur-Yvette 91190, France

e.renzi@lboro.ac.uk

HIGHLIGHTS

- We present a numerical wave flume based on a higher-order Moving Particle Semi-Implicit Method (NWF-MPS).
- We introduce a novel artificial viscosity term to prevent particle clustering and to reduce spurious numerical oscillations.
- The model is used to successfully reproduce waves of engineering interest in linear and nonlinear regimes, using fewer particles than needed by other Lagrangian methods.

1 INTRODUCTION

The Moving Particle Semi-Implicit Method is a meshless Computational Fluid Dynamics (CFD) model based on a Lagrangian description of the fluid flow. In Lagrangian models, the fluid is discretised into computational particles, which act as calculations points where the hydrodynamic quantities (such as velocity and pressure) are calculated.

Applications of particle based models to wave dynamics date back to three decades ago, when the Smoothed Particle Hydrodynamics (SPH) method, originally developed in the 1970's for problems in astrophysics, was extended to solve free-surface flows [1]. The development of MPS started much later, around the beginning of this century, as an extension of the finite volume method [2]. MPS has several advantages as compared to SPH, such as a simplified approach to spatial discretisation and a lower sensitivity to the kernel choice [3].

Several authors have proposed MPS applications to water waves, including wave breaking, wave-ship interaction and landslide tsunamis (see [3, 4] and references therein). However, there is still lack of systematic MPS modelling of design waves in a numerical wave flume (NWF).

Here we report novel results stemming from the recent work of [3], in which a higher-order MPS model was developed to reproduce linear and nonlinear waves.

2 NUMERICAL MODEL

We consider a viscous and weakly compressible fluid flow governed by the continuity and Navier-Stokes equations, respectively

$$\frac{\mathrm{D}\rho}{\mathrm{D}t} + \rho \nabla \cdot \mathbf{u} = 0, \tag{1}$$

and

$$\frac{\mathrm{D}\mathbf{u}}{\mathrm{D}t} = -\frac{1}{\rho}\nabla P + \nu \nabla^2 \mathbf{u} + \mathbf{g}. \tag{2}$$

In the latter, $\mathrm{D}/\mathrm{D}t$ is the Lagrangian derivative, $\nabla = (\partial/\partial x, \partial/\partial y)^T$ is the nabla operator, ρ is density, P is pressure, ν is kinematic viscosity and $\mathbf{g} = (0, -g)^T$, $g = 9.807\,\mathrm{ms}^{-2}$ is gravity. Following [5, 6, 7], a weakly compressible formulation is used for the density, so that

$$\rho = \rho^0 + \frac{\mathrm{d}\rho}{\mathrm{d}P}\,\mathrm{d}P, \tag{3}$$

where ρ^0 is the constant ambient density and $c = (\mathrm{d}P/\mathrm{d}\rho)^{1/2}$ is the speed of sound in water.

2.1 MPS Formalism

The MPS method solves a discretised form of the governing equations (1)–(2), calculated at particle i at the k-th instant t^k. This is achieved by using a weighted average over all the neighbouring particles $j = 1, ..., N_i$, where the weight function is given by

$$w(r, r_e) = \begin{cases} r_e/r - 1 & \text{if } r < r_e \\ 0 & \text{if } r \geq r_e \end{cases}. \tag{4}$$

In the latter, r_e is an effective radius of interaction. Summing the weight functions calculated at all the neighbouring particles of the i-th target particle gives the particle number density

$$n_i = \sum_{j \neq i}^{N_i} w\left(r_{ji}, r_e\right), \tag{5}$$

where $\mathbf{r}_{ji} = \mathbf{r}_j - \mathbf{r}_i$, $r_{ji} = |\mathbf{r}_{ji}|$, and $\mathbf{r}_i$ is the position of particle i.

2.2 Numerical Solution

The governing equations are then solved numerically using a predictor-corrector scheme, where the ith particle velocity $\mathbf{u}_i$ is first calculated at an intermediate step t^*, without considering the pressure gradient:

$$\mathbf{u}_i^* = \mathbf{u}_i^k + \left(\nu \left\langle \nabla^2 \mathbf{u} \right\rangle_i^k + \mathbf{g}\right) \Delta t. \tag{6}$$

The value is then corrected by accounting for the pressure contribution:

$$\mathbf{u}_i^{k+1} = \mathbf{u}_i^* - \frac{1}{\rho} \left\langle \nabla P \right\rangle_i^{k+1} \Delta t, \tag{7}$$

where Δt is the time discretisation. Eq. (7) is fully determined once the pressure is known. The pressure solves the Poisson equation

$$-\frac{1}{\rho_0} \left\langle \nabla^2 P \right\rangle_i^{k+1} + \frac{\alpha}{\Delta t^2} P_i^{k+1} = \frac{n_i^* - 2n_i^k + n_i^{k-1}}{n^0 \Delta t^2} + B \frac{n_i^k - n_i^{k-1}}{n^0 \Delta t} + \Gamma \frac{n_i^k - n^0}{n^0}, \tag{8}$$

where $\alpha = 1/(\rho c^2)$, $B = 500$, $\Gamma = 50,000$ as recommended by [8]. In (8) the Laplacian is given by

$$\left\langle \nabla^2 P \right\rangle_i^k = \frac{4}{\lambda^0 n^0} \sum_{j \neq i} \left(P_j^k - P_i^k\right) w\left(r_{ji}, r_e\right), \tag{9}$$

where

$$\lambda^0 = \frac{1}{n^0} \sum_{j \neq l} \left(r_{jl}^0\right)^2 w\left(r_{jl}^0, r_e\right) \tag{10}$$

is a weighted average at time $t = 0$, and l is an internal fluid particle. Substitution of (9) in (8) yields a linear system for the P_i^k's. Once the pressure is known from solving (8), the pressure gradient in (7) is calculated with the minimum pressure $\hat{P}_i^{k+1}$ in the neighbourhood of the i-th particle:

$$\langle \nabla P \rangle_i^{k+1} = \mathbf{C}_i^{-1} \cdot \left(\frac{1}{n^0} \sum_{j \neq i}^{N_i} \frac{P_j^{k+1} - \hat{P}_i^{k+1}}{\left(r_{ji}^*\right)^2} \mathbf{r}_{ji}^* \, w\left(r_{ji}^*, r_e\right) \right), \tag{11}$$

where the 2×2 matrix $\mathbf{C}_i$ is given by

$$\mathbf{C}_i = \frac{1}{n^0} \sum_{j \neq i}^{N_i} \frac{\mathbf{r}_{ji}^*}{r_{ji}^*} \otimes \frac{\left(\mathbf{r}_{ji}^*\right)^T}{r_{ji}^*} \, w\left(r_{ji}^*, r_e\right), \tag{12}$$

see [3, 8, 9]. To prevent particle clustering and tensile instability, we add an additional viscous term to the predictor step:

$$\left\langle \frac{\mathrm{D}\mathbf{u}}{\mathrm{D}t} \right\rangle_i^k = \frac{\delta \, c}{n^0} \sum_{i \neq j}^{N_i} \left(\frac{\mathbf{u}_{ji}^k \cdot \mathbf{r}_{ji}^k}{\left(r_{ji}^k\right)^2 + 0.01 \, r_e^2} \right) \left(\frac{r_e}{r_{ji}^k} \right)^2 \frac{\mathbf{r}_{ji}^k}{r_{ji}^k}, \tag{13}$$

where δ is an artificial viscosity parameter.

Appropriate boundary conditions must be applied on the free surface and at the solid boundaries. On the free surface, we request that the pressure be atmospheric, i.e. $P = 0$. In other words, we only consider the excess pressure over the atmospheric value. On the solid boundaries, we request a no-slip condition, so that the velocity is zero at boundary particles. Waves are generated using a numerical wavemaker at the left end of the flume, based on a dynamic boundary method (DBM). For more details on the implementation of those conditions into the computational algorithm, we refer interested readers to [3].

3 APPLICATIONS

The NWF-MPS model has been validated with respect to available analytical and experimental data. An extensive validation exercise, including detailed convergence studies, is available in [3]. Here we report an application of the above model to nonlinear wave propagation in a channel. More applications, including random seas and highly nonlinear dynamics, will be presented at the Workshop.

Figure 1 shows the time series of second-order Stokes waves generated in the flume, compared with Madsen's analytical formula [10]. The wavemaker generates a first-order component and a second-order bound wave, which is known to steepen the crests and broaden the troughs. The flume is 15 m long and 0.64 m deep, the wave height is 0.15 m and the period is 2 s. To prevent unwanted reflections from the end wall of the flume, a relaxation zone has been introduced at the end of the tank. The total number of particles is 42,236 and the time step is 0.001 s.

There is very good agreement between the analytical and numerical data. The correlation coefficient is $R = 0.988$ and the root mean square error is $E = 0.01$. We remark that a similar configuration was studied by [11] with an SPH solver. Interestingly, [11] obtained similar convergence results, but with an order $O(10^5)$ particles, as opposed to $O(10^4)$ needed by the NWF-MPS model.

4 CONCLUSIONS

We presented a novel Numerical Wave Flume based on a higher-order Moving Particle Semi-Implicit method (NEW-MPS). A peculiar aspect of the model is the addition of an artificial

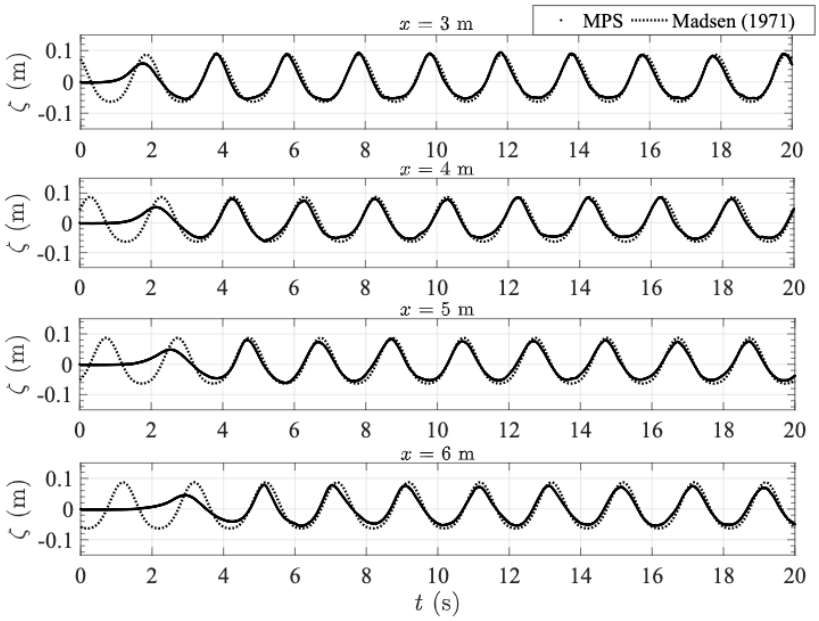

Figure 1: Comparison between MPS data and Madsen's analytical formula

viscosity term that prevents tensile instability and particle clustering, thus allowing to propagate waves even at large times. The model is able to reproduce design waves of engineering interest, such as second-order Stokes waves. Further examples on random sea states and wave-structure interactions will be presented at the Workshop.

REFERENCES

[1] Monaghan, J. 1994. *Simulating free surface flows with SPH. J. Comput. Phys. 110*, 399–406.

[2] Koshizuka, S., and Oka, Y. 1996. *Moving-particle semi-implicit method for fragmentation of incompressible fluid. Nucl. Sci. Eng. 123*, 421–434.

[3] Renzi, E., and Dias, F. 2021. *Application of a Moving Particle Semi-Implicit Numerical Wave Flume (MPS-NWF) to model design waves. Coast. Eng.*, 104066.

[4] Gotoh, H., and Khayyer, A. 2018. *On the state-of-the-art of particle methods for coastal and ocean engineering.* Coast. Eng. J. 60(1), 79–103.

[5] Renzi, E., and Dias, F. 2014. *Hydro-acoustic precursors of gravity waves generated by surface pressure disturbances localised in space and time. J. Fluid Mech. 754*, 250–262.

[6] Renzi, E. 2017. *Hydro-acoustic frequencies of the weakly compressible mild-slope equation. J. Fluid Mech. 812*, 5–25.

[7] Michele, S., and Renzi, E. 2020. *Effects of the sound speed vertical profile on the evolution of hydroacoustic waves. J. Fluid Mech. 883*, A28.

[8] Kondo, M., and Koshizuka, S. 2011. *Improvement of stability in moving particle semi-implicit method.* Int. J. Numer. Meth. Fluids 65(638–654).

[9] Koshizuka, S., Shibata, K., Kondo, M., and Matsunaga, T. 2018. *Moving Particle Semi-Implicit Method.* Academic Press, United Kingdom.

[10] Madsen, O. 1971. *On the generation of long waves. J. Geophys. Res. 76*, 8672—-8683.

[11] Altomare, C., Dominguez, J., Crespo, A., Gonzalez-Cao, J., Suzuki, T., Gomez-Gesteira, M., and Troch, P. 2017. *Long-crested wave generation and absorption for SPH-based DualSPHysics model. Coast. Eng. 127*, 37–54.

Trapped waves within the blocking frequency under compressed sea ice and two-dimensional current

Sunanda Saha[1*], Santu Das[2], Swaroop Nandan Bora[3]
[1]Department of Mathematics, School of Advanced Sciences, Vellore Institute of Technology, Vellore - 632014, India
[2]Mathematical and Computational Sciences, Physical Sciences Division, Institute of Advanced Study in Science and Technology, Guwahati - 781035, India
[3]Department of Mathematics, Indian Institute of Technology Guwahati, Guwahati - 781039, India
*Corresponding author: sunanda.saha@vit.ac.in

1. INTRODUCTION

The objective of the current work is to analyze blocking and trapping of flexural-gravity waves that propagate along the coupled water and floating structure surface. As the first step, we need to understand what these waves are and why they are required to be studied. Trapped waves are the waves with finite total energy which exist near the submerged structure and die out as they propagate away from the structure. On the other hand, the wave blocking is a phenomenon in which the rate of wave energy propagation vanishes and is mathematically expressed through linear water theory by the vanishing of the group velocity. The primary cause of such a phenomenon is an opposing current in the ocean which creates a hydrodynamic horizon and blocks the wave. A number of subsequent relevant studies which illustrate the impact of compression and ocean current on wave blocking are available in [1, 2, 3]. In the above-mentioned studies on flexural-gravity wave blocking accounted for the influence of compression but considered only unidirectional ocean currents. The work has been extended to two-dimensional uniform ocean current by [4] where they have also studied the trapped wave for a horizontal submerged circular cylinder. However, in their work, the trapped mode frequency spectrum inside the blocking frequency was not discussed in detail. In the present study , an attempt is made to extend the work of [4] to find the trapped wave mode inside the frequency band of blocking.

2. MATHEMATICAL FORMULATION AND SOLUTION FRAMEWORK

The domain for this physical problem is a homogeneous fluid bounded above by an ice cover and below by a flat and rigid bottom. The Cartesian coordinate framework is chosen so that the z-axis points vertically upward and the xy-plane is horizontal. Hence $z = -h$, $z = f < 0\,(x = 0)$ and $z = 0$, respectively, denote the mean position of the flat bottom, the axis of the cylinder, and the mean ice-covered surface, respectively. The region of the problem under consideration is $-\infty < x, y < \infty$, $-h < z < 0$ with an effect of two-dimensional ocean current acting along the xy-plane. Utilizing the linear water wave theory, the complex velocity potential satisfies the three-dimensional Laplace's equation and takes up the following form in the presence of ocean current

$$\Phi(x, y, z, t) = U_1 x + U_2 y + \phi(x, y, z, t), \tag{1}$$

where U_1 and U_2 are the components of the current along the x- and y-directions, respectively. The upper surface boundary condition is of Neumann type as described in [4]:

$$\left(D\partial_z^4 - Q\partial_z^2 + g + m_0\partial_t^2\right)\frac{\partial\phi}{\partial z} = \left(\partial_t + U_1\partial_x + U_2\partial_y\right)^2\phi \ \text{ on } \ z = 0, \tag{2}$$

with $D = Ed^3/\{12\rho(1-\nu^2)\}$; $Q = N/\rho$; $m_0 = \rho_p d/\rho$. The ice-cover parameters are E, ν, d, N and ρ_p, which, respectively, denote Young's modulus, Poisson's ratio, thickness, uniform in-plane compressive force and the density. Water density is denoted by ρ and the acceleration due to gravity by g.

The bottom boundary condition due to the flat and rigid bed is

$$\frac{\partial \phi}{\partial z} = 0, \quad \text{on} \quad z = -h. \tag{3}$$

The incident wave angle with the positive x- direction is denoted by α and the angular frequency by ω. The wavenumber of the plane progressive wave that is denoted by k satisfies the following dispersion relation:

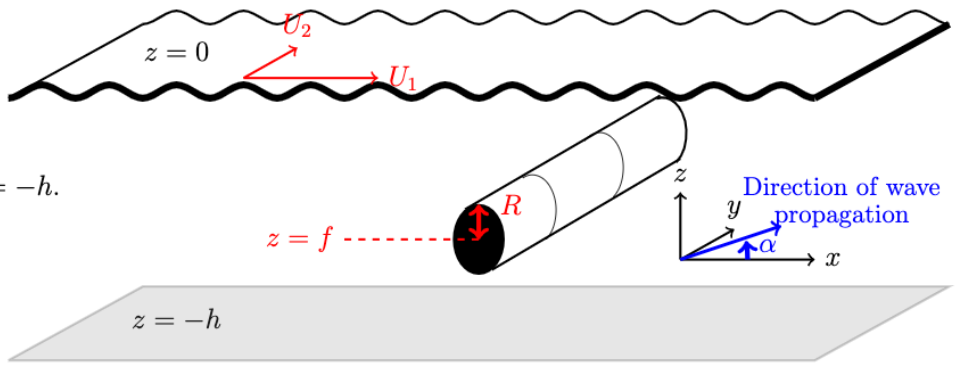

Figure 1: Schematic diagram of the problem (following [4].)

$$G(u) = F_+(u)e^{-2uh} - F_-(u) = 0, \tag{4}$$

where

$$F_\pm(u) = u\big(Du^4 - Qu^2 + g\big) \pm \Big[\omega - u(U_1\cos\alpha + U_2\sin\alpha)\Big]^2. \tag{5}$$

The multipoles with singularity at the axis of the cylinder satisfying the governing equation (1), and boundary conditions (2) and (3) can be written as

$$\phi_n = \phi_n^a(r,\theta)\cos(by - \omega t) + \phi_n^s(r,\theta)\sin(by - \omega t), \tag{6}$$

with

$$\phi_n^s(r,\theta) = K_n(br)\cos n\theta + \sum_{p=0}^{\infty} d_{pn} I_p(br)\cos p\theta, \tag{7}$$

$$\phi_n^a(r,\theta) = K_n(br)\sin n\theta + \sum_{m=0}^{\infty} c_{mn} I_m(br)\sin m\theta, \tag{8}$$

where $v = b\cosh u$; $I_n(br)$ and $K_n(br)$ are the n-th order modified Bessel functions of the first and second kind, respectively, with argument br; c_{mn} and d_{pn} have the following representations:
$c_{mn} = (-1)^m \epsilon_n \int_0^\infty \sinh mu \sinh nu \Big[A(v)e^{vf} + A(v)e^{-v(f+2h)} + e^{-2v(f+h)}\Big]\, du,$
$d_{pn} = (-1)^p \epsilon_n \int_0^\infty \cosh pu \cosh nu \Big[A(v)e^{vf} + A(v)e^{-v(f+2h)} + e^{-2v(f+h)}\Big]\, du,$ with $\epsilon_0 = 1, \epsilon_n = 2, n \geq 1$ and $A(v) = F_+(v)\frac{(-1)^n e^{vf} + e^{-v(f+2h)}}{G(v)}$. The linear combinations of all these symmetric and anti-symmetric multipoles when pass through the body boundary condition on the surface of the cylinder give rise to a system of homogeneous linear equations $A\mathbf{x} = 0$. For numerical computation of trapped modes, we need to truncate the order of the matrix and locate the frequency for which the determinant of the truncated matrix A vanishes.

Before we compute the trapping frequency in the blocking range, it is imperative to look into the integral that arises in c_{mn} and d_{pn}. It has singularity when $G(v) = 0$. Inside the blocking frequency band, except at the terminal frequencies (primary and secondary blocking) and the point of inflexion, there are three distinct positive real roots, i.e., k_1, k_2 and k_3, and each of them induces a singularity for the integral. Consequently, there are three choices of the incident wavenumber, namely k_j $(j = 1, 2, 3)$, and we term these waves as the first (for k_1), second (for k_2) and third (for k_3) choice. Therefore, the singular points for the j-th choice are given by

$$L_{ij} = \cosh^{-1}\left[\frac{k_i}{k_j \sin\alpha}\right] \quad \text{for} \quad i = 1, 2, 3,$$

and the corresponding integral can be suitably expressed as the sum of the principal value integrals which can be evaluated by employing the method used in [5]. We will restrict ourselves to first and third choice for evaluating the trapped frequencies.

3 NUMERICAL RESULTS

In this section, the results on trapping phenomena will be discussed in the blocking range when both the currents are acting in opposite direction. Other choices of the currents will be discussed during the presentation. The graphs are shown for the first and third choices of the incident wavenumber. The non-dimensionalized positions of the cylinder and the water depth are kept fixed at $f = -1.01$ and $h = 6$. The flexural rigidity of the floating ice and the compressive force acting on it are kept invariant as $D = 0.01$ and $Q = 1.5\sqrt{D}$.

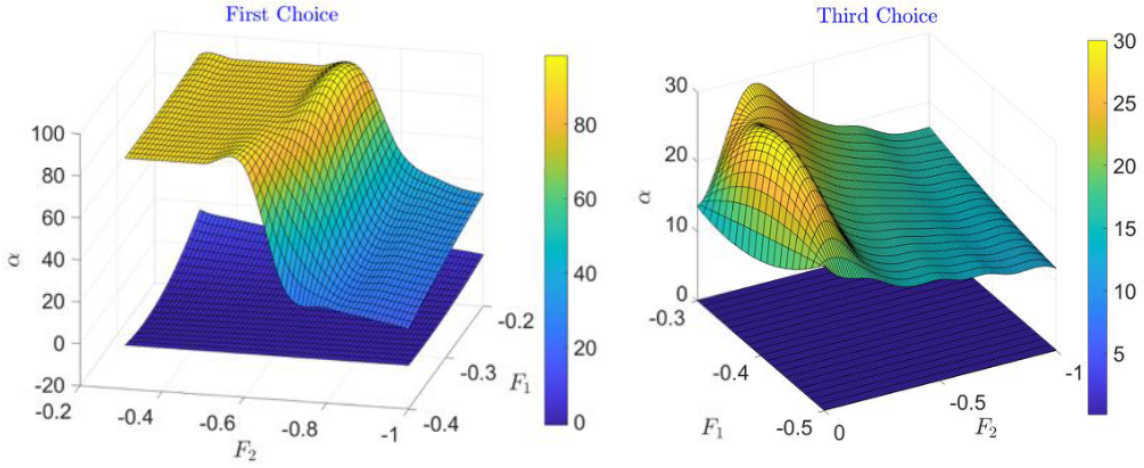

Figure 2: The surface plot of α_{min} and α_{max} for both the choices when the current varies.

The optimum range of α by varying both the opposite currents is shown with the help of surface plots (figure 2). Considering the first choice, the trapped mode exists for $\alpha \in (0, 20°)$ for $F_1 = -0.4$ and $F_2 = -1.0$ (left panel). As we reduce the magnitude of F_2, the range widens and reaches the full range, i.e., $\alpha \in (0, 90°)$. However, with a decrease in the magnitude of F_1, the lower limit of α increases and leads to a narrower α band. Hence, a lower magnitude of F_2 along with a higher magnitude of F_1 is the favourable choice for getting the maximum range of existence of the trapped modes at any value of α. While considering the third choice (right panel), the lower bound of α remains constant at $0°$ and the upper bound monotonically increases with a decrease in the magnitude of F_1. However, when the magnitude of F_1 decreases, then α_u starts bending and hence obtain maximal value for certain F_2.

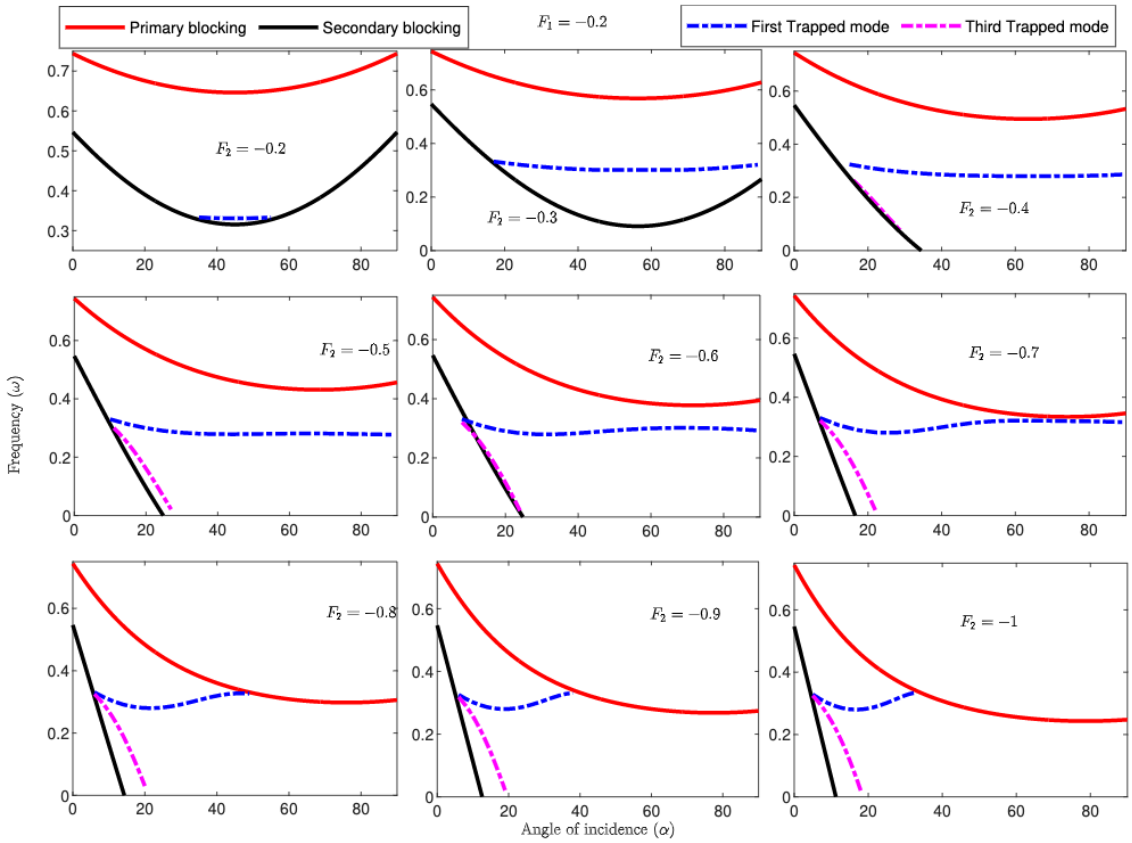

Figure 3: The range of trapped mode frequencies within the blocking range when F_2 varies.

Based on the discussion of the range of α in figure 2, the frequency pattern for trapped modes can be understood from figure 3. We fix the value of F_1 at -0.2 and vary F_2 from -1.0 to -0.2 to obtain the trapped modes frequencies. It can be clearly observed that when $F_2 = -1.0$, the trapped mode exists for both the choices of propagating modes confined within a specific range of incidence angle α. With a decrease in the magnitude of F_2, the trapped frequency for the third propagating mode overlaps with the secondary blocking frequency and dies out. However, the first trapped mode exists for a wider range of α, which also shrinks for $F_2 = -0.2$.

REFERENCES

[1] Das, S., Sahoo, T., and Meylan, M. 2018. Dynamics of flexural gravity waves: from sea ice to Hawking radiation and analogue gravity. Proc. R. Soc. A 474 (2209), 20170223.

[2] Das, S., Kar, P., Sahoo, T., and Meylan, M. 2018. Flexural-gravity wave motion in the presence of shear current: wave blocking and negative energy waves. Phys. Fluids 30 (10), 106606.

[3] Das, S., Sahoo, T., and Meylan, M. 2020. An investigation of the properties of flexural-gravity wave propagation in a coupled submerged and floating plate system. European Journal of Mechanics-B/Fluids 82, 123–134.

[4] Das, S., and Saha, S. 2021. A transit through the trapping and blocking of flexural-gravity wave: Impact of two-dimensional current and in-plane compression. Phys. Fluids 33(11), 116603.

[5] Hao, Z., and Wu, B. 2020. Three-dimensional Green-function method to predict the water wave radiation of a submerged body with ice cover. Appl. Ocean Res. 101, 102297.

37^{th} *International Workshop on Water Waves and Floating Bodies, Italy, April 10-13, 2022.*

Analysis of the pressure field in a breaking wave.

Y.-M. Scolan
ENSTA-Bretagne, IRDL UMR 6027 (France)
yves-marie.scolan@ensta-bretagne.fr

Highlights

- numerical simulation of breaking wave in a sloshing tank,
- analysis of the onset of critical jets,
- spatial/temporal of the pressure field and its differential properties: gradient, Hessian matrix.

1) Introduction

The present abstract is concerned with highly nonlinear breaking wave in a rectangular tank. This kinematics is obtained by forcing the motion of the tank with a simple cyclic horizontal motion. As a result a plunging breaker is simulated. The same result could be probably obtained by simulating a dam-breaking case, starting from an initial potential energy and setting hence the total amount of available energy. However the experience shows that we can inject much more energy in the fluid thanks to the forced motion of the tank. In addition to the interest of being experimentally reproducible, the forced movement also has the advantage of injecting a quantity of energy much greater than the maximum potential energy reached during the simulation. The cyclic horizontal motion appears to be the simplest way to isolate some critical sequences when studying the loads on the walls of the tank (see Karimi *et al*, 2016). It is not the objective of the present study to assess the global or local loads. More interestingly it is observed in the present simulated highly nonlinear wave, the onset of critical jets that can appear suddenly along the free surface in the close vicinity of the nascent overturning crest leading to a plunging breaker. Some of these observations have been already commented in previous papers (see Scolan and Etienne, 2021).

The pionnering works by Longuet-Higgins (1980) provide us with mathematical tools to better anticipate the onset of highly accelerated flow when dealing with nonlinear free surface flows. Here in order to comment the mechanism of appearance of critical jets, it is proposed to analyze more deeply the temporal/spatial variations of the pressure. The principle is as follows; it is clear that a zero pressure gradient close to a free surface where the pressure itself vanishes, induce locally a high pressure gradient and consequently a high Lagrangian acceleration. However it is crucial to identify the mechanism according which a vanishing pressure gradient, particularly a local maximum, can occur close to the free surface. In that purpose higher order derivatives of the pressure are calculated, in particular its Hessian matrix and its eigenvalues and eigenvectors.

Among the critical jets the flip-through phenomenon (see Cooker and Peregrine, 1990) is already well known. Here other configurations are described and new types of critical jet are commented.

2) Governing equations

Basically, the equations are posed in the Potential Theory. The numerical software solves the fully nonlinear free surface boundary conditions. A desingularized technique avoids the discretization of an integral equation. The conformal mapping of the interior of the tank makes it possible to reduce the number of unknowns to the positions of the markers at the free surface only (see Scolan, 2010). The velocity potential is transported by the free surface markers. In the fluid the complex potential reads

$$F(z,t) = \sum_{j=1}^{N} q_j(t) G(w, W_j(t)) \tag{1}$$

where the complex coordinate w is the image of the complex coordinate z in the physical plane through the mapping function $w = -\cos\frac{\pi z}{L}$, L being the length of the rectangular tank. The intensity of the source # j is q_j and $W_j = g(Z_j)$ is the complex coordinate of the source # j in the transformed plane w. G is the complex potential of this source plus its mirror image with respect to the axis $\Im(w) = 0$; hence G meets the impermeability condition on the walls. The complex potential F describes the fluid motion in a coordinate attached to the tank. When the tank is in horizontal forced motion, additional terms appear. The pressure follows from Bernoulli equation written here in its complex form

$$F_{,t} + \frac{1}{2}|F_{,z}|^2 + \frac{p}{\rho} + \gamma(z,t) = 0 \tag{2}$$

where γ accounts for the acceleration fields (gravity and horizontal tank motion). Euler equation relates the pressure gradient to the velocity $\vec{u}$ as

$$\vec{u}_{,t} + (\vec{u}\cdot\vec{\nabla})\vec{u} + \frac{\vec{\nabla}p}{\rho} = \vec{\gamma} \tag{3}$$

where $\vec{\gamma}$ accounts for the acceleration fields (gravity and horizontal tank motion). The sum of the first two terms gives the Lagrangian acceleration $\frac{d\vec{u}}{dt}$. Due to the zero pressure condition at the free surface, the gradient of the pressure $\vec{\nabla}p$ is always oriented in the normal direction to the free surface, pointing into the fluid. In the present study, we also analyze the variations of the Hessian matrix that reads

$$\mathbf{H} = \begin{pmatrix} p_{,x^2} & p_{,xy} \\ p_{,xy} & p_{,y^2} \end{pmatrix} \tag{4}$$

This is a symmetric matrix and by using the following notations

$$f = \rho|F_{,z^2}|^2, \qquad A = \rho\left(F_{,z^3}\overline{F}_{,z} + F_{,z^2t}\right) = R + iI \tag{5}$$

the coefficients of the Hessian matrix are

$$p_{,x^2} = -f - R, \qquad p_{,y^2} = -f + R, \qquad p_{,xy} = I \tag{6}$$

The expressions of the eigenvalues λ and the eigenvectors $\vec{v}$ of the matrix $\mathbf{H}(x,y,t)$ then reads

$$\lambda_1 = -f + |A|, \qquad \lambda_2 = -f - |A|, \tag{7}$$

$$\vec{v}_1 = \frac{1}{\sqrt{2|A|}}\begin{pmatrix} sg(I)\sqrt{|A|-R} \\ \sqrt{|A|+R} \end{pmatrix}, \qquad \vec{v}_2 = \frac{1}{\sqrt{2|A|}}\begin{pmatrix} sg(I)\sqrt{|A|+R} \\ -\sqrt{|A|-R} \end{pmatrix} \tag{8}$$

where $sg(I)$ denotes the sign of I. The Gaussian curvature Ω is the determinant of the matrix $\mathbf{H}$. This is the product of the eigenvalues, $\Omega = \lambda_1\lambda_2$. The inverse of each eigenvalue is also the curvature radius of the surface $p(x,y)$ along their corresponding principal directions defined by the eigenvectors. It is worth noting that one of the eigenvalues (denoted λ_2) is always negative meaning that the curvature of the surface $p(x,y)$ is "oriented down" along the direction of $\vec{v}_2$. λ_1 can change sign when $f = |A|$. As we are looking for zero of pressure gradient $p_{,x} = p_{,y} = 0$, we distinguish two cases. When both eigenvalues are negative, the Gaussian curvature is positive, indicating a local maximum. Otherwise, it is a saddle point. As we track the minimum of the pressure gradient over time and space, we shall seek the location where $||\vec{\nabla}p||$ is minimum or even vanishes. It is shown that this also occurs when $\vec{\nabla}p$ and $\vec{v}_1$ are parallel, leading to search for the change of sign of the following quantity

$$v = Ip_{,y} - (R + |A|)p_{,x} \tag{9}$$

2) Illustrative results

The locations where v changes of sign is illustrated with a black line in the following figure (left).

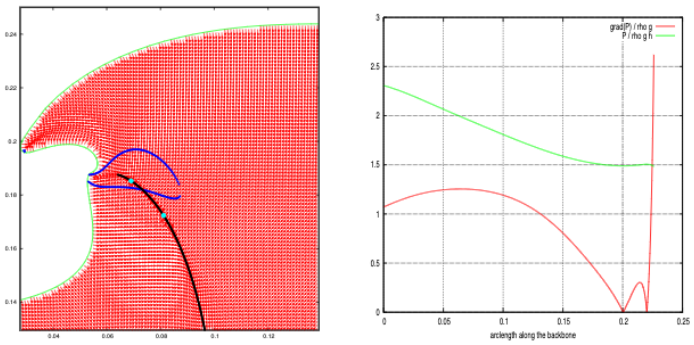

The vector field corresponds to the normalized pressure gradient. The blue line encloses the region of positive Gaussian curvature. The two light blue spots show the location of a saddle point and a local maximum of the pressure in the region where $\Omega > 0$. The black line $v = 0$ can be described with an arclength and in the present case, this line starts from the bottom. The right figure shows the spatial variation of $\frac{p}{\rho g h}$ and $\frac{||\vec{\nabla} p||}{\rho g}$ along the line $v = 0$. The pressure reaches a threshold $\frac{p}{\rho g h} \approx 1.5$ in the region $\Omega > 0$, then the pressure must vanish at the free surface, hence leading to a pressure gradient which can be greater than $\frac{||\vec{\nabla} p||}{\rho g} > 300$. This is the mechanism that makes appear and develop the critical jet.

The part of the free surface where high kinematics is expected is located between the left wall and the tip of the nascent overturning crest. When a plunging breaker fully develops, this region is oftenly called the barrel by the surfers. It is proven that the maximum acceleration and the maximum of velocity are observed in the barrel (see Yasuda *et al*, 1997). In this region several type of critical flows can appear. Before the barrel is well formed Peregrine (2003) shows that the flip-through appears to be the result of a competition between the run-up at the wall and the advancing crest front towards the wall. The free surface rather looks like a parabola whose curvature radius shrinks until the free surface flips leading to a small jet (see Cooker, 2009). At this instant the acceleration can reach very high values (more than ten thousand times the gravity). The shape of the free surface before this occurs is analyzed by Longuet-Higgins (2001). In particular he proposes to flatten the trough drawn by the free surface at the wall. As a consequence he observes a local growth that precedes the launch of a jet, the whole sequence is called the bazooka effect (see the fig. 6 in Longuet-Higgins, 2001). Actually this "bazooka" looks like a standard flip-through. In the present study the initial local growth is called a pre-bazooka effect. Indeed this local growth is the sign of appearance of a new type of jet as illustrated below

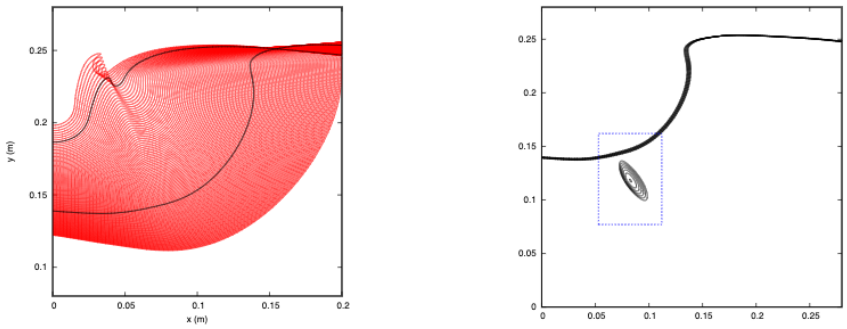

The left figure shows the successive free surface profiles for a case where a pre-bazooka appears. Two particular instants are emphasized with black lines. The first instant corresponds to the change of sign of the curvature radius along the free surface, hence announcing the local growth. Before this instant, it is observed that the Gaussian curvature Ω becomes positive at a single point

inside the fluid just below the location where the pre-bazooka will appear. Then this region of positive Gaussian curvature increases until hitting the free surface. There is a strong correlation between the change of sign of the curvature radius along the free surface and the change of sign of the Gaussian curvature as shown in Scolan and Etienne (2021). The reason is $\vec{v}_2$ is oriented normally to the free surface as $\vec{\nabla} p$. Here the local change of sign of Ω announces an event as a premonitory sign. Unfortunately this is not observed in Longuet-Higgins' computations. One reason could be that not enough kinetic energy is available. The second instant of interest corresponds to the maximum acceleration reached during this simulation. This occurs in the trough on the left of the nascent inverted crest. In the present case this maximum acceleration does not exceed 400 times the gravity. There is common feature of all overturning crests, the main one like the small one in a critical jet; the crest turns towards the region where the Lagrangian acceleration is maximum. It is also noticeable that the free surface as a parabolic profile at the wall. As a consequence a flip-through is likely to occur. In the present case the small inverted crest (similar to a "tuft of hair" on the head of the wave) breaks before the onset of the flip-through. A parametrical analysis in terms of the mean water depth h shows an inversion of chronology; the flip-through occurs before the breaking inverted crest.

The present analysis the pressure field allows to revisit some recent studies concerning the occurrence of wave breaking (see Barthelemy *et al*, 2018 among others). This proposed criterion is the ratio of the horizontal fluid velocity at the wave crest to the phase velocity. This is a ratio of kinematic quantities and it is found that there is a threshold above which the wave breaks. This threshold varies slightly depending on the type of wave and on the type of bathymetry. It is proposed here that there could also exist a dynamic criterion which would link the Lagrangian acceleration to the pressure gradient. Preliminary numerical tests consists of a dam breaking case that leads to a soliton that breaks (or not). The quantities $||\frac{d\vec{u}}{dt}||$ and $||\vec{\nabla} p||$ are calculated along the line where $v = 0$ which links the maximum free surface elevation to the bottom of the tank. A maximum of $\rho||\frac{d\vec{u}}{dt}||/||\vec{\nabla} p||$ exists along the line $v = 0$. This maximum has a threshold depending on whether or not the wave breaks.

3) References

• Longuet-Higgins, M.S. 1980, A Technique for Time-Dependent Free-Surface Flows. Proceedings of the Royal Society of London. Series A, Mathematical and Physical Sciences, **371**, 441-451.

• Cooker, M.J., Peregrine, D.H., 1990, A model of breaking wave impact pressures. Proc. 22nd Conf. Coastal Engineering, Holland ASCE, 1473-1486.

• Karimi M.R., L. Brosset, J.-M. Ghidaglia, M.L. Kaminski, 2016, Effect of ullage gas on sloshing, Part II: Local effects of gas-liquid density ratio. Eur. J. of Mech. B/Fluids, **57**, 82-100.

• Scolan, Y.-M., 2010, Some aspects of the flip-through phenomenon: A numerical study based on the desingularized technique J. Fluid Struc., **26**, Issue 6, 918-953.

• Scolan, Y.M., Etienne, S., 2021, Properties of the pressure field in highly nonlinear free surface flows with critical jet. J. Eng Math, 128, 4.

• Longuet-Higgins M. S. , 2001, Vertical jets from standing waves; the bazooka effect, IUTAM Symposium on Free Surface Flows, Kluwer Academic Publishers, 195-203.

• Yasuda T., Mutsuda H., Mizutani N. 1997, Kinematics of overturning solitary waves and their relations to breaker types Coastal Engineering, **29**, Issues 3-4, 317-346.

• Cooker, M.J., 2009, The flip-through of a plane inviscid jet with a free surface. Journal of Engineering Mathematics, **67**, (1-2), 137-152.

• Peregrine, D. H., 2003, Water-wave impact on walls, Annual Review of Fluid Mechanics Vol. 35, 23-43.

• Barthelemy, X., Banner, M., Peirson, W., Fedele, F., Allis, M., & Dias, F., 2018, On a unified breaking onset threshold for gravity waves in deep and intermediate depth water. J. Fluid Mech., 841, 463-488.

Impulsive impact of a body submerged in an open container

Y.A. Semenov[1] yuriy.a.semenov@gmail.com
Y.N. Savchenko[1] hydro.ua@gmail.com
G.Y. Savchenko[1] lenchik123@ukr.net

[1]Institute of Hydromechanics of the NAS of Ukraine, Kyiv, Ukraine

The concept of impulsive fluid/structure interaction widely used to study an initial stage of violent water impact flows, for which a strong couple between the nonlinear and unsteady effects may result in an extremely large hydrodynamic pressure and the force, respectively. Among the earliest work is that by Lagrange (1783) and Joukowskii (1884), in which the product of the density times the velocity potential is interpreted as the pressure impulse needed to suddenly impel a fluid from rest to its present velocity.

This concept has received much extension with application to aircrafts landing on water surface (von Karman, 1929), steep waves that suddenly hit coastal or marine structures (Cooker and Peregrine, 1995), impulsive motion of the submerged cylinder (Greenhow, 1987; Tyvand and Miloh, 1995) and impulsive sloshing in containers (Tyvand and Miloh, 2012), dam-break flows (Korobkin and Yilmaz, 2009), impact of blunt bodies onto a free surface (Howison, Ockendon and Wilson, 1991).

Impulsive impact of a body fully submerged into the half-space of the liquid was studied by (Semenov, Savchenko and Savchenko, 2021) using integral hodograph method. In the present study we extend the solution for the cases of containers or open channels of finite depth.

Boundary-value problem

A sketch of the physical domain is shown in figure 1(a). The body submerged below flat free surface is symmetric respect to Y-axis, therefore only half of the flow region is considered. Before the impact, $t = 0$, the body and the liquid are at rest. At time $t = 0^+$ the body is suddenly set into motion with acceleration a directed downwards such that, during infinitesimal time interval $\Delta t \to 0$, the speed of the body reaches the value $U = a\Delta t$. The problem of a rigid body moving in a fluid body is kinematically equivalent to the problem of a fluid body moving around a fixed rigid body with acceleration a of the bottom of the container or channel. We define a non-inertial Cartesian system of coordinates XY attached to the body at point A, and an inertial system of coordinates $X'Y'$ attached to the container. The body and the container are assumed to have an arbitrary shape, which can be defined by the slope of the boundary including the body and the container as a function of the arclength coordinate S, $\delta = \delta(S)$. The liquid is assumed to be ideal and incompressible, and the flow is irrotational. The gravity and surface tension effects are ignored.

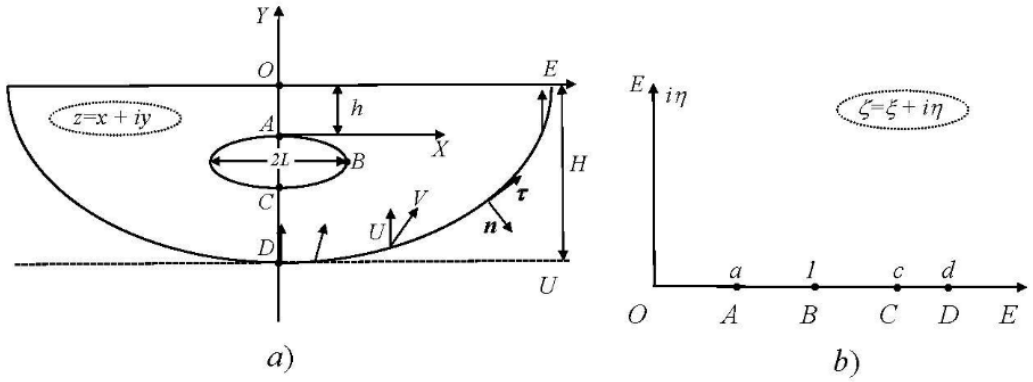

Figure 1. (a) The physical z-plane with the container and submerged body, (b) the parameter, or ζ–plane.

For two-dimensional inviscid, incompressible, irrotational flow we can introduce a complex potential $W(Z) = \Phi(x, y) + i\Psi(x, y)$ with $Z = X + iY$.

By integrating Bernoulli's equation

$$\frac{\partial \Phi}{\partial t}+\frac{p}{\rho}+\frac{|V|^2}{2}=\frac{p_a}{\rho}+\frac{U^2}{2}\cdot \tag{1}$$

over the infinitesimal time interval $\Delta t \to 0$ and taking into account that the integral of the third term tends to zero, one can obtain

$$P=\int_0^{\Delta t} p dt=-\rho\Phi, \tag{2}$$

where P is the impulsive pressure. Here, $|V|$ is the velocity magnitude, p and p_a are the hydrodynamic pressure and the pressure on the free surface, respectively.

The vertical impulse force F_y is obtained by integrating the impulse pressure over the body surface,

$$F_y=-2\rho\int_{S_A}^{S_C}\Phi(S)\cos(n,y)\,dS=\mathrm{mL^2U}, \tag{3}$$

where S is the arc length coordinate along the body surface; S_A and S_C are the arcthlength coordinates of points A and C; m is the coefficient of the added mass. The multiplier "2" appears to account force acting on the whole body. Since we consider the body symmetric respect to y-axis, the horizontal impulse force equals zero. As it follows from equation (3), the coefficient of the added mass in the coordinate system XY is defined as

$$m=-2\rho\int_{S_A}^{S_C}\phi(s)\cos(n,y)\,ds. \tag{4}$$

In the paper Semenov, Savchenko and Savchenko (2021) it was shown that the added mass coefficients in the coordinate systems $X'Y'$ and XY are related as follows

$$m'=m-\rho A^* U, \tag{5}$$

where A^* is the cross-sectional area of the body.
The problem is to determine the velocity potential $\phi(x,y)$ immediately after the impact.

Conformal mapping

We introduce the complex potential $w(z)=\phi(x,y)+i\psi(x,y)$, where $\psi(x,y)$ is the stream function. To find the complex potential $w(z)$ directly is a challenge; therefore, we introduce an auxiliary parameter plane, or ζ -plane. We formulate boundary-value problems for the complex velocity function, dw/dz, and for the derivative of the complex potential, $dw/d\zeta$, both defined in the ζ -plane. Then the derivative of the mapping function is obtained as $dz/d\zeta = (dw/dz)/(dw/d\zeta)$, and its integration provides the mapping function $z=z(\zeta)$ relating the coordinates in the parameter and physical planes.

The boundary value problem for the complex velocity, dw/dz, is identical to the case of infinite depth of the liquid studied Semenov, Savchenko and Savchenko (2021). Therefore, we have

$$\frac{dw}{dz}=v_\infty\left(\frac{\zeta-a}{\zeta+a}\right)^{\frac{1}{2}}\left(\frac{\zeta-c}{\zeta+c}\right)^{\frac{1}{2}}exp\left[\frac{1}{\pi}\int_a^\infty\frac{d\beta_b}{d\xi}ln\left(\frac{\zeta-\xi}{\zeta+\xi}\right)d\xi-\frac{i}{\pi}\int_0^\infty\frac{dln\,v}{d\eta}ln\left(\frac{\zeta-i\eta}{\zeta+i\eta}\right)d\eta-i\frac{\pi}{2}\right], \tag{5}$$

where $\beta_b(\xi)=\delta(\xi)-\gamma(\xi)$ is the slope of the flow boundary as the function of the coordinate ξ, and $\gamma(\xi)$ is the angle between the velocity vector and the flow boundary. The body is considered to be fixed; therefore, the angle $\gamma(\xi)=\pi$ at interval $a\le\xi\le c$ corresponding to the body, and $\gamma(\xi)$ has to be determined at the interval $d\le\xi<\infty$ corresponding to the bottom surface. At the interval $c\le\xi\le d$, $\delta(\xi)=\frac{3\pi}{2}$ and $\gamma(\xi)=\pi$, i.e. $d\beta_b/d\xi=0$. The function $v(\eta)$ is the modulus of the velocity on the free surface just after the impact.

Now we formulate boundary value problem for the derivative of the complex potential, $dw/d\zeta$.

$$\vartheta(\zeta) = arg\left(\frac{dw}{d\zeta}\right) = arg\left(\frac{dw}{ds}\frac{ds}{d\zeta}\right) = arg\left(\frac{dw}{ds}\right) + \begin{cases} 0, & \zeta = \xi, \\ -\frac{\pi}{2}, & \zeta = i\eta, \end{cases} = \begin{cases} \pi, & 0 \le \xi \le d,\ \eta = 0, \\ \gamma(\xi), & d \le \xi < \infty,\ \eta = 0, \\ \frac{\pi}{2}, & 0 \le \eta < \infty,\ \xi = 0. \end{cases} + \begin{cases} 0, & \zeta = \xi, \\ -\frac{\pi}{2}, & \zeta = i\eta, \end{cases} \tag{6}$$

Equation (6) determines the argument of the complex function $dw/d\zeta$ on the whole fluid boundary, or on the real and imaginary axes of the ζ-plane. The integral formula (Semenov & Yoon (2009)),

$$F(\zeta) = K\exp\left[\frac{1}{\pi}\int_{\infty}^{0}\frac{\partial\vartheta}{\partial\xi}\ln\left(\varsigma^2-\xi^2\right)d\xi + \frac{1}{\pi}\int_{0}^{\infty}\frac{\partial\vartheta}{\partial\eta}\ln\left(\varsigma^2+\eta^2\right)d\eta + i\vartheta_{\infty}\right], \tag{7}$$

determines the complex function which satisfies boundary condition (6). Here, K is a real factor, $\vartheta(\zeta) = \arg[F(\zeta)]$, $0 < \xi < \infty, \eta = 0$ and $0 < \eta < \infty, \xi = 0$, $\vartheta_{\infty} = \vartheta(\zeta)_{|\zeta|\to\infty}$. We evaluate the integrals over each step change of the function $\vartheta(\zeta)$, and finally obtain the expression for the derivative of the complex potential in the ζ -plane as

$$\frac{dw}{d\zeta} = \frac{K}{\sqrt{d^2-\zeta^2}}exp\left[-\frac{1}{\pi}\int_0^{\infty}\frac{d\gamma}{d\xi}ln(\xi^2-\zeta^2)d\xi + i\theta_{\infty}\right]. \tag{8}$$

Free surface boundary conditions

The velocity generated by the impact is perpendicular to the free surface, or it is directed in y-direction. Accordingly, the argument of the complex velocity (5) is

$$arg\left(\frac{dw}{dz}\Big|_{\zeta=i\eta}\right) = -\frac{\pi}{2}, \quad 0 \le \eta \le \infty. \tag{9}$$

Taking the argument of the complex velocity from (5), we obtain the following integral equation respect to the function $\frac{\mathrm{d}\ln v}{d\eta}$

$$\frac{1}{\pi}\int_0^{\infty}\frac{dln\,v}{d\eta'}ln\left|\frac{\eta'-\eta}{\eta'+\eta}\right|d\eta' + tan^{-1}\frac{\eta}{a} + tan^{-1}\frac{\eta}{c} + \frac{1}{\pi}\int_a^{\infty}\frac{d\beta_b}{d\xi}2tan^{-1}\frac{\eta}{\xi}d\xi = 0, \tag{10}$$

Equation (10) is the Fredholm integral equation of the first kind with the logarithmic kernel. The solution takes the form (Semenov, Savchenko and Savchenko, 2021).

$$v(\eta) = \sqrt{\eta^2+a^2}\sqrt{\eta^2+c^2}\exp\left(\frac{1}{\pi}\int_a^{\infty}\frac{\mathrm{d}\beta_b}{d\xi}\ln(\eta^2+\xi^2)d\xi\right). \tag{11}$$

The parameters a, c and K are determined using the depth of submergence h, length of the low side BC and upper side AB of the plate.

Kinematic boundary condition on the solid surfaces

By integrating the derivative of the mapping function along the real axis of the parameter plane, we can determine the spatial coordinate along the body as a function of the parameter variable

$$s_b(\xi) = \int_0^{\xi}\left|\frac{dz}{d\zeta}\right|_{\zeta=\xi'}d\xi' \tag{12}$$

Since the function $\beta_b(s) = \delta(s) - \gamma(s)$ is known along the body and bottom surfaces, the function $\beta_b = \beta_b(\xi)$ is determined from the following integro-differential equation:

$$\frac{d\beta_b}{d\xi} = \frac{d\beta_b}{ds}\frac{ds_b}{d\xi}. \tag{13}$$

The angle $\gamma(s)$ along the bottom surface is determined from the condition

$$\beta\left|\frac{dw}{dz}\right|_{\zeta=\xi}\sin\gamma = 1, \quad d \le \xi < \infty. \tag{14}$$

Results

The added mass coefficients m' according to definition (5) are shown the in the Table for the flat plate submerged in the open channel

h/L	0.2	0.3	0.5	1	2	3	4	4.5	4.75
(H-h)/L	4.8	4.7	4.5	4	3	2	1	0.5	0.25
m'	2.162	2.302	2.514	2.828	3.009	3.119	3.386	4.374	4.706

Table 1. Added mass coefficient for the depth of the channel H/L=5.

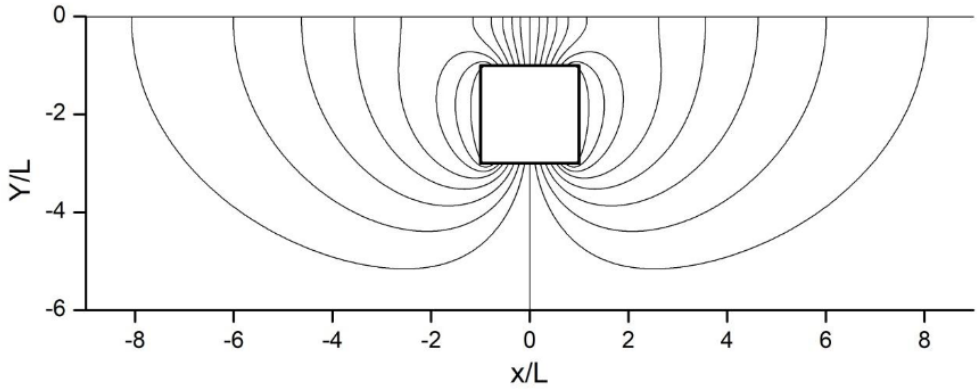

Figure 1. Streamline patterns for the impulsive motion of the square 2L× 2L in the coordinate system attached to the channel bottom.

References

Cooker, M.J., Peregrine, D.H. (1995) Pressure-impulse theory for liquid impact problems, J. Fluid Mech. 297, 193-214.

Greenhow, M. and Yanbao, L. (1987) Added masses for circular cylinders near or penetrating fluid boundaries-review, extension and application to water-entry, -exit and slamming. *Ocean Engineering*, 14 (4). pp. 325 - 348.

Havelock, T., H. (1949) The wave resistance of a cylinder started from rest. Q. J. Mech. Appl. Maths, 2, 325-334.

Howison, S., Ockendon, J., Wilson, S. (1991) Incompressible water-entry problems at small deadrise angles, Journal of Fluid Mechanics 222 (1), 215–230.

Joukowskii, N.E. 1884 On impact of two spheres, one of which floats in liquid. *Mat. Otd. Novorossiiskogo Obshchestva Estestvoispytatelej* 5, 43–48.

von Karman, T. (1929) The impact of seaplane oats during landing. Washington, DC:NACA 1929; Tech. Note 321.

Korobkin, A., Yilmaz, O. (2009) The initial stage of dam-break flow. J Eng Math 63, 293–308.

Lagrange, J.-L. 1783 Memoire sur la theorie du mouvement des fluides. *Nouv. Mem. Acad. Sci. Berlin* 12, 151–188.

Joukowskii, N.E. 1884 On impact of two spheres, one of which floats in liquid. *Mat. Otd. Novorossiiskogo Obshchestva Estestvoispytatelej* 5, 43–48.

Semenov, Y.A., Savchenko, Y.N. and Savchenko, G.Y. 2021 Impulsive impact of a submerged body. J. Fluid Mech. *vol.* 919, R4.

Tyvand, P. A.; Miloh, T. (1995) Free-surface flow due to impulsive motion of a submerged circular cylinder. *J. Fluid Mech. 286,* 67–101.

Tyvand, P.A. and Miloh, T. (2012) Incompressible impulsive sloshing J. Fluid Mech. 708, pp. 279_302.

Steady-state motion of a load on an ice cover with linearly variable thickness in a channel

Konstantin Shishmarev[1,3], Kristina Zavyalova[1] and Tatyana Khabakhpasheva[2]
[1]Department of differential equations, Altai State University, Barnaul, Russia
[2]Lavrentyev Institute of Hydrodynamics SB RAS, Novosibirsk, Russia
[3]E-mail: shishmarev.k@mail.ru

1 INTRODUCTION AND FORMULATION OF THE PROBLEM

The main part of the flexural-gravity wave research was carried out for ice covers of infinite extent. However, majority of the ice tanks, where scientific and technical experiments with ice cover are conducted, have finite dimensions and rectangular cross-sections. For this reason, studying the features of waves in channels and how they differ from waves in unbounded sheets is highly important. Under natural conditions, the ice cover is not homogeneous. Due to different reasons its thickness, density and stiffness are not constant. This paper considers the case of an ice cover whose thickness varies linearly, and ice density and stiffness are assumed to be constant. Similar problem for an ice plate with constant thickness was studied in [1], [2].

The response of a viscoelastic ice cover to a load moving along a frozen channel is considered. The channel is of rectangular section with a finite depth H ($-H < z < 0$) and a finite width $2b$ ($-b < y < b$), the channel is of infinite extent in the x direction. Here $Oxyz$ is a Cartesian coordinate system. The problem is studied within the linear theory of hydroelasticity (see, e.g., [3]). Liquid in the channel is inviscid, incompressible and covered with ice. The ice cover is modeled by a thin viscoelastic plate with given constant density ρ_i and rigidity $D(y)$, where $D(y) = Eh_i^3(y)/[12(1-\mu^2)]$, E is the Young's modulus for ice, μ is the Poisson's ratio for ice and $h_i(y)$ is variable thickness of the ice cover. A Kelvin–Voigt model of viscoelastic ice is used in this study. The constitutive equation of this model is $\sigma = E(\epsilon + \tau\partial\epsilon/\partial t)$, where σ is the stress, ϵ is the strain, τ is the so-called retardation time and t is the time. Ice oscillations caused by a load moving along a center line of the channel with constant speed U. The load is modeled by a localized smooth pressure distribution. Flow beneath the plate caused by ice deflections is potential.

The ice deflection $w(x, y, t)$ satisfies the equation of a thin viscoelastic plate

$$M(y)\frac{\partial^2 w}{\partial t^2} + \left(1 + \tau\frac{\partial}{\partial t}\right) Lw = p(x, y, 0, t) + P(x, y, t) \quad (-\infty < x < \infty, -b < y < b, z = 0), \quad (1)$$

where L is a differential operator,

$$L = D(y)\Delta^2 + 2D_y\left(\frac{\partial^3}{\partial y^3} + \frac{\partial^3}{\partial x^2\partial y}\right) + D_{yy}\left(\frac{\partial^2}{\partial y^2} + \mu\frac{\partial^2}{\partial x^2}\right),$$

$\Delta^2 = \partial^4/\partial x^4 + 2\partial^4/\partial x^2\partial y^2 + \partial^4/\partial y^4$, $M(y) = \rho_i h_i(y)$ is the mass of the ice plate per unit area, $P(x, y, t)$ is the external pressure and $p(x, y, 0, t)$ is a liquid pressure at the ice/liquid interface. The external pressure $P(x, y, t)$ moves along the central line of the channel with constant magnitude P_0 and is described by

$$P(x, y, t) = -P_0 P_1\left((x - Ut)/b\right) P_2\left(y/b\right) \quad (-\infty < x < \infty,\ -b < y < b), \quad (2)$$

$$P_1(\widetilde{x}) = \big(\cos(\pi c_1\widetilde{x}) + 1\big)/2 \ \ (c_1|\widetilde{x}| < 1), \quad P_1(\widetilde{x}) = 0 \ \ (c_1|\widetilde{x}| \geq 1), \quad \widetilde{x} = (x - Ut)/b,$$

$$P_2(\widetilde{y}) = \big(\cos(\pi c_2 \widetilde{y}) + 1\big)/2 \;\; (c_2|\widetilde{y}| < 1), \quad P_2(\widetilde{y}) = 0 \;\; (c_2|\widetilde{y}| \geq 1), \qquad \widetilde{y} = y/b,$$

where c_1 and c_2 are non-dimensional parameters of the external load characterizing the size of the pressure area. The hydrodynamic pressure $p(x, y, 0, t)$ at the ice-liquid interface is given by the linearised Bernoulli equation,

$$p(x, y, 0, t) = -\rho_\ell \varphi_t - \rho_\ell g w \quad (-\infty < x < \infty, \; -b < y < b), \tag{3}$$

where g is the gravitational acceleration, ρ_ℓ is the density of the liquid and $\varphi(x, y, z, t)$ is the velocity potential of the flow beneath the ice cover. The velocity potential $\varphi(x, y, z, t)$ satisfies Laplace's equation in the flow region and the boundary conditions

$$\varphi_y = 0 \;\; (y = \pm b), \quad \varphi_z = 0 \;\; (z = -H), \quad \varphi_z = w_t \;\; (z = 0). \tag{4}$$

The ice cover is frozen to the walls, which is modeled by the clamped conditions

$$w = 0, \quad w_y = 0 \qquad (-\infty < x < \infty, \;\; y = \pm b). \tag{5}$$

The term with $\tau\partial/\partial t$ in the equation of viscoelastic plate (1) describes the damping of ice plate oscillations, so they decay far away from the moving load, where $|(x - Ut)| \to \infty$.

One case of linear change in the ice thickness is considered: the ice thickness varies symmetrically across the channel, being the smallest at the center of the channel and the largest at the channel walls. The main parameters of the thickness are its average h_*, minimum h_0 and maximum h_1 values. Then $h_i(y)$ can be written in the form:

$$h_i(y) = h_0(1 + \alpha_1 |y/b|), \quad \alpha_1 = (h_1 - h_0)/h_0, \quad h_i(0) = h_0, \;\; h_i(\pm b) = h_1. \tag{6}$$

The formulated problem is solved in non-dimensional variables denoted by tilde. The half-width of the channel b is taken as the length scale, the ratio b/U as the time scale, and the pressure magnitude P_0 as the pressure scale. The non-dimensional depth of the channel H/b is denoted by h. The moving coordinate system $(\widetilde{x}, \widetilde{y}, \widetilde{z})$ with the origin at the centre of the load is introduce by

$$\widetilde{y} = y/b, \quad \widetilde{x} = (x - Ut)/b, \quad \widetilde{z} = z/b, \quad \widetilde{t} = Ut/b.$$

We are concerned with a steady-state solution in the moving coordinate system,

$$w(x, y, t) = w(\widetilde{x}L + Ut, L\widetilde{y}, t) = w_{sc} \, \widetilde{w}(\widetilde{x}, \widetilde{y}),$$

$$\varphi(x, y, t) = \varphi(\widetilde{x}L + Ut, L\widetilde{y}, t) = \varphi_{sc} \, \widetilde{\varphi}(\widetilde{x}, \widetilde{y}, \widetilde{z}),$$

where w_{sc} and φ_{sc} are the scales of the ice deflection and the velocity potential correspondingly. The scales are chosen as $w_{sc} = P_0/(\rho_\ell g)$ and $\varphi_{sc} = (UP_0)/(\rho_\ell g)$. The scale h_{sc} of the ice thickness, $\widetilde{h}_i(\widetilde{y}) = h_i(y)/h_{sc}$, is equal to h_0.

In the non-dimensional variables the problem reads (tildes are omitted further)

$$mh\mathrm{Fr}^2 h_i w_{xx} + \beta\Big(1 - \varepsilon\frac{\partial}{\partial x}\Big)\left[h_i^3\nabla^4 w + 6h_i^2 h_{i,y}(w_{yyy} + w_{xxy}) + 6h_i h_{i,y}^2(w_{yy} + \mu w_{xx})\right] + w = \\ = h\mathrm{Fr}^2\varphi_x - P_1(x)P_2(y) \quad (-\infty < x < \infty, \quad -1 < y < 1, \quad z = 0), \tag{7}$$

$$\nabla^2\varphi = 0 \qquad (-\infty < x < \infty, \;\; -1 < y < 1, \;\; -h < z < 0), \tag{8}$$

$$\varphi_z = -w_x \quad (z = 0), \qquad \varphi_y = 0 \quad (y = \pm 1), \qquad \varphi_z = 0 \quad (z = -h), \tag{9}$$

$$w = 0, \quad w_y = 0 \qquad (y = \pm 1), \qquad w, \varphi \to 0 \qquad (|x| \to \infty). \tag{10}$$

Here $\beta = D_*/(\rho_l g b^4)$, $D_* = E h_{sc}^3/[12(1-\mu^2)]$, $\varepsilon = (\tau U)/b$, $m = (\rho_i h_{sc})/(\rho_\ell b)$ and $\mathrm{Fr} = U/\sqrt{gH}$ is the Froude number.

The solution of the problem (7) – (10) depends on seven non-dimensional parameters h, m, β, ε, Fr, c_1, c_2 and on the non-dimensional ice thickness $h_i(y)$. These parameters describe the aspect ratio of channel, characteristics of ice and of the applied load. We shall determine the deflection w and strain distribution in the ice cover for given values of these parameters.

METHOD OF THE SOLUTION AND DISCUSSION

The coupled problem (7) – (10) is solved with the help of the Fourier transform in the x direction. The plate equation (7) provides

$$\beta(1-i\xi\varepsilon)\left[h_i^3(w^F_{yyyy} - 2\xi^2 w^F_{yy} + \xi^4 w^F) + 6h_i^2 h_{i,y}(w^F_{yyy} - \xi^2 w^F_y) + 6h_i h_{i,y}^2(w^F_{yy} - \mu\xi^2 w^F)\right] + \\ +(1 - mh\mathrm{Fr}^2\xi^2 h_i)w^F = i\xi h\mathrm{Fr}^2\varphi^F - P^F(\xi, y), \quad (11)$$

where

$$w^F(\xi, y) = \frac{1}{\sqrt{2\pi}}\int\limits_{-\infty}^{\infty} w(x,y)e^{-i\xi x}dx, \qquad w(x,y) = \frac{1}{\sqrt{2\pi}}\int\limits_{-\infty}^{\infty} w^F(\xi,y)e^{i\xi x}dx. \qquad (12)$$

The Fourier transform is also applied to the rest of the equations in (7) – (10). The solution for the Fourier image of the ice deflections $w^F(\xi, y)$ is sought in the form of an infinite series of normal vibration modes of an elastic beam taking into account the variable thickness of ice. In the linear case, these modes are described by Bessel functions (see, i.e., [4]) and are orthogonal with a weight. After determining the modes, the principal coordinates in the series for the Fourier image of ice deflections are determined. These principal coordinates depend on the Fourier transform parameter ξ and will be complex-valued due to the coefficients in the equation (11). The Fourier image of the flow velocity potential, which is appeared in (11), is determined by the method of separation of variables from the corresponding boundary-value problem taking into account the kinematic condition. In the end, the dimensionless ice deflections $w(x, y)$ are defined as the inverse Fourier transform applied to $w^F(\xi, x)$ (second equation in (12)). Number of the mods is reduced to a finite number $Nmod$. The limits of integration in the inverse Fourier transform are limited and the resulting integrals are calculated numerically for each mode. The convergence of the numerical solution is checked by varying the number of modes and the integration parameters. For a plate of constant thickness, the solution method is the same as the method used in [1].

Calculations of the ice response were carried out for parameters of the problem corresponding to the experimental ice tank at the Sholem Aleichem Amur State University in Birobidzhan (see [5]): $H = 1$ m, $2b = 3$ m, ice thickness in the tank is chosen to be equal to 0.0035 m. The parameters of ice and liquid in the calculations were: $\rho_i = 917$ kg/m^3, $\rho_\ell = 1024$ kg/m^3, $\mu = 0.3$, $E = 4.2 \cdot 10^9$ Pa, $\tau = 0.1$ s. Minimum and maximum values of the ice thickness and speed of the load U change in the calculations. The average thickness h_* in all calculations did not change and is equal to 0.0035 m.

The shape of ice deflections significantly depends on the speed of the load. It is known that there is an infinite number of dispersion relations in a channel and, accordingly, an infinite number of hydroelastic waves possibly propagating along a channel. A hydroelastic wave will propagate from the moving load with its speed if a phase speed equal to the load speed is existed. Long waves propagate behind, and short ones in the front of the load. However, a change in the ice thickness leads to a change in the characteristics of hydroelastic waves and,

therefore, the combination of waves propagating from the load can be different. Two minimum phase speeds for the considered channel are shown in Figure 1a. The solid lines show the results for a plate with constant thickness $h_i = 0.0035$ m, the dashed lines show the results for the plate with linear thickness for $h_0 = 0.002$ m, and the dotted lines show the results for the plate with linear thickness for $h_0 = 0.001$ m. For example, at a load speed $U = 2$ m/s, the first wave (for the first minimum phase speed) always propagates from the load, but the presence of the second wave depends on the change in the ice thickness. In the presented case, such a wave exists only for $h_0 = 0.001$ m.

Dimensionless ice deflections along the center line of the channel are shown in Figure 1b. The solid thick line shows the ice deflections for a plate with constant thickness $h_* = 0.0035$ m, the thin solid line – for a plate with variable thickness $h_0 = 0.002$ m and the dotted line – for $h_0 = 0.001$ m. Waves in front of the load are not observed due to the strong damping effect. Amplitude of the waves behind the load increases together with an increase in the change in the ice thickness. It is seen that the length of the observed waves propagating behind the load increases and the effect of damping decreases.

The main focus of the study is on the effect of the non-uniform ice thickness on the ice deflections and strain distribution. More detailed numerical results will be presented at the Workshop.

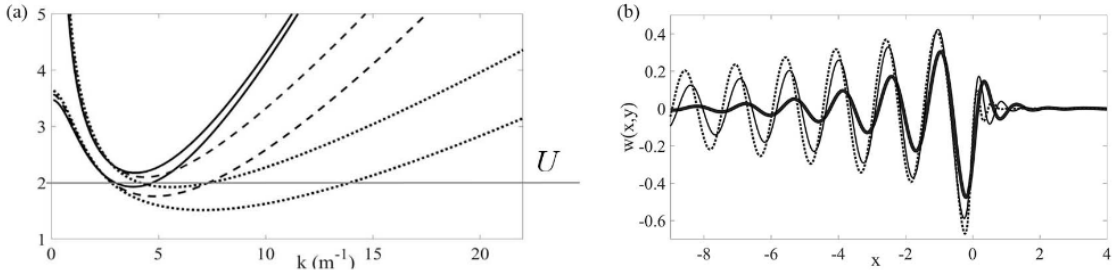

Figure 1: Phase speeds of periodic hydroelastic waves propagating in the channel **(a)**. The ice deflections along the center line of the channel for $U = 2$ m/s **(b)**.

Acknowledgment
The study was funded by RFBR and TUBITAK according to the research project 20-58-46009 "Loads on engineering structures in sea ice".

REFERENCES

1. Shishmarev K.A.; Khabakhpasheva T.I.; Korobkin A.A. The response of ice cover to a load moving along a frozen channel. *Appl. Ocean Res.* **2016**, *59*, 313–326.

2. Batyaev, E.A.; Khabakhpasheva, T.I. Hydroelastic waves in a channel covered with a free ice sheet. *Fluid Dyn. 2015* **50(6)**, *775–788.*

3. Squire, V.A.; Hosking, R.; Kerr, A.; Langhorne, P.J. *Moving loads on ice plates*; Dordrecht: Kluwer, 1996.

4. Taha M.H.; Abohadima S. Mathematical model for vibrations of non-uniform flexural beams. *Enging Mech.* **2008**, *15(1)*, 3–11.

5. Pogorelova, A.V.; Zemlyak, V.L.; Kozin, V.M. Moving of a submarine under an ice cover in fluid of finite depth. *J. Hydrodyn.* **2019**, *31(3)*, 562–569.

A very simple park interaction factor

Charitini Stavropoulou and Malin Göteman

Department of Electrical Engineering, Uppsala University, Uppsala, Sweden
E-mail address of the presenting author: malin.goteman@angstrom.uu.se

Highlights An approximate q-factor is derived, and compared to the exact q-factor, computed by multiple scattering theory. The simple q-factor can be used to get a quick estimate of the park interaction in point-absorber wave energy parks, without carrying out any hydrodynamic computation for the park. The approximate method is evaluated as function of wave parameters and number of interacting devices.

1 Introduction

There is a vast literature on the wave-structure interaction and energy absorption in wave energy parks. Various analytical and numerical methods have been developed to solve the wave field of scattered and radiated waves within arrays of floating bodies, to analyse aspects such as optimal configurations, annual energy absorption, or power fluctuations [1–5]. The most common approach when studying large parks is to solve the fluid-structure interaction within the assumptions of linear potential flow theory, but extensions to higher non-linear interactions has also been developed. In many applications, such as economic or reliability optimization of large wave energy systems, thousands of iterations are needed to reach convergence [6]. In such situations, it is not feasible to carry out detailed analysis of the hydrodynamic interaction within the park during each iteration.

The q-factor, defined as the ratio between the total energy and the energy absorbed by the N WECs in isolation, is often used to evaluate the interaction between the devices. The simplest approach is assuming $q = 1$, i.e., to simply neglect all interactions between the wave energy converters (WECs) and assume that the total energy absorption is $P_{\text{tot}} = NP_1$, where N is the number of WECs in the park, and P_1 is the average energy absorption of a single isolated WEC in that sea state. This is often an overestimation of the park performance, as the interaction within wave energy arrays is typically destructive, at least when averaged over different sea states and wave directions, which is the realistic approach.

Here, another approach is presented. A very simple, approximate park interaction q-factor is derived. Using only knowledge of the energy absorption of a single WECs, as well as the number of WECs in the park and the size of the park, it can be used to estimate the total energy absorption of the park (the array layout is not required as an input). As compared to the simplest assumption of neglecting interaction, this approach typically gives an underestimation for the energy production, as it only includes the destructive interactions between WECs, and not the positive. It can thus be used as a lower bound for the performance. The approximate q-factor is compared to the exact q-factor, computed using multiple scattering theory. For a range of park configurations, with different number of WECs and different array layouts, the approximate method produces similar results.

Acknowledgedly, the approximate q-factor does not provide any fundamentally new insights into the fluid dynamics in wave energy parks. For this, accurate analytical, numerical, and/or experimental methods are needed. The method merely provides a very simple tool to estimate the interaction and performance, and can be of great use in many applications where the accurate methods are not feasible.

2 Theory

Consider a wave energy park of N point-absorbing wave energy converters (WECs), each consisting of a cylindrical surface buoy of radius $R = 3$ m connected to a linear generator at the sea bed. From the buoy oscillation driven by the waves, the WEC will absorb energy P_1, which will depend on the sea state parameters, the WEC dimensions and mass, and power take-off (PTO) settings. In terms of the capture width ratio (CWR) τ, the energy absorption is written $P_1 = \tau DJ$, where $J = \rho g^2/(64\pi)H_s^2T_e$ is the energy flux defined in terms of the significant wave height H_s and energy period T_e of the waves.

Due to the presence and motion of the WECs, the total wave field in the park will be a superposition of scattered and radiated waves of all buoys. To determine the total energy absorption, P_{tot}, the full hydrodynamic interaction between all bodies must be determined, which is a challenging problem for large parks.

The park interaction factor, or q-factor, is defined as

$$q = \frac{P_{\text{tot}}}{NP_1}. \tag{1}$$

In most realistic cases and for large parks, the q-factor is below 1, showing that the total energy absorption of the park is less than if the N WECs were operating in isolation. If the energy absorption for single WECs and the q-factor is known, the total power of the park can thus be computed according to Eq. (1). Here, the analytical multiple scattering method is utilized to compute P_{tot} in Eq. (1), using the numerical implementation of [7]. In this approach, hydrodynamic interaction between all WECs in the park is computed semi-exactly, within the limits of linear potential flow theory, up to truncation $\Lambda_z = 40$ for the vertical eigenfunctions (evanescent modes) and $\Lambda_\theta = 3$ for the angular eigenfunctions.

The approximate method is now introduced. Given a park of N WECs deployed in an ocean area $L_{\text{park}} \times L_{\text{park}}$, the park layout is assumed as $\sqrt{N}$ rows of WECs along the length of the park L_{park}, with $\sqrt{N}$ WECs in each row. We further assume that the power absorbed by row j is only affected by the energy absorbed by the rows preceding it (as measured in the direction of the waves), i.e. shadowing effects are included, but no positive interaction. The energy absorbed by the $\sqrt{N}$ devices in the first row perpendicular to the incident waves is then $\sqrt{N}\tau DJ$, where again, τ is the CWR. Since the energy absorbed by the first row is not available to the second row, the available energy flux to row 2 is $J(1 - \tau D\sqrt{N}/L_{\text{park}})$. Consequently, the energy absorbed by row 2 is approximately $\sqrt{N}\tau DJ(1 - \tau D\sqrt{N}/L_{\text{park}})$. In the same way, the energy absorbed by row j is approximately

$$P_{\text{abs,row } j} = \sqrt{N}\tau DJ \left(1 - \frac{\tau D\sqrt{N}}{L_{\text{park}}}\right)^{j-1}. \tag{2}$$

To this end, we introduce the parameter

$$s = 1 - \alpha\tau, \tag{3}$$

where $\alpha = D\sqrt{N}/L_{\text{park}}$ is the ratio of the total device width in a row and the length of the row. The parameter s satisfies $0 < s < 1$, and for few devices in the park as well as for small CWR τ, $s \to 1$. The total energy absorbed by the park during each hour can then be obtained as a geometric sum over the $\sqrt{N}$ rows,

$$P_{\text{tot}}^{\text{approx}} = \sum_{j=1}^{\sqrt{N}} P_{\text{abs,row } j} = \sqrt{N}\ \tau D\ J \sum_{j=1}^{\sqrt{N}} s^{j-1} = \sqrt{N}\ \tau D\ J \frac{1 - s^{\sqrt{N}}}{1 - s} = NP_1 q^{\text{approx}} \tag{4}$$

where we identified the approximate q-factor in expression (4) as

$$q^{\text{approx}} = \frac{1 - s^{\sqrt{N}}}{\big(1 - s\big)\sqrt{N}}. \tag{5}$$

When the number of devices in the park decrease, the park interaction tends to unity $q^{\text{approx}} \to 1$, implying that the interaction between the devices can be neglected and the power can be computed as $P_{\text{tot}}^{\text{approx}} = NP_1$. It decreases with increasing number of devices N, with increasing CWR τ or device width D, and with decreasing park area. The park interaction in Eq. (5) thus behaves as expected: it acts as a destructive shadowing effect which reduces the total power of the park, an effect which grows with more densely populated parks, and it can be neglected when the WECs in the park are few or separated by large distances.

3 Results

Figure 1 shows the results for the approximate q-factor, as compared to the exact results, and the case of neglected park interactions ($q = 1$). For the exact model, both parks with a square layout $\sqrt{N} \times \sqrt{N}$ have been modelled, as well as parks with random layouts. In the random layouts, the positions of the N WECs have been chosen randomly, with a minimum distance of $4R$ between devices. The park size has been increased according to number of WECs, such that the average distance to the closest neighbour stays approximately the same (15.1–22.6 m). Each park with random layouts has been modelled three times, as the results will differ for different WEC coordinates. An example of a park layout is shown in Fig. 2.

The single WEC performance will be different in different sea states and for different PTO damping values Γ. The results are therefore shown for two different sea states, characterised by (H_s, T_p) values equal to (1 m, 7 s) and (2 m, 12 s), and damping $\Gamma = 320$ kNs/m and 570 kNs/m, respectively. The PTO damping values are approximately the optimal damping values for a single WEC corresponding to those sea states, but similar results are obtained also for non-optimal damping values. Note that the computation for the approximate q-factor does not require any computation of the hydrodynamic interaction in the park, and the results could therefore be computed up to infinitely many devices with no computational effort. To enable a comparison with the exact results, however, we have here restricted the figures to 100 WECs.

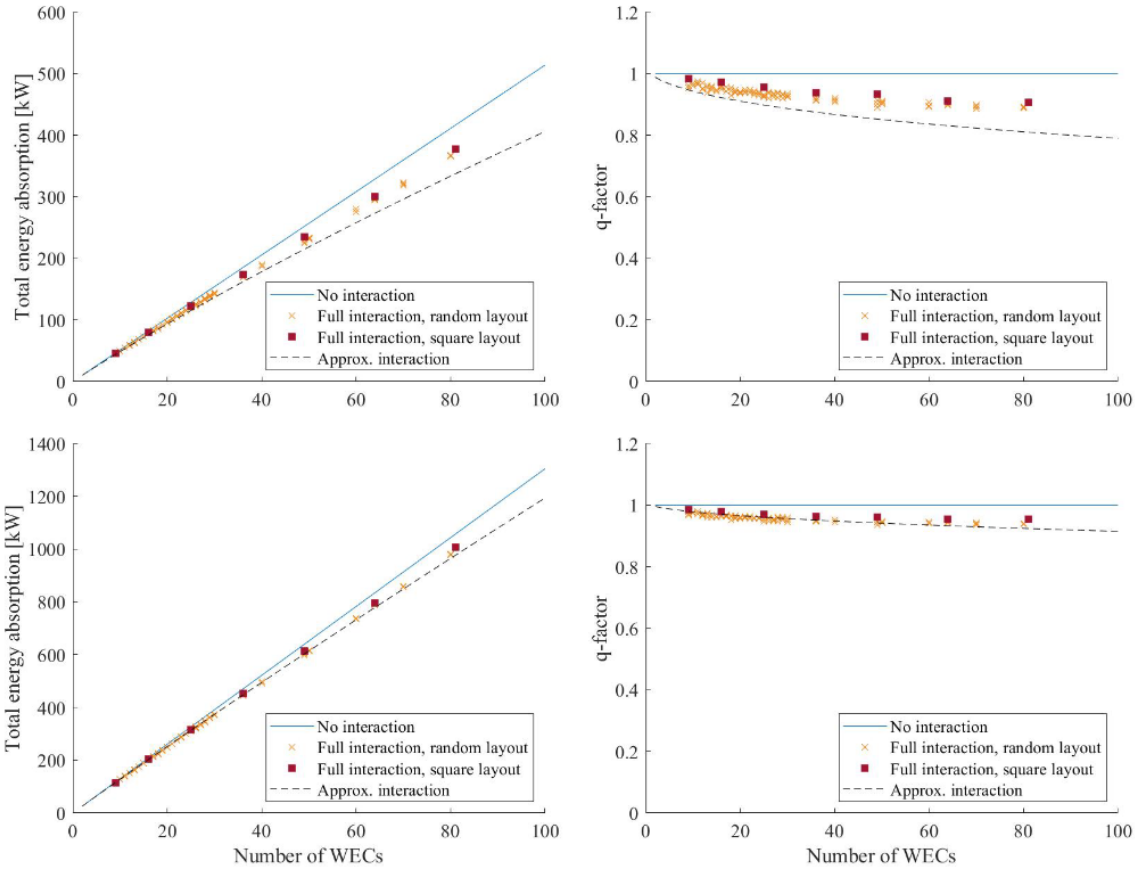

Figure 1: Performance of the q-factor as compared to the case of no interaction ($P_{\text{tot}} = NP_1$) and full interaction, computed using multiple scattering. Results shown for wave energy parks of increasing sizes (9-81 WECs). *Top row:* Sea state characterized by significant wave height $H_s = 1$ m and peak period $T_p = 7$ s, and a PTO damping of 320 kNs/m; *Bottom row:* significant wave height $H_s = 2$ m and peak period $T_p = 12$ s, with a PTO damping of 570 kNs/m.

To evaluate the approximate method further, and in particular the dependency on the wave climate, the square park with 81 WECs is evaluated in all the sea states corresponding to the annual wave climate at the WaveHub site, UK [8], with significant wave height H_s in the range 0.25–6.25 m and peak period T_p in the range 4.5–14.8 s. The results are shown in Fig. 2 in terms of the ratio $P_{\text{tot}}/P_{\text{tot}}^{\text{approx}}$ as function of the CWR for single WECs. The peak period of each individual sea state is indicated by the colorbar. Each sea state is simulated for a range of 9 different PTO dampings 190–750 kNs/m. The results corresponding to the optimal PTO damping for each sea state is highlighted with black circles.

As can be seen from the figure, the ratio between the exact and the approximate total energy is linearly dependent on the CWR. A low CWR gives an agreement close to 1, whereas higher CWR values correspond to a disagreement between P_{tot} and $P_{\text{tot}}^{\text{approx}}$ of up to 18.6%. The same relation holds true for the peak period; a better agreement for the total power is obtained in sea states with long peak periods, and worse agreement at short peak periods. This corresponds well to the results of Fig. 1, where the "range" between the approximate and no interaction lines is more narrow in the case with longer peak period (bottom plots), implying a closer agreement between the approximate and exact results. The linear relationship can be understood from the definition of the approximate interaction factor in Eq. (5). Using Eq. (1) and (4) for the exact and approximate energy absorption, their ratio becomes an expression that can be Taylor expanded around $s = 1$, or equivalently $\alpha\tau = 0$,

$$\frac{P_{\text{tot}}}{P_{\text{tot}}^{\text{approx}}} = \frac{q}{q^{\text{approx}}} = q\,\frac{(1-s)\sqrt{N}}{1-s^{\sqrt{N}}} = q\Big(1+\tfrac{1}{2}(\sqrt{N}-1)\alpha\tau+\tfrac{1}{12}(N-1)(\alpha\tau)^2+\tfrac{1}{24}(N-1)(\alpha\tau)^3+\mathcal{O}\big((\alpha\tau)^4\big)\Big). \quad (6)$$

Expanding also the q-factor as a linear function in the CWR, $q = q_0 + q_1\tau$, gives a polynomial expansion for the ratio in Eq. (6). For a park of $N = 81$ WECs, this expression becomes, to linear order,

$$\frac{P_{\text{tot}}}{P_{\text{tot}}^{\text{approx}}} = q_0\big(1+4\alpha\tau\big) + q_1\tau + \mathcal{O}\big(\tau^2\big) \quad (7)$$

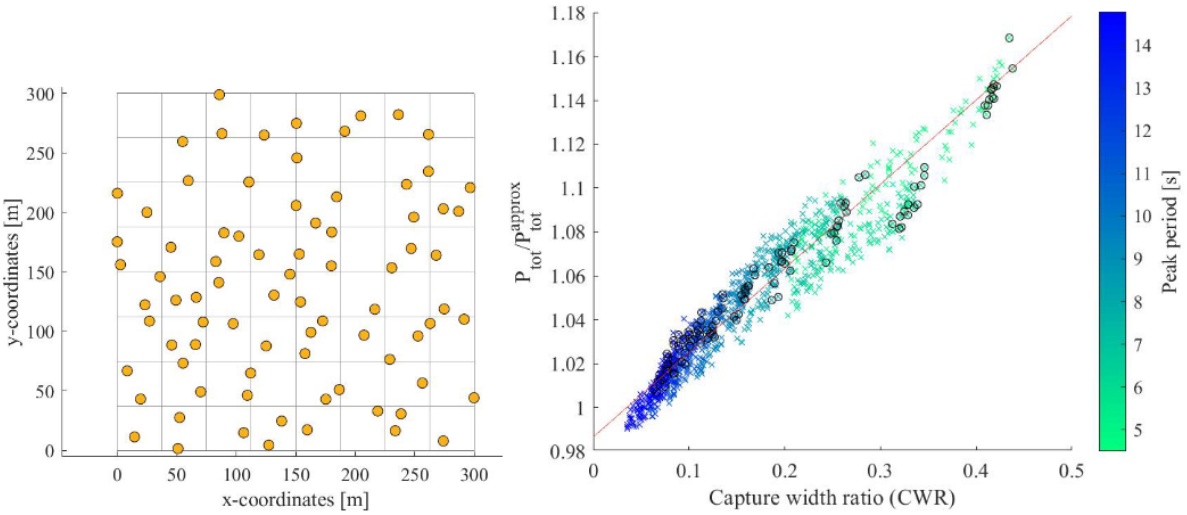

Figure 2: *Left:* Example of a random park layout of 81 WECs. In the square layout, the WECs are instead positioned on the 9×9 grid nodes. *Right:* Ratio of the total park power computed using full multiple scattering (P_{tot}) and the approximate method ($P_{\mathrm{tot}}^{\mathrm{approx}}$), for all sea states corresponding to an annual wave climate at the WaveHub site, UK. The ratio is shown as function of CWR for single WECs, and the peak period for each sea state is shown. The simulations corresponding to a PTO damping optimal for the particular sea state are highlighted with black circles. The simulations are carried out for a square park with 81 WECs. The expression for the plotted line is given in Eq. (7).

In Fig. 2, the line shown is the expression in Eq. (7), where the values q_0 and q_1 have been determined from fitting the data for the q-factor to a linear function of the CWR τ.

4 Conclusions

A simple expression for the park interaction q-factor has been derived, which can be used as an estimate of the total energy absorption of large wave energy parks. Only destructive interactions are taken into account, implying that the approximate interaction model can be used to estimate a lower bound for the absorbed energy.

The approximate q-factor and the resulting approximate energy absorption has been compared to exact values (computed using analytical multiple scattering) for many parks with 9-81 WECs, with both gridded and random layouts. To evaluate the performance as function of wave parameters, the comparison has been carried out for all sea states corresponding to an annual wave climate at the WaveHub site, UK. The results agree fairly well, with a better approximation obtained at higher wave periods and smaller CWR (of single devices). A linear relationship between the exact and approximate absorbed energy is obtained as function of the CWR.

It should be highlighted, that the strength of the approximate method lies not within its accuracy, but within its simplicity. Whereas the computation of hydrodynamic interactions within a large park of 100 WECs can require days of computational effort, even when parallel cores on HPC clusters are utilized, the estimate using the approximate q-factor is a simple multiplication of scalars.

References

[1] SA Mavrakos and P Koumoutsakos. Hydrodynamic interaction among vertical axisymmetric bodies restrained in waves. *Applied Ocean Research*, 9(3):128–140, 1987.

[2] A Babarit. On the park effect in arrays of oscillating wave energy converters. *Renewable Energy*, 58:68–78, 2013.

[3] P Siddorn and R Eatock Taylor. Diffraction and independent radiation by an array of floating cylinders. *Ocean Engineering*, 35(13):1289–1303, 2008.

[4] X Garnaud and CC Mei. Wave-power extraction by a compact array of buoys. *J. Fluid Mech.*, 635:389–413, 2009.

[5] G Tokić and D Yue. Hydrodynamics of large wave energy converter arrays with random configuration variations. *J. Fluid Mech.*, 923, 2021.

[6] M Göteman, M Giassi, J Engström, and J Isberg. Advances and challenges in wave energy park optimization—a review. *Frontiers in Energy Research*, 8:26, 2020.

[7] M Göteman, J Engström, M Eriksson, and J Isberg. Fast modeling of large wave energy farms using interaction distance cut-off. *Energies*, 8(12):13741–13757, 2015.

[8] J Sjolte, G Tjensvoll, and M Molinas. Power collection from wave energy farms. *Applied Sciences*, 3(2):420, 2013.

The Cauchy-Poisson problem for a fluid with a shear flow and non-uniform compressed ice cover

Izolda V. Sturova
Lavrentyev Institute of Hydrodynamics of SB RAS, Novosibirsk, 630090, Russia
E-mail: sturova@hydro.nsc.ru

1 INTRODUCTION

The study of the unsteady motion of a heavy fluid arising due to the action at the initial time of impulse pressure or an elevation of the horizontal equilibrium surface of the fluid (the so-called Cauchy - Poisson problem) is one of the classical problems of wave hydrodynamics, which has been studied in some detail for the case of a homogeneous incompressible inviscid fluid, when its upper boundary is free, and the fluid is initially at rest (see, e.g., the famous review of Wehausen and Laitone, 1960 [1]).

In recent years, more complex formulations of this problem have been actively studied. The axisymmetric initial disturbance created on the surface of a fluid under an ice cover without taking into account the compressive forces was carried out by Maiti and Mandal (2005) [2]. In the initial state, the fluid is at rest and its depth is infinite. The initial disturbances were either in the form of an impulsive pressure distributed over a certain region of the ice-cover or an initial displacement of the ice-cover.

The 3-D Cauchy-Poisson problem for a fluid with a shear flow and a surface tension on the free surface was studied by Ellingsen (2014) [3]. In an unperturbed state, the linear shear flow is given for only one component of the horizontal fluid velocity. Li and Ellingsen (2015) [4] considered a similar problem without taking into account surface tension for the case of an initial pressure impulse condition. The results obtained showed that a shear current has a significant impact on the transient wave motions. The shear current introduced asymmetry between upstream and downstream waves, resulting in asymmetric wave patterns. Experimental observations performed by Smeltzer et al. (2019) [5] confirmed the effects predicted by the theory.

This paper presents a solution to a linear 3-D unsteady problem of hydroelasticity on the generation of water waves due to prescribed initial axisymmetric disturbance in the ocean with an ice-cover modelled as a thin elastic plate. For an ice cover, longitudinal, transverse and shear compressive forces are taken into account. Beneath the upper boundary of the fluid, there is a linear shear current with two horizontal velocity components. The integral representation of solution that describes the behavior of the ice cover is constructed. The 2-D case of this problem is considered by Sturova (2022) [6].

2 MATHEMATICAL FORMULATION

We consider an infinitely extended ice cover of constant thickness h and density ρ_1 floating on the surface of an ideal incompressible fluid of depth H. The Cartesian coordinate system x, y, z is introduced so that the x and y axes lie on the unperturbed horizontal upper boundary of the fluid, and the z axis is directed vertically upwards. The velocity vector of the unperturbed flow is denoted by $\mathbf{V} = (U(z), V(z), 0)$, where the velocity components along the x and y axes have a linear dependence

$$U(z) = U_0 + \alpha z, \quad V(z) = V_0 + \beta z.$$

At the initial instant of time $t = 0$, the upper boundary of fluid is deviated from the horizontal position. Let us denote the arising perturbations of the fluid velocity by $\mathbf{v} = (u, v, w)$. The development of the subsequent wave motion in the fluid is described by the linearized Euler equations

$$\Big(\frac{\partial}{\partial t} + \mathbf{V} \cdot \nabla\Big)\mathbf{v} + w\frac{d\mathbf{V}}{dz} + \frac{1}{\rho}\nabla p = 0, \quad \text{div } \mathbf{v} = 0, \tag{1}$$

where $p(x, y, z, t)$ is the hydrodynamic pressure, ρ is the fluid density.

The assumption of no cavitation between the ice and fluid at any time gives kinematic and dynamic conditions at $z = 0$:

$$\frac{\partial \eta}{\partial t} + U_0 \frac{\partial \eta}{\partial x} + V_0 \frac{\partial \eta}{\partial y} = w, \tag{2}$$

$$D\Delta_2^2 \eta + Q_1 \frac{\partial^2 \eta}{\partial x^2} + Q_2 \frac{\partial^2 \eta}{\partial y^2} + 2Q_3 \frac{\partial^2 \eta}{\partial x \partial y} + M \frac{\partial^2 \eta}{\partial t^2} + \rho g \eta = p, \quad \Delta_2 \equiv \frac{\partial^2}{\partial x^2} + \frac{\partial^2}{\partial y^2}. \tag{3}$$

Here, $\eta(x, y, t)$ is the vertical deflection of the ice cover, its cylindrical rigidity is equal to $D = Eh^3/[12(1-\nu^2)]$, $M = \rho_1 h$; E, ν are Young's modulus and Poisson's ratio of ice cover; Q_1, Q_2, Q_3 are longitudinal, transverse and shear forces (compression for positive values and tensile for negative values) along the corresponding directions and g is acceleration due to gravity. It what follows, we will consider the action of only compressive forces, i.e., $Q_j \geq 0$ $(j = 1, 2, 3)$. In the dynamic condition (3), the first term describes the elastic properties of the ice cover, the sum of the next three terms represents the compressive stresses in it, and the fifth term is its inertial properties. In what follows, it is assumed that the inertial term is small in comparison with other terms and can be neglected.

The no-flow condition is satisfied on a flat horizontal bottom

$$w = 0 \quad (z = -H). \tag{4}$$

The initial conditions are as follows:

$$\eta = \eta_0(r), \quad |\mathbf{v}| = 0 \quad (t = 0), \quad r = \sqrt{x^2 + y^2}, \tag{5}$$

where $\eta_0(r)$ is axisymmetric initial elevation of the upper fluid boundary.

To solve the initial-boundary value problem (1)-(5), the double Fourier transform is used

$$\tilde{u}(\lambda, \mu, z, t) = \iint\limits_{-\infty}^{+\infty} u(x, y, z, t) \exp[-i(\lambda x + \mu y)] dx dy. \tag{6}$$

Similar transforms are introduced for other required functions.

Let us perform the Fourier transforms for the system of equations (1) and using the boundary condition (4), we obtain

$$\tilde{w} = A(\lambda, \mu, t) \sinh[k(z + H)], \quad k^2 = \lambda^2 + \mu^2,$$

where $A(\lambda, \mu, t)$ is an undetermined function. Based on the conditions (2) and (3), we have

$$\tilde{p}|_{z=0} = -\frac{\rho}{k} \{ [\dot{A} + i\zeta_1 A] \cosh(kH) - \frac{i\zeta_2}{k} A \sinh(kH) \},$$

where a dot denotes a time derivative, $\zeta_1(\lambda, \mu) = \lambda U_0 + \mu V_0$, $\zeta_2(\lambda, \mu) = \lambda\alpha + \mu\beta$. As a result, the equation for determining $\tilde{\eta}(\lambda, \mu, t)$ has the form

$$\ddot{\tilde{\eta}} + i\Big[2\zeta_1 - \frac{\zeta_2}{k} \tanh(kH)\Big] \dot{\tilde{\eta}} + \Big[\Big(\frac{k}{\rho}\zeta_3 + \frac{\zeta_1\zeta_2}{k}\Big) \tanh(kH) - \zeta_1^2\Big] \tilde{\eta} = 0 \tag{7}$$

with initial conditions

$$\tilde{\eta} = \tilde{\eta}_0(k), \quad \dot{\tilde{\eta}} = 0 \quad (t = 0), \tag{8}$$

where $\zeta_3(\lambda, \mu) = Dk^4 - \lambda^2 Q_1 - \mu^2 Q_2 - 2\lambda\mu Q_3 + \rho g$.

Following Ellingsen (2014) [3], we obtain the dispersion relation as the functional relation between the frequency ω and the wave vector $\mathbf{k} = (k\cos\theta, k\sin\theta)$ for flexural gravity waves in the problem under consideration

$$\omega(k, \theta) = \sqrt{\omega_0^2 + \zeta_4^2} - \zeta_4, \tag{9}$$

where

$$\omega_0(k, \theta) = \sqrt{\frac{k}{\rho}\zeta_3 \mathrm{th}(kH)}, \quad \zeta_4(k, \theta) = \frac{\zeta_2 \mathrm{th}(kH)}{2k}, \quad \theta = \arctan\frac{\mu}{\lambda}.$$

Here the function $\omega_0(k,\theta)$ is the dispersion relation for waves in a fluid without a velocity shear. Taking into account the inertial term in Eq. (3), i.e. for $M \neq 0$, the dispersion relation $\omega_0(k,\theta)$ was given by Bukatov et al. (1991) [7], Bukatov (2017) [8], Sturova (2021) [9]. For the existence of a real value of frequency $\omega(k,\theta)$, it is necessary that the radicand in Eq. (9) be non-negative for all values $0 \le \theta \le 2\pi$. This condition guarantees the stability of the floating plate.

The solution to Eq. (7) with initial conditions (8) has the form

$$\tilde{\eta} = \tilde{\eta}_0 \exp(i\zeta_5 t)\big[\cos(\zeta_6 t) - \frac{i\zeta_5}{\zeta_6}\sin(\zeta_6 t)\big], \quad \zeta_5(k,\theta) = \zeta_4 - \zeta_1, \quad \zeta_6(k,\theta) = \omega + \zeta_4.$$

For initial elevation $\eta_0(r) = a\exp(-br^2)$ after the double Fourier transform (6), we have

$$\tilde{\eta}_0(k) = \frac{\pi a}{b}\exp\Big(-\frac{k^2}{4b}\Big).$$

After performing the inverse Fourier transforms and switching to a moving coordinate system

$$X = x - U_0 t, \; Y = y - V_0 t,$$

we obtain a solution for the vertical deflection of the ice cover

$$\eta(x,y,t) = \frac{a}{4\pi b}\int_0^{2\pi} d\theta \int_0^{\infty} k\exp\Big(-\frac{k^2}{4b}\Big)\Big[1 + \frac{\gamma(k,\theta)}{\sigma(k,\theta)}\Big]\cos\psi(k,\theta,t)dk, \tag{10}$$

where

$$\gamma(k,\theta) = (\alpha\cos\theta + \beta\sin\theta)\tanh(kH)/2 - k(U_0\cos\theta + V_0\sin\theta),$$

$$\sigma(k,\theta) = \sqrt{\omega_0^2(k,\theta) + [(\alpha\cos\theta + \beta\sin\theta)\tanh(kH)/2]^2},$$

$$\omega_0(k,\theta) = \sqrt{k\tanh(kH)[Dk^4 - Q(\theta)k^2 + g\rho]}, \quad Q(\theta) = Q_1\cos^2\theta + Q_2\sin^2\theta + Q_3\sin(2\theta),$$

$$\psi(k,\theta,t) = (X\cos\theta + Y\sin\theta)k - \omega(k,\theta)t, \quad \omega(k,\theta) = \sigma(k,\theta) - (\alpha\cos\theta + \beta\sin\theta)\tanh(kH)/2.$$

The resulting solution (10) becomes axisymmetric only in the absence of the main flow, i.e. $U(z) = V(z) = 0$, and uniform compression of the ice cover $Q_1 = Q_2$, $Q_3 = 0$:

$$\eta(r,t) = \frac{a}{2b}\int_0^{\infty} k\exp\Big(-\frac{k^2}{4b}\Big)J_0(kr)\cos[\bar{\omega}_0(k)t]dk,$$

where

$$\bar{\omega}_0(k) = \sqrt{k\tanh(kH)(Dk^4 - Q_1k^2 + g\rho)},$$

J_0 is the zeroth order Bessel function of the first kind.

Wave patterns of the ice deflections $\eta(x,y,t)/a$ are shown in Fig. 1(a-f) at the two time instants: $t\sqrt{g/H} = 5$ (Fig. 1(a,c,e)) and $t\sqrt{g/H} = 10$ (Fig. 1(b,d,f)). The following input data are used:

$$E = 5\ GPa,\ h = 0.5\ m,\ \nu = 0.3,\ \rho = 1025\ kg/m^3,\ H = 20m,\ b = 2/H^2.$$

The values $Q_j = 0$ $(j = 1,2,3)$ are used for Fig. 1(a,b) and the values $(Q_1,Q_2,Q_3) = (1.5,1.2,0.5)\sqrt{g\rho D}$ are used for Fig. 1 (c-f). The values $(\alpha,\beta) = (1,0.6)\sqrt{g/H}$, $(U_0,V_0) = (0.6,0.4)\sqrt{gH}$ are used for Fig. 1 (a,b,e,f) and the values $\alpha = \beta = 0$, $U_0 = V_0 = 0$ are used for Fig. 1 (c,d). For each case, the bold black closed curve shows the shape of the wave front, which is defined as $c(K,\theta)t/H$, where $c(k,\theta) = \omega(k,\theta)/k$ is the phase velocity of flexural gravity wave, the value of the wave number $K = 2\sqrt{b}$, at which the degree of the exponential factor in Eq. (10) is equal to -1, and θ varies from 0 to 2π.

More detailed numerical results will be presented at the Workshop.

REFERENCES

[1] Wehausen J.V., Laitone E.V. 1960 Surface waves. *Handbuch der Physik.* **9**, 446-778.

[2] Maiti P., Mandal B.N. 2005 Water waves generated due to initial axisymmetric disturbances in

water with an ice-cover. *Arch. Appl. Mech.* **74**(9), 629-636. DOI 10.1007/s00419-005-0384-7
[3] Ellingsen S.Å. 2014 Initial surface disturbance on a shear current: The Cauchy-Poisson problem with a twist. *Phys. Fluids.* **26** (8), 082104. http://dx.doi.org/10.1063/1.4891640
[4] Li Y., Ellingsen S.Å. 2015 Initial value problems for water waves in the presence of a shear current. *Proc. 25th Intern. Ocean and Polar Eng. Conf.* **3**, 543-549.
[5] Smeltzer B.K., Æsøy E., Ellingsen S.Å. 2019 Observation of surface wave patterns modified by sub-surface shear currents. *J. Fluid Mech.* **873**, 508-530. doi:10.1017/jfm.2019.424
[6] Sturova I.V. 2022 The Cauchy-Poisson problem for fluid with an ice cover in the presence of shear current (Two-dimensional case). *Fluid Dyn.* **57**(1), 45-54. DOI:10.1134/S0015462822010104
[7] Bukatov A.E., Zharkov V.V., Zav'yalov D.D. 1991 Three-dimensional bent-gravity waves with non-uniform compression. *J. Appl. Mech. and Techn. Phys.* **32**(6), 867-872.
https://doi.org/10.1007/BF00850629
[8] Bukatov A.E. 2017 *Waves in the sea with a floating ice cover.* Sevastopol: FSBSI MHI. 360 p. [in Russian] htpp://mhi-ras.ru/news/news_201802151133.html
[9] Sturova I.V. 2021. The effect of non-uniform compression of an elastic plate floating on the fluid surface on the development of unsteady flexural-gravity waves. *Fluid Dyn.* **56**(2), 211-218. DOI:10.1134/S0015462821020117

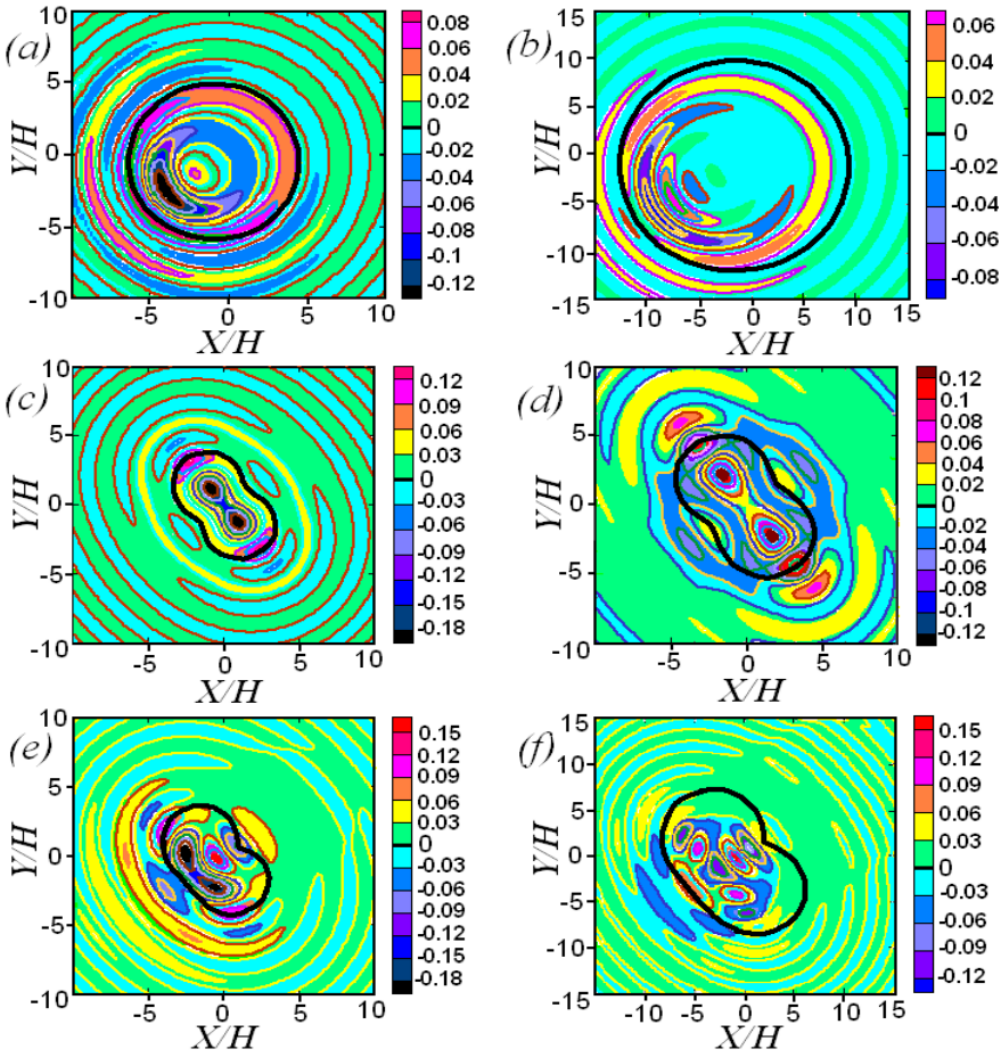

Figure 1.

Body-Exact Computations of Vertical Plane Motions

(Abstract for the 37th International Workshop on Water Waves and Floating Bodies, Giardini Naxos, Italy, 2022)

Rahul Subramanian[1], **Robert F. Beck**[2]
[1]Department of Ocean Engineering, Texas A&M University, Galveston, USA
[2]Department of Naval Architecture and Marine Engineering, University of Michigan, Ann Arbor, USA
Presenting author: rbeck@umich.edu

1 INTRODUCTION

Assessing the motion response of a vessel is a crucial component of the ship design process. The heave and pitch motions and subsequent accelerations are critical for assessing the inertial loads at key locations and have bearing on the dynamic structural loading and proper prediction of slamming probabilities and impact.

Computational methods employing the potential flow theory, formulate the problem either in the time-domain or the frequency domain. Although frequency domain codes have proven to be fairly accurate, robust and computationally fast, they are inherently restricted by the assumption of small wave amplitude because of the linear formulation. Time-domain based methods on the other hand have a major advantage in being able to model different degrees of nonlinearity, as reviewed in [1]. The sophistication level of these so called "blended method" codes can be chosen based on the particular problem being solved, the required accuracy level and available computational resources. Validation studies ([2], [3]) have shown increased accuracy in forward speed and capability in handling large motions when compared with linear frequency domain methods.

This paper presents the application of an efficient time-domain "blended-method" formulation to predict the ship motions of a vessel under forward speed. Computations are done specifically for vertical plane motions in head seas in order to compare with experimental data. The computer program is based on the body-exact time-domain strip theory developed by [4], which was extended to predict maneuvering in waves ([5]). Over the years, the physics models have been continuously updated to improve the predictions ([6], [7]). The strip theory approach allows for faster computational times when compared to fully three-dimensional methods. The free surface boundary conditions are transferred to a "representative surface" as explained in the section below. The body boundary condition is applied below the intersection surface of the incident wave and the exact body position at each time step. Accounting for the changing wetted surface ensures that the nonlinear radiation and diffraction wave loads are also captured in addition to the nonlinear Froude-Krylov and hydrostatic loads. Computations have been performed for the KCS and KVLCC2, representing two different modern hull forms. The results have been compared with available experiments and predictions from other numerical methods.

2 MATHEMATICAL FORMULATION

The fluid flow for the wave body problem is considered inviscid, irrotational, incompressible and unsteady. Since most ocean going vessels are relatively slender, a strip theory formulation is adopted, where the three-dimensional problem is solved as a series of individual two-dimensional problems.

The strip wise two-dimensional potential $\phi = \phi(y, z, t; x)$ satisfies the Laplace equation at each frame such that $\nabla^2\phi(y, z, t; x) = 0$. Three different coordinate frames are used as shown in Figure 1. An inertial Earth fixed frame with origin at O_e is used to keep track of the vessel translational motions and the Euler angles. The boundary value problem is formulated in a hydrodynamic frame that translates and rotates in the horizontal plane with the body. A body fixed frame is used to solve the equations of motion. The hydrodynamic frame follows the ship such that its origin O_h is always in a vertical line with the origin of the body fixed frame, O_b.

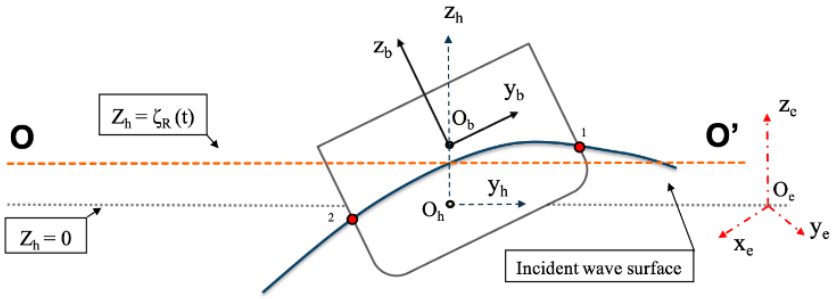

Figure 1: Schematic showing the details at a station. The free surface boundary conditions are transferred to the representative surface given by $z_h = \zeta_R(t)$. The origins of the three frames are denoted by O. (Schematic shows vessel in general non-head sea condition)

In the present formulation, the free surface boundary conditions are applied on a "representative surface", indicated by (line) O-O' in Figure 1 given by $z_h = \zeta_R(t)$. Here, $\zeta_R(t)$ is a representative free-surface at each station, given by $\zeta_R(t) = \eta_I(x_h = x_{station}, y_h = 0, t)$. Here, η_I, $x_{station}$, and y_h represent the incident wave elevation, longitudinal location of a station and the y coordinate y_h in the hydrodynamic frame ($y_h = 0$ indicates intersection of incident wave with z axis of hydrodynamic frame), respectively. The quasi-linear kinematic and dynamic free surface boundary conditions written in the moving hydrodynamic frame, applied on the $z_h = \zeta_R(t)$ plane (line in 2-D) are as follows

$$\frac{\delta\eta}{\delta t} = \frac{\partial\phi}{\partial z} + V\frac{\partial\eta}{\partial y} + x_h\dot{\psi}\frac{\partial\eta}{\partial y} + v_m\frac{\partial\eta}{\partial y} - \mu\eta \tag{1}$$

$$\frac{\delta\phi}{\delta t} = -g\eta + V\frac{\partial\phi}{\partial y} + x_h\dot{\psi}\frac{\partial\phi}{\partial y} + v_m\frac{\partial\phi}{\partial y} + \dot{\zeta}_R(t)\frac{\partial\phi}{\partial z} - \mu\phi \tag{2}$$

Here $\frac{\delta}{\delta t}$ refers to the time derivative taken by following a free surface node. The terms η and x_h represent the free surface wave elevation measured from the calm water surface, and the longitudinal position of the station in the hydrodynamic frame, respectively. Additional terms are picked up to account for the horizontal (v_m) and vertical ($\dot{\zeta}_R(t)$) movement of the free surface nodes wrt the hydrodynamic frame. The moving node velocity v_m accounts for the lateral movement of each free surface node. This is necessary in a body-exact formulation. The last term in the equations (1) and (2) are the damping terms that are added to generate artificial damping at the beach to satisfy the far-field condition at the edge of the domain. Details for the numerical beach can be found in [8].

The body boundary condition can thus be written in terms of its individual components for the diffraction (ϕ_D) and radiation (ϕ_R) potentials,

$$\nabla\phi_D \cdot \mathbf{N} = -\nabla\phi_I \cdot \mathbf{N} \quad \text{on } S_B(t) \tag{3}$$

$$\nabla\phi_R \cdot \mathbf{N} = \tilde{\mathbf{v}} \cdot \mathbf{N} \quad \text{on } S_B(t) \tag{4}$$

The velocity $\tilde{\mathbf{v}}$ used in Equation (4) is the velocity of a point on the body surface after removing the time-varying mean velocity components in the horizontal plane. Therefore, the velocity $\tilde{\boldsymbol{v}}$ is evaluated as $\tilde{\mathbf{v}} = \mathbf{v} - \mathbf{v_{avg}}$, where $\mathbf{v}$ represents the complete velocity of a node with respect to the earth fixed frame and includes the rotational velocity components, and $\mathbf{v_{avg}}$ denotes the time-varying mean velocity components in surge, sway and due to rotation in yaw, given by ($u_{avg} - y\dot{\Psi}_{avg}$, $v_{avg} + x\dot{\Psi}_{avg}$, 0). The variables u_{avg}, v_{avg} and $\dot{\Psi}_{avg}$ denote the average surge, sway and yaw velocities, respectively. The averaging is done over an encounter wave period.

The mixed boundary value problem (Equations 1 - 4) is solved for the perturbation potentials ϕ_R and ϕ_D and their derivatives. In the present work, a source distribution technique is used. De-

Main Particular	KCS	KVLCC2
$Type$	$Containership$	$VLCC$
L	230 m	320 m
B	32.18 m	58 m
T	10.8 m	20.8 m
C_B	0.65	0.81
Fn	0.33	0.142

Table 1: Main Particulars of Analyzed Vessels (Full Scale)

singularised sources are placed above the free surface nodes and constant strength panels are used on the body.

The pressure at any point on the hull surface is calculated using Bernoulli's equation as shown below

$$\frac{p}{\rho} + \left.\frac{\partial \phi}{\partial t}\right|_e + \frac{1}{2}\nabla\phi \cdot \nabla\phi + gz = 0 \tag{5}$$

where $\left.\frac{\partial \phi}{\partial t}\right|_e$ represents the temporal derivative of the perturbation potential with respect to the earth fixed frame. A direct formulation is used to set up a BVP for this term, often called the "acceleration potential". Details of this formulation can be found in [8]. The pressure is integrated over the hull surface to obtain the hydrostatic and external hydrodynamic forces and moments acting on the hull at a given instant in time. In the present study, all forces are computed by integrating the corresponding pressure components on the intersection surface of the exact body position and the incident wave surface. The body accelerations are computed by solving a fully nonlinear 6-DOF equations of motion solver. A 4^{th} order Adams-Bashforth-Moulton predictor-corrector scheme is used to time-step the equations of motion and solve for the evolution of the free surface.

3 RESULTS AND DISCUSSION

The simulations were set up and performed for two modern hull forms shown in Table 1. The KCS represents a high speed containership, and the KVLCC2 a slow speed large crude carrier. Based on convergence studies, a time step size of $T_e/100$ is used, T_e being the encounter period. On average, a total of 50 body panels are used for a full station. The free surface extends to 4 wavelengths on each side of the body, including 2 for the numerical beach, and the simulations are run for 15 encounter periods to obtain steady state solutions. The origin of the body frame is at the intersection of the calm water plane and the center-plane at the midship.

The response amplitude operators in head seas were extracted using an FFT of the force time history over the last two encounter wave periods. The comparisons with available experiments and other codes are shown in Figures 2 and 3. The predictions compare very favourably compared to the experiments with a general tendency to slightly over-estimate heave and show excellent agreement for pitch. The experimental data for the KCS was obtained from [9], and for the KVLCC2 from [10] (experiment 1) and CEHIPAR [11] (corresponding to experiment 2). Better agreement is seen for the KCS in heave and pitch compared to the linear frequency domain code MDLHydroD ([12]). For the KVLCC2, the 3D Rankine source based BEM ([11]) shows better agreement for heave at larger wavelengths, whereas the present body-exact computations are able to better capture the pitch motions throughout the frequency range.

REFERENCES

[1] Beck, R. F., and Reed, A. M. Modern computational methods for ships in a seaway. In *Transactions SNAME* (2001), pp. 1–51.

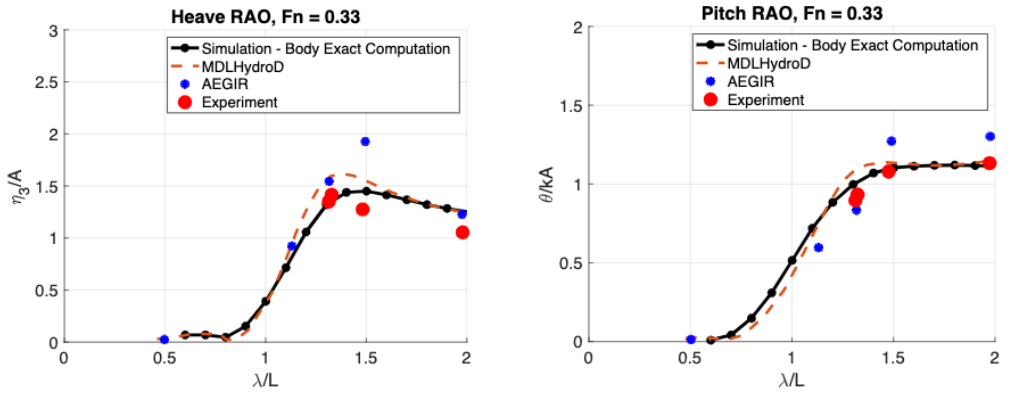

Figure 2: Vertical Plane Motions of KCS in Head Seas.

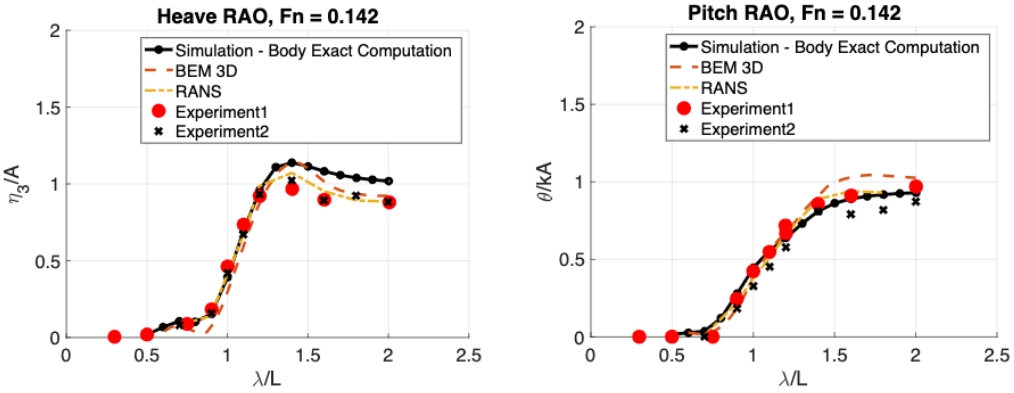

Figure 3: Vertical Plane Motions of KVLCC2 in Head Seas

[2] Pawlowski, J. S., and Bass, D. W. 1991. *A Theoretical and Numerical Model of Ship Motions in Heavy Seas. SNAME Transactions 9*, 319–352.

[3] Huang, Y., and Sclavounos, P. D. 1998. *Nonlinear Ship Motions. Journal of Ship Research 42*, 120–130.

[4] Bandyk, P. J. 2009. *A body-exact strip theory approach to ship motions computations.* PhD thesis, The University of Michigan, Department of Naval Architecture and Marine Engineering.

[5] Subramanian, R., and Beck, R. F. 2015. *A time-domain strip theory approach to maneuvering in a seaway. Ocean Engineering 104*, 107–118.

[6] Subramanian, R., and Beck, R. F. An improved body-exact method to predict the maneuvering of ships in a seaway. In *Proceedings of the 38th International Conference on Ocean, Offshore& Arctic engineering, Glasgow, Scotland, UK* (2019), ASME.

[7] Subramanian, R., and Beck, R. F. Effect of wave height on maneuverability of ships in waves. In *SNAME Maritime Convention, Tacoma, Washington, USA* (2019), SNAME.

[8] Subramanian, R. 2012. *A time domain strip theory approach to predict maneuvering in a seaway.* PhD thesis, The University of Michigan, Department of Naval Architecture and Marine Engineering.

[9] Simonsen, C. D., Otzen, J. F., Joncquez, S., and Stern, F. 2013. *EFD and CFD for KCS heaving and pitching in regular head waves. Marine Science Technology 18*, 435–459.

[10] Park, D., Lee, J., and Kim, Y. 2015. *Uncertainty analysis for added resistance experiment of KVLCC2 ship. Ocean Engineering 95*, 143–156.

[11] Lyu, W., and Moctar, O. 2017. *Numerical and experimental investigations of wave-induced second order hydrodynamic loads. Ocean Engineering 131*, 197–212.

[12] Guha, A., and Falzarano, J. 2015. *The effect of hull emergence angle on the near field formulation of added resistance. Ocean Engineering 105*, 10–24.

A study of a fixed trapezoidal section in regular waves using a generalized weak-scatterer model

Chao Tong[1], Yanlin Shao[1*], Harry B. Bingham[1], Finn-Christian W. Hanssen[2]

1: Department of Mechanical Engineering, Technical University of Denmark, 2800 Lyngby, Denmark
2: NTNU AMOS, Department of Marine Technology, NTNU, Trondheim, Norway

1 Introduction

The original weak-scatterer (OWS) hypothesis, pioneered by Pawlowski [1], assumes a vertical displacement of the scattered wave elevation from the underlying incident wave, which leads to an inconsistency when the surface-piercing structure has flares near the waterline. Thus, the predicted waterline position using the superposition of the incident and scattered waves will separate from the surface of the structure, particularly for incident waves with large amplitudes and structures with large flare angles. With this in mind, we have re-derived the free-surface boundary conditions based on a generalized weak-scatterer (GWS) approximation to avoid this inconsistency. The basic idea of GWS is that the fully nonlinear (FN) free-surface conditions are linearized about the incident wave surface, but using a Taylor expansion along an arbitrary direction which can be manually prescribed in practice according to the geometry of the structure. In this way, we can precisely capture the waterline position on the structure at each time step of the solution. Accordingly, expressions for the wave loads acting on the structure based on direct pressure integration are also derived based on the same assumption.

2 Generalized weak-scatterer approximation

A Cartesian coordinate system Oxz is defined with its origin located at the mean water level and the Oz axis oriented positively upwards. For a surface-piercing structure with a large flare, like a wedge or a ship bow, it is reasonable to introduce a direction tangential to the structure's surface to track the waterline intersection. In this case, we assume that the total velocity potential and the free surface displacement $(\varphi, \mathbf{r})$ can be split into the incident component $(\varphi_I, \mathbf{r}_I)$ and the scattered component $(\varphi_S, \mathbf{r}_S)$, where $\mathbf{r}_I = (x_I, \eta_I)$ and $\mathbf{r}_S = (x_S, \eta_S)$:

$$\varphi = \varphi_I + \varphi_S, \qquad \mathbf{r} = \mathbf{r}_I + \mathbf{r}_S. \tag{1}$$

Same as in the OWS hypothesis, we introduce a small parameter ϵ to denote the smallness of the quantities associated with the scattered waves, and assume that $\varphi_S/\varphi_I \in O(\epsilon)$ and $r_i^S/r_i^I \in O(\epsilon), (i = 1, 2, 3)$, where r_i^I and r_i^S represent position components of $\mathbf{r}_I$ and $\mathbf{r}_S$, respectively.

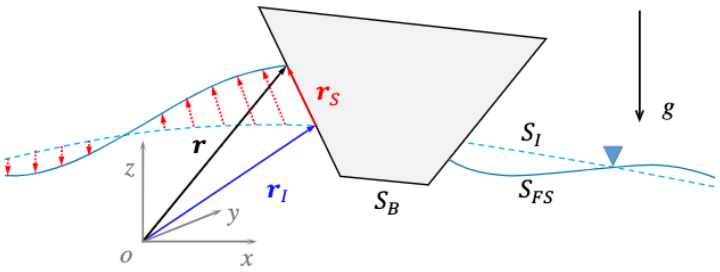

Figure 1: An illustration of wave-structure interaction problem within the frame of weak-scatterer approximation.

An arbitrary Lagrangian-Eulerian (ALE) approach is adopted to track the wave markers. On the instantaneous free surface, the kinematic and dynamic free-surface boundary conditions in the inertial reference frame are expressed as:

$$\frac{\delta \eta}{\delta t} = \frac{\partial \varphi}{\partial z} - (\nabla \varphi - \mathbf{V}) \cdot \nabla \eta, \qquad \frac{\delta \varphi}{\delta t} = -g\eta - \frac{1}{2} \nabla \varphi \cdot \nabla \varphi + \mathbf{V} \cdot \nabla \varphi. \tag{2}$$

Inserting (1) into (2), taking the Taylor series expansion of the free-surface boundary conditions from the incident wave along an arbitrary direction, and neglecting terms higher than the first order in ϵ, finally we

*Corresponding author. E-mail addresses: yshao@mek.dtu.dk

obtain the free-surface boundary conditions for the scattered wave:

$$\frac{\delta\eta_S}{\delta t} =\frac{\partial\varphi_S}{\partial z} - (\nabla\varphi_I - \mathbf{V})\cdot\nabla\eta_S - \nabla\varphi_S\cdot\nabla\eta_I - \nabla\left(\frac{\partial\eta_I}{\partial t} - \frac{\partial\varphi_I}{\partial z} + \nabla\varphi_I\cdot\nabla\eta_I\right)\cdot\mathbf{r}_S \quad \text{at } \mathbf{r}=\mathbf{r_I}, \tag{3}$$

$$\frac{\delta\varphi_S}{\delta t} =- g\eta_S - (\nabla\varphi_I - \mathbf{V})\cdot\nabla\varphi_S - \nabla\left(\frac{\partial\varphi_I}{\partial t} + g\eta_I + \frac{1}{2}\nabla\varphi_I\cdot\nabla\varphi_I\right)\cdot\mathbf{r}_S \quad \text{at } \mathbf{r}=\mathbf{r_I}. \tag{4}$$

Here $\mathbf{V}$ is a prescribed velocity which is tangential to the boundary of the surface-piercing structure at the waterline, meaning that $\mathbf{V}$ and $\mathbf{r}_S$ are parallel to each other at the free-surface intersection. Away from the structure, the direction of $\mathbf{V}$ is gradually changed to purely vertical. The unit direction vector of $\mathbf{r}_S$ is defined as $\mathbf{l}_S = (l_1, l_2)$, and the vertical component of $\mathbf{V}$ is $V_2 = \partial\eta_I/\partial t + \mathbf{V}\cdot\nabla\eta_I$ for a fixed structure. The relation between $\mathbf{V}$ and $\mathbf{r}_S$ gives $\mathbf{V} = (l_1V_2/l_2, V_2)$ straightforwardly.

For the Neumann boundaries, a no-flux condition normal to the structure surface should be satisfied on the instantaneous wetted body surface: $\partial\varphi_S/\partial n = -\partial\varphi_I/\partial n + \mathbf{V_b}\cdot\mathbf{n}$, while on the stationary seabed or tank walls: $\partial\varphi_S/\partial n = 0$. The governing equation for the scattered potential field is the Laplace equation $\nabla^2\varphi_S = 0$. Enclosed by the described mixed Dirichlet-Neumann boundaries, a BVP can be formulated and solved.

The instantaneous pressure on the structure surface can be computed from Bernoulli's equation:

$$P = -\rho(\varphi_t + \frac{1}{2}|\nabla\varphi|^2 + gz). \tag{5}$$

where ρ is the fluid density. Therefore, the hydrodynamic forces $\mathbf{F}_{hydro} = (f_1, f_2, f_3)$ and moments $\mathbf{M}_{hydro} = (f_4, f_5, f_6)$ can subsequently be obtained by integrating the pressure over the structure's wetted surface. The integrals over the exact wetted body surface S_{WB} are split into two parts: one is over the wetted body surface S_{WB}^I below the intersection between the body and the incident wave, and the other is introduced because of the scattered wave:

$$f_i = -\iint_{S_{WB}} Pn_i\,\mathrm{d}s = -\iint_{S_{WB}^I} Pn_i\,\mathrm{d}s - \iint_{\Delta S} Pn_i\,\mathrm{d}s, \tag{6}$$

where n_i are the six components of the generalized unit normal vector, $(n_1, n_2, n_3) = \mathbf{n}$, and $(n_4, n_5, n_6) = \mathbf{r}_b\times\mathbf{n}$. Here $\mathbf{n}$ points into the fluid. The second term due to the scattered waves can also be separated into two parts for convenience:

$$-\iint_{\Delta S} Pn_i\,\mathrm{d}s = \rho\iint_{\Delta S}\left(\varphi_t + \frac{1}{2}|\nabla\varphi|^2\right)n_i\,\mathrm{d}s + \rho\iint_{\Delta S} gzn_i\,\mathrm{d}s = \Pi_1 + \Pi_2. \tag{7}$$

Since the integrand of Π_1 is not a constant within the strip area ΔS but a function of $\mathbf{r}_S$, in order to obtain the integral, taking the Taylor expansion of the integrand at the incident wave position at the incident wave $\mathbf{r}_I$ yields

$$\begin{aligned}\Pi_1 =&\rho\iint_{\Delta S}\left(\left[\varphi_t + \frac{1}{2}\left[\nabla\varphi\right|^2\right]_{\text{at }\mathbf{r}_I} + \left[\nabla\left(\varphi_t + \frac{1}{2}|\nabla\varphi|^2\right)\cdot(\mathbf{r}-\mathbf{r}_I)\right]_{\text{at }\mathbf{r}_I} + O(\epsilon^2)\right)n_i\,\mathrm{d}s\\ \approx&\rho\oint_{\Gamma_I} r_S\left(\varphi_t + \frac{1}{2}|\nabla\varphi|^2\right)n_i\,\mathrm{d}\Gamma + \rho\oint_{\Gamma_I}\frac{1}{2}r_S^2\left[\nabla\left(\frac{\partial\varphi_I}{\partial t} + \frac{1}{2}\nabla\varphi_I\cdot\nabla\varphi_I\right)\cdot\mathbf{l}_S\right]n_i\,\mathrm{d}\Gamma,\end{aligned} \tag{8}$$

where Γ_I indicates the waterline of the structure due to the incident wave. r_S is the amplitude of $\mathbf{r}_S$ with the same sign as the vertical component of $\mathbf{r}_S$, and θ denotes the angle between the vector $\mathbf{r}_S$ and the z-axis in the inertial coordinate system so that $\eta_S = r_S\cos\theta$. As for the second integral Π_2,

$$\Pi_2 =\rho\iint_{\Delta S} gzn_i\,\mathrm{d}s = \rho\oint_{\Gamma_I}\int_0^{r_S} g(\eta_I + z_S)n_i\,\mathrm{d}r\mathrm{d}\Gamma = \rho\oint_{\Gamma_I}\frac{1}{2}g(2\eta_I r_S + r_S^2\cos\theta)n_i\,\mathrm{d}\Gamma. \tag{9}$$

The hydrodynamic loads on the structure can be finally assembled as

$$\begin{aligned}f_i =&\rho\iint_{S_{WB}^I}\left(\varphi_t + \frac{1}{2}|\nabla\varphi|^2 + gz\right)n_i\,\mathrm{d}s + \rho\oint_{\Gamma_I} r_S\left(\varphi_t + \frac{1}{2}|\nabla\varphi|^2 + g\eta_I\right)n_i\,\mathrm{d}\Gamma\\ &+\rho\oint_{\Gamma_I}\frac{1}{2}r_S^2\left[\nabla\left(\frac{\partial\varphi_I}{\partial t} + \frac{1}{2}\nabla\varphi_I\cdot\nabla\varphi_I\right)\cdot\mathbf{l_S} + g\cos\theta\right]n_i\,\mathrm{d}\Gamma.\end{aligned} \tag{10}$$

It can be observed that the magnitude for the main wetted body surface integral is of $O(1)$, for the first waterline integral is of $O(\epsilon)$ and for the second waterline integral is of $O(\epsilon^2)$, respectively.

3 Stability analysis

A fixed trapezoidal cylinder with large flare angle subject to an incident wave is considered. By observing the GWS free surface boundary conditions in Eqn.(3) and (4), it can be seen that there exist convective terms, which make the condition similar to that for a seakeeping problem for a ship with forward speed. When the forward speed becomes significant, instability may occur if an explicit time-integration scheme is applied without special treatment of the convective terms. Here, a linear matrix-based eigenvalue stability analysis is performed to understand the stability properties of the numerical algorithms. We consider the 2D linearized kinematic and dynamic GWS free-surface boundary conditions containing the x-convective terms in matrix form:

$$\frac{\delta}{\delta t}\begin{pmatrix}\eta_S\\ \tilde{\varphi}_S\end{pmatrix}=\begin{pmatrix}-U_x\frac{\partial}{\partial x} & \frac{\partial}{\partial z}\\ -g & -U_x\frac{\partial}{\partial x}\end{pmatrix}\begin{pmatrix}\eta_S\\ \tilde{\varphi}_S\end{pmatrix}, \tag{11}$$

where the convective velocity is defined as $U_x=\frac{\partial\varphi_I}{\partial x}-V_x$, η_S is the scattered wave elevation, and $\tilde{\varphi}_S=\varphi_S(x,0,t)$ is the scattered velocity potential at the mean water level. The space-discretized form of Eqn. (11) can be written as

$$\frac{\delta}{\delta t}\begin{pmatrix}\{\eta_S\}\\ \{\tilde{\varphi}_S\}\end{pmatrix}=\begin{pmatrix}[U][D_x^f] & [\Theta_z]\\ -g[I] & [U][\Theta_x]\end{pmatrix}\begin{pmatrix}\{\eta_S\}\\ \{\tilde{\varphi}_S\}\end{pmatrix}\Rightarrow\frac{\delta\{q\}}{\delta t}=[J]\{q\}. \tag{12}$$

Here $\{q\}=[\eta_{S,1},\eta_{S,2},\cdots,\eta_{S,N_m},\tilde{\varphi}_{S,1},\tilde{\varphi}_{S,2},\cdots,\tilde{\varphi}_{S,N_m}]^{\mathrm{T}}=[\{\eta_S\};\{\tilde{\varphi}_S\}]$, where N_m is the number of wave markers. $[I]$ is an identity diagonal matrix, while $[U]$ is a diagonal matrix containing the convective velocities of the wave markers. The matrix operator $[D_x^f]$ differentiates η_S with respect to x, whose non-zero elements are the weighting coefficients of a specific finite difference scheme. The global equation system is recalled

$$[A]\{\varphi_S\}=\{b\}\doteq[Q]\{\tilde{\varphi}_S\}, \tag{13}$$

where $[Q]$ is an operator matrix to distribute the free surface boundary conditions $\{\tilde{\varphi}_S\}$ into the corresponding positions of the global boundary value vector $\{b\}$. By doing this, after some simple manipulations, we can get expressions for $[\Theta_x]$ and $[\Theta_z]$:

$$[\Theta_x]=[D_x^c][A]^{-1}[Q],\quad [\Theta_z]=[D_z^c][A]^{-1}[Q], \tag{14}$$

in which $[D_x^c]$ and $[D_z^c]$ are operator matrices to take the x and z derivative of $\{\tilde{\varphi}_S\}$ at $z=0$.

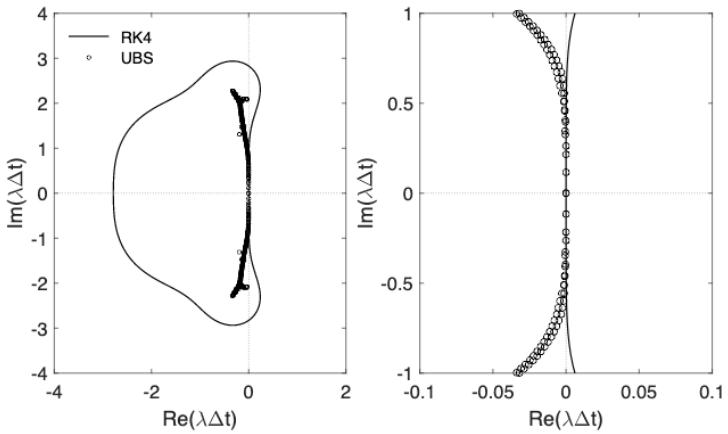

Figure 2: Eigenvalues of a 3^{rd}-order upwind-biased scheme for the wave steepness $kH=0.2$. Zoomed-in view near the origin is also displayed in the right plot.

For the discretization of the free-surface boundary conditions discussed above, the eigenvalues of the matrix $[J]$ can be computed numerically. To guarantee stability, all the eigenvalues of matrix $[J]$ multiplied by the time step Δt must be inside the stability region for a given time stepping scheme. In our study, the 4^{th}-order explicit Runge-Kutta (RK4) scheme is used.

There are two convective derivatives in both the dynamic and kinematic free-surface conditions, i.e. $\partial\varphi_S/\partial x$ and $\partial\eta_S/\partial x$, which are calculated by a 3^{rd}-order upwind-biased scheme (UBS) to ensure stability. At Neumann boundaries, we require ghost nodes outside the fluid domain to calculate the convective derivatives. If upwind markers on the free surface can be found, then extrapolation is used; otherwise, a Neumann boundary condition is imposed to compute the values on the ghost points. Here a linearized Neumann

boundary condition is provided as reference:

$$\frac{\partial \eta_S}{\partial n} = \frac{1}{g}\frac{\partial}{\partial t}\left(\frac{\partial \varphi_I}{\partial n}\right). \tag{15}$$

In general, instability issues come mainly from the wave markers on the lee side of the structure, but the scheme is applied everywhere. The stability eigenvalues for the 3^{rd}-order upwind-biased scheme (UBS) are shown in Fig. 2. It can be seen from the zoomed-in plot that all eigenvalues are inside the stability region of the RK4 scheme. More details of the stability analysis can be found in [3].

4 Numerical application

A fixed trapezoidal ship section with a flare angle $\theta = 30°$, semi-submerged in regular waves is studied here. The flare angle θ is defined as the angle between the side wall of the section and the vertical direction in the inertial coordinate system Oxz that is located at the middle of the tank at the mean water level. The wave tank has a length $L = 8L_w$, the water depth is $h = L_w$, and the length of the damping zone is $L_{damp} = 2L_w$. The incident wavelength is set as $L_w = 2.5$ m in our simulations and the wave period is T. The wave height $H = 0.11$ m. The incident wave is generated by the stream function theory [2]. The bottom breadth of the trapezoidal section is $B = 0.2L_w$ and the draught is $d = 0.1L_w$.

A detailed demonstration of the dynamic fluid pressure distribution over the instantaneous wetted body surface, and the wave profile close to the waterline points for this fixed trapezoidal ship section in waves with $H = 0.11$ m is presented in Fig. 3. The snapshots represent different time instants during the 31^{st} wave period. Generally speaking, the consistency between the GWS and FN models [4] is deemed satisfactory and promising for both the wave elevation and the pressure distribution. Note that the pressure distribution of the GWS solutions in Fig. 3 results from the intersection between the incident wave and the structure, corresponding to the mean wetted body surface integral in Eqn. (10). The difference between the OWS and GWS can not be demonstrated here due to the lack of space and will be presented during the workshop.

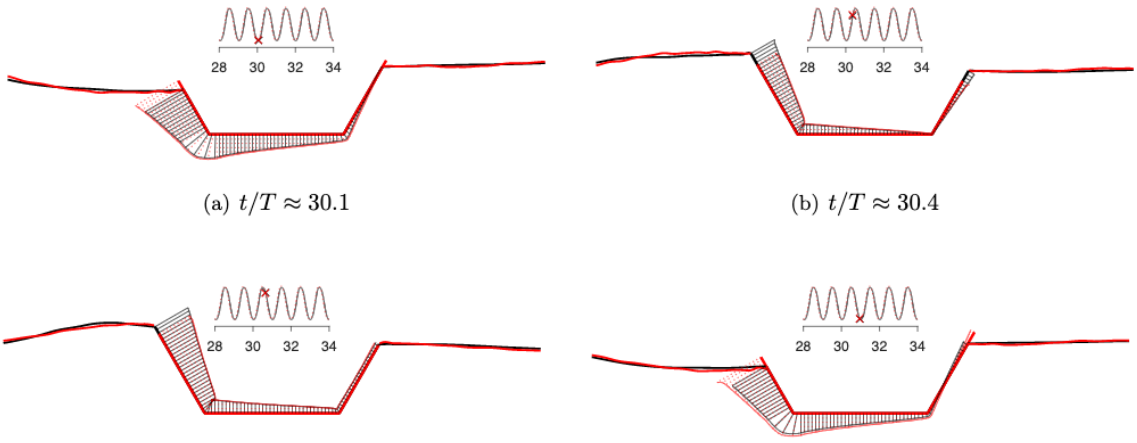

(a) $t/T \approx 30.1$ (b) $t/T \approx 30.4$

(c) $t/T \approx 30.7$ (d) $t/T \approx 31$

Figure 3: Dynamic pressure distribution and free surface elevation near waterline on the body at different time instants. The analysis of the GWS solutions (red) is compared with the FN solutions (black). The corresponding time instants are indicated with red and black cross in the time series of horizontal force.

Acknowledgment

This work is funded by the Chinese Scholarship Council (No.201906230317) and the Department of Mechanical Engineering at Technical University of Denmark.

References

[1] Pawlowski, J., 1994. A nonlinear theory of ship motion in waves .

[2] Rienecker, M., Fenton, J., 1981. A fourier approximation method for steady water waves. Journal of fluid mechanics 104, 119–37.

[3] Tong, C., Shao, Y., Bingham, H.B., Hanssen, F.C.W., . A generalized weak-scatterer approximation for nonlinear wave-structure interaction in marine hydrodynamics (submitted) .

[4] Tong, C., Shao, Y., Bingham, H.B., Hanssen, F.C.W., 2021. An adaptive harmonic polynomial cell method with immersed boundaries: Accuracy, stability, and applications. International Journal for Numerical Methods in Engineering 122, 2945–80.

Experimental and numerical 2D wedge entry in water with entrained air

Martin van der Eijk and Peter R. Wellens
Maritime & Transport Technology, Delft University of Technology, The Netherlands
m.vandereijk@tudelft.nl

HIGHLIGHTS

Air entra in water has a significant and reducing effect on the maximum forces during extreme (wave) impacts. Experimental and numerical methods used together can lead to a better understanding of physics. Combined results show that the difference between aerated impacts and those without air can be 12% for 5% air content.

EXPERIMENTAL & NUMERICAL COMPARISON

Maritime floating bodies are often designed to endure extreme water wave events. Examples of these impact loading events are hull entries, waves slamming onto the hull, or green water onto the deck. A simplification of such an event can result in a better understanding of the physics involved. An example is a 2D simplified cross-section of the floating body [1, 2, 3, 4], a wedge, in a drop test.

A high-speed falling wedge experiment is conducted at the Delft University of Technology. The experiment is built to investigate the effect of air in water on the impact. The experimental results are used to validate our numerical model. The literature, we found, does not yet feature data of high-speed 2D entries followed by emergences, including compressible effects. The wedge used for this experiment has a deadrise angle of 15 degrees. A Froude number up to 6.5 ($\approx$7.0[m/s]) is reached.

The experimental setup is illustrated in fig. 1. The domain size and the water level are designed such that their influence on the initial impact is negligible and a large impact speed is reached. The experimental tests are done for three different weights of the wedge; 4.0[kg], 5.0[kg], and 10[kg], representing 0.8, 1.0 (neutrally buoyant), and 2.0 times the buoyancy. Every weight is released at least five times. The measurement equipment are two light gates for measuring the speed, two accelerometers of 100g and 200g (AS28E and ADXL377), and a camera.

The numerical method is an extension of [5]. The method is a Volume-of-Fluid based method that uses a cut-cell method and full geometric piecewise linear reconstruction. The governing equations for fully-compressible two-phase flows are solved. The fluid-structure interaction is solved monolithicly. Second-order integration schemes to capture the dynamics during the impact are used. The method makes use of the one-fluid formulation and matches the mass and momentum flux to prevent momentum losses [6].

The acceleration signals are filtered using Fourier analysis. The frequencies caused by the structure of the setup are removed. The speed measurement is used as calibration for the acceleration time signals. The variation between the impact speeds of the different weights (6.65, 6.80, and 7.03[m/s] respectively) is up to 5.5%, caused by friction losses during falling. The maximum accelerations, including the variation, are illustrated in fig. 2a.

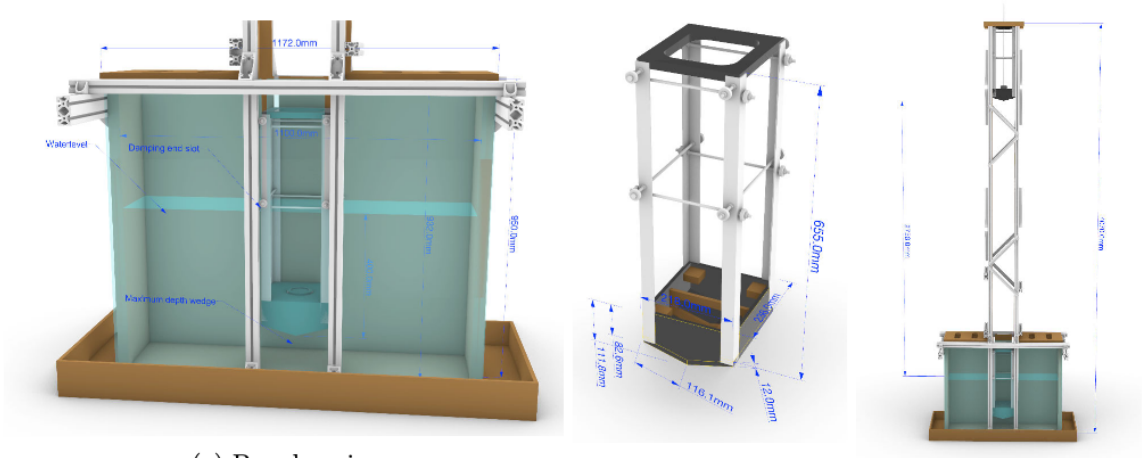

(a) Box domain.

(b) Wedge.

(c) Droptower.

Figure 1: Experimental setup.

The results of the 200g accelerometer in fig. 2 match better with the numerical results than the 100g accelerometer. The Fourier analysis of the 100g accelerometer data shows to be more sensitive to environmental effects, like structural vibrations, than the 200g accelerometer. The accuracy of the 100g accelerometer is debatable as the wedge impacts are higher than 100g.

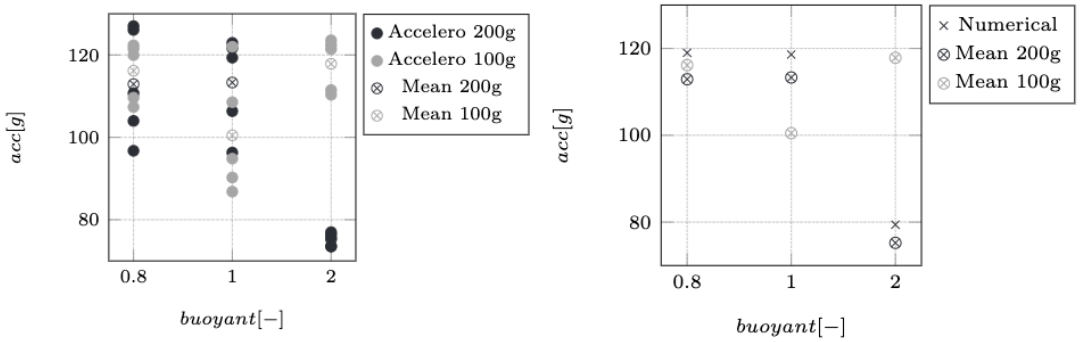

(a) Variation experiment.

(b) Numerical and experiment.

Figure 2: Comparison max. accelerations experimentel data & numerical results.

In fig. 3 the free surface is extracted from the camera recordings and is compared with the numerical results. The contour extraction of the recordings has problems with representing the mixed air-water jets. The numerical results correspond well with the video frames. In fig. 3a and fig. 3b a circle is drawn showing the difference between the numerical free surface and the contour extraction. When comparing these to the video frames, the numerical results seems to be in good agreement. In fig. 3b a returning jet attached to the sidewall penetrates the free surface and is captured by both methods.

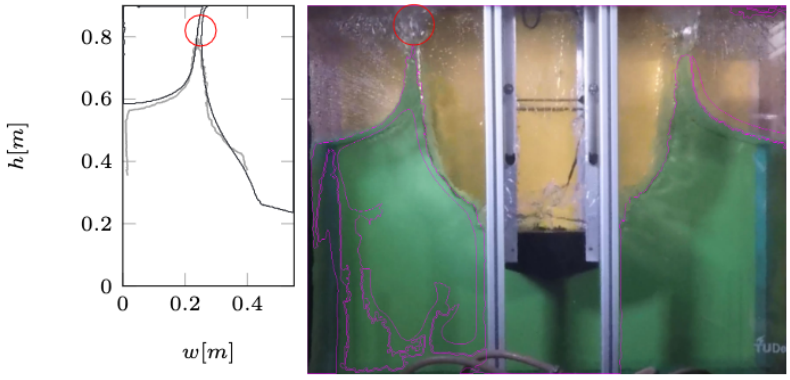

(a) Max. penetration depth.

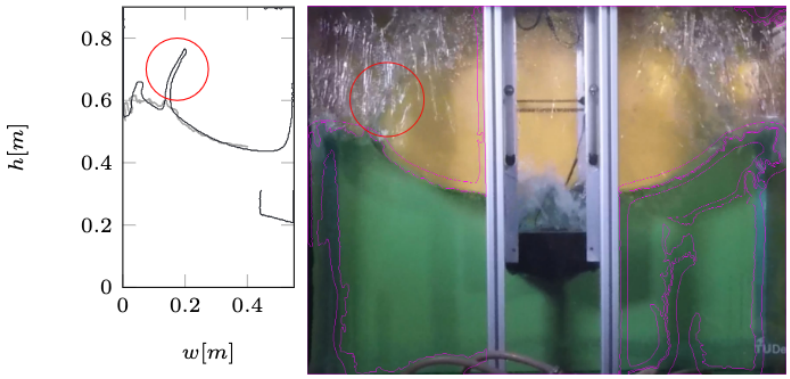

(b) Upward motion.

Figure 3: Comparison free surface experimental data & numerical results for 0.8x buoyant; – experiment, – numerical result.

AERATION

In reality, breaking in heavy seas can lead to air entrainment. The air content can remain in the water for several wave periods. Assuming the mixture of air and water homogeneous modifies the compressibility up to several orders of magnitude. General methods used for the design stage of maritime floating bodies often do not account for the air content, which is likely to be one percent or higher [7, 8]. Our numerical method [5] has been modified to account for these compressible effects, including the air content.

Numerical simulations of the 0.8x buoyant wedge at a speed of 6.65[m/s] are performed. The numerical domain is the same as the domain illustrated in fig. 1a. The air content is varied, showing the effect on the maximum acting force. The results are shown in tab. 1.

The results show that an increase of air content for a constant impact speed results in a cushioning effect on the maximum acceleration. This cushioning effect corresponds to other experimental results [9, 10] The air content results in increased compressibility. The compressibility of a mixture can be indicated by a Mach number which is the ratio of the flow speed and speed of sound for a homogeneous mixture [10].

Air content [%]	Max. acc. [g]	Diff. with 0% air [%]	Mach number
0 (Exp., 200g)	113.7	-	0.02
1 (Exp., 200g)	109.1	-4	0.2
0 (Exp., 100g)	116.1	-	0.02
1 (Exp., 100g)	119.5	+3	0.02
0	119.0	-	0.02
0.1	115.5	-3	0.08
1	112.5	-6	0.2
5	104.6	-12	0.5

Table 1: Maximum acting accelerations.

CONCLUSION

An experimental setup has been presented that can be used to investigate the effect of aeration on the accelerations during impact with a 2D cross-section. Also, the results are used to validate an in-house numerical model. The numerical and experimental results are in good agreement regarding the maximum accelerations. The combination of the experiment and numerics gives a better insight into physics. Increasing the air content for the numerical simulations showed a large and nonlinear decrease of the maximum accelerations. Air in water should be considered in the final design process of maritime floating bodies enduring extreme water events.

REFERENCES

[1] Colicchio, G., Greco, M., Miozzi, M., and Lugni, C. Experimental and numerical investigation of the water-entry and water-exit of a circular cylinder. In *24th International Workshop on Water Waves and Floating Bodies* (2009), pp. 19–22.

[2] van der Eijk, M., and Wellens, P. 2020. *Experimental and numerical assessment of vertical accelerations during bow re-entry of a RIB in irregular waves. International Shipbuilding Progress*, 1–26.

[3] Ni, B., and Wu, G. 2017. *Numerical simulation of water exit of an initially fully submerged buoyant spheroid in an axisymmetric flow.* Fluid Dynamics Research 49(4), 045511.

[4] Tenzer, M., Moctar, O. e., and Schellin, T. E. 2015. *Experimental investigation of impact loads during water entry.* Ship Technology Research 62(1), 47–59.

[5] van der Eijk, M., and Wellens, P. R. 2019. *A compressible two-phase flow model for pressure oscillations in air entrapments following green water impact events on ships. International Shipbuilding Progress*, 1–29.

[6] Zuzio, D., Orazzo, A., Estivalèzes, J.-L., and Lagrange, I. 2020. *A new efficient momentum preserving Level-Set/VOF method for high density and momentum ratio incompressible two-phase flows. Journal of Computational Physics 410*, 109342.

[7] Bullock, G., Crawford, A., Hewson, P., Walkden, M., and Bird, P. 2001. *The influence of air and scale on wave impact pressures.* Coastal Engineering 42(4), 291–312.

[8] Peregrine, D., and Thais, L. 1996. *The effect of entrained air in violent water wave impacts. Journal of Fluid Mechanics 325*, 377–397.

[9] Mai, T., Mai, C., Raby, A., and Greaves, D. 2019. *Aeration effects on water-structure impacts: Part 1. drop plate impacts. Ocean Engineering 193*, 106600.

[10] Elhimer, M., Jacques, N., Alaoui, A. E. M., and Gabillet, C. 2017. *The influence of aeration and compressibility on slamming loads during cone water entry. Journal of Fluids and Structures 70*, 24–46.

Efficient Computation of the Linear Radiation Problem using a Spectral Element Method

Jens Visbech[1], **Allan P. Engsig-Karup**[1], **and Harry B. Bingham**[2]
[1] Department of Applied Mathematics and Computer Science
[2] Department of Mechanical Engineering
Technical University of Denmark, 2800 Kgs. Lyngby, Denmark
s161975@student.dtu.dk or jenshaakon@gmail.com

1 INTRODUCTION

Estimating the hydrodynamic characteristics of bodies interacting with ocean waves is of key importance in ocean engineering. Solving the wave-structure interaction problem has been a topic of research for many years, especially using linearized potential flow theory which generally captures the majority of the physics for typical marine structures. Linear theory allows for a decomposition of the potential into radiation and diffraction parts, where the focus of this abstract lies on the former.

For modelling the linear interactions between floating bodies and ocean waves, the impulsive time-domain formulation has been widely used and studied [1], and in recent years the pseudo-impulsive approach has gained renewed attention [2]. The basic concept for these impulsive methods is to force the floating object with an impulse (or pseudo-impulse) in velocity and measure the resultant force on the body. The Fourier transform of the force divided by the Fourier transform of the body motion conveniently determines the added mass and damping coefficients for all frequencies.

Despite the work by Robertson & Sherwin (1999) [3] suggesting an inherent mesh-instability problem with the spectral element method (SEM) applied to free surfaces waves, significant progress for pure wave propagation and wave-structure interaction using SEM have been made over the last half-decade starting with Engsig-Karup, Eskilsson & Bigoni (2016) [4]. Using this high-order numerical discretization method allows for exceptional geometrical flexibility, high accuracy and efficiency, and an optimal $\mathcal{O}(n)$ scaling of the computational effort. This latter property is achieved in combination with p-multigrid techniques [5, 6]. For a further review of the SEM and its beneficial capabilities see [7].

This abstract seeks to highlight recent progress towards developing a computational tool in the setting of linear potential flow using a pseudo-impulsive approach combined with a higher-order SEM. This ultimately enables all of the aforementioned features of this numerical method, including curvilinear elements, unstructured meshes, different radiation conditions, and much more.

2 GOVERNING EQUATIONS

In a general 3D setting, $d = 3$, an Eulerian Cartesian coordinate system is adopted, where the xy-axis represents the horizontal plane, and the vertical z-axis is defined as positive in the upwards direction. These axes span the entire fluid domain, $\Omega \subset \mathbb{R}^d$, which is bounded by the free surface (FS), $\Gamma^{FS} \subset \mathbb{R}^{d-1}$, and the bathymetry, $\Gamma^b \subset \mathbb{R}^{d-1}$. Also, Ω is bounded by the the body surface, $\Gamma^{body} \subset \mathbb{R}^{d-1}$, the far-field boundary, $\Gamma^\infty \subset \mathbb{R}^{d-1}$, and potentially also a symmetry boundary, $\Gamma^{sym} \subset \mathbb{R}^{d-1}$. The depth is denoted by $z = -h(\boldsymbol{x})$, where $\boldsymbol{x} = (x, y)$, and the free surface is defined as $z = \eta(\boldsymbol{x}, t)$, where the time domain is $T : t \geq 0$. Notations for the 2D setting are illustrated in Figure 1.

Applying the theory of linear potential flow, enables the general solution for wave-structure interactions to be decomposed into independently solvable parts, where the focus of this abstract lies upon the k radiation potentials, ϕ_k. In the following, we will use the notation: $\nabla = (\partial_x, \partial_y)$, where e.g. ∂_x is the derivative with respect to x.

The temporal development is governed by the linearized kinematic and dynamic free surface boundary conditions

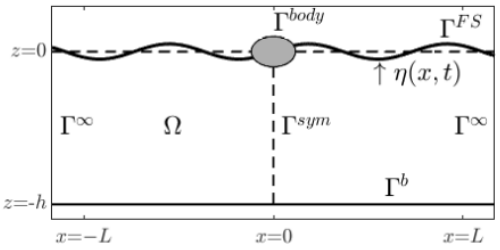

Figure 1: Notations for the 2D physical domain, Ω.

$$\partial_t \eta = \tilde{w}_k \quad \text{and} \quad \partial_t \tilde{\phi}_k = -g\eta \quad \text{on} \quad \Gamma^{FS}, \tag{1}$$

where the "$\sim$"-notation indicates quantities evaluated on Γ^{FS}, i.e. $\tilde{\phi}_k = \phi_k(\boldsymbol{x}, 0, t)$ and $\tilde{w}_k = \partial_z \phi_k|_{z=0}$.

Combined with the free surface conditions, the continuity equation, in the form of a Laplace problem, governs the spatial domain with an in-homogeneous Dirichlet boundary condition on Γ^{FS} and a homogeneous Neumann boundary condition on Γ^b,

$$(\nabla, \partial_z)^2 \phi_k = 0 \quad \text{for} \quad -h \leq z \leq 0, \tag{2}$$

$$\phi_k = \tilde{\phi}_k \quad \text{on} \quad \Gamma^{FS}, \quad \text{and} \quad \partial_n \phi_k = 0 \quad \text{on} \quad \Gamma^b, \tag{3}$$

where ∂_n is the derivative in the normal direction to the boundary. For the body boundary condition on Γ^{body}:

$$\partial_n \phi_k = \dot{\xi}_k n_k \quad \text{on} \quad \Gamma^{body}, \quad \text{where } n_k = \begin{cases} \boldsymbol{n} & k = 1,2,3 \\ \boldsymbol{r} \times \boldsymbol{n} & k = 4,5,6 \end{cases} \tag{4}$$

in which $\boldsymbol{n}$ is the normal vector and $\boldsymbol{r}$ is the position vector of a point on Γ^{body}. Furthermore, ξ_k denotes the displacement of the body, which is to be modelled as a Gaussian, so that a tailored frequency content governed by the spatial resolution, is released into the system. See [2] for more details. The Gaussian should be modelled in such a way that the displacement at $t = 0$, is practically zero, which in combination with a zero-imposed velocity potential at the free surface, will form the initial conditions for (1).

It can be computationally beneficial to impose a symmetry boundary, Γ^{sym}, on the symmetry-axis of the body. For symmetrical and anti-symmetrical problems these are given as

$$\partial_{\boldsymbol{x}} \phi_k = 0 \quad \text{or} \quad \phi_k = 0 \quad \text{on} \quad \Gamma^{sym}. \tag{5}$$

On the far-field boundary, Γ^{∞}, appropriate actions should be taken to avoid reflections that could influence the frequency content of the solution. Combinations of various approaches have been used: 1) a simple grid stretching technique, 2) classical relaxation zone techniques, and/or 3) an in-homogeneous Neumann-type Sommerfeld boundary condition.

2.1 Added mass and damping coefficients

From [2] it can be shown that the added mass and damping coefficients can be computed via the Fourier transform, $\mathcal{F}(\cdot)$, of the discrete displacement and force time signals as

$$\omega^2 a_{jk} - \mathrm{i}\omega b_{jk} = \frac{\mathcal{F}\{F_{jk}(t)\}}{\mathcal{F}\{\xi_k(t)\}}, \tag{6}$$

where $F_{jk}(t)$ is the radiation force for mode j caused by an impulse in mode k. This can be computed by integrating the linear dynamic pressure over the wetted body surface, Γ^{body}.

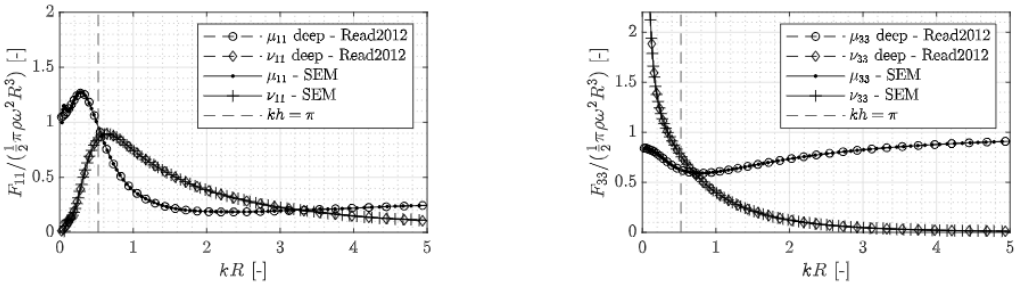

Figure 2: Numerical results for a surging (left) and a heaving (right) cylinder using 4th order polynomials.

3 NUMERICAL SOLUTION

The Laplace problem given by (2) and its associated boundary conditions are discretized using the SEM in a 2D setting, hereby splitting the fluid domain, Ω, into non-overlapping triangular elements with curvilinear sides - if needed - in an unstructured way so that the mesh is more refined at Γ^{FS} and Γ^{body} than in the rest of the spatial domain. On this discrete domain, global piece-wise continuous polynomial finite element basis functions of order P will represent the solution, thus leading to a sparse linear system of equations

$$\boldsymbol{A}\boldsymbol{\phi_k} = \boldsymbol{b}, \quad \boldsymbol{A} \in \mathbb{R}^{DOF \times DOF}, \quad \boldsymbol{b} \in \mathbb{R}^{DOF}. \tag{7}$$

The governing temporal equations given by (1) will be evolved in time using a classical explicit four-stage Runge-Kutta time integration scheme in combination with a conservative global CFL condition to ensure conditional stability. The time steep is chosen to be $\Delta t = \frac{\mathrm{Cr}\,\Delta x_{\min}}{u_{\max}}$, where Cr is the Courant number, $\mathrm{Cr} \in [0.5\ ;\ 1]$, $\Delta x_{\min}$ is the minimum grid spacing on the free surface elements, and $u_{\max}$ is the asymptotic limit of the linear wave celerity, i.e. $u_{\max} = \sqrt{g/k\tanh(kh)}$.

The evaluation of the time derivatives in the Bernoulli equation for the pressure are computed by finite difference schemes with fourth-order accuracy to accordance with the time integration scheme. Finally, the Fourier transforms in (6) are evaluated using a fast Fourier transform.

4 NUMERICAL CASES AND RESULTS

At present moment, the 2D implementation has been validated extensively by achieving spectral convergence (fixed mesh and increasing polynomial order) and algebraic convergence rates (fixed polynomial order and decreasing uniform element sizes) for affine and curvilinear triangular elements, on structured and unstructured meshes. Also, the solver has been validated against different known benchmarks. A 3D implementation is in progress from which results will be presented at the workshop including the aforementioned validation analysis.

The case studies that are presented are heavily inspired by those presented in [8] using a finite difference solver, hence showing normalised results for a half-submerged cylinder (radius: $R = 0.5$ and depth: $h = 3$). The finite difference solver [8] on an overset grid was validated against analytical infinite-depth solutions calculated using a multipole method.

From Figure 2 the surge-surge and heave-heave results in terms of non-dimensional added mass and damping coefficients for a cylinder are plotted with the numerical results from [8]. The results show excellent visual agreement, ultimately confirming the legitimacy and correctness of the SEM model. Similar results were obtained for the barge case from the reference abstract.

To show the promising geometrical flexibility features of the model, a simple 2D version of a tetra spar buoy has been implemented, see Figure 3. A symmetry boundary, Γ^{sym}, is applied on the left boundary. The geometry of the structure is: Top part is $B = 10$ m wide, straight vertical part is B long, length of leg (measured at the top part of each leg) is $3B$, width of the leg is $B/4$, and angle between the legs is $\pi/2$.

The added mass and damping coefficients are given in non-dimensional form by

$$\tilde{a}_{jk} = \frac{a_{jk}}{\frac{1}{2}\pi\rho L_c^2}, \quad \tilde{b}_{jk} = \frac{b_{jk}}{\frac{1}{2}\pi\rho\omega L_c^2}, \tag{8}$$

where L_c is a characteristic length of the structure taken to be the leg length, $L_c = 3B$.

The preliminary results for this geometrically demanding structure are shown in Figure 4.

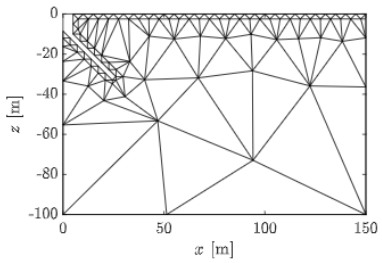

Figure 3: Illustration of an unstructured mesh for a 2D simplified version of a 3D tetra spar bouy.

5 ACKNOWLEDGEMENTS

The computations were performed on resources provided by the DTU Computing Center (DCC) at the Technical University of Denmark.

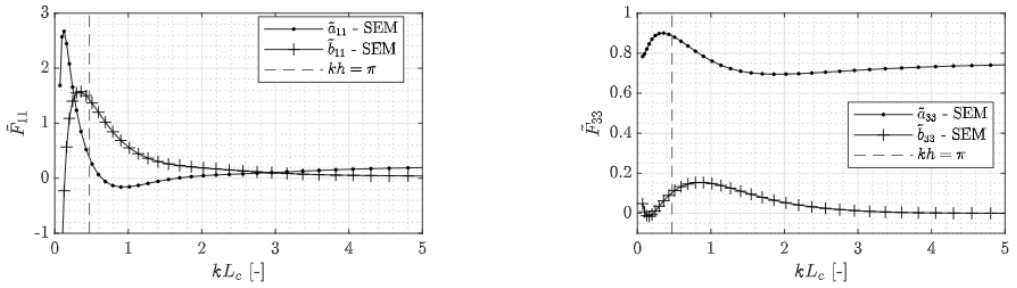

Figure 4: Numerical results for surging (left) and a heaving (right) 2D tetra spar buoy geometry with $h = 20B$.

REFERENCES

[1] Bingham, H. B. 1994. *Simulating ship motions in the time domain.* PhD thesis, Massachusetts Institute of Technology.

[2] Amini-Afshar, M., and Bingham, H. B. 2017. *Solving the linearized forward-speed radiation problem using a high-order finite difference method on overlapping grids.* Applied Ocean Research 69(1), 220–244.

[3] Robertson, I., and Sherwin, S. 1999. *Free-surface flow simulation using hp/spectral elements.* Journal of Computational Physics 155(1), 26–53.

[4] Engsig-Karup, A., Eskilsson, C., and Bigoni, D. 2016. *A stabilised nodal spectral element method for fully nonlinear water waves.* Journal of Computational Physics 318(1), 1–21.

[5] Engsig-Karup, A. P., and Laskowski, W. L. 2021. *An efficient p-multigrid spectral element model for fully nonlinear water waves and fixed bodies.* Int. J. Num. Meth. Fluids 93(9), 2823–2841.

[6] Mortensen, L., Laskowski, W., Engsig-Karup, A., Eskilsson, C., and Monteserin, C. Simulation of nonlinearwaves interacting with a heaving body using a *p*-multigrid spectral element method. In *The 31st International Ocean and Polar Engineering Conference* (2021), OnePetro.

[7] Xu, H., Cantwell, C., Monteserin, C., Eskilsson, C., Engsig-Karup, A., and Sherwin, S. 2018. *Spectral/hp element methods: Recent developments, applications, and perspectives.* Journal of Hydrodynamics 30(1), 1–22.

[8] Read, R., and Bingham, H. B. 2012. *Solving the linear radiation problem using a volume method on an overset grid. IWWWFB27.*

The wave-induced drift of objects of finite size

Q. Xiao[1], R. Calvert[2,4], S.Q. Yan[3], T. Adcock[1], T.S. van den Bremer[1,4]
[1]Department of Engineering Science, University of Oxford, Oxford, UK
[2]School of Engineering, University of Edinburgh, Edinburgh, UK
[3]School of Mathematics, Computer Science and Engineering, City, University of London, UK
[4]Department of Civil Engineering and Geosciences, TU Delft, Delft, Netherlands
Presenting author, email: qian.xiao@eng.ox.ac.uk

1 INTRODUCTION

An understanding of wave-induced transport on the ocean surface is critical for the marine ecosystem health and ocean-related industries. Example applications are transport of plastic, oil patches and large ice floes. An unrestrained object floating in a field of surface gravity waves will normally experience a net drift in the direction of wave propagation in addition to the oscillatory motion associated with the waves. The net drift typically only becomes relevant over time scales much longer than the wave period due to the relatively small drift speeds. Unlike an idealized fluid parcel[1], an object of finite size may display non-Lagrangian drift behaviour[2]. This study examines the time-averaged transport of floating objects under the influence of regular waves in deep water. By using a hybrid numerical model that employs a fully nonlinear potential-flow model to capture the wave field and a Navier-Stokes (NS) model to calculate the detailed flow patterns near objects, our model encompasses both viscous effects and nonlinear wave-body interactions. A group of objects with different size, draft (submergence) and shape are investigated in the presence and absence of viscosity in the simulations. Their effects on drift and the mechanisms involved are explored.

2 NUMERICAL MODEL

The hybrid model QaleFOAM, employed in this study, is based on domain-decomposition method, which couples the QALE-FEM (Quasi Arbitrary Lagrangian-Eulerian Finite Element Method) model with the two-phase incompressible Navier-Stokes (NS) model InterDyMFOAM in OpenFOAM[3]. The domain is divided into two parts: the large outer domain is simulated by QALE-FEM to capture the waves, and a small inner domain, near the floating object, is solved by the NS model. In the NS model, both the air and water phases are assumed incompressible, and the VOF (volume of fluid) method is used to identify the phases and their interfaces. The coupling approach employed in this paper is a one-way coupling, which means that at the interfaces, the NS model only takes as input the solutions of QALE-FEM solver but does not feed its solutions back. For the 2D simulations performed in this paper, the front and back interfaces in the NS domain are empty, and a laminar viscosity model is used. The right interface of the NS domain is equipped with a passive wave absorber[3]. The left interface of the NS domain is coupled with the QALE-FEM, where the wave generated in the QALE-FEM domain using a flap wavemaker is transferred into the NS domain. A similar wave absorber is also equipped in the left interface to absorb the reflected/radiated waves from the objects. Note that although we do not deal with roll motions in this abstract, i.e. the results below are obtained with the approximation that the objects are not allowed to rotate, the effects of rotation on drifts will be reported on in the presentation and future publication.

3 NUMERICAL RESULTS

Drift of fluid parcels: We consider ideal fluid parcels, regarded as infinitely small objects, on regular waves in deep water with two different frequencies (low frequency ω=4.09 rad/s and high frequency ω=7.85 rad/s). For each frequency, a series of waves are simulated with different wave amplitudes, corresponding to different wave steepnesses ranging from 0.03 to 0.13, and the horizontal drift velocities of fluid particles are calculated to make comparison with the theoretical Stokes drift. First shown in [1], the horizontal component of Stokes drift velocity $\bar{u}_{sd}$ is given by

$$\bar{u}_{sd} = a^2 \omega k e^{2kz} = \varepsilon^2 \frac{\omega}{k} e^{2kz}, \tag{1}$$

where a denotes wave amplitude, ω is angular frequency, k is wave number and ε=ka is the wave steepness. The mean drift velocities of fluid particles in quasi-steady state are obtained by applying the best linear fit to its horizontal trajectory and determining the slope of the linear fit line. A comparison between the numerical results and theoretical Stokes drift is given in Fig.1. The theoretical Stokes drift is obtained by Eq. 1, in

which z is equal to the vertical position of the tracked particles z_p. A non-dimensional velocity $\bar{u}_p / c$, where $c=\omega/k$ is the phase speed of the waves, is employed. Excellent agreement is achieved between the numerical results and the theoretical solution for cases of both higher and lower frequencies with various wave steepnesses validating our model and confirming its ability to predict the drift velocity of an infinitely small object. Convergence tests of three target quantities (surface elevation η, mean Eulerian velocity u_E and drift rates $\bar{u}_p$ of a fluid parcel) have been carried out for both grid mesh resolution as well as the length of the relaxation zone. In the interest of brevity, the results are not shown here.

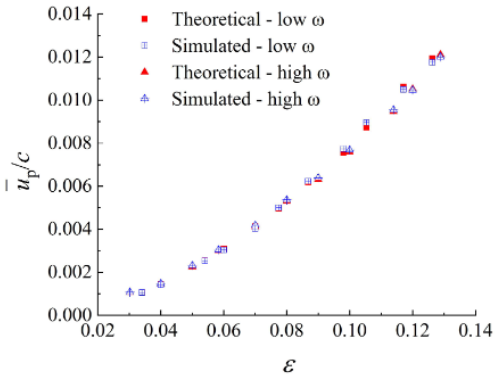

Figure 1 Horizontal drift velocities of fluid parcels.

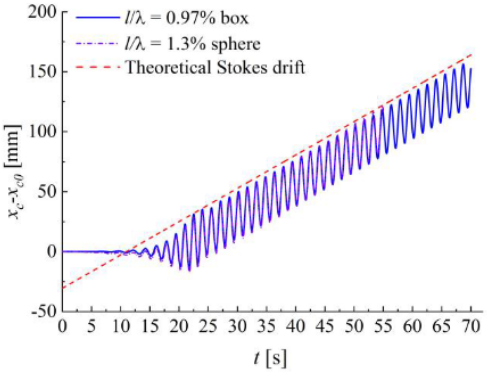

Figure 2 Example of horizontal trajectory of a small object.

Drift of very small objects: We next examine the drift of objects that are small relative to the wavelength but where there still is some wave/body interaction. Experiments support the intuition that when an object is small enough, its behaviour becomes purely Langrangian[4]. Two different object shapes are examined here: a rectangular box and a sphere. The wave condition is chosen from the above simulation as the case with ω=4.09 rad/s, ka=0.034. The size of the rectangular box is l=0.036 m (l/λ=1%), in which λ indicates the wavelength, l the length of the box in the direction of wave propagation. The diameter of the sphere is D =0.05 m (D/λ=1.3%). Both objects have the same density of ρ=500 kg/m^3. The height of the box and the radius of the sphere are chosen to make sure that the object will not be submerged by the waves.

The time history of the horizontal motion of the centre of mass x_c of both objects is given in Fig. 2 and compared with the theoretical Stokes drift. The initial position (t=0 s) of the centre of mass of the objects is given by x_{c0}. Satisfactory agreement is observed between the simulated results and the theoretical Stokes drift, validating the model and confirming that the drift of very small objects is equal to the Stokes drift.

Table 1 Scale parameters of the objects.

l/λ	1%	2%	3%	4%	5%	6%	7%	8%	9%	10%
D (m)	0.05	0.074	0.11	0.15	0.19	0.22	0.258	0.294	0.332	0.369
l (m)	0.036	0.074	0.11	0.15	0.19	0.22	0.258	0.294	0.332	0.369
h (m)	0.05	0.1	0.15	0.2	0.25	0.3	0.35	0.4	0.45	0.5

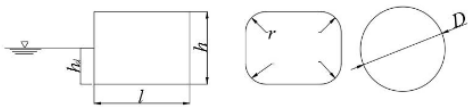

Figure 3 Shapes of the objects.

Drift of objects of different sizes and shapes: Drift motions of objects of different sizes and shapes are examined here in the waves with low steepness. The shape of the objects along with the definitions of the scale parameters are given in Fig. 3. We define the following dimensionless parameters: relative object size is described by l/λ or D/λ; the radius of the corners of the round-cornered box is described by $r/(h/2)$, the density of all the objects ρ=500 kg/m^3. To investigate how size and shape of an object affect its transport and what role viscosity plays, we conduct a series of simulations with three object shapes and a range of sizes: a box with sharp corners, a box with round corners, and spheres. For the box with round corners, we set $r/(h/2)$=0.24. The relative size of objects, measured by wavelength, ranges from 1% up to 10% in 1%-point steps. The detailed scale parameters of the objects are given in Tab. 1. The difference between a sharp-

cornered box (SC) and round-cornered box (RC) is only the corner type, and the differences between a round-cornered box and a sphere (SP) with equivalent size are the submerged shape and submergence of the object. The simulations are performed with and without viscosity. Fig. 4 (a) provides the celerity-normalized drift velocity $\bar{u}_c / c$ as a function of relative object size. The vertical motion magnitudes Z_a are shown in Fig. 4 (b) as a function of relative object size, in which the magnitude is the time-averaged value after the quasi-steady state has been achieved.

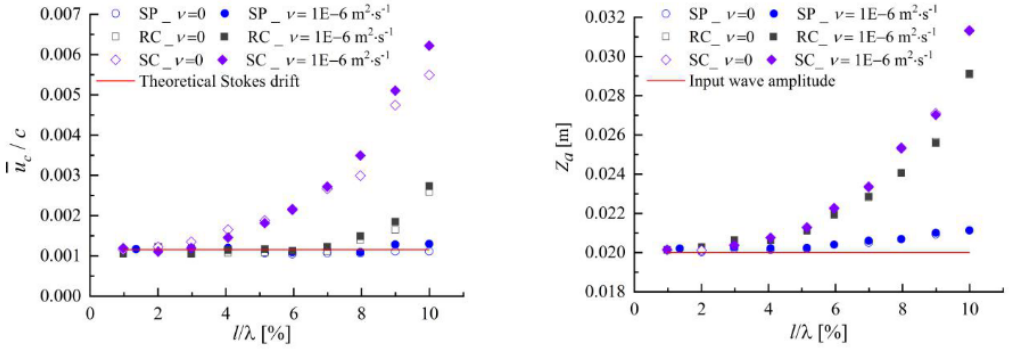

(a) Horizontal drift velocities of differently shaped objects (b) Vertical motion amplitude of differently shaped objects

Figure 4 Simulation results for different objects with viscosity (ν =10^{-6} m$^2 \cdot$ s^{-1}) and without viscosity (ν =0).

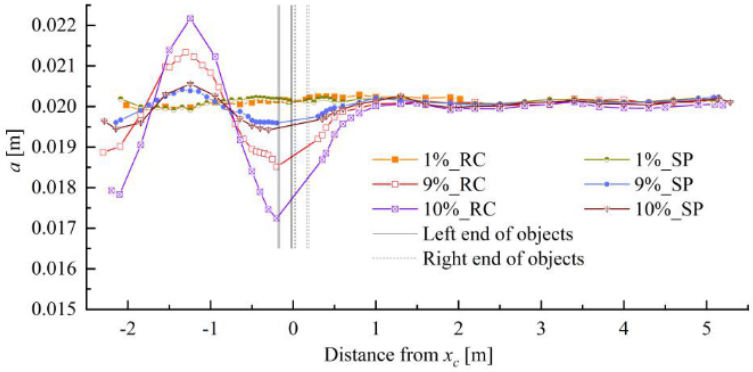

Figure 5 Distribution of amplitude of the surface elevation along horizontal direction

We start by examining the objects that experience the largest increases in drift, the group of sharp-cornered box (SC), as shown in Fig. 4 (a). We observe that when the box is very small, its drift rate is equal to the Stokes drift, while, as the box becomes larger, the drift speed is enhanced significantly along with an increase of the vertical motion magnitude. This phenomenon is clearly visible with and without viscosity. The enhanced drift is less observable for the cases of round-cornered box (RC) with relative size less than 7%, but becomes more discernible as size increases. The trends are similar whether or not viscosity is included. However, for spheres (SP), as depicted in the figure, no obvious enhancement of drift speed is found in the absence of viscosity even when the relative size is as large as 10%. In the presence of viscosity, small, enhanced drift is observed as the sphere becomes larger.

There is a large difference between the sharp-cornered boxes and the two other object types. Following scrutiny of the fluid fields during the simulations we found that, for sharp-cornered boxes, significant additional vorticity is generated around the sharp corners compared with the round-cornered boxes and the spheres, which manifest no obvious vorticity (no figures shown here for brevity). Although we do not explore the effect of vorticity in depth here, it is evident that the effects of flow separation, viscosity and vorticity are important factors in determining wave-induced drift. The discrepancy between the drift speeds of the round-cornered box and the sphere becomes large when the relative size of the object is larger than 7%. The increased drift is always accompanied by an increase of the amplitude of the vertical motion, as shown in the Fig. 4 (a) and (b). To further explain this phenomenon, we conduct an analysis of the wave field for round-cornered boxes and spheres. Fig. 5 depicts the wave amplitude as a function of the horizontal distance to the centre of mass of the objects for cases of 9% and 10% relative size for the round-cornered box (RC) and the sphere (SP). The results for 1% relative size are also given for comparison. A standing wave pattern

forms, and there are differences in the surface elevation amplitude on both sides of the objects; the differences are larger for larger boxes. This pattern is less clear for round-cornered boxes with a relative size smaller than 7% (not presented here for brevity) and for spheres, as seen in Fig. 5. This explains the previous observation that spheres in the absence of viscosity do not experience any observable increase in drift unlike the round-cornered boxes of equivalent size. The diffraction-based mechanism involved will be discussed further in the presentation and in future publications.

Here, we further examine the role played by viscosity. Compared with the result for spheres in the absence of viscosity (no significant drift increase for all sizes), enhanced drift becomes evident when the sphere is larger than 8% relative size and when viscosity is considered. For the round-cornered boxes, for which the standing wave pattern only comes into play for relatively large boxes, when this pattern is small, which is the case of objects smaller than 7% relative size, the presence of viscosity contributes to the drift increase in a way consistent with the spheres. As the round-cornered box becomes larger, the draft (submergence) of the box becomes larger, and the standing wave pattern becomes a dominant driver for drift increase. Viscosity works to promote the enhanced drift and yields a larger drift increase compared to the case without viscosity included.

For the sharp-cornered boxes, when the object has a relative size of 1%, viscosity has no influence on the drift, and drift is equal to the Stokes drift. For objects of relative size smaller than 5%, the presence of viscosity slightly reduces the drift enhancement, whereas for the cases of relative size larger than 6%, the drift velocity of the cases with viscosity included experience greater increase compared with their non-viscous counterparts. The influence of viscosity is a combination of its influence on vorticity and their effect on drift directly.

4 CONCLUSION

The effects that size, shape, and submergence impose on the mean drift motions of objects subjected to regular waves in deep water with low wave steepness are explored using a numerical model that both encompasses viscous effects and can model wave-body interaction. The results for fluid parcels and very small objects compare well with the theoretical Stokes drift. The simulations are carried out with and without viscosity for several different objects of different size, shape, and submergence. The dependence of mean drift rates on these factors is investigated. We identify two mechanisms that can explain increased drift, at a rate faster than the Stokes drift: viscosity and wave amplitude imbalance between the two sides of the object as part of a standing wave pattern resulting from diffraction by the object. Both these mechanisms come into play as the size of the object becomes larger. We note that our model is further validated by comparing the linear motion of the object and the surface elevation distribution with the results from a boundary element method. The results are consistent with the limited experimental evidence and analytical analysis[2,5-6]. Ongoing work concerning the effect of submerged shape and submergence on drift through diffraction will be reported on in the presentation.

Acknowledgement

This research work was supported by the China Scholarship Council-PAG Oxford Scholarship.

REFERENCES

[1] Stokes G G. 1880. *On the theory of oscillatory waves*. Transactions of the Cambridge philosophical society.

[2] Calvert, R., McAllister, M. L., Whittaker, C., Raby, A., Borthwick, A. G. L., & Van Den Bremer, T. S. 2021. *A mechanism for the increased wave-induced drift of floating marine litter*. Journal of Fluid Mechanics, 915.

[3] Yan, S., Wang, J., Wang, J., Ma, Q., & Xie, Z. 2020. *CCP-WSI blind test using qaleFOAM with an improved passive wave absorber*. International Journal of Offshore and Polar Engineering, 30(01), 43-52.

[4] Van Den Bremer, T. S., Whittaker, C., Calvert, R., Raby, A., & Taylor, P. H. 2019. *Experimental study of particle trajectories below deep-water surface gravity wave groups*. Journal of Fluid Mechanics, 879, 168-186.

[5] He, M., Ren, B., & Qiu, D. H. 2016. *Experimental study of nonlinear behaviors of a free-floating body in waves*. China Ocean Engineering, 30(3), 421-430.

[6] Huang, G., Law, A. W. K., & Huang, Z. 2011. *Wave-induced drift of small floating objects in regular waves*. Ocean Engineering, 38(4), 712-718.

Numerical Simulation of Turbulent Structures under Breaking Waves

Zhihua Xie[1,3], **Maurizio Brocchini**[2], **Pengzhi Lin**[3]
[1]School of Engineering, Cardiff University, Cardiff, CF24 3AA, UK
[2]Department of Civil and Building Engineering, and Architecture, Universit a Politecnica delle Marche, 60131 Ancona, Italy
[3]State Key Laboratory of Hydraulics and Mountain River Engineering, Sichuan University, China
E-mail Address of the presenting author: zxie@cardiff.ac.uk

HIGHLIGHTS

- A large-eddy simulation model is developed to simulate turbulent two-phase flows under breaking waves with pre- and post-breaking processes.
- The 3D Piece-wise Linear Interface Calculation Volume-of-Fluid (PLIC-VOF) is implemented for interface capturing.
- The surface tension effect is considered for the bubble and droplet break-up and coalescence.

1 INTRODUCTION

Wave breaking plays an important role in marine hydrodynamics, wave-structure interaction, air-sea interaction, surf zone dynamics, and nearshore sediment transport [1]. With the development of the numerical methods for the Navier–Stokes equations and free surface flows, several numerical studies have been performed to further our understanding of breaking waves, such as periodic waves in the surf zone [2, 3, 4], focusing wave [5], deep-water breaking waves in a periodic domain [6, 7, 8, 9, 10, 11], and shallow-water breaking waves over complex topography [12], which have provided much insight into the kinematics and dynamics of breaking waves, including the overturning jet and the subsequent splash-up process. In this study, a 3D large-eddy simulation based two-phase flow model is developed to investigate the turbulent vortical structures under the breaking waves, with the surface tension effect being taken into account for the small-scale bubble and droplet break-up and coalescence process. In addition, a Cartesian cut-cell method is developed to deal with complex topography and wave-structure interaction, which can provide detailed information on the impact force and energy dissipation during wave breaking.

2 MATHEMATICAL MODEL

The large-eddy simulation (LES) approach is adopted in this study, for which the large-scale turbulence is resolved and a subgrid-scale model is employed to compute the unresolved scales of turbulence. The governing equations used for incompressible two-phase flow are based on the spatially filtered Navier–Stokes equations, given as:

$$\boldsymbol{\nabla} \cdot \bar{\boldsymbol{u}} = 0, \tag{1}$$

$$\frac{\partial(\rho\bar{\boldsymbol{u}})}{\partial t}+\boldsymbol{\nabla}\cdot(\rho\bar{\boldsymbol{u}}\otimes\bar{\boldsymbol{u}})=-\boldsymbol{\nabla}\bar{p}+\boldsymbol{\nabla}\cdot[\mu(\boldsymbol{\nabla}\bar{\boldsymbol{u}}+\boldsymbol{\nabla}^{T}\bar{\boldsymbol{u}})]+\rho\boldsymbol{g}+\sigma\kappa\tilde{\mathbf{n}}\delta+\boldsymbol{\nabla}\boldsymbol{\tau}^{\mathrm{sgs}}, \tag{2}$$

where the overbar $\bar{\cdot}$ denotes the spatial filtering over the grid in Cartesian coordinates (x, y, z), $\bar{\boldsymbol{u}}=(\bar{u},\bar{v},\bar{w})$ is the filtered velocity vector and $\bar{p}$ is the filtered pressure. t is the time, $\boldsymbol{g}$ is the gravitational acceleration vector, ρ and μ are the density and dynamic viscosity of the fluid, σ is the surface tension coefficient, κ is the interfacial curvature, $\tilde{\mathbf{n}}$ is the interface unit normal, δ is the Dirac delta function.

The term $\boldsymbol{\tau}^{\mathrm{sgs}}=\rho(\overline{\bar{\boldsymbol{u}}\bar{\boldsymbol{u}}}-\overline{\boldsymbol{u}\boldsymbol{u}})$ is the subgrid-scale (SGS) stress tensor and the anisotropic part of the SGS term is modelled by an eddy-viscosity model of the form:

$$\boldsymbol{\tau}^{\mathrm{sgs}}-\frac{1}{3}\mathrm{trace}(\boldsymbol{\tau}^{\mathrm{sgs}})\boldsymbol{I}=2\mu_t\bar{\boldsymbol{S}}, \tag{3}$$

where $\boldsymbol{I}$ is the unit tensor and $\bar{\boldsymbol{S}}$ is the strain rate tensor of the resolved field. μ_t is the turbulent eddy viscosity defined as:

$$\mu_t=\rho C_d\bar{\Delta}^2\left|\bar{\boldsymbol{S}}\right|,\text{and}\left|\bar{\boldsymbol{S}}\right|=\sqrt{2\bar{\boldsymbol{S}}\bar{\boldsymbol{S}}}, \tag{4}$$

with the cut-off length scale $\bar{\Delta}=(\Delta x\Delta y\Delta z)^{1/3}$ and the coefficient C_d is calculated by the dynamic SGS model in the present study.

The momentum equation is closed with the constitutive relations for the density and dynamic viscosity of the fluid

$$\rho=F\rho_{\mathrm{w}}+(1-F)\rho_{\mathrm{a}}, \tag{5}$$

$$\mu=F\mu_{\mathrm{w}}+(1-F)\mu_{\mathrm{a}}, \tag{6}$$

where the subscripts w and a denote fluid water and air, respectively. F is the volume fraction of water and the air-water interface is governed by

$$\frac{\mathrm{d}F}{\mathrm{d}t}=\frac{\partial F}{\partial t}+\bar{\boldsymbol{u}}\cdot\boldsymbol{\nabla}F=0. \tag{7}$$

These equations complete the mathematical description of the two-phase flow model.

3 NUMERICAL METHODS

A Cartesian grid multiphase flow solver (Xdolphin3D), based on the 3D LES approach, is used for the computations. The governing equations are discretised using the finite volume method on a staggered Cartesian grid. The advection terms are discretised using a high-resolution scheme, combining high order accuracy with monotonicity, whereas the gradients in the pressure and diffusion terms are obtained using a central difference scheme. A Cartesian cut-cell method [13] is developed to deal with the complex topography. The PISO algorithm is employed in the present study for the pressure-velocity coupling and a second-order backward Euler method is used for the time derivative. In this study, the model has been further developed to capture the air-water interface by a geometric PLIC-VOF (Piece-wise Linear Interface Calculation Volume-of-Fluid) method [14], and the continuum surface force model is implemented for the surface tension effect. The multiphase flow code Xdolphin3D has already been extensively verified and validated through numerous test cases for breaking waves [12], wave-structure interaction [15], and LES studies of free surface flows over rough beds [16].

4 RESULTS AND DISCUSSION

The third-order Stokes wave in a periodic domain is considered here, similar to previous 2D [6, 7] and 3D [8, 9, 10, 11] studies. The simulation is initialised with a modified potential solution of water waves, the third-order Stokes wave solution for the air-water interface and velocity potential [17] in the water. The velocity in the air is initialised as zero as little is known in the air. The computational domain of $L \times L \times 0.5L$ (where L is the wave length) is discretised by a uniform mesh $512 \times 512 \times 256$ in the streamwise, vertical, and spanwise direction. Periodic boundary conditions are used in both streamwise and spanwise direction. The corresponding Reynolds number and Weber number are $Re = 10^5$ and $We = 100$, respectively.

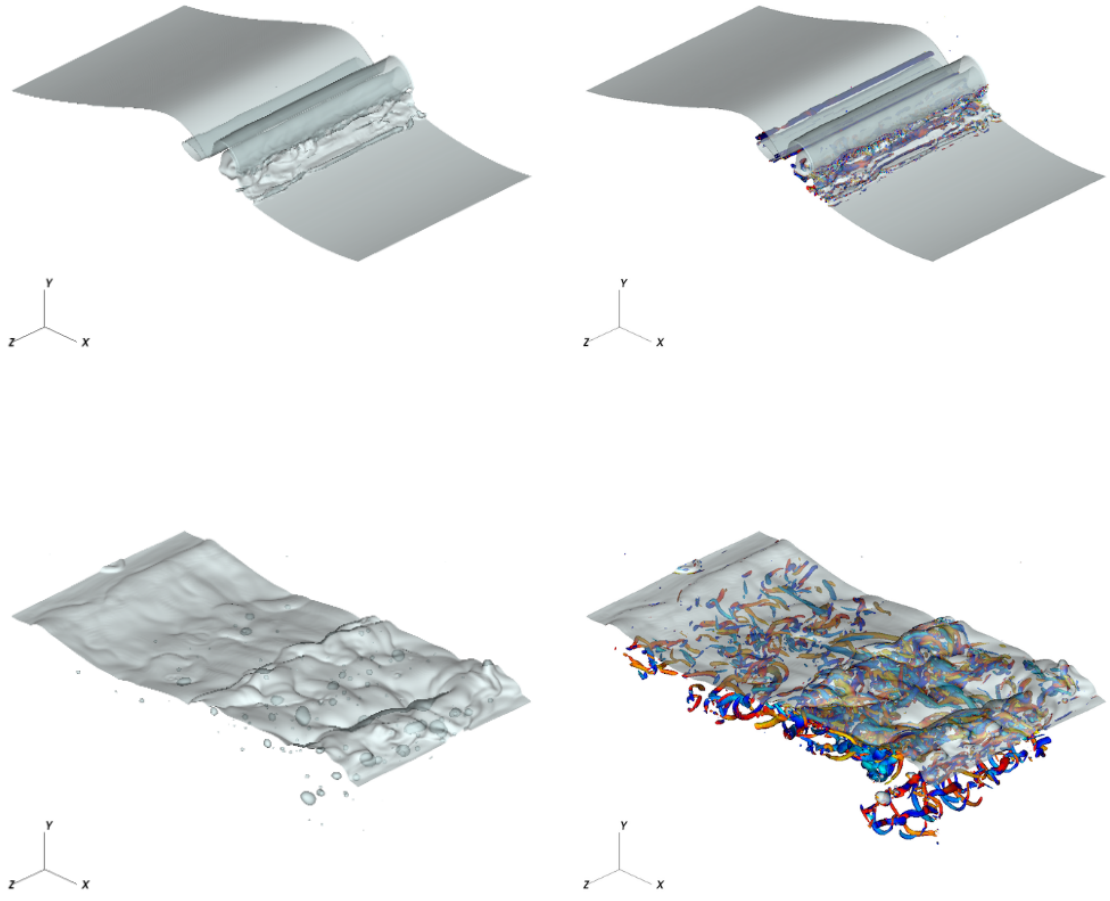

Figure 1: Snapshots of air-water interface (left panel) together with their vortex structures identified by the λ_2 method (right panel) at two instants during wave-breaking process.

Figure 1 shows some snapshots of the air-water interface and the vortex structures during wave breaking processes. It can be seen that the splash-up is generated when the plunging jet hits the water surface ahead. Small-scale bubbles and droplets are generated during the wave-breaking process. There is complex vortex structure-bubble interaction during the coalescence.

More results of the kinematics and dynamics of 3D breaking waves interaction with fixed and moving bodies will be presented at the workshop.

ACKNOWLEDGMENTS

This work was financially supported by the Engineering and Physical Sciences Research Council (EPSRC) through grant (EP/V040235/1), the Royal Society Newton Advanced Fellowship (NAF/R1/201156) and International Exchanges (IES/R2/202095), and the Open Fund of the State Key Laboratory of Hydraulics and Mountain River Engineering at Sichuan University (SKHL1904). The financial support from the MIUR PRIN 2017 Project, titled "FUNdamentals of BREAKing wave-induced boundary dynamics – FUNBREAK" (Grant Number 20172B7MY9) is also gratefully acknowledged.

REFERENCES

[1] Brocchini, M., and Peregrine, D. H. 2001. *The dynamics of strong turbulence at free surfaces. Part 1. Description. Journal of Fluid Mechanics 449*, 225–254.

[2] Lin, P., and Liu, P. L. F. 1998. *A numerical study of breaking waves in the surf zone. Journal of Fluid Mechanics 359*, 239–264.

[3] Watanabe, Y., Saeki, H., and Hosking, R. J. 2005. *Three-dimensional vortex structures under breaking waves. Journal of Fluid Mechanics 545*, 291–328.

[4] Lakehal, D., and Liovic, P. 2011. *Turbulence structure and interaction with steep breaking waves. Journal of Fluid Mechanics 674*, 522–577.

[5] Derakhti, M., and Kirby, J. T. 2016. *Breaking-onset, energy and momentum flux in unsteady focused wave packets. Journal of Fluid Mechanics 790*, 553–581.

[6] Chen, G., Kharif, C., Zaleski, S., and Li, J. 1999. *Two-dimensional Navier-Stokes simulation of breaking waves.* Physics of Fluids 11(1), 121–133.

[7] Iafrati, A. 2009. *Numerical study of the effects of the breaking intensity on wave breaking flows. Journal of Fluid Mechanics 622*, 371–411.

[8] Lubin, P., and Glockner, S. 2015. *Numerical simulations of three-dimensional plunging breaking waves: generation and evolution of aerated vortex filaments. Journal of Fluid Mechanics 767*, 364–393.

[9] Deike, L., Melville, W. K., and Popinet, S. 2016. *Air entrainment and bubble statistics in breaking waves. Journal of Fluid Mechanics 801*, 91–129.

[10] Wang, Z., Yang, J., and Stern, F. 2016. *High-fidelity simulations of bubble, droplet and spray formation in breaking waves. Journal of Fluid Mechanics 792*, 307–327.

[11] Chan, W. H. R., Johnson, P. L., Moin, P., and Urzay, J. 2021. *The turbulent bubble break-up cascade. Part 2. Numerical simulations of breaking waves. Journal of Fluid Mechanics 912.*

[12] Xie, Z. 2015. *A two-phase flow model for three-dimensional breaking waves over complex topography. Proceedings of the Royal Society A 471*, 20150101.

[13] Xie, Z., and Stoesser, T. 2020. *A three-dimensional Cartesian cut-cell/volume-of-fluid method for two-phase flows with moving bodies. Journal of Computational Physics 416*, 109536.

[14] Gueyffier, D., Li, J., Nadim, A., Scardovelli, R., and Zaleski, S. 1999. *Volume-of-fluid interface tracking with smoothed surface stress methods for three-dimensional flows.* Journal of Computational Physics 152(2), 423–456.

[15] Xie, Z., Stoesser, T., Yan, S., Ma, Q., and Lin, P. 2020. *A Cartesian cut-cell based multiphase flow model for large-eddy simulation of three-dimensional wave-structure interaction. Computers & Fluids 213*, 104747.

[16] Xie, Z., Lin, B., Falconer, R., Nichols, A.N. Tait, S., and Horoshenkov, K. 2021. *Large-eddy simulation of turbulent free surface flow over a gravel bed. Journal of Hydraulic Research.* , in press.

[17] Deike, L., Popinet, S., and Melville, W. 2015. *Capillary effects on wave breaking. Journal of Fluid Mechanics 769*, 541–569.

Local resonances within an array of C-shaped cylinders in water waves

J. Xu[1], D.Z. Ning[1], L. Chen[1, 2], C.W. Zhang[1], B. Teng[1]

[1]State Key Laboratory of Coastal and Offshore Engineering, Dalian University of Technology, Dalian, 116024, China.

[2]Oceans Graduate School, Faculty of Engineering and Mathematical Sciences, The University of Western Australia, M053, Perth WA 6009, Australia.

1. Introduction

Recently, the interaction between waves and periodic structures has attracted considerable attention, noting various resonance behaviors, e.g. the so-called Bragg resonance for uniform periodic ripples [1], and rainbow trapping for graded or chirped arrays in which the properties of the array spacing or elements vary spatially [2]. The concepts built on these resonance mechanisms have been proposed for coastal protection by blocking certain waves [3] or for amplifying wave-energy harvesting by focusing wave energy of different frequencies at different spatial locations [2].

It is well recognized that these resonances of periodic solid structures (e.g. bottom mounted vertical cylinders) occur when the wavelength is comparable to the periodic spacing of the structures [4]. Thus, the proposed concepts/systems normally fail to function in long-wave regime [5]. This is crucial as tsunamis and storm swells are in this category.

Metamaterials, consisting of e.g. split-ring/tube or C-shaped cylinder arrays, in acoustics are known to be able to incur a new type of resonance at frequencies far below those of conventional Bragg resonances [4]. This provides attractive alternatives in the water-wave context. Hu et al. [6] and Dupont et al. [7] have demonstrated that the propagation of low-frequency water waves through a line of C-shaped cylinders is indeed prohibited, and Bennetts et al. [8] extended the concept by grading the cylinder properties. Although Chalmers et al. [9] argued that the formation of this low-frequency-type resonance may be associated with the resonance of the air column within each individual resonator, the underlying mechanics applied to water waves, including the effects of wave nonlinearity and water viscosity, remain unclear.

This work investigates nonlinear water wave propagation through a line array of C-shaped cylinders with an emphasis on identifying and characterizing this low-frequency-type resonance. The so-called band diagram derived using the Bloch theorem is used for identifying the frequency bands/gaps within which the wave transmission/propagation is blocked. The band diagram is initially proposed for solid-state physics of semiconductors, and is extended to water waves by e.g. Evans and Porter [10], and McIver [11]. The local wave fields are detailed for investigating the captured resonant behaviors using first linear potential flow theory and latter more sophisticated CFD-based simulations. The effects of various wave parameters and dimensions of the C-shaped cylinder are also analyzed.

2. Results and Discussion

We consider a water domain of infinite horizontal extent (defined as along x-axis), and constant finite depth h (defined as along z-axis). The vertical coordinate z points upwards, with its origin coinciding with the mean water level, and $z = -h$ denoting the bottom. The domain is bounded by a flat bottom and by a free surface, and a line array of M vertical C-shaped cylinders are placed along the centerline of the domain; details referred to Figs. 3-4. The spacings between adjacent C-shaped cylinders in x and y directions are labelled as a and b, respectively, and the individual C-shaped cylinder is characterized by its outer radius R_1, inner radius R_2, and opening l_n - see Fig. 1 left in which a periodic unit is shown. This unit is used to obtain the band diagram using Bloch theorem; details to be followed.

As mentioned above, the problem of wave-periodic structure interaction is first considered within the framework of linear potential flow theory; the flow motion can then be described by the velocity potential,

$$\Phi(x,y,z,t)=\mathrm{Re}\left\{\phi(x,y)\frac{\cosh\left(k(z+h)\right)}{\cosh(kh)}e^{i\omega t}\right\} \tag{1}$$

where t is the time, and ϕ is depth independent, hence, satisfies the Helmholtz equation in the fluid domain,

$$\left(\nabla^2+k^2\right)\phi=0 \tag{2}$$

where k is the wavenumber, satisfying the dispersion relation $\omega^2=gk\tanh(kh)$ with ω being the angular wave frequency, and g the acceleration due to gravity.

The no-flow boundary conditions are applied on the surfaces of the C-shaped cylinders and the flat bottom,

$$\nabla\phi\cdot\mathbf{n}=0 \tag{3}$$

where $\boldsymbol{n}$ is the outward unit normal vector.

In Bloch theorem, the solutions for infinite periodic structures, Eqs. (1-3), are resolved within a periodic unit as shown in Fig. 1 (left); the boundaries of which should then satisfy [11],

$$\phi(a,y)=e^{iq_1a}\phi(0,y) \quad \text{and} \quad \partial\phi(a,y)/\partial x=e^{iq_1a}\partial\phi(0,y)/\partial x \quad \text{in the } x \text{ direction} \tag{4}$$

$$\phi(x,b)=e^{iq_2b}\phi(x,0) \quad \text{and} \quad \partial\phi(x,b)/\partial y=e^{iq_2b}\partial\phi(x,0)/\partial y \quad \text{in the } y \text{ direction} \tag{5}$$

where q_1 and q_2 are the x- and y-components of Bloch wave vector defined in the reciprocal space, respectively, and can be complex numbers in water waves [11]. For given q_1a ($\in[0, \pi]$) and q_2 ($= 0$; as only wave propagation along x-axis is considered), the solutions for the eigenvalues k are obtained by solving Eq. (2) using the finite element method; the first three eigenvalues are considered in this work, see e.g. Fig. 1 (right; solid lines).

The numerical solutions are first used to reproduce the experiments in Dupont et al. [8] for validation. As in Dupont et al., $a = b = 0.65$ m, $R_1 = 0.15$ m, $R_2 = 0.145$ m, and $l_n = 0.16$ m. Firstly, the calculated band diagram considering infinite arrays is shown in Fig. 1 right. It can be seen that there are two frequency ranges (characterized by ka; and shaded by blue) within which no real values of q_1 can be found. These are so-called stopping bands (or band gaps). As a result, the incident wave of the frequency in these stopping bands is blocked by the periodic structure; the wave amplitude is attenuated and eventually decreases to zero as infinite number of cylinders is considered. The frequencies outside the stopping bands are otherwise formed the so-called passing bands within which the waves can propagate freely through the array with changes only in phase. It is found that the band gap $ka\in[3.08, 3.88]$ corresponds to the well-known Bragg resonances associated with the periodic nature of the array [9], and the band gap $ka\in[1.96, 2.80]$ falls in the category of low-frequency-type resonances.

Then the array of three C-shaped cylinders is considered, facilitating a direct comparison with the experiments (only finite number of cylinders can be considered in laboratory). The absorbing boundary conditions (the method of numerical beach is applied in this work) are applied at the left and right ends of the numerical flumes for absorbing reflected waves from the domain. The calculated transmission coefficients are compared with the experimental data in Fig. 2. It can be seen that the

transmission coefficients are nearly zero or very small in two separated regions, which are overlapped with the band gaps identified in Fig. 1. Main trend is captured by the present numerical solutions, although differences are observed. This could be due to the energy dissipation and wave breaking at the slits in the experiments; details will be presented at the workshop.

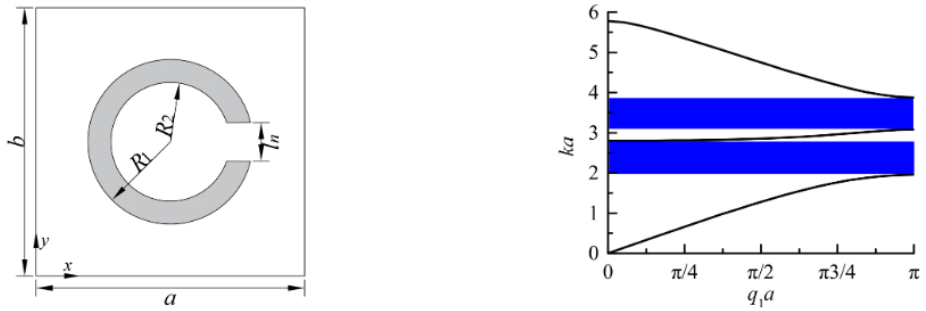

Fig. 1 Layout of a periodic unit of a line array of infinite C-shaped cylinders (left) and the band diagram calculated using Bloch therom (right). The band gaps are shaded by blue. $a = b = 0.65$ m, $R_1 = 0.15$ m, $R_2 = 0.145$ m, and $l_n = 0.16$ m.

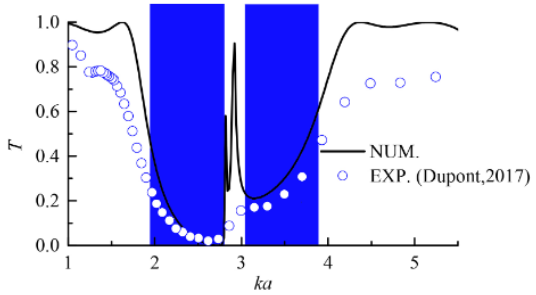

Fig. 2 Comparison of numerical results of the transmission coefficient with experiment data. (M = 3; $a = b = 0.65$ m, $R_1 = 0.15$ m, $R_2 = 0.145$ m, and $l_n = 0.16$ m)

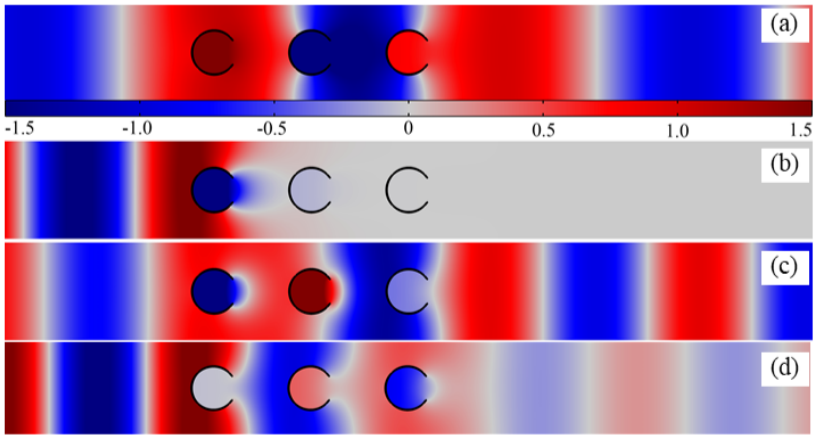

Fig. 3 Contour of non-dimensional free surface elevations at $ka = 1.63$ (a), 2.74 (b), 2.92 (c) and 3.27 (d).

Figs. 3(a) ~ (d) show the contour of non-dimensional free surface elevations for four typical frequencies, $ka = 1.63$, 2.74, 2.92 and 3.27, respectively. As expected, no resonance occurs and the waves of frequencies outside the band gaps are free to propagate through the array, see Figs. 4 (a) and (c). While the wave energy of frequency $ka = 2.74$ in the second band gap and $ka = 3.17$ in the first band gap are blocked by the array; the differences is that for the former, only the first cylinder plays the role (Fig. 3 (b)), and the latter the amplitude attenuation starts at the first cylinder and evolves

along the array (Fig. 3(d)). This suggests that the resonance mechanism associated with the second band maybe a locally behavior incurred by the individual periodic unit, and the resonance in the first band should arise due to the periodic nature of the structure, consistent with the Bragg-type resonances. We note that similar resonance phenomenon in the second lower frequency band is observed by Elford et al. [4] in acoustic waves.

This is then further investigated by running numerical experiments with one and five C-shaped cylinders and results are shown in Fig. 4. It can be seen that the resonance still occurs even if there is only one C-shaped cylinder. Meanwhile, comparisons between Fig. 3 (b) and Fig. 4 show that the modes of resonance are the same around the first cylinder for the three cases considered. It indicates that this low-frequency-type resonance is indeed a locally resonance, and may be caused by the wave resonance in the cavity. More results regarding the effect of nonlinearity etc. will be presented at the workshop.

Fig. 4 Contour of non-dimensional free surface elevations at ka = 2.74 for cases with one (a) and five (b) C-shaped cylinders. For color maps see Fig. 3.

Acknowledgements

This work is supported by the LiaoNing Revitalization Talents Program (Grant No. XLYC2002033), Liaoning BaiQianWan Talents Program (Grant No. 2020921007) and Fundamental Research Funds for the Central Universities (Grant No. DUT21LAB116).

References

[1] Zhang, S. B., Chen, L., Ning, D. Z., & Teng, B. *Multi-Bragg reflections over a periodic submerged structure*. The 36h International Workshop on Water Waves and Floating Bodies, Seoul, Korea, 25-28 April, 2021

[2] Archer, A. J., Wolgamot, H. A., Orszaghova, J., Bennetts, L. G., Peter, M. A., & Craster, R. V. 2020. *Experimental realization of broadband control of water-wave-energy amplification in chirped arrays*. Physical Review Fluids, 5(6), 062801.

[3] Liu, H. W., Liu, Y., & Lin, P. 2019. *Bloch band gap of shallow-water waves over infinite arrays of parabolic bars and rectified cosinoidal bars and Bragg resonance over finite arrays of bars*. Ocean Engineering, 188, 106235.

[4] Elford, D. P., Chalmers, L., Kusmartsev, F. V., & Swallowe, G. M. 2011. *Matryoshka locally resonant sonic crystal*. The Journal of the Acoustical Society of America, 130(5), 2746-2755.

[5] Hu, X., Chan, C. T., Ho, K. M., & Zi, J. 2011. *Negative effective gravity in water waves by periodic resonator arrays*. Physical review letters, 106(17), 174501.

[6] Hu, X., Yang, J., Zi, J., Chan, C. T., & Ho, K. M. 2013. *Experimental observation of negative effective gravity in water waves. Scientific Reports*, 3(1), 1-4.

[7] Dupont, G., Remy, F., Kimmoun, O., Molin, B., Guenneau, S., & Enoch, S. 2017. *Type of dike using C-shaped vertical cylinders*. Physical Review B, 96(18), 180302.

[8] Bennetts, L. G., Peter, M. A., & Craster, R. V. 2018. *Graded resonator arrays for spatial frequency separation and amplification of water waves*. Journal of Fluid Mechanics, 854.

[9] Chalmers, L., Elford, D. P., Kusmartsev, F. V., & Swallowe, G. M. 2009. *Acoustic band gap formation in two-dimensional locally resonant sonic crystals comprised of Helmholtz resonators*. International Journal of Modern Physics B, 23(20n21), 4234-4243.

[10] Evans, D. V., & Porter, R. 1999. *Trapping and near-trapping by arrays of cylinders in waves*. Journal of Engineering Mathematics, 35(1), 149-179.

[11] McIver, P. 2000. *Water-wave propagation through an infinite array of cylindrical structures*. Journal of Fluid Mechanics, 424, 101-125.

Influence of Rigid/Deformable Foil Shape on the Hydrodynamic Loads and Performance

Huili Xu[1,*], Marilena Greco[1,2], Claudio Lugni[1,2]
[1]Centre for Autonomous Marine Operations and System (AMOS), Department of Marine Technology, NTNU, Trondheim, Norway
[2]CNR-INM, Institute of Marine Engineering, Rome, Italy
hui-li.xu@ntnu.no

1 INTRODUCTION

Many swimming fishes can be considered as underwater bio vehicles with high hydrodynamic efficiency and performance, such as low resistance, high speed, and good maneuverability. The basis source of their propulsion forces is the control of vortices produced by their oscillating bodies and fins. Inspired by fish, the thrust-producing harmonically oscillating foils have been studied extensively through both experimental and numerical techniques. In the present work, various two-dimensional (2D) flapping foils are studied with focus on the influence of rigid and deformable fish-like profiles on the hydrodynamic loads and performance. Herein, a morphing strategy of the foil is pursued to combine the advantages of the rigid foils with different shapes, that is, to maximize the thrust and efficiency while minimizing the required mean input power during pitching motion.

2 MODELLING AND METHODOLOGY

In order to understand better the flapping performances of foils with different profiles in a proper manner, three symmetric hydrofoils with the same chord length c are examined, as shown in fig. 1.

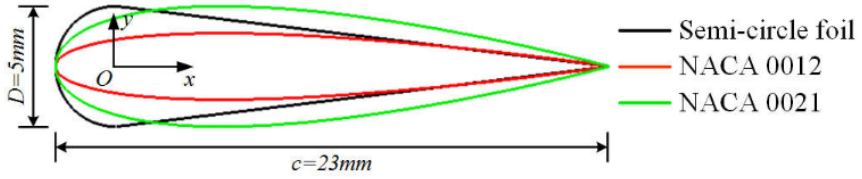

Figure 1: Schematic view of the examined fish-like foil profiles

The tear-shaped foil with a semicircular leading edge and a triangular form in the aft is adopted from a reference experiment [1]. The trailing edge of NACA 0012 foil is as sharp as the semi-circle foil, but its maximum thickness D is ~43% smaller. In contrast, we selected NACA 0021 foil that has the same maximum thickness as the semi-circle foil, but it is thicker in the aft part. Each foil was studied in the following scenario: placed in a uniform current with constant inflow speed U in the horizontal direction parallel to the x-axis and forced to perform pitching motions (about O and z-axis). The angular motions are described by $\theta(t) = \theta_0 \sin(\omega t)$. Here $\omega = 2\pi f$ is the angular frequency, and θ_0 is the maximum pitching angle. During the prescribed motion, the foil is aligned with the inflow at $\omega t = n\pi$ (with $n = 1,2,\dots$) and reaches the extreme inclined positions at $\omega t = n\pi + \pi/2$ (maximum rotation to the top) and $n\pi + 3\pi/2$ (maximum rotation to the bottom). In this work, the foils are studied with the following parameters: $f = 2.244s^{-1}$, $\theta_0 = 0.153rad$ (i.e., peak-to-peak amplitude at the trailing edge $A = 6.25mm$) and the chord-based Reynolds number, $Re = Uc/\nu$ (ν is the kinematic viscosity of fluid), is set as $Re = 1173$, i.e., consistent with the reference experimental study where quasi-2D mechanisms in the fluid-body interactions are documented.

The simulations are performed as 2D within a stepwise research strategy and using a thoroughly validated finite-volume-based code in the OpenFOAM platform based on a collocated grid. The

PIMPLE algorithm is employed for solving the incompressible Navier-Stokes equations, which combines PISO (Pressure Implicit with Splitting of Operator) and SIMPLE (Semi-Implicit Method for Pressure Linked Equations) algorithms. A second-order scheme is used for the space discretization, and the implicit Euler scheme is chosen for the time discretization as compromise between numerical accuracy and computational cost. To handle the large motions of pitching foil, the overset grid method is employed in this work [2]. The computational domain around the flapping foil is defined by a rectangle extending 5.2 chords upstream and 6.5 chords downstream. The domain transverse dimension is $-3.26c < y < 3.26c$, which is the same as the tunnel width in the reference experiment. Detailed boundary conditions are shown in fig. 2 and numerical-convergence analysis for this hydrodynamic problem can be found in [3]. Due to the linear interpolation between grids in openFOAM, the overset mesh is constructed so that the outermost layer of the moving mesh has comparable cell size as the background grid. Therefore, the employed grid has 3640 hexahedral cells in the overset region and 288000 structured cells for the background mesh.

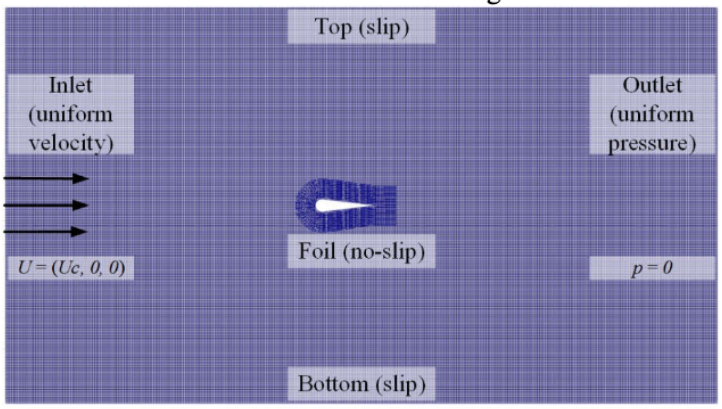

Figure 2: Computational domain and boundary conditions for the flapping foil

Additionally, all simulations are run on supercomputer VILJE nodes (Intel Xeon E5-2670) using 2 nodes (32 cores) per simulation and FRAM nodes (Intel E5-2683v4 2.1 GHz) with 1 node (32 cores) per simulation.

3 INFLUENCE OF RIGID FOIL SHAPE

The investigations of the three rigid foils focus on their thrust force F_x, input power requirement P and propulsion efficiency η. The corresponding nondimensional coefficients are defined, respectively, as $C_x = F_x/0.5\rho U^2 c$, $C_P = P/0.5\rho U^3 c$, and $\eta = F_x U/P = C_x/C_P$. Here ρ is the density of the fluid, P is the mechanical power required to activate the foil, calculated as $P = M_z\dot{\theta}$, with M_z the hydrodynamic torque. Based on the above definitions, the foil experiences thrust when $C_x < 0$ and requires input power when $C_P < 0$.

The steady-state behaviors of horizontal-force and power coefficients within one complete oscillation period for the three rigid hydrofoils are shown in fig. 3. Under the aforementioned conditions, the NACA 0012 and NACA 0021 foils are associated with thrust generation and drag generation, respectively, and the semi-circle foil is at the drag-thrust transition. C_x and C_P in the three cases are periodic with a period half of the pitching period, which is expected due to the symmetry of the foils and of their rotational motion with respect to the x-axis. Their extreme values occur nearly at the same phases ωt; this is exactly true for C_P and nearly true for C_x. In addition, the inflection points of the C_P curve practically synchronize with the extremes of the C_x curve, i.e., maximum instantaneous thrust/drag force. However, there are obvious differences among the results of the three foils. From the plots, the C_x curves for the NACA 0012 and semi-circle foils have similar oscillation amplitude,

while the one for the NACA 0021 foil has a slightly smaller value. This indicates that the force oscillation amplitude is dominated by mechanisms connected with the shape of the trailing edge and increases for sharper/thinner geometries. Besides, the NACA 0021 and semi-circle foils experience similar maximum drag (positive C_x), occurring slightly after the foil has passed its mean position, while the NACA 0012 foil has a smaller maximum drag; this confirms the primary role of the maximum thickness in the forward part of the foil for this force contribution. The C_P histories of the semi-circle foil and NACA 0012 foil practically coincide. The NACA 0021 foil has the same maximum C_P, but its minimum value at $\omega t = 7\pi/8$ has a smaller magnitude than that documented by the other two foils. Because the pitching frequency and amplitude are the same, the only reason for this is the torque experienced by the hydrofoils, as shown in the right plot of fig. 3. When the foils move from the extreme positions to the mean positions, the torque for NACA 0021 foil becomes smaller than for the other foils. This confirms the importance of the trailing edge shape in this case, and highlights that a thicker trailing edge leads to lower input power requirement. The influence of the foil shape can also be studied from the analysis on the pressure and friction components of the hydrodynamic force.

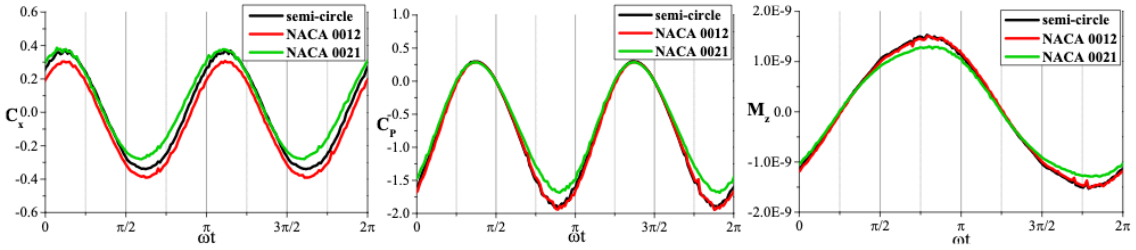

Figure 3: Steady-state horizontal force and input power coefficients and torque for the three rigid foils

4 INFLUENCE OF DEFORMABLE FOIL SHAPE

The analysis of the rigid flapping foils showed that the NACA 0012 foil is associated to the largest thrust but experiences the largest hydrodynamic torque, which might pose possible issues for robustness. This leads to the following research question: can we identify a morphing-foil strategy so to generate a thrust similar to that of the NACA 0012 foil while reducing the hydrodynamic torque to a level comparable to that of the NACA 0021 foil?

A first attempt to combine these advantages within a foil morphing strategy is to enforce that the foil becomes thicker when close to the mean position and thinner when close to the extreme positions. Therefore, the thickness of the foil profile is forced to change in time according to the law: $D(t) = D_0 + D_1(t) = D_0 + a_D(\cos(2\omega t + \phi) - 1)$, with D_0 the mean value and $D_1(t)$ the oscillating part with an amplitude a_D, a period half of the pitching period and a phase ϕ with respect to the pitching motion of the foil, set to zero as first attempt. To pursue our scope, the deformation parameters are chosen so to ensure that the foil profile is morphed between the NACA 0012 and NACA 0021 foils, as illustrated in fig. 4.

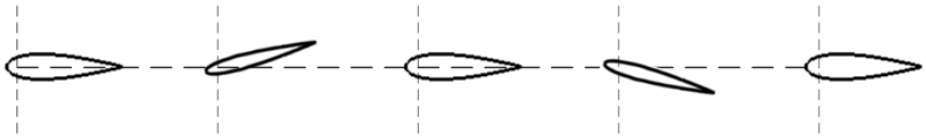

Figure 4: Schematic showing foil morphing between NACA 0012 and 0021 during one oscillation period

This deformable NACA foil is studied under the same pitching condition as for the rigid cases ($f = 2.244s^{-1}$ and $\theta_0 = 0.153rad$). Fig. 5 compares the horizontal force and power from the rigid and

deformable NACA foils. From the plots of C_x, the horizontal force for the deformable NACA foil is not in phase with those for the rigid foils. The deformable NACA foil generates the maximum thrust force (minimum C_x) at the extreme positions and experiences the largest drag just before reaching the mean positions. Its minimum C_x value is the same as for the blunt NACA 0021 foil, however, its maximum C_x value is even smaller than that for the streamlined NACA 0012 foil. Therefore, the deformable NACA foil generates a time-averaged thrust force, which is slightly smaller than that of the NACA 0012 foil, while the NACA 0021 foil suffers a mean drag. The time histories of C_P prove that the deformable NACA foil requires as less power as NACA 0021 foil to perform the prescribed pitching motion.

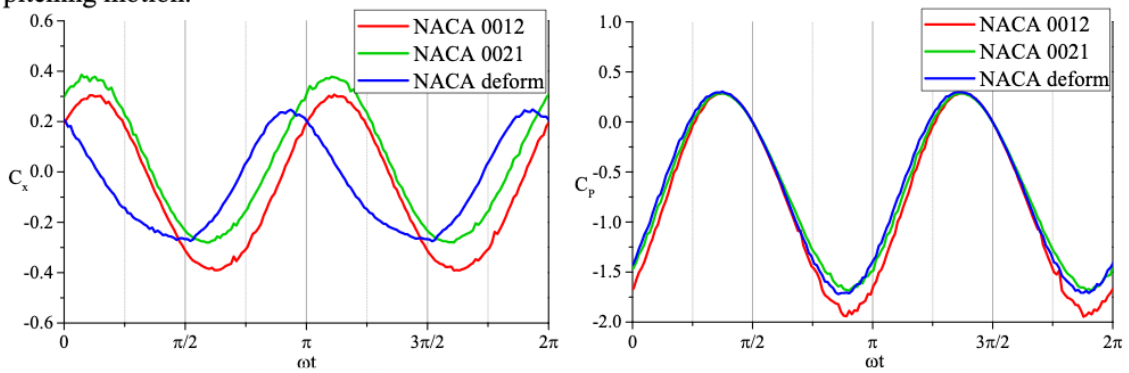

Figure 5: Steady-state horizontal force and input power coefficients for rigid and deformable NACA foils

This attempt proves that a morphing strategy could serve to our scope. This brings to the next research question: is it possible to identify an optimized morphing strategy so to maximize the mean thrust and efficiency while minimizing the required mean input power? To answer to this question, the phase ϕ has been systematically changed while keeping the other deformation parameters unchanged. The results of such investigation will be presented in the workshop.

5 CONCLUSIONS

Three rigid foils with different profiles and a series of deformable foils are studied under the same flapping conditions to investigate the influence of rigid/deformable foil shape on the hydrodynamic loads and performances. Here, a morphing-foil strategy based on the NACA 0012 and NACA 0021 foils is proposed and developed in the OpenFOAM platform to combine the advantages of the rigid foils. The results support that this strategy could enable to achieve large thrust force and high efficiency while reducing the requirement for input power.

ACKNOWLEDGEMENT

The work is sponsored by the Research Council of Norway through the Centre of Excellence funding scheme, project number 223254, AMOS. The simulations were performed on resources provided by UNINETT Sigma2 - the National Infrastructure for High Performance Computing and Data Storage in Norway.

REFERENCES

[1] Godoy-Diana, R., Aider, J. L., & Wesfreid, J. E., 2008. *Transitions in the wake of a flapping foil*. Phys. Rev. E, 77(1), 016308.

[2] Siddiqui, M. A., Xu, H. L., Greco, M., & Colicchio, G., 2020. *Analysis of Open-Source CFD Tools for Simulating Complex Hydrodynamic Problems*. In International Conference on Offshore Mechanics and Arctic Engineering (Vol. 84409, p. V008T08A036). American Society of Mechanical Engineers..

[3] Xu, H. L., Greco, M., & Lugni, C., 2021. *2D Numerical Study on Wake Scenarios for a Flapping Foil*. In International Conference on Offshore Mechanics and Arctic Engineering (Vol. 85185, p. V008T08A033). American Society of Mechanical Engineers.

(*Abstract for the 37th International Workshop on Water Waves and Floating Bodies, Giardini Naxos, Italy, 2022*)

On the modulation of a plane wave to oblique perturbations in finite water depth

Jiacheng Yang[1*] , Jinyu Yao[1] and Xinshu Zhang[1†]

[1]State Key Laboratory of Ocean Engineering, Shanghai Jiao Tong University, Shanghai 200240, China

Highlights

- The instability regions are re-drawn by ZE with kernels in a Hamiltonian form.
- The growth rates in arbitrary water depth by the HOS method and the discretized form of ZE are summarized and the results agree well with each other in particular for the most unstable modes.
- There is a reduction of modulational instability with decreasing the depth and there is still modulational instability in terms of $k_0h = 0.8$, which leads to a strong amplitude growth.

1 Introduction

For two-dimensional modulational instability, a carrier wave can be perturbated with a pair of collinear sidebands and the water depth plays an essential role. There is an evident threshold of the dimensionless water depth $k_0h = 1.363$ (k_0 is the wavenumber of the carrier wave and h is the water depth), which was first found by Benjamin (1967) and Whitham (1967), and confirmed by Janssen & Onorato (2007). As the result of the finite water depth, the wave-induced current and mean surface elevation are generated, which weakens the modulational instability and makes less focusing of the wave energy. Further more, it disappears when $k_0h < 1.363$ and hence the uniform wave train is stable.

However, for three-dimensional cases, a carrier wave is perturbated by a pair of oblique sidebands. Different from the former, the modulational instability can be triggered even when $k_0h < 1.363$. Benney & Roskes (1969) indicated that the unstable regions are limited in a narrow and approximately straight domain in any water depth except $k_0h = 0.38$ where the domain reduces to a straight line. In addition, by using an integro-differential equation of Zakharov (1968), Crawford *et al.* (1981) obtained the horn shape unstable region in the condition of infinite water depth. Stiassnie & Shemer (1984) further studied the same topic with the same approach but in finite water depth and the instability domain. The maximum growth rates were compared with those in McLean (1982). The experiment by Toffoli *et al.* (2013) and the numerical simulations by Fernandez *et al.* (2014) also confirmed the same conclusion and indicated that the modulational instability cannot sustain a substantial amplitude growth for the relative water depth $k_0h < 0.8$. The selected sideband is located at the angle of about 35° on the wavenumber plane, which is based on the nonlinear Schrödinger equation. The experimental results also showed a larger limiting k_0h because a dissipative process is involved inevitably.

In the present study, combined with theoretical analyses by the Zakharov integro-differential equation, direct numerical simulations of the Euler equations are performed using a higher-order spectral method to investigate the modulational instability in finite water depth, in particular for oblique sidebands. The instability regions are also re-drawn by the Zakharov equation with kernels in a Hamiltonian form. Another objective is to find out the threshold water depth where the modulational instability diminishes for oblique cases within the scope of the Zakharov equation.

2 Theoretical Model

The Benjamin-Feir instability of Stokes waves can be considered as a special quartet or a degenerate case of the four-wave resonant. The carrier wave is counted twice and satisfies $\boldsymbol{k_1} = \boldsymbol{k_2} = (k_0, 0)$. The two sidebands $\boldsymbol{k_3} = \boldsymbol{k_1} + (K_x, K_y)$ and $\boldsymbol{k_4} = \boldsymbol{k_1} - (K_x, K_y)$ whose phases are shifted by $-\pi/4$ satisfy

$$2\boldsymbol{k_1} = \boldsymbol{k_3} + \boldsymbol{k_4},\ |2\omega_1 - \omega_3 - \omega_4| < O(\epsilon^2), \tag{1}$$

where ϵ is the wave steepness, $\boldsymbol{k_j}$ are the wavenumbers and ω_j are the angular frequencies.

According to Crawford *et al.* (1981), Stiassnie & Shemer (1984) and Mei *et al.* (2005), the theoretic analyses are started by the discretized differential equations based on the well-known Zakharov equation (ZE),

$$\mathrm{i}\frac{\mathrm{d}B_1}{\mathrm{d}t} = (T_{1111}|B_1|^2 + 2T_{1313}|B_3|^2 + 2T_{1414}|B_4|^2)B_1 + 2T_{1134}e^{\mathrm{i}\Delta_{1134}t}B_1^*B_3B_4, \tag{2}$$

$$\mathrm{i}\frac{\mathrm{d}B_3}{\mathrm{d}t} = (2T_{3131}|B_1|^2 + T_{3333}|B_3|^2 + 2T_{3434}|B_4|^2)B_3 + T_{3411}e^{-\mathrm{i}\Delta_{1134}t}B_1^2B_4^*, \tag{3}$$

$$\mathrm{i}\frac{\mathrm{d}B_4}{\mathrm{d}t} = (2T_{4141}|B_1|^2 + 2T_{4343}|B_3|^2 + T_{4444}|B_4|^2)B_4 + T_{4311}e^{-\mathrm{i}\Delta_{1134}t}B_1^2B_3^*, \tag{4}$$

*Presenting author
†xinshuz@sjtu.edu.cn

where B_j are the wave action amplitudes and T with different subscripts are the interaction kernels of ZE.

As only the short-time solution of the equation is concerned, it is reasonable to take the assumption that the initial amplitudes of two sidebands are far less than that of the carrier wave (i.e., $|B_3|, |B_4| \ll |B_1|$). The solutions to the equations linearized through the zeroth order and the first order can be obtained as

$$B_1 = \beta_1 e^{-\mathrm{i}T_{1111}|\beta_1|^2 t},\ \beta_1 = B_1(0), \tag{5}$$

$$B_3 = \beta_3 e^{-\mathrm{i}(\frac{1}{2}\Delta_{1134}+T_{1111}|\beta_1|^2+\sigma)t},\ \beta_3 = B_3(0), \tag{6}$$

$$B_4 = \beta_4 e^{-\mathrm{i}(\frac{1}{2}\Delta_{1134}+T_{1111}|\beta_1|^2-\sigma^*)t},\ \beta_4 = B_4(0), \tag{7}$$

where the relation between the wave amplitude a_j and the wave action amplitude B_j satisfies $a_j = \frac{1}{\pi}\sqrt{\frac{\omega_j}{2g}}|B_j|$ and $\Delta_{1134} = 2\omega_1 - \omega_3 - \omega_4$ is the detuning factor.

The eigenvalue σ is given as $\sigma = (T_{3131} - T_{4141})\beta_1^2 \pm \sqrt{D}$ with

$$D = \left[\frac{1}{2}\Delta_{1134} + (T_{1111} - T_{3131} - T_{4141})\beta_1^2\right]^2 - T_{3411}T_{4311}\beta_1^4, \tag{8}$$

which is the essential criterion of modulation instability. If the value of D is positive, the wave train will be stable and B_3 and B_4 will maintain the initial values. On the contrary, the growth rate is defined as the imaginary part of σ, i.e., Im $\sigma = \sqrt{-D}$ when D is negative, and B_3 and B_4 will increase exponentially over time. Thus the growth rates in finite depth are able to form complete characterization.

A limitation for the application of ZE in finite depth is that the kernels with the form of T_{1111} and T_{1212} are non-unique. Fortunately, the former one has been resolved by Stiassnie & Shemer (1984) and Janssen & Onorato (2007) and the expression of the latter one is given by Stiassnie & Gramstad (2009). The kernels we use in the present work are consistent with those by Janssen & Onorato (2007) and Janssen (2009), which are slightly different from those by Stiassnie & Shemer (1984) and Stiassnie & Gramstad (2009). And the two expressions are identical under the condition of the exact four-wave resonant.

Another limitation is that for stationary wave steepness, ZE is not suitable for the particularly small water depth, in which there will be an abnormal increase for the growth rate. Zakharov (1999) discussed that the weakly-nonlinear theory has narrow frames of applicability in shallow water.

3 Direct Numerical Simulations

The numerical model with a higher-order spectral (HOS, Dommermuth & Yue (1987), West *et al.* (1987)) method is applied to validate the predictions of growth rate. According to the potential flow theory, the velocity potential $\phi(\boldsymbol{x}, z, t)$ in the fluid domain satisfies the Laplace equation $\nabla_{\boldsymbol{x}}^2\phi + \phi_{zz} = 0$. The nonlinear kinematic and dynamic surface boundary conditions are rewritten as

$$\frac{\partial \eta}{\partial t} = \left(1 + |\nabla_{\boldsymbol{x}}\eta|^2\right) W - \nabla_{\boldsymbol{x}}\phi^S \cdot \nabla_{\boldsymbol{x}}\eta,\ \text{at } z = \eta(\boldsymbol{x}, t), \tag{9}$$

$$\frac{\partial \phi^S}{\partial t} = -g\eta - \frac{1}{2}|\nabla_{\boldsymbol{x}}\phi^S|^2 + \frac{1}{2}\left(1 + |\nabla_{\boldsymbol{x}}\eta|^2\right) W^2,\ \text{at } z = \eta(\boldsymbol{x}, t), \tag{10}$$

where $\nabla_{\boldsymbol{x}}$ is the horizontal gradient operator, $\phi^S(\boldsymbol{x}, t) = \phi(\boldsymbol{x}, z = \eta(\boldsymbol{x}, t), t)$ is the velocity potential of the free surface, and $W(\boldsymbol{x}, t) = \phi_z|_{z=\eta}$ is the vertical velocity at the free surface. In addition, we assume a constant water depth h and the vertical velocity at the bottom is zero, that is, $\phi_z|_{z=-h} = 0$.

The HOS method is a Fourier spectral collocation method (also called a pseudo-spectral method), by which $\nabla_{\boldsymbol{x}}\eta$ and $\nabla_{\boldsymbol{x}}\phi^S$ are able to be solved. As for W, a series of expansions in wave steepness ϵ is performed up to the HOS order $M = 3$, which is chosen to capture the third-order non-linearity in the modulational instability. In addition, a 4th-order Runge–Kutta time integration with $\Delta t = T_1/32$ is applied and there is no relaxation period because the nonlinear initial conditions for the elevation and the velocity potential are applied. The code for the HOS method is developed in house and a GPU acceleration algorithm is adopted to make it more efficient (see Liu & Zhang (2019)).

In this study, we consider a square computational domain with periodic boundary conditions of $L_x \times L_y = 50\lambda_1 \times 50\lambda_1$ (λ_1 is the wavelength corresponding to $\boldsymbol{k_1}$) with $N_x \times N_y = 1024 \times 1024$ to ensure enough nodes in one wavelength and $\boldsymbol{k_1} = (1, 0)$ m^{-1} with $\lambda_1 = 6.28$ m. Thus, the wavenumber resolution is $\mathrm{d}k_x = \mathrm{d}k_y = 0.02$ m^{-1}, which allows us to accurately extract the changes of the carrier wave and sidebands. The initial surface and velocity potential are obtained by superimposing the carrier wave $(k_0, 0)$ which propagates along the x direction and two sidebands $(k_0 + K_x, K_y)$ and $(k_0 - K_x, -K_y)$. The amplitudes of perturbations are only one percent of the carrier-wave amplitude which is denoted by a_0 for a long steady increase.

4 Results

As results of Eq. (8) with the kernels by Janssen & Onorato (2007) and Janssen (2009), the unstable regions of modulational instability from $k_0h = 0.8$ to $k_0h = 1.78$ and $k_0h = 100$ (i.e., infinite water depth) are shown by contour maps in Fig. 1 with the typical dimensionless wave steepness $k_0a_0 = 0.10$. The maximum growth rate is marked by $\Diamond$. The threshold of the dimensionless water depth $k_0h = 1.363$ can be clearly detected and the

values on the x-axis become zero when $k_0h < 1.363$. As for three-dimensional cases, the unstable regions are distributed in a relatively wide horn-like domain for $k_0h > 1.363$ and along a narrow arc for $k_0h < 1.363$. It is worth noting that the second unstable region appears for $k_0h < 1.0$, which is located at $K_x/k_0 > 0.8$. It is also reported by Stiassnie & Shemer (1984) and Gramstad & Trulsen (2011). This paper concentrates on the main unstable region and the cases of the second unstable region are not included.

The cases for direct numerical simulations by the HOS method are marked in the Fig. 1 with △ and also listed in the Tab. 1. These are the sidebands with the largest growth rate under the corresponding water depth at relatively lower but reasonable resolution. It is caused by the limitation of the resolution of computational domain and only the sidebands matching the resolution are selected for the convenience of wavenumber spectrum analysis. Nevertheless, without loss of generality, the growth rates of the sidebands △ for the actual calculation are almost the same as the prediction ◊ by ZE although the locations are slightly different from each other.

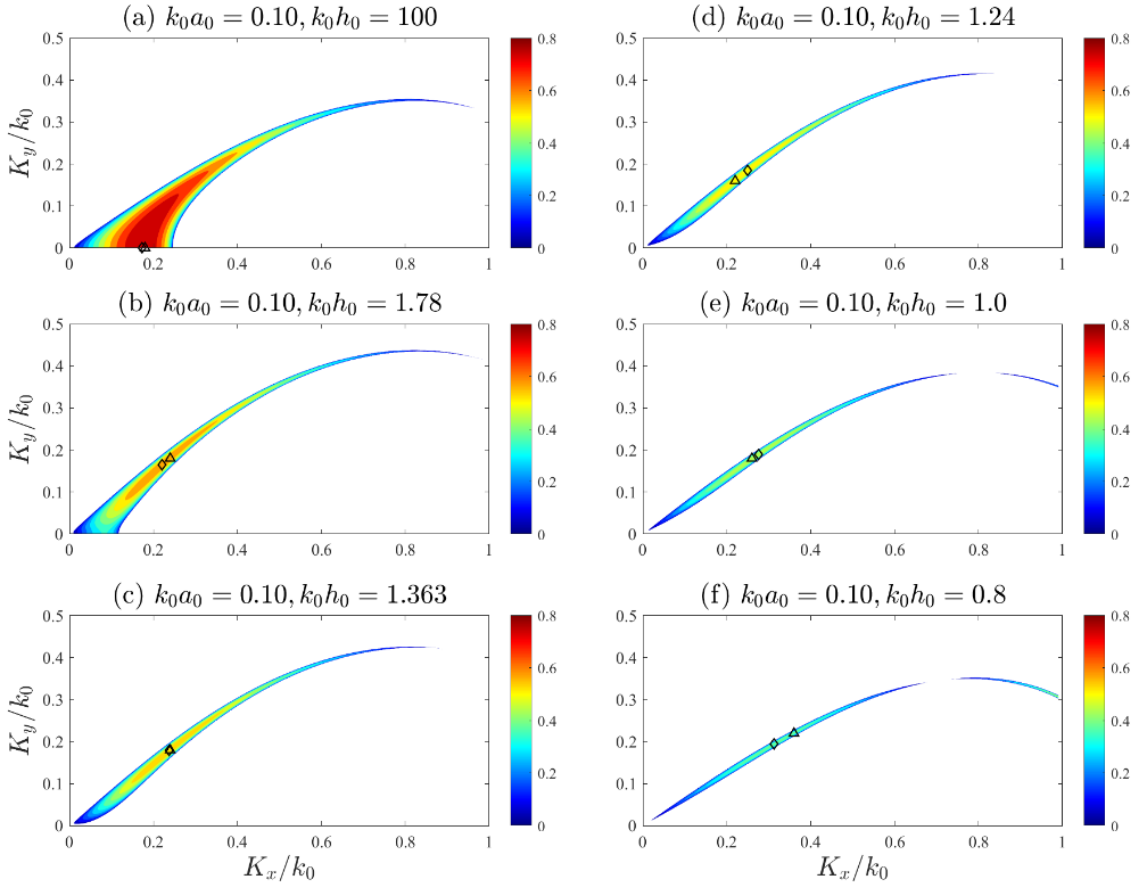

Figure 1: The non-dimensional growth rate G' in different water depths for $k_0a_0 = 0.10$.

The detailed results are summarized in Tab. 1. For results by ZE, the growth rate $G = \mathrm{Im}\sigma$ is directly calculated by Eq. (8). The dimensionless growth rate is defined as $G' = \mathrm{Im}(\sigma)/\frac{1}{2}\omega_0 k_0^2 a_0^2$. For results by HOS method, the growth rate is estimated by data fitting using a least-squares method. The average amplitude of the upper and lower sideband, which is normalized by the initial amplitude of the carrier wave, is used for calculation. The length of the data is about $50T_1$. For example, the slope of $50T_1$ to $100T_1$ in Fig. 2 is considered as the growth rate. It is found that the results by the HOS method are in good agreement with those by ZE for all the cases. The maximum growth rate decreases with decreasing depth, which indicates the reduction of the modulational instability. The most unstable mode occurs only in deep water when the sidebands are collinear with the carrier wave, whereas in finite depth the region with an angle around 35° exhibits the strongest modulational instability.

In Fig. 2, analyses in wavenumber space are performed and the amplitudes of two sidebands (the magenta solid line for $\boldsymbol{k_3}$, the blue solid line for $\boldsymbol{k_4}$ and the black dash dot line for the average) and the carrier wave (the black solid line) are plotted at each time step. The prediction of ZE is also plotted as the black dash line for comparison. It can be seen from the figure that the amplitudes of the sidebands increase rapidly while the amplitude of the carrier wave decreases. The slopes of the sidebands by ZE and the HOS method are almost the same. The steady growth time of the sidebands (the straight line segments for the sidebands in Fig. 2) increases with decreasing the depth. However, there is no significant difference for the maximum values that the sidebands can reach (the first peak of the sideband growth curve) in different depths.

When modulation occurs, the energy of the carrier wave is transferred to the upper and lower sidebands.

Table 1: Cases of the numerical simulations.

Case	k_0h	k_0a_0	K_x/k_0	K_y/k_0	G		G'	
					ZE	HOS	ZE	HOS
A1	100	0.10	0.18	0	0.0126	0.0127	0.8059	0.8078
B1	1.78	0.10	0.24	0.18	0.0094	0.0096	0.6198	0.6295
C1	1.363	0.10	0.24	0.18	0.0085	0.0086	0.5783	0.5883
D1	1.24	0.10	0.22	0.16	0.0079	0.0080	0.5497	0.5543
E1	1.0	0.10	0.26	0.18	0.0065	0.0066	0.4741	0.4805
F1	0.8	0.10	0.36	0.22	0.0051	0.0051	0.3998	0.4003

The amplitudes of two sidebands increase exponentially in the wavenumber space. In the real physical space, the maximum free-surface elevation will increase with the time. The amplification of the wave amplitude is also an appropriate criterion for assessing the modulational instability. Fig. 3 illustrates the temporal evolution of the maximum wave elevation which is normalized by the initial amplitude of the carrier wave. The continuous increase gives another evidence for the modulational instability. In addition, for deep water, the maximum wave elevation can reach a relatively higher value in less time than that for the shallower water.

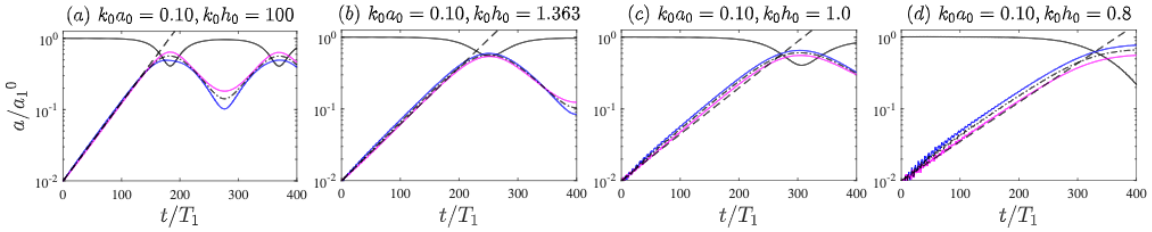

Figure 2: Temporal evolution of the amplitudes of the carrier wave and sidebands in several different depths.

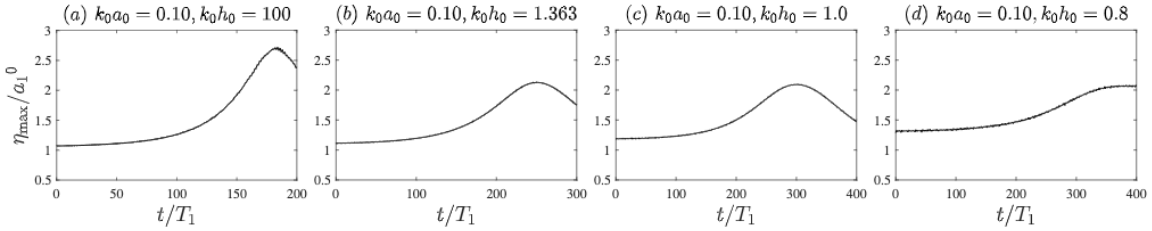

Figure 3: Temporal evolution of the normalised maximum elevation of the free surface in several different depths.

References

Benjamin, T. B. 1967 Instability of periodic wavetrains in nonlinear dispersive systems. *Proc. R. Soc. Lond. A* **299** (1456), 59–76.

Benney, D. J. & Roskes, G. J. 1969 Wave instabilities. *Stud. Appl. Math.* **48** (4), 377–385.

Crawford, D. R., Lake, B. M., Saffman, P. G. & Yuen, H. C. 1981 Stability of weakly nonlinear deep-water waves in two and three dimensions. *J. Fluid Mech.* **105** (-1), 177–191.

Dommermuth, D. & Yue, D. K. P. 1987 A higher-order spectral method for the study of nonlinear gravity waves. *J. Fluid Mech.* **187**, 267–288.

Fernandez, L., Onorato, M., Monbaliu, J. & Toffoli, A. 2014 Modulational instability and wave amplification in finite water depth. *Nat. Hazard. Earth Sys.* **14** (3), 705–711.

Gramstad, O. & Trulsen, K. 2011 Hamiltonian form of the modified nonlinear schrödinger equation for gravity waves on arbitrary depth. *J. Fluid Mech.* **670**, 404–426.

Janssen, P. A. E. M. 2009 On some consequences of the canonical transformation in the hamiltonian theory of water waves. *J. Fluid Mech.* **637**, 1–44.

Janssen, P. A. E. M. & Onorato, M. 2007 The intermediate water depth limit of the zakharov equation and consequences for wave prediction. *J. Phys. Oceanogr.* **37**, 2389–2400.

Liu, S. & Zhang, X. 2019 Extreme wave crest distribution by direct numerical simulations of long-crested nonlinear wave fields. *Appl. Ocean Res.* **86**, 141–153.

McLean, J. W. 1982 Instabilities of finite-amplitude gravity waves on water of finite depth. *J. Fluid Mech.* **114**, 331–341.

Mei, C. C., Stiassnie, M. & Yue, D. K. P. 2005 *Theory and Applications of Ocean Surface Waves, Part 2: Nonlinear Aspects*. World Scientific.

Stiassnie, M. & Gramstad, O. 2009 On Zakharov's kernel and the interaction of non-collinear wavetrains in finite water depth. *J. Fluid Mech.* **639** (639), 433–442.

Stiassnie, M. & Shemer, L. 1984 On modifications of the zakharov equation for surface gravity waves. *J. Fluid Mech.* **143**, 47–67.

Toffoli, A., Fernandez, L., Monbaliu, J., Benoit, M., Gagnaire-Renou, E., Lefevre, J. M., Cavaleri, L., Proment, D., Pakozdi, C., Stansberg, C. T., Waseda, T. & Onorato, M 2013 Experimental evidence of the modulation of a plane wave to oblique perturbations and generation of rogue waves in finite water depth. *Phys. Fluids* **25** (9), 091701.

West, B. J., Brueckner, K. A. & Janda, R. S. 1987 A new numerical method for surface hydrodynamics. *J. Geophys. Res.* **92** (11), 11803–11824.

Whitham, G. B. 1967 Non-linear dispersion of water waves. *J. Fluid Mech.* **27** (2), 399–412.

Zakharov, V. E. 1968 Stability of periodic waves of finite amplitude on the surface of a deep fluid. *J. Appl. Mech. Tech. Phys.* **9** (2), 190–194.

Zakharov, V. E. 1999 Statistical theory of gravity and capillary waves on the surface of a finite-depth fluid. *Eur. J. Mech. B* **18** (3), 327–344.

(*Abstract for the 37th International Workshop on Water Waves and Floating Bodies, Giardini Naxos, Italy, 2022*)

Nonlinear Effect on Ship Generated Mini-tsunamis

Jinyu Yao[1]*, Xinshu Zhang[1], Robert F. Beck[2]

[1]State Key Laboratory of Ocean Engineering, Shanghai Jiao Tong University, Shanghai 200240, China

[2]Department of Naval Architecture and Marine Engineering, University of Michigan, Ann Arbor MI 48109, USA

1 Introduction

The condition of waves generated by a ship in steady motion in finite depth water varies with the ship's speed U. The depth Froude number $Fr = \frac{U}{\sqrt{gh}}$ (where g is the acceleration of gravity and h is the water depth) is widely adopted to measure the velocity. If a ship moves with a subcritical speed ($Fr < 1$) in water with a flat bottom, a wave wake and a depression along the ship are formed. The phenomenon called 'squat' happens when the depth is shallow (Tuck, 1966). Under the near-critical and supercritical conditions, nonlinear effects can not be ignored. Ertekin *et al.* (1984) found a series of solitons in the experiment when $Fr > 1$. The solitons begin to break at $Fr = 1.2$ and are replaced by a hydraulic jump at $Fr = 1.3$. Chen & Sharma (1995) used a Kadomtsev-Petviashvili equation to investigate a slender ship moving in a shallow channel. As for $Fr = 0.9$, 1.0, 1.1, they obtained similar results with Ertekin *et al.* (1984). In addition, they also considered the influence of the channel width on the amplitude of solitons and the period of the first two solitons. Wu (1987) explained the basic mechanism of the formation of upstream solitons and studied the nonlinear stability based on the forced Korteweg-de Vries equation. Li & Sclavounos (2002) investigated the three-dimensional nonlinear waves generated by a ship traveling at different speeds in an unbounded domain. The parabolic crestline of solitons is shown in shallow water and parabolic water humps are formed when $Fr > 1.2$.

Recently, different from the nonlinear solitons mentioned above, a new type of upstream wave named 'mini-tsunami' was observed in Norway (Grue, 2017). Mini-tsunamis are generated when large ships travel across a shallow depth variation with subcritical speed. These ship-induced upstream waves can cause erosion, and it is worth investigating them.

Because the amplitude and wavelength of mini-tsunamis are 2 m and 100 m, respectively, linear free-surface boundary conditions were used by Grue (2017). The ship was modelled by a moving pressure distribution. He studied the influence of channel width and the ship's velocity on the amplitude of mini-tsunamis. Later, he developed a model for a real ship geometry and explained the generation process of mini-tsunamis (Grue, 2020). The results showed that the differences between the calculations for a real ship geometry and those for a pressure distribution are not obvious.

The slope of a mini-tsunamis, which is defined as the ratio between the height and the length, is in the linear regime, so linear free-surface boundary conditions were used in two papers of Grue. However, the nonlinear effects have not been studied and the importance of nonlinearity is still unclear. With this motivation, we used a High-Order Spectral (HOS) method and a Boussinesq model, FUNWAVE-TVD, to model the nonlinear evolution of the free surface over a variable bottom. Comparing the results of the HOS model, FUNWAVE-TVD and Grue's method, we can examine the nonlinear effects in different conditions where the ship's draft and velocity are the main variables.

2 Fully nonlinear numerical models

2.1 HOS model with variable bathymetry (HOS-VB)

A potential flow formalism is used and the flow can be described by a velocity potential ϕ (Gouin *et al.*, 2017). The two horizontal axes are x and y, and the horizontal computational domain can be defined as $L_x \times L_y$. The vertical axis z points upwards and the mean water level is at $z = 0$. Based on the potential flow assumption, the governing equation is the Laplace equation: $\nabla\phi = 0$. The surface potential $\phi^S(x, y, z, t) = \phi(x, y, \eta(x, y, t), t)$ is introduced here, then the nonlinear free-surface boundary conditions are

$$\eta_t + \nabla_1\phi^S \cdot \nabla_1\eta - (1 + \nabla_1\eta \cdot \nabla_1\eta)\phi_z(x, y, \eta, t) = 0, \quad at\ z = \eta \tag{1}$$

$$\phi_t^S + g\eta + \frac{1}{2}\nabla_1\phi^S \cdot \nabla_1\phi^S - \frac{1}{2}(1 + \nabla_1\eta \cdot \nabla_1\eta)\phi_z^2(x, y, \eta, t) = -\frac{p}{\rho}, \quad at\ z = \eta \tag{2}$$

where $\nabla_1 = (\frac{\partial}{\partial x}, \frac{\partial}{\partial y})$, η is the free-surface elevation, ρ, g and p are the water density, gravitational acceleration and ship pressure distribution, respectively. The total depth $-h = -h_0 + \beta(x, y)$ where h_0 is the average bottom

*Presenting author

and β is the bottom variation. The bottom boundary condition reads

$$\nabla_1\phi\cdot\nabla_1\beta-\phi_z(x,y,-h_0+\beta)=0,\quad at\ z=-h_0+\beta. \tag{3}$$

The computational domain is periodic in the x and y directions, which can be expessed by :

$$(\phi;\eta)(x=0,y,z,t)=(\phi;\eta)(x=L_x,y,z,t), \tag{4}$$
$$(\phi;\eta)(x,y=0,z,t)=(\phi;\eta)(x=x,L_y,z,t), \tag{5}$$

If the vertical velocity on the free surface, $\phi_z(x,y,\eta)$, can be solved, the time stepping of ϕ and η can be continued based on Eqns. (1) and (2).

In order to calculate ϕ_z, we use a truncated power series to express the potential, $\phi=\sum_{m=1}^{M}\phi^{(m)}$. Then we define $\phi^{(m)}=\phi_{h_0}^{(m)}+\phi_\beta^{(m)}$, where $\phi_{h_0}^{(m)}$ satisfies the flat bottom ($z=-h_0$) boundary condition: $\frac{\partial\phi_{h_0}^{(m)}}{\partial z}(x,y,-h_0,t)=0$, while $\phi_\beta^{(m)}$ still satisfies Eqn. (3). Therefore, $\phi_{h_0}^{(m)}$ and $\phi_\beta^{(m)}$ can be expressed as:

$$\phi_{h_0}^{(m)}=\sum_p\sum_q A_{pq}^{(m)}(t)\frac{\cosh(k_{pq}(z+h_0))}{\cosh(k_{pq}h_0)}e^{\mathrm{i}k_{xp}x+\mathrm{i}k_{yq}y} \tag{6}$$

$$\phi_\beta^{(m)}=\sum_p\sum_q B_{pq}^{(m)}(t)\frac{\sinh(k_{pq}z)}{\cosh(k_{pq}h_0)}e^{\mathrm{i}k_{xp}x+\mathrm{i}k_{yq}y}, \tag{7}$$

where $k_{xp}=p\frac{2\pi}{L_x}$, $k_{yq}=q\frac{2\pi}{L_y}$ and $k_{pq}=|(k_{xp},k_{yq})|$. Then the modal amplitudes $A_{pq}^{(m)}(t)$ and $B_{pq}^{(m)}(t)$ can be solved by a Fast Fourier Transform. More specifically, $B_{pq}^{(m)}(t)$, which is a function of $A_{pq}^{(m)}(t)$, can be computed by the following method:

We assume $\frac{\beta}{h_0}\ll 1, O(\frac{\beta}{h_0})\equiv O(\frac{\partial\beta}{\partial x})\equiv O(\frac{\partial\beta}{\partial y})$, then the bottom condition in Eqn. (3) can be expressed by a Taylor expansion. The Taylor series of the free surface and the variable bottom are truncated at different orders. More specifically, M for the free surface and M_b for the variable bottom. Therefore, $\phi_\beta^{(m)}=\sum_{l=1}^{M_b}\phi_\beta^{(m,l)}$. If we keep terms in Eqn. (3) at the same order, we have

$$\begin{aligned}
\left[\frac{\partial\phi_\beta^{(m)}}{\partial z}\right]_{z=-h_0} &= \sum_{l=1}^{M_b}\left(\frac{\partial\phi_\beta^{(m,l)}}{\partial z}\right)_{z=-h_0}\\
&= \sum_{l=1}^{M_b}\frac{\partial}{\partial x}\left[\frac{\beta^l}{l!}\frac{\partial^{l-1}}{\partial z^{l-1}}\left(\frac{\partial\phi_{h_0}^{(m)}}{\partial x}\right)\right]_{z=-h_0}+\sum_{l=1}^{M_b}\frac{\partial}{\partial y}\left[\frac{\beta^l}{l!}\frac{\partial^{l-1}}{\partial z^{l-1}}\left(\frac{\partial\phi_{h_0}^{(m)}}{\partial y}\right)\right]_{z=-h_0}\\
&+ \sum_{l=1}^{M_b}\sum_{j=1}^{l-1}\frac{\partial}{\partial x}\left[\frac{\beta^j}{j!}\frac{\partial^{j-1}}{\partial z^{j-1}}\left(\frac{\partial\phi_\beta^{(m,l-j)}}{\partial x}\right)\right]_{z=-h_0}+\sum_{l=1}^{M_b}\sum_{j=1}^{l-1}\frac{\partial}{\partial y}\left[\frac{\beta^j}{j!}\frac{\partial^{j-1}}{\partial z^{j-1}}\left(\frac{\partial\phi_\beta^{(m,l-j)}}{\partial y}\right)\right]_{z=-h_0}
\end{aligned} \tag{8}$$

$B_{pq}^{(m)}(t)$ can be solved by Eqn. (8).

2.2 FUNWAVE-TVD

The open-source FUNWAVE-TVD solver is based on a fully nonlinear Boussineq model (Chen *et al.*, 2000). The moving pressure distributions in the FUNWAVE-TVD and HOS model are the same and defined as:

$$p(x,y,t) = \rho gTf(x,t)q(y,t). \tag{9}$$

$$f(x,t) = \begin{cases} cos^2[\frac{\pi(|x-x^*(t)|-\frac{1}{2}\alpha L)}{(1-\alpha L)}] & \frac{1}{2}\alpha L\le|x-x^*(t)|\le\frac{1}{2}L\\ 1 & |x-x^*(t)|\le\frac{1}{2}\alpha L\end{cases} \tag{10}$$

$$q(y,t) = \begin{cases} cos^2[\frac{\pi(|y-y^*(t)|-\frac{1}{2}\beta B)}{(1-\beta B)}] & \frac{1}{2}\beta B\le|y-y^*(t)|\le\frac{1}{2}B\\ 1 & |y-y^*(t)|\le\frac{1}{2}\beta B\end{cases} \tag{11}$$

where L,B,T are the ship's length, width and draft, respectively. The center position of the ship is (x^*,y^*). α and β are the coefficients which control the shape of the draft region in x and y directions, respectively.

3 Results and discussion

Numerical simulations are performed by the two fully nonlinear models and the linear model in Grue (2017). Following the information of Color Fantasy which is the ship documented by Grue (2017), we use a small-scale model to simulate it. The results may be as a reference for the future experiments. In all simulations, the ship's length is $L=2$ m and its beam is $B=0.5$ m. The steady velocity of the ship is defined as U_0, and a start-up process is imposed at the initial moment: $U=U_0\sin(t/T_0)$ for $0\le t\le\frac{\pi T_0}{2}$ where $T_0=30\sqrt{h_1/g}$ and $h_1=0.3$. The computational domain is $L_x\times L_y=307.2$ m $\times$ 2 m and the total number of nodes is $N_x\times N_y=8192\times128$.

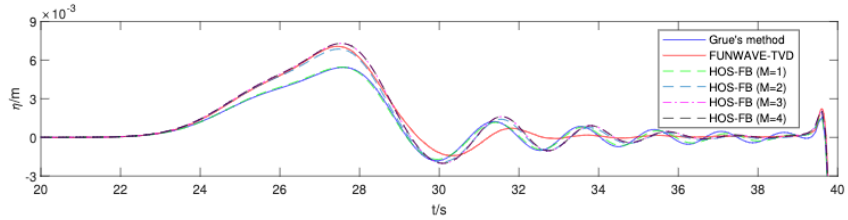

Figure 1: The upstream wave elevation induced by the start-up process on a flat bottom as recorded by the probes in different computations. $U_0 = 1.3$ m/s, $h = 0.45$ m, $Fr = U_0/\sqrt{gh} = 0.62$, $\frac{h}{T} = 4.5$.

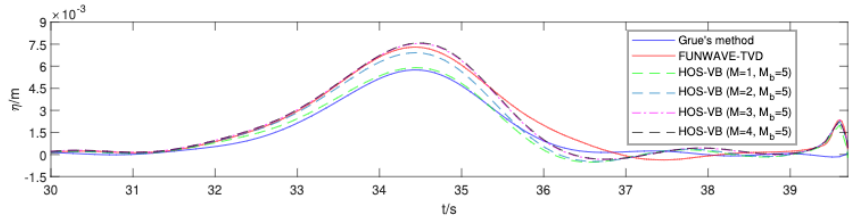

Figure 2: The upstream wave elevation induced by a variable bottom as recorded by the probes in different computations. $U_0 = 1.3$ m/s, $\Delta h = 0.75$ m, $h_0 = 0.825$ m, $Fr = U_0/\sqrt{gh_0} = 0.46$, $\frac{h_0}{T} = 8.25$.

First, we consider the influence of nonlinear effects on upstream waves induced by the ship's start-up process on a flat bottom. The velocity is $U_0 = 1.3$ m/s, the draft is $T = 0.1$ m and the depth is $h = 0.45$ m. Therefore, the non-dimensional parameter $\frac{h}{T} = 4.5$. A numerical wave probe is placed at 49.28 m in front of the initial position of ship and both of them are placed in the half-width line of the tank. The wave amplitudes at the probe that are calculated by different models are displayed in Fig. 1. As for the HOS model with flat bottom (HOS-FB), different nonlinear orders are tested, i.e. $M = 1, 2, 3, 4$. As shown in the figure, the front wave, whose peak is recorded at approximately 27.8 s, is induced by the start-up of the ship. The wave amplitudes calculated by the HOS-FB ($M = 3$) and HOS-FB ($M = 4$) are almost the same, which means that the results are converged. Although nonlinear free-surface boundary conditions are used, HOS-FB ($M = 1$) which concentrates on the first-order terms has the same wave amplitude as Grue's model. Both of them are 5.45 mm, which verifies the linear result. If the nonlinear order in HOS is set to 2, the wave peak reaches 6.86 mm. It means that the second-order nonlinearity plays an obvious role. Considering the FUNWAVE-TVD and HOS with a higher order, we find the wave amplitudes increase to approximately 7.10 mm. In order to compare the linear result and nonlinear result, and quantify the role of nonlinearity, we define a parameter $\mu = \frac{|H_{\mathrm{HOS-VB(M=3)}} - H_{\mathrm{Grue}}|}{H_{\mathrm{Grue}}} \times 100\%$, then $\mu = 33.95\%$ for this flat bottom condition. To sum up, nonlinearity plays an important role in the upstream wave generated by the start-up of the ship.

Next, we investigate the nonlinear effect on the upstream waves induced by a variable bottom. The depth change $\Delta h = 0.75$ m, the average water depth $h_0 = 0.825$ m, and $\frac{h_0}{T} = 8.25$. The depth change is modeled by a function of $\beta = -\frac{1}{2}\Delta h + \frac{1}{2}\Delta h[tanh(0.35(x - x_a)) - tanh(0.35(x - x_b))]$ where the midpoints of two depth changes x_a, x_b are 128.1 m and 179.1 m, respectively. The ship starts at the position which is 25 m in front of x_a with a start-up process and two probes are placed at $x_{p1} = 152.4$ m and $x_{p2} = 174.45$ m, respectively. The case with $U_0 = 1.3$ m/s is considered first. In Fig. 2, the wave whose peak is at approximately 34.5 s is generated by the variable bottom. Comparing the calculations in HOS-VB model with different orders, we can see the wave amplitude is converged at $M = 3$. As for the linear model and low-order HOS-VB model, the results of Grue's method and HOS-VB ($M = 1$) model are almost the same. If the second-order nonlinear terms are considered, the weak peak grows to 6.92 mm. The wave amplitudes in the nonlinear models including FUNWAVE-TVD, HOS-VB ($M = 3$) are approximately 7.54 mm, which is 1.80 mm higher than those in Grue's model. Comparing the linear and high-order nonlinear results, we get $\mu = 31.13\%$ which represents an obvious nonlinear effect. Therefore, it seems that the nonlinearity can not be ignored.

In order to investigate the nonlinear effect systematically, we use different values of T and U_0 and set $T = 0.10$ m, $U_0 = 1.3$ m/s as a reference. The draft remains 0.1 m and U_0 is chosen as 1.1 m/s and 1.5 m/s,

Table 1: The values of μ in different working conditions.

T	h_0/T	U_0	Fr	μ	U_0	Fr	T	h_0/T	μ
		1.1 m/s	0.39	26.11%			0.05 m	16.50	14.53%
0.10 m	8.25	1.3 m/s	0.46	31.13%	1.3 m/s	0.46	0.10 m	8.25	31.13%
		1.5 m/s	0.53	47.04%			0.15 m	5.50	50.81%

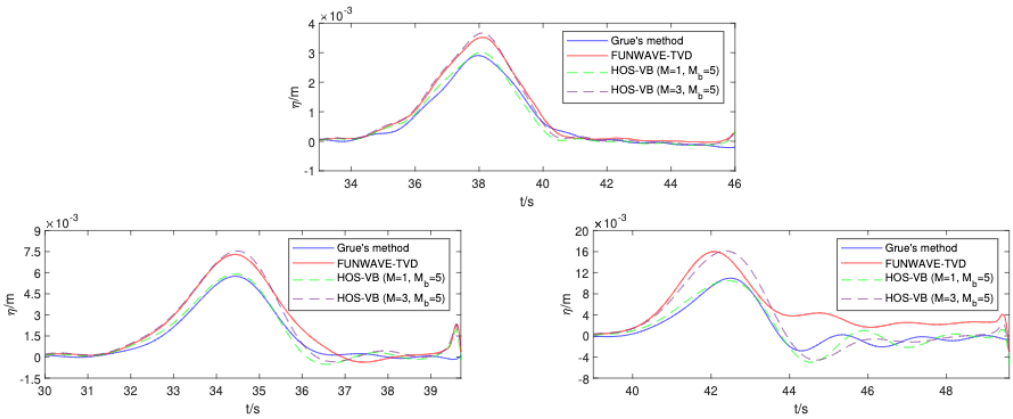

Figure 3: The sensitivity of the nonlinear effect on the upstream elevation to ship speed. (a) $U_0 = 1.1$ m/s, $Fr = 0.39$, the probe is placed at x_{p1}. (b) $U_0 = 1.3$ m/s, $Fr = 0.46$, the probe is placed at x_{p1}. (c) $U_0 = 1.5$ m/s, $Fr = 0.53$, the probe is placed at x_{p2}.

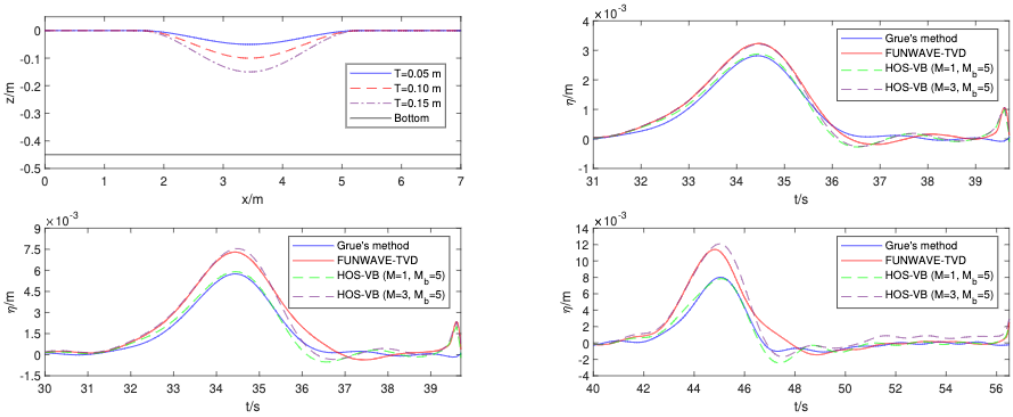

Figure 4: The sensitivity of the nonlinear effect on the upstream elevation to ship's draft. (a) Comparison of pressure distribution with different values of draft at longitudinal section in center plane with the shallow water depth. (b) $T = 0.05$ m, $\frac{h_0}{T} = 16.50$, the probe is placed at x_{p1}. (c) $T = 0.10$ m, $\frac{h_0}{T} = 8.25$, the probe is placed at x_{p1}. (d) $T = 0.15$ m, $\frac{h_0}{T} = 5.50$, the probe is placed at x_{p2}.

respectively. The Froude numbers $Fr = U_0/\sqrt{gh_0}$ of the two conditions are 0.39 and 0.53, respectively. The results with different velocities are drawn in the Fig. 3. μ in different conditions are shown in Table 1. It is evident that μ increases with the steady velocity. That means the nonlinear effect is more important when the Froude number is high. Finally, U_0 remains 1.3 m/s and the draft is chosen as 0.05 m, 0.10 m and 0.15 m. Therefore, $\frac{h_0}{T}$ of the three conditions are 16.50, 8.25 and 5.50, respectively. The results with different drafts are displayed in the Fig. 4. In Fig. 4(a) pressure distribution with different values of draft at a longitudinal section in the center plane is compared with the shallow water depth. By analyzing the value of μ in Table 1, we find the nonlinearity is more obvious in conditions with a larger draft. μ can even increase to 50.81% when the draft is 0.15 m. It can be concluded that the nonlinear effects have an influence on the upstream wave generated by the depth change and is more significant when the parameter $\frac{h_0}{T}$ is small or the depth Froude number is high.

References

Chen, Q., Kirby, J. T., Dalrymple, R. A., Kennedy, A. B. & Chawla, A. 2000 Boussinesq modeling of wave transformation, breaking, and runup ii: 2d. *J. Waterw. Port. Coast. Ocean. Eng.* **126** (1), 48–56.

Chen, X. N. & Sharma, S. D. 1995 A slender ship moving at a near-critical speed in a shallow channel. *J. Fluid Mech.* **291** (1), 263–285.

Ertekin, R. C., Webster, W. C. & Wehausen, J. V. 1984 Ship-generated solitons. In *Proc. 15th Symp. Nav. Hydrodyn, Hamburg*.

Gouin, M., Ducrozet, G. & Ferrant, P. 2017 Propagation of 3d nonlinear waves over an elliptical mound with a high-order spectral method. *Eur. J. Mech. B Fluids.* **63**, 9–24.

Grue, J. 2017 Ship generated mini-tsunamis. *J. Fluid Mech.* **816**, 142–166.

Grue, J. 2020 Mini-tsunami made by ship moving across a depth change. *J. Waterw. Port. Coast. Ocean. Eng.* **146** (5), 04020023.

Li, Y. & Sclavounos, P. D. 2002 Three-dimensional nonlinear solitary waves in shallow water generated by an advancing disturbance. *J. Fluid Mech.* **470** (1), 383–410.

Tuck, E. O. 1966 Shallow-water flows past slender bodies. *J. Fluid Mech.* **26** (1), 81–95.

Wu, T. Y. 1987 Generation of upstream advancing solitons by moving disturbances. *J. Fluid Mech.* **184** (1), 75–99.

Wave-passing by ships in a single file formation

Zhi-Ming Yuan

Dep. of Naval Architecture, Ocean & Marine Engineering, University of Strathclyde

HIGHLIGHTS

- Discover the wave-passing phenomenon by ships in a single file configuration
- Distinct wave interference phenomenon was found between individual ships

1 INTRODUCTION

It has been commonly observed on open waters that ducklings/goslings follow their mothers in a single file configuration. A recent research by Yuan et al. (2021) reveals the reason of such formation locomotion observed in nature: wave interference. Their findings are different from the existing literatures on formation movement by flying birds or swimming fishes, in which the vortices in wakes were considered as the main reason for energy savings by group locomotion (Liao 2007). When a body is moving on the free water surface, its resistance components are fundamentally different from those moving in a single media. A distinct Kelvin wave pattern will be observed on the interface between the air and water in the wake of the moving body, accompanied by a wave making resistance to the body, which is one of the major components of the total resistance. Therefore, it is essential to investigate the wave interactions among bodies travelling in highly organized groups. It was found by Yuan et al. (2021) that when a duckling swims at the "sweet spot" behind its mother, a destructive wave interference phenomenon occurs and the wave resistance of the duckling turns positive, pushing the duckling forward. More interestingly, this *wave-riding* benefit could be sustained by the rest of the ducklings in a single-file line formation. Starting from the 3rd one in a queue, the wave resistance of individuals gradually tended towards zero, and a delicate dynamic equilibrium is achieved. Each individual under that equilibrium acted as a wave passer, passing the waves energy to its trailing one without any energy losses. It inspires the present study to investigate the ships in a single file configuration and to see if we can learn this *wave-riding* and *wave-passing* skills from the waterfowl to improve our design of waterborne traffic and to eventually design a water train of minimized wave-making resistance.

As commented by Ellingsen (2021) that the benefits of *wave-riding* and *wave-passing* are not exclusive to waterfowl, but could equally apply to boats and vessels at a larger scale. A recent project, Sea Train, initiated by the US Defense Advanced Research Projects Agency (DARPA 2020), is envisioned to consist of four or more unmanned surface vehicles travelling in a row formation with the objective to minimize the collective wave-making resistance by creating 'the equivalent of a long parallel mid-body', as shown in *Figure 1*. Compared to a ship with a long parallel mid-body, multiple short ships in a single file configuration could achieve many benefits, e.g. better mobility, manoeuvrability, flexibility, etc. By intuition, one may think the multiple short ships might generate more waves than the single long ship, hence pocessing a larger wave-making resistance. The objective of this study is to quantify how much wave-resistance is increased or reduced by ships in single file formation, comparing to that of a single ship.

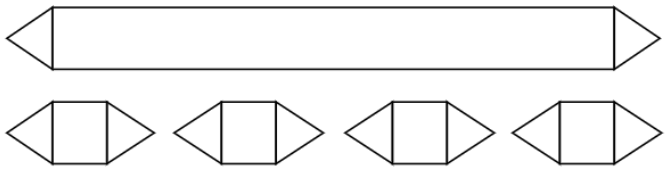

Figure 1. Upper half: a ship with very long parallel mid-body; lower half: four ships in a single file formation.

2 METHDOLOGY AND ASSUMPTIONS

The present study focuses on the wave-making problem, and no attempts are made to address the force or interaction caused by the viscosity of the fluid. The fluid domain can be described by using a velocity potential

that satisfies Laplace equation. The three-dimensional boundary element method used in (Yuan, He et al. 2015) can then be applied to solve the Laplace equation and calculate the wave-making resistance with an implementation of linearized free-surface boundary condition.

In the case study, the ship model is represented by a simple Wigley hull with B/L=1/4 and T/L=1/10, where B, L and T are ship breadth, length and draft respectively. Let's define R_s as the wave resistance of a single ship travelling solely in calm water. In a single file formation, all the individual ships are exactly the same, and the wave resistance for the n-th body in the formation is denoted by R_n, where n=0 represents the leading ship, and n=1 indicates the first coach in the train (the first trailing ship after the leading one). The wave drag reduction coefficient C_{DR} can be defined as

$$C_{DR} = \left(1 - \frac{R_n}{R_S}\right) \times 100\% \qquad (1)$$

The coefficient C_{DR} can be used to quantify the intensity of hydrodynamic interaction. $C_{DR} > 0$ indicates the wave resistance is reduced in a formation due to the hydrodynamic interaction; whilst $C_{DR} < 0$ represents an increase of wave resistance. No interaction is found at $C_{DR} = 0$, and the wave resistance is the same as that of independent moving. Obviously, it is desired by the trailing ships to get a C_{DR} as large as possible.

3 RESULTS AND DISCUSSIONS

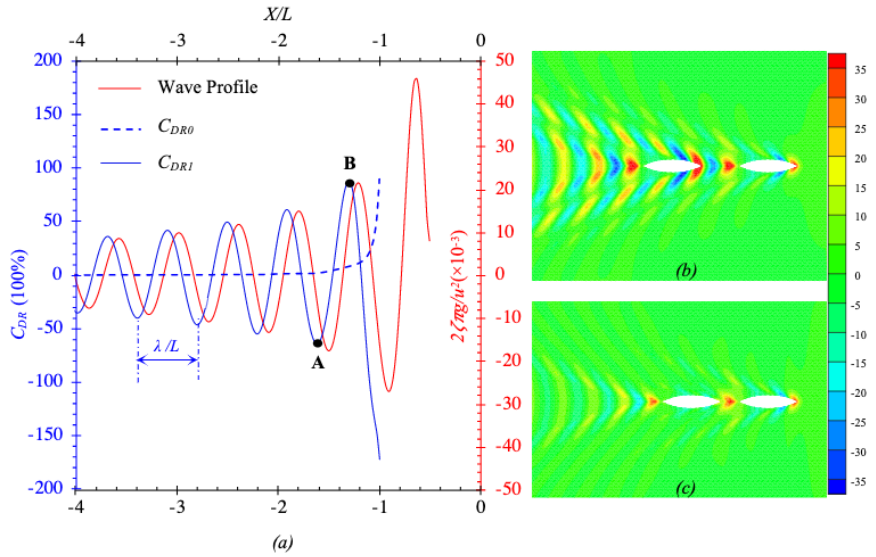

Figure 2. (a) C_{DR} of the trailing ship (n=1, blue solid curve) and the leading ship (blue dash curve) at Fr=0.3. Point A and B on the blue solid curve corresponds to two typical wave drag reduction positions. The red solid curve is the wave profile on the centre line behind the leading ship. λ is the wavelength. (b) Wave pattern when the trailing ship is swimming at position A. (c) Wave pattern when the trailing ship is swimming at position B.

Let's firstly put the trailing ship on the centre line behind the leading ship and let it gradually approach the leading ship from -4L to -1L. The wave drag reduction of both the trailing ship and leading ship, and the wave patterns, are shown *Figure 2*. There are three main findings from the results in *Figure 2*.

1) The trailing ship has equal probability to experience an increased drag (C_{DR} <0) and reduced drag (C_{DR} >0) by following the leading ship's wake, depending on its relative position to the leading ship, as shown by the solid blue curve in *Figure 2* (a). The trailing ship's C_{DR} curve exhibits a periodical property, fluctuating around a neutral value. The oscillation amplitude decays as the trailing ship stays in positions further downstream. The decay rate matches very well with that of the waves propagating to the far-field downstream. The distance (d) between two consecutive crests on C_{DR} curve is approximately a wavelength (λ). Since the wavelength on the centre line behind a moving body is speed dependent ($\lambda=2\pi U^2/g$), we could always find the best energy saving position of the trailing ship by adjusting its distance to the leading one. The maximum wave drag reduction of 96% is found at the first crest of C_{DR} curve, indicating the trailing ship's total wave drag is only 4% of a single ship moving

solely at the same speed. The amplitude of the curve is subject to a decrease as the leading-to-trailing ship distance increases. At the 5th crest, where the trailing ship is 3.7*L* away from its leader, the trailing ship could still receive up to 36% of wave drag reduction. The other side of the coin is that some regions exist where the drag increases. In particular, a -172% drag reduction is observed at position *X/L*=-1, where the trailing ship's bow is contacting the leading ship's stern.

2) It is not a surprise that the trailing ship is subject to a strong hydrodynamic interaction when travelling at the leading ship's wake. However, would the leading ship receive a drag reduction due to the presence of the trailing ship, leading to mutual benefit in a formation movement? The calculations provide the evidence to support this hypothesis that the trailing ship moving close behind a leading ship will also assist the leader. It can be seen from the blue dashed curve in *Figure 2* (a) that the wave drag of the leading ship can be reduced by 90% when the trailing ship is moving directly behind her. The pressure distributed over the rear part of the leading ship is increased due to the trailing ship's frontal waves. As a result, the leading ship receives benefit by riding the trailing ship's bow wave. However, at this position, the trailing ship is the looser. Its wave drag reduction becomes -172%, which indicates the trailing ship has to spend more than twice its efforts to overcome the wave drag, compared to that when travelling independently. A win-win situation is observed when the trailing ship is swimming at position B, where the leading ship saves 8% and the trailing ship saves 96% of its wave drag. This kind of mutual benefit is essential to configurate the optimal formation of a water train, as it could save on the amount of energy as a whole. As the separation increases, this benefit of the leader's drag reduction diminishes rapidly. There is nearly no interactive effect on the leading ship as the separation becomes larger than a trailing ship's body length.

3) Why can the trailing ship save energy when it swims at position B, while it consumes more energy at position B? The wave patterns in *Figure 2* (b) and (c) help to reveal these reasons. When the trailing ship is riding the waves at position B, a destructive wave interference phenomenon is observed, as shown in *Figure 2* (b). The wave cancellation mainly occurs in the leading ship's aft wedge region. The phase of the waves generated by the trailing ship is different from that of leading ship's waves. By superposition, the downstream waves are partially cancelled. Taking the leading ship and trailing ship as a whole system ("0+1"), it requires less work done by the system to maintain the resultant wave energy. As the waves are confined downstream within a Kelvin wedge, the leading ship can only receive very limited benefit from wave cancellation. In contrast, when the trailing ship is swimming on the waves at position A, a constructive wave interference is observed. The extra energy carried by the amplified waves is mainly extracted from the trailing ship's energy expenditure due to the downstream propagation nature of the Kelvin waves. It coincides with the fact that drag increases at position A, as shown in *Figure 2*.

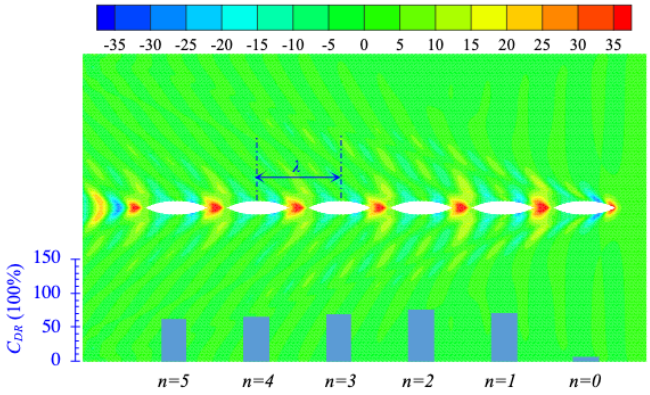

Figure 3. The optimum swimming formation by a leading ship (*n*=0) followed by trailing ship(s) in an array of 5. The contour is the wave pattern by "0+5" in an optimum formation. *n* represents the *n*-th trailing ship in the formation. The columns represent the wave drag reduction of the *n*-th individual *n*.

Assuming the first trailing ship (*n*=1) stays at a position with maximum wave drag reduction (position B), let's put the second trailing ship (*n*=2) to follow "*0*+1". Obviously, the wave energy generated by the leading ship

has been partly extracted by the 1st trailer. The aft wedge region in *Figure 2* (c) may not provide enough energy for the 2nd trailer to achieve the same amount of drag reduction as the first one. This leads to other interesting questions, if there is more than one trailing ships following a leading ship: 1) what is the best configuration? 2) how much wave drag can be saved by each individual in a formation? To answer these questions on "*0+n*", a large computation needs to be performed by repeating the above-mentioned process of "0+1", and we can find the best position for each individual in sequence from the 1st to the n^{th} body, and eventually an optimum formation can be obtained.

Figure 3 shows the optimum swimming formation of "*0+5*" system. The separation between adjacent trailing ships is nearly uniform, i.e. a wave length. The most exciting finding from the results in Figure 3 is a *wave-passing* phenomenon. The leading ship generates the waves in the wake, leaving energy potentially available for the trailing ships to extract. As the first trailer is moving directly behind the leading ship, it is supposed to receive the best benefit. However, its wave drag reduction is slightly less than the 2nd trailer, whose C_{DR}=102%, in which 100% is used to overcome its wave drag, and the remaining 2% turns to be a propulsive force. Although the wave drag reduction fluctuates around 90% (one possible reason of the fluctuation is the numerical error in the calculation, in which only limited positions are calculated), the remaining wave energy is still sufficient for the rest of the trailing ships to gain a large stable wave drag reduction, indicating the benefit of wave drag reduction is passed from the 1st trailer to the last one in a queen. This *wave-passing* phenomenon can also be observed in the wave patterns shown in Figure 3. The waves behind the leading ship are passed by its trailer, and then the same waves are maintained behind each ship. Repeating this process, the wave energy initiated from the leading ship will eventually reaches the *n*-th trailing ship, regardless of the separation.

It should be noted that not all the trailing ships receive a 100% of wave drag reduction. This is different from the observation by Yuan et al. (2021), in which the size of the leading one in a formation is much larger than the trailing individuals. As a results, the leading one could initiate sufficient waves for the trailers to ride and to pass. Therefore, when designing a water train, the size and hull form of the engine ship could be an important factor, which determines how much drag reduction can be achieved by the trailing coaches. The idea case is to design a configuration that all the trailing coaches received 100% of wave drag reduction, so that the train made by multiple short ships could be equivalent of a single long parallel mid-body.

REFERENCES

Ellingsen, S. Å. (2021). "Getting the ducks in a row." Journal of Fluid Mechanics **932**.

Liao, J. C. (2007). "A review of fish swimming mechanics and behaviour in altered flows." Philos Trans R Soc Lond B Biol Sci **362**(1487): 1973-1993.

Yuan, Z.-M., et al. (2021). "Wave-riding and wave-passing by ducklings in formation swimming." Journal of Fluid Mechanics **928**.

Yuan, Z. M., et al. (2015). "Ship-to-Ship Interaction during Overtaking Operation in Shallow Water." Journal of Ship Research **59**(3): 172-187.

Two-Dimensional Planing in Water of Finite Depth

Zhihang Zhang
Department of Naval Architecture and Marine Engineering
University of Michigan, Ann Arbor, USA
ZhihangZ@Umich.edu

Kevin J. Maki
Department of Naval Architecture and Marine Engineering
University of Michigan, Ann Arbor, USA
KJMaki@UMich.edu

Lawrence J. Doctors
School of Mechanical and Manufacturing Engineering
The University of New South Wales, Sydney, Australia
L.Doctors@UNSW.edu.au

Highlights

The traditional deep-water analysis of planing is extended to the case where the water has a finite depth. There are remarkable and strong depth phenomena, which are predicted by the potential-flow and the computational fluid dynamics analyses. Furthermore, the formulation of Newman and Poole (1962, Equation 10) is shown to apply to the sudden drop in the wave-resistance component of the total inviscid drag at the critical speed.

1 Introduction

A detailed summary of the early work by Sedov (1936), Maruo (1951), Maruo (1956), Maruo (1957), Maruo (1959), Squire (1957) and Sedov (1965, Chapter VII), can be found in the work of Doctors (1974).

In all cases, the planing surface is represented by an unknown pressure distribution, which is to be found. Doctors (1974) developed a simple approach in which the pressure is composed of overlapping triangular elements, as depicted in Figure 1(a).

Here we extend the work to include the effects of finite depth and we complement the results with computational fluid dynamics (CFD).

2 Potential-Flow Theory

We follow the classic inviscid-flow approach and assume linearized kinematic and dynamic conditions at the free surface, as well as the kinematic condition on the bottom. The wave elevation for a pressure patch was given by Doctors (2018a, Equation 12.12). For the current application, we only require the zeroth (transverse or two-dimensional) term in the summation of the wave components:

$$\zeta(x) = \frac{1}{\pi}\int_0^\infty \mathrm{d}k\, k^2 \exp(\mathrm{i}kx)\,\mathcal{U}/f - \left\langle \mathrm{i}k^2 \exp(\mathrm{i}kx)\,\mathcal{U}\Big/\frac{\mathrm{d}f}{\mathrm{d}k}\right\rangle - \delta(x)\,, \tag{1}$$

$$f = k^2 - k_0 k \tanh(kd)\,, \tag{2}$$

$$\mathrm{d}f/\mathrm{d}k = 2k - k_0 \tanh(kd) - k_0 kd\,\mathrm{sech}^2(kd)\,, \tag{3}$$

$$k_0 = g/U^2\,, \tag{4}$$

where k is the wave number, f is the dispersion relationship and k_0 is the fundamental circular wave number. Equation 1 applies only to a pressure element which is symmetric fore-and-aft – as in the present case. The static depression in Equation 1 is $\delta(x)$.

The solution for k in the implicit equation for $f = 0$ in Equation 2 can be found in the usual way by using the Newton-Raphson iteration with the assistance of its derivative in Equation 3. For

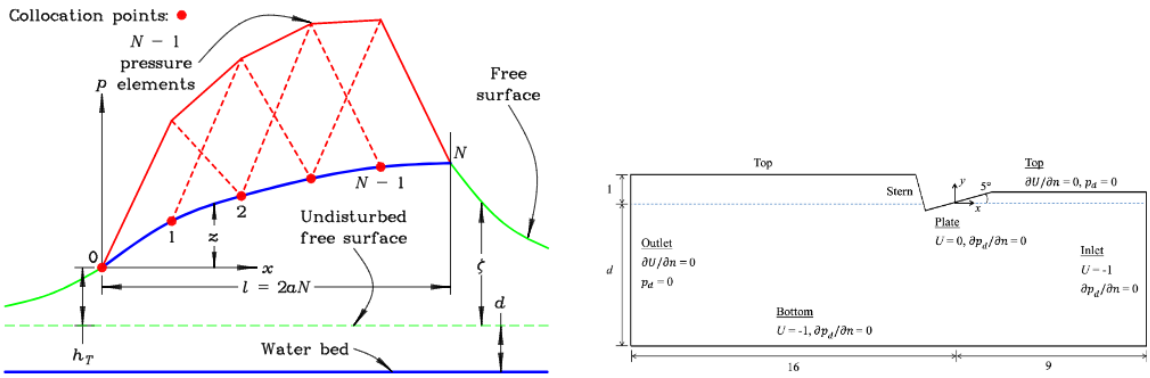

(a) Triangular Pressure Elements

(b) Computational Domain

Figure 1: Definition of the Problem

subcritical speeds, $F_d = U/\sqrt{gd} < 1$, the second term in Equation 1 is evaluated for this solution. For supercritical speeds there is no solution and this term is to be ignored; this is indicated by the $\langle\rangle$ notation.

The Kochin function $\mathcal{U}$ for a triangular element was given by Doctors (2018b, Section 8.3) as

$$\mathcal{U} \;=\; \delta_0 \cdot 2a \cdot [\sin(ka)/ka]^2 \,, \tag{5}$$

in which δ_0 is the nominal (peak) static depression for the pressure element.

3 Results for Influence Function

The influence function in Equation 1 for various test cases has been checked with the deep-water analytic formula developed by Doctors (1974). It has also been verified for the case of finite water depth with the work of Maki, Broglia, Doctors and Di Mascio (2012).

4 Computational Fluid Dynamics

A two-phase flow solver, which is based on the open-source CFD library OpenFOAM, is used to model the nonlinear viscous-fluid flow around the planing plate. The Reynolds-averaged Navier-Stokes (RANS) equations are used to govern both the water and air.

Figure 1(b) shows the computational domain with boundary conditions and dimensions. For the present simulations, the flow speed $U = 1$, gravity $g = 1$, and trim angle $\alpha = 5°$ are fixed. Three different water depths are studied; $d = 16$, 2, and 0.5. Other fluid parameters include the water density $\rho = 998.8$, air density $\rho_a = 1$, water kinematic viscosity $\nu = 1.09\times10^{-6}$ and air kinematic viscosity $\nu_a = 1.48\times10^{-5}$.

Other details of the solver and numerical setup can be found in Garland and Maki (2012) and Kramer, Maki and Young (2013).

5 Results for Planing

The pressure distribution p in Figure 2(a) has been nondimensionalized using the wetted length l and the lift L. The finite-depth potential-flow method is compared with the CFD data using the no-slip boundary condition. The Froude number F based on the wetted length is not a selected round number, because this length is not prescribed in the CFD method.

The dimensionless trailing-edge elevation is plotted against the Froude number for a selection of dimensionless depths d/l in Figure 2(b). The singular behavior of the elevation in the region near the critical speed is evident. It is pleasing to see the close agreement between the potential-flow predictions and the three CFD-computed points. In particular, the bizarre result of a positive trailing-edge elevation for the relatively-shallow-water case of $d/l = 0.3460$ is confirmed.

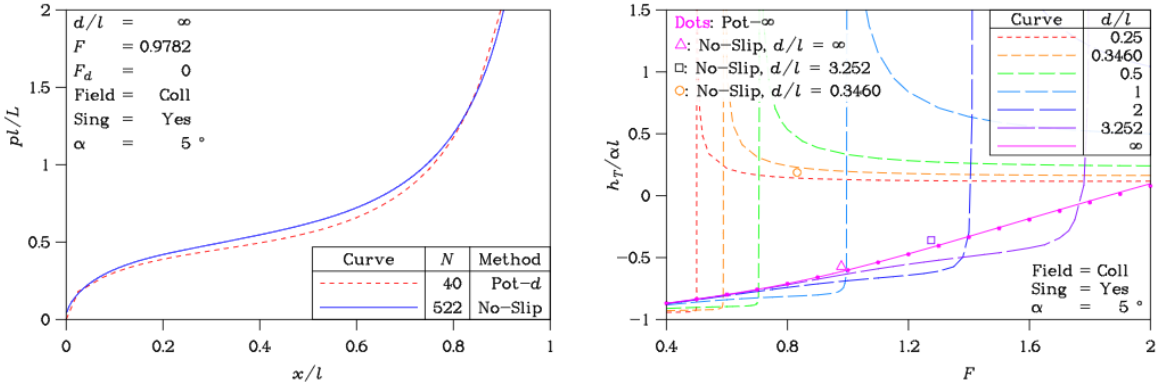

(a) Pressure

(b) Trailing-Edge Elevation

Figure 2: Pressure Distribution and Trailing-Edge Elevation

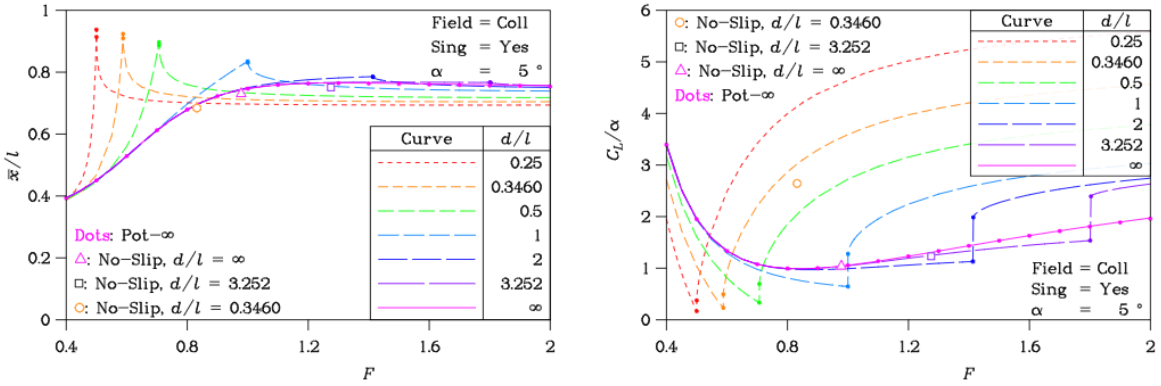

(a) Center of Pressure

(b) Lift

Figure 3: Center of Pressure and Lift

The dots represent data from the deep-water-only method described by Doctors (1974). They provide confirmation of the coding in the new finite-depth software.

The dimensionless center of pressure $\overline{x}/l$ is plotted in Figure 3(a). The potential-flow predictions indicate that there is extreme, but not singular, behavior near the critical speed. Once again, the CFD deep-water and finite-depth points lie extremely close to the potential-flow curves.

The lift coefficient per unit trim angle C_L/α is shown in Figure 3(b). There is a sudden rise in the lift at the critical speed. The CFD deep-water point falls slightly below the potential-flow curve. The two finite-depth CFD data points are in very close agreement with the potential-flow predictions.

The potential-flow wave-resistance coefficient is plotted in Figure 4(a). The wave resistance drops to zero at the critical speed because this is a two-dimensional problem.

This sudden drop is related to the loss of the second term in Equation 1. It was first discovered by Newman and Poole (1962, Equation 10) for a pressure distribution. The same result was derived by Doctors (2018b, Section 5.5) for a displacement vessel with weight W in a channel of width w:

$$\Delta R_W \quad = \quad \frac{3W^2}{2\rho g w d^2} \quad \text{with} \quad w \equiv 1 \,. \tag{6}$$

Here we can substitute $W = L = \frac{1}{2}\rho U^2 l \cdot C_L$ and $R_W = \frac{1}{2}\rho U^2 l \cdot C_W$ into Equation 6. We also note that $F_d = 1$ and $w \equiv 1$. After some algebra it can be show that

$$\Delta C_W / C_L^2 \quad = \quad (3/4) \cdot (l/d) \,. \tag{7}$$

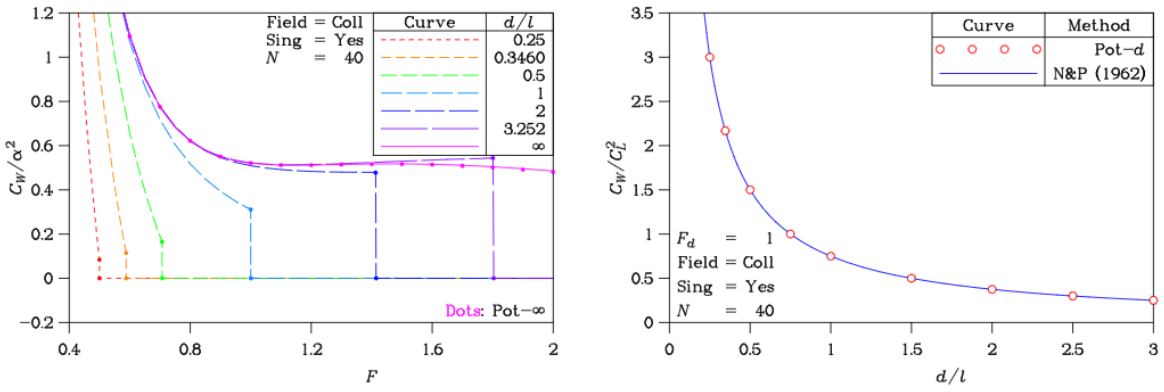

(a) Coefficient

(b) Drop at Critical Speed

Figure 4: Wave Resistance

The two sides of Equation 7 are plotted in Figure 4(b) and this remarkable phenomenon is verified for the planing case. However, we note that the planing surface also generally suffers spray resistance, which is to be considered separately.

6 Concluding Comments

Further work is required to resolve the minor discrepancies between the predictions of the lift between the potential-flow and the CFD calculations. The differences might be attributed to nonlinear effects and the presence of viscosity in the CFD analysis.

Long-term plans include extension of this work to the three-dimensional case.

7 References

Doctors, L. J. (1974): "Representation of Planing Surfaces by Finite Pressure Elements", *Proc. Fifth Australasian Conference on Hydraulics and Fluid Mechanics*, Christchurch, New Zealand, Vol. 2, pp 480–488, December.

Doctors, L. J. (2018a): *Hydrodynamics of High-Performance Marine Vessels*, Printed by CreateSpace, an Amazon.com Company, Charleston, South Carolina, Second Edition, Vol. 2, pp 423–885+ii, January.

Doctors, L. J. (2018b): *Hydrodynamics of High-Performance Marine Vessels*, Printed by CreateSpace, an Amazon.com Company, Charleston, South Carolina, Second Edition, Vol. 1, pp 1–421+li, January.

Garland, W. R. and Maki, K. J. (2012): "A Numerical Study of a Two-Dimensional Stepped Planing Surface", *J. Ship Production and Design*, Vol. 28, No. 2, pp 60–72, May.

Kramer, M. R., Maki, K. J., and Young, Y. L. (2013): "Numerical Prediction of the Flow Past a 2-D Planing Plate at Low Froude Number", *Ocean Engineering*, Vol. 70, pp 110–117, September.

Maki, K. J., Broglia, R., Doctors, L. J., and Di Mascio, A. (2012): "Nonlinear Wave Resistance of a two-Dimensional Pressure Patch Moving on a Free Surface", *Ocean Engineering*, Vol. 39, pp 62–71, January.

Maruo, H. (1951): "Two Dimensional Theory of the Hydroplane", *Proc. First Japan National Congress for Applied Mechanics*, pp 409–415.

Maruo, H. (1956): "Hydrodynamic Researches of the Hydroplane (Part 1)", *J. Zosen Kiokai*, Vol. 91, pp 9–16, September.

Maruo, H. (1957): "Hydrodynamic Researches of the Hydroplane (Part 2)", *J. Zosen Kiokai*, Vol. 92, pp 57–63, April.

Maruo, H. (1959): "Hydrodynamic Researches of the Hydroplane (Part 3)", *J. Zosen Kiokai*, Vol. 105, pp 23–26, July.

Newman, J. N. and Poole, F. A. P. (1962): "The Wave Resistance of a Moving Pressure Distribution in a Canal", *Schiffstechnik*, Vol. 9, No. 45, pp 21–26, January.

Sedov, L. I. (1936): "Two Dimensional Problem of Planing on the Surface of a Heavy Fluid", *Trudy Konferentsii po Teorii Volnovogo Sprotivleniya*, Moscow, pp 7–30.

Sedov, L. I. (1965): *Two-Dimensional Problems in Hydrodynamics and Aerodynamics*, Interscience Publishers, New York, NY, Translated from the Russian and edited by Chu, C.K., Cohen, H., and Seckler, B., 427+xv pp.

Squire, H. B. (1957): "The Motion of a Simple Wedge along the Water Surface", *Proc. Royal Society of London*, Series A, Vol. 243, No. 1232, pp 48–64, December.

Extension of MCC-FS model to bottom time-varying problems

B.B. Zhao[1], T.Y. Zhang[1], L.J. Li[1], Z. Wang[1,2,*], W.Y. Duan[1], M. Hayatdavoodi[1,3]

[1] College of Shipbuilding Engineering, Harbin Engineering University, Harbin, China

[2] Qingdao Innovation and Development Center of Harbin Engineering University, Qingdao, China

[3] School of Science and Engineering, University of Dundee, Dundee, UK

*zhan.wang@hrbeu.edu.cn

Highlights

- Equations of the Miyata-Choi-Camassa model that includes the free-surface effect (MCC-FS model) are extended to solve bottom time-varying problems.
- Waves generated by a moving obstacle on the bottom in a two-layer fluid system with a free surface is numerically simulated by use of the extended MCC-FS model.

1 Introduction

Internal wave is a common phenomenon in nature. Internal waves are generated by disturbances in the density stratified lakes and oceans. The model derived by Miyata (1985), Choi & Camassa (1999) (MCC, hereafter) is widely used to study large-amplitude internal waves in a two-layer fluid system. However, most of the studies on the MCC model are confined to the flat-bottom cases (Camassa et al., 2006; Jo & Choi, 2008; Kodaira et al., 2016; La Forgia & Sciortino, 2019; Zhao et al., 2020) or the cases where bottom only varied with space (Choi & Camassa, 1996; Choi et al., 2020).

For time-varying bottom in a two-layer fluid system, Grue et al. (1997) studied internal waves generated by a moving obstacle on the bottom by solving Euler's equations under the rigid-lid assumption (Euler-RL solution). Zhao et al. (2014) and Zhao & Duan (2014) used the two-layer high-level Green-Naghdi model to investigate the free-surface effect on the generated internal waves by comparing with Euler-RL solution of Grue et al. (1997).

In this paper, we will extend the MCC model that includes the free-surface effect (MCC-FS model) to solve bottom time-varying problems. This paper is organized as follows. The governing equations and boundary conditions of the extended MCC-FS model are described in Section 2. Numerical results of internal waves generated by a moving obstacle on the bottom in a two-layer fluid system with a free surface are presented and discussed in Section 3. Conclusions are reached in Section 4.

2 MCC-FS model

In this paper, we consider a two-layer fluid system with a free surface, shown in Figure 1. The two fluids are assumed to be inviscid, immiscible and incompressible. The origin of the Cartesian coordinate system is at the undisturbed interface between the two fluids. The mass densities of the upper and lower layers are ρ_1 and ρ_2, respectively. The undisturbed depths of the upper and lower layers are h_1 and h_2, respectively. The free surface, interface and bottom are expressed by $z = \eta_1(x, t)$, $z = \eta_2(x, t)$ and $z = \eta_3(x, t)$, respectively.

In the MCC-FS model, the governing equations include the mass conservation equations and the momentum conservation equations (Euler's equations), which in two dimensions can be written as

$$\frac{\partial u_i}{\partial x} + \frac{\partial w_i}{\partial z} = 0 \quad (i = 1, 2), \tag{1}$$

$$\frac{\partial u_i}{\partial t} + u_i \frac{\partial u_i}{\partial x} + w_i \frac{\partial u_i}{\partial z} = -\frac{1}{\rho_i} \frac{\partial p_i}{\partial x} \quad (i = 1, 2), \tag{2a}$$

$$\frac{\partial w_i}{\partial t} + u_i \frac{\partial w_i}{\partial x} + w_i \frac{\partial w_i}{\partial z} = -\frac{1}{\rho_i} \frac{\partial p_i}{\partial z} - g \quad (i = 1, 2), \tag{2b}$$

where u and w are horizontal and vertical velocity components, respectively, p is the pressure and g is gravitational acceleration. $i = 1$ represents the variables for the upper-fluid layer and $i = 2$ represents the variables for the lower-fluid layer.

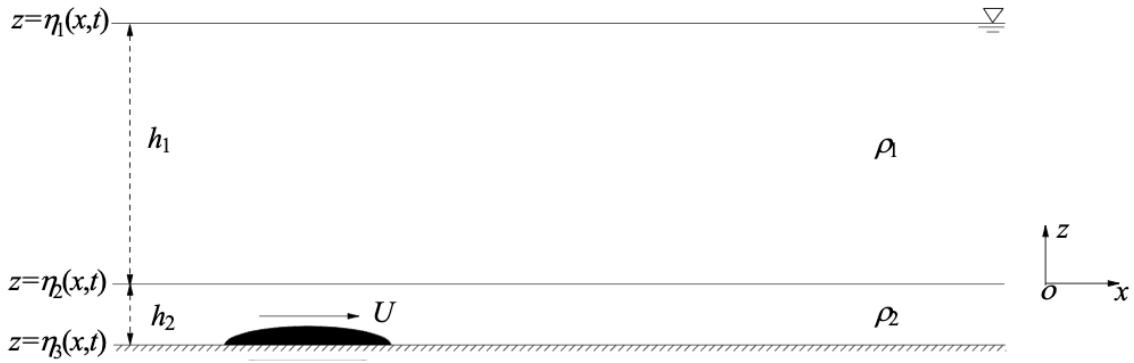

Figure 1 Sketch of a two-layer fluid system with a free surface

The boundary conditions for the upper-fluid layer are written as

$$w_1 = \frac{\partial \eta_1}{\partial t} + u_1 \frac{\partial \eta_1}{\partial x}, \quad \hat{p}_1 = 0 \quad \text{at } z = \eta_1(x,t), \tag{3a}$$

$$w_1 = \frac{\partial \eta_2}{\partial t} + u_1 \frac{\partial \eta_2}{\partial x} \quad \text{at } z = \eta_2(x,t), \tag{3b}$$

The boundary conditions for the lower-fluid layer are written as

$$w_2 = \frac{\partial \eta_2}{\partial t} + u_2 \frac{\partial \eta_2}{\partial x} \quad \text{at } z = \eta_2(x,t), \tag{4a}$$

$$w_2 = \frac{\partial \eta_3}{\partial t} + u_2 \frac{\partial \eta_3}{\partial x} \quad \text{at } z = \eta_3(x,t). \tag{4b}$$

The dynamic boundary condition at the interface between the two-fluid layers is written as

$$\overline{p}_1 = \hat{p}_2 \quad \text{at } z = \eta_2(x,t). \tag{5}$$

In the MCC-FS model, the depth-averaged horizontal velocity for each layer is defined as

$$\overline{u}_i(x,t) = \frac{1}{\eta_i - \eta_{i+1}} \int_{\eta_{i+1}}^{\eta_i} u_i(x,z,t)\mathrm{d}z \quad (i = 1,2). \tag{6}$$

The equations of the MCC-FS model for the flat bottom, i.e., $z = \eta_3(x, t) = -h_2$, can be written as (see e.g., Kodaira et al., 2016)

$$\frac{\partial \zeta_1}{\partial t} + \frac{\partial (\zeta_1 \overline{u}_1)}{\partial x} = 0, \quad \zeta_1 = \eta_1 - \eta_2, \tag{7a}$$

$$\frac{\partial \zeta_2}{\partial t} + \frac{\partial (\zeta_2 \overline{u}_2)}{\partial x} = 0, \quad \zeta_2 = \eta_2 - \eta_3, \tag{7b}$$

$$\frac{\partial \overline{u}_1}{\partial t} + \overline{u}_1 \frac{\partial \overline{u}_1}{\partial x} + g \frac{\partial}{\partial x}(\zeta_1 + \zeta_2) = \frac{1}{3\zeta_1} \frac{\partial}{\partial x}\left(\zeta_1^3 G_1\right) - \frac{1}{2\zeta_1} \frac{\partial}{\partial x}\left(\zeta_1^2 D_1^2 \zeta_2\right) + \frac{\partial \zeta_2}{\partial x}\left(\frac{1}{2}\zeta_1 G_1 - D_1^2 \zeta_2\right), \tag{7c}$$

$$\frac{\partial \overline{u}_2}{\partial t} + \overline{u}_2 \frac{\partial \overline{u}_2}{\partial x} + g \frac{\partial}{\partial x}\left(\frac{\rho_1}{\rho_2}\zeta_1 + \zeta_2\right) = \frac{1}{3\zeta_2} \frac{\partial}{\partial x}\left(\zeta_2^3 G_2\right) + \frac{\rho_1}{\rho_2} \frac{\partial}{\partial x}\left(\frac{1}{2}\zeta_1^2 G_1 - \zeta_1 D_1^2 \zeta_2\right), \tag{7d}$$

where

$$G_i(x,t) = \frac{\partial^2 \overline{u}_i}{\partial x \partial t} + \overline{u}_i \frac{\partial^2 \overline{u}_i}{\partial x^2} - \left(\frac{\partial \overline{u}_i}{\partial x}\right)^2, \quad D_i \equiv \frac{\partial}{\partial t} + \overline{u} \frac{\partial}{\partial x}. \tag{8}$$

In this paper, we extend the MCC-FS model to study the physical problem where the bottom varies with time and space, and hence Equations (7c) - (7d) are modified. The derivation process will be presented in the workshop.

3 Numerical results

Here, we numerically study the internal waves generated by a moving ellipse obstacle on the bottom in a two-layer fluid system with a free surface as shown in Figure 1. The parameters are the same as those given by Grue et al. (1997). Mass densities of the upper and lower layers are $\rho_1 = 787.3\text{kg/m}^3$ and $\rho_2 = 1000\text{kg/m}^3$, respectively. Undisturbed depths of the upper and lower layers are $h_1 = 0.12$m and $h_2 = 0.03$m, respectively. The major-semi axis and the minor-semi axis of the moving ellipse obstacle are $L_{1/2} = 10h_2 = 0.3$m and $B_{1/2} = 0.1h_2 = 0.003$m, respectively. The constant velocity of the obstacle is $U = 1.1c_0 = 0.252$m/s, where $c_0 = [gh_1h_2(\rho_2-\rho_1)/(\rho_2h_1+\rho_1h_2)]^{1/2}$ is the linear long-wave speed. The initial

center position of the moving obstacle is at $x = 0$m.

We use the MCC-FS model to simulate the physical problem in time domain. We note that this case belongs to the shallow-configuration case ($h_1/h_2 = 4/1$) and the MCC-FS model can provide accurate results. Snapshots of the surface-wave elevation, internal-wave elevation and bottom at two different moments are shown in Figure 2.

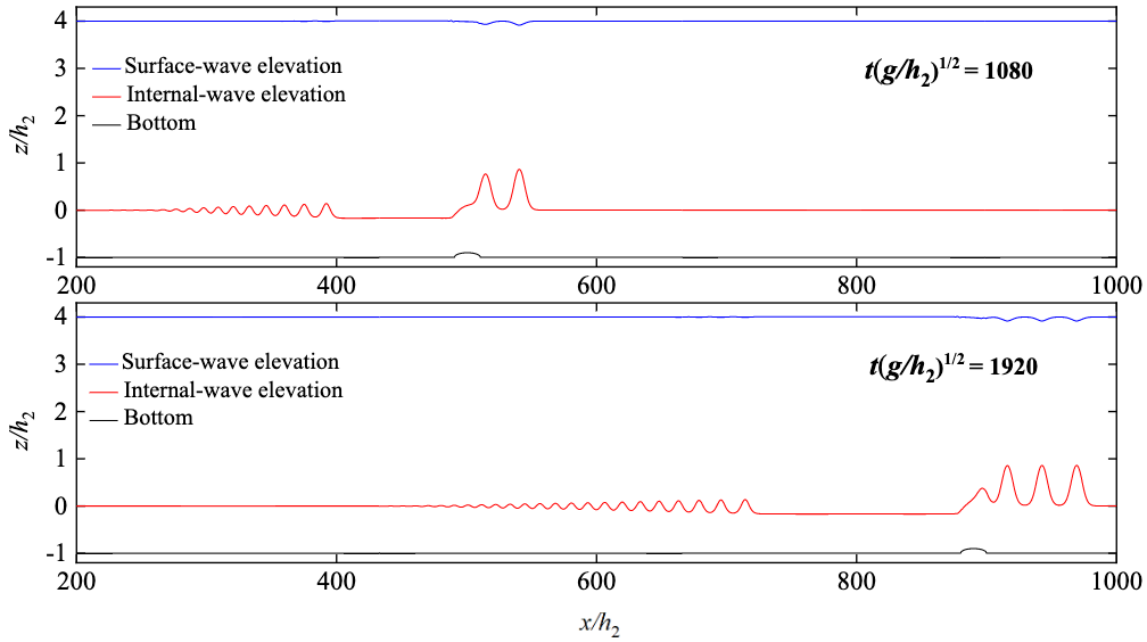

Figure 2 Snapshots of the elevations at different moments

As shown in Figure 2, surface waves in the depression form and internal waves in the elevation form are generated. With the time marching, the number of generated waves increases. At $t\,(g/h_2)^{1/2} = 1920$, three complete surface waves with amplitude $b/h_2 = -0.08$ and three complete internal waves with amplitude $a/h_2 = 0.86$ are observed.

Next, we compare the internal-wave elevation results of the MCC-FS model with the results of the computational fluid dynamics (CFD) software, STAR-CCM+ and Euler-RL solution of Grue et al. (1997) and at $t\,(g/h_2)^{1/2} = 1920$, as shown in Figure 3. We note that in the STAR-CCM+ simulations, the free-surface effect is included.

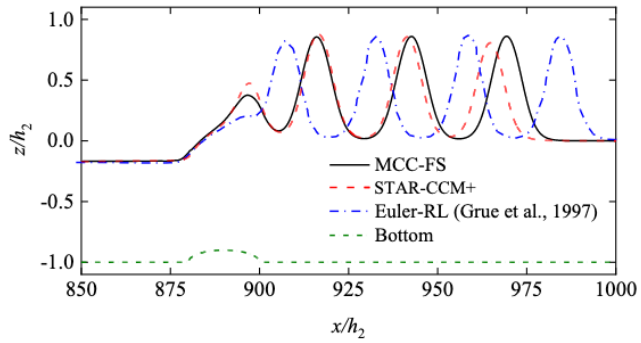

Figure 3 Comparison of internal-wave elevation obtained by the MCC-FS model, STAR-CCM+ and Euler-RL solution of Grue et al. (1997) at $t\,(g/h_2)^{1/2} = 1920$

From Figure 3, we observe that four complete internal waves have been generated through the Euler-RL solution. While results of the MCC-FS model and STAR-CCM+ show that only three complete internal waves have been generated. Furthermore, the wave speed is smaller in the MCC-FS and STAR-CCM+ results compared with the Euler-RL solution. These differences are caused by the rigid-lid approximation introduced by Grue et al. (1997). Since the density ratio between the two fluids is not close to 1, the free-surface effect should be considered (Lamb, 1932), which is also observed in results shown in Figure 3.

The surface-wave elevation obtained by the MCC-FS model and STAR-CCM+ at $t\,(g/h_2)^{1/2} = 1920$ is shown in Figure 4. We observe that three complete surface waves in the depression form have been generated. The amplitude of

the surface waves reaches $b/h_2 = -0.08$, which also implies that the free-surface effect should be included for this case where $\rho_1 / \rho_2 = 0.7873$.

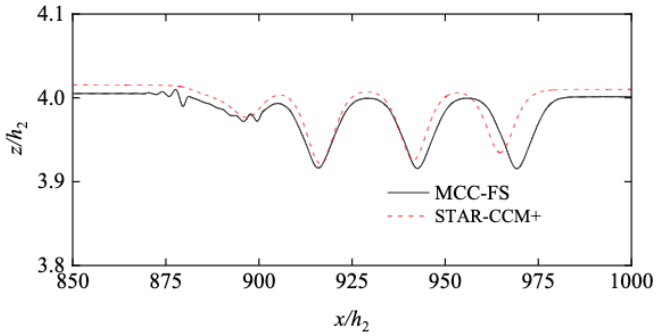

Figure 4 Surface-wave elevation obtained by the MCC-FS model and STAR-CCM+ at $t\,(g/h_2)^{1/2} = 1920$

4 Conclusions

In this paper, we extend the equations of the MCC-FS model to solve bottom time-varying problems. The internal waves generated by a moving obstacle on the bottom in a two-layer fluid system with a free surface is then numerically simulated. By comparing the MCC-FS results with the STAR-CCM+ results and the Euler-RL solution of Grue et al. (1997), we find that the number of generated waves is fewer and the wave speed is smaller when the free-surface effect is considered. Since the density ratio between the two fluids is not always close to 1, the rigid-lid approximation introduces larger errors in this case and the free-surface effect should be considered.

Acknowledgments

The first and fifth authors' (B.B. Zhao and W.Y. Duan) work is supported by the National Natural Science Foundation of China (No. 11972126) and the Heilongjiang Touyan Innovation Team Program.

References

[1] Miyata, M. (1985). An internal solitary wave with large amplitude. La Mar, 23: 43-48.
[2] Choi, W. & Camassa, R. (1999). Fully nonlinear internal waves in a two-fluid system. Journal of Fluid Mechanics, 396: 1-36.
[3] Camassa, R., Choi, W., Michallet, H., Rusas, P.-O. & Sveen, J.K. (2006). On the realm of validity of strongly nonlinear asymptotic approximations for internal waves. Journal of Fluid Mechanics, 549: 1-24.
[4] Jo, T.-C. & Choi, W. (2008). On Stabilizing the Strongly Nonlinear Internal Wave Model. Studies in Applied Mathematics, 120(1): 65-85.
[5] Kodaira, T., Waseda, T., Miyata, M. & Choi, W. (2016). Internal solitary waves in a two-fluid system with a free surface. Journal of Fluid Mechanics, 804: 201-223.
[6] La Forgia, G. & Sciortino, G. (2019). The role of the free surface on interfacial solitary waves. Physics of Fluids, 31: 106601.
[7] Zhao, B.B., Wang, Z., Duan, W.Y., Ertekin, R.C., Hayatdavoodi, M. & Zhang, T.Y. (2020). Experimental and numerical studies on internal solitary waves with a free surface. Journal of Fluid Mechanics, 899, A17.
[8] Choi, W. & Camassa, R. (1996). Weakly nonlinear internal waves in a two-fluid system. Journal of Fluid Mechanics, 313, 83-103.
[9] Choi, W., Zhi, C. & Barros, R. (2020). High-order unidirectional model with adjusted coefficients for large-amplitude long internal waves. Ocean Modelling, 151: 101643.
[10] Grue, J., Friis, H.A., Plam, E. & Rusas, P.O. (1997). A method for computing unsteady fully nonlinear interfacial waves. Journal of Fluid Mechanics, 351, 223-252.
[11] Zhao, B.B., Duan, W.Y., Ertekin, R.C. & Webster, W.C. (2014). Recent progress on the GN model for a two-layer flow. 29th International Workshop on Water Waves and Floating Bodies, Osaka, Japan.
[12] Zhao, B.B. & Duan, W.Y. (2014). Fluid-sheet water-wave theory—GN wave model. Tsinghua University Press (in Chinese).
[13] Lamb, H. (1932). Hydrodynamics, Dover.

Abstract for 37th IWWWFB, Giardini Naxos, Italy - April 10-13, 2022

Water wave interaction with an annular metamaterial cylinder

S. Zheng[a], R. Porter[b], H. Liang[c], D. Greaves[a]

a School of Engineering, Computing & Mathematics, University of Plymouth, Drake Circus, Plymouth PL4 8AA, United Kingdom
siming.zheng@plymouth.ac.uk; deborah.greaves@plymouth.ac.uk
b School of Mathematics, University of Bristol, Woodland Road, Bristol BS8 1UG, United Kingdom
richard.porter@bristol.ac.uk
c Technology Centre for Offshore and Marine, Singapore (TCOMS), 118411, Singapore
liang_hui@tcoms.sg

Highlights

We study water wave scattering by an annular metamaterial cylinder, which is composed of a series of radially aligned closely spaced plates, with both analytical and numerical methods.

- We find there can be hardly any back scattering for a wide range of wave frequencies;
- The resonant frequencies are predicted, around which the near non-back-scattering generally happens;
- We observe and theoretically prove that there is not any scattered wave contribution at the center point of the annular metamaterial cylinder.

1 Mathematical model

An annular metamaterial cylinder subjected to unidirectional regular waves in water of finite depth h is considered. The annular cylinder with its inner and outer radii denoted as $R_{\rm i}$ and R, respectively, is composed of a periodic array of infinitely–thin vertical plates aligned with the radial direction. A global Cartesian coordinate system $Oxyz$ is chosen with the mean free–surface coinciding with the (x, y)–plane, Oz placed at the axis of the cylinder pointing vertically upwards, and Ox coinciding with the incident wave direction. Hence the fluid bottom is at $z = -h$. Moreover, a cylindrical coordinate system, $Or\theta z$, are chosen for the purpose of convenience of mathematical expression. Fluid is allowed to flow in gaps between adjacent plates and waves are supported by the free surface. The effect of these plates of annular cylinder allows waves to propagate in the Or–direction only. The fluid domain can be divided into an annular domain, which fills the annular metamaterial cylinder, an exterior domain, representing the fluid domain outside the metamaterial cylinder extending towards infinity horizontally, and a inner region.

We assume that all amplitudes are small enough that linear theory applies and we make the usual assumptions that the fluid is inviscid, incompressible and its motion is irrotational. We denote the fluid velocity potential by $\Phi(x, y, z, t)$. It is further assumed that all motion is time–harmonic with angular frequency ω. Thus, we can write

$$\Phi(x, y, z, t) = \mathrm{Re}\{\phi(x, y, z)\mathrm{e}^{-\mathrm{i}\omega t}\}, \tag{1}$$

where Re denotes the real part. Thus ϕ is the spatial velocity potential which is independent of time, i.e., t. i is the imaginary unit. The spatial velocity potential satisfies Laplace equation,

$$\bigtriangledown^2 \phi = 0 \quad \text{in the water}, \tag{2}$$

and the boundary conditions at sea bed and free surface.

Within the fluid in the annular cylinder, Eq. (2) also holds although it is confined to narrow disconnected domains bounded by thin plates aligned with the radial direction of the $Or\theta z$ coordinate. Writing Eq. (2) in coordinate $Or\theta z$ and imposing the boundary conditions on the channel walls, it shows that the field within the whole of the annular cylinder is governed by an effective medium governing equation involving the reduced Laplacian:

$$\left(\frac{\partial^2}{\partial r^2} + \frac{1}{r}\frac{\partial}{\partial r} + \frac{\partial^2}{\partial z^2}\right)\phi = 0. \tag{3}$$

See also [1, 5] who employed the same models. Eq. (3) conservation of mass for an irrotational flow in which the motion perpendicular to the plates is inhibited.

Expressions of spatial velocity potential in different domains.–The spatial velocity potential in the exterior domain can be expressed as

$$\phi_{ext} = \phi_I + Z_0(z)\sum_{n=0}^{\infty} A_n H_n(kr)\cos(n\theta), \tag{4}$$

where ϕ_I represents the velocity potential of incident waves. The second term denotes the components contributed by the waves scattered from the cylinder. A_n are the unknown coefficients to be determined; H_n denotes the Hankel function of the first kind of order n; $Z_0(z) = \frac{\cosh[k(z+h)]}{\cosh(kh)}$; k is associated with propagating waves, and it is the positive real root of the dispersion relation for the exterior domain

$$\omega^2 = gk\tanh(kh), \tag{5}$$

where g denotes the acceleration due to gravity.

For the plane incident waves with amplitude A, angular frequency ω and wave direction $\beta = 0$, ϕ_I can be expressed in the coordinate systems of $Oxyz$ and $Or\theta z$, respectively, as

$$\phi_I = -\frac{\mathrm{i}gA}{\omega}\mathrm{e}^{\mathrm{i}kx}Z_0(z) = -\frac{\mathrm{i}gA}{\omega}Z_0(z)\sum_{n=0}^{\infty}\epsilon_n\mathrm{i}^n J_n(kr)\cos(n\theta), \tag{6}$$

where J_n is the Bessel function of the first kind of order n. ϵ_0=1, and ϵ_n=2 for $n > 0$.

The spatial velocity potentials in the interior and annular domains can be expressed as

$$\phi_{int}(r,\theta,z) = Z_0(z)\sum_{n=0}^{\infty}B_n J_n(kr)\cos(n\theta), \tag{7}$$

and

$$\phi_{ann}(r,\theta,z) = Z_0(z)\sum_{n=0}^{\infty}[C_n J_0(kr) + D_n Y_0(kr)]\cos(n\theta), \tag{8}$$

respectively, in which B_n, C_n, and D_n are unknown coefficients to be determined; Y_0 denotes the Bessel function of the second kind (also known as the Neumann function) of order 0.

The unknown coefficients, A_n, B_n, C_n, and D_n, in the expressions of the velocity potentials can be calculated by satisfying the continuity of the field in terms of pressure and flux across the interfaces of the annular, exterior, and interior domains, resulting in four sets of equations, i.e.,

$$\begin{pmatrix} J_n(kR_\mathrm{i}) & 0 & -J_0(kR_\mathrm{i}) & -Y_0(kR_\mathrm{i}) \\ J_n'(kR_\mathrm{i}) & 0 & -J_0'(kR_\mathrm{i}) & -Y_0'(kR_\mathrm{i}) \\ 0 & H_n(kR) & -J_0(kR) & -Y_0(kR) \\ 0 & H_n'(kR) & -J_0'(kR) & -Y_0'(kR) \end{pmatrix} \begin{pmatrix} A_n \\ B_n \\ C_n \\ D_n \end{pmatrix} = \frac{\mathrm{i}gA}{\omega}\epsilon_n\mathrm{i}^n \begin{pmatrix} 0 \\ 0 \\ J_n(kR) \\ J_n'(kR) \end{pmatrix}, \tag{9}$$

for the four unknown coefficients.

Wave elevation and the far-field scattering amplitude.–The wave elevation can be expressed as

$$\eta(r,\theta) = \frac{\mathrm{i}\omega}{g}\phi|_{z=0}. \tag{10}$$

The far–field scattering amplitude A_S that is independent of r and z is expressed as

$$A_S(\theta) = \frac{\mathrm{i}\omega}{g\pi}\sum_{m=0}^{\infty}(-\mathrm{i})^m A_m\cos(m\theta). \tag{11}$$

Resonance within the annular metamaterial ring.–Analogous to the gap resonance by two side-by-side barges [3], we impose the homogeneous Dirichlet-type condition at open ends of the channel ends giving rise to

$$\begin{cases} C_m J_0(kR_\mathrm{i}) + D_m Y_0(kR_\mathrm{i}) = 0, \\ C_m J_0(kR) + D_m Y_0(kR) = 0. \end{cases} \tag{12}$$

The condition that the above equation system has nontrivial solutions requires

$$J_0(k_j R_\mathrm{i})Y_0(k_j R) - J_0(k_j R)Y_0(k_j R_\mathrm{i}) = 0, \tag{13}$$

where $k_j \in \mathbb{R}^+$ for $j = 1, 2, 3, \cdots$ denotes the jth root, which is associated to the jth resonant frequency. If we substitute the large-argument asymptotic forms of Bessel functions and Neumann functions, we will get $k_j(R - R_\mathrm{i}) \approx j\pi$, which is in line with the Fabry-Pérot resonance condition [4]. For $R_\mathrm{i}/R = 0.5$, the first three resonance frequencies correspond to $kR = 6.246, 12.547, 18.836$.

Broadband near non-back-scattering.–We demonstrate that there can be hardly any back scattering for a wide range of wave frequencies (see Fig. 1). The near non-back-scattering generally happens around the predicted resonant frequencies. There are a series of spikes observed on the curves of $|A_S|/A - kR$ at the non-resonant wave conditions around $kR = 4.0$, 9.0, and 16.0. The forward-scattering coefficient $|A_S(0)|/A$ presents an overall step-shaped growth with the increase of kR. The three resonant frequencies in the computed range of wave conditions

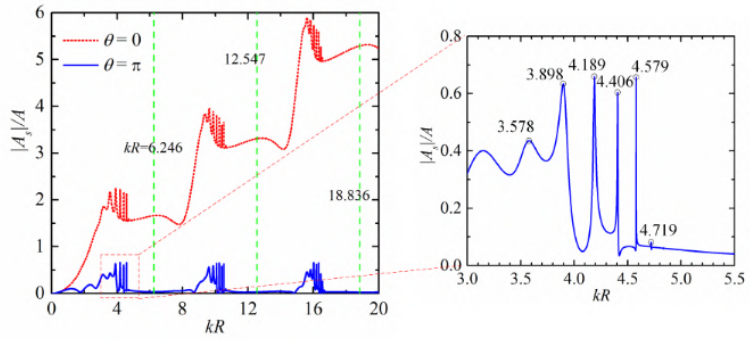

Figure 1: Frequency response of the far-field scattering coefficient in terms of $|A_S|/A$ at $\theta = 0$ and π, $R/h = 1.0$, $R_i/R = 0.5$. The green dash lines represent the positions of the resonant frequencies.

and four other wave frequencies associated to the peaks of the curve of $|A_S(\pi)|/A - kR$ around $kR = 4.0$ are selected to be examined in details that follow.

The near-field wave fields in terms of the wave amplitude and the instantaneous wave response at $t = 0$ for the three resonant frequencies and the four none-resonant frequencies are plotted in Figs. 2 and 3, respectively. An excellent agreement between the numerical and analytical results are obtained (Figs. 2a vs. 2b), giving confidence in the present analytical model for solving water scattering problem by an annular metamaterial cylinder.

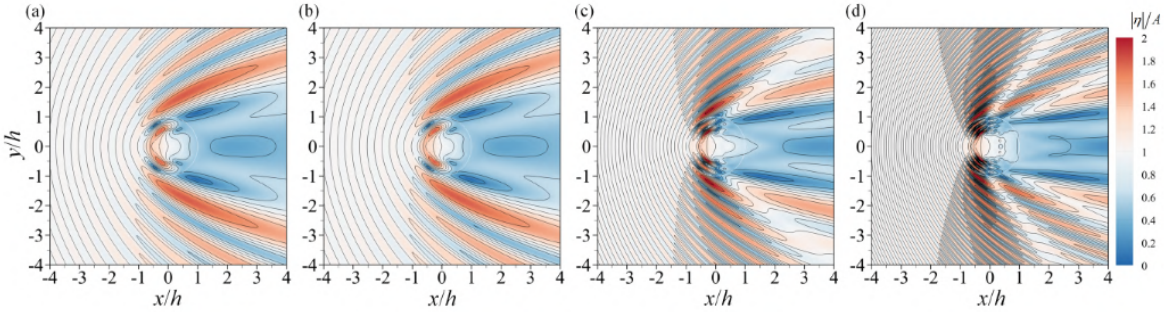

Figure 2: The maximum free surface amplitude, $R/h = 1.0$, $R_i/R = 0.5$: (a) numerical results [2]; (b)-(d) analytical results. (a)-(b) $kR = 6.246$; (c) $kR = 12.547$; (d) $kR = 18.836$. For the numerical results, the annular metamaterial cylinder is composed of 128 infinitely-thin vertical plates aligned with the radial direction and uniformly distributed all over the angular direction.

For the resonant wave frequencies, the waves are attenuated after passing through the annular metamaterial cylinder because of the fluid-structure interaction. The larger the incident wavelength, the wider the 'open angle' of the attenuated domain at the lee side of the annular metamaterial cylinder. The diffracted waves are generated at the front-side half-ring of the annular metamaterial cylinder and, taking that as a centre, propagate outwards in all directions. The diffracted waves are perfectly transmitted through each small channel with no phase delay. For the jth resonant frequency, which satisfies $k_j(R - R_i) \approx j\pi$, i.e., the length of each channel is $j/2$ times as large as the wavelength, j regions of large amplitude of the diffracted waves are generated and developed at the channels over $\theta \in (0.5\pi, \pi)$, and ultimately travel outwards in the open sea with different propagating directions. The waves are found to travel in curved paths in the metamaterial annular domain. When the waves cross the boundary between the metamaterial region and the exterior open sea, there is a sudden change in propagating direction, resulting in 'wave refraction'. For the non-resonant wave frequencies, there is a phase delay when diffracted waves are transmitted through each small channel, showing an 'impedance effect'. A 'sloshing' type motion of the diffracted waves along the x-axis is observed at the annular domain. Consequently, the diffracted waves are generated all over the annular metamaterial cylinder and, taking the out edge as a series of sources, propagate outwards.

Non-scattering at the center point.–We observe that the amplitude of the wave response at $r = 0$ is 1.0 regardless of the wave frequencies, e.g., see Fig. 2-3. This can be theoretically explained and approved with our model. Since $J_0(0) = 1.0$ and $J_m(0) = 0$ for $m > 0$, the wave response at $r = 0$ reads $\eta(0, \theta) = \mathrm{i}\omega B_0/g$. In the present model, we have $B_0 = -\mathrm{i}gA/\omega$, which gives $\eta(0, \theta) = A$. This means the wave motion at the center of the annular metamaterial cylinder is identical to the incident waves in terms of both amplitude and phase, i.e.,

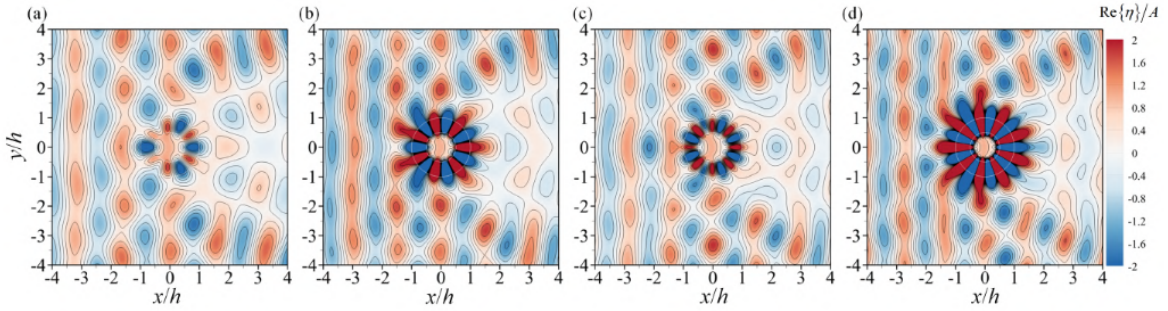

Figure 3: The instantaneous free surface at $t = 0$, $R/h = 1.0$, $R_i/R = 0.5$: (a) $kR = 3.898$; (b) $kR = 4.189$; (c) $kR = 4.406$; (d) $kR = 4.579$.

non-scattering at the center point.

Wave near-trapping.–By allowing k to become complex we can consider solutions which represent localised wave oscillations that exist in the absence of incident wave forcing. Such modes are defined by solutions to

$$f(n,k) = \det \mathbf{A}(n,k) = 0, \tag{14}$$

where $\mathbf{A}(n,k)$ denotes the coefficient matrix in Eq. (9). Figure 4 shows the roots of $f(n,k) = 0$ in the complex kR plane. The roots for $n = 5 \sim 10$ close to the real axis around $kR = 4.0$ are $3.557 - 0.108$i, $3.909 - 0.038$i, $4.188 - 0.010$i, $4.406 - 0.002$i, $4.579 - 2.7 \times 10^{-4}$i, and $4.720 - 3.0 \times 10^{-5}$i, respectively. It is clear that the first cluster of the spikes of the response as shown in Fig. 1 can be associated with these roots, i.e., the spikes at frequencies corresponding to near-trapping are related to the near-vanishing of the determinant.

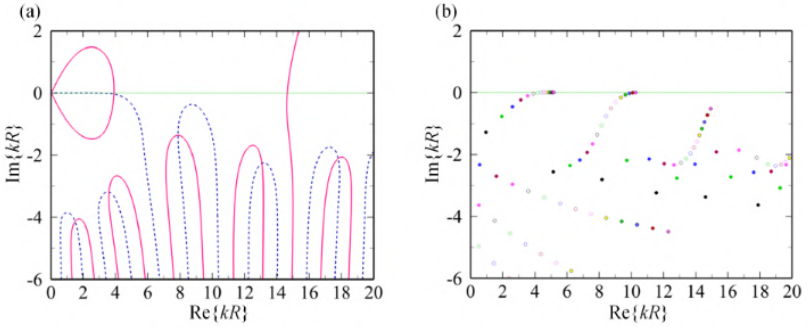

Figure 4: Wave near-trapping for $R/h = 1.0$, $R_i/R = 0.5$: (a) Location of the roots of $f(n,k) = 0$ in the complex kR plane for $n = 6$. The blue dashed lines identify the contours $\mathrm{Re}\{f(n,k)\} = 0$, whereas the pink solid lines correspond to the contours $\mathrm{Im}\{f(n,k)\} = 0$; (b) Location of zeros of determinant as n varies from 1 to 15.

The research was supported by Open Research Fund Program of State Key Laboratory of Hydroscience and Engineering (Tsinghua University) [grant number sklhse-2021-E-02]. R.P. acknowledges support from the EPSRC [grant number EP/V04740X/1]. D.G. gratefully acknowledges the EPSRC for supporting part of this work through the Supergen ORE Hub, EP/S000747/1.

References

[1] A. U. Jan and R Porter. Transmission and absorption in a waveguide with a metamaterial cavity. *The Journal of the Acoustical Society of America*, 144(6):3172–3180, 2018.

[2] H. Liang, S. Zheng, Y. Shao, K. H. Chua, Y. S. Choo, and D. Greaves. Water wave scattering by impermeable and perforated plates. *Phys. Fluids*, 33(7):077111, 2021.

[3] B. Molin. On the piston and sloshing modes in moonpools. *J. Fluid Mech.*, 430:27–50, 2001.

[4] M. M. Sadeghi, Sucheng Li, Lin Xu, Bo Hou, and Huanyang Chen. Transformation optics with Fabry-Pérot resonances. *Sci. Rep.*, 5:8680, 2015.

[5] S. Zheng, R. Porter, and D. Greaves. Wave scattering by an array of metamaterial cylinders. *J. Fluid Mech.*, 903:A50, 2020.

Experimental study on wave breaking and evolution of wave groups with high steepness

K. Zheng, B.B. Zhao*, W.Y. Duan

College of Shipbuilding Engineering, Harbin Engineering University, Harbin, China
* zhaobinbin@hrbeu.edu.cn

HIGHLIGHTS:

- ●. Laboratory experiments are conducted in deep-water wave tank to study characteristics of breaking waves arising from the evolved wave train.
- ●. The peaks of the evolved wave envelop have different performance between the mild breaking and severe breaking wave conditions with respect to the elevation and the numbers.

1 INTRODUCTION

The evolution of wave groups is often investigated to study the nonlinear effect of deep-water waves. Su [1] performs typical experiments on the wave train evolution with limited number of waves per packet. The regular wave train evolves into a number of envelope solitons. Despite a varying degree of wave breaking are observed in the evolved wave train, they only summarize some qualitative phenomenon on the breaking waves. The similar work following Su [1], concentrates on the evolution of non-breaking wave train with moderate steepness [2]. The experimental investigation on the breaking waves arisen from the evolution of strongly nonlinear wave trains is not sufficient in Su [1] and rarely to be reported after his work. The main motivation of our research is to study the wave breaking characteristic in regular wave trains by the physical experiments.

The details on experimental set-ups are introduced in Section 2. The measurements are presented in Section 3. In Section 4, some calculations are presented based on the High Level Irrotational Green-Naghdi (HLIGN) equations implemented with wave breaking model and compared with the laboratory measurement. Summaries and conclusions of this study are provided in Section 5.

2 EXPERIMENTAL FACILITY AND SET-UP

The experiments are conducted in the Fluid Mechanics laboratory of Harbin Engineering University. A sketch of the wave flume is shown in Fig. 1. The wave flume is 25.0m long, 2.0m wide and the water depth is fixed at 1.0m.

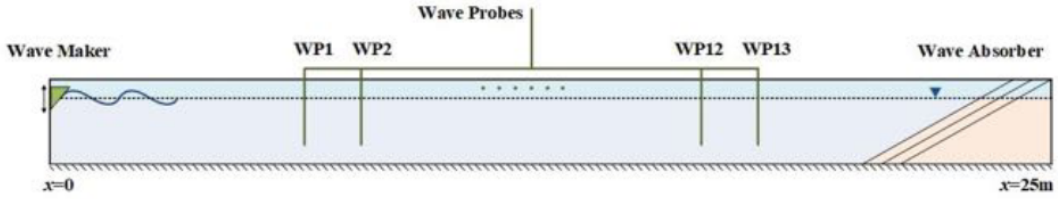

Fig. 1 Sketch of the physical wave tank.

Two experimental wave conditions are considered here, and these are list in Tab.1. The initial wave steepness is the ratio of initial wave height H and the wave length λ. The linear dispersion relation is used to calculate wave length from the wave period T. A settling time of approximately 10 minutes between two successive measurements is sufficient for the water in the tank to become calm.

Tab. 1 Physical test cases

Case	T (s)	H (m)	H/λ	Breaking condition
SR1012	1.0	0.12	0.08	Mild breaking
SR1016		0.16	0.10	Severe breaking

Plunger type wave generator move in the vertical direction to generate regular waves at one end of the tank. The total operating time of the wave maker is T_{stop}=10.0s for each case. The ramping time, which is the time that the wave maker oscillates from still to the maximum position, is T_{ramp}=3.0s. On the other end of the tank, there is a multi-layer sponger-type wave absorber. This absorber is found effective in damping the incoming waves. Thirteen capacitance type wave probes are placed in a line along the wave tank. All probes record the time history of surface elevation simultaneously. The sampling frequency is 50Hz. The location of each wave probe from the wave maker is list in Tab. 2.

Tab. 2 Location of wave probes, measured from the wave-maker end of the tank

No.	1	2	3	4	5	6	7	8	9	10	11	12	13
x (m)	4.5	5.5	7.0	8.5	10.0	11.5	13.0	14.5	16.0	17.5	18.6	19.0	20.5

As shown in Tab.1, wave groups with different wave steepness are considered. The wave breaking observed in the wave tank are remarked as 'Mild breaking' and 'Severe breaking' although this is a qualitative and relative indication of the wave breaking conditions. As an example, two moments of the breaking surface elevation for cases SR1012 and SR1016 corresponding to the `Mild breaking' and `Severe breaking', respectively, are given in the following Fig. 2.

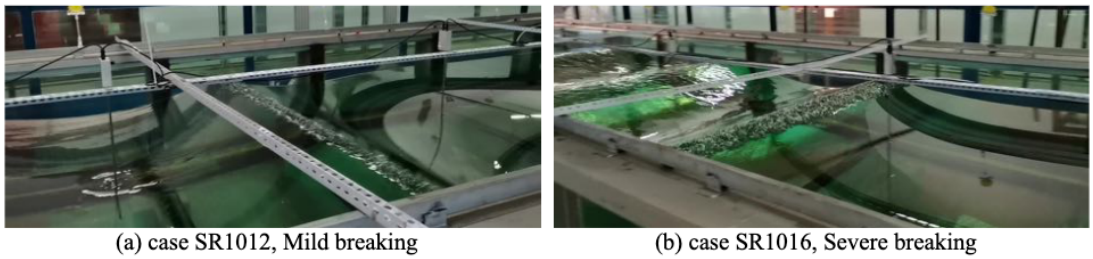

(a) case SR1012, Mild breaking (b) case SR1016, Severe breaking

Fig. 2 Photos of breaking moments of (a) mild breaking and (b) severe breaking.

3 EXPERIMENTAL MEASUREMENTS

In this section, time series of surface elevation recorded by the 13 wave gauges are presented in the following figures for cases SR1012 and SR1016.

3.1 Case SR1012

The experimental measurements of the mild breaking case, SR1012, is presented in Fig. 3. The black lines show the wave gauges' data of surface elevation, and the red lines indicate the upper envelop. The upper envelop is obtained by a data analyzing software based on the percentile filter algorithm.

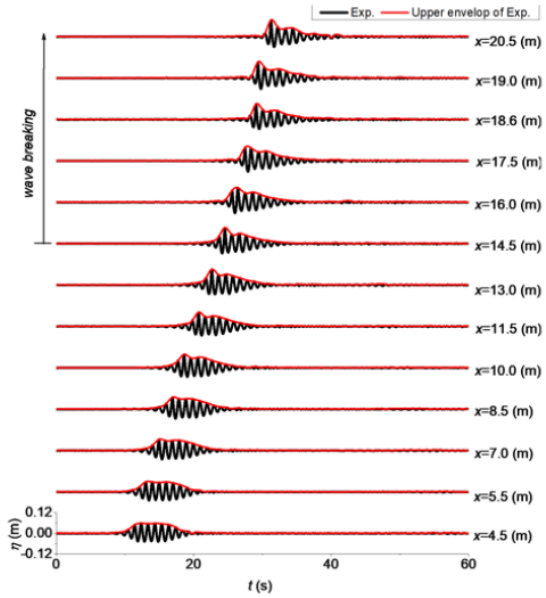

Fig. 3 Evolution of wave surface elevation measured by the wave gauges in the wave flume for case SR1012

As indicated in Fig. 3, wave breaking occurs at $x \geq 14.5$m. The uniform wave train gradually evolves and becomes non-uniform from $x = 4.5$m to $x = 20.5$m. The envelop peak at the leading side, which is in the left side of the wave train seen in Fig.3, is getting higher during the evolution.

3.2 Case SR1016

The experimental measurements of the severe breaking case, SR1016, is presented in Fig. 4.

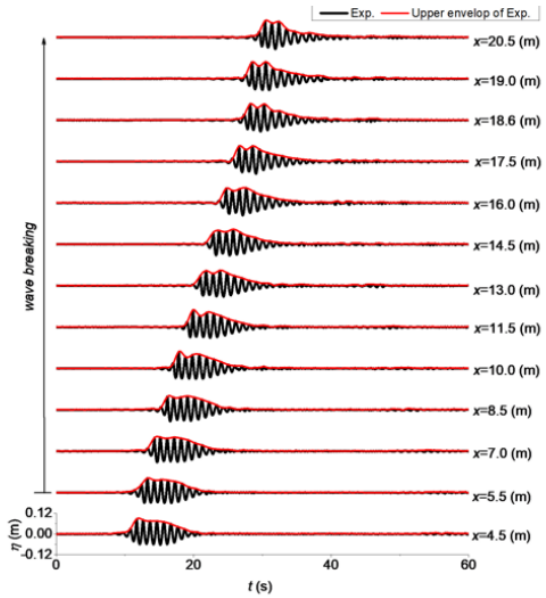

Fig. 4 Evolution of wave surface elevation measured by the wave gauges in the wave flume for case SR1016

Different with that observed in Fig. 3, wave breaking occurs at $x \geq 5.5$m for case SR1016. It means that the wave breaking occurs earlier as the increasing of initial wave steepness. The performance on the envelop is also different between these two wave trains seen in Figs. 3 and 4 at the same location. For the SR1016, two envelop peaks with similar elevation are observed. More

quantitative results will be presented on the workshop to show the relation between the profile of wave train and the wave breaking.

4 NUMERICAL SIMULATION WITH HLIGN EQUATIONS

The numerical simulations are also performed by use of HLIGN equations with the eddy viscosity wave breaking model proposed by Tian [3] for the same cases as the laboratory experiments. The comparison between the converged HLIGN results (red line) and the experimental data (black dot) for three wave probes, $x=4.5$m, $x=11.5$m, $x=18.6$m, is presented in the following Fig. 5 for severe breaking case SR1016.

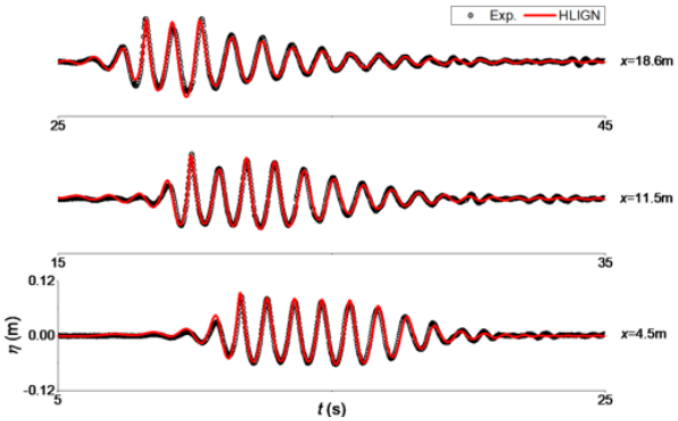

Fig. 5 Comparison of time series of wave evolution in the tank, measured by the wave gauges, in laboratory (dot), and calculated by HLIGN model (line), for case SR1016, Severe breaking.

Following some suggestions of Tian [3], excellent agreement is obtained in Fig. 5 between the experimental measurements and the results of HLIGN equations with wave breaking model.

5 CONCLUSIONS

The evolution of deep-water gravity wave groups with high steepness is studied in this paper. Laboratory experiments on the modulation of strongly nonlinear wave trains are conducted in deep water to investigate the wave breaking effect. The envelop profile of surface elevation time series depends on the evolution of the wave train with different initial wave steepness. One distinct envelop peak is observed at the leading side of the evolved wave train for the mild breaking case (SR1012). However, two envelop peaks with similar elevation are observed for the severe breaking case (SR1016) as the evolution of wave train. Good agreement is observed between the laboratory measurements and the calculations given by HLIGN equations with wave breaking model. More quantitative results and discussions will be presented on the workshop.

ACKNOWLEDGEMENTS

The second and third authors' (B.B. Zhao and W.Y. Duan) work is supported by the National Natural Science Foundation of China (Nos. 11772099), the Heilongjiang Touyan Innovation Team Program.

REFERENCES

[1] Su, M.Y., 1982. *Evolution of groups of gravity waves with moderate to high steepness*. Physics of Fluids 25, 2167-2174.

[2] Zheng, K., Zhao, B.B., Duan, W.Y., Ertekin, R.C., Chen, X.B., 2016. *Simulation of evolution of gravity wave groups with moderate steepness*. Ocean Modelling 98, 1-11.

[3] Tian, Z.G., Perlin, M., Choi, W., 2012. *An eddy viscosity model for two-dimensional breaking waves and its validation with laboratory experiments*. Physics of Fluids 24, 036601.

Study on Numerical PMM Tests in Incident Waves

Zhang Zhu, Byung-Soo Kim, Shuguang Wang, *Yonghwan Kim

Department of Naval Architecture and Ocean Engineering, Seoul National University, Seoul, Korea
*yhwankim@snu.ac.kr

1 INTRODUCTION

Recently, extensive researches are being carried out to understand the ship manoeuvring performance in waves. Since the coupled seakeeping-manoeuvring effect is getting more important, the conventional manoeuvring simulation methods should be enhanced or a new theory must be developed. One of the typical methods is the two-time-scale model, and its works enhanced by considering the steady-flow induced coupling effect [1] and the bilinear model for wave drift force computation [2] have emphasized the necessity to investigate the wave effect on ship manoeuvring coefficients.

The traditional Planar Motion Mechanism (PMM) test originally designed to generate a group of body manoeuvring coefficients (also named manoeuvring derivatives or hydrodynamic coefficients) is based on the experiment in calm sea, therefore the PMM test in incident waves must be considered to this end. Analysing a static motion in waves is relatively straightforward, whereas the dynamic PMM tests that are proposed under the quasi-steady assumption still have some unknowns when the incident waves are presented.

This study mainly discusses a comparison between the static drift test and the dynamic sway test. These two tests have very different motion patterns: one has static motion and another one has dynamic harmonic motion. However, they can generate the same manoeuvring coefficients with respect to sway velocity. Comparing with the static drift test could provide an indirect understanding of the dynamic PMM test.

2 TEST OVERVIEW

2.1 Numerical Model

To carry out the PMM test under various wave conditions, a numerical circular tank is chosen to overcome the physical limitations of traditional towing or manoeuvring tanks. The numerical tank is built by using the PMM module of the *snuMHLFoam* package that the Marine Hydrodynamic Lab of Seoul National University develops based on the OpenFOAM+ v1912 platform. A moving circular domain is considered for the numerical computation and a typical wave pattern is shown in Fig. 1. The current circular computational domain has a diameter of 5λ where λ is the wavelength. Correspondingly, a circular wave forcing region of forcing length λ is implemented at the circular boundary using the exponential forcing function. A quaternion-based body motion algorithm is used to handle the ship motion that is combined with prescribed PMM movement and wave-induced motions.

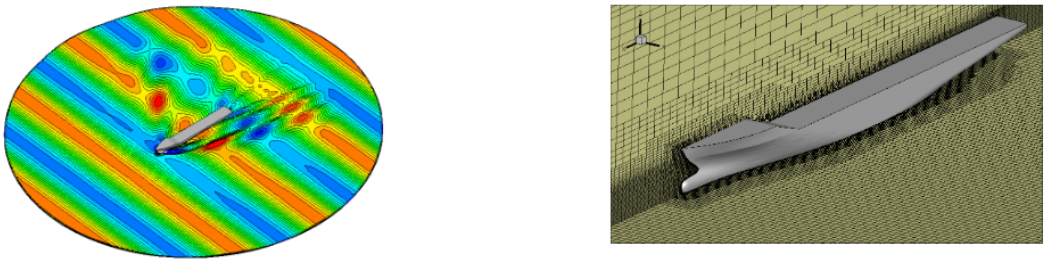

(a) Wave pattern inside the circular computational domain (b) Mesh structure near hull

Fig. 1 The numerical model

The time-step Δt is selected to be $T_e/\Delta t = 500$ where T_e is the wave encounter period. The mesh resolution around the free-surface is specified as $H/\Delta z = 16$, $\lambda/\Delta x = 120$, where Δx and Δz indicate the horizontal and vertical size of the mesh covering the propagating waves, and H is the wave height. Boundary layer mesh is applied to ensure a $y+$ field that is generally less than 30 near the bow region. The validation works of the

present numerical solver are not shown here, but it has generally achieved satisfactory results on both the KCS PMM test in calm-sea and the KCS seakeeping tests.

2.2 Test Condition

The test model is a 3.07-meter KCS bare hull with the Froude number of 0.16, following the model condition used by the direct manoeuvring test in wave [3]. A static drift test with drift condition $\beta_0 = 18°$ ($v' = v/U = 0.309$) and a pure sway test with the sway condition, $v_0' = v_0/U = 0.309$ and $\omega_0' = 1.90$, are considered in this work. For the static drift test, the drift angle β_0 is defined as atan(-v/u), where u and v represent the surge velocity and sway velocity of ship static motion. For the pure sway test that ship has a harmonic sway velocity $v = v_0 \cdot \cos(\omega_0 \cdot t)$, v_0 represents the maximum sway velocity, and ω_0 is sway frequency. U is the ship total velocity determined by Froude number. The ship has a fixed roll condition, and its heave and pitch motion are released during the PMM motion. The current work chooses one wave condition that the wavelength λ/L is 1.0 and the wave slope H/λ is 1/60, and several wave directions are considered.

2.3 Wave Added Force/Moment

Table 1. The added force/moment components of interest

	Static drift test	Pure sway test
Added sway force	$Y_{AW}^{(0)} = Y_{\text{wave}}^{(0)} - Y_{\text{calm}}^{(0)}$	$Y_{AW}^{(1,\cos)} = Y_{\text{wave}}^{(1,\cos)} - Y_{\text{calm}}^{(1,\cos)}$
Added yaw moment	$N_{AW}^{(0)} = N_{\text{wave}}^{(0)} - N_{\text{calm}}^{(0)}$	$N_{AW}^{(1,\cos)} = N_{\text{wave}}^{(1,\cos)} - N_{\text{calm}}^{(1,\cos)}$

Table 1 lists the added force/moment components that are mainly considered in this work, some are the mean components and some are the harmonic components depending on the test type and target manoeuvring coefficients. For the components listed in Table 1, the term "*AW*" indicates the values increased in waves, the terms "wave" and "calm" indicate the results obtained under wave condition and calm-sea condition respectively. The superscript $^{(0)}$ and $^{(1,\cos)}$ represent the mean component and the 1st-order cosine component of force and moment obtained by discrete Fourier transform. The pure sway test generates the periodical and nonlinear force/moment signals so the Fourier transform is performed based on the prescribed sway frequency which is much lower than the wave encounter frequency. Fig. 2 compares the original signals and the reconstructed signals of the sway force obtained from the pure sway test.

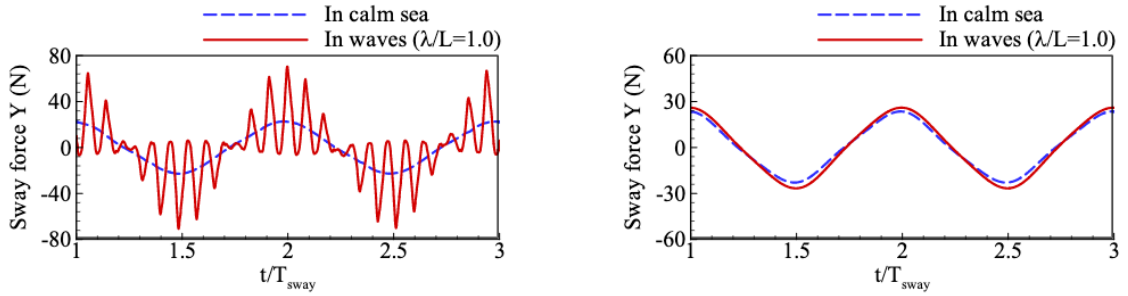

(1) The original signals from numerical computation (2) The reconstructed signals by Fourier transform

Fig. 2 The sway force signals of the pure sway test. ($\omega_0' = 1.90$, $v_0' = 0.309$)

3 RESULT AND DISCUSSION

Ship dynamic PMM test is proposed under a quasi-steady assumption that some considerations such as memory effect [4][5] would become more concerned when incident waves are involved. Meanwhile, the accuracy of the force/moment components that are directly obtained by the Fourier transform is also questionable. Therefore, a comparison is carried out using the pure sway test and static drift test since both two tests can provide the manoeuvring coefficients Y_v, Y_{vvv}, N_v, N_{vvv} that represent the derivatives of sway force and yaw moment with respect to sway velocity; a comparison on the development of flow fields, such as wave pattern, could help to understand those concerns for the dynamic test in waves.

Fig. 3(a) compares the sway force signal obtained under calm-sea condition. The blue dashed-dotted line is the steady result of the static drift test. The red line represents the periodical result of the pure sway test, and the black dashed line is the sway velocity of the pure sway test. The sway force signal of the pure sway test have nonlinear components, but its out-of-phase component is almost equal to the steady value of the static drift test, as observed in Fig. 3(a). It means that two tests could generate very similar results as well as the corresponding manoeuvring coefficients, which could also show the reliability of the present numerical model. Similar agreements are also observed in Fig. 3(b) which compares the results obtained under waves. Although the signal of sway test shows a high-frequency oscillation of varying amplitude which is caused by the varying ship sway velocity in waves, the results of the two tests have almost matched signals at the phase that target sway velocity is reached.

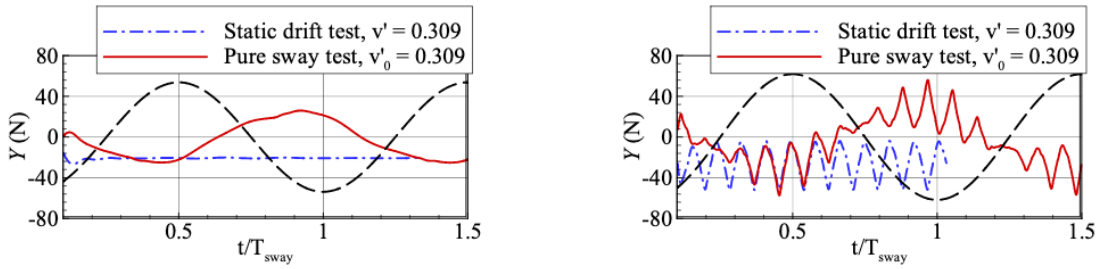

(a) in calm-sea condition (b) in wave condition, λ/L=1.0

Fig. 3 Comparison on the sway force *Y* between the two tests
(black dashed line: the sway velocity history of pure sway test)

The agreement of the two tests can also be observed from the history of wave patterns. For Fig. 5, t is the time instant, T_e is the wave encounter period and T_0 is the prescribed sway period. Static drift test has a constant sway velocity v'. For the wave patterns of the pure sway test shown by Fig. 5, subfigure (b) is the time instant ($2.5T_0$) that the swaying ship has reached the target sway velocity v_0', and very similar wave patterns are observed comparing with that of static drift test. Subfigure 5(f) indicates a phase that the ship also reached the target sway speed but it is under a negative swaying condition, and the sequential wave development is almost identical to that of the positive swaying stage.

< Static drift test, β_0 = 18°, v' = 0.309 >

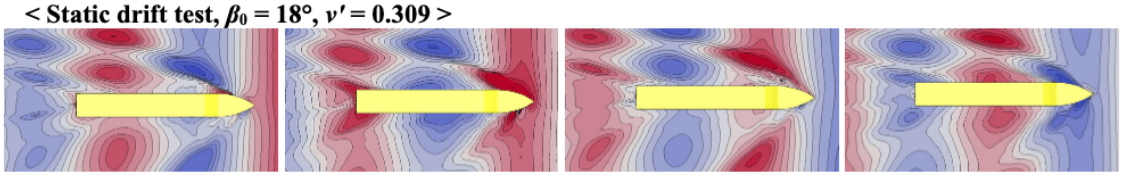

(a) $t = 12T_e - 0.25T_e$ (b) $\boldsymbol{t = 12T_e}$ (c) $t = 12T_e + 0.25T_e$ (d) $t = 12T_e + 0.5T_e$

< Pure sway test, ω_0' = 1.90, v_0' = 0.309 >

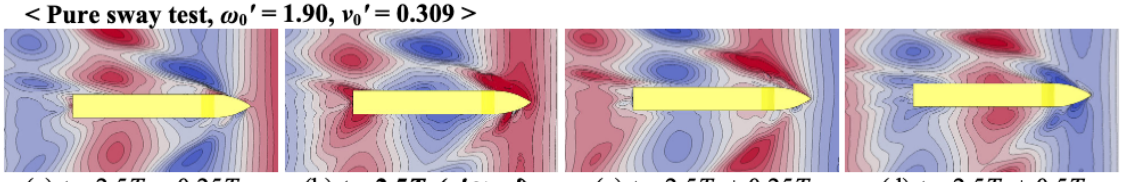

(a) $t = 2.5T_0 - 0.25T_e$ (b) $\boldsymbol{t = 2.5T_0\ (v' \approx v_0')}$ (c) $t = 2.5T_0 + 0.25T_e$ (d) $t = 2.5T_0 + 0.5T_e$

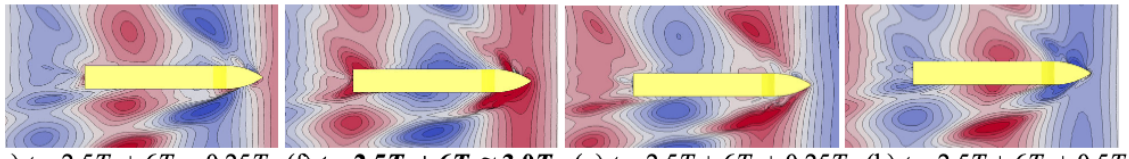

(e) $t = 2.5T_0 + 6T_e - 0.25T_e$ (f) $\boldsymbol{t = 2.5T_0 + 6T_e \approx 3.0T_0}$ (g) $t = 2.5T_0 + 6T_e + 0.25T_e$ (h) $t = 2.5T_0 + 6T_e + 0.5T_e$

Fig. 4 Comparison on the sequential wave patterns between the static drift test and the pure sway test

Fig. 5 compares the results of two tests under various wave directions. The relative direction between the static drift motion and incident wave is shown in Fig. 5, $\chi = 180°$ indicates the head sea condition and $\chi = 90°$ indicates the beam sea condition. The added sway force has been normalized by ($\rho g A^2 B^2/L$) and the added yaw moment has been normalized by ($\rho g A^2 B^2$). The pure sway test has provided agreeable results compared with that of static drift test at various wave heading directions, indicating a satisfactory quasi-steadiness for the current dynamic sway test. Meanwhile, Fig. 5 shows a tendency that bow quartering waves generally provide strong added force and moment, which means the increased derivative Y_v and N_v of sway force and yaw moment with respect to sway velocity.

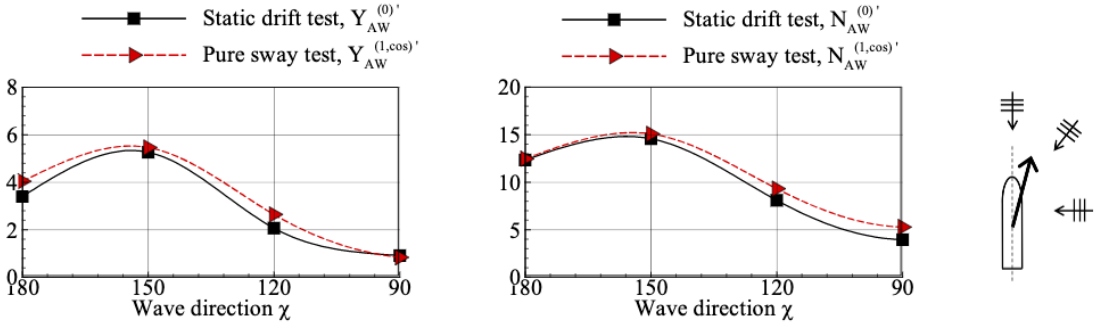

(1) Added sway force (2) Added yaw moment

Fig. 5 Comparison between the static drift test ($v' = 0.309$) and the pure sway test ($\omega_0' = 1.90$, $v_0' = 0.309$)

4 CONCLUSIONS

This study has applied the numerical tank to carry out the pure sway test and the static drift test under incident waves. Through the comparison between these two tests, the following conclusions can be made:

- By comparing with the static drift test, the dynamic sway test has generated very similar force component and sequential wave development at its motion stage of interest, which indicates an acceptable quasi-steadiness for the current dynamic PMM test in waves. Therefore, this numerical model is possible to be extended to more complicated PMM motions, such as the pure yaw test and the combined drift-yaw test, to observe other manoeuvring coefficients with respect to wave conditions.
- The application of numerical tank to PMM tests has shown more advantages than the conventional indoor tanks, for example, the unlimited space for captive motion in waves and the more detailed observation of flow fields.

ACKNOWLEDGEMENT

This study was supported by the Lloyd's Register Foundation (LRF)-Funded Research Center at Seoul National University. Their support is greatly appreciated.

REFERENCES

[1] Lee, J.H., Kim, Y., 2020. Study on Steady Flow Approximation in Turning Simulation of Ship in Waves. *Ocean Eng.*, Vol. 195, 106645.

[2] Lee, J.H., Nam, B.W., Lee, J-H., Kim Y., 2021. Development of Enhanced Two-Time-Scale Model for Simulation of Ship Maneuvering in Ocean Waves. *J. of Marine Sci. and Eng.*, 9, 700.

[3] Yasukawa H., Hasnan M.A.A., Matsuda A., 2021. Validation of 6-DOF Motion Simulations for Ship Turning in Regular Waves. *J. of Marine Sci. and Tech.*, Vol. 26, 1096-1111.

[4] Newman, J.N., 1966. Some Hydrodynamic Aspects of Ship Maneuverability. *Proceeding of 6th Symposium on Naval Hydrodynamics*, Washington DC, USA.

[5] ITTC, 2021. Captive Model Test. *ITTC Recommended Procedures and Guidelines*, 7.5-02-06-02.